Ying-Pin Chen
Sajid Bashir
Jingbo Louise Liu *Editors*

Nanostructured Materials for Next-Generation Energy Storage and Conversion

Hydrogen Production, Storage, and Utilization

MATERIALS.SPRINGER.COM

Springer

Nanostructured Materials for Next-Generation Energy Storage and Conversion

Ying-Pin Chen • Sajid Bashir
Jingbo Louise Liu
Editors

Nanostructured Materials for Next-Generation Energy Storage and Conversion

Hydrogen Production, Storage, and Utilization

With 161 Figures and 19 Tables

Springer

Editors
Ying-Pin Chen
Department of Chemistry
Texas A&M University
College Station, Texas, USA

Sajid Bashir
Department of Chemistry
Texas A&M University–Kingsville
Kingsville, Texas, USA

Jingbo Louise Liu
Department of Chemistry
Texas A&M University–Kingsville
Kingsville, Texas, USA

ISBN 978-3-662-53512-7 ISBN 978-3-662-53514-1 (eBook)
DOI 10.1007/978-3-662-53514-1

Library of Congress Control Number: 2017936057

Printed on acid-free paper

This Springer imprint is published by Springer Nature
The registered company is Springer-Verlag GmbH Germany
The registered company address is: Heidelberger Platz 3, 14197 Berlin, Germany

Preface

The purpose of this monograph is to answer questions related to the substitution of fossil fuels in vehicles, home, or industry using hydrogen for either direct use or as an energy carrier in the generation of electricity. It is projected that mobility via electrical means will increase during the next 50 years and will become a significant component of the energy portfolio. A factor in achieving this is the utilization of hydrogen as stored energy, which is appealing because it further addresses greenhouse gas emissions, leads to lower environmental pollution, and will further reduce the dependency on oil from foreign governments.

Although there are a number of reviews, special journal issues, and books on hydrogen, none deal with the important but neglected topics of hydrogen generation and storage, which are specifically addressed here. Topics discussed in this monograph include the advantages and disadvantages of hydrogen compared with other fuels; strategies related to the photocatalytic evolution of hydrogen, including activation of hydrogen using transition metal complexes; separation of hydrogen using polymeric materials; current and future technologies used towards hydrogen storage using a metal–organic framework, porous carbon networks, or organic polymer systems or metal hydrides; and techniques for characterization of hydrogen adsorption sites in various materials.

The technical means to generate and store hydrogen are currently feasible, although many hurdles remain in relation to the efficiency of hydrogen generation, its storage, and the cost effectiveness of its implementation for mobile and stationary power. These technical problems will be overcome, just as artificial light enabled societies to be productive during the sunset hours and the wheel, rail, and sea allowed increased mobility of people and goods; however, good commerce also dictates fiscal profit and here the technologies have to provide equivalent energy cheaper than coal or gasoline—a realization that cannot be overlooked or ignored, but is not the focus here.

In this book, each author puts forward his or her vision regarding hydrogen storage (adsorption and desorption), providing an overview of the technical merits of the approach and its benefits. We as editors have also included a summary in the form of ▶ Chap. 10, which reviews tangential ideas discussed by the authors throughout the book as well as providing a discussion of policy, infrastructure, cost analysis, and data regarding the practical feasibility of using hydrogen in a

test model vehicle. Any errors, omissions, or faults are ours and we welcome feedback and comment.

Any project, be it a white paper on legislature, doctoral thesis, book chapter, review article, or grant proposal, is an intense and almost always team effort; this monograph is no different, which we acknowledge here. We would like to thank both Antje Endemann, for day-to-day management, and Sharon George of Springer-Verlag GmbH (Berlin and Heidelberg, Germany) for taking an idea based on our work within the American Chemistry Society (ACS) divisions of Energy and Fuels (Dr. Liu) and Colloid and Surface Chemistry (Drs. Liu and Bashir) and turning it into this book. We also wish to acknowledge the support received from senior university administration at Texas A&M University–Kingsville.

Lastly, we pay our respects to Sir David MacKay (1967–2016), author of the book *Sustainable Energy – Without the Hot Air* (UIT Cambridge, 2008. ISBN 0-9544529-3-3), who died of cancer in 2016. His work led the way for a whole new generation of scientists and engineers to consider the environment and the impact our work will have on it when thinking about energy and how best to generate, store, and use it. Thank you, Sir MacKay—your legacy will endure.

To conclude, we provide a brief look ahead to why we believe hydrogen and fuel cells are the way forward, and briefly summarize its costs and our projections regarding what might transpire over the next 50 years.

The Carbon Economy: Current Dilemma

A central truth is that any combustion of carbon-containing materials will generate carbon dioxide (CO_2), a greenhouse gas, as shown in the Keeling and Whorf CO_2 plot from 1960 to 1980, and extended to 2010, clearly showing an upwards CO_2 trajectory as measured at Mauna Loa, Hawaii. While the reason for this rise in CO_2 may be disputed, it acknowledged a rise to 398 ppm (seasonal minima) or 404 ppm (weighted monthly average, February 2016 [1]) that cannot be ignored. The global land and ocean surface temperature (at 500 millibar height pressure) was 0.88 °C (August 2015), the highest for any August on records held since 1880. In 2015, six months held the highest temperature since records began, while Alaska, western Canada, central USA, and western/southeastern Asia were cooler than average, linking global record CO_2 levels with global record temperature variations [2], which suggests that CO_2 levels should be lowered to 300 ppmv as shown in buried polar ice [3]. It is not the toxicity of CO_2 that is problematic (since it is toxic at 5% [4]), but the resulting global warming and changes in weather patterns [5]. Bulk CO_2 is released through combustion and respiration, with coal-fired power plants releasing 1.5 million metric tons or 76% of total emissions associated with electricity generation [6] in addition to fine soot particles [7]. The fossil fuel supply-side economics are dominated by the USA, which utilizes more fossil fuel resources than any other country [8]; therefore, some countries are shifting to petroleum substitutes such as tar sand or heavy oil, which generate more CO_2 per mole due to their higher carbon content, thus releasing more CO_2 into the atmosphere. In 2014,

approximately 4 trillion kilowatt hours of electricity were generated in the USA, 67% of which was from fossil fuels (coal, natural gas, and petroleum)—only 7% was from renewable resources (biomass, geothermal, solar, and wind), 6% from hydropower, and 19% from nuclear power; by 2050, this mix should shift towards more renewable resources, which are projected to rise from 7% to 50% [9].

Is a Hydrogen Economy Feasible or Desirable? During the high oil price of 1970, Linden outlined the advantages of a hydrogen economy [10], which was briefly popular in the 1920s to 1930s via electrolysis of water using hydroelectricity; however, the Hindenburg blimp disaster in New Jersey, USA in 1937 [11] and rising costs of electrolysis moved the economy towards coal and petroleum (despite recent evidence that hydrogen was not the primary cause of the accident [12]), causing the use of fossil fuels to be dominant in transport and energy production today.

The use of hydrogen is attractive as it is the lightest stable element (one proton and one electron, but is stable as a diatomic molecule; 2.016 amu, density 0.0838 kg/m^3 at 760 mmHg and 298 K), combustion of which produces water. Unlike natural gas, hydrogen is not a primary source of energy but rather a carrier of energy (e.g., electricity) as it must be extracted from other sources such as water or hydrocarbons, requiring an input of energy. Since hydrogen is a diatomic molecule, both electrons can have the same spin state (ortho) or opposite spin states (para); at 300 K the majority of hydrogen is ortho (75%) and at cryogenic temperatures it is para. At $<$20 K, the temperature at which gaseous hydrogen becomes a liquid [13], pressurization to 195 pounds per square inch will increase the boiling temperature to 33 K; however, further compression does not raise the boiling temperature. Comparison of hydrogen (H_2) with methane (CH_4) and methanol (CH_3OH) reveal that hydrogen has the lowest density and energy density but the highest energy per unit mass (H_2: 0.0838 kg/m^3, CH_4: 0.71, CH_3OH: 799; H_2: 10.8 MJ/m^3, CH_4: 32.6, CH_3OH: 14,500; and H_2: 33.3 kWh/kg; CH_4: 12.8, CH_3OH: 5.0 at 760 mmHg and 298 K [14]). Hydrogen gas also exhibits an excellent higher heating value (water as a liquid) or lower heating value (water as steam), which represents the amount of energy capable of doing work (141.9 and 111.9 kJ/g for hydrogen, 55.5 and 50.0 kJ/g for CH_4, and 20.0 and 18.1 kJ/g for CH_3OH, respectively) and, as stated earlier, combustion of hydrogen produces no carbon, only water. Since hydrogen gas is an energy carrier, it needs to be generated from other carbon-based feed stocks, such as steam reformation of CH_4, a water gas shift reaction, gasification of coal, and electrolysis of water, all of which require energy and in the case of carbon feed stocks also generates CO_2. To make practical sense, the generated CO_2 would need to be sequestered or generated from biomass gasification-generating carbon monoxide and H_2 and be carbon neutral, since plants would use CO_2 during photosynthesis and release it during gasification. However, although feasible, these methods are more expensive than generation of electricity from coal or are comparable with the price of gasoline (below US$2/gallon). To meet the current demand of 4 trillion kilowatt hours of electricity would require a considerable increase in the utilization of biomass, more land for windmills, more dams for hydroelectric power, or 5000–10,000 1 GW nuclear fission power plants (ignoring the problem of disposal of nuclear by-products) [15].

The use of solar energy to power the electrolysis of water appears to be an attractive approach; however, solar energy is expensive and costs more than the US$0.02/kWh cost using coal. If costs are ignored, however, there is sufficient sunlight to provide the required energy needs by 2050 [16]. Solar power can be used to meet the energy shortfall, is the largest single potential source of energy, and is currently utilized by plants in photosynthesis, which can be used for biofuels. In addition, sunlight can be converted to electrical energy through photovoltaics or to heat for thermal storage. The current limitation in the use of switchgrass is economic, which may be offset using artificial photosynthetic systems. Water splitting [H_2O (l) $\rightarrow$ H_2 (g) + ½O_2 (g)] is endothermic [$\Delta G^\circ = 237.2$ kJ/mol, $\Delta E^\circ = -1.23$ V; $E_{practical} = 1.50$ V] and is dependent on pH, electrode potential, and cell design [17], and since water does not absorb visible light, either electrical potential or a chromophore or semiconductor are required to absorb sunlight and generate electron–hole pairs, or, alternatively, heat is needed to thermochemically split water at approximately 2500 K [18]. Lastly, biochemical means [6 H_2O + 6 CO_2 12 hν $\rightarrow$ 6HCOOH + 3O_2].

In answer to our question, hydrogen generation is technically feasible, it is desirable to reduce CO_2 and other pollutant emissions, and it is potentially practical in the form of fuel cells.

Why Hydrogen and Fuel Cells? Greenhouse gas emissions from vehicles were 1500 million metric tons CO_2 equivalent or 27% of the total greenhouse gas emissions in 2013[19]—even a modest decrease could yield substantial savings in terms of CO_2 emissions, as well as in CH_4, nitrous oxide, and hydrofluorocarbons, by using electrochemical conversion of hydrogen (and air) to electricity (and water) using different electrolytes such as polymer–electrolyte (or proton exchange) membrane fuel cells (PEMFCs) (operated at 60–80 °C) in contrast with solid oxide yttrium-stabilized zirconia fuel cells (SOFCs [20]) (which operate at 1000 °C), which are used for generation of stationary power. PEMFCs are attractive as portable forms of power [21] as they have near-zero emissions and a fuel cell has efficiencies in the order of $\geq$80% or 60% in practice, much greater than heat engines [22]. However, they cost around US$120/kW compared with US$20/kW for a heat engine [23]. This higher operating cost is due to use of nobel metals as the catalyst and fuel cell designs that are not as robust as heat engines and are susceptible to catalyst poisoning, gasket membrane oxidation, and cracking [24].

To reduce fossil fuel use in transport from 27% to even 20% would require increased incorporation of solar technologies in the generation of hydrogen, using a photocatalyst (▶ Chap. 1) or hydrogen activation (▶ Chap. 2), improvements in the storage of hydrogen (the focus of this book, ▶ Chaps. 3, ▶ 4, ▶ 5, ▶ 6, and ▶ 7), use of metal hydrides in generation of hydrogen (▶ Chap. 8), and a greater understanding of the chemistry and physics behind hydrogen adsorption in resins and polymers systems (▶ Chap. 9) and the economics of hydrogen generation, CO_2, and water splitting and the infrastructure of the hydrogen economy (▶ Chap. 10). Advances in photovoltaics, fuel cells, and batteries produced at costs comparable with current petroleum-based engines will make this a reality by 2050.

Acknowledgment

We wish to thank the Robert A. Welch Foundation and the College of Arts and Sciences and Office of the Provost at Texas A&M University–Kingsville for their assistance. In addition, we thank the program chairs of Energy and Fuels and Colloid and Surface Chemistry divisions of the American Chemical Society for the opportunity to run or moderate symposia at their technical sessions. Lastly, we thank the production team at Springer for their assistance in copy editing this and the other book chapters.

Author Contributions

Dr. Bashir wrote the first draft. Dr. Liu edited the first draft, assisted with the physiochemical data, and submitted the manuscript to the publishers.

Department of Chemistry
Texas A&M University–Kingsville
Kingsville, TX, USA

S. Bashir
J. Liu

References

1. NOAA, Trends in atmospheric carbon dioxide (2016), http://www.esrl.noaa.gov/gmd/ccgg/trends/. Retrieved 29 Mar 2016
2. NOAA, Global analysis - August 2015 (2015), http://www.ncdc.noaa.gov/sotc/global/201508. Retrieved 29 Mar 2016
3. J.R. Petit, J. Jouzel, D. Raynaud, N.I. Barkov, J.M. Barnola, I. Basile, et al., Vostok ice core data for 420,000 years. IGBP PAGES/World Data Center for Paleoclimatology Data Contribution Series, 76 (2001)
4. InspectAPedia. Toxicity of carbon dioxide gas exposure, CO_2 poisoning symptoms, carbon dioxide exposure limits http://inspectapedia.com/hazmat/Carbon_Dioxide_Hazards.php. Retrieved 29 Mar 2016
5. D.S. Ojima, W.J. Parton, D.S. Schimel, J.M. Scurlock, T.G. Kittel, Modeling the effects of climatic and CO_2 changes on grassland storage of soil C, in *Terrestrial Biospheric Carbon Fluxes Quantification of Sinks and Sources of CO_2* (Springer Netherlands, 1993), pp. 643–657
6. US Energy Information Administration (EIA), How much of the U.S. carbon dioxide emissions are associated with electricity generation? http://www.eia.gov/tools/faqs/faq.cfm?id=77&t=11. Retrieved 29 Mar 2016
7. G. Pershagen, Z. Hrubec, U. Lorich, P. Rönnqvist, Acute respiratory symptoms in patients with chronic obstructive pulmonary disease and in other subjects living near a coal-fired plant. Arch. Environ. Health. 39(1), 27–33 (1984)
8. IAE, Oil market report charts (2016), https://www.iea.org/oilmarketreport/omrpublic/charts/. Retrieved 29 Mar 2016

9. EIA, What is U.S. energy generation by energy source? (2015), https://www.eia.gov/tools/faqs/faq.cfm?id=427&t=3. Retrieved 29 Mar 2016
10. H.R. Linden, The evolution of an energy contrarian. Ann. Rev. Energy Environ. 21(1), 31–67 (1996)
11. F. Rigas, S. Sklavounos, Evaluation of hazards associated with hydrogen storage facilities. Int. J. Hydrog. Energy 30(13), 1501–1510 (2005)
12. L. Liao, I. Pasternak, A review of airship structural research and development. Prog. Aerosp. Sci. 45(4), 83–96 (2009)
13. J.W. Leachman, R.T. Jacobsen, S.G. Penoncello, E.W. Lemmon, Fundamental equations of state for parahydrogen, normal hydrogen, and orthohydrogen. J. Phys. Chem. Ref. Data 38(3), 721–748 (2009)
14. M. Momirlan, T.N. Veziroglu, The properties of hydrogen as fuel tomorrow in sustainable energy system for a cleaner planet. Int. J. Hydrog. Energy 30(7), 795–802 (2005)
15. N.S. Lewis, D.G. Nocera, Powering the planet: chemical challenges in solar energy utilization. Proc. Natl. Acad. Sci. U S A 103(43), 15729–15735 (2006)
16. V. Fthenakis, J.E. Mason, K. Zweibel, The technical, geographical, and economic feasibility for solar energy to supply the energy needs of the US. Energy Policy 37(2), 387–399 (2009)
17. K. Domen, J.N. Kondo, M. Hara, T. Takata, Photo-and mechano-catalytic overall water splitting reactions to form hydrogen and oxygen on heterogeneous catalysts. Bull. Chem. Soc. Jpn. 73(6), 1307–1331 (2000)
18. M.D. Archer, J.R. Bolton, Requirements for ideal performance of photochemical and photovoltaic solar energy converters. J. Phys. Chem. 94(21), 8028–8036 (1990)
19. EPA, Reducing emissions from transportation (2014), https://www3.epa.gov/climatechange/ghgemissions/sources/transportation.html. Retrieved 29 Mar 2016
20. B.D. James, D.A. DeSantis, J.M. Moton, C. Houchins, II.A.1: Hydrogen pathways analysis for solid oxide fuel cell (SOFC) and dark fermentation (2015), https://www.hydrogen.energy.gov/pdfs/progress15/ii_a_1_james_2015.pdf. Retrieved 29 Mar 2016
21. A.F. Ghenciu, Review of fuel processing catalysts for hydrogen production in PEM fuel cell systems. Curr. Opin. Solid State Mater. Sci. 6(5), 389–399 (2002)
22. S. Verhelst, R. Sierens, Hydrogen engine-specific properties. Int. J. Hydrog. Energy 26(9), 987–990 (2001)
23. J. Ogden, High hopes for hydrogen. Sci. Am. 295(3), 94–101 (2006)
24. M.L. Perry, T.F. Fuller, A historical perspective of fuel cell technology in the 20th century. J. Electrochem. Soc. 149(7), S59–S67 (2002)

Contents

List of Contributors

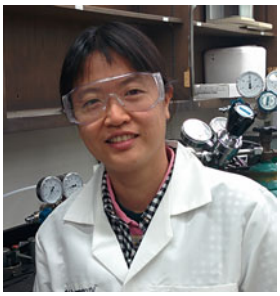

Ying-Pin Chen earned two degrees in Chemical Engineering and Materials Science from National Cheng Kung University, Taiwan. Continuing her interest in materials with electrical properties, she completed her M.S. in photonics and display technique at National Chiao Tung University, where she focused on advanced thin-film transistors (TFTs) and organic photovoltaics. She then joined AU Optronics, the largest and leading display manufacturer in Taiwan, as a senior integration engineer responsible for yield improvement and failure mode diagnosis on TFT panels as well as supervising operators' on-site work. Building on this sound knowledge and industrial experience, she began her Ph.D. studies at Texas A&M University in 2010, under the guidance of Dr. Hong-Cai Zhou. She has worked on X-ray structural determination and fundamental research into gas kinetic behaviors in metal–organic frameworks (MOFs). Being active in her chosen field (h-index = 20), she has participated in more than 30 MOF projects using her X-ray technology skills and co-authored three book chapters and 43 peer-reviewed journal articles. In the future, she aims to focus on materials science relating to crystallographic characterizations.

Sajid Bashir received his Ph.D. in Analytical Chemistry from the University of Warwick, England, in 2001 and has also been a postgraduate research associate at Cornell University conducting research in the field of plant genetics. He is an Associate Professor at Texas A&M University–Kingsville (TAMUK) and was a faculty member and student team fellow at the Lawrence Berkeley National Laboratory (2011–2013). Dr. Bashir has directed and participated in more than ten projects supported by the Welch Foundation, TAMUK, the Texas Workforce Commission, and the US National Institutes of Health. He has co-authored book chapters and peer-reviewed journal articles and delivered more than a dozen presentations at various scientific conferences. Dr. Bashir is also a

fellow and Chartered Chemist (CChem) of the Royal Society of Chemistry (FRSChem) as well as a Chartered Scientist (CSci). During his service at TAMUK, he has trained more than 100 students at both undergraduate and graduate levels and has created online courses and established safety training protocols in conjunction with the Risk Management.

Jingbo Liu received her Ph.D. in Materials Science and Engineering from the University of Science and Technology, Beijing, China in 2001. She was promoted to a tenured Associate Professor at Texas A&M University–Kingsville (TAMUK) because of her outstanding creativity and productivity regarding nanostructured materials preparation, characterization, and understanding of fundamental physical and chemical properties of nanoparticles, nanofilms, and nanotubes, as well as applications of engineered nanomaterials in alternative energy and biological science. Currently, Dr. Liu is the DEBI faculty fellow at the US Air Force Research Laboratory and user affiliate at the Lawrence Berkeley National Laboratory. She has established the highest power density to advance performance of proton exchange membrane fuel cells and directed a new paradigm to apply metal–organic frameworks in disinfection science. Dr. Liu has authored and co-authored textbooks, books and book chapters, and more than 70 peer-reviewed journal articles. She has also reviewed dozens of journal articles and served as a National Science Foundation (NSF) panelist and chaired the proposal review panel. During her 10-year service at TAMUK, she taught >5000 students, and trained >120 undergraduate students and 20 graduate students to conduct leading-edge research. She has received tens of awards (such as a JSPS invitation fellowship and Israel faculty fellowship) and directed and/or participated in more than 15 projects supported by the NSF (USA, China), Natural Sciences and Engineering Research Council (NSERC) (Canada), American Chemical Society Petroleum Research Funds, R. Welch Foundation, and Department of Education as principal investigator (PI), co-PI, and senior personnel. She has also received dozens of travel funds to attend NSF, US Department of Energy, and US National Institutes of Health workshops.

Yi-Hsien Yu received his M.S. in Environmental Engineering from the National Taiwan University, Taipei, Taiwan in 2007. In 2010, he enrolled at Texas A&M University (TAMU), Texas, USA and joined its Department of Materials Science and Engineering in 2011. He is currently working under the supervision of Dr. Zhengdong Cheng in the Department of Chemical Engineering at TAMU. His research interests are focused on the study and synthesis of nanomaterials for energy applications, including solar materials,

phase-changing materials, and nanosurfactants for enhanced oil recovery. He has published several peer-reviewed papers related to semiconducting materials and photocatalytic hydrogen production.

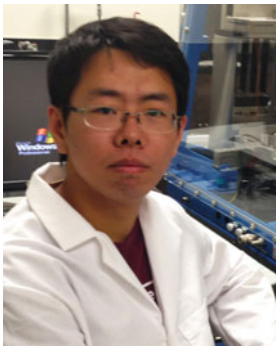

Shuai Yuan received his B.Sc. in chemistry from Shandong University, China in 2012. He joined Prof. Hong-Cai Zhou's research group in the same year at Texas A&M University as a graduate research assistant. His research interests include the development of new porous materials and their energy-related applications.

Dr. Zhengdong Cheng received his Ph.D. in Physics from Princeton University, USA in 1999. He was promoted to a tenured Associate Professor in 2010 at Texas A&M University (TAMU) due to his outstanding creativity and productivity relating to research into complex fluids and soft matter. He focuses on the self-organization of intelligent colloids and anisotropic particles, the fabrication of photonic crystals and integrated photonic circuits, solar hydrogen production via water splitting, and the application of microfluidics to bio-encapsulation. The techniques developed are applicable to the modeling of phase transitions and liquid crystal materials, the engineering of nanocomposites and semiconductors of light, solar energy harvesting, and a wide range of therapeutic treatments. Dr. Cheng has authored and co-authored more than 80 textbooks, books, book chapters, and peer-reviewed journal articles. He has chaired and organized professional conferences, such as American Institute of Chemical Engineering national meetings, American Physics Society meetings, and the China Soft Matter Day Symposium. Dr. Cheng is the Associate Editor of the *American Society of Gravity and Space Research Journal*. He was awarded the William Keeler Memorial Award (Contribution) by Dwight Look College of Engineering, TAMU in February 2015. In addition, he directed and participated in projects supported by the National Science Foundation (NSF) (USA, China), NASA, American Chemical Society Petroleum Research Funds, industrial, and TAMU as principal investigator (PI), co-PI, and senior personnel. During his 11-years at TAMU, he has taught more than 1000 students and trained more than 20 undergraduate students and nearly 20 graduate students to conduct leading-edge research. He served as NSF (CMP, center proposal site review, and Materials Research Science and Engineering Center [MRSEC]), National

Institute of Food and Agriculture (NIFA). He has also served as a journal editor on many publications and has reviewed hundreds of peer-reviewed journal papers.

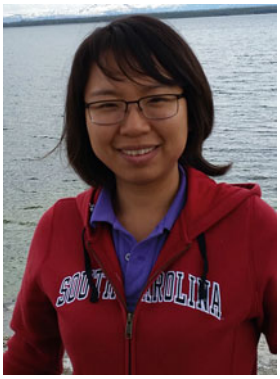

Dr. Yuwei Kan graduated from Jilin University, China in 2008 with a B.Eng. degree in chemical engineering. She obtained her Ph.D. degree in inorganic chemistry at the University of South Carolina–Columbia under the guidance of Professor Richard D. Adams in 2013. Dr Kan. developed a novel synthetic method to synthesize ruthenium and osmium carbonyl cluster complexes with heavy main group bridging ligands, and investigated reaction mechanisms and the unsaturation nature of high-nuclearity metal cluster complexes using computational calculation. She also synthesized a series of new Os–Ge and Os–Ge–Au carbonyl cluster complexes with bridging hydride ligands, investigated the dynamic behavior of hydrides using 2D variable temperature–nuclear magnetic resonance (VT-NMR) experiments, and elucidated Au–Ge bonding based on density functional theory (DFT) calculations. After her graduation, Dr. Kan joined Professor Abraham Clearfield's lab in the Department of Chemistry at Texas A&M University as a postdoctoral research associate in 2014. Her research is focused on surface modification of inorganic layered materials for various applications. She has initiated layer-by-layer assembly of thin-film metal–organic frameworks on 2D layered zirconium phosphate nanoplatelets and studied gas adsorption and catalytic properties. She is also involved in several interdisciplinary research projects, such as design and synthesis of zirconium phosphates and their derivatives as a lubricant additive in motor oil and design of surface-modified zirconium phosphate nanoplatelets for drug delivery. Dr. Kan has author and co-authored more than ten peer-reviewed journal articles.

Dr. Qiang Zhang received his B.S. in chemistry from Jilin University, China in 2008, working on rare earth metal-based fluorescent nanomaterials. He then joined the Department of Chemistry and Biochemistry at the University of South Carolina and started to work on transition metal cluster complexes and earned his Ph. D. in inorganic chemistry in 2013, earning straight 'A' scores and publishing 20 peer-reviewed articles. Following this, he moved to the Department of Chemistry at Texas A&M University for postdoctoral training and switched his research topic to metal–organic frameworks for applications in energy storage, catalysis, sensing, and separation. He is currently an Assistant Professor in the Department of Chemistry at Washington State University. His research focus is concentrated on innovative catalyst design for C–H activation and hydrogen production. The long-term goal is to use solar energy to produce alternative energy sources through green

chemical processes to supply civilization with clean energy. He was awarded the IPMI (International Precious Metal Institute) Metro New York Chapter Award and The Guy F. Lipscomb Award for the Best Graduate Student while in graduate school. He is also a co-principal investigator for a National Science Foundation-funded Small Business Initiative Research program. He has co-authored 30 peer-reviewed journal publications and has delivered ten presentations at national meetings and conferences.

Dr. Xiayun Huang graduated from Donghua University, China in 2007 with a B.Eng. degree in polymer science and engineering. She then received her M.Sc. degree in polymer chemistry and physics with a focus on nanohybrid composites from Shanghai Jiao Tong University in 2010. An interest in building block sheet structures led Dr. Huang to the Adaptive Soft and Colloidal Materials Lab at Texas A&M University (TAMU) where she pursued her doctoral studies from 2010 to 2014. During her Ph.D. she was involved in research on functional hybrid polyelectrolyte multilayer films and colloids using the layer-by-layer technique. Dr. Huang is currently a postdoctoral research associate in the Experimental Soft Matter Lab at TAMU, working on multilayer assembly at the surface and interface via microfluidic technique and liquid crystal self-assembly. Dr. Huang has author and co-authored more than 12 book chapters and peer-reviewed journal articles, two of which have been featured as cover stories, one as the American Chemical Society (ACS) highlight, and one was highlighted in the TAMU news. She has been invited to present her work at national and international conferences and is a member of the ACS, American Physical Society (APS), Materials Research Society (MRS), and Women in Science and Engineering (WISE). Dr. Huang has also served as a reviewer for more than 18 peer-reviewed journals and was selected to serve on the Award Selection Committee for the Ethel Ashworth-Tsutsui Memorial Awards for Mentoring and Research.

Dr. Haiqing Yao received her B.S. in Chemistry from Wuhan University, China in 2007 and graduated with an M.S. in organic chemistry from Nankai University in 2010, following which she began her Ph.D. study at the Polymer Technology Center laboratory at Texas A&M University under the supervision of Professor Hung-Jue Sue; she received her Ph.D. in Materials Science and Engineering in May 2015. Dr. Yao has worked at the Kaneka US Material Research Center at Kaneka Americas Holding, *Inc.* as a research scientist since May 2015. Her research focus is the study of the colloidal stability of nanoparticles and their applications in polymer nanocomposites, and chemical and physical functionalization of carbon nanotubes and graphene and their applications in

polymer nanocomposites and nanotechnology. She has published 14 research articles in peer-reviewed journals and has joined many international conferences.

Dervis Emre Demirocak received his Ph.D. in Mechanical Engineering from the University of South Florida, USA, after which he worked as a postdoctoral researcher in the Center for Automotive Research at Ohio State University. He joined the Department of Mechanical and Industrial Engineering at the Texas A&M University–Kingsville as an Assistant Professor in February 2015. He has published more than ten peer-reviewed articles, and his research interests include hydrogen storage, carbon capture and storage, thermal energy storage, degradation of Li-ion batteries, and solar thermal power generation and cooling.

Lanfang Zou obtained her B.S. in chemistry from Nanjing University, China in 2012. She attended Texas A&M University the same year, pursuing her Ph.D. in inorganic chemistry under the guidance of Prof. Hong-Cai Zhou. Her work is focused on the synthesis and functionalization of novel stable metal–organic frameworks (MOFs) and porous polymer networks (PPNs) for practical applications such as gas storage, separation, and heterogeneous catalysis. So far, she has participated in more than ten MOF/PPN projects utilizing her skills in organic synthesis, MOFs design, and PPN construction. She has co-authored seven peer-reviewed journal articles and also has substantial clean energy-related grant experience, having been responsible for technical reviews, quarterly progress reporting, guiding researchers towards completion of technical deliverables, and primary liaison for collaborating teams. In the future, she would like to further develop functional MOFs and PPNs for practical applications. Currently, she is working at Department of Process and Analytical Chemistry, Merck Research Laboratories, Merck and Co. Inc., Rahway, NJ 07065, USA.

Dr. Hong-Cai Zhou obtained his Ph.D. in 2000 from Texas A&M University under F.A. Cotton. After a postdoctoral stint at Harvard University with R.H. Holm, he joined the faculty of Miami University, Oxford in 2002. He rose to the rank of a full professor within 6 years by working on the preparation and application of metal–organic frameworks (MOFs). He moved to Texas A&M University in 2008 and was promoted to a Davidson Professor of Science in 2014 and a Robert A. Welch Chair in Chemistry in 2015. In June 2013, he became an

associate editor for *Inorganic Chemistry (ACS)*. Since 2003, he has obtained more than US$17,000,000 funding externally and published over 210 peer-reviewed papers with more than 25,000 citations and an h-index of 72. His awards include a Research Innovation Award from Research Corporation in 2003, a National Science Foundation (NSF) CAREER Award in 2005, a Cottrell Scholar Award from Research Corporation in 2005, the 2006 Miami University Distinguished Scholar – Young Investigator Award, the 2007 Faculty Excellence Award from Air Products, as well as the 2010 Department of Energy Hydrogen Program Special Recognition Award as a main contributor to the Hydrogen Sorption Center of Excellence. In 2014, he received a JSPS Invitation Fellowship. In 2014, he was the only chemist in the Texas A&M University system listed as a Highly Cited Researcher by Thomson Reuters based on his 2002–2012 publications, and he was one of only seven on this list in 2015 based on his 2003–2013 publications. He has been the Director for the Center for Electrochemical Systems and Hydrogen Research in Texas A&M University since 2016.

Mathieu Bosch was born in Hampton, Virginia, USA and worked full-time for several years before attending the University of Houston starting in 2010. He graduated Summa Cum Laude, with honors in Chemistry in May 2013 and has been a graduate student at Texas A&M University since, studying under Prof. Hong-Cai 'Joe' Zhou. His research interests lie in the synthesis and characterization of novel advanced porous materials for catalysis and energy storage.

Dr. Sesha Srinivasan received his Ph.D. in physics from one of the premier institutions in India, the Banaras Hindu University (BHU), and Center of Excellences in Physics. He was instrumental in developing hydrogen-fueled motorcycles in India and was invited to be a guest speaker at the prestigious 80th Indian Science Congress in 2009. Dr. Srinivasan is one of the inaugural faculty members at Florida Polytechnic University and is currently teaching Physics and Engineering courses. He has served as a tenure track Assistant Professor of Physics at Tuskegee University in the State of Alabama from fall 2009 until spring 2014. Prior to his teaching endeavor, Dr. Srinivasan worked in various capacities such as Research Assistant Professor, Senior Researcher, and Post-Doctoral Fellow at the University of Hawaii Department of Chemistry from 2002 to 2004 and at the University of South Florida Clean Energy Research Center (USF-CERC) Tampa, Florida from 2004 to 2009. Dr. Srinivasan is currently serving as a full member of Sigma-Xi and is a Physics Congress Committee member of Sigma-Pi-Sigma, faculty liaison of the Florida Academy of Sciences, and faculty advisor of the Society of Physics Students Florida

Polytechnic University chapter. He has served as a panel review member of the National Science Foundation, Qatar National Research Foundation, Conrad Innovation Challenge, and Department of Defense's National Defense Science and Engineering Graduate (NDSEG) and Science, Mathematics & Research for Transformation (SMART) programs. Dr. Srinivasan has two US patents and two patent disclosures and has published seven book chapters, more than 75 peer-reviewed journal publications, and many more conference proceedings. He has been awarded research grants (>US$0.5 million) from NSF-EAGER (National Science Foundation–Early-concept Grants for Exploratory Research), the Office of Naval Research, Dauphin Island Sea Lab (British Petroleum), Quantum Sphere Inc., and Florida Energy Systems Consortium, as well as a Florida Polytechnic University internal seed grant. Dr. Srinivasan has served as an advisor and faculty mentor for six Ph.D. theses and 15 Masters' dissertations. He has served as a guest editor for the *Journal of Nanomaterials* and is currently serves as an Associate Editor for DeGruyter Open publications in physics, materials science, and astronomy. He can be reached at ssrinivasan@flpoly.org.

Dr. Weigang Lu received his Bachelor Degree in Chemistry from Nanjing University, China in 1995 and his Ph.D. in Organic Chemistry from Sun Yat-Sen University in 2002. After independent research at Sun Yat-Sen University (2002–2005) and a period as a visiting-scholar at the Hong Kong University of Science and Technology (2005–2008), he joined Prof. Hong-Cai Zhou's research group at Texas A&M University as a postdoctoral researcher and later as an assistant research scientist (2008–2015). His research interest is focused on the development of porous organic polymers and their clean energy-related applications. Since 2010, Dr. Lu has authored more than 20 peer-reviewed research papers with over 2000 citations and has reviewed hundreds of peer-reviewed papers for journals such as *Chemical Society Reviews*, *Journal of the American Chemical Society*, *Energy & Environment Science*, *Nature Communications*, *Chemical Communications*, *Chemistry – A European Journal*, *Nanoscale*, *Chemistry of Materials*, *Journal of Materials Chemistry*, etc.

Photocatalytic Hydrogen Evolution

1

Yi-Hsien Yu, Yuan Shuai, and Zhengdong Cheng

Abstract

With the foreseeable depletion of fossil fuels and their significant contribution to greenhouse gas emissions, the development of an alternative energy source has become an urgent research field. Among renewable energy resources, solar energy is the largest exploitable resource by far. In view of the intermittency of sunlight, if solar energy is to be a major energy source, it must be converted and stored. An especially attractive approach is to store solar-converted energy in the form of chemical bonds, i.e., by solar-driven water splitting. This chapter will give a brief introduction to the fundamental principles of semiconductor-based photoelectrochemical water splitting into hydrogen and oxygen. The semiconductor photocatalysts for photoelectrochemical water splitting are introduced in details. Strategies to optimize solar to hydrogen conversion efficiencies by

Author Contribution: The chapter was compiled by Dr. Zhengdong Cheng (corresponding author). The subsections were researched by Yi-Hsien Yu and Shuai Yuan. The revision was done by Dr. J. Liu and Dr. S. Bashir.

Y.-H. Yu
Department of Materials Science and Engineering, Texas A&M University, College Station, TX, USA
e-mail: myrzr@tamu.edu

Y. Shuai
Department of Chemistry, Texas A&M University, College Station, TX, USA
e-mail: shuai.yuan@chem.tamu.edu

Z. Cheng (✉)
Department of Macromolecular Science, Fudan University, Shanghai, China

Department of Materials Science and Engineering, Texas A&M University, College Station, USA

Mary Kay O'Connor Process Safety Center, Artie McFerrin Department of Chemical Engineering, Texas A&M University, College Station, USA
e-mail: zcheng@tamu.edu

Y.-P. Chen et al. (eds.), *Nanostructured Materials for Next-Generation Energy Storage and Conversion*, DOI 10.1007/978-3-662-53514-1_1

optimization of light harvesting semiconductors, surface catalysis, and devices design will also be described.

Contents

1.1 Introduction

The supply of clean, effective, and sustainable energy is one of the most challenging tasks in the twenty-first century. In 2012, worldwide primary energy consumption was 147,899, terawatt-hour (TWh), which is an average energy consumption rate of 16.9 terawatt (TW) [1, 2]. Yet global power consumption is projected to rise to 28 TW if population and economic growth projections continue. Developing alternative energies to reduce greenhouse gas accumulation and to reserve depletion of fossil fuel is necessary. Solar energy has the largest theoretical potential among renewable energy resources. The amount of solar radiation received by the Earth (~23,000 TW) is much higher than annual global energy consumption (~16 TW) (Fig. 1.1). There are three major problems to utilizing solar energy. First, as photon

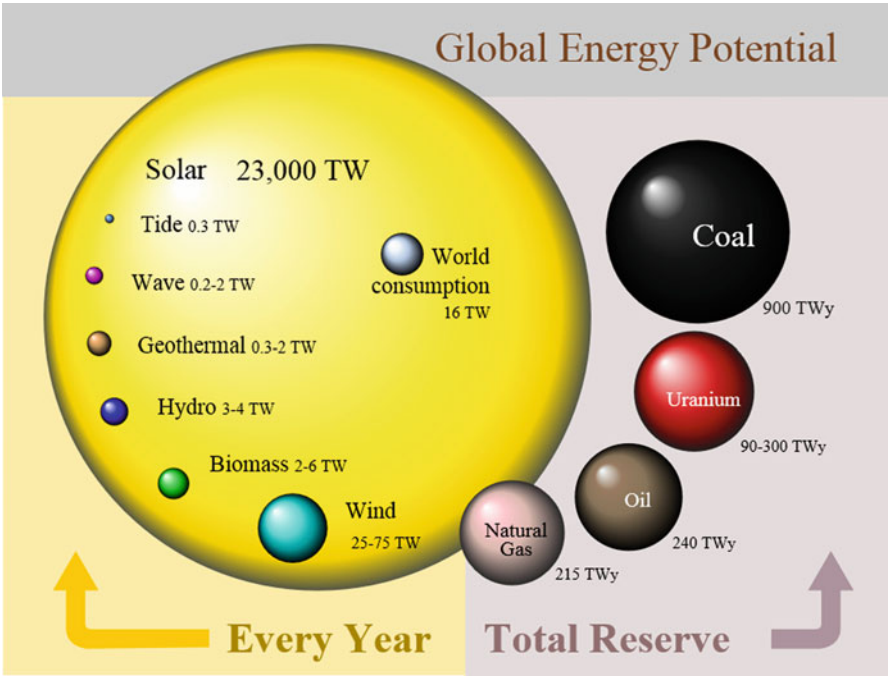

Fig. 1.1 Global energy potential by source. Total recoverable reserves are shown for the finite resources. Yearly potential is shown for the renewables (Reprinted with permission from Ref. [3]. Copyright 2009 IEA SHC)

energy, the solar energy needs to be converted into usable energy such as electricity. Second, solar energy strongly depends on the weather and time. In addition, the availability of solar energy strongly depends on a region's geographic position and land availability. In view of the intermittency of solar energy, it must be converted and stored on demand to the end user.

An efficient system for solar energy conversion and storage is the photosynthetic system developed by nature 3.4 billion years ago. The photosystem 2 in chloroplast stroma absorbs sun light and split water, generating hydrogen (H_2) and oxygen (O_2) [4]. On the other side of the membrane, photosystem 1 reduces proton and generates nicotinamide adenine dinucleotide phosphate-oxidase (NADPH). The NADPH further participated into the formation of sugar. Water oxidation reaction and hydrogen reduction reaction is well separated by membrane. As a result, carbon dioxide (CO_2) and water is converted to sugar and oxygen. During this process, the solar energy is stored in chemical bonds. Inspired by nature, people realize that solar energy can be converted and stored in the form of chemical bonds following be utilized for producing oxygen from water and reduced fuel such as hydrogen or other hydrocarbon species. In 1972, Fujishima found that some semiconductor, such as TiO_2, can split water into

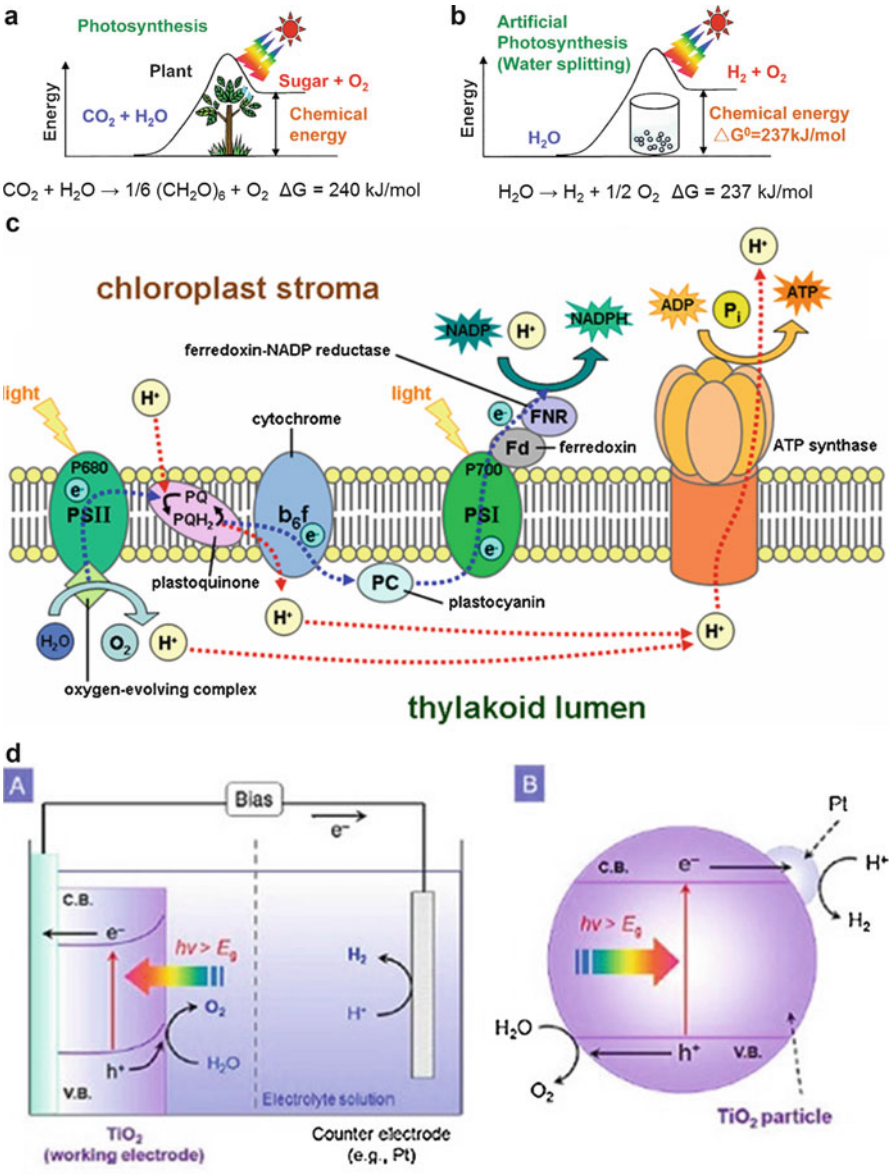

Fig. 1.2 Photosynthesis by green plants and photocatalytic water splitting as an artificial photosynthesis (Reprinted with permission from Ref. [6]. Copyright 2009 Royal Society of Chemistry)

O_2 and H_2 under ultraviolet (UV) irradiation [5]. This reaction is similar to photosynthesis by green plants and therefore is regarded as an artificial photosynthesis, which attracted the attention of chemists for decades (Fig. 1.2).

1.2 Fundamental Mechanisms

For fundamental principles of photocatalytic water-splitting, see cited reviews [6–9]. Herein, we briefly introduce the basic concepts that are necessary for the understanding of photocatalytic water-splitting.

The reaction of water splitting is a simple process. It can be realized by an electrolytic cell with an electrical power source connected to two electrodes (typically made from some inert metals such as platinum, Pt), which are placed in the water. Cathode will receive electrons and generate hydrogen at the interface. Similarly, oxygen from water oxidation will be produced at the anode. The electrode potential can be easily calculated by Nernst equation. The hydrogen and oxygen evolution reaction are pH dependent. But the total potential to split water is always 1.23 V, which is corresponding to the free energy change for the conversion of one molecule of H_2O to H_2 and 1/2 O_2 under standard conditions ($\Delta G = 237.2$ kJ/mol).

$$\text{Oxygen Evolution Reaction (OER)}: \quad H_2O \rightarrow \frac{1}{2}O_2 + 2H^+ + 2e^- \qquad E^0_{OER} = 1.23 \text{ V vs NHE} \tag{1.1}$$

$$\text{Hydrogen Evolution Reaction (HER)}: \quad 2H^+ + 2e^- \rightarrow H_2 \qquad E^0_{OER} = 1.23 \text{ V vs NHE} \tag{1.2}$$

$$\text{Overall}: \quad H_2O \rightarrow \frac{1}{2}O_2 + H_2,\ E = E^0_{OER} - E^0_{HER} = -1.23 \text{ V} \tag{1.3}$$

$$E = E^0 - \frac{RT}{nF}\ln\frac{a_{\text{Red}}}{a_{\text{Ox}}} \tag{1.4}$$

$$E_{HER} = E^0_{HER} - \frac{RT}{2F}\ln\frac{P_{H_2}}{[H^+]^2} \tag{1.5}$$

$$E_{\text{OER}} = E^0_{\text{OER}} - \frac{RT}{2F}\ln\frac{1}{[H^+]^2(P_{O_2})^{1/2}} \tag{1.6}$$

where **R** is 8.314 (J mol^{-1} K^{-1}); **E** = half–cell potential (V) of the oxidized and reduced species (mol/L); **n** = moles of electrons transferred per mole of reactants; **T** the absolute temperature (K); and **F** as the Faraday constant (96,500 C mol^{-1}).

To use a semiconductor to drive this reaction with light, the semiconductor needs to provide a voltage that is larger than 1.23 volt (V). The semiconductor must be able to absorb radiant light with photon energies of at least 1.23 electron-volt (eV, equal to wavelengths of about 1000 nm or shorter) and use the energy to split water into H_2

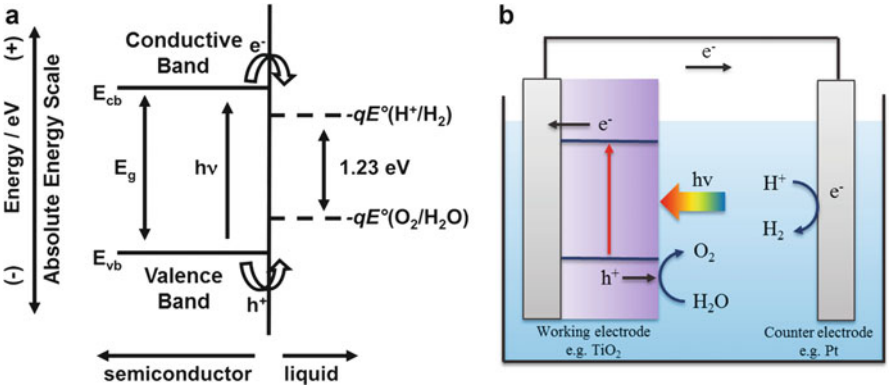

Fig. 1.3 (**a**) Water splitting on an ideal semiconductor material (Reprinted with permission from Ref. [10]. Copyright 2010 American Chemical Society). (**b**) Simplified scheme of water splitting cells

and O_2. In the ideal case, a single semiconductor material having a band gap energy (E_g) larger than 1.23 eV, and having a conduction band-edge energy (E_{cb}) more negative than electrochemical potentials E° (H^+/H_2) and valence band-edge energy (E_{vb}) more positive than electrochemical potentials E° (O_2/H_2O), can drive the hydrogen evolution reaction (HER) and oxygen evolution reaction (OER) under illumination. A simplified model of water splitting cell by an ideal semiconductor material is illustrated in Fig. 1.3. Semiconductor separates photo excited electron–hole pairs. The electrons reduce H^+ to produce H_2, while the holes oxidize water generating O_2. But this model is simply based on thermodynamics and is far from reality. The surface chemistry of semiconductors and kinetics also needs to be considered.

For the semiconductor chemistry, the basic concept is the Fermi levels. Fermi level is defined as the thermodynamic work required to add one electron to the body. It describes energy of carriers. The Fermi level of different materials is shown in Fig. 1.4 to illustrate the filling of the electronic density of states in various types of materials at equilibrium. Here the vertical axis is energy, while the horizontal axis is the density of states for a particular band in the material listed. For a metal, the Femi level is the position of half-filled orbital. For a semiconductor, it lies between conduction band and valence band. If the semiconductor is p-type, Fermi level is close to the valence band because the valance band is not fully occupied. Similarly, for n-type semiconductor, some of the conduction band is filled, so Fermi level is close to conduction band. In semiconductors, the bands are close enough to the Fermi level to be thermally populated with electrons or holes.

The semiconductor itself can separate charges, but cannot generate photo voltage. It needs a surface or interface. Semiconductor-solution contact provides the surface. When semiconductor is contact with liquid, a Fermi energy difference exists. Electrons will flow to the liquid just like water goes downhill. As a result, the semiconductor will

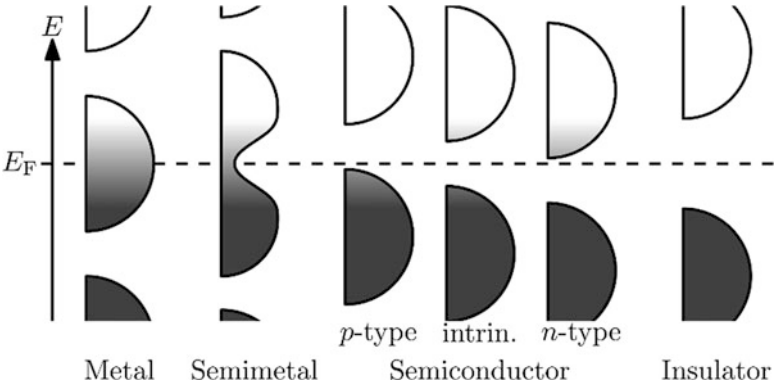

Fig. 1.4 Schematic illustration of Fermi level of different materials. The *vertical* axis is energy while the *horizontal* axis is the density of states for a particular band in the material listed

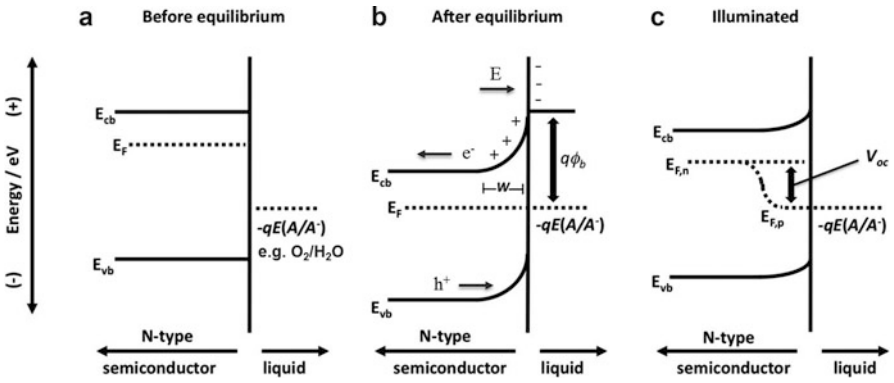

Fig. 1.5 The band energetics of a semiconductor/liquid contact are shown in three cases: (**a**) before equilibration between the two phases, (**b**) after equilibration, but in the dark, and (**c**) in quasi-static equilibrium under steady state illumination (Reprinted with permission from Ref. [10]. Copyright 2010 American Chemical Society)

have excess positive charge, while the liquid surface bears negative charge. An electric field is generated by the electric double layer. This electric field will hinder the electron flow from semiconductor to liquid and favor the holes moving from semiconductor to the liquid. Under illumination, electron–hole pair can be generated. The Fermi level describes the carrier energy in equilibrium. Illumination yields nonequilibrium electron and hole populations, which is described by quasi-Fermi level. The quasi-Fermi level of electrons and holes is shown in Fig. 1.5. The effective photo voltage that is generated by a semiconductor is the energy difference between electron Fermi level and hole Fermi level, named as open circuit voltage. It determines the reactions that

can be driven by that system. Even though the semiconductors have an appropriate band position and large-enough band gap, water splitting is not possible unless the photo voltage is greater than 1.23 V.

In order to drive the water splitting reaction, we also need to take the kinetics into consideration. When reaction happens, the current going through electrode will change the potential of electrode from the thermodynamically expected potential. The change is called overpotential. Tafel equation describes the relationship between the current and the overpotential. η stands for the overpotential, I is the observed current, and I_0 is the exchange current. The Tafel slope, b, mainly depends on the temperature. According to the Tafel equation, the over potential increases with current and decreases with exchange current. The exchange current is a constant, which depends on the electrode properties, for example, the material and the surface area. Here we define current density, which is the current over area. The exchange current density only depends on the material of electrode and it describes the catalytic performance of this material. Because the exchange current density depends on the material, one way to increase the exchange current density is to cover the electrode with other materials as catalyst.

$$\text{Tafel equation}: \quad \eta = b \log \frac{I}{I_0} \tag{1.7}$$

$$\text{Exchange current density}: \quad J_0 = \frac{I_o}{S} \tag{1.8}$$

Taken the semiconductor chemistry and overpotential into consideration , a comprehensive scheme of water splitting cells can be illustrated (Fig. 1.6a). A semiconductor with appropriate band edge position that crosses the water oxidation and reduction levels is adopted to generate enough photovoltage. In order to drive the reaction, effective photovoltage (V_{oc}) needs to be larger enough to overcome the over potential. Taking all these factors into consideration, experimentally, we need to ensure a band gap of 2.4 V [11].

During the photocatalytic water splitting, several processes happen on the semiconductor photocatalyst. These includes light absorption of the semiconductor photocatalyst, generation of electron and hole pairs, recombination of the excited charges, separation of charges, migration of the charges, trap of excited charges, and transfer of excited charges to water or other molecules (Fig. 1.6b) [12]. All of these processes have to be taken into account for the generation of hydrogen by the semiconductor photocatalyst system. Apparently, any process that generates and keeps the excited electron–hole pairs will contribute to the hydrogen generation efficiency. Likewise, any process that consumes electrons without generating hydrogen should be avoided. For charge-generation process, the semiconductor should efficiently absorb light and avoid light scattering and reflection. Second, the semiconductor should have a high efficiency in generating excited charges, rather than generating heat using the absorbed photons. Two important competitive processes, the charge recombination and separation/migration processes, largely affect the efficiency of the photocatalyst. Charge recombination

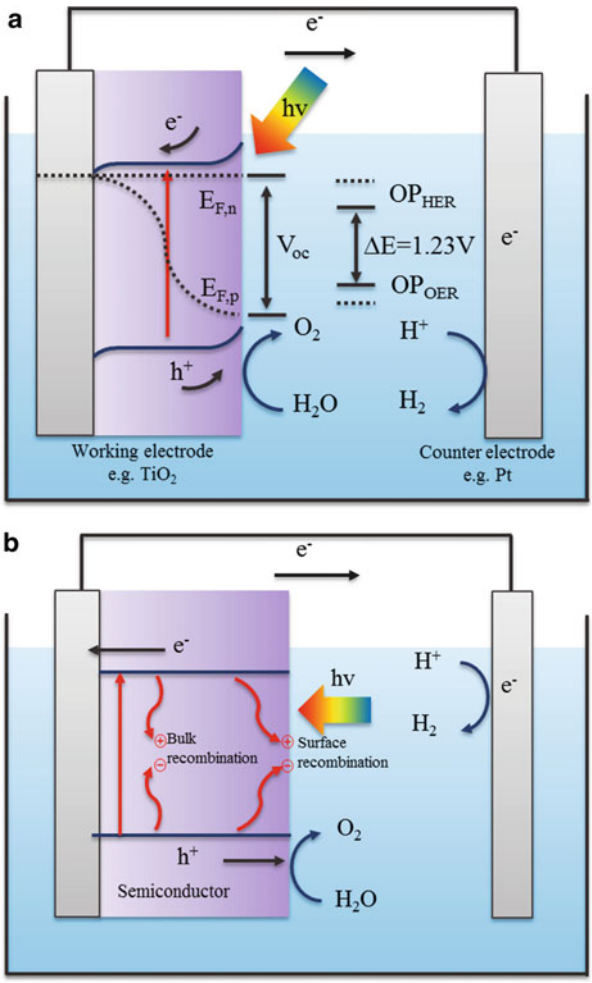

Fig. 1.6 (**a**) Comprehensive scheme of water splitting cells including the semiconductor chemistry and overpotential; (**b**) Processes happening on the semiconductor during photocatalytic water splitting

reduces the excited electorns/holes generating phonons or heat. Charge recombination includes surface recombination and bulk recombination, which are both classified as deactivation processes. On the other hand, charge separation and migration is an activation process. The charge recombination will be reduced by the efficient charge separation and transport, which is fundamentally important for photocatalytic water splitting. Two preconditions are required in the development of high-efficiency semiconductor materials for the water splitting: (a) The photocatalyst band gap should be sufficient to both harvest solar light and to drive water splitting reaction to completion; and (b) efficient charge separation to minimize electron–hole recombination is necessary and allows fast charge transport.

With a general understanding of the mechanism of solar water splitting cell, we turn to the evaluation of the cell efficiency. Overall solar-to-hydrogen (STH) efficiency is the most important parameter to characterize a photoelectrochemical (PEC) device. The STH

efficiency is the single value by which all solar water splitting cell can be reliably ranked against one another. However, the STH efficiency strongly depends on the experimental condition, for example, the light resources. In order to compare the activities of photocatalysts under different reaction conditions, quantum yield is selected as a criterion. In fact, the observed quantum efficiency (apparent quantum yield) is expected to be smaller than the real quantum yield because the number of absorbed photons is usually less than that of incident photons. It is worth noting that the quantum yield is different from the STH efficiency that is usually used for solar cells evaluation. The number of photocatalysts with reasonable solar energy conversion efficiency is limited by now, maybe because of insufficient measurement. However, the efficiency of photocatalytic water splitting should be evaluated by solar energy conversion efficiency [11].

Diagnostic efficiency: Apparent quantum yield (AQY)

$$\text{Apparent quantum yield } (\%) = \frac{\text{Number of the reacter electrons}}{\text{Number of the incident photons}} \times 100\% \quad (1.9)$$

Benchmark efficiency: Solar-to-hydrogen efficiency (STH)

$$\text{STH} = \frac{(\text{mol } H_2/\text{s}) \times (237{,}000 \text{ J/mol})}{P \text{ (W/cm}^2) \times \text{S (cm}^2)} \times 100\% \quad (1.10)$$

$$= \frac{j_{sc}(\text{A/cm}^2) \times (1.23 \text{ V}) \times \eta_F}{P(\text{W/cm}^2) \times \text{Area(cm}^2)} \times 100\% \quad (1.11)$$

where **P** is incident illumination power density and **S** is illuminated electrode area.

1.3 Semiconductor Photocatalysts

Until the middle of the 1980s, it has been mainly focused on $SrTiO_3$ and TiO_2 as particulate photocatalysts for hydrogen generation from water [13, 14]. Since the 1990s, many tantalates and niobates and have been reported as efficient photocatalysts [15]. Zinco oxide (ZrO_2) has also been found to be a highly active photocatalyst, exhibiting high activity that can split water even without a cocatalyst [16]. Later, tungsten-based metal oxides such as $AMWO_6$ (A = Rb, Cs; M = Nb, Ta) were reported to be active under UV for water splitting [17]. To date, a large number of semiconducting materials have been developed as water splitting photocatalysts. Figure 1.7 shows the groups of metallic elements that can form metal oxide materials with suitable band gap structures which have been applied as photocatalysts for water splitting. Based on their electronic configurations, these photocatalysts can be typically classified into four groups: (a) d^0 metal (e.g., Ti^{4+}, Zr^{4+}, Nb^{5+}, Ta^{5+}, W^{6+}, and Mo^{6+}) oxide photocatalysts; (b) d^{10} metal (e.g., In^{3+}, Ga^{3+}, Ge^{4+}, Sn^{4+}, and Sb^{5+}) oxide photocatalysts; (c) f^0 metal (e.g., Ce^{4+}) oxide photocatalysts; and (d) a small group of nonmetal oxide photocatalyst (e.g., Ge_3N_4). Other metal oxides with d^0 or d^{10} electronic configurations, such as Zn^{2+} and V^{5+} [18, 19], are also expected to be

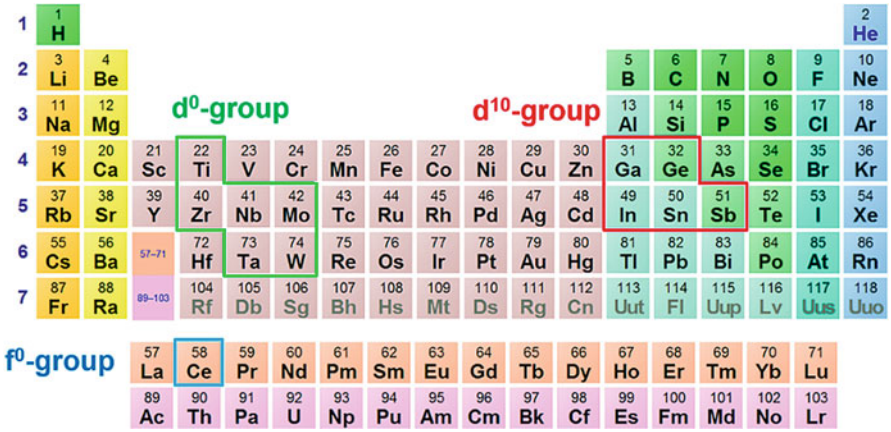

Fig. 1.7 Principal metal oxides for photocatalytic water splitting

acting as photocatalysts. However, there are no reported studies on such photocatalysts for water splitting with reasonable activity and stability.

A wide range of metal oxide photocatalysts have been reported to date. Some of them have achieved high quantum efficiencies (as high as 30–50%) under UV irradiation [20, 21]. Nevertheless, most of the metal oxide semiconductors respond only to UV, which accounts less than 5% of solar energy. The valence bands of d^0 or d^{10} metal oxides usually consist of O-2p orbitals, which are located at $>+3$ V (vs. NHE). The conduction band of such semiconductors is expected to be more negative than the water reduction potential in order to generate hydrogen. Therefore, the band gap of the material will inevitably be larger than 3 eV, rendering them inactive in the visible-light region.

1.4 d^0 Metal Oxide Photocatalyst

1.4.1 Group 4 Elements (Ti, Zr)-Based Oxides

As the first reported photocatalyst for water splitting under UV irradiation, it has been extensively studied [5]. TiO_2 is reported to split water from water vapor, liquid water, and aqueous solutions containing electron donor [22–24]. The colloidal TiO_2 was found to efficiently generate H_2 under UV irradiation when combined with ultrafine Pt and RuO_2 particles [22]. Later, it was found that additions of NaOH or Na_2CO_3 can facilitate water splitting on the Pt/TiO_2 photocatalyst [25]. The metal ions doping was reported to enhance the photocatalytic activity of TiO_2. For example, Ga doped TiO_2 powder could stoichiometrically split water under UV irradiation, whereas TiO_2 solid did not show any activity [26]. When combined with

a second metal oxide semiconductor such as SnO_2, ZrO_2, Cu_xO, and Ag_xO, photocatalytic activity of TiO_2 was also improved. All of the mixed metal oxides displayed higher hydrogen evolution rates from aqueous solutions containing electron donors than TiO_2 alone [27]. When TiO_2 nanoparticles were dispersed in the mesoporous materials such as Mobil Composition of Matter No.41 (MCM-41) and MCM-48, it showed higher photocatalytic activity for hydrogen evolution under UV irradiation than bulk TiO_2 [28].

Many titanates are also known as efficient photocatalysts for water splitting under UV irradiation. For example, the layered titanates, $Na_2Ti_3O_7$, $K_2Ti_2O_5$, and $K_2Ti_4O_9$, were active in photocatalytic H_2 evolution from aqueous methanol solutions even without presence of noble metal cocatalyst [29]. These layered titanates can be modified by ion-exchange [30]. The H^+-exchanged $K_2Ti_2O_5$ exhibited a high activity for hydrogen generation with a quantum yield of up to 10%. After being pillared with SiO_2 in the interlayers, the photocatalytic activity of $K_2Ti_4O_9$ was enhanced, which is in agreement with the increased surface area [31]. NiO-loaded $SrTiO_3$ powder was also found to be active for water splitting into H_2 and O_2 [32]. The NiO cocatalyst for H_2 evolution is usually activated by H_2 reduction and subsequent O_2 oxidation to form a NiO/Ni double layer structure that facilitates electron migration from photocatalyst to the cocatalyst [33] with high efficiency using NiO as cocatalyst. The photocatalytic activity of $SrTiO_3$ was also improved by a modified preparation route or metal cations doping such as La^{3+} and Ga^{3+} [34].

Sayama and Arakawa firstly reported the photocatalytic decomposition of pure water proceeded over ZrO_2 powder under UV irradiation [35]. The activity was affected significantly by the nature of the additive to the solution. Specifically, the addition of sodium carbonate (Na_2CO_3) or sodium hydrogen bicarbonate ($NaHCO_3$) led to a remarkable increase in the activity of hydrogen evolution [36]. Barium zirconate ($BaZrO_3$) with a cubic perovskite structure can efficiently split water under UV irradiation with a quantum yield up to 3.7% [37]. Two factors contribute to the photoactivity of $BaZrO_3$. First, the highly negative conduction band position provides enough driving force for hydrogen generation. Second, the conduction bands, which mainly composed of Zr-4d orbitals are largely dispersed, facilitates the fast charge transfer. The photocatalytic activities for hydrogen evolution of lanthanide zirconium oxides, $Ln_2Zr_2O_7$ (Ln: La, Ce, Nd, and Sm), have also been investigated. Hydrogen gas was clearly evolved in a water suspension of $La_2Zr_2O_7$, $Sm_2Zr_2O_7$, and $Nd_2Zr_2O_7$ under the irradiation of a 500-W Xenon lamp.

1.4.2 Group 5 Elements (Nb, Ta)-Based Oxides

Pure Nb_2O_5, with a band gap of 3.4 eV, is not active for water splitting under UV irradiation [38]. However, it can produce H_2 from methanol aqueous solutions when modified with Pt as a cocatalyst [39]. It was demonstrated that mesoporous Nb_2O_5 revealed photocatalytic activity 20 times higher for hydrogen evolution than a bulk

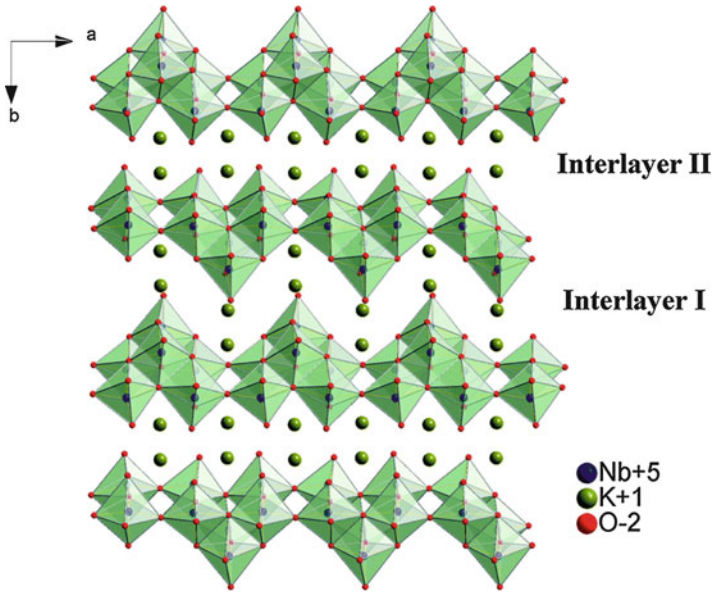

Fig. 1.8 Structural diagram of $K_4Nb_6O_{17}$

Nb_2O_5 without any porosity. Besides Nb_2O_5, a number of niobates can serve as photocatalyst to produce H_2 and O_2 from water under UV irradiation. $K_4Nb_6O_{17}$ is the first example of a niobate photocatalyst that showed high and stable activity for H_2 evolution from aqueous methanol solution without cocatalyst [40]. $K_4Nb_6O_{17}$ has a layered structure: Niobium oxide forms the layer and potassium ions intercalate between each layer (Fig. 1.8). There are two kinds of interlayers: One contains water molecules and potassium ions, whereas the other contains only potassium ions. The interlayer potassium ions between each niobium oxide sheet can be exchanged with other ions. H_2 evolution proceeds in one interlayer with a nickel cocatalyst, while O_2 evolution occurs in another interlayer. It is the characteristic of the $K_4Nb_6O_{17}$ photocatalyst that H_2 evolution sites are separated from O_2 evolution sites [41]. $Rb_4Nb_6O_{17}$ with similar layered structure can also efficiently split water under UV irradiation [42]. Some other alkaline-metal niobates such as $ANbO_3$ (A = Li, Na, K) and $Cs_2Nb_4O_{11}$ also catalyzed water splitting under UV irradiation when modification with Pt, RuO_2, or NiO as cocatalysts [43].

Tantalum oxides are known as efficient UV-driven water splitting photocatalysts. Tantalum (V) oxide Ta_2O_5 alone can only produce a very small amount of H_2 from pure water [38]. When modification with NiO and RuO_2 as cocatalysts, it displayed much better activity for water splitting [44]. Mesoporous Ta_2O_5 was found to be an active catalyst for photocatalytic water splitting with NiO loading

[45]. Although the walls of the mesoporous Ta_2O_5 were amorphous, the photocatalytic activity was higher than that of crystallized Ta_2O_5. This was attributed to the small wall thickness of mesoporous Ta_2O_5 that favors the migration of electron to the surface. Many tantalates with layered perovskite as the bond structure are also shown activity towards water splitting. For example, Kudo and coworkers reported that the photocatalytic activity of NiO/$NaTaO_3$ is remarkably increased by doping of lanthanide ions [46, 47]. At the optimized condition, NiO (0.2 weight-percent, wt%)/$NaTaO_3$:La (2%) photocatalyst shows high activity for hydrogen generation from water at wavelength of 270 nm with an apparent quantum yield of 56%. Production of H_2 and O_2 can be directly observed. It is interesting that hydrogen and oxygen generation simultaneously happens on the same nanoparticle without significant back reaction, which is not usual as water reduction and oxidation are completely opposite reactions. This phenomena can be attributed to the band structure and morphology of NiO (0.2 wt%)/$NaTaO_3$:La (2%), which will be discussed in detail.

1.4.3 Group 6 Elements (W, Mo) and Other d^0 Elements-Based Oxides

The heterogeneous photocatalysts based on tungstates and molybdates are less commonly reported in the field of water splitting. Inoue and coworkers reported that $PbWO_4$ acted as high and stable photocatalyst for the stoichiometric decomposition of water when RuO_2 was loaded [48]. The large dispersions of the valence bands and conduction bands are responsible for the good photocatalytic performance. For comparison, the $CaWO_4$, with similar crystal structure, is found to be photocatalytically inactive, which is attributed to the small dispersion in the conduction band. A novel silicotungstic acid (SWA)-SiO_2 photocatalyst is developed by impregnating SWA on a silica support [49], which stoichiometrically can split water into H_2 and O_2. The photoactive sites in SiO_2 acted as a donor source for hydrogen, while the SWA acted as an inhibitor that prevents the charge recombination.

1.4.4 d^{10} Metal Oxide Photocatalyst

d^{10} metal oxides such as ZnO and In_2O_3 have been reported as photocatalysts for a long time. However, they are not suitable photocatalyst for water splitting because of photocorrosion and the positive conduction band position. On the other hand, various typical metal oxides with d^{10} (In^{3+}, Ga^{3+}, Ge^{4+}, Sn^{4+}, Sb^{5+}) configurations have been shown to be active towards photochemical water-splitting under UV irradiation. For example, Ni-loaded Ga_2O_3 shows excellent photocatalytic activity for overall water splitting [50]. Doping of other metal cations such as Zn^{2+}, Ca^{2+}, Sr^{2+}, and Ba^{2+} can efficiently be effectively improve the photoactivity

[51]. Among them, Ni/Zn-Ga_2O_3 shows highest performance, with an apparent quantum yield for of ~20% [52]. Those materials consist of d^{10} metal ions with distorted octahedral or tetrahedral geometry, which is believed to be responsible for the photocatalytic activity [53–55].

1.4.5 f^0 Metal Oxide Photocatalyst

It was found that the f^0 metal oxides themselves only show limited photocatalytic activity towards water splitting. They are often combined with other metal oxides [56]. When RuO_2 was loaded as cocatalyst, the Sr^{2+}-doped CeO_2 shows activity for H_2 and O_2 generation from water. Ce (III) oxide supported zeolites showed higher photocatalytic activity for water splitting than bulk metal oxide [57]. $BaCeO_3$ were also reported to produced H_2 and O_2 from methanol aqueous solutions and $AgNO_3$ aqueous solutions, respectively [58].

1.4.6 Nonmetal Oxide Photocatalyst

Many nonmetal oxides with small band-gaps can efficiently produce H_2 from water when sacrificial agents are used. For example, suspensions of ZnS can produce hydrogen from SO_3^{2-} solutions with high quantum yield up to 90% under UV irradiation [59]. InP can generate H_2 from water when inorganic sacrificial agents are used [60]. However, there are only a few reports on the monoxide photocatalyts that can split pure water into H_2 and O_2. Domen and coworkers studied the photocatalytic activity of GaN towards water splitting which reveals that it strongly depends on the catalyst and the preparation of material [61]. Zn^{2+}, Mg^{2+}, and Be^{2+} doping of GaN give a more active and stable photocatalyst [62]. Ge_3N_4 was another effective nitride photocatalyst for overall water splitting when combined with RuO_2 as cocatalyst [63].

In order to utilize solar energy, it is important to the development visible light responsive photocatalysts that utilize solar light to split water. However, until the first half of the 1990s, only a few chalcogenides and metal oxides were known to be photocatalytically active under visible light [64]. Some metal chalcogenides, such as CdS and CdSe, with proper band position for visible light-driven water splitting, are not stable in the water oxidation reaction. The S^{2-} and Se^{2-} anions are more susceptible to oxidation than water, as a result, CdS or CdSe catalyst itself is easier to be oxidized and causes photocorrosion [65]. Although WO_3 functions as a stable photocatalyst for O_2 evolution under visible light in the presence of an appropriate electron acceptor, the conduction band is too positive for water reduction. Figure 1.9c depicts a schematic illustration of band position of typical photocatalysts.

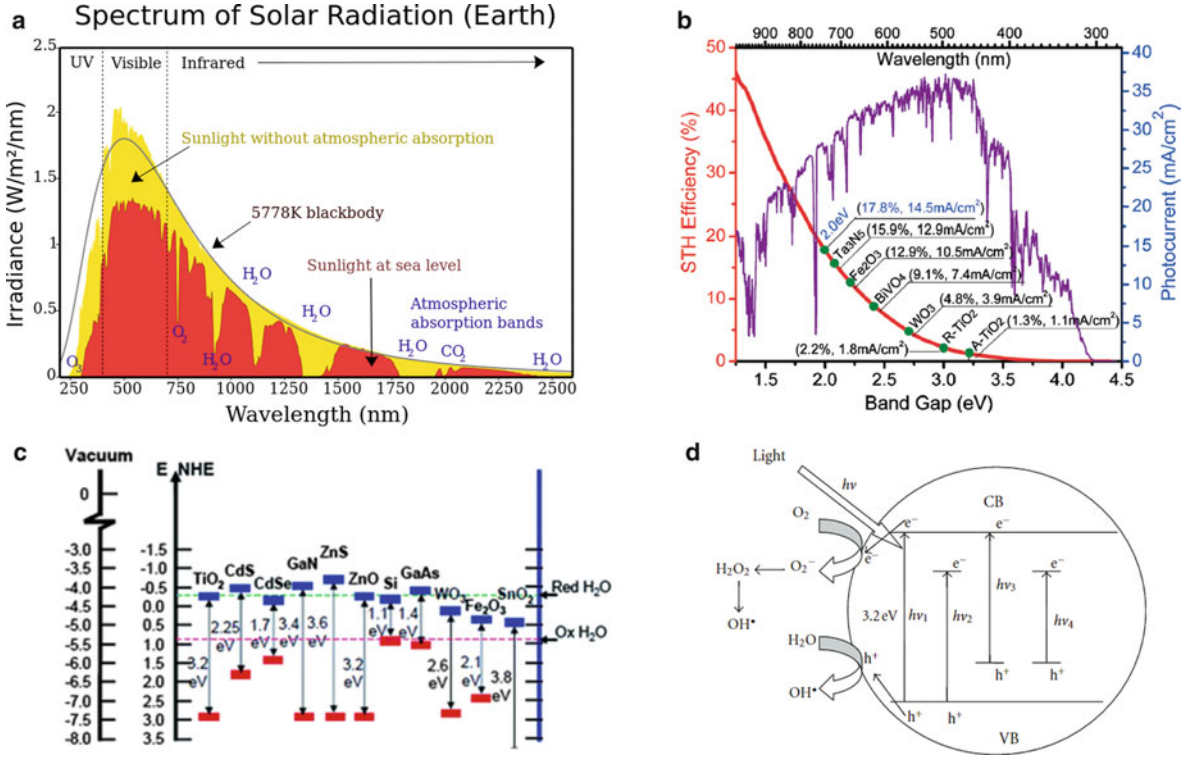

Fig. 1.9 (**a**) Solar spectra (Reprinted with permission from Ref. [66]. Copyright Wikimedia Foundation, Inc.). (**b**) Theoretical efficiency limits for semiconductors [67] (Reprinted with permission from Ref. [67]. Copyright The Royal Society of Chemistry). (**c**) Schematic illustration of band structures of several semiconductor photocatalysts, which presents the above-mentioned dilemma [67] (Reprinted with permission from Ref. [67]. Copyright The Royal Society of Chemistry). (**d**) Schematic representation of the mechanism of photocatalytic titanium dioxide particles (TiO_2: $h\nu1$, Fe-TiO_2: $h\nu2$, N-TiO_2: $h\nu3$, Fe-N-TiO_2: $h\nu4$). [68] (Reprinted with permission from Ref. [68]. Copyright Hindawi Publishing Corporation)

1.5 Approaches to Modify Electronic Band Structure

To solve this problem, efforts have been made to develop new visible light absorbing photocatalysts and to modify the photo-response of known photocatalyst to visible region. Several effective approaches have been developed to enhance the visible light absorption of photocatalysts for visible light-driven water splitting: (a) metal or/and nonmetal doping, (b) dye sensitization, (c) control the band structure by solid solutions, and (d) cocatalyst loading.

1.5.1 Doping

Here the main lattice is modified through addition or substitution, and depending on method, degree, and effect, the terms employed are doping or metal-insertion. In this context, the band gap is altered through addition of dopant cofactors.

1.5.2 Metal Ion Doping

Metal ion doping is an effective approach to modify the visible light response of wide band gap photocatalysts. A number of studies have been carried out on the metal doping of photocatalysts over the past decades. These host materials include TiO_2 [68], $SrTiO_3$ [69], and $La_2Ti_2O_7$ [70]. Figure 1.9d depicts the mechanism of metal ion doping to create active photocatalysts. Metal doping creates impurity energy levels in the forbidden band of wide band gap semiconductor. It can either be a donor level more positive than the original valence band or an acceptor level more negative than the original conduction band. As a result, the band gap is narrowed, which gives a visible light active photocatalyst.

As the most commonly studied materials, TiO_2 photocatalyst is exclusively adopted as a host material. TiO_2 with different doping metal ions have been reported to improve the visible-light absorption and photocatalytic activities, including V, Ni, Cr, Mo, Fe, Sn, Mn, and so on [68]. Although, the changed-color of TiO_2 powder with doping of transition metal cations can be observed, the photocatalytic activity drastically decreases even under band gap excitation due to formation of recombination centers. In order to develop efficient visible light responsive photocatalysts, the suitable dopants are needed. For example, codoping of Cr^{3+}/Ta^{5+}, Cr^{3+}/Sb^{5+}, and Ni^{2+}/Ta^{5+} can effectively increase the visible light absorption of $SrTiO_3$ [71]. The resulting materials can generate H_2 from aqueous methanol solutions under visible light with Pt cocatalyst. The dopants form electron donor levels in the forbidden band of the host materials, resulting in visible light response. When Ti^{4+} is replaced with Cr^{3+} or Ni^{2+}, the charge becomes unbalanced. This may result in the formation of recombination centers. Codoped metal cations such as Nb^{5+}, Ta^{5+}, and Sb^{5+} compensate the charge imbalance, which maintains the efficiency and visible light absorption.

1.5.3 Nonmetal Doping

In another approach, nonmetals are doped in wide band gap photocatalysts to adjust their visible light response. Different from metal doping, nonmetal doping is less likely to form donor level above the original valence band. Usually, the doping element forms a donor level above the original valence band which negatively shifts the valence band edge. A variety of wide band gap photocatalysts have been reported as the host materials for nonmetal doping, including Ti-based oxides [72], Zr-based oxides, Nb-based oxides [73], Ta-based oxides, etc. [74]. Nonmetal dopants, such as N, C, S, P, B, F, I, Cl, and Br, also have been extensively studied. For example, Ramakrishna and coworkers [75] compared the photoconversion efficiency (PEC) between TiO_2 and nitrogen-doped TiO_2 (N-TiO_2) and found that N dopants helped to narrow bandgap. Hence, the resulting efficiency of N-TiO_2 was 10 times higher than that of TiO_2 alone. Chen and coworkers [76] reported a PEC cell using photoanode made of carbon-doped ZnO and a 26.6% of incident photon-to-current efficiency (IPCE) irradiated under monochromatic wavelength of 400 nm was achieved. Xu and coworkers [77] studied the doping effect of sulfur on mesoporous carbon nitride (g-C_3N_4) for photocatalytic hydrogen evolution. They found that S-doping helped to lower the edge of conduction band by 0.25 eV, resulting in a 30 times more active than that of undoped g-C_3N_4. The studies have proved that nonmental doping is another effective route to engineering the bandgap of semiconductors.

1.5.4 Solid Solutions

In the doped photocatalysts, the energy level formed by dopant is usually discrete and thus not convenient for migration of electrons/holes. Besides, the formation of recombination sites by the dopant is inevitable. Therefore, other methods are needed to form continuous band and avoid charge recombination center. Forming solid solutions between wide and narrow band gap semiconductors is another promising approach. Varying the ratio of the compositions of the narrow and the wide band gap semiconductor in the solid solution is able to adjust the band gap and position. Domen and coworkers have reported a systematic study on GaN-ZnO solid solutions [78]. The band gaps of both GaN and ZnO are larger than 3 eV. So the solid solution of GaN and ZnO is expected to have a band gap greater than 3 eV, concerning the large band gap of GaN and ZnO. However, a much narrower band gap is observed for GaN-ZnO solid solution than expectation. This is attributed to the *p-d* repulsion between the N-2*p* and Zn-3*d* orbitals which shifted the valence-band maximum upward without affecting the conduction-band minimum [79]. As a result, the band position of GaN-ZnO solid solution can be adjusted by changing the composition of solid solution. At optimized condition, the GaN-ZnO solid solutions were able to split water under visible light with a quantum yield of 2.5% when $Rh_{2-y}Cr_yO_3$ was loaded as a cocatalyst [80]. The charge combination within the solid solution is largely prevented compared with doped sample, which explains the high photocatalytic performance of $Rh_{2-y}Cr_yO_3/(Ga_{1-x}Zn_x)(N_{1-x}O_x)$ system.

1.5.5 Dye Sensitization

Dye sensitization is another powerful method to enhance the visible-light harvesting of wide band gap semiconductors [81]. It has been actively studied in solar energy conversion systems including dye-sensitized solar cells [82] and dye-sensitized photocatalytic reactions [83]. The dye-sensitized solar cell has attracted much attention since the work by work O'Regan and Grätzel, owing to its stability, low cost, and efficiency [84]. The mechanism of dye-sensitizing usually involves the excitation of the dye and charge transfer from the dye to the semiconductor. The dye adsorbed onto the semiconductor is excited by visible light, and thus electrons are injected into the conduction band of the semiconductor in which water is reduced to H_2. The oxidized dye molecules received electrons from the electron donor and then are substantially reduced and regenerated.

Ruthenium (II) complex dyes are widely used as sensitizer for photocatalytic hydrogen production systems [85]. Besides, many other transition-metal complexes such as polypyridine complexes, phthalocyanine, alizarine, and metalloporphyrins with metal centers including Pt (II), Co (II), Zn (II), and Cr (III) have also been used as sensitizers [86]. The transitional metal complexes exhibit high efficiency and reasonable stability when combined with wide band gap photocatalysts for visible light-driven H_2 generation. However, the cost of some transition-metal complexes, especially Ru complexes, is too expensive to commercialize. Therefore, metal-free dyes, such as porphine, melocyanine, xanthene, and coumarin dyes, have also been developed [87].

1.5.6 Cocatalyst Loading

1.5.6.1 Noble Metal Cocatalyst

Transition metals have been extensively used to improve the efficiency of semiconductor, especially noble metals (Pt, Pd, Rd, Au, Ag, etc.). The mechanism could be described as the follows. When the electron–hole pairs generated by light irradiation, the hole will stay in the bulk semiconductor and the electron will migrate to cocatalyst and accumulated on the surface of cocatalyst (in this case, Pt is the cocatalyst). The reason is that the Fermi energy level of noble metal cocatalyst is always lower than that of semiconductor. As a result, cocatalyst loading improves the charge separation as well as the reduced possibilities of recombination. However, noble metal nanoparticles were not considered as photosensitizer until recently. The discovery of generation of hot-electron (electrons are not in thermal equilibrium with the atoms) induced by surface plasmon resonance (SPR) was found to be beneficial to photocatalytic hydrogen evolution. When the free electrons entrapped in a properly designed nanostructure oscillating with same frequency of incident light, eventually resonance occurred and intense electromagnetic field is generated [88]. The energetic carriers are capable of transferring energy to neighboring semiconductors. For example, Ingram and Linic [89] found that using Au as plasmonic-metal sensitizer incorporated with nitrogen-doped TiO_2

($N\text{-}TiO_2$), the photocurrent increased 10 times higher than that of $N\text{-}TiO_2$ alone. Cronin and coworkers [90] studied the gold particles coated TiO_2 films for photocatalytic hydrogen evolution. They observed a 66 times enhancement on generated photocurrent when gold particles were coated with TiO_2 film under 633 nm irradiation. Kim and coworkers [91] studied the size and surface density effects of gold nanoparticles on TiO_2-coated SnO_2 nanoparticles as well as photocatalytic activity. With appropriate amount of deposition of gold nanoparticles, the SPR excited gold particles can inject electrons to the CB of TiO_2 and enhance the efficiency of photocatalyst. The SPR effect depends on the size, shape, and nanostructure of the metals. Hence, this mechanism is considered as a new route to design the nanostructure and to harvest light using the entire solar spectrum, even beyond [92].

1.5.6.2 Nontransition-Metal Cocatalyst

A considerable number of transition-metal oxides, transition-metal hydroxide, transition-metal sulfide, and nonmetal oxide have been developed to enhance photocatalytic hydrogen evolution as cocatalyst. The nontransition-metal cocatalysts are believed to enhance the migration of photo-induced charge carriers and transfer to the active sites on the surface of photocatalyst.

The transition-metal oxides, such as RuO_2, NiO, and $K_4Ce_2M_{10}O_{30}$ ($M = Ta, Nb$), are also well known as effective cocatalysts [10, 93, 94]. Cocatalysts are generally accepted whose function is to trap electrons and enhance charge separation. Jaegermann and coworkers [95] studied the heterojunction of RuO_2/TiO_2 in details. It was realized that the enhanced photocatalytic activity resulted from band alignment at interface of RuO_2/TiO_2 caused by metallic behavior of RuO_2, then further improved the separation of photo-induced electron–hole pairs. Moreover, Toupance and coworkers [96] performed electron spin resonance (ESR) spectroscopy on the O^-, Ti^{3+}, and O^{2-} trapping center of charge carriers in RuO_2/TiO_2 composites and studied the mechanism of photocatalytic reaction. It was confirmed that the electrical conductivity was improved after deposition of RuO_2 forming the heterojunction of RuO_2/TiO_2, and consequently, the rate of charge separation and recombination rapidly increased. The electron spin resonance (ESR) analysis also confirmed that electrons were trapped at Ti^{3+}. Therefore, the photocatalytic reaction for RuO_2/TiO_2 in a methanol/water system can be described as follows:

$$RuO_2/TiO_2 + h\nu \rightarrow e^-(TiO_2) + h^+(RuO_2) \tag{1.12}$$

$$h^+ + CH_3OH \rightarrow \cdot CH_2OH + H^+ \tag{1.13}$$

$$\cdot CH_2OH \rightarrow HCHO + H^+ + e^- \tag{1.14}$$

$$2H_2O + 2e^- \rightarrow H_2 + 2OH^- \tag{1.15}$$

and the overall reaction is

$$CH_3OH \overset{h\upsilon,\ catalyst}{\rightarrow} HCHO + H_2 \tag{1.16}$$

The obtained formaldehyde could be further oxidized to formic acid, which is oxidized to carbon dioxide along with generation of hydrogen as follows:

$$HCHO + H_2O \overset{h\upsilon,\ catalyst}{\rightarrow} HCOOH + H_2 \tag{1.17}$$

$$HCOOH \overset{h\upsilon,\ catalyst}{\rightarrow} CO_2 + H_2 \tag{1.18}$$

Xu and Xu [97] reported a series of nickel-based cocatalysts (Ni, $Ni(OH)_2$, NiS, and NiS_2) for photocatalytic hydrogen production. They found the kinetics of electrochemical adsorption and desorption was accelerated when NiS coupled with CdS as follows:

$$NiS + e^- + H^+ \rightarrow HNiS \tag{1.19}$$

$$HNiS + e^- + H^+ \rightarrow NiS + H_2 \tag{1.20}$$

The coupling NiS/CdS not only improved the transportation of charge carriers, but improved the resistance to photocorrosion on CdS.

In addition to noble metal and nontransition metal, transition metal sulfides have been found to be good candidates as cocatalyst. Guo and coworkers [98] studied the effect of a series of transition metal sulfide, MnS, NiS, CuS, CoS, SnS, and Ag_2S, as cocatalyst deposited on $ZnIn_2S_4$. The result indicated that the deposition of all transition metal sulfides was able to enhance photocatalytic hydrogen evolution in terms of improved charge separation and inhibited charge recombination.

1.6 Nanostructure of Semiconductors

In semiconductor materials, size is a crucial factor for transfer and recombination of electron–hole pairs. The architectures of semiconductor also have been proven to play an important role in the photocatalytic hydrogen generation system with respect to electron transfer and efficient charge separation. From zero dimensional (0-D, quantum dots, nanoparticles), one dimensional (1-D, nanowires, nanotubes, nanoribbons), two dimensional (2-D, nanoplatelets, nanosheets), to three dimensional systems, each of categories exhibits uniqueness on performance.

1.6.1 0-D Material

Quantum dots (QDs) are nanocrystals with a few nanometers in diameter (2–10 nm). QDs have attracted lots of attention owing to their tuneable and size-dependent

electronic properties. The bandgap of QDs would vary due to the quantum confinement effect, which bandgap increases when size of nanomaterial reduces. In photocatalytic hydrogen generation, QDs usually work as a sensitizer with another semiconductor. Osterloh and coworkers [99] studied the photocatalytic hydrogen generation depending on the size of QDs ranging from 1.75 to 4.81 nm. Enhanced electron transfer between semiconductor and redox couple in solution with raised thermodynamic potential due to the widening bandgap was confirmed. Li and coworkers [100] used dual QDs, CdS, and CdSe, to sensitize double sided ZnO nanowire. Compared to single-sided photoanode, the efficiency of charge collection was substantially improved with assistance of QDs because of the direct interaction between QDs and ZnO nanowires. The possibility of fine tuning of QDs allows us to engineer desired photovoltaic devices.

When the size of nanomaterials increases to larger than 10 nm but less than 100 nm is considered as nanoparticles. Compared to bulk materials, the reduction in diameter usually leads to the increase of surface area and available active sites for photocatalysis taking place. TiO_2 nanoparticles are one of the most extensively studied nanoparticles. Syu and Liu [101] fabricated mesoporous N-TiO_2 nanoparticles for hydrogen generation from water-methanol aqueous solution. The resulting products have specific surface area ranging from 27 up to 67 m^2/g. With appropriate amount of nitrogen doping, the highest yield of generated hydrogen was about 8.9 μmol/h/g photocatalyst owing to the mesoporous TiO_2 with high surface area as active site. Mao and coworkers [102] used self-doped TiO_2 nanoparticles (hydrogenated TiO_2) to increase solar absorption for photocatalysis of water to produce hydrogen. The bandgap of hydrogenated-TiO_2 was 1.54 eV after bandgap engineering and was very stable without any degradation in a 22-day period. However, it was generally accepted that electron transfer would be limited in 0-D nanostructures because of lack of continuous conducting pathway.

1.6.2 1-D Material

In contrast to 0-D semiconductors, 1-D nanostructures are expected to have better charge transfer properties because of the shorter distance for recombination of charge carriers [103, 104]. One-dimensional (1 D) TiO_2 nanostructures have been widely investigated as catalysts in photocatalytic systems or in photovoltaic devices. The strategies to improve photocatalytic performance are similar, such as QDs loading, cocatalyst, doping, and dye sensitizer loading. Other nanowire semiconductors were studied as well. For example, Balbuena and coworkers [105] reported the hydrogen evolution using organic molecules functionalized Zn_3P_2 combined with the theoretical analysis. They found the organic functional groups not only prevented Zn_3P_2 nanowire from degradation, but also improved the electron transfer from interior to the surface of nanowire. Zheng and coworkers [106] studied different nanowires-based photoanode for PEC cell including TiO_2, α-Fe_2O_3, ZnO,

and $BiVO_4$. The TiO_2 nanowire photoanode showed the highest photocurrent density among the investigated samples. After a rapid flame treatment, the photocurrent increased by 2.7 times. Li and coworkers [107] used hydrogen-treated TiO_2 (H:TiO_2) nanowires for PEC water splitting. The pristine TiO_2 nanowires only showed 0.24% solar-to-hydrogen (STH) efficiency, while H:TiO_2 showed a significant improvement to 1.63%. Other 1-D nanostructures, such as nanotube, nanoribbon, and nanorod, also have been studied [108–110]. Wang and coworkers designed an Au/TiO_2 nanotube photoelectrode and produced a photocurrent density of ~150 μA cm^{-2} [108]. Amal and coworkers studied photocatalytic activity of sodium titanate ($Na_{1.48}H_{0.52}Ti_3O_7$), sodium hexatitanate ($Na_2Ti_6O_{13}$), and hydrogen titanate ($H_2Ti_3O_7$) nanoribbons. They found the hydrogen evolution rate of $Na_2Ti_6O_{13}$ was 10 times higher than TiO_2 nanorods owing to the tunnel structure beneficial for separation of electrons and holes [109]. Domen and coworkers fabricated vertically aligned Ta_3N_5 nanorod for photoeletrochemical water splitting. A photocurrent density was improved by 3.2 times compared to that of a thin film electrode. Recent studies indicate that 1 D nanomaterials are one of the desired nanostructures for photocatalytic hydrogen evolution.

1.6.3 2-D Material

In recent years, many 2-D materials are found to be promising for photocatalytic hydrogen evolution, such MoS_2, graphene/graphite combined with semiconductors. The graphene is a two-dimensional material with good electrical conductivity. Dai and coworkers [111] reported that uniformly dispersed MoS_2 nanosheet in reduced graphene oxide (RGO) network improved the HER by the synergistic effects of chemical and electrical coupling properties. Although the MoS_2/RGO was not used for photocatalytic hydrogen evolution, the results indicated that the conducting network could be considered as a network to form heterojunction of semiconductor/graphene photocatalysts. Peng and coworkers [112] investigated the synthesis of MoS_2/CdS/RGO at different pH values. At neutral pH, MoS_2 preferred to deposit on CdS, while at high pH (11), preferred to deposit on RGO. It is interesting that when MoS_2 was deposited on the surface of CdS, the light absorbance and photocatalyticity of the composite material were reduced. In contrast, when MoS_2 was deposited on RGO instead of CdS, the electron transfer was improved. As a result, the MoS_2/CdS/RGO synthesized at high pH (alkaline) showed better photocatalytic hydrogen evolution activity. Jin and coworkers [113] found that exfoliated metallic 1 T-MoS_2/Si electrodes showed improved photocurrent and could be considered as a potential alternative of noble metal catalyst for solar-driven hydrogen evolution. Wang and coworkers [114] investigated MoS_2 supported on different morphology of carbon network including multiwall carbon nanotube (MWCNT), mesoporous carbon (MC), graphene oxide (GO), and reduced graphene oxide (RGO). Their results showed that the resistance of MoS_2 was reduced with incorporation of carbon-based

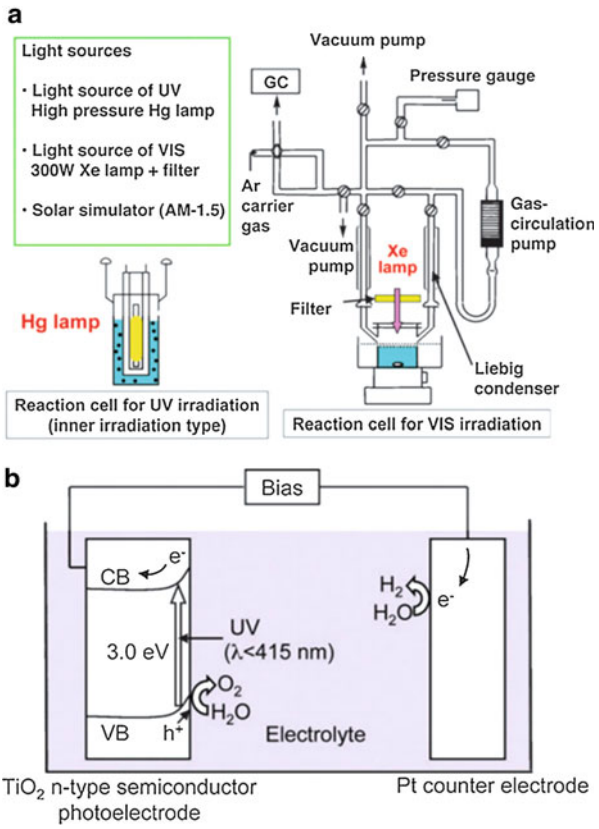

Fig. 1.10 (**a**) An example of the experimental setup for photocatalytic water splitting (Reprinted with permission from Ref. [6] from the Royal Society of Chemistry). (**b**) Honda–Fujishima effect-water splitting using a TiO_2 photoelectrode (Reprinted with permission from Ref. [115]. Copyright 1972 Nature Publishing Group)

materials. Among investigated carbon materials, amorphous MoS_2-loaded RGO showed the highest activity. The studies also revealed that the design of the hetero-junction is important for efficient composite photocatalyst.

Photocatalytic system. Due to its simplicity and intuition, photocatalytic hydrogen evolution from powder photocatalysts suspension has received considerable interests. In general, the photocatalysis system is composed of a simulated solar light equipped with and without a cutoff filter, an air-tight water-jacked reactor for controlling the temperature of system, and connected to a gas chromatography for analysis of gas composition, as shown in Fig. 1.10a. However, the drawbacks are not evitable: (1) hard to separate inactive photocatalyst, (2) hard to apply to a continuous flow system, and (3) hard to avoid the aggregation of photocatalyst.

Another common apparatus for water-splitting is shown in Fig. 1.10b. The photocatalysts are preloaded on a substrate, usually conducting glasses, as a photoelectrode and the noble metal, Pt, is acting as counter electrode. When the photoelectrode is exposed to a light source, the photocurrent is generated and the photo-induced electron will migrate to the counter electrode and then reduce the hydrogen

ion into hydrogen. The main disadvantages are: (1) setup is more sophisticated and (2) sometimes external bias is needed to initiate the reaction.

Recently, Jaramillo and coworkers [116] evaluated technical and economic feasibility of four types of centralized facilities for solar-driven hydrogen evolution based on two types of apparatus mentioned above. The powdered-suspension-based system operates at the lowest cost, \$1.6/kg H_2 generated. However, the safety and operation issues need to be conquered. Meanwhile, the operation cost of photoelectrode-based system can be enhanced by improving efficiency of photocatalysts.

1.7 Sacrificial Reagents

In recent studies, sacrificial reagents (SRs) have been extensively used for photocatalytic evolution. It has been reported that using sacrificial reagents is able to repress the combination of charge carriers and further improve the quantum efficiency. Shangguan and coworkers [117] compared several commonly used SRs including Na_2SO_3, Na_2S, KI, EDTA-Na, CH_3OH, $AgNO_3$, and $Fe(NO_3)_3$ in a Pt/TiO_2 photocatalysis system. Their results revealed that CH_3OH was the most effective electron donor for photocatalytic reduction of water forming hydrogen. In general, sacrificial reagents are acting as a hole scavenger to prevent charge recombination. The function of a hole scavenger (methanol in this case) could be described as follows [118]:

$$MeOH \rightarrow H_2CO + H_2 \tag{1.21}$$

$$H_2CO + H_2O \rightarrow H_2CO_2 + H_2 \tag{1.22}$$

$$H_2CO_2 \rightarrow CO_2 + H_2 \tag{1.23}$$

More recently, using glycerol as a sacrificial reagent becomes more and more popular because glycerol is produced as a byproduct in the production of biodiesel. Hebalkar and coworkers [119] used copper ion impregnated TiO_2 as catalyst and 5% glycerol ($C_3H_8O_3$) aqueous solution as a sacrificial reagent to perform photocatalytic hydrogen evolution. A maximum hydrogen production rate of 290 μmol h^{-1} was obtained using 2 wt% Cu_2O/TiO_2 photocatalytst under solar irradiation. However, there was no hydrogen produced without assistance of glycerol. The photocatalytic reaction can be described as follows:

$$C_3H_8O_3 + 3H_2O \rightarrow 7H_2 + 3CO_2 \tag{1.24}$$

It also can be observed that obtained hydrogen was partially contributed by the SRs used. Therefore, it is important to take into account the effect of SRs when evaluating the performance of photocatalyst.

1.8 Overall Water Splitting

In 1972, Fujishima and Honda's pioneering work [5] revealed that overall water splitting was feasible by illuminating the TiO_2 electrode with UV-light. Although intense efforts have been made in the past few decades, hydrogen obtained directly from photocatalysis is still facing challenging issues: (1) quantum efficiency remains to be improved, (2) efficient photocatalysts are made of rare and costly materials, (3) ability to efficiently split water requires additional energy, (4) sacrificial agents are needed, and (5) a large overpotential is needed for oxidation of water to oxygen.

Bao and coworkers [120] fabricate CoO nanoparticles from micropowder for overall water splitting without assistance of cocatalyst and sacrificial agent (Fig. 1.11a, approximately H_2:O_2 = 2:1) and a STH efficiency of 5% was obtained. Bulk CoO particle is not regarded as a good candidate for photocatalysis due to its

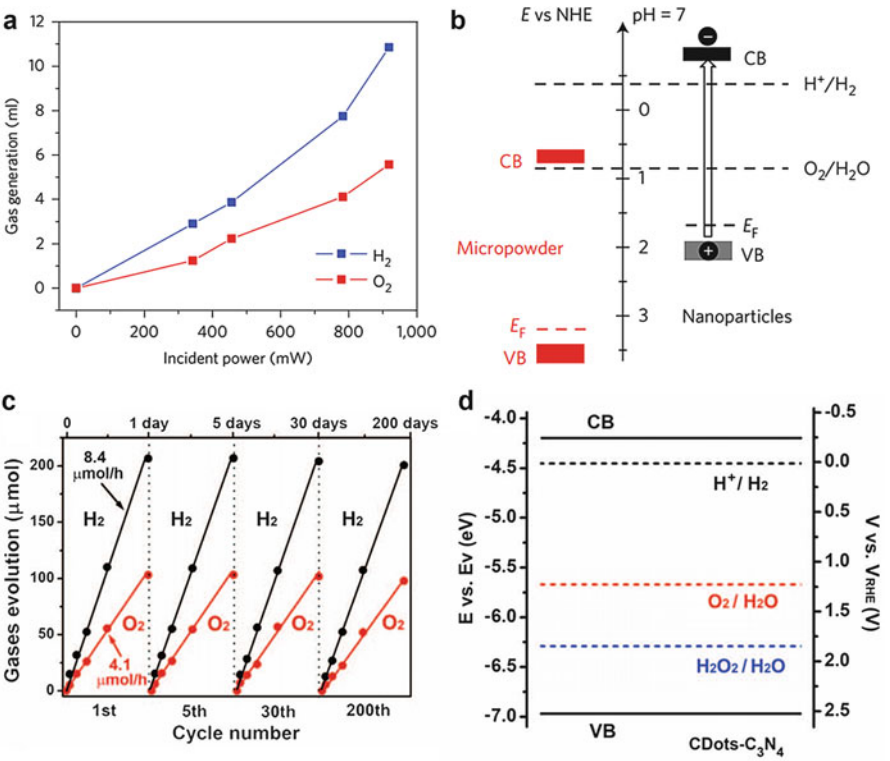

Fig. 1.11 (**a**) Production of hydrogen and oxygen from CoO nanoparticles (12 mg) as a function of incident laser power. The laser wavelength is 532 nm. (**b**) Band positions of CoO nanocrystals and micropowders according to the bandgaps and flat-band potentials [120]. (**c**) Typical time course of H_2 and O_2 production from water under visible light irradiation catalyzed by CDots-C_3N_4. (**d**) Band structure diagram for CDots-C_3N_4 [121]. ([**a**, **b**] Reprinted with permission from Ref. [120]. Copyright 2014 Nature Publishing Group. [**c**, **d**] Reprinted with permission from Ref. [121]. Copyright 2014 Nature Publishing Group)

CB position is more positive than hydrogen reduction potential. However, the qualitative difference of bandgap edge can be seen in Fig. 1.11b due to the quantum confinement effect; hence, necessary requirements were met for overall water splitting.

Later, Kang and coworkers [121] proposed a two-electron pathway using a metal-free photocatalysis, carbon nanodot-carbon nitride (CDots-C_3N_4.), for efficient water splitting under visible light illumination. Instead of a typical four-electron process for water splitting, they found a two-electron process which might be possible to be applied to water splitting:

The typical four-electron process for water-splitting is listed below:

$$2H_2O \rightarrow O_2 + 2H_2 \tag{1.25}$$

$$H_2 \text{ generation}: \quad 4H^+ + 4e^- \rightarrow 2H_2 \tag{1.26}$$

$$O_2 \text{ generation}: \quad 2H_2O \rightarrow O_2 + 4H^+ + 4e^- \ (1.23 \text{ eV}) \tag{1.27}$$

Two-electron pathway is as follows:

First step:

$$2H_2O \rightarrow H_2O_2 + H_2 \tag{1.28}$$

$$H_2 \text{ generation}: \quad 2H^+ + 2e^- \rightarrow H_2 \tag{1.29}$$

$$H_2O_2 \text{ generation}: \quad 2H_2O \rightarrow H_2O_2 + 2H^+ + 2e^- \ (1.78 \text{ eV}) \tag{1.30}$$

Second step: disproportionate reaction of hydrogen peroxide

$$H_2O_2 = \frac{1}{2}O_2 + H_2O \ \ \Delta G = -106.1 \text{ kJ/mol } (-1.1 \text{ eV}) \tag{1.31}$$

It can be realized that four-electron process is more thermodynamically favorable for water splitting. However, a higher reaction rate might be achieved that water is first oxidized to hydrogen peroxide and hydrogen followed by disproportionation of hydrogen peroxide. An overall solar energy conversion efficiency of 2% is achieved by the low-cost, earth-abundant, and environmental-friendly photocatalyst.

1.9 Perovskite-Structure Photocatalyst

Some metal oxides, such as $ATaO_3$ (A = Li, Na, and K), have similar perovskite-like structures, which is composed of corner-sharing TaO_6 octahedra between them [122]. The A cation strongly affects the photocatalytic activities of $ATaO_3$. The A cations influence the Ta–O–Ta bond angles, which are 143° for $LiTaO_3$, 163° for

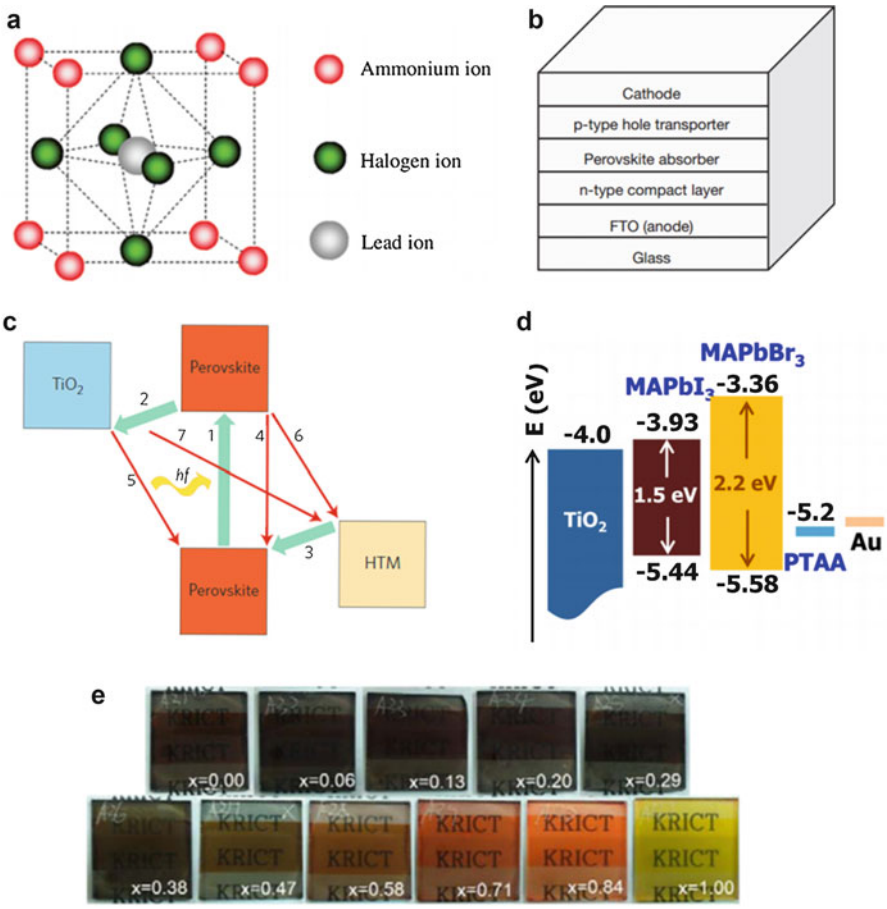

Fig. 1.12 (**a**) Crystal structures of perovskite compounds (Reprinted with permission from Ref. [124]. Copyright 2009 American Chemical Society). (**b**) Generic structure of a planar heterojunction *p–i–n* perovskite solar cell [125] (Reprinted with permission from Ref. [121]. Copyright 2014 Nature Publishing Group). (**c**) Schematic diagram of energy levels and electron transfer processes in a perovskite solar cell [126] (Reprinted with permission from Ref. [126]. Copyright 2014 Nature Publishing Group). (**d**) The conduction band minimum (CBM) and the valence band maximum (VBM) of $MAPbI_3$, $MAPbBr_3$, and TiO_2 are represented in eV, (**e**) Photographs of 3D $TiO_2/MAPb(I_{1-x}Br_x)_3$ bilayer nanocomposites on FTO glass substrates (MA: CH_3NH_3) [127] ([**d**, **e**] Reprinted with permission from Ref. [127]. Copyright 2013 American Chemical Society)

$NaTaO_3$, and 180° for $KTaO_3$. Excited energy or electron–hole pair in the crystal migrates more easily and the band gap becomes narrower when the bond angle approaches 180° [123]. Therefore, $KTaO_3$ demonstrates the highest delocalization of excited energy and smallest band-gap. It is expected to be the best photocatalyst in this system. However, the valence band of $KTaO_3$ is not negative enough to donate electrons to NiO cocatalyst. On the other hand, $NaTaO_3$ have a suitable band edge position and reasonable delocalization of excited energy. That is why it shows the

highest photocatalytic activity among those materials. As shown in Fig. 1.12a, the conduction band level of the $NaTaO_3$ photocatalyst is higher than that of NiO and the excited energy is delocalized in the $NaTaO_3$ crystal so that the exited electrons in the conduction band of the $NaTaO_3$ can transfer to the NiO. In conclusion, the high activity of NiO/$NaTaO_3$ is due to the suitable band structure.

1.10 Perovskite Solar Cell

In the past few years, a new class of solar cell, organic-inorganic metal halide perovskite solar cells, have emerged as a promising material for light harvesting. The perovskite is presented as the formula of ABX_3, where A is methylammonium cation, B is lead cation and X is halogen anion [CH_3NH_3X, where X is Cl, Br, or I]. The crystal structure is depicted in Fig. 1.12a. In 2012, Miyasaka and coworkers [124] were the first to report efficient organometal halide perovskites whose efficiency was 3.81%. To date, the highest energy conversion efficiency has researched a confirmed 20.1%. Although the perovskite solar cell will encounter degradation when exposed to ultraviolet irradiation and moisture, the rapidly improvement of efficiency makes it possibly an alternative of silicon based solar cells.

The generic structure of a perovskite solar cell is shown in Fig. 1.12b. In a perovskite solar cell, a perovskite absorber with or without metal oxide scaffold is sandwiched between electron and hole transport layer (HTM), followed by electrodes. Upon light irradiation, the charge carriers are created in the absorber layer and travel through the pathway accordingly to the transport layers, electrodes, and the interface. Hence, it is essential to manipulate the carriers moving along the desired pathway in order to improve power conversion efficiency (PCE).

The possible route of light harvesting for perovskites is depicted in Fig. 1.12c, which is similar to a typical semiconductor. Some key steps are involved: (1) generation of electron–hole pairs by light energy absorption, (2) electrons migrate to conduction band (CB) of TiO_2, (3) photo-induced holes migrate from the HTM, 2,2′,7,7′-tetrakis-(*N*,*N*-di-*p*-methoxyphenyl-amine)-9,9′-spirobifluorene (*spiro*-MeOTAD) in this case, and (4) electron–hole pairs recombination, back charge transfer of TiO_2/interface, perovskite/HTM (5,6), and back transfer between TiO_2/HTM (7). In order to improve performance, (1)–(3) is the desired route and undesired route (4)–(7) should be avoided if possible.

Miyasaka and coworkers [124] used a self-organization process to deposit nanocrystalline particles of $CH_3NH_3PbX_3$ (X = Br, I) on a mesoporous film of TiO_2 layer coated on a fluorine-doped SnO_2 transparent conductive glass (FTO) as a photoanode. A Pt-coated FTO glass was used as the counter electrode (cathode) and the cell was assembled with filling in an organic electrolyte solution containing lithium halide and halogen. The PCE reached 3.13% for the $CH_3NH_3PbBr_3$ perovskite solar cell and increased to 3.81% when bromide was replaced with iodide ($CH_3NH_3PbI_3$). Although all the devices were not stable, their work leads to a new direction of solar cell.

Subsequently, Grätzel, Park and coworkers [128] employed similar structure but replaced the liquid electrolyte with a solid state sensitizer, *spiro*-MeOTAD, as HTM which was previously used for organic LEDs [129]. It was found that the instability of liquid cell was caused by dissolution of perovskite particles into iodide electrolyte. Therefore, the resulting all-solid-state perovskite solar cell yielded promising power conversion efficiency (PCE) of 9.7% and was stable in a 500 h of durability test. Later on, Snaith and coworkers [130] reported a meso-superstructured solar cell delivering a PCE of 10.9% along with several important findings. First, they found iodide-chloride mixed halide perovskite solar cell provided with better stability as well as performance compared to that of pure iodide cell. Second, using a thin perovskite layer coated insulate material, Al_2O_3, as a scaffold, was able to improve the open-circuit voltage and then boosted the PCE to 10.9%. Third, perovskite material was found not just to be a sensitizer but with ability to transfer both of carriers to corresponding terminals. Their work simplified the multijunction devices by eliminating the requirement for the lattice matching in conventional multijunction solar cells.

A PCE of 12% was achieved by Grätzel, Seok, and coworkers [131] while using poly-triarylamine (PTAA) as a HTM. Various organic compounds were investigated including poly-3-hexylthiophene (P3HT), poly-[2,1,3-benzothiadiazole-4,7-diyl [4,4-bis(2-ethylhexyl)-4H-cyclopenta[2,1-b:3,4-b′]dithiophene-2,6-diyl]] (PCPDTBT), (poly-[[9-(1-octylnonyl)-9H-carbazole-2,7-diyl]-2,5-thiophenediyl-2,1,3-benzothiadiazole-4,7-diyl-2,5-thiophenediyl]) (PCDTBT), and poly-triarylamine (PTAA) as optional HTMs or electron-blocking layers. They realized the combination of a 3-dimentional composites of $TiO_2/CH_3NH_3PbI_3$ and complementary well-matched polymeric hole conductors were the key to good performance.

The Seok's group [127] further improved the PCE to 12.3% combining similar structures and mixed-halide perovskite material ($CH_3NH_3PbI_{3-x}Br_x$). The contents of Br were found to play an important role in the mixed-halide cell. The band configuration is shown in Fig. 1.12d and the synthesized mixed-halide perovskite cell is shown in Fig. 1.12e. The highest initial efficiency could be obtained among investigated cells was with low Br content due to a lower bandgap. On the other hand, cells with high Br content showed good resistance to humidity. In addition, the advantage of using mixed-halide perovskite ($CH_3NH_3PbI_{3-x}Br_x$) as light absorber is that it has been proven that photogenerated charge carriers in mixed-halide perovskite ($CH_3NH_3PbI_{3-x}Br_x$) are with higher diffusion distance compared to that of pure iodide cell that is >1000 nm [132], suggesting charge carriers are able to diffuse through the perovskite layer.

The key factor makes a significant improvement of PCE from ~3% to >10% is the utilization of solid-state spiro-MeOTAD as HTM. The preparation of solid-state HTM by solution-processed method is to dissolve *spiro*-MeOTAD into solvent following by spin-coating on perovskite-coated TiO_2 and then thermal evaporation of solvent [128]. Snaith and coworkers developed perovskite cell by vapor-processed method and compared to solution-processed TiO_2 compact layer as well as perovskite layer. Figure 1.13a, b shows the top view of SEM images, and Fig. 1.13c, d shows the SEM images of cross-section area of obtained perovskite

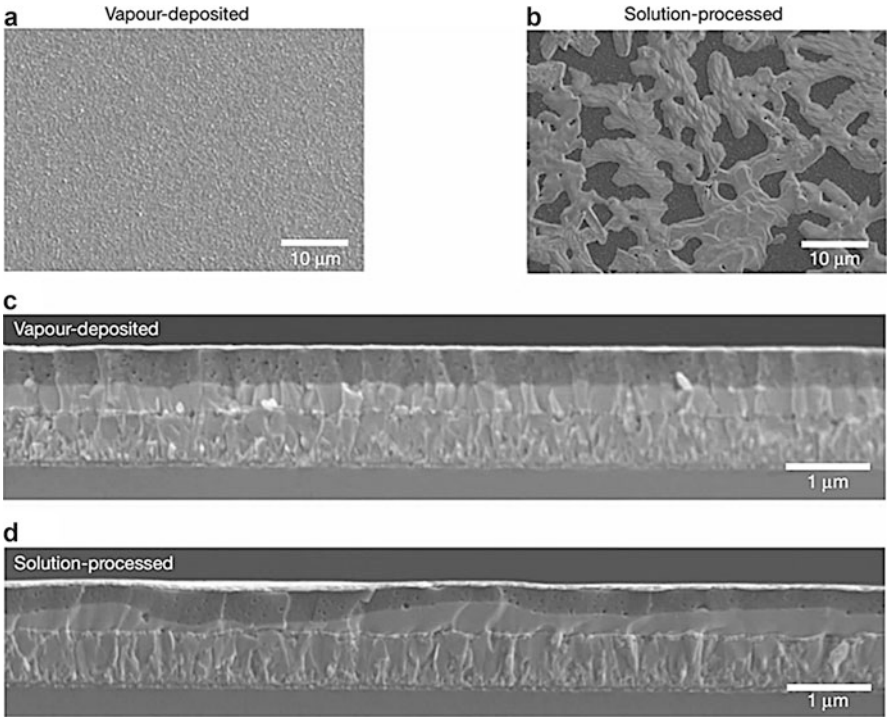

Fig. 1.13 Thin-film topology characterization. (**a**, **b**) SEM top views of a vapor-deposited perovskite film (**a**) and a solution-processed perovskite film (**b**). (**c**, **d**) Cross-sectional SEM images under lower magnification of completed solar cells constructed from a vapor deposited perovskite film (**c**) and a solution-processed perovskite film (**d**) [125] (Reprinted with permission from Ref. [125]. Copyright 2013 Nature Publishing Group)

film. It was observed that the solution-processed perovskite film did not fully cover the whole layer, while the perovskite film prepared by vapor-deposited was uniform and had a better coverage. The cross-sectional SEM images showed both of the perovskite film and HTM layer were flat and uniform. In contrast, solution-processed perovskite film and HTM layer presented undulation characteristics with varied thickness. Therefore, the transport of charge carriers might be beneficial from the uniform structure prepared by the vapor-deposited perovskite film and HTM layer. The PCE are 8.6% and 15.4% for solution-processed and vapor-deposited cell, respectively.

spiro-MeOTAD mainly involves in the perovskite solar cells. However, it is costly because it has to be synthesized at extremely low temperature, which would raise the overall cost of perovskite solar cell. Recently, the effect of different HTM on charge recombination in perovskite solar cell was investigated by Johansson and coworkers [133]. spiro-OMeTAD, P3HT, and 4-(diethylamino)-benzaldehyde diphenylhydrazone (DEH) were used as HTM layer. They studied the lifetime of photogenerated electrons in the devices and found spiro-OMeTAD had the best

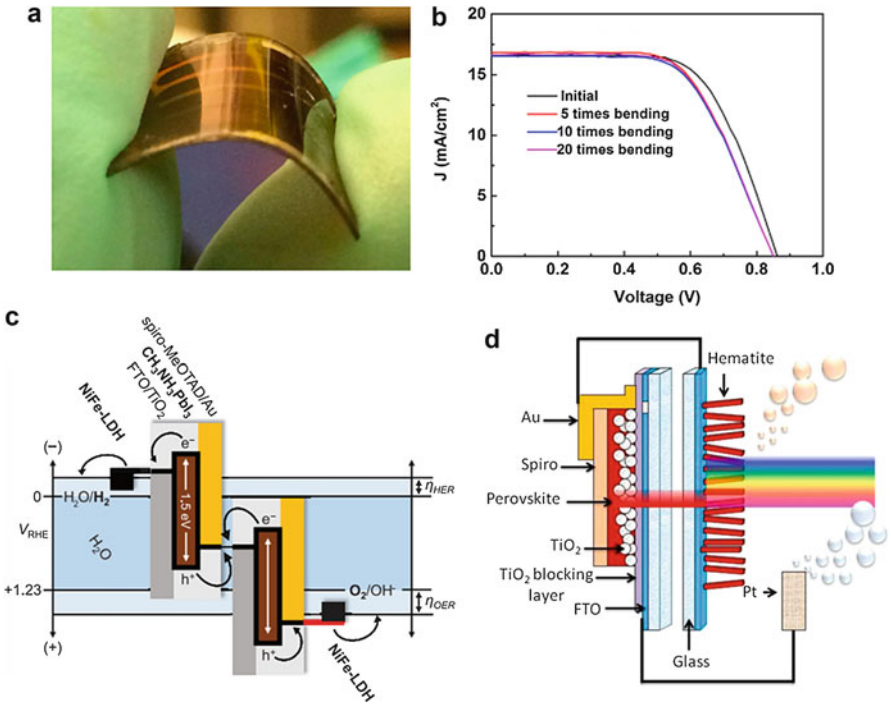

Fig. 1.14 (**a**) Photo image of flexible perovskite solar cells on PET/ITO substrate, and (**b**) device performance of the perovskite solar cells on PET/ITO flexible substrate before and after bending [136] (Reprinted with permission from Ref. [136]. Copyright 2014 American Chemical Society). (**c**) A generalized energy schematic of the perovskite tandem cell for water splitting [139] and (**d**) Schematic of the dual junction perovskite solar cell/hematite photoanode tandem cell [141] (Reprinted with permission from Ref. [141]. Copyright 2015 American Chemical Society)

performance among investigated HTMs. Etgar and coworkers [134] studied mixed-halide perovskite without HTM and found any composition of perovskites were capable of acting as light harvester as well as HTM. A PCE of 8.54% was realized under 1 sun illumination. Their work proves the possibilities of developing HTM-free perovskite solar cell.

The fabrication of perovskite solar cell usually requires high temperature for the sintering of the compact layer of TiO_2, which might limit its application. In 2013, Snaith and coworkers [135] attempted to reduce the processing temperature from 500 °C to <150 °C while kept PCE up to 12.3%. Al_2O_3-coated FTO glass was selected to replace TiO_2 as mesoporous film and all of the processing steps were maintained below 150 °C. Subsequently, Yang and coworkers [135] developed a solution-processing method to fabricate perovskite solar cell under 120 °C using a flexible conductive polyethylene terephthalate (PET)/ITO substrate and a PCE of 9.2% was realized. It is worth noticing that bending test was performed on the flexible device as shown in Fig. 1.14a, b. The results showed the performance of the device

was well-kept after up to 20 times bending. The low-temperature processing method broadens the usage of the perovskite solar cells for wearing and portable devices.

Although a PCE of 20.1% was achieved, maintaining long-term stability of perovskite solar cell is still challenging. Moreover, it is competitive with fossil fuels in terms of low cost and high efficiency for using solar energy as a sustainable energy source. Water photolysis by perovskite solar cell provides with the possibility owing to recent progress. The water splitting requires at least 1.23 V as a thermodynamic driving force, but overpotentials of 1.8–2 V associated with the kinetics are usually needed. Open-circuit voltages of at least 0.9 V and up to 1.5 V were reported recently [137, 138], suggesting that two cells connected in series would be sufficient to boost the reaction.

Grätzel and coworkers [139] produced perovskite solar cell with a PCE of 17.3% and connected two cells in series combined with earth-abundant electrocatalysts (NiFe layered double hydroxides in this case) as shown in Fig. 1.14c. Their photoelectrochemical system generated a 12.3% water-to-hydrogen efficiency, which is close to a theoretical upper limit of 17.8%. Although result was promising, the current density dropped to 80% of original value after 2 h of operation, indicating that it is essential to improve the stability. Another attempt was made by Mathews and coworkers. Hematite (Fe_2O_3) was incorporated with perovskite solar cell forming a single tandem cell (Fig. 1.14d) whose photo-potential (1.87 V) was higher than thermodynamic and kinetic requirements (1.6 V) and a STH efficiency of 2.4% was achieved. Kamat and coworkers developed a tandem cell composed of $BiVO_4$ as photoanode along with single-junction perovskite solar cell [140]. The all-solution processed procedure enables a low-cost photoelectrochemical water-splitting system with a solar-to-hydrogen (STH) conversion efficiency of 2.5% at neutral pH.

1.11 Summary and Future Prospects

Hydrogen obtained from photocatalytic system and photovoltaic devices is a promising alternative energy source in terms of sustainability. The fundamental knowledge and techniques developed in the earlier years are useful and provide with better understanding on design new materials and devices. Many factors that affect the solar energy conversion efficiency need to be considered toward effective photocatalytic hydrogen production system.

The rapidly increased efficiency, ease of processing, and earth-abundance of perovskite solar cell makes it possibly to be commercialized in next few years. Multiple attempts have been made to achieve long-term stability and to reduce toxicity because lead presented in the structure. A premium product would be brought to market combining both perovskite and existing technologies in the near future.

Acknowledgment S. Yuan was supported by U. S. Department of Energy, Office of Science, Office of Basic Energy Sciences (DE-SC0001015) and Texas A&M Energy Institute Graduate Fellowship Program Funded by ConocoPhillips. Y.-H. Yu would like to thank for the valuable discussion with Dr. Balbuena and Dr. Vaddiraju in Department of Chemical Engineering, Texas A&M University.

References

1. P. Moriarty, D. Honnery, What is the global potential for renewable energy? Renew. Sust. Energ. Rev. **16**, 244–252 (2012)
2. N.S. Lewis, D.G. Nocera, Powering the planet: chemical challenges in solar energy utilization. Proc. Natl. Acad. Sci. **103**, 15729–15735 (2006)
3. R. Perez, M. Perez, A fundamental look at energy reserves for the planet. IEA SHC Solar Update **50**, 2–3 (2009)
4. B. Jagannathan, J.H. Golbeck, in *Encyclopedia of Microbiology*, ed. by M. Schaechter, 3rd edn. (Academic, Oxford, 2009), pp. 325–341
5. A. Fujishima, K. Honda, Photolysis-decomposition of water at the surface of an irradiated semiconductor. Nature **238**, 37–38 (1972)
6. A. Kudo, Y. Miseki, Heterogeneous photocatalyst materials for water splitting. Chem. Soc. Rev. **38**, 253–278 (2009)
7. M. Gratzel, *Energy Resources Through Photochemistry and Catalysis* (Elsevier, Amsterdam, 2012)
8. X. Wang, K. Maeda, A. Thomas, K. Takanabe, G. Xin, J.M. Carlsson, K. Domen, M. Antonietti, A metal-free polymeric photocatalyst for hydrogen production from water under visible light. Nat. Mater. **8**, 76–80 (2009)
9. K. Maeda, K. Domen, New non-oxide photocatalysts designed for overall water splitting under visible light. J. Phys. Chem. C **111**, 7851–7861 (2007)
10. M.G. Walter, E.L. Warren, J.R. McKone, S.W. Boettcher, Q. Mi, E.A. Santori, N.S. Lewis, Solar water splitting cells. Chem. Rev. **110**, 6446–6473 (2010)
11. Z. Chen, H.N. Dinh, E. Miller, *Photoelectrochemical Water Splitting. Standards, Experimental Methods, and Protocols* (Springer, New York, 2013)
12. X. Chen, S. Shen, L. Guo, S.S. Mao, Semiconductor-based photocatalytic hydrogen generation. Chem. Rev. **110**, 6503–6570 (2010)
13. K. Domen, S. Naito, M. Soma, T. Onishi, K. Tamaru, Photocatalytic decomposition of water vapour on an NiO–$SrTiO_3$ catalyst. J. Chem. Soc. Chem. Commun. **12**, 543–544 (1980). doi:10.1039/C39800000543
14. S. Sato, J. White, Photodecomposition of water over Pt/TiO_2 catalysts. Chem. Phys. Lett. **72**, 83–86 (1980)
15. K. Domen, A. Kudo, A. Shinozaki, A. Tanaka, K.-I., Maruya, T. Onishi, Photodecomposition of water and hydrogen evolution from aqueous methanol solution over novel niobate photocatalysts. J. Chem. Soc. Chem. Commun. 356–357 (1986). doi:10.1039/C39860000356
16. K. Sayama, H. Arakawa, Effect of carbonate addition on the photocatalytic decomposition of liquid water over a ZrO_2 catalyst. J. Photochem. Photobiol. A Chem. **94**, 67–76 (1996)
17. S. Ikeda, T. Itani, K. Nango, M. Matsumura, Overall water splitting on tungsten-based photocatalysts with defect pyrochlore structure. Catal. Lett. **98**, 229–233 (2004)
18. J. Ye, Z. Zou, M. Oshikiri, A. Matsushita, M. Shimoda, M. Imai, T. Shishido, A novel hydrogen-evolving photocatalyst $InVO_4$ active under visible light irradiation. Chem. Phys. Lett. **356**, 221–226 (2002)
19. H.M. Chen, C.K. Chen, Y.C. Chang, C.W. Tsai, R.S. Liu, S.F. Hu, W.S. Chang, K.H. Chen, Quantum dot monolayer sensitized ZnO nanowire – array photoelectrodes: true efficiency for water splitting. Angew. Chem. **122**, 6102–6105 (2010)
20. M. Machida, J.-I. Yabunaka, T. Kijima, Efficient photocatalytic decomposition of water with the novel layered tantalate $RbNdTa_2O_7$. Chem. Commun. 1939–1940 (1999). doi:10.1039/A905246A
21. S. Ikeda, M. Hara, J.N. Kondo, K. Domen, H. Takahashi, T. Okub, M. Kakihana, Preparation of a high active photocatalyst, $K_2La_2Ti_3O_{10}$, by polymerized complex method and its photocatalytic activity of water splitting. J. Mater. Res. **13**, 852–855 (1998)
22. D. Duonghong, E. Borgarello, M. Graetzel, Dynamics of light-induced water cleavage in colloidal systems. J. Am. Chem. Soc. **103**, 4685–4690 (1981)

23. S.-H. Lee, Y. Park, K.-R. Wee, H.-J. Son, D.W. Cho, C. Pac, W. Choi, S.O. Kang, Significance of hydrophilic characters of organic dyes in visible-light hydrogen generation based on TiO_2. Org. Lett. **12**, 460–463 (2009)
24. C. Xiaobo, Titanium dioxide nanomaterials and their energy applications. Chin. J. Catal. **30**, 839–851 (2009)
25. M. Anpo, S. Dohshi, M. Kitano, Y. Hu, M. Takeuchi, M. Matsuoka, The preparation and characterization of highly efficient titanium oxide-based photofunctional materials. Annu. Rev. Mater. Res. **35**, 1–27 (2005)
26. J. Chae, J. Lee, J.H. Jeong, M. Kang, Hydrogen production from photo splitting of water using the Ga-incorporated TiO_2s prepared by a solvothermal method and their characteristics. Bull. Kor. Chem. Soc. **30**, 302–308 (2009)
27. B. Zieliñska, E. Borowiak-Palen, R.J. Kalenczuk, Photocatalytic hydrogen generation over alkaline-earth titanates in the presence of electron donors. Int. J. Hydrog. Energy **33**, 1797–1802 (2008)
28. D. Zhao, S. Budhi, A. Rodriguez, R.T. Koodali, Rapid and facile synthesis of Ti-MCM-48 mesoporous material and the photocatalytic performance for hydrogen evolution. Int. J. Hydrog. Energy **35**, 5276–5283 (2010)
29. M. Shibata, A. Kudo, A. Tanaka, K. Domen, K.-I. Maruya, T. Onishi, Photocatalytic activities of layered titanium compounds and their derivatives for H_2 evolution from aqueous methanol solution. Chem. Lett. **16**, 1017–1018 (1987)
30. M.R. Allen, A. Thibert, E.M. Sabio, N.D. Browning, D.S. Larsen, F.E. Osterloh, Evolution of physical and photocatalytic properties in the layered titanates $A_2Ti_4O_9$ (A = K, H) and in nanosheets derived by chemical exfoliation. Chem. Mater. **22**, 1220–1228 (2009)
31. M. Machida, X.W. Ma, H. Taniguchi, J.-I. Yabunaka, T. Kijima, Pillaring and photocatalytic property of partially substituted layered titanates, $Na_2Ti_{3-x}M_xO_7$ and $K_2Ti_{4-x}M_xO_9$ (M = Mn, Fe, Co, Ni, Cu). J. Mol. Catal. A Chem. **155**, 131–142 (2000)
32. K. Domen, S. Naito, T. Onishi, K. Tamaru, M. Soma, Study of the photocatalytic decomposition of water vapor over a nickel (II) oxide-strontium titanate ($SrTiO_3$) catalyst. J. Phys. Chem. **86**, 3657–3661 (1982)
33. K. Domen, A. Kudo, T. Onishi, Mechanism of photocatalytic decomposition of water into H_2 and O_2 over NiO-$SrTiO_3$. J. Catal. **102**, 92–98 (1986)
34. K. Domen, S. Naito, T. Onishi, K. Tamaru, Photocatalytic decomposition of liquid water on a NiO/$SrTiO_3$ catalyst. Chem. Phys. Lett. **92**, 433–434 (1982)
35. K. Sayama, H. Arakawa, Photocatalytic decomposition of water and photocatalytic reduction of carbon dioxide over zirconia catalyst. J. Phys. Chem. **97**, 531–533 (1993)
36. K. Sayama, H. Arakawa, Effect of Na_2CO_3 addition on photocatalytic decomposition of liquid water over various semiconductor catalysis. J. Photochem. Photobiol. A Chem. **77**, 243–247 (1994)
37. Y. Yuan, X. Zhang, L. Liu, X. Jiang, J. Lv, Z. Li, Z. Zou, Synthesis and photocatalytic characterization of a new photocatalyst $BaZrO_3$. Int. J. Hydrog. Energy **33**, 5941–5946 (2008)
38. K. Sayama, H. Arakawa, K. Domen, Photocatalytic water splitting on nickel intercalated A 4 $Ta_xNb_{6-x}O_{17}$ (A = K, Rb). Catal. Today **28**, 175–182 (1996)
39. X. Chen, T. Yu, X. Fan, H. Zhang, Z. Li, J. Ye, Z. Zou, Enhanced activity of mesoporous Nb_2O_5 for photocatalytic hydrogen production. Appl. Surf. Sci. **253**, 8500–8506 (2007)
40. K. Domen, A. Kudo, M. Shibata, A. Tanaka, K.-I. Maruya, T. Onishi, Novel photocatalysts, ion-exchanged $K_4Nb_6O_{17}$, with a layer structure. J. Chem. Soc. Chem. Commun. **23**, 1706–1707 (1986)
41. A. Kudo, K. Sayama, A. Tanaka, K. Asakura, K. Domen, K. Maruya, T. Onishi, Nickel-loaded $K_4Nb_6O_{17}$ photocatalyst in the decomposition of H_2O into H_2 and O_2: structure and reaction mechanism. J. Catal. **120**, 337–352 (1989)
42. K. Sayama, A. Tanaka, K. Domen, K. Maruya, T. Onishi, Photocatalytic decomposition of water over a Ni-loaded $Rb_4Nb_6O_{17}$ catalyst. J. Catal. **124**, 541–547 (1990)

43. Y. Miseki, H. Kato, A. Kudo, Water splitting into H_2 and O_2 over $Cs_2Nb_4O_{11}$ photocatalyst. Chem. Lett. **34**, 54–55 (2005)
44. H. Kato, A. Kudo, New tantalate photocatalysts for water decomposition into H_2 and O_2. Chem. Phys. Lett. **295**, 487–492 (1998)
45. Y. Takahara, J.N. Kondo, T. Takata, D. Lu, K. Domen, Mesoporous tantalum oxide. 1. Characterization and photocatalytic activity for the overall water decomposition. Chem. Mater. **13**, 1194–1199 (2001)
46. A. Kudo, H. Kato, Effect of lanthanide-doping into $NaTaO_3$ photocatalysts for efficient water splitting. Chem. Phys. Lett. **331**, 373–377 (2000)
47. H. Kato, K. Asakura, A. Kudo, Highly efficient water splitting into H_2 and O_2 over lanthanum-doped $NaTaO_3$ photocatalysts with high crystallinity and surface nanostructure. J. Am. Chem. Soc. **125**, 3082–3089 (2003)
48. H. Kadowaki, N. Saito, H. Nishiyama, H. Kobayashi, Y. Shimodaira, Y. Inoue, Overall splitting of water by RuO_2-loaded $PbWO_4$ photocatalyst with $d^{10}s^2$-d^0 configuration. J. Phys. Chem. C **111**, 439–444 (2007)
49. T.-V. Nguyen, K.-J. Kim, O.-B. Yang, Photocatalytic water decomposition for hydrogen production over silicotungstic acid–silica photocatalyst. J. Photochem. Photobiol. A Chem. **173**, 56–63 (2005)
50. X. Zhang, Z. Ai, F. Jia, L. Zhang, X. Fan, Z. Zou, Selective synthesis and visible-light photocatalytic activities of $BiVO_4$ with different crystalline phases. Mater. Chem. Phys. **103**, 162–167 (2007)
51. H. Xu, H. Li, C. Wu, J. Chu, Y. Yan, H. Shu, Z. Gu, Preparation, characterization and photocatalytic properties of Cu-loaded $BiVO_4$. J. Hazard. Mater. **153**, 877–884 (2008)
52. J. Sato, N. Saito, H. Nishiyama, Y. Inoue, New photocatalyst group for water decomposition of RuO_2-loaded p-block metal (In, Sn, and Sb) oxides with d10 configuration. J. Phys. Chem. B **105**, 6061–6063 (2001)
53. J. Sato, N. Saito, H. Nishiyama, Y. Inoue, Photocatalytic water decomposition by RuO_2-loaded antimonates, $M_2Sb_2O_7$ (M = Ca, Sr), $CaSb_2O_6$ and $NaSbO_3$, with d^{10} configuration. J. Photochem. Photobiol. A Chem. **148**, 85–89 (2002)
54. J. Sato, H. Kobayashi, K. Ikarashi, N. Saito, H. Nishiyama, Y. Inoue, Photocatalytic activity for water decomposition of RuO_2-dispersed Zn_2GeO_4 with d^{10} configuration. J. Phys. Chem. B **108**, 4369–4375 (2004)
55. H. Kadowaki, J. Sato, H. Kobayashi, N. Saito, H. Nishiyama, Y. Simodaira, Y. Inoue, Photocatalytic activity of the RuO_2-dispersed composite p-block metal oxide $LiInGeO_4$ with d^{10}-d^{10} configuration for water decomposition. J. Phys. Chem. B **109**, 22995–23000 (2005)
56. G.R. Bamwenda, T. Uesigi, Y. Abe, K. Sayama, H. Arakawa, The photocatalytic oxidation of water to O_2 over pure CeO_2, WO_3, and TiO_2 using Fe^{3+} and Ce^{4+} as electron acceptors. Appl. Catal. A Gen. **205**, 117–128 (2001)
57. H. Kadowaki, N. Saito, H. Nishiyama, Y. Inoue, RuO_2-loaded Sr^{2+}-doped CeO_2 with d^0 electronic configuration as a new photocatalyst for overall water splitting. Chem. Lett. **36**, 440–441 (2007)
58. Y. Yuan, J. Zheng, X. Zhang, Z. Li, T. Yu, J. Ye, Z. Zou, $BaCeO_3$ as a novel photocatalyst with 4f electronic configuration for water splitting. Solid State Ionics **178**, 1711–1713 (2008)
59. J.F. Reber, K. Meier, Photochemical production of hydrogen with zinc sulfide suspensions. J. Phys. Chem. **88**, 5903–5913 (1984)
60. T. Ohmori, H. Mametsuka, E. Suzuki, Photocatalytic hydrogen evolution on InP suspension with inorganic sacrificial reducing agent. Int. J. Hydrog. Energy **25**, 953–955 (2000)
61. K. Maeda, K. Teramura, N. Saito, Y. Inoue, K. Domen, Photocatalytic overall water splitting on gallium nitride powder. Bull. Chem. Soc. Jpn. **80**, 1004–1010 (2007)
62. N. Arai, N. Saito, H. Nishiyama, K. Domen, H. Kobayashi, K. Sato, Y. Inoue, Effects of divalent metal ion (Mg^{2+}, Zn^{2+} and Be^{2+}) doping on photocatalytic activity of ruthenium oxide-loaded gallium nitride for water splitting. Catal. Today **129**, 407–413 (2007)

63. J. Sato, N. Saito, Y. Yamada, K. Maeda, T. Takata, J.N. Kondo, M. Hara, H. Kobayashi, K. Domen, Y. Inoue, RuO_2-loaded β-Ge_3N_4 as a non-oxide photocatalyst for overall water splitting. J. Am. Chem. Soc. **127**, 4150–4151 (2005)
64. M. Matsumura, Y. Saho, H. Tsubomura, Photocatalytic hydrogen production from solutions of sulfite using platinized cadmium sulfide powder. J. Phys. Chem. **87**, 3807–3808 (1983)
65. A.B. Ellis, S.W. Kaiser, J.M. Bolts, M.S. Wrighton, Study of n-type semiconducting cadmium chalcogenide-based photoelectrochemical cells employing polychalcogenide electrolytes. J. Am. Chem. Soc. **99**, 2839–2848 (1977)
66. *Sunlight*. The Free Encyclopedia Wikipedia, Wikimedia Foundation, Inc. Retrieved 10, March, 2016, from https://en.wikipedia.org/wiki/Sunlight
67. J. Li, N. Wu, Semiconductor-based photocatalysts and photoelectrochemical cells for solar fuel generation: a review. Catal. Sci. Technol. **5**, 1360–1384 (2015)
68. X. Chen, S.S. Mao, Titanium dioxide nanomaterials: synthesis, properties, modifications, and applications. Chem. Rev. **107**, 2891–2959 (2007)
69. J. Liu, G. Chen, Z. Li, Z. Zhang, Electronic structure and visible light photocatalysis water splitting property of chromium-doped $SrTiO_3$. J. Solid State Chem. **179**, 3704–3708 (2006)
70. D.W. Hwang, H.G. Kim, J.S. Lee, J. Kim, W. Li, S.H. Oh, Photocatalytic hydrogen production from water over M-doped $La_2Ti_2O_7$ (M = Cr, Fe) under visible light irradiation ($\lambda > 420$ nm). J. Phys. Chem. B **109**, 2093–2102 (2005)
71. H. Kato, A. Kudo, Visible-light-response and photocatalytic activities of TiO_2 and $SrTiO_3$ photocatalysts codoped with antimony and chromium. J. Phys. Chem. B **106**, 5029–5034 (2002)
72. T. Lindgren, J.M. Mwabora, E. Avendaño, J. Jonsson, A. Hoel, C.-G. Granqvist, S.-E. Lindquist, Photoelectrochemical and optical properties of nitrogen doped titanium dioxide films prepared by reactive DC magnetron sputtering. J. Phys. Chem. B **107**, 5709–5716 (2003)
73. K. RavindranathanáThampi, Highly active meso–microporous TaON photocatalyst driven by visible light. Chem. Commun. 268–270 (2005). doi:10.1039/b413250e
74. X. Qiu, Y. Zhao, C. Burda, Synthesis and characterization of nitrogen-doped group IVB visible-light-photoactive metal oxide nanoparticles. Adv. Mater. **19**, 3995 (2007)
75. V.J. Babu, M.K. Kumar, A.S. Nair, T.L. Kheng, S.I. Allakhverdiev, S. Ramakrishna, Visible light photocatalytic water splitting for hydrogen production from N-TiO2 rice grain shaped electrospun nanostructures. Int. J. Hydrog. Energy **37**, 8897–8904 (2012)
76. Y.G. Lin, Y.K. Hsu, Y.C. Chen, L.C. Chen, S.Y. Chen, K.H. Chen, Visible-light-driven photocatalytic carbon-doped porous ZnO nanoarchitectures for solar water-splitting. Nanoscale **4**, 6515–9 (2012)
77. J. Hong, X. Xia, Y. Wang, R. Xu, Mesoporous carbon nitride with in situ sulfur doping for enhanced photocatalytic hydrogen evolution from water under visible light. J. Mater. Chem. **22**, 15006 (2012)
78. K. Maeda, T. Takata, M. Hara, N. Saito, Y. Inoue, H. Kobayashi, K. Domen, GaN: ZnO solid solution as a photocatalyst for visible-light-driven overall water splitting. J. Am. Chem. Soc. **127**, 8286–8287 (2005)
79. M. Yashima, H. Yamada, K. Maeda, K. Domen, Experimental visualization of covalent bonds and structural disorder in a gallium zinc oxynitride photocatalyst $(Ga_{1-x}Zn_x)(N_{1-x}O_x)$: origin of visible light absorption. Chem. Commun. **46**, 2379–2381 (2010)
80. K. Maeda, K. Teramura, D. Lu, T. Takata, N. Saito, Y. Inoue, K. Domen, Photocatalyst releasing hydrogen from water. Nature **440**, 295–295 (2006)
81. S. Anderson, E.C. Constable, M.P. Dare-Edwards, J.B. Goodenough, A. Hamnett, K.R. Seddon, R.D. Wright, Chemical modification of a titanium (IV) oxide electrode to give stable dye sensitisation without a supersensitiser. Nature **280**, 571–573 (1979)
82. N. Robertson, Catching the rainbow: light harvesting in dye-sensitized solar cells. Angew. Chem. Int. Ed. **47**, 1012–1014 (2008)
83. T.-V. Nguyen, J.C. Wu, C.-H. Chiou, Photoreduction of CO_2 over ruthenium dye-sensitized TiO_2-based catalysts under concentrated natural sunlight. Catal. Commun. **9**, 2073–2076 (2008)

84. B. O'regan, M. Grätzel, A low-cost, high-efficiency solar cell based on dye-sensitized colloidal TiO_2 films. Nature **353**, 737–740 (1991)
85. P. Wang, S.M. Zakeeruddin, J.E. Moser, M.K. Nazeeruddin, T. Sekiguchi, M. Grätzel, A stable quasi-solid-state dye-sensitized solar cell with an amphiphilic ruthenium sensitizer and polymer gel electrolyte. Nat. Mater. **2**, 402–407 (2003)
86. V. Zakharenko, A. Bulatov, V. Parmon, Pt (alizarine) 2 complex adsorbed on titanium dioxide as a sensitizer in photocatalytic evolution of dihydrogen. React. Kinet. Catal. Lett. **36**, 295–300 (1988)
87. S. Mathew, A. Yella, P. Gao, R. Humphry-Baker, F.E. CurchodBasile, N. Ashari-Astani, I. Tavernelli, U. Rothlisberger, K. NazeeruddinMd, M. Grätzel, Dye-sensitized solar cells with 13% efficiency achieved through the molecular engineering of porphyrin sensitizers. Nat. Chem. **6**, 242–247 (2014)
88. C. Clavero, Plasmon-induced hot-electron generation at nanoparticle/metal-oxide interfaces for photovoltaic and photocatalytic devices. Nat. Photonics **8**, 95–103 (2014)
89. D.B. Ingram, S. Linic, Water splitting on composite plasmonic-metal/semiconductor photoelectrodes: evidence for selective plasmon-induced formation of charge carriers near the semiconductor surface. J. Am. Chem. Soc. **133**, 5202–5 (2011)
90. Z. Liu, W. Hou, P. Pavaskar, M. Aykol, S.B. Cronin, Plasmon resonant enhancement of photocatalytic water splitting under visible illumination. Nano Lett. **11**, 1111–6 (2011)
91. S.T. Kochuveedu, D.-P. Kim, D.H. Kim, Surface-plasmon-induced visible light photocatalytic activity of TiO_2 nanospheres decorated by Au nanoparticles with controlled configuration. J. Phys. Chem. C **116**, 2500–2506 (2012)
92. M. Rycenga, C.M. Cobley, J. Zeng, W. Li, C.H. Moran, Q. Zhang, D. Qin, Y. Xia, Controlling the synthesis and assembly of silver nanostructures for plasmonic applications. Chem. Rev. **111**, 3669–712 (2011)
93. Y. Kuo, C.D. Frye, M. Ikenberry, K.J. Klabunde, Titanium–indium oxy(nitride) with and without RuO_2 loading as photocatalysts for hydrogen production under visible light from water. Catal. Today **199**, 15–21 (2013)
94. M. Tian, W. Shangguan, J. Yuan, L. Jiang, M. Chen, J. Shi, Z. Ouyang, S. Wang, $K_4Ce_2M_{10}O_{30}$ (M = Ta, Nb) as visible light-driven photocatalysts for hydrogen evolution from water decomposition. Appl. Catal. A Gen. **309**, 76–84 (2006)
95. M.T. Uddin, Y. Nicolas, C. Olivier, T. Toupance, M.M. Müller, H.-J. Kleebe, K. Rachut, J. Ziegler, A. Klein, W. Jaegermann, Preparation of RuO_2/TiO_2 mesoporous heterostructures and rationalization of their enhanced photocatalytic properties by band alignment investigations. J. Phys. Chem. C **117**, 22098–22110 (2013)
96. M.T. Uddin, O. Babot, L. Thomas, C. Olivier, M. Redaelli, M. D'Arienzo, F. Morazzoni, W. Jaegermann, N. Rockstroh, H. Junge, T. Toupance, New insights into the photocatalytic properties of RuO_2/TiO_2 mesoporous heterostructures for hydrogen production and organic pollutant photodecomposition. J. Phys. Chem. C **119**, 7006–7015 (2015)
97. Y. Xu, R. Xu, Nickel-based cocatalysts for photocatalytic hydrogen production. Appl. Surf. Sci. **351**, 779–793 (2015)
98. S. Shen, X. Chen, F. Ren, C.X. Kronawitter, S.S. Mao, L. Guo, Solar light-driven photocatalytic hydrogen evolution over $ZnIn_2S_4$ loaded with transition-metal sulfides. Nanoscale Res. Lett. **6**, 290 (2011)
99. M.A. Holmes, T.K. Townsend, F.E. Osterloh, Quantum confinement controlled photocatalytic water splitting by suspended CdSe nanocrystals. Chem. Commun. **48**, 371–3 (2012)
100. G. Wang, X. Yang, F. Qian, J.Z. Zhang, Y. Li, Double-sided CdS and CdSe quantum dot co-sensitized ZnO nanowire arrays for photoelectrochemical hydrogen generation. Nano Lett. **10**, 1088–92 (2010)

101. S.-H. Liu, H.-R. Syu, One-step fabrication of N-doped mesoporous TiO_2 nanoparticles by self-assembly for photocatalytic water splitting under visible light. Appl. Energy **100**, 148–154 (2012)
102. X. Chen, L. Liu, P.Y. Yu, S.S. Mao, Increasing solar absorption for photocatalysis with black hydrogenated titanium dioxide nanocrystals. Science **331**, 746–750 (2011)
103. A. Wolcott, W.A. Smith, T.R. Kuykendall, Y. Zhao, J.Z. Zhang, Photoelectrochemical water splitting using dense and aligned TiO_2 nanorod arrays. Small **5**, 104–11 (2009)
104. K. Nakata, A. Fujishima, TiO_2 photocatalysis: Design and applications. J. Photochem. Photobiol. C: Photochem. Rev. **13**, 169–189 (2012)
105. G. Ramos-Sanchez, M. Albornoz, Y.H. Yu, Z. Cheng, V. Vasiraju, S. Vaddiraju, F. El Mellouhi, P.B. Balbuena, Organic molecule-functionalized Zn_3P_2 nanowires for photochemical H_2 production: DFT and experimental analyses. Int. J. Hydrog. Energy **39**, 19887–19898 (2014)
106. I.S. Cho, M. Logar, C.H. Lee, L. Cai, F.B. Prinz, X. Zheng, Rapid and controllable flame reduction of TiO_2 nanowires for enhanced solar water-splitting. Nano Lett. **14**, 24–31 (2014)
107. G. Wang, H. Wang, Y. Ling, Y. Tang, X. Yang, R.C. Fitzmorris, C. Wang, J.Z. Zhang, Y. Li, Hydrogen-treated TiO2 nanowire arrays for photoelectrochemical water splitting. Nano Lett. **11**, 3026–33 (2011)
108. Z. Zhang, L. Zhang, M.N. Hedhili, H. Zhang, P. Wang, Plasmonic gold nanocrystals coupled with photonic crystal seamlessly on TiO_2 nanotube photoelectrodes for efficient visible light photoelectrochemical water splitting. Nano Lett. **13**, 14–20 (2013)
109. K. Kiatkittipong, A. Iwase, J. Scott, R. Amal, Photocatalysis of heat treated sodium- and hydrogen-titanate nanoribbons for water splitting, H_2/O_2 generation and oxalic acid oxidation. Chem. Eng. Sci. **93**, 341–349 (2013)
110. Y. Li, T. Takata, D. Cha, K. Takanabe, T. Minegishi, J. Kubota, K. Domen, Vertically aligned Ta_3N_5 nanorod arrays for solar-driven photoelectrochemical water splitting. Adv. Mater. **25**, 125–31 (2013)
111. Y. Li, H. Wang, L. Xie, Y. Liang, G. Hong, H. Dai, MoS_2 nanoparticles grown on graphene: an advanced catalyst for the hydrogen evolution reaction. J. Am. Chem. Soc. **133**, 7296–9 (2011)
112. Y. Li, H. Wang, S. Peng, Tunable photodeposition of MoS_2 onto a composite of reduced graphene oxide and CdS for synergic photocatalytic hydrogen generation. J. Phys. Chem. C **118**, 19842–19848 (2014)
113. Q. Ding, F. Meng, C.R. English, M. Caban-Acevedo, M.J. Shearer, D. Liang, A.S. Daniel, R.J. Hamers, S. Jin, Efficient photoelectrochemical hydrogen generation using heterostructures of Si and chemically exfoliated metallic MoS_2. J. Am. Chem. Soc. **136**, 8504–7 (2014)
114. X. Xia, Z. Zheng, Y. Zhang, X. Zhao, C. Wang, Synthesis of MoS_2-carbon composites with different morphologies and their application in hydrogen evolution reaction. Int. J. Hydrog. Energy **39**, 9638–9650 (2014)
115. A. Fujishima, K. Honda, Electrochemical photolysis of water at a semiconductor electrode. Nature **238**, 37–38 (1972)
116. B.A. Pinaud, J.D. Benck, L.C. Seitz, A.J. Forman, Z. Chen, T.G. Deutsch, B.D. James, K.N. Baum, G.N. Baum, S. Ardo, H. Wang, E. Miller, T.F. Jaramillo, Technical and economic feasibility of centralized facilities for solar hydrogen production via photocatalysis and photoelectrochemistry. Energy Environ. Sci. **6**, 1983 (2013)
117. H. Liu, J. Yuan, W. Shangguan, Photochemical reduction and oxidation of water including sacrificial reagents and Pt/TiO_2 catalyst. Energy Fuel **20**, 2289–2292 (2006)
118. N. Alenzi, W.-S. Liao, P.S. Cremer, V. Sanchez-Torres, T.K. Wood, C. Ehlig-Economides, Z. Cheng, Photoelectrochemical hydrogen production from water/methanol decomposition using Ag/TiO_2 nanocomposite thin films. Int. J. Hydrog. Energy **35**, 11768–11775 (2010)

119. K. Lalitha, G. Sadanandam, V. Durga Kumari, M. Subrahmanyam, B. Sreedhar, N.Y. Hebalkar, Highly stabilized and finely dispersed Cu_2O/TiO_2: a promising visible sensitive photocatalyst for continuous production of hydrogen from glycerol: water mixtures. J. Phys. Chem. C **114**, 22181–22189 (2010)
120. L. Liao, Q. Zhang, Z. Su, Z. Zhao, Y. Wang, Y. Li, X. Lu, D. Wei, G. Feng, Q. Yu, X. Cai, J. Zhao, Z. Ren, H. Fang, F. Robles-Hernandez, S. Baldelli, J. Bao, Efficient solar water-splitting using a nanocrystalline CoO photocatalyst. Nat. Nanotechnol. **9**, 69–73 (2014)
121. J. Liu, L. Yang, N. Liu, Y. Han, X. Zhang, H. Huang, Y. Lifshitz, S.-T. Lee, J. Zhong, Z. Kang, Metal-free efficient photocatalyst for stable visible water splitting via a two-electron pathway. Science **347**, 970–974 (2015)
122. H. Kato, A. Kudo, Water splitting into H_2 and O_2 on alkali tantalate photocatalysts $ATaO_3$ (A = Li, Na, and K). J. Phys. Chem. B **105**, 4285–4292 (2001)
123. M. Wiegel, M. Emond, E. Stobbe, G. Blasse, Luminescence of alkali tantalates and niobates. J. Phys. Chem. Solids **55**, 773–778 (1994)
124. A. Kojima, K. Teshima, Y. Shirai, T. Miyasaka, Organometal halide perovskites as visible-light sensitizers for photovoltaic cells. J. Am. Chem. Soc. **131**, 6050–6051 (2009)
125. M. Liu, M.B. Johnston, H.J. Snaith, Efficient planar heterojunction perovskite solar cells by vapour deposition. Nature **501**, 395–8 (2013)
126. M.A. Green, A. Ho-Baillie, H.J. Snaith, The emergence of perovskite solar cells. Nat. Photonics **8**, 506–514 (2014)
127. J.H. Noh, S.H. Im, J.H. Heo, T.N. Mandal, S.I. Seok, Chemical management for colorful, efficient, and stable inorganic-organic hybrid nanostructured solar cells. Nano Lett. **13**, 1764–9 (2013)
128. H.S. Kim, C.R. Lee, J.H. Im, K.B. Lee, T. Moehl, A. Marchioro, S.J. Moon, R. Humphry-Baker, J.H. Yum, J.E. Moser, M. Gratzel, N.G. Park, Lead iodide perovskite sensitized all-solid-state submicron thin film mesoscopic solar cell with efficiency exceeding 9%. Sci. Rep. **2**, 591 (2012)
129. J. Salbecka, N. Yu, J. Bauerb, F. Weissörtel, H. Bestgenb, Low molecular organic glasses for blue electroluminescence. Synth. Met. **91**, 209–215 (1997)
130. M.M. Lee, J. Teuscher, T. Miyasaka, T.N. Murakami, H.J. Snaith, Efficient hybrid solar cells based on meso-superstructured organometal halide perovskites. Science **338**, 643–647 (2012)
131. J.H. Heo, S.H. Im, J.H. Noh, T.N. Mandal, C.-S. Lim, J.A. Chang, Y.H. Lee, H.-j. Kim, A. Sarkar, M.K. Nazeeruddin, M. Grätzel, S.I. Seok, Efficient inorganic–organic hybrid heterojunction solar cells containing perovskite compound and polymeric hole conductors. Nat. Photonics **7**, 486–491 (2013)
132. S.D. Stranks, G.E. Eperon, G. Grancini, C. Menelaou, M.J.P. Alcocer, T. Leijtens, L.M. Herz, A. Petrozza, H.J. Snaith, Electron-hole diffusion lengths exceeding 1 micrometer in an organometal trihalide perovskite absorber. Science **342**, 341–344 (2013)
133. D. Bi, L. Yang, G. Boschloo, A. Hagfeldt, E.M. Johansson, Effect of different hole transport materials on recombination in $CH_3NH_3PbI_3$ perovskite-sensitized mesoscopic solar cells. J. Phys. Chem. Lett. **4**, 1532–6 (2013)
134. S. Aharon, B.E. Cohen, L. Etgar, Hybrid lead halide iodide and lead halide bromide in efficient hole conductor free perovskite solar cell. J. Phys. Chem. C **118**, 17160–17165 (2014)
135. J.M. Ball, M.M. Lee, A. Hey, H.J. Snaith, Low-temperature processed meso-superstructured to thin-film perovskite solar cells. Energy Environ. Sci. **6**, 1739 (2013)
136. J. You, Z. Hong, Y.M. Yang, Q. Chen, M. Cai, T.-B. Song, C.-C. Chen, S. Lu, Y. Liu, H. Zhou, Y. Yang, Low-temperature solution-processed perovskite solar cells with high efficiency and flexibility. ACS Nano **8**, 1674–1680 (2014)
137. S. Ryu, J.H. Noh, N.J. Jeon, Y. Chan Kim, W.S. Yang, J. Seo, S.I. Seok, Voltage output of efficient perovskite solar cells with high open-circuit voltage and fill factor. Energy Environ. Sci. **7**, 2614 (2014)

138. E. Edri, S. Kirmayer, M. Kulbak, G. Hodes, D. Cahen, Chloride inclusion and hole transport material doping to improve methyl ammonium lead bromide perovskite-based high open-circuit voltage solar cells. J. Phys. Chem. Lett. **5**, 429–33 (2014)
139. J. Luo, J.-H. Im, M.T. Mayer, M. Schreier, M.K. Nazeeruddin, N.-G. Park, S.D. Tilley, H.J. Fan, M. Grätzel, Water photolysis at 12.3% efficiency via perovskite photovoltaics and Earth-abundant catalysts. Science **345**, 1593–1596 (2014)
140. Y.S. Chen, J.S. Manser, P.V. Kamat, All solution-processed lead halide perovskite-$BiVO_4$ tandem assembly for photolytic solar fuels production. J. Am. Chem. Soc. **137**, 974–81 (2015)
141. D. Gurudayal, M. Sabba, H. Kumar, L.H. Wong, J. Barber, M. Gratzel, N. Mathews, Perovskite-hematite tandem cells for efficient overall solar driven water splitting. Nano Lett. **15**, 3833–9 (2015)

Transition Metal Complexes for Hydrogen Activation

2

Yuwei Kan and Qiang Zhang

Abstract

Hydrogen activation is a very important industrial process for hydrogenation reactions and ammonia production. The hydrogen splitting and hydride transfer process can be classified as homolytic and heterolytic cleavage of molecular hydrogen on mono- and multinuclear transition metal centers. Hydrogenase enzymes have inspired researchers in the field of organometallic chemistry to develop small molecule structural models of active sites and thus to mimic the biological system to activate molecular hydrogen. Multinuclear cluster complexes, including those containing heavy main group metals, can bind hydrogen molecule under mild conditions in a reversible fashion. This chapter aims at providing introductory review to cover various types of transition metal complexes that can split molecular hydrogen. The interaction between hydrogen molecule and metal centers, which determines the distance between two hydrogen atoms, will affect hydrogen splitting. The mechanism of such interactions will be discussed in details. Hydrogenation reactions catalyzed by transition metal complexes or heterogeneous nanocatalysts derived from metal cluster complexes will also be introduced.

Author Contribution: The chapter context was mainly compiled by Dr. Y. Kan under the supervision of Dr. Q. Zhang. The introduction part, chemical expression, and the revision of other subsections were examined and corrected by Dr. J. Liu and Dr. S. Bashir.

Y. Kan
Department of Chemistry, Texas A&M University, College Station, TX, USA

Department of Chemistry, Washington State University, Pullman, WA, USA
e-mail: yuwei.kan@chem.tamu.edu

Q. Zhang (✉)
Department of Chemistry, Washington State University, Pullman, WA, USA
e-mail: q.zhang@wsu.edu

Y.-P. Chen et al. (eds.), *Nanostructured Materials for Next-Generation Energy Storage and Conversion*, DOI 10.1007/978-3-662-53514-1_2

Abbreviations

BAr^F	$[B\{C_6H_3(CF_3)_2\}_4$
Bn	Benzyl
bq	7,8-Benzoquinolato
CDA	Cyclododecane
CDE	Cyclododecene
CDT	Cyclododecatriene
COD	1,5-Cyclooctadiene
Cp	η^5-Cyclopentadienyl
Cy	Cyclohexyl
DFT	Density functional theory
depe	1,2-bis(diethylphosphino)ethane
dppe	1,2-bis(diphenylphosphino)ethane
EAC	Ethyl (Z)-1-acetamidocinnamate
EPR	Electron paramagnetic resonance
EXAFS	Extended X-ray absorption fine structure
Fc	Ferrocene
NMR	Nuclear magnetic resonance
PCy_3	Tricyclohexylphosphine ligand
P^iPr^3	Triisopropylphosphine ligand
PR_2	Phosphido ligand
PR_3	Phosphine ligand
Py	Pyridine
ROP	Ring opening polymerization
TOF	Turnover Frequency
Tp	Trispyrazolylborate

Contents

2.1 Introduction and Background

Hydrogen gas (H_2) as an energy carrier has historically played an important role, for example production of synthetic methanol through steam reforming by BASF in Leuna, Germany, in 1923, and plays a vital role in a variety of industrial processes,

Scheme 2.1 $W(CO)_3(PR_3)_2(H_2)$ discovered by Kubas in 1984

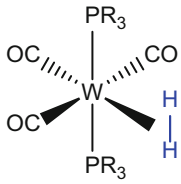

such as hydrogenation reactions, the production of ammonia (NH_3) from H_2 and nitrogen (N_2) that greatly supports the world's agriculture; and the processing of petrochemical in which crude oil is treated with H_2. Hydrogen is also considered as valuable future fuel which is environmental friendly. It attracts considerable attention to scientists all over the world to develop new plans for hydrogen storage and production. H_2 molecule has a very low chemical reactivity due to the very strong, nonpolar covalent bond, which holds together the two hydrogen atoms. In order to improve the efficient utilization of H_2, transition metal catalysts are often required to facilitate H–H bond splitting process.

The activation of molecular hydrogen by transition metal complexes is of great importance in organometallic chemistry and is an essential step in understanding catalytic hydrogenation processes [1, 2]. The interaction of H_2 with transition metal complexes results in the perturbance of H–H bond which leads to the formation of a mono- or dihydride complex. Since the discovery of the first transition metal hydride complex, $H_2Fe(CO)_4$, in 1931 by Hieber, along with the development of various characterization techniques, such as single crystal X-ray diffraction analyses and neutron scattering, a vast number of transition metal hydride complexes were synthesized, characterized [3, 4], and can be used in homogeneous hydrogenation system [5, 6]. Thousands of papers and lots of review articles were published on this subject [7, 8]. However, the hydrogen activation mechanism was not established until 1980s. Particularly, the discovery of the first stable dihydrogen complex which contains intact molecular H_2 in transition metal complex, $W(CO)_3(PR_3)_2(H_2)$ (where PR_3 is a phosphine ligand), by Kubas in 1984 significantly propelled the development of the field of hydrogen activation (as shown in Scheme 2.1) [9].

There are numerous review articles and book chapters published in recent years provide important summaries regarding the theories and properties of transition metal dihydrogen complexes [10–14]. H_2 interacts with metal center in a side-on (η^2) mode (as shown in Scheme 2.2) by donating its two σ electrons to a vacant metal *d* orbital, forming a nonclassical 3-center 2-electron (3c–2e) bond, which elongates the H–H bond. The stability of η^2-H_2 complex depends on the strength of electron back-donation from a filled *d* orbital of the metal center to the σ^* orbital of H_2. Therefore, in some cases the strong back-donation causes the splitting of dihydrogen to dihydride complexes with elongated H–H bond distance (as shown in Scheme 2.3) [11].

As mentioned in the beginning of the introduction, hydrogenation reaction is one of the most important industrial processes. Most hydrogenation reactions [$RCH = CH_2 + H_2 \rightarrow RCH_2CH_3$ (R = alkyl, aryl)] use hydrogen gas to reduce or saturate organic compounds. Transition metal complexes are commonly involved as

Scheme 2.2 Bonding mode of η^2-H_2 complex and dihydride complex

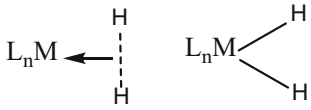

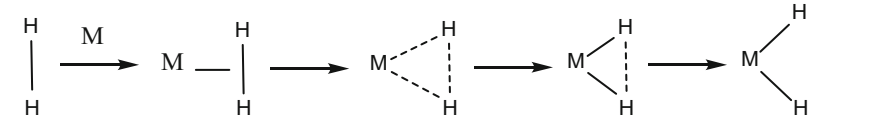

Scheme 2.3 H–H bond distances from crystallography and NMR

either homogeneous [e.g., $C_{10}H_{14}O$ +1 atm H_2 + $RhCl(PPh_3)_3$ where PPh_3 is triphenylphosphine → $C_{10}H_{16}O$] or heterogeneous [e.g., C_8H_6 + 1 atm H_2 + [5% Pd-$CaCO_3$ + $Pb(OCOCH_3)_2$ + C_9H_7N] → C_8H_8] catalysts to facilitate this process and improve the selectivity of desired hydrogenation product [15–17]. Transition metal complexes, such as Rh, Ir complexes, are long known to homogenously catalyze hydrogenation reaction by promoting molecular hydrogen activation [18, 19]. Transition metal hydrides are normally involved as intermediates in the catalytic cycle. Wilkinson's catalyst, $RhCl(PPh_3)_3$, was discovered in 1965 as the first highly active homogenous hydrogenation catalyst that is used under mild conditions [20]. It is well known to catalyze hydrogenation of alkene (as shown in Scheme 2.4) to alkane. In this catalytic cycle, one bulky triphenylphosphine ligand on $RhCl(PPh_3)_3$ is readily lost to form highly unsaturated 14-electron rhodium complex $RhCl(PPh_3)_2$ due to steric effect, followed by rapid oxidative addition of hydrogen molecule to produce 16-electron dihydride complex $RhClH_2(PPh_3)_2$. The next step, alkene is coordinated to rhodium via π donation and followed by intramolecular hydride transfer to yield alkyl hydride intermediate, $RhH(alkyl)Cl(PPh_3)_2$, which finally results in alkane product and regenerates $RhCl(PPh_3)_2$ through reductive elimination.

Other than Wilkinson's catalyst, there are two other famous cationic homogenous hydrogenation catalysts: one is rhodium based Schrock-Osborn catalyst [21], $[Rh(COD)(PPh_3)_2]^+$, (where COD = 1,5-cyclooctadiene) and the other one is iridium based Crabtree's catalyst $[Ir(COD)(PCy_3)(Py)]^+$ (Py = pyridine, Cy = cyclohexyl) [22]. They are more active and effective for hydrogenation reaction than Wilkinson's catalyst. The cationic metal center is more electrophilic than neutral metal center and thus fosters the coordination of alkene, which is the essential reaction rate determination step. These catalysts also exhibit high activity in the hydrogenation of hindered alkene. Notably, Crabtree's catalyst even catalyze the hydrogenation of tetra-substituted olefin compounds, while Wilkinson's and Schrock-Osborn catalysts do not. The hydrogenation rate of various substituted olefins with different Ir and Rh catalysts is shown in Table 2.1 [22].

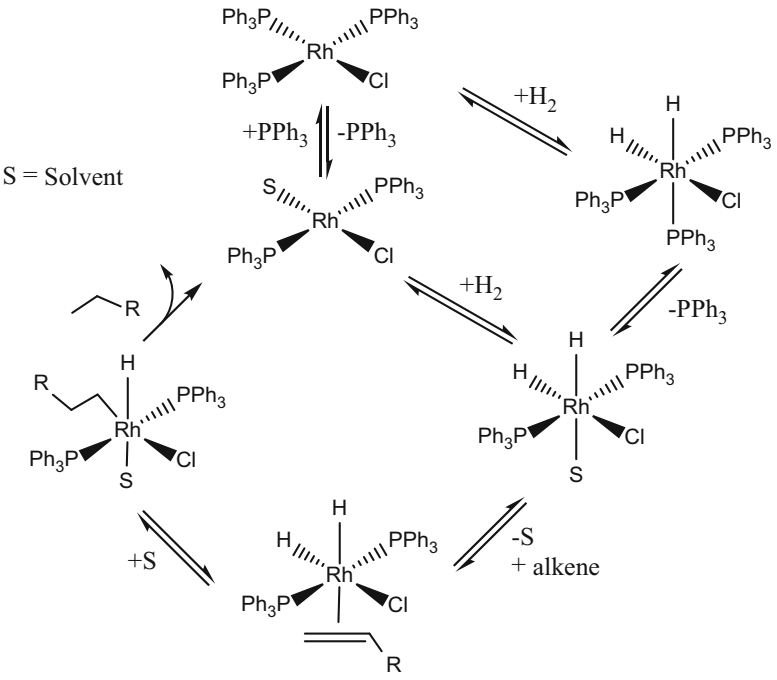

Scheme 2.4 Catalytic hydrogenation of alkene by Wilkinson's catalyst

Table 2.1 Rates[a] of hydrogenation of substituted olefins with different catalysts

Catalyst	Temp °C	Solvent	Substrate			
			1-hexene	Cyclo-hexene	1-Methyl-cyclohexene	2,3-Dimethyl-but-2-ene $Me_2C = CMe_2$
$[Ir(COD)(PCy_3)(py)]^+$	0	CH_2Cl_2	6400	4500	3800	4000
$[Ir(COD)(PMePh_2)_2]^+$	0	CH_2Cl_2	5100	3800	1900	50
	0	acetone	~10	0	0	0
$[Rh(COD)(PPh_3)_2]^+$	25	CH_2Cl_2	4000	10	–	0
$HRuCl(PPh_3)_3$	25	C_6H_6	9000	7	–	0
$RhCl(PPh_3)_3$	25	C_6H_6/ EtOH	650	700	13	0
	0	C_6H_6/ EtOH	60	70	–	0

[a]In mol of substrate reduced (mol of catalyst)$^{-1}$ h^{-1}

Heterogeneous catalytic hydrogenation is more widely used in industry. Heterogeneous catalysts are present in different phase from reactants, which are often recovered and recycled for cost savings. Heterogeneous hydrogenation reaction occurs on the interfaces of catalysts and reactants. In other words, adsorption of reactant,

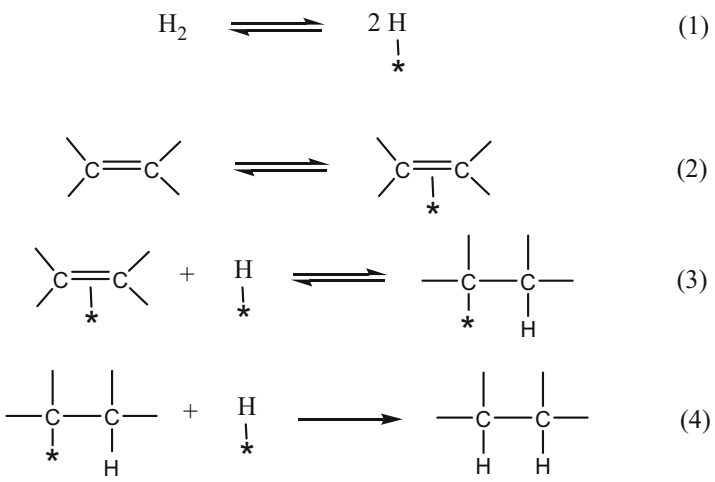

Fig. 2.1 The alkene hydrogenation mechanism proposed by Horiuti-Polanyi.

hydrogenation chemical reaction, and desorption of product must take place on the surface of catalysts [23]. The bond of reactant should be weakened or broken with the formation of reactive intermediates. An example is provided to illustrate the hydrogenation of alkene using a heterogeneous catalyst (Fig. 2.1). Hydrogen is adsorbed to the catalyst surface, followed by the cleavage of H–H σ bond to form more reactive M–H bonds. C=C π bond of alkene is weakened by adsorption to catalyst surface and then reacts with the activated hydrogen in a stepwise process to eventually yield alkane. This mechanism for alkene hydrogenation was proposed by Horiuti and Polanyi in 1934 [24].

Heterogeneous catalysts are normally transition metal, metal alloy, or metal oxides. The catalyst can be deposited on support with high surface area to forester hydrogen diffusion and promote interaction between catalysts and reactants. Heterogeneous catalysis seems to be far away from the area of organometallic chemistry at the first sight; however, surface organometallic species are often involved during the process of hydrogenation. Moreover, transition metal cluster complexes have been used as precursors to generate heterogeneous catalyst. Cluster chemistry can also serve as effective structural model to study the behavior of small molecules on metal surfaces in chemisorbed processes, which is known as the cluster-surface analogy [25, 26]. Further discussion will be provided in Sect. 2.2.

Hydrogenase enzymes are also one important class of compounds that are known for the activation of hydrogen in biological system. They are active redox enzymes that catalyze reversible oxidation of hydrogen to protons (Eq. 2.1). There are mainly three types of active sites in hydrogenase, [Fe]-only hydrogenase, dinuclear [FeFe] hydrogenases, and [NiFe] hydrogenases. A reversible hydrogen oxidation reaction is shown in Eq. 2.1.

$$H_2 \rightleftharpoons 2H^+ + 2e^- \tag{2.1}$$

X-ray crystallography and spectroscopic analyses revealed that the active sites at hydrogenase enzymes are organometallic complexes of Fe or Ni. While precious metal catalysts are majorly used in industry, nature has its unique way to reversibly activate hydrogen by using first row transition metals. Synthetic organometallic chemists are inspired by nature to pursue the synthesis of first row transition metal complexes by mimicking the function of hydrogenase in order to obtain efficient and inexpensive catalysts for hydrogen oxidation and production. This chemistry has been developed explosively since 2000 when the comprehensive review article came out by Marcetta Y. Darensbourg [27]. This book chapter (Sect. 2.2.2) will mainly focus on the introduction of structure model of the active site on hydrogenase, and a few examples of hydrogen activation process by the synthetic organometallic complexes will also be provided.

2.2 Molecular Complexes for Hydrogen Activation

2.2.1 Hydrogen Activation by Mononuclear Transition Metal Complexes

The majority well-studied organometallic compounds for hydrogen activation are mononuclear transition metal complexes. Metal dihydrogen complexes are stabilized by electronic synergistic effect of σ electron donation from dihydrogen and electron backdonation from *d* orbital of metal center to the σ^* orbital of dihydrogen (Scheme 2.5). There are two different ways to split H–H bond by transition metal complexes: homolytic cleavage and heterolytic cleavage (Scheme 2.6). Homolytic cleavage of H_2 results in a pair of hydrogen atoms, each with one electron. Heterolytic cleavage of H_2 results in a proton and a hydride anion with two electrons.

2.2.1.1 Homolytic Cleavage of H_2

Homolytic cleavage is also referred as the model of oxidative addition of hydride to metal centers through H_2 cleavage. Complexes with nucleophilic metal centers that have low oxidation states favor homolytic H_2 cleavage. In homolytic cleavage, the

Scheme 2.5 M-σ bond for η^2-H_2 complex

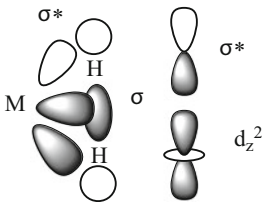

Scheme 2.6 Pathways for H–H bond cleavage

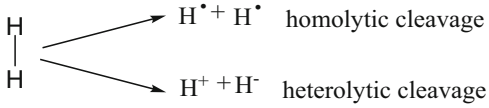

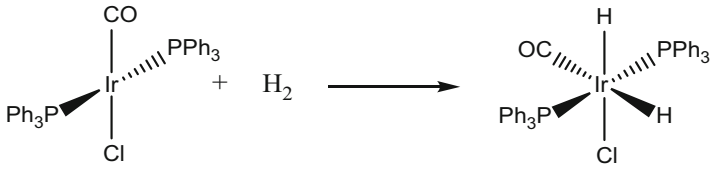

Scheme 2.7 Homolytic cleavage of H_2 by $IrCl(CO)(PPh)_2$

strong electron back-donation from metal center to σ^* orbital of H_2 weakens the H–H bond; thus, H_2 acts more as Lewis acid to accept electrons from *d* orbital of metal atom and eventually incorporate with metal center to yield metal hydride complex. Vaska made significant demonstration of homolytic hydrogen cleavage for Ir (I) complex (Vaska's compound) to yield dihydride Ir (III) complex in 1962 (Scheme 2.7) [28]. Increasing the basicity of metal center leads to stronger electron backdonation to H–H σ^* orbital, which further improves H_2 activation (the cleavage of H–H bond). This process is essentially oxidative addition of two hydrides to the metal center, and as a consequence the oxidation state of metal center increases by two. Wilkinson's catalyst as shown in Scheme 2.4 in the introduction part is an excellent example for homolytic H_2 cleavage. In this process, the crucial dihydride intermediate complex $RhClH_2(PPh_3)_2$ is formed by rapid homolytic H_2 cleavage from an unobserved dihydrogen intermediate complex $Rh(H_2)Cl(PPh_3)_2$ [29], and the oxidation state of rhodium increases from +1 to +3. It is worth mentioning here that the oxidation state of metal can be also increased by only one instead of two in homolytic H_2 cleavage. Examples are hydrogen activation by cobalt complexes, $[Co(CN)_5]^{3-}$ and $Co_2(CO)_8$; the oxidation state of Co in $[Co(CN)_5]^{3-}$ increases from +2 to +3, while for $Co_2(CO)_8$ increases from 0 to +1 (Eq. 2.2) with the formation of monohydride cobalt complexes instead of dihydride complexes [17]. Late transition metals (3*d* to 4*d* to 5*d*) have more diffused *d* orbitals than that of early transition metals which can result in more basic metal with more $d(M)$–$\sigma(H^-)$ orbital overlap and thus provides stronger M–H bond. For example, $Mo(H_2)(CO)(dppe)_2$ is a dihydrogen complex, while the $WH_2(CO)(dppe)_2$ is a dihydride complex [30]. Another example is that $V(H_2)Cp(CO)_3$ possesses η^2-H_2 coordination, $Nb(H_2)Cp(CO)_3$ exists in equilibrium with dihydride complex $NbH_2Cp(CO)_3$, whereas $TcH_2Cp(CO)_3$ is a very stable dihydride complex [31].

Homolytic H_2 Cleavage of $[Co(CN)_5]^{3-}$ and $Co_2(CO)_8$

$$\begin{aligned} 2\left[Co(CN)_5\right]^{3-} + H_2 &\rightarrow 2\left[HCo(CN)_5\right]^{3-} \\ Co_2(CO)_8 + H_2 &\rightarrow 2HCo(CO)_4 \end{aligned} \tag{2.2}$$

Steric effect of ligand plays a very important role in stabilizing metal dihydrogen ligand. Bulky ligand can stabilize dihydrogen ligand and inhibit the dihydrogen cleavage. Heinekey et al. synthesized PMe_3 analogy of Kubas complexes $(PCy_3)_2W(CO)_3H_2$ and $(P^iPr_3)_2W(CO)_3H_2$ (PCy_3 is the tricyclohexylphosphine ligand and

Scheme 2.8 Equilibrium existence of $(PR_3)_2W(CO)_3(H_2)$ and $(PR_3)_2W(CO)_3H_2$ in solution, R=Cy and *i*-Pr

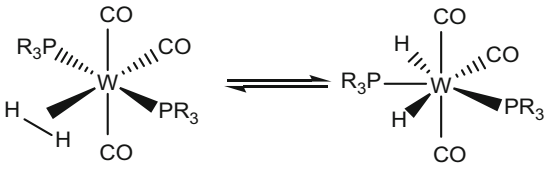

Scheme 2.9 Reaction of Mo $(CO)(PR_2C_2H_4PR_2)_2$ with H_2

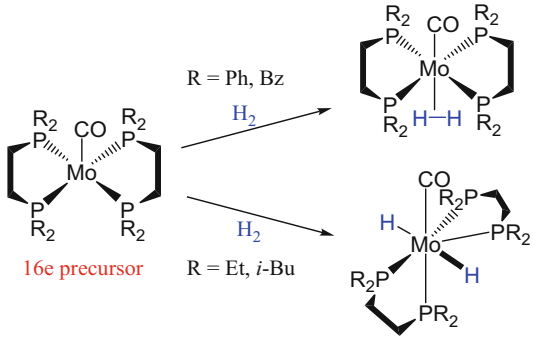

P^iPr_3 is the triisopropylphosphine ligand) by photochemical synthesis [32]. By using less bulky PMe_3 ligand, it has been shown that no tungsten dihydrogen complex was observed based on NMR study at various temperatures, whereas in Kubas complexes (Scheme 2.8), NMR observation confirmed the co-existence of dihydrogen complex $(PCy_3)_2W(CO)_3(H_2)$ and dihydride complex $(PCy_3)_2W(CO)_3H_2$ in equilibrium, with the domination of dihydrogen form. Another examples can be demonstrated by reaction of $Mo(CO)(PR_2C_2H_4PR_2)_2$ (where $PR_2C_2H_4PR_2$ is a diphosphine ligand) with hydrogen; dihydrogen complex $Mo((H_2)(CO)(PR_2C_2H_4PR_2)_2$ is produced when using bulky phenyl ligand, whereas oxidative addition of two hydride ligand occurs when using smaller ethyl ligand (Scheme 2.9) [33].

Other than the nature of metal center itself, electronic effect of ancillary ligand has great influence to electron backdonation of metal center to H_2 as well. Replacing electron-accepting ligand to electron-donating ligand enhances metal basicity and promotes the backdonation of M to H_2 and thus causes easier H_2 activation. It can also be demonstrated by $Mo(CO)(PR_2C_2H_4PR_2)_2$. Although the size of *i*-Bu is similar to Ph, H_2 cleavage occurs when using *i*-Bu ligand because $P^iBu_2C_2H_4P^iBu_2$ ligand is more electron-donating than $PPh_2C_2H_4PPh_2$ (Scheme 2.9). This ligand effect can also apply to transition metal polynuclear cluster complexes (detail will be discussed in Sect. 2.2.1.2). Some other examples for electronic and ligand effect are shown in Table 2.2 [34].

2.2.1.2 Heterolytic Cleavage of H_2

Heterolytic cleavage is a more prevalent hydrogen activation process for transition metal complexes and hydrogenase enzymes. In this process, molecular hydrogen is first polarized and splitted to hydride ion (H^-) and proton (H^+), resulting in the formation of metal hydride complex and protonation of an assisting Lewis donor,

Table 2.2 Examples of effects of variation of metal, ligand, or charge on dihydrogen versus polyhydride coordination

Dihydrogen complex	Polyhydride complex
$Mo(H_2)(CO)(dppe)_2$	$WH_2(CO)(dppe)_2$
$CpMn(H_2)(CO)_2$	$CpReH_2(CO)_2$
$TcCl(H_2)(dppe)_2$	$TcH_3(dppe)_2$
$[MH(H_2)(PR_3)_4]^+$ (M=Fe, Ru)	$[OsH_3(PPh_3)_4]^+$
$MH(H_2)(PR_3)_3$ (M=Fe, Ru)	$OsH_4(PR_3)_3$
$[TpOs(H_2)(PPh_3)_2]^+$	$[CpOsH_2(PPh_3)_2]^+$
$TpRuH(H_2)(PR_3)$	$CpRuH_3(PR_3)$

depe = 1,2-bis(diethylphosphino)ethane, R = alkyl
dppe = 1,2-bis(diphenylphosphino)ethane, Tp = trispyrazolylborate

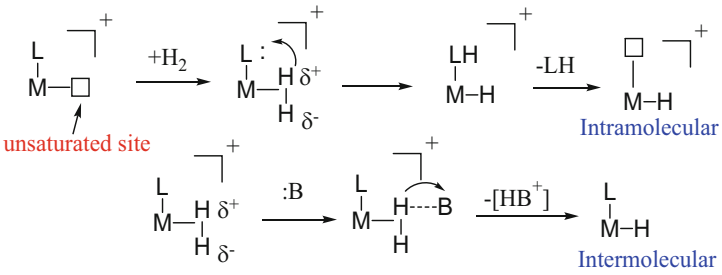

Scheme 2.10 Two pathways for heterolytic cleavage of H_2

which is a basic molecule or ligand. The assisting Lewis donor, either intramolecular basic ligand or an external basic molecule, is presence to assist hydrogen cleavage by inducing polarization to H_2. This eventually leads to the migration of H^+ to the base and the coordination of H^- to metal center to form metal monohydride (Scheme 2.10). The first example of heterolytic η^2-H_2 cleavage by cationic complex was shown by Crabtree in 1985. Cationic dihydrogen iridium complex, $[IrH(H_2)(PPh_3)_2(bq)]^+$, (bq = 7,8-benzoquinolato) was synthesized by treating its corresponding aquo iridium complex with hydrogen, and intermolecular heterolysis of η^2-H_2 on $[IrH(H_2)(PPh_3)_2(bq)]^+$ occurred by deprotonation of H_2 in the presence of strong external base MeLi [35].

Unlike homolytic H_2 cleavage, complexes with electrophilic metal center favor heterolytic cleavage of H_2. The electron poor metal center has low ability to backdonate electrons to σ^* H_2. Therefore, the stability of M–H_2 bond is determined by the electron accepting ability of both the proton acceptor from Lewis base and the metal acceptor from hydride. Increasing basicity of ligand, such as H_2O or Cl ligand, can enhance the electron polarization of hydrogen and cause heterolytic cleavage of H_2. For intramolecular heterolytic cleavage, basic ligand at *cis* position or close to η^2-H_2 facilitates proton transfer. On the other hand, electron withdrawing ligand,

Scheme 2.11 $IrCl_2H(H_2)(PR_3)_2$ with Cl *cis* to H_2 (*left-hand side*) and Cl *trans* to H_2 (*right-hand side*)

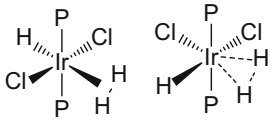

such as CO ligand, helps make metal center more electrophilic, especially at *trans* position to η^2-H_2; it reduces electron backdonation of M to η^2-H_2 greatly and thus stabilizes η^2-H_2 coordination. Conversely, σ donor ligand at *trans* position weakens η^2-H_2 coordination by reducing electron donation from η^2-H_2 to M. The degree of H_2 activation can be judged by H–H distance from X-ray or neutron diffraction and NMR coupling constant J_{HD}. This *trans* effect can be illustrated by $IrCl_2H(H_2)(PR_3)_2$, when Cl is in trans position to H_2, d_{HH} is 0.81 Å; on the other hand, d_{HH} is 1.4 Å with Cl *cis* to H_2 [36] (Scheme 2.11).

Besides the electrophilicity nature of ligand and metal, the charge of the metal center effect is another important factor to determine H_2 activation. It has to be considered with ligand *trans* effect together for heterolytic H_2 activation. In general, cationic metal center and electron withdrawing ligand at *trans* position greatly reduces electron backdonation and shortens H–H distance, which enhances the stability of dihydrogen complex. Strong σ donor ligand and neutral metal complexes favor heterolytic H_2 activation. The metal charge effect can be shown by the comparison of $MoH_2(PR_3)_5$ and $[Fe(H_2)(PH_3)_5]^{2+}$. $MoH_2(PR_3)_5$ is a pure dihydride complex [37] versus $[Fe(H_2)(PH_3)_5]^{2+}$, which is a dihydrogen complex with very short H–H distance by theoretical calculation [38].

2.2.1.3 Transition Metal Complex as Homogenous Hydrogenation Catalysts

Transition metal complexes are widely used as homogenous catalysts in hydrogenation, hydroformylation [39], and hydrogen oxidation reactions to promote the activation of hydrogen [40, 41]. As stated in introduction part, Wilkinson's catalyst made an impressive example of homolytic H_2 cleavage in homogenous hydrogenation reaction. James published two review articles in 1970s which thoroughly reviewed a variety of homogenous hydrogenation mononuclear transition metal complexes of earlier days.

Asymmetric hydrogenation plays a very important role in industry where high quality precise chemical synthesis is desired, such as in pharmaceuticals, fragrances, and agrochemicals. Transition metal catalysts containing chiral diphosphine ligand have been demonstrated to significantly enhance product steroselectivity in hydrogenation reactions (Scheme 2.12) [42–44]. In the 1970s, Monsanto company developed Rh (I) complexes containing chiral diphosphine DIPAMP for asymmetric hydrogenation across unsymmetrical C=C to synthesize L-DOPA in industrial scale which is an essential drug for treatment of Parkinson's disease [45, 46]. This invention made significant milestone on the development of enantioselective

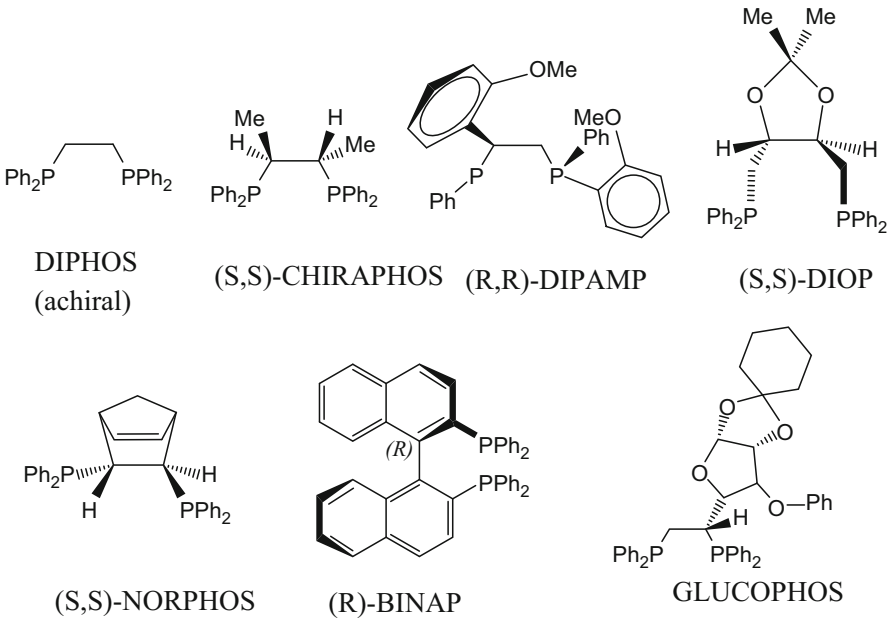

Scheme 2.12 Structures of selected chiral diphosphines

catalysis for its recognition as the first industrial asymmetric synthesis, and the inventor, William S. Knowles, shared one quarter of Nobel Prize in 2001 for his development of chiral catalyst. The asymmetric hydrogenation catalyzed by Rh-DIPAMP cation yield spectacular enantioselectivity of 95% ee (Eq. 2.3). The reaction mechanism of asymmetric hydrogenation by the Rh(I) chiral diphosphine catalyst has been demonstrated by Halpern [47] and it is the most studied mechanism for asymmetric hydrogenation. In catalytic hydrogenation cycle by Wilkinson's catalyst, which is also an Rh (I) complex (see Scheme 2.4), reversible oxidative addition of H_2 to form rhodium dihydride complex is involved as an essential catalytic intermediate. Such dihydride mechanism can also be applied to Rh (I) catalyzed asymmetric hydrogenation, although it is proposed that unsaturated mechanism is also suitable to explain the catalytic cycle. The difference between these two mechanisms is not practically important because the resulting steroselectivity in the catalytic reaction is always the same [48]. Scheme 2.13 presents the mechanism of asymmetric hydrogenation of ethyl (Z)-1-acetamidocinnamate (EAC) by using Rh(I)-diphosphine catalyst. First, solvent molecules that are coordinated to Rh complex dissociate and are displaced by EAC through olefinic π bond and carbonyl interaction with Rh (I) center, followed by oxidative addition of H_2 to the Rh (I) forming Rh (III) dihydride intermediate. Subsequently,

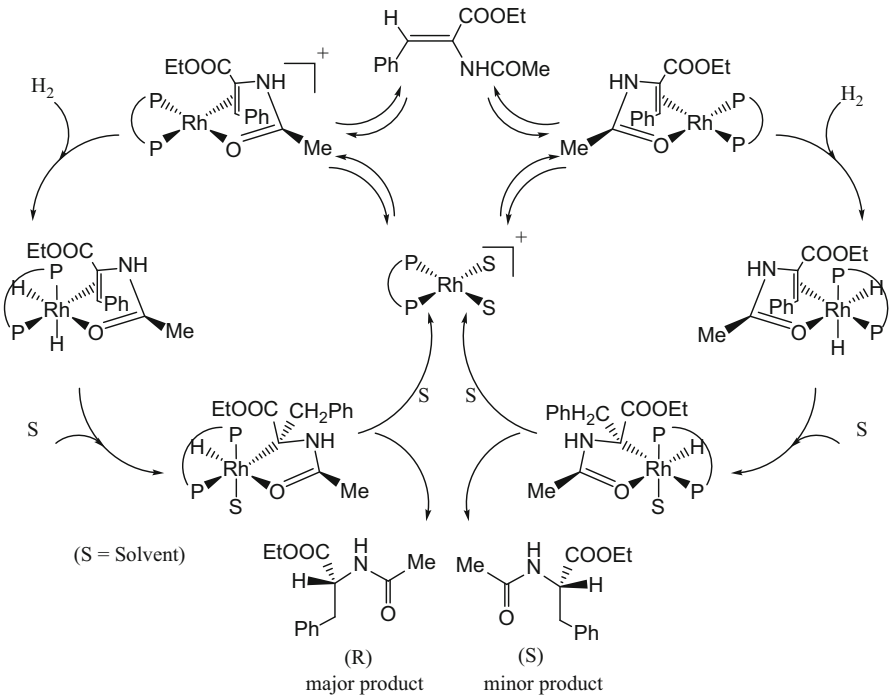

Scheme 2.13 Mechanism of Rh-diphosphine-catalyzed hydrogenation of ethyl (Z)-1-acetamido-cinnamate (EAC)

one of the hydrides on Rh (III) centers migrates to the coordinated olefinic bond to form Rh-alkyl σ bond with one solvent molecule coordinated back to the metal center. Final reduction phenylalanine is eliminated with the other hydride and regenerate the initial catalyst. In theory, two diastereoisomers of phenylalanine products should be produced when the chiral ligand possesses C2 symmetry, because the olefin can bind to Rh complex center by either the *re* face or the *si* face at the first step in the catalytic cycle. However, practically, high enantioselectivity product of (R) enantiomer is achieved. Kinetic studies for Rh (I) CHIRAPHOS catalyst explained the reason: at the rate determining oxidative addition of H_2 step, the intermediates for both (R) and (S) enantiomer form rapidly, but the intermediate for (R) enantiomer is produced much faster than that for (S) enantiomer, which leads to the preference of (R) enantiomer as the major final product. Experimental studies have shown that using CHIRAPHOS ligated Rh (I) complex for asymmetric hydrogenation of methyl-(Z)-1-acetamido-cinnamate also results in the same analogous enantiomer as the above with good selectivity [49] (Scheme 2.13).

The Monsanto synthesis of L-DOPA using catalytic asymmetric chiral Rh(I) complex

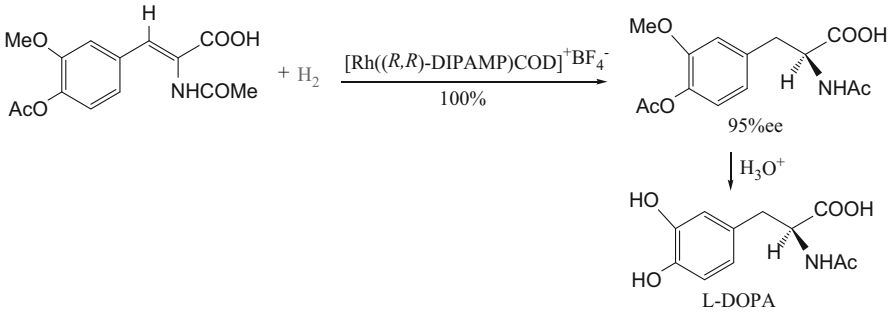

(2.3)

Other than Rh (I)-diphosphine complex catalysts, chiral Ru (II)-diphosphine complex catalysts, particularly Ru (II)-BINAP catalyst, are also exceptional for stereoselective organic synthesis in industry. Ru (II)-BINAP catalysts are discovered by Ryōji Noyori who is recognized as one of the Nobel Laureates in Chemistry and shared half of prize with William S. Knowles in 2001. Ryōji Noyori introduced chiral Ru catalyst catalysts for asymmetric hydrogenation of ketones, aldehydes, and imines. The Ru (II)-BINAP catalysts exhibit spectacular high steroselectivity of asymmetric hydrogenation and the product is even predictable, depending on if (S)- or (R)-BINAP ligand is used. Example here is given for the asymmetric hydrogenation of β-keto carboxylic ester (Scheme 2.14). In this catalytic cycle, Ru (II)-BINAP complex first activates dihydrogen by heterolytic cleavage to form Ru-monohydride intermediate and HX by the loss of one halide ligand (X = halide). The ketone ester compound coordinates to ruthenium center with the loss of another coordinated solvent molecule. Due to the chirality of BINAP ligand, in the next step, proton transfer occurs to the carbon atom on ketone, followed by the elimination of hydrogenated ester with the coordination of solvent ligand, and the ruthenium complex can activate H_2 again by heterolytic cleavage to catalyze the reaction cycle [50]. Noyori made tremendous progress in improving the selectivity for the ketone hydrogenation products. Lots of scientists over the world continue investigating this type of chiral Ru catalyst for different kinds of asymmetric ketone hydrogenation.

Hydrogen oxidation reaction split molecular hydrogen into two protons and two electrons, which converts the chemical energy of H–H bond to electric energy. Among the three types of active hydrogenases, [FeFe] hydrogenases and [NiFe] hydrogenases are the most studied. The hydrogen activation reactivity is not only influenced by the organometallic active site of hydrogenase, it is also greatly affected by its surrounding enzyme matrix. The reactivity of H_2 activation is very sensitive to ligand selection. Inspired by the nature of biological system, scientists use the basic ligand, such as pendant amine group to facilitate proton transfer for transition metal complexes. Earth-abundant transition metals, such as Ni, Fe, Mn, are used to

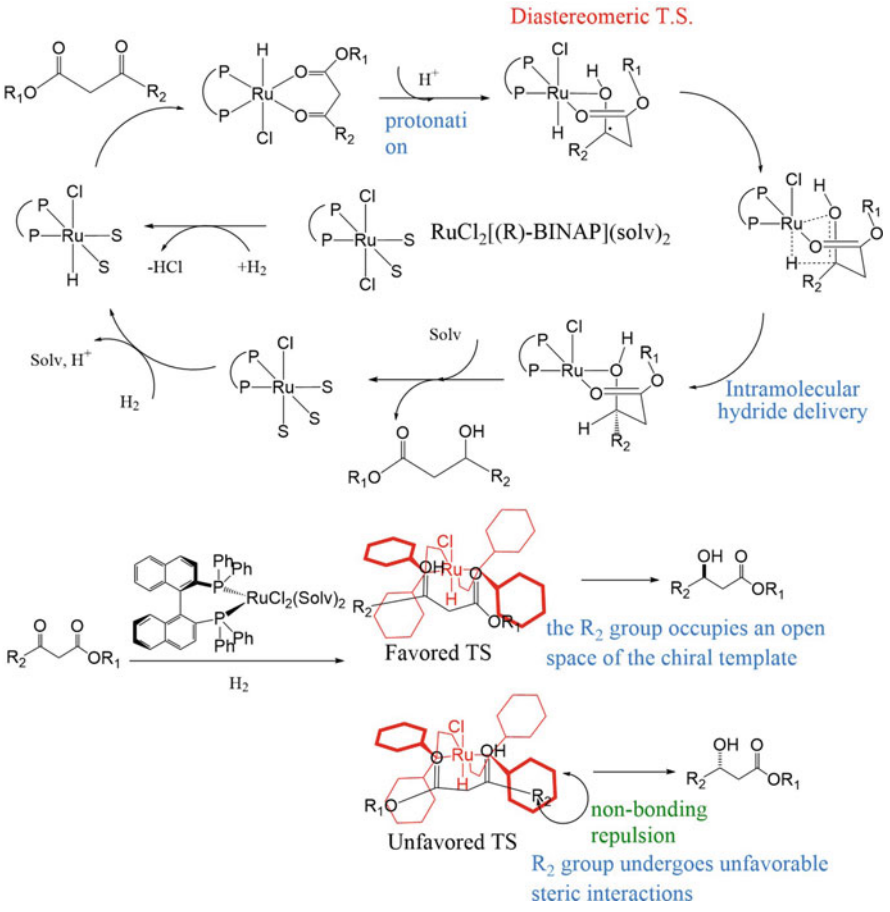

Scheme 2.14 Mechanism of Ru(II)-BINAP catalyzed substrate-directed ketone hydrogenation

catalyze hydrogen oxidation reaction. Recently, a mononuclear iron complex, $Cp^{C6F5}Fe(P^{tBu}{}_2N^{Bn}{}_2)H$, is shown to be efficient molecular catalyst for hydrogen oxidation reaction (1.0 atm, 22 °C) at the highest turnover frequencies of 2.0 s^{-1} among all iron complex catalysts reported to date (Scheme 2.15) [51]. Pendant amine group is used as σ-donor ligand to assist intramolecular H_2 cleavage in the catalytic cycle. *Tert*-butyl groups can avoid competitive binding of exogeneous amine base and favor dihydrogen coordination in the cycle. In this catalytic cycle, Fe (II)–H is first oxidized to Fe (III)–H cation complex, followed by the proton transfer to the adjacent pendant amine group. By the intermolecular deprotonation of exogeneous amine base, Fe (II)-H cation is reduced to neutral Fe (I), which is then electrochemically oxidized to Fe (II) complex. Fe (II)-H_2 is formed as intermediate with H_2 uptake, followed by H_2 heterolytic cleavage, which is promoted by the pendant amine group. In the final step of this catalytic cycle, exogeneous amine base

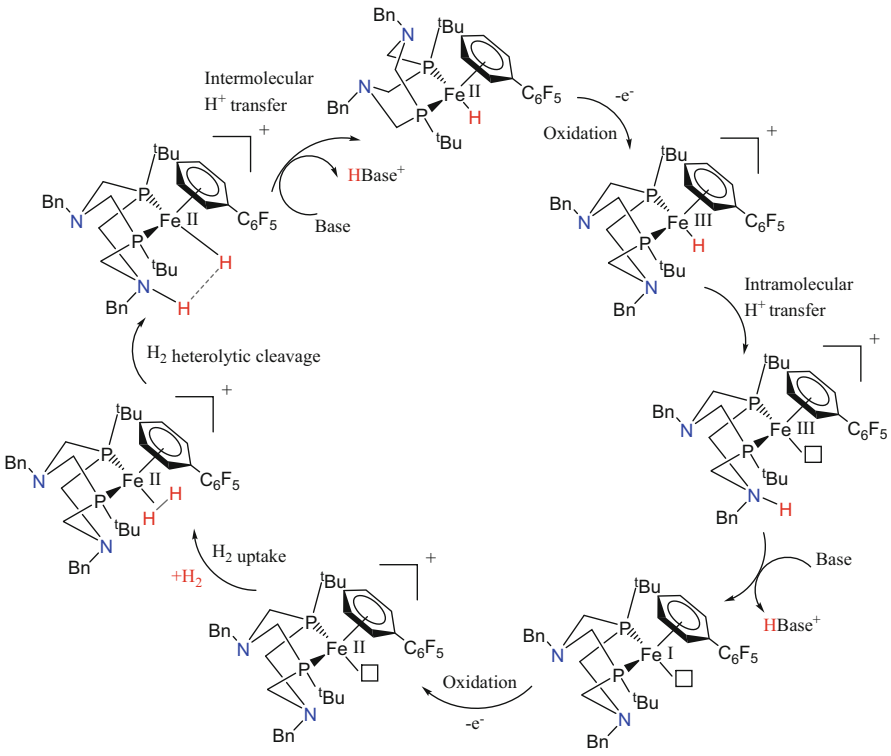

Scheme 2.15 Proposed mechanism for electrocatalytic oxidation of H_2 [51]. (Bn = benzyl)

deprotonates again to complete the catalytic cycle and regenerates Fe (II)-H complex.

2.2.2 Heterometallic Cluster Complexes for Hydrogen Activation

2.2.2.1 Heterometallic Cluster Complexes for Hydrogen Activation and Homogenous Hydrogenation Catalysis

Transition metal cluster chemistry made tremendous development over the last 50 years. A metal cluster complex can be defined as the compound that contains two or more metal atoms that are held together by direct and substantial metal–metal bonds. It can serve as effective structural model to study chemisorbed process on metal surfaces, which is known as the cluster-surface analogy [25, 26]. Therefore, investigating hydrogen activation process by using metal cluster complexes is particularly of great importance for the study of heterogeneous hydrogenation catalysis. Furthermore, the characterization of cluster compounds in solution and the solid state by using spectroscopic (particularly infrared, NMR and mass spectrometry) and

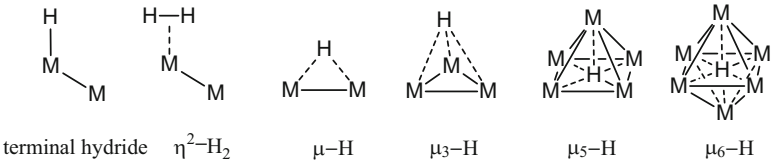

Fig. 2.2 Hydrogen bonding mode in metal cluster complexes. Terminal hydride (η^1-H) and dihydrogen side on coordination (η^2-H_2) as the same with mononuclear complexes, bridging hydride with different number of metals (μ-H, μ_3-H, μ_5-H, μ_6-H)

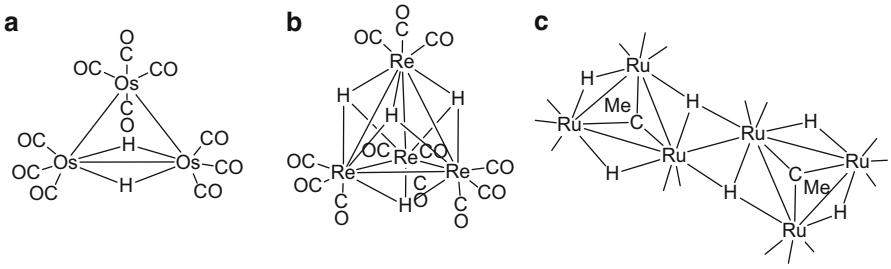

Fig. 2.3 Examples of unsaturated polynuclear metal complexes containing bridging hydride ligands

diffraction techniques (single-crystal X-ray and neutron diffraction) can provide insightful understanding for metal surfaces at the atomic and molecular levels.

Heteronuclear metal cluster complexes include the electron-precise polyhedral cluster complexes in which all the metal atoms have the closed shell 18 electron configuration, as well as the complexes in which the metal atoms interact with each other by forming delocalized bonds that can be explained by polyhedral skeletal electron pair theory [52]. Electronic unsaturation in metal complexes captured great attention to organometallic chemists. It can be found as a vacant coordination site or metal–metal multiple bonds in cluster complexes. Any polynuclear transition metal cluster complexes that can activate hydrogen must contain vacant molecular orbital (electronically unsaturated) or undergo ligand dissociation by heat or light to generate unsaturated coordination site before interacting with hydrogen. Metal skeleton rearrangement can also provide unsaturated site during the process for hydrogen activation. In mononuclear transition metal complexes, hydrogen interacts with metal center by either coordinated hydride or side-on η^2-H_2 (Scheme 2.2 and 2.3) [53]. In transition metal cluster complexes, hydrogen can form delocalized bonds to bridge metal atoms in a variety of bonding mode (Fig. 2.2). Delocalized hydrogen can also disguise the unsaturation of polynuclear metal cluster complexes, such as the 46-electron triosmium complex $Os_3(CO)_{10}(\mu\text{–}H)_2$ [54], **A**, the 56–electron tetrarhenium complex $Re_4(CO)_{12}(\mu\text{–}H)_4$ [55], **B**, and higher nuclear clusters such as the hexaruthenium carbonyl complex with 92 electrons $[Ru_3(CO)_8(\mu_3\text{-CMe})(\mu\text{-}H)_2(\mu_3\text{-}H)]_2$ [56], **C** (shown in Fig. 2.3). Particular detail is provided for compound **A**, which is formed by H_2 addition to $Os_3(CO)_{10}(NCMe)_2$ due to labile NCMe

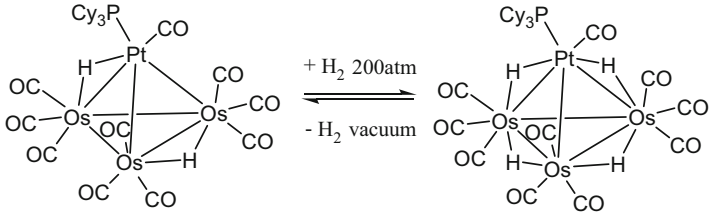

Scheme 2.16 $PtOs_3(CO)_{10}(PCy_3)(\mu\text{-}H)_2$ reacts with H_2 under 200 atm to $PtOs_3(CO)_{10}(PCy_3)(\mu\text{-}H)_4$. The loss of one equivalent H_2 occur upon vacuum

ligand dissociation. Many transition metal cluster complexes can interact with H_2 without ligand dissociation or metal cluster rearrangement to yield metal-hydride complexes; however, some of the reactions only precede under relatively harsh condition. For example, unsaturated bimetallic cluster $PtOs_3(CO)_{10}(PCy_3)(\mu\text{-}H)_2$ is two-electron short and shown to reversibly take up 1 equivalent of H_2, but this hydrogen addition requires a high H_2 pressure of 200 atm (Scheme 2.16).

On the other hand, some transition metal cluster complexes readily take up hydrogen under very mild condition. Weller and coworkers have reported a series of highly electronically unsaturated hydrogen rich polynuclear metal cluster complexes, $[Rh_6(PR_3)_6H_{12}][Y]_2$ (R = *i*Pr, Cy; Y = $[B\{C_6H_3(CF_3)_2\}_4]$ or 1-H-*closo*-$CB_{11}Me_{11}^-$), which are formed from condensation of mononuclear complex $[(R_3P)_2Rh(nbd)][Y]$ (nbd = norbornadiene) under hydrogen [57]. The structure of the Rh_6 complex consists of an octahedral cluster of six Rh atoms with wide range of Rh–Rh distance 2.7181(3)–3.0597(5) Å and each of the 12 hydride ligands bridges one Rh–Rh, which is known to elongate metal–metal bond. Interestingly, $[Rh_6(PR_3)_6H_{12}][BAr^F{}_4]_2$ (R = *i*-Pr, Cy; BAr^F = $[B\{C_6H_3(CF_3)_2\}_4]$ is found to be capable of rapidly adding two molecules of H_2 under 1 atm either in CH_2Cl_2 or in crystalline form to give 16 hydride cluster complex $[Rh_6(PR_3)_6H_{16}][BAr^F{}_4]_2$ without any metal cluster rearrangement. Upon the influence of vacuum, two hydrogen molecules dissociate from the 16-hydride complex and regenerate its 12-hydride precursor (Scheme 2.17) [58]. The resulting 16-hydride cluster is also highly unsaturated which contains 80 electrons (saturated octahedral transition metal cluster should contain 86 electrons). This is due to steric effect of bulky PR_3 ligand, which acts as shield to prevent molecules from disturbing metal core except the smallest H_2 and thus stabilizing the whole cluster.

Adams and Captain have shown that the 12-electron $[M(PBu^t{}_3)_2]$ (M=Pd or Pt) is an exceptional reagent that can be introduced to some transition metal carbonyl complexes to synthesize stable, highly unsaturated mix metal cluster complexes [59, 60]. The resulting polynuclear-mixed metal cluster complexes contain bulky $PBu^t{}_3$ ligand to provide large steric effect to shield the metal core atoms and exhibit high reactivity for hydrogen activation. Bimetallic cluster complex $[Pt_3Re_2(CO)_6(PBu^t{}_3)_3]$ can be obtained from the reaction of $Re_2(CO)_{10}$ with Pt $(PBu^t{}_3)_2$ in octane reflux (125 °C). The resulting complex is highly unsaturated with only 62 electrons, which is 10 electrons shorter than that of a saturated trigonal

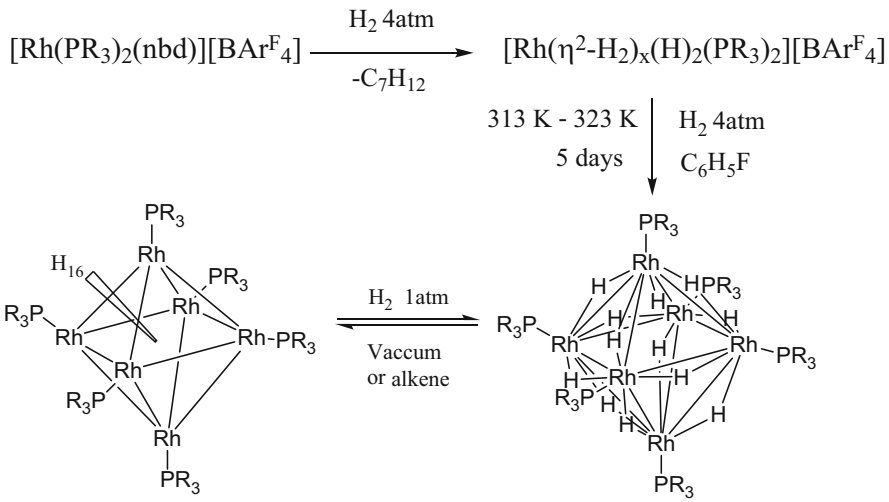

Scheme 2.17 $[Rh_6(PR_3)_6H_{12}][BAr^F{}_4]_2$ (R = *i*Pr, Cy; BAr^F = $[B\{C_6H_3(CF_3)_2\}_4]$ can add two equivalents of hydrogen reversibly under very mild conditions

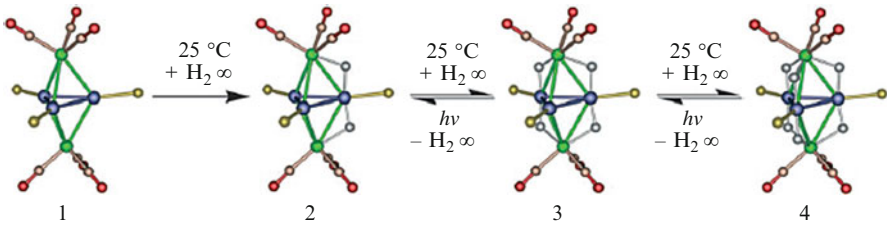

Fig. 2.4 Reversible addition of H_2 to the $\{Pt_3Re_2\}$ cluster complex **1**. *Blue* Pt, *green* Rh, *yellow* P, *red* O, *light brown* C, *gray* H [63] (Reproduced with permission from Ref. [63]. Copyright © 2009 American Chemical Society)

bipyramidal cluster. This complex has very unusual reactivity and is capable of sequentially adding three equivalent of H_2 at room temperature and reversibly eliminating two equivalent of H_2 under UV irradiation (Fig. 2.4) [61]. In this process, H_2 is activated and added to the metal cluster by forming hydrido ligands that bridge Pt–Re without any ligand dissociation. The mechanism for H_2 addition at multiple metal centers was investigated by density functional theory (DFT) calculation, which suggests that hydrogen activation on platinum atom is more energetically favorable than on rhenium atom [62]. For the addition of H_2 from **1** to **2**, computational experiment indicated that H_2 activation can undergo two possibilities, both of which involve multiple metal atoms (Fig. 2.5). For the 1st pathway, H_2 activation occurs on two Pt metal atoms by H_2 interaction with one Pt center in a η^2-H_2 mode as transition state, followed by heterolytic cleavage of H–H to form bridging hydrido ligand and a free hydride ligand. For the 2nd pathway, two Pt atoms and one Re

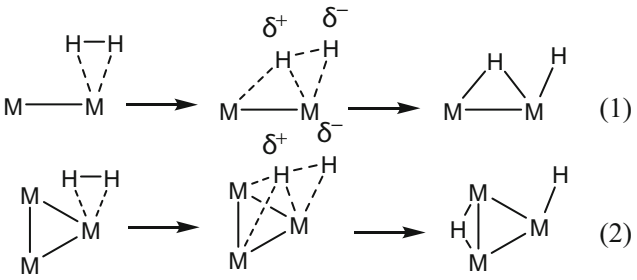

Fig. 2.5 Schematic representation of the two-center (*1*) and three-center (*2*) activation of dihydrogen observed in the transition states

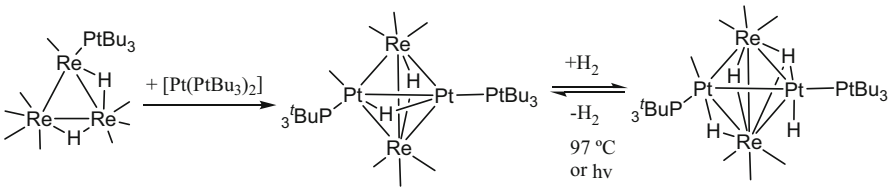

Scheme 2.18 $Pt_2Re_2(CO)_7(PtBu^t_3)_2(\mu\text{-}H)_2$ synthesis and reversible H_2 addition

atoms are involved in the H–H cleavage: η^2-H_2 is activated to form a hydrido ligand across Pt–Re bond and a terminal hydride on Pt atom through heterolytic cleavage.

Another unsaturated Pt–Re bimetallic cluster complex $Pt_2Re_2(CO)_7(PtBu^t_3)_2(\mu\text{-}H)_2$ can also reversibly take up H_2. This cluster complex has only 54 electrons for the tetrahedral Pt_2Re_2 core. One equivalent of H_2 can be added to form $Pt_2Re_2(CO)_7(PtBu^t_3)_2(\mu\text{-}H)_4$ with four briding hydrido ligand at room temperature 1 atm and can be eliminated under high temperature or UV irradiation (Scheme 2.16). Late transition metals, such as Pt, Pd, Rh, Ir, tend to initiate hydrogen activation in transition metal cluster complexes. Computational method indicated the heterolytic cleavage of H_2 that involved multiple metal atoms. These transition metal cluster complexes have low lying lowest unoccupied molecular orbital (LUMO) that readily take up two electrons from hydrogen molecule (Scheme 2.18).

Moreover, transition metal carbonyl cluster complexes exhibit superior properties as homogeneous hydrogenation catalysts. Although in some metal cluster catalytic system, it is indeed the mononuclear metal fragment, which is formed after the loss of ligands from the cluster that actually acts as the catalysts; [64] there are still some examples where catalysis is achieved by intact clusters complexes. In the homogenous metal cluster catalyzed hydrogenation reaction, one or more metal atoms in the cluster can serve as an active site to convert the reactants into products, and the cluster catalyst is an integral part of the catalytic cycle. For example, the complex $Pt_3Ru_6(CO)_{20}(\mu_3\text{-}PhC_2Ph)(\mu_3\text{-}H)(\mu\text{-}H)$ has been shown to be an effective catalyst for the hydrogenation of diphenylacetylene to (Z)-stilbene under mild condition [65]. In this layer segregated metal cluster complex, the central triangular layer contains

three platinum atoms, while each of the two outer triangle layers contains three ruthenium atoms. Kinetic study showed that the rate of (Z)-stilbene formation is inverse first-order function with respect to the CO pressure which indicated the CO ligand dissociation must be involved to initiate the catalytic cycle. Mechanism of this hydrogenation reaction was proposed, see Scheme 2.19. An electronically unsaturated cluster complex **A** was the active catalytic species formed by the dissociation of one CO ligand at Pt atom, followed by the activation of H_2 to a proposed complex **B** with four hydrido ligand. And then alkyne was inserted to the cluster complex, which is the rate determination step (r.d.s) because it was demonstrated that (Z)-stilbene formation was first-order dependent on alkyne concentration. Bridging hydrido ligands were transferred to hydrogenate alkyne which was then eliminated to reform the active species **A**. The formation of (Z)-stilbene was observed at a turnover frequency of 47 h^{-1}, suggesting the effective catalytic property of $Pt_3Ru_6(CO)_{20}(\mu_3\text{-}PhC_2Ph)(\mu_3\text{-}H)(\mu\text{-}H)$ as a homogenous hydrogenation catalyst (Scheme 2.19).

2.2.2.2 Biomimetic Model Complexes for Hydrogen Activation

Hydrogenases are enzymes to catalyze reversibly hydrogen activation to proton and electron (Eq. 2.1). The prosthetic group of hydrogenase is an iron-sulfur cluster as shown in Fig. 2.6. The Fe_4S_4 "Cubane" cluster is attached directly to one of the Fe atoms through a cysteine thiol bridge. This is believed to be the most possible structure of the active site with one CN^- and CO on each Fe and a bridging CO on the Fe–Fe bond. The Fe–Fe bond (2.6 Å) is a typical Fe–Fe distance in dithio-bridged organometallic Fe–Fe compounds. It is worth to note that the two sulfur atoms are connected through a three-atom bridge, the middle atom is identified as nitrogen and the other two are carbon atoms. This secondary amine group is very important as it participates in the di-hydrogen activation process, namely heterolysis of H_2. The "Cubane" cluster acts as electron donor in the redox process. The cyanide groups are strong electron donating ligands, which helps to stabilize the oxidized form of the di-iron unit. The coordinated water molecule is also very important, since in the hydrogen activation reactions, the coordinated water molecules have to be completely replaced by dihydrogen molecules. If the water is replaced by a CO ligand, the iron-sulfur cluster will lose its hydrogen activation capability, as CO is much stronger ligand compared to water and dihydrogen and it is impossible for dihydrogen to replace coordinated CO.

The dihydrogen activation on such a cluster has been well studied. Although numerous mechanisms have been derived along the way, the key steps of dihydrogen activation process are somewhat similar. As illustrated in Scheme 2.20, the dihydrogen activation and hydrogen production can reversibly occur on [FeFe] hydrogenase. Taken into account the dihydrogen activation as an example, under hydrogen atmosphere, the hydrogen molecule competes with the coordinated water molecule to coordinate to one of the iron atoms. The H–H σ-bond donates its two bonding electrons to the iron open site to form an agostic interaction. The dihydrogen is then quickly split between the acid (the iron atom) and base (the amino group) through a heterolytic cleavage. This intermediate is neutral. In the next

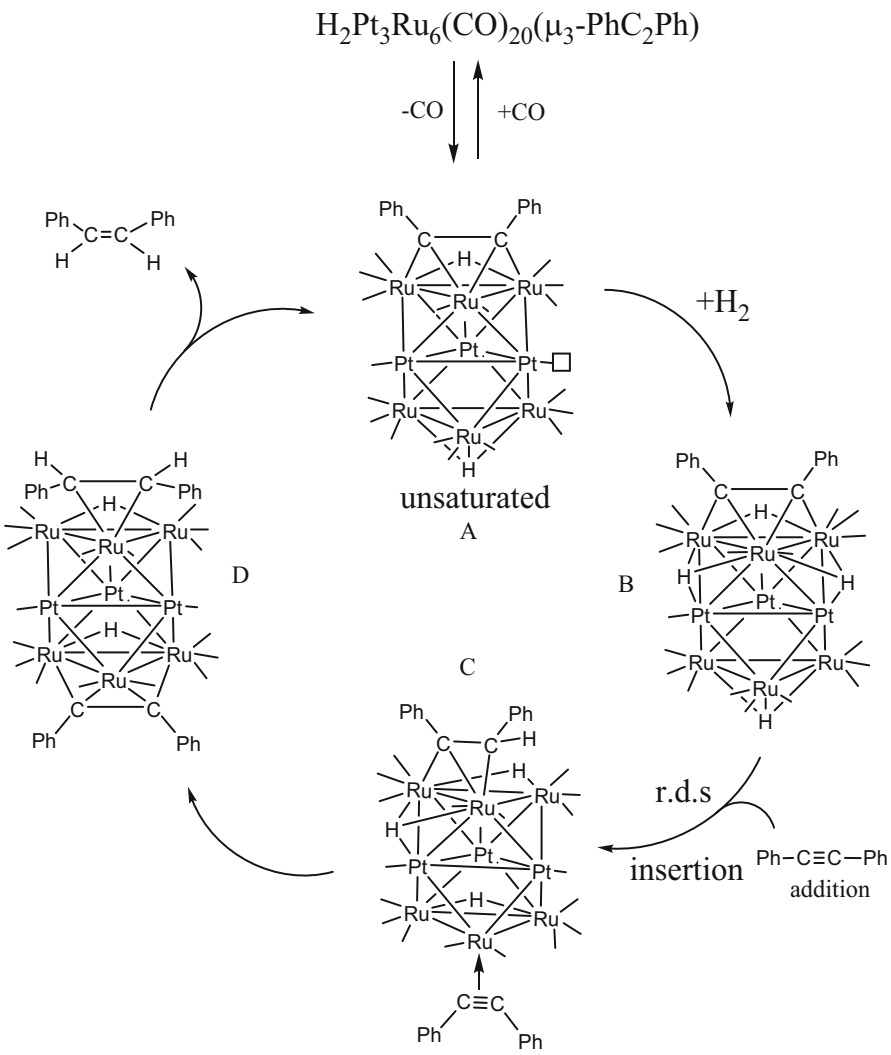

Scheme 2.19 Proposed mechanism for the catalytic process of hydrogenation of diphenylacetylene to (Z)-Stilbene by use of $Pt_3Ru_6(CO)_{20}(\mu_3\text{-}PhC_2Ph)(\mu_3\text{-}H)(\mu\text{-}H)$ complex as catalyst. CO ligands are omitted for clarity

step, the proton on the amine group is pumped away through the protein channel, which leaves the H–Fe–Fe as an anion. As stated above, the Cubane Fe_4S_4 is an electron shuttle, which can provide electrons or take electrons away from the H_2ases. In this scenario, the Cubane takes two electrons away from the cluster and resulted in the formation of a cationic Fe–Fe cluster. The terminal hydride, at the same time, migrates to the bridging position to stabilize the oxidized metal centers. There are two pathways from the cationic intermediate, again between the competing

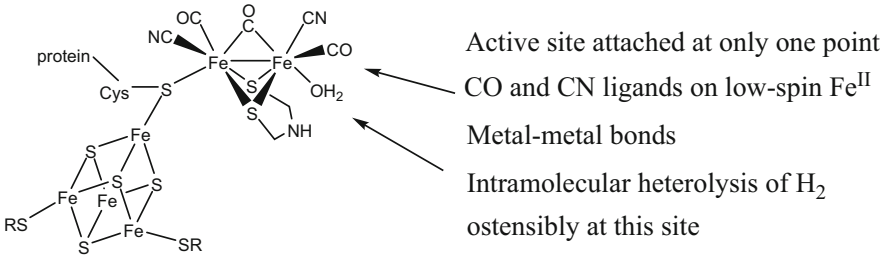

Fig. 2.6 The prosthetic group of hydrogenase is an iron-sulfur cluster

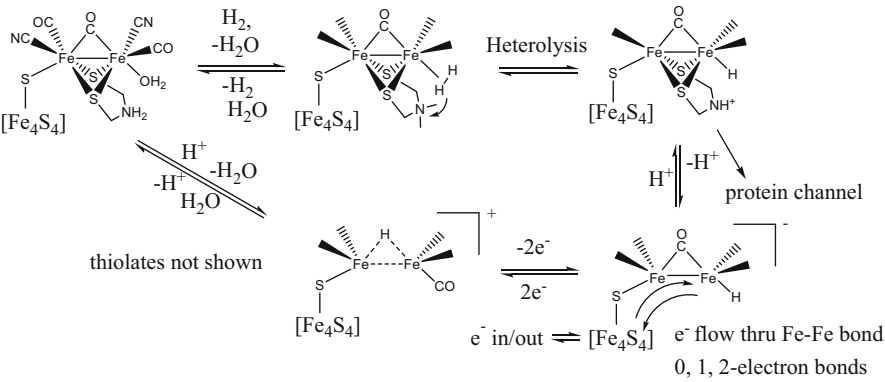

Scheme 2.20 Hydrogen activation and hydrogen production mechanism on [FeFe]hydrogenase

coordination of hydrogen and water molecules. The cleavage of the proton results in an open iron coordination site, which is either occupied by a water molecule to generate the original H_2ases or occupied by a dihydrogen to form the H_2 bonded (agostic interaction) Fe–Fe cluster to complete the catalytic cycle (Scheme 2.20).

Compared to the Fe only hydrogenase, the structure of the [NiFe]hydrogenase is quite different. The structure was obtained by protein X-ray crystallography from sulfate-reducing bacteria. In combining with infrared spectroscopic analyses, the active site on [NiFe]hydrogenase was found to be $(S\text{-}Cys)_4Ni(\mu\text{-}X)Fe(CO)(CN)_2$ (Fig. 2.7a). It consists of heteronuclear Fe and Ni atoms, which are held together by two μ-S-cysteines bridged ligands (π-donors) and a third bridging ligand of a hydride, hydroxide, or hydroperoxide. The distance between two metal atoms ranges from about 2.9 Å for the oxidized state to about 2.5 Å for the reduced state of [NiFe] hydrogenase [66–68]. Iron atom presents the similar coordination environment as $Fe(CO)(CN)_2$ with [FeFe]hydrogenase but with two cyanide ligands. The iron remains its oxidation state at +2 and a low spin ($S = 0$) system, while the actual redox active site is nickel site, which is additionally coordinated to two terminal S-cysteines ligands. The oxidation state of Ni changes between +2 and +3 in its various redox forms of enzyme. It is believed that dihydrogen binding occurs on Ni site in [NiFe]

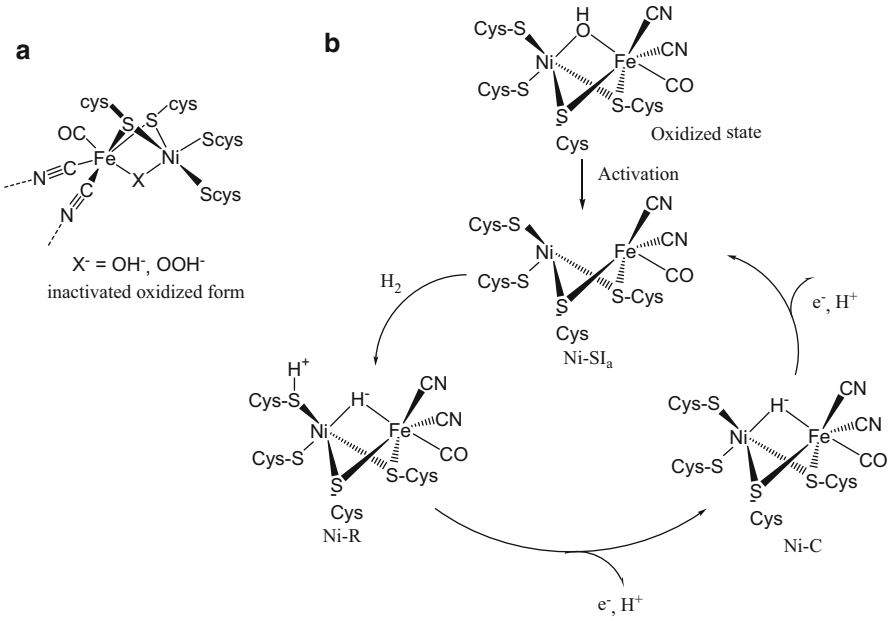

Fig. 2.7 (**a**) Drawing of the active site of [NiFe]hydrogenase. (**b**) Proposed catalytic reaction mechanism of [NiFe] hydrogenase

hydrogenase, due to the fact that CO inhibition binds at the open site of Ni [69] and Ni position presents just at the end of H_2 transfer channel [70]. However, controversy has arisen from DFT calculation which suggests that Fe site is where dihydrogen binding occurs, because the vacant coordination site of d^6 Fe favors direct binding of dihydrogen [71]. Recently, DFT calculation revealed that both coordination geometry and the spin state of Ni affect hydrogen activation efficiency in [NiFe]hydrogenase [72]. Regardless of the dihydrogen binding position, heterolytic cleavage leads to the formation of one bridging hydride and a proton bonded to one terminal cysteines ligand [73]. The [NiFe]hydrogenase can reversibly activate hydrogen as metal catalyst. Several redox states of Ni present as intermediates in the catalytic cycle. First, it is activated by the cleavage of bridging X ligand to form activated reduced state known as Ni-SI_a, and the dihydrogen is heterolytic cleaved to form Ni-R state with a bridging hydride and proton on terminal cysteines ligand. Nickel is then oxidized to +3 oxidation state by losing one electron and yields Ni-C state accompanying by the loss of proton on the terminal cysteines ligand. The bridging hydride ligand between Fe and Ni atoms in this state was confirmed by electron paramagnetic resonance (EPR) techniques [74, 75]. Catalytic cycle is complete by further loss of hydride to yield back to Ni-SI_a state (Fig. 2.7b).

Inspired by the beauty of bio-system, chemists have been making great effort on synthesizing functional models of [FeFe]hydrogenase and [NiFe]hydrogenase active site to mimic their excellent hydrogen activation and production [76–78]. Hundreds

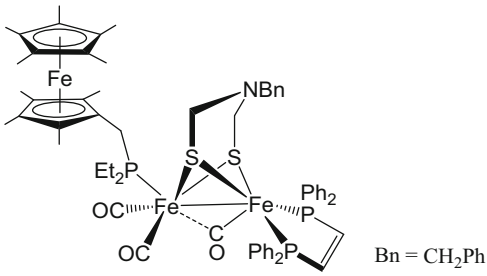

Fig. 2.8 Drawing of the synthetic model complex $Fe_2[(SCH_2)_2NBn](CO)_3(FcP^*)(dppv)$

of papers have been published regarding this subject, among which the majority are associated with [FeFe]hydrogenase and di-iron complexes. For example, recently Rauchfuss and Camara made significant progress on modeling the structural feature of [FeFe]hydrogenase by incorporating redox active ligand $Cp^*Fe(C_5Me_4CH_2PEt_2)$ (called *FcP**) to catalyze H_2 oxidation in the presence of oxidant and base (Fig. 2.8) [79]. The FcP* ligand simulates the function of the Fe_4S_4 cluster, and it is stable in two oxidation state both at Fe (II) and Fe (III). The coordination environment of the distal iron is also very crucial for hydrogen activation. It consists of square pyramidal geometry of iron with dithiolate, diphosphine, and CO ligands, which makes the coordination site that locates at opposite side of CO ligand to be available for H_2 binding. $FcBAr^F{}_4$ is used as oxidant to oxidize ferrocenyl group from Fe (II) to Fe (III) and di-iron unit from Fe(I)Fe(I) to Fe(I)Fe(II). H_2 is uptaken and heterolytic cleaved by dication $[Fe_2[(SCH_2)_2NBn](CO)_3(FcP^*)(dppv)]^{2+}$, followed by electron redistribution to +2 oxidation state for two distal iron and ferrocenyl group. Excess $P(o\text{-tolyl})_3$ is also provided to remove hydride on NBn, meanwhile bridging CO ligand is cleaved and coordinates to distal Fe in a terminal fashion with the formation of $[(\mu\text{-H})Fe_2[(SCH_2)_2NBn](CO)_3(FcP^*)(dppv)]^+$ (Scheme 2.21).

2.3 Supported Nanoclusters for Hydrogenation Reactions

Heterogeneous catalytic hydrogenations are most important reactions in many industrial processes, which accounts for 10–20% reactions to produce chemicals, such as the production of pharmaceuticals, naphtha reforming for petrochemicals. Heterogeneous catalysts are used over homogeneous catalysts in industry because of their high recyclability and low cost. Supported metal catalysts are of importance in heterogeneous catalysts, for which the catalytic active metals are anchored on solid supports (such as organic polymers and inorganic oxides) or entrapped in zeolite. These supported metal catalysts often incorporate a second catalytic metal forming supported bimetallic cluster catalysts to enhance catalytic properties. The presence of two metal species can improve product selectivity, enhance the catalyst lifetime, and increase catalytic activity [80]. The catalytic performance improvement is achieved by cooperative interactions between the different metal species, which is known as synergistic effect [81]. Platinum group metal containing bimetallic

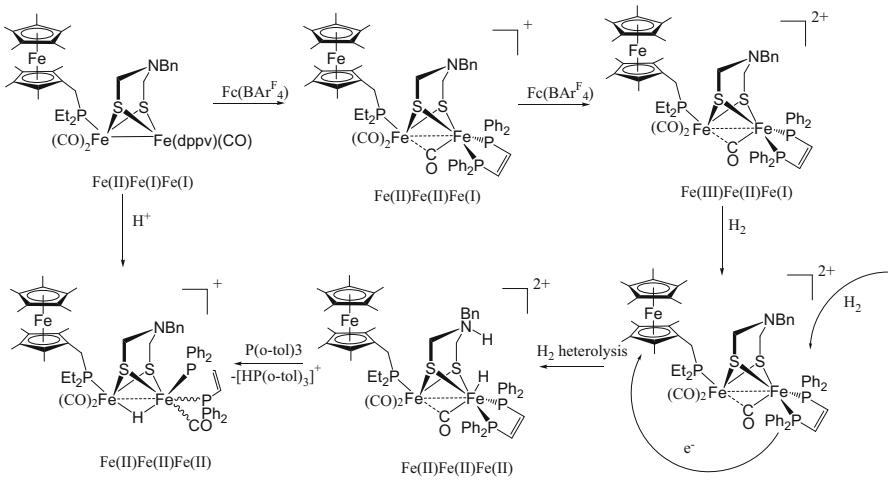

Scheme 2.21 Hydrogen activation process for $Fe_2[(SCH_2)_2NBn](CO)_3(FcP^*)(dppv)$ [79]

catalysts are extensively used in petroleum reforming for converting low-octane rating petroleum naphtha to high-octane gasoline [82–85]. The first bimetallic catalyst in industry for petroleum reforming is alumina-supported Pt–Re catalysts in 1969 [86, 87]. Later alumina-supported Pt–Ir and Pt–Sn bimetallic catalysts were discovered to exhibit superior catalytic properties compared to monometallic Pt catalysts [88]. The catalytic species are generally much smaller in size (average size 10–50 Å) and dispersed on the support compared to bulky metals. Especially in supported bimetallic catalysts, some of metals can form alloy-like nanocluster when they are small in size, rather than form bulky metal alloy in large scale. Catalytic activity is substantially affected by the size of the supported bimetallic catalysts. It is expected that the difference between bulky and small size bimetallic catalysts increases with decreasing of the particle size [89, 90]. Herein, only supported nanoclusters with particles size smaller than 10 Å are discussed. These nanoclusters typically contain less than 10 metal atoms, which can be considered as good models to investigate the influence of cluster structure to catalytic properties. Only heterogeneous hydrogenation reactions will be exhibited as examples to demonstrate the catalytic performance of supported nanocluster catalysts.

The most commonly used and inexpensive method for the synthesis of supported nanocluster catalysts is incipient wetness impregnation. The metal precursors are dissolved in aqueous or organic solvents, and catalyst support with the same pore volume as the metal precursor's solution is then mixed. Afterwards, the mixture is dried or calcined at elevated temperature to remove solvent, resulting in supported bimetallic catalysts with active metal species on the surface of support [91–93]. This is the simplest method and does not require any complex equipment. However, compared to supported nanocluster catalysts, the bimetallic particles made from this method are relatively large forming alloy species. Besides, the interaction of

difference metal precursors is not strong enough to form uniform bimetallic species during deposition, so that it is difficult to identify the precise structure of bimetallic particles prepared from incipient wetness impregnation [94].

Controlled synthesis of supported bimetallic catalysts is highly desired so that the structures of bimetallic species and their influence on the catalytic property can be investigated. It is anticipated that stronger interaction between two metals significantly influence catalytic property compared to supported monometallic catalyst. By using molecular transition metal cluster complexes as precursors to prepare bimetallic cluster catalyst, the bimetallic interaction can be maximized and measured. Metal–metal bonds are "premade" before deposition on the solid support. These transition metal cluster complexes (most with carbonyl ligands) precursors have been demonstrated as excellent candidates for hydrogen activation, which is an essential step in hydrogenation reaction.

2.3.1 Transition Metal Cluster Complexes as Precursors for Heterogeneous Hydrogenation

Transition metal carbonyl complexes contain carbonyl ligands that bond terminally to one transition metal atom or coordinate to two or more transition metal atoms in a bridging fashion. The transition metal–carbonyl bonding interaction involves σ-bonding of the CO ligand to the empty *d* orbital of the transition metal, as well as the π back bonding from a filled metal *d* orbital to an empty π^* orbital of CO ligand (Fig. 2.9). The CO ligand has a high tendency to stabilize metal–metal bonding in cluster complexes due to the capability of CO ligand to reduce electron density on the metal through π-backbonding. The first metal carbonyl complex, $Ni(CO)_4$, was discovered by Ludwig Mond in 1890, which is an intermediate used to produce pure nickel metal by the Mond process [95]. Transition metal cluster complexes used as homogenous and heterogeneous catalysts have drawn significant attention to chemists since 1960s [96]. Mix-metal cluster complexes not only can be used as homogenous catalysts in organic solution (Sect. 2.2.2.1), due to the synergism among multiple catalytic systems derived from mix-metal centers, they can also be used in heterogeneous catalytic system in which metal cluster derived particles are anchored on solid supports. Many transition metal cluster complexes have been shown to serve as precursors to generate heterogeneous catalysts for a variety of

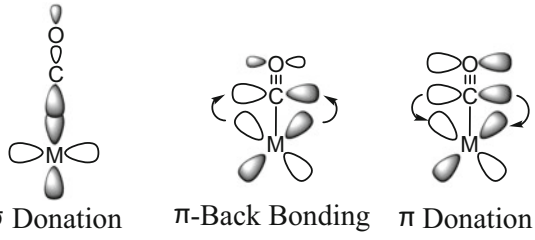

Fig. 2.9 The bonding between a terminal carbonyl ligand and transition metal atom

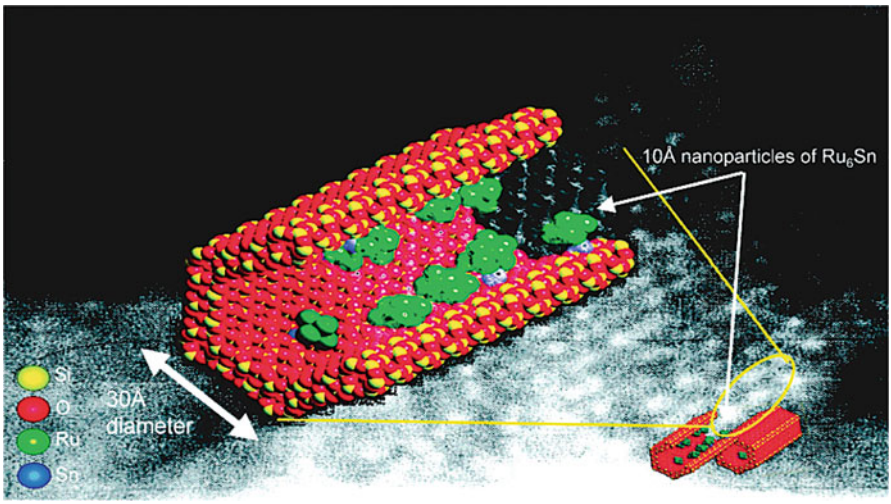

Fig. 2.10 Computer graphic illustration of Ru_6Sn nanoparticles encapsulated on the inner surface of silica on an enlarged SEM image of the same system (Reproduced with permission from Ref. [97]. Copyright © 2003 American Chemical Society)

important industrial processes [97, 98], such as petroleum reforming, hydrogenation, and dehydrogenation reactions. There are several advantages to use transition metal cluster complexes as precursors to make heterogeneous catalysts.

1. Heterogeneous catalysis is a surface phenomenon which is greatly influenced by interaction between reactant species and catalyst. Intensive efforts have being made to reduce the size of the heterogeneous catalysts to nanoscale so that metal catalysts can be more finely dispersed which can significant improve the catalytic efficiency. Transition metal cluster complexes are limited in size. Most of the metal cluster complexes contains less than ten metal atoms. Highly condensed metal cluster is also found, such as palladium clusters Pd_{69} [99], and Pd_{145} [100], for which the diameters are in nanometer scale and have close-packed frameworks described as *ccp* (cubic close-packed) stacking layers. These cluster complexes have been considered as proper model for the study of very small transition metal particles and metal surface chemisorption on heterogeneous catalysts [101]. Particularly for transition metal carbonyl complexes in which the transition metals are in low oxidation states, the carbonyl ligands can be readily removed under thermal treatment which also makes the resulting bare clusters to anchor firmly on the oxide support (Fig. 2.10). The resulting bare cluster catalysts are very small in size with more surface to volume ratio, therefore provide better catalyst exposure to the reactant species, and improve the catalytic activity. Moreover, the firm attachment of bare cluster to oxide support can significantly minimize the catalyst coalesce and sintering, and thus increase catalysts lifetime and reduce the cost.

Table 2.3 List of metal couples in molecular mixed-metal clusters used as precursors to heterogeneous catalysts

Catalyzed reactions	Supported bimetallic cluster catalyst
Hydrogenation of C–C multiple bonds	Ta–Rh, Ta–Ir
	Mo–Fe, Mo–Ru, Mo–Co, Mo–Rh, Mo–Ir, Mo–Ni, Mo–Pd, Mo–Pt
	W–Fe, W–Co, W–Ni, W–Pt
	Fe–Ru, Fe–Co
	Ru–Os, Ru–Co, Ru–Ni, Ru–Pd, Ru–Pt, Ru–Cu, Ru–Ag
	Os–Ni
	Co–Rh, Rh–Pt
	Pt–Cu, Pt–Au
Hydrogenation of CO and CO_2	Cr–Ru, Cr–Co, Cr–Pt
	Mo–Fe, Mo–Ru, Mo–Os
	Mo–Co, Mo–Rh, Mo–Ni
	W–Os, W–Rh, W–Ir, W–Pt
	Mn–Fe, Mn–Ru, Mn–Co, Re–Os
	Fe–Ru, Fe–Os
	Fe–Co, Fe–Rh, Fe–Ir, Fe–Pd, Fe–Pt
	Ru–Os, Ru–Co, Ru–Rh, Ru–Ni
	Os–Rh, Os–Ni, Co–Rh, Co–Cu
Hydrogenation of aldehydes and ketones	Mo–Co, Mo–Rh, Ru–Pt
	Os–Ni, Co–Cu, Co–Zn

2. Various characterization techniques can be applied to metal carbonyl complexes to confirm the well-defined structure (discussed in Sect. 2.2.2.1). Furthermore, for mix-metal carbonyl cluster complexes, the stoichiometry of different metal species can be guaranteed from cluster synthesis and the integrity of clusters still retained when undergo decarbonylation process to make supported nanocatalyst. The structural information and dispersion of bare metal clusters on oxide support at atomic level can be determined by X-ray absorption spectroscopy (EXAFS: extended X-ray absorption fine structure), high resolution electron microscopy, etc. By comparison, conventional incipient wetness impregnation method cannot guarantee the uniform dispersion and integrity of mix metal stoichiometry due to weak interaction of the precursors.
3. Heterogeneous catalysis is more prevalent in industry than homogenous catalysis. It has been long established that bimetallic catalysts exhibit superior catalytic performance than that of monometallic catalysts in petroleum industry. Using bimetallic cluster complexes as heterogeneous catalyst precursor can provide a deeper insight into such synergistic effect due to the fact that cluster complexes contain direct metal–metal bond can be better characterized at the atomic and molecular level [102–105]. A list of the different supported bimetallic cluster catalysts used for the catalysis of various hydrogenation reactions is given in Table 2.3. A comprehensive review for the catalytic performance of each

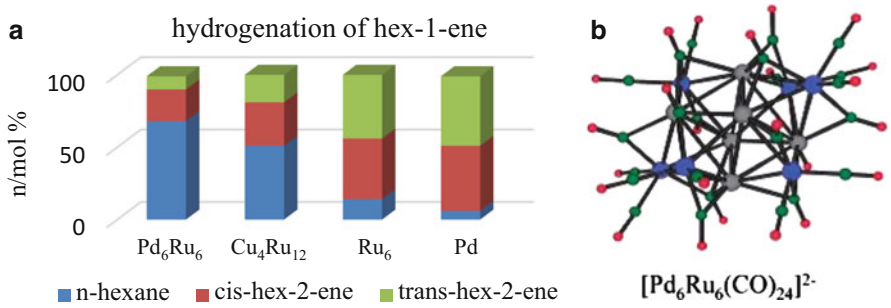

Fig. 2.11 (**a**) Bar chart summarizing the relative performances and selectivities of the Pd_6Ru_6 and Cu_4Ru_{12} catalysts when compared to monometallic Ru_6 and Pd nanocatalysts for the hydrogenation of hex-1-ene. (**b**) Parent anionic metal carbonyl complex from naked Pd_6Ru_6 nanoparticle (17 Å diameter for the bimetallic core catalysts) (Reproduced with permission from Ref. [97]. Copyright © 2003 American Chemical Society)

supported bimetallic catalyst is given in a review article published by Buchwalter Rosé, and Braunstein recently [106]. A few examples of supported ruthenium and palladium bimetallic nanocatalysts are provided in this book chapter. Thomas and Johnson et al. [107] have reported alkene hydrogenation catalyzed by bimetallic Pd-Ru and Cu-Ru nanoparticles, which were prepared from mix-metal carbonyl cluster complexes $[Pd_6Ru_6(CO)_{24}]^{2-}$ and $[Ru_6C(CO)_6Cu_2Cl]^{2-}$, respectively. The prepared nanocatalysts are uniformly dispersed nanoparticles, about 1.5 nm in diameter. The metal oxide loaded nanocatalysts were prepared by making a slurry of corresponding metal clusters in diethyl ether and methylene chloride with oxide support, such as mesoporous silica MCM-41 (pore size is approximately 3.0 nm), followed by activation of the encapsulated clusters upon heating at about 200 °C in vacuo. Structural retention of the clusters was confirmed by EXAFS showing the unchanged metal–metal bond. The hydrogenation of hex-1-ene, dodec-1-ene, and naphthalene were performed using these bimetallic PdRu and CuRu nanocatalyst with the comparison of individual monometallic Pd and Ru catalyst. The results of this catalytic hydrogenation of hex-1-ene are shown in a column chart in Fig. 2.11; the bimetallic nanocatalyst are much superior compared to monometallic Ru and Pd nanocatalysts for n-hexane selectivity. Also, the TOF (Turnover Frequency) for Pd_6Ru_6 and Cu_4Ru_{12} is 20 and 10 times more than that of Ru and Pd catalysts, respectively.

Thomas and Johnson demonstrated significantly that a number of anchored bimetallic nanocatalysts generated from cluster complexes exhibit high catalytic activity and product selectivity for a series of single-step hydrogenation under low temperature (353–373 K). These are efficient hydrogen activation processes, which featured direct hydrogenation in only one step. Some of the industrial essential organic compounds have been demonstrated to be made by hydrogenation in a single step. Such catalytic reactions are desired in industry to address

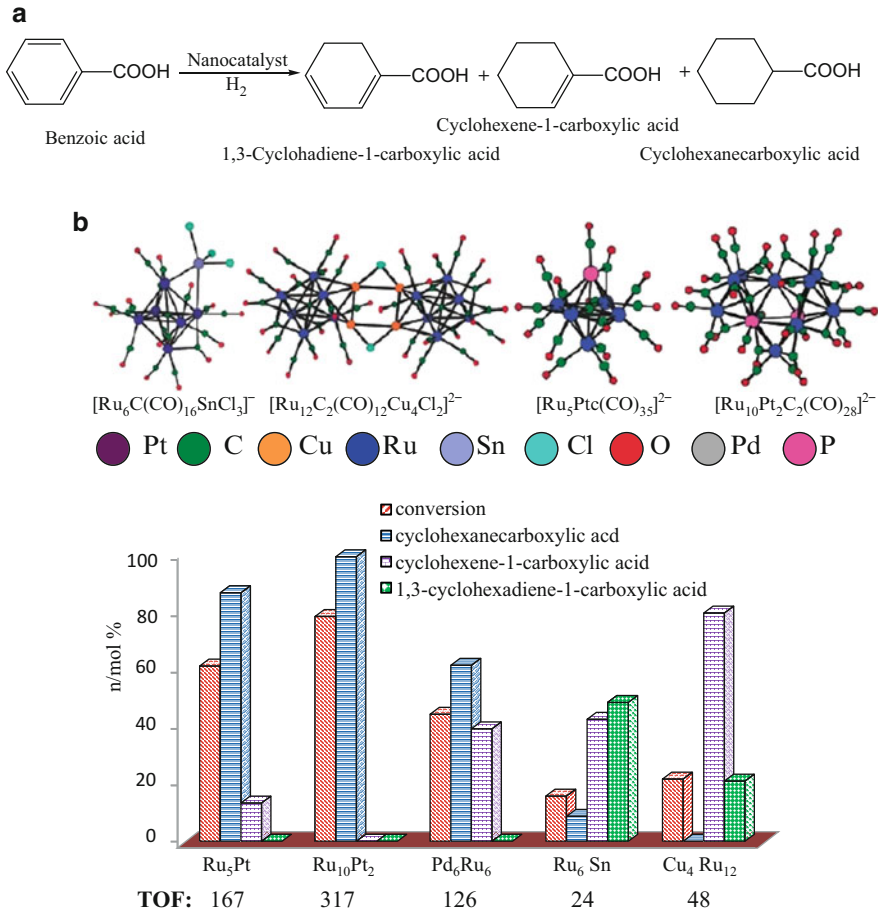

Fig. 2.12 (**a**) The products from the hydrogenation of benzoic acid. (**b**) Parent anionic metal carbonyl complex from naked Ru_5Pt_1, $Ru_{10}Pt_2$, Ru_6Sn, and Cu_4Ru_{12} nanocatalysts nanoparticle, and bar chart summarizing the relative performances and selectivity of the Ru_5Pt and $Ru_{10}Pt_2$ catalysts when compared to other bimetallic nanocatalysts for the hydrogenation of benzoic acid. Reaction conditions: benzoic acid: 2.5 g; catalyst, 50 mg; H_2 pressure, 20 bar; Solvent: C_2H_5OH 75 mL; temperature 373 K; time 24 h; TOF = $[(mol_{subst})(mol_{cluster})^{-1}\ h^{-1}]$ (Reproduced with permission from Ref. [97]. Copyright © 2003 American Chemical Society)

environmental problems, including the decline of petroleum feedstock and generation of unnecessary byproducts. An example is given here for the production of cyclohexane-carboxylic acid by the hydrogenation of benzoic acid using cluster complex derived nanocatalysts, Ru_5Pt_1, $Ru_{10}Pt_2$, Pd_6Ru_6, Ru_6Sn, and Cu_4Ru_{12}. Three products could be obtained from the hydrogenation of benzoic acid (Fig. 2.12a), but only the fully hydrogenated product cyclohexane-carboxylic acid is desired because it has been used to produce Caprolactam, which is a precursor to

synthesize Nylon 6 via ring opening polymerization (ROP) in industry. The selectivity results of this catalytic hydrogenation are shown in Fig. 2.12b; the RuPt bimetallic nanocatalyst is the most efficient catalyst in terms of selectivity and conversion compared to other nanocatalysts. Interestingly, when larger metal cluster complexes were used as the catalyst precursor, $Ru_{10}Pt_2$ has the same Ru:Pt ratio as Ru_5Pt; an increase in reagent conversion was observed. Remarkably, the catalyst generated from $Ru_{10}Pt_2$ shows almost 100% selectivity for the desired product at almost double the TOF (Turnover Frequency) compared to that generated from the Ru_5Pt cluster.

2.3.2 Heavy Main Group Metal Modified Transition Metal Clusters as Supported Catalysts for Hydrogenation

Main group metals, such as group 14 and 15 elements, Ge [108–110], Sn [111–120], Bi [121, 122], Sb, have been shown to be valuable modifiers for transition metal-based catalysts to enhance their catalytic performance and lifetime of the catalysts, especially Pt-based bimetallic catalysts. Bismuth on oxide supports has been shown to catalyze the oxidation of certain hydrocarbons efficiently [121, 122]. Transition metal–bismuth bimetallic catalysts also attracted significant attention since the discovery of bismuth–molybdate catalysts in the 1980s, which catalyzes the important industrial process for the ammoxidation of propylene to acrylonitrile [123]. Studies of the mechanism of this reaction have been suggested that bismuth is responsible for the abstraction of hydrogen from propylene through the Bi-O bond. Heterogeneous nanocatalysts of compositions Re_2Bi_2, Re_2Sb_2, Re_2Sb derived from molecular cluster of $Re_2(CO)_8(\mu\text{-}BiPh_2)_2$, $Re_2(CO)_8(\mu\text{-}SbPh_2)_2$, and $Re_2(CO)_8(\mu\text{-}SbPh_2)(\mu\text{-}H)$, respectively, have been used in the synthesis of niacin (vitamin B3) for the liquid-phase ammoxidation of 3-picoline to nicotinonitrile (an intermediate to niacin) under mild condition [124]. Later, one step synthesis of niacin by oxidation of 3-picoline using APB (acetylperoxyborate) was achieved by using Ir_3Bi and Ir_5Bi_3 nanocatalysts, obtained by thermal activation of the clusters $[Ir_3(CO)_9(\mu_3\text{-}Bi)]$ and $[Ir_5(CO)_{10}(\mu_3\text{-}Bi)_2(\mu_4\text{-}Bi)]$ [125]. The heterometallic complex $[Bi_2Pd_2(O_2CCF_3)_{10}(HO_2CCF_3)_2]$ was used as precursor to prepare carbon-supported PdBi catalyst for the oxidation of D-glucose [126].

Tin has also been shown as valuable modifier to many other transition metal catalysts. Iridium-tin catalysts have been shown to have high selectivity for dehydrogenation of propane to propene [127]. Nickel-tin catalysts have been shown to produce hydrogen catalytically from biomass-derived oxygenated hydrocarbons [128]. Platinum-tin nanoparticles supported on alumina that are used as dehydrogenation and aromatization catalysts have shown to be even more effective than Pt-Re and Pt-Ir bimetallic catalysts in petroleum reforming [19]. The platinum-tin catalysts possess increased reforming selectivity and reduced poisoning by weakening Pt-C bonds that lead to the formation of coke. Many studies have been conducted to try to

understand the role of tin in bimetallic catalysts considering the fact that Pt surface should be poisoned by even small traces of metallic tin [21]. Dautzenberg and Biloen have suggested that tin divides the surface to very small ensembles of platinum atoms (ensemble effect); thus, the hydrogenolysis and isomerization can be suppressed to reduce coke formation [129, 130]. However, Burch and Garla proposed that tin modifies the electronic properties of the small platinum particles (ligand effect), which is attributed to the higher stability and selectivity. Lead has also been used as catalytic modifier in bimetallic transition metal catalysts, but to a lesser extent and not in heterogeneous catalysis system. For instance, a Pd–Pb complex [$PdPb(OAc)_4$] (where OAc is the acetate, $C_2H_3O_2$ ligand) was used in the benzylic acyloxylation of alkyl aromatics in liquid phase [131].

Among these heavy main group metal modifiers, group 14 elements, germanium and tin draw particular extensive attention for heterogeneous hydrogenation reactions [132]. Rh-Ge bimetallic catalysts supported on alumina prepared by surface redox reaction exhibited exceptional product selectivity of citral hydrogenation to the unsaturated alcohols (nerol and geraniol), which are crucial feedstock for several industries, such as flavor, fragrance, and pharmaceutical industry. On the other hand, the monometallic rhodium catalysts lead to the undesired saturated aldehyde (citronellal) as major product [108]. Tin-containing nanoscale catalysts platinum-tin, rhodium-tin, and ruthenium-tin anchored with mesoporous silica are shown to exhibit remarkable selectivity for the selective hydrogenation (as shown in Fig. 2.13a) of 1,5,9-cyclododecatriene (CDT) to produce cyclododecene (CDE) [133]. By contrast, hydrogenation of CDT by using most simple catalysts readily gives cyclododecane (CDA) as the final product from which all three C=C bonds are hydrogenated. However, CDE is more desired product which is the vital feedstock in many industrial processes. The lone C=C double bond in CDE is easily functionalized and thus can be used to produce a variety of C12 products including precursors to polyesters and nylon-12. Bimetallic organometallic transition metal cluster complexes are used as precursors to prepare the catalysts which are synthesized by deposition of organometallic cluster complexes from solution onto silica supports such as Davison type 911, following by ligand removal by heating in vacuo for 1 h at 473 K. The corresponding parent cluster complexes used for the nanocatalysts of $PtSn_2$, $RhSn_2$, and $RuSn_2$ are $(COD)Pt(SnPh_3)_2$, (COD = 1,5-cyclooctadiene), $Rh_3(CO)_6(SnPh_3)_2(\mu\text{-}SnPh)_2$, and $Ru(CO)_4(SnPh_3)_2$, respectively. To compare the catalytic performance with the pure PGM (platinum group metals), $Pt(COD)_2$, $Rh_4(CO)_{12}$, and $Ru_3(CO)_{12}$ were used as the precursors to prepare the corresponding monometallic catalysts in the same way as those bimetallic catalysts. The result of the catalytic performance is shown in Fig. 2.13b, which clearly shows in exceptional selective hydrogenation of cluster-derived supported tin-containing bimetallic catalysts. Moreover, Ru-Sn nanocatalysts with different ratios of Ru:Sn from molecular cluster complexes $[Ru_4(\mu_4\text{-}SnPh)_2(CO)_{12}]$, $[Ru_4(\mu_4\text{-}SnPh)_2(\mu\text{-}SnPh_2)_2(\mu\text{-}CO)_2(CO)_8]$, $[Ru_4(\mu_4\text{-}SnPh)_2(\mu\text{-}SnPh_2)_4(CO)_8]$, $[Ru_6(\mu_6\text{-}C)(CO)_{16}(\mu\text{-}SnCl_3)]^-$, and $PtRu_5(CO)_{16}(\mu\text{-}SnPh_2)(\mu_6\text{-}C)$ are also evaluated for

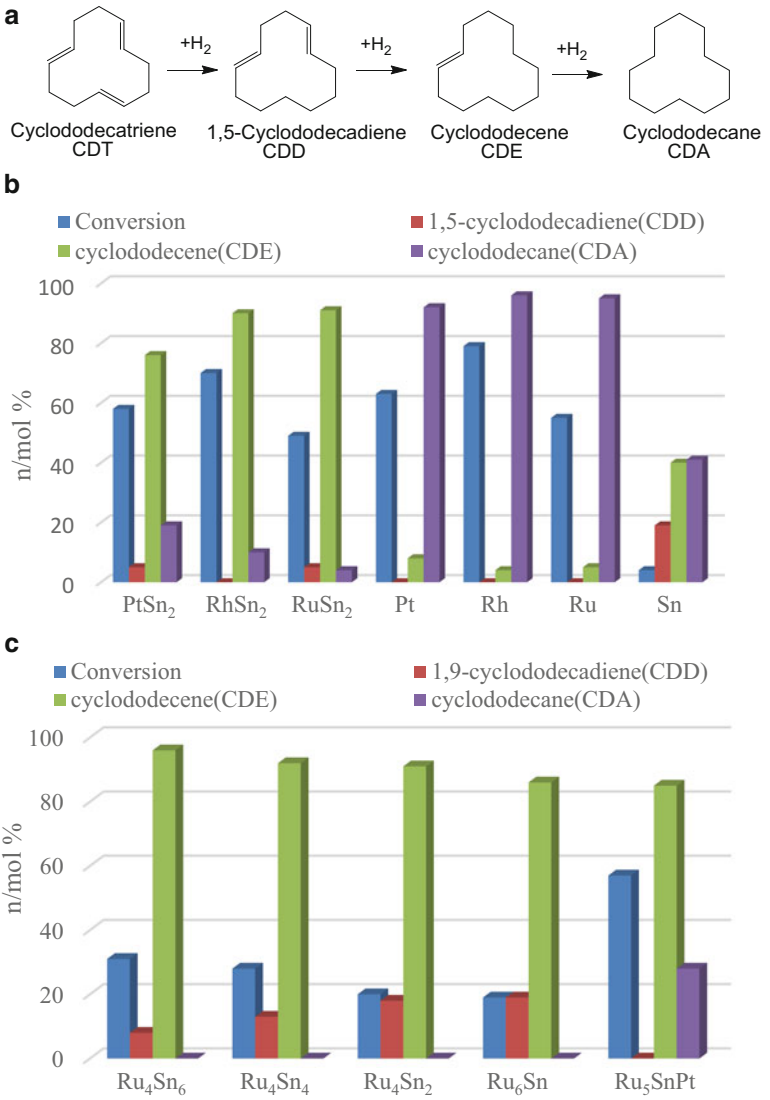

Fig. 2.13 (**a**) Stepwise hydrogenation reaction of 1,5,9-cyclododecatriene (CDT). (**b**) Effect of tin in the selective hydrogenation of CDT using anchored monometallic and bimetallic cluster catalysts. (**c**) Comparison of catalytic performance of Ru_4Sn_6, Ru_4Sn_4, Ru_4Sn_2, Ru_6Sn, and Ru_5SnPt. Reaction conditions: substrate 50 g, catalyst 25 mg (cluster anchored on mesopore 2% metal loading), H_2 pressure 30 bar, T = 373 K, t = 8 h. n/mol% represents the conversion (%) into product

selective hydrogenation of CDT (result see Fig. 2.13c). By incorporation of tin as modifier to platinum group metals, the selectivity and catalytic efficiency are significantly enhanced.

2.4 Summary

Hydrogen is considered as the most possible alternative energy carrier, and the activation of H–H bond is a very important aspect of chemistry. Hydrogen activation plays a very important role in hydrogenation, hydro-formylation, and hydrogenolysis processes which are key reactions in chemical refining, fuel production, and drug development. Transition metal complexes have been extensively studied as dihydrogen activation catalysts. Considerable amount of efforts have been made during the last century in order to design and synthesis of promising complexes as homogenous or heterogeneous catalysts for hydrogen activation or to serve as biomimetic models to study the hydrogen activation or production mechanisms. In the course of pursuing insights about hydrogen activation, researchers have developed numbers of techniques and methodologies to assist the characterization of reaction intermediates. For example, the development of single crystal X-ray analysis and proton NMR spectroscopy has helped with the determination of complex structures that involve hydrogen molecule or hydrogen atoms. In some rare cases, neutron diffraction is used to precisely locate hydrogen atoms. If iron is involved in the complex, Mössbauer spectroscopy can also be used to determine the oxidation states of the iron centers. It is no doubt that computational chemistry, especially DFT calculations in conjunction with other characterization methods, contributed tremendously to the development of this field.

This chapter summarized some history and recent development in the field of transition metal complexes that are important in hydrogen activation. The hydrogen activation can be classified into two categories, homolytic and heterolytic cleavage. The former normally happens on mononuclear metal complexes, while in most of the cases, dihydrogen molecule will undergo heterolytic cleavage to form a proton and a hydride. Dinuclear transition metal cluster complexes are vital in hydrogen activation not only because they are easy to prepare, but they also play crucial roles in biological systems, namely hydrogenase. Multinuclear transition metal cluster complexes, interestingly, can bind hydrogen molecule reversibly under mild conditions. Numbers of these cluster complexes show very high activity and selectivity for hydrogenation reactions either in solution or deposited on support. In sum, the transition metal complexes in hydrogen activation is a very interesting and important topic which has made considerable progress. With the assistance of current resources and technology, hydrogen activation mechanism will be fully established, which will play an important role in designing new catalysts and will greatly impact the chemical industry and contribute considerably to our daily life.

Acknowledgement The technical support from the Departments of Chemistry at Texas A&M University and Washington State University were duly acknowledged.

References

1. J.N. Armor, Catalysis and the hydrogen economy. Catal. Lett. **101**(3–4), 131–135 (2005)
2. J.M. Thomas, R. Raja, B.F.G. Johnson, S. Hermans, M.D. Jones, T. Khimyak, Bimetallic catalysts and their relevance to the hydrogen economy. Ind. Eng. Chem. Res. **42**(8), 1563–1570 (2003)
3. S.S. Bath, L. Vaska, Five-coordinate hydrido-carbonyl complexes of rhodium and iridium and their analogy with CoH(CO)4. J. Am. Chem. Soc. **85**(21), 3500–3501 (1963)
4. F. Maseras, A. Lledós, E. Clot, O. Eisenstein, Transition metal polyhydrides: from qualitative ideas to reliable computational studies. Chem. Rev. **100**(2), 601–636 (2000)
5. W. Hieber, F. Leutert, Zur Kenntnis des koordinativ gebundenen Kohlenoxyds: Bildung von Eisencarbonylwasserstoff. Naturwissenschaften **19**(17), 360–361 (1931)
6. P.J. Craig, The organometallic chemistry of the transition metals. R H Crabtree, John Wiley and Sons (Wiley Interscience), New York, Chichester, Brisbane, Toronto, Singapore, 1988. £36.45. ISBN 0 471853062. Appl. Organomet. Chem. **3**(6), 563 (1989)
7. P.J. Brothers, Heterolytic activation of hydrogen by transition metal complexes, in *Prog. Inorg. Chem.* (Wiley, New York, 2007), pp. 1–61
8. M.M.T. Khan, A.E. Martell, 1 – Activation of molecular hydrogen, in *Activation of Small Inorganic Molecules*, ed. by M.M.T.K.E. Martell (Academic, New York, 1974), pp. 1–77
9. G.J. Kubas, R.R. Ryan, B.I. Swanson, P.J. Vergamini, H.J. Wasserman, Characterization of the first examples of isolable molecular hydrogen complexes, $M(CO)_3(PR_3)_2(H_2)$ (M = molybdenum or tungsten; R = Cy or isopropyl). Evidence for a side-on bonded dihydrogen ligand. J. Am. Chem. Soc. **106**(2), 451–452 (1984)
10. J. Kubas Gregory, Molecular hydrogen complexes: coordination of a.sigma. bond to transition metals. Acc. Chem. Res. **21**(3), 120–128 (1988)
11. G.J. Kubas, *Metal Dihydrogen and Bond Complexes: Structure Theory and Reactivity* (Kluwer Academic/Plenum Publishers, New York, 2011), p. 472
12. P.G. Jessop, R.H. Morris, Reactions of transition metal dihydrogen complexes. Coord. Chem. Rev. **121**, 155–284 (1992)
13. H. Berke, Conceptual approach to the reactivity of dihydrogen. ChemPhysChem **11**(9), 1837–1849 (2010)
14. G.J. Kubas, Fundamentals of H2 binding and reactivity on transition metals underlying hydrogenase function and H2 production and storage. Chem. Rev. **107**(10), 4152–4205 (2007)
15. J. Halpern, The catalytic activation of hydrogen in homogeneous, heterogeneous, and biological systems, in *Advances in Catalysis*, ed. by D.D. Eley, P. W. S., B.W. Paul, vol 11 (Academic, New York, 1959), pp. 301–370
16. C. Pettinari, F. Marchetti, D. Martini, Metal complexes as hydrogenation catalysts, in *Comprehensive Coordination Chemistry II*, ed. by J.A.M.J. Meyer (Pergamon, Oxford, 2003), pp. 75–139
17. B.R. James, Hydrogenation reactions catalyzed by transition metal complexes, in *Adv. Organomet. Chem.* ed. by F.G.A. Stone, W. Robert, vol 17 (Academic, New York, 1979), pp. 319–405
18. L.A. Oro, D. Carmona, Rhodium, in *The Handbook of Homogeneous Hydrogenation* (Wiley-VCH Verlag GmbH, Weinheim, 2008), pp. 2–30
19. R.H. Crabtree, Iridium, in *The Handbook of Homogeneous Hydrogenation* (Wiley-VCH Verlag GmbH, Weinheim, 2008), pp. 31–44
20. J.A. Osborn, F.H. Jardine, J.F. Young, G. Wilkinson, The preparation and properties of tris (triphenylphosphine)halogenorhodium(I) and some reactions thereof including catalytic homogeneous hydrogenation of olefins and acetylenes and their derivatives. J. Chem. Soc. A: Inorg. Phys. Theor. (0), 1711–1732 (1966)
21. R.R. Schrock, J.A. Osborn, Catalytic hydrogenation using cationic rhodium complexes. 3. The selective hydrogenation of dienes to monoenes. J. Am. Chem. Soc. **98**(15), 4450–4455 (1976)

22. R. Crabtree, Iridium compounds in catalysis. Acc. Chem. Res. **12**(9), 331–337 (1979)
23. P. Gallezot, Hydrogenation – heterogeneous, in *Encyclopedia of Catalysis* (Wiley, New York, 2002)
24. I. Horiuti, M. Polanyi, Exchange reactions of hydrogen on metallic catalysts. Trans. Faraday Soc. **30**, 1164–1172 (1934)
25. E.L. Muetterties, T.N. Rhodin, E. Band, C.F. Brucker, W.R. Pretzer, Clusters and surfaces. Chem. Rev. **79**(2), 91–137 (1979)
26. E.L. Muetterties, S.T. Olin, Metal clusters in catalysis VIII. Reduction of triple bonds. Bull. Soc. Chim. Belg. **85**(7), 451–470 (1976)
27. M.Y. Darensbourg, E.J. Lyon, J.J. Smee, The bio-organometallic chemistry of active site iron in hydrogenases. Coord. Chem. Rev. **206–207**, 533–561 (2000)
28. L. Vaska, J.W. DiLuzio, Activation of hydrogen by a transition metal complex at normal conditions leading to a stable molecular dihydride. J. Am. Chem. Soc. **84**(4), 679–680 (1962)
29. C.E. Johnson, R. Eisenberg, Stereoselective oxidative addition of hydrogen to iridium(I) complexes. Kinetic control based on ligand electronic effects. J. Am. Chem. Soc. **107**(11), 3148–3160 (1985)
30. G.J. Kubas, R.R. Ryan, D.A. Wrobleski, Molecular hydrogen complexes of the transition metals. 3. Evidence for a new complex, $Mo(CO)(dppe)_2(H_2)$, and for solution equilibrium between dihydrogen and dihydride forms, M-.eta.2-H2.dblarw. H-M-H, in $M(CO)_3(PR_3)_2(H_2)$. J. Am. Chem. Soc. **108**(6), 1339–1341 (1986)
31. M.T. Haward, M.W. George, P. Hamley, M. Poliakoff, Dihydride versus dihydrogen complex; the photochemical reaction of $(\eta^5\text{-}C_5H_5)M(CO)_4$(M = V, Nb and Ta) with hydrogen in solution at both cryogenic and room temperatures. J. Chem. Soc. Chem. Commun. (16), 1101–1103 (1991)
32. D.M. Heinekey, J.K. Law, S.M. Schultz, Kubas complexes revisited: novel dihydride complexes of tungsten. J. Am. Chem. Soc. **123**(50), 12728–12729 (2001)
33. G.J. Kubas, R.R. Ryan, C.J. Unkefer, Molecular hydrogen complexes. 5. Electronic control of $\eta^2\text{-}H_2$ vs. dihydride coordination. Dihydride structure of $MoH_2(CO)(R_2PC_2H_4PR_2)_2$ for R = Et, iso-Bu versus $\eta^2\text{-}H_2$ for R = Ph. J. Am. Chem. Soc. **109**(26), 8113–8115 (1987)
34. G.J. Kubas, C.J. Burns, J. Eckert, S.W. Johnson, A.C. Larson, P.J. Vergamini, C.J. Unkefer, G.R.K. Khalsa, S.A. Jackson, O. Eisenstein, Neutron structure and inelastic-neutron-scattering and theoretical studies of molybdenum complex $Mo(CO)(H_2)[(C_6D_5)_2PC_2H_4P(C_6D_5)_2]_2{\cdot}4.5C_6D_6$, a complex with an extremely low barrier to hydrogen rotation. Implications on the reaction coordinate for H-H cleavage to dihydride. J. Am. Chem. Soc. **115**(2), 569–581 (1993)
35. R.H. Crabtree, M. Lavin, C-H and H-H bond activation; dissociative vs. nondissociative binding to iridium. J. Chem. Soc. Chem. Commun. (12), 794–795 (1985)
36. A.N. Khlobystov, A.J. Blake, N.R. Champness, D.A. Lemenovskii, A.G. Majouga, N.V. Zyk, M. Schröder, Supramolecular design of one-dimensional coordination polymers based on silver(I) complexes of aromatic nitrogen-donor ligands. Coord. Chem. Rev. **222**(1), 155–192 (2001)
37. J. Tomàs, A. Lledós, Y. Jean, The Kubas complex revisited. A theoretical study of dihydrogen addition and structure of the dihydride form. Organometallics **17**(2), 190–195 (1998)
38. F. Maseras, M. Duran, A. Lledos, J. Bertran, Molecular hydrogen complexes with a hydride ligand. An ab initio study on the iron hydride, $[Fe(PR_3)_4H(H_2)]^+$, system. J. Am. Chem. Soc. **113**(8), 2879–2884 (1991)
39. J. Pospech, I. Fleischer, R. Franke, S. Buchholz, M. Beller, Alternative metals for homogeneous catalyzed hydroformylation reactions. Angew. Chem. Int. Ed. **52**(10), 2852–2872 (2013)
40. S. Tan, C.T. Williams, An in situ spectroscopic study of prochiral reactant–chiral modifier interactions on palladium catalyst: case of alkenoic acid and cinchonidine in various solvents. J. Phys. Chem. C **117**(35), 18043–18052 (2013)
41. S. Tan, J. Monnier, C. Williams, Kinetic study of asymmetric hydrogenation of α, β-unsaturated carboxylic acid over cinchona-modified Pd/Al_2O_3 catalyst. Top. Catal. **55**(7–10), 512–517 (2012)

42. R. Noyori, H. Takaya, BINAP: an efficient chiral element for asymmetric catalysis. Acc. Chem. Res. **23**(10), 345–350 (1990)
43. T. Hayashi, Chiral monodentate phosphine ligand MOP for transition-metal-catalyzed asymmetric reactions. Acc. Chem. Res. **33**(6), 354–362 (2000)
44. M.J. Burk, Modular phospholane ligands in asymmetric catalysis. Acc. Chem. Res. **33**(6), 363–372 (2000)
45. W.S. Knowles, Asymmetric hydrogenation. Acc. Chem. Res. **16**(3), 106–112 (1983)
46. W.S. Knowles, Application of organometallic catalysis to the commercial production of L-DOPA. J. Chem. Educ. **63**(3), 222 (1986)
47. J. Halpern, 2 – Asymmetric catalytic hydrogenation: mechanism and origin of enantioselection, in *Asymmetric Synthesis*, ed. by J.D. Morrison (Academic, San Diego, 1985), pp. 41–69
48. I.D. Gridnev, T. Imamoto, On the mechanism of stereoselection in Rh-catalyzed asymmetric hydrogenation: a general approach for predicting the sense of enantioselectivity. Acc. Chem. Res. **37**(9), 633–644 (2004)
49. C.R. Landis, J. Halpern, Asymmetric hydrogenation of methyl (Z)-.alpha.-acetamidocinnamate catalyzed by [1,2-bis(phenyl-o-anisoyl)phosphino)ethane]rhodium(I): kinetics, mechanism and origin of enantioselection. J. Am. Chem. Soc. **109**(6), 1746–1754 (1987)
50. R. Noyori, T. Ohkuma, M. Kitamura, H. Takaya, N. Sayo, H. Kumobayashi, S. Akutagawa, Asymmetric hydrogenation of β-keto carboxylic esters. A practical, purely chemical access to β-hydroxy esters in high enantiomeric purity. J. Am. Chem. Soc. **109**(19), 5856–5858 (1987)
51. T. Liu, D.L. DuBois, R.M. Bullock, An iron complex with pendent amines as a molecular electrocatalyst for oxidation of hydrogen. Nat. Chem. **5**(3), 228–233 (2013)
52. D.M.P. Mingos, Polyhedral skeletal electron pair approach. Acc. Chem. Res. **17**(9), 311–319 (1984)
53. A.S. Weller, J.S. McIndoe, Reversible binding of dihydrogen in multimetallic complexes. Eur. J. Inorg. Chem. **2007**(28), 4411–4423 (2007)
54. R.W. Broach, J.M. Williams, Interaction of hydrogen and hydrocarbons with transition metals. Neutron diffraction study of di-.mu.-hydrido-decacarbonyltriosmium, $(\mu\text{-H})_2Os_3(CO)_{10}$, containing a four-center four-electron hydrogen-osmium (H_2Os_2) bond. Inorg. Chem. **18**(2), 314–319 (1979)
55. R.D. Wilson, R. Bau, The molecular structure of dodecacarbonyltetra-.mu.3-hydrotetrarhenium. Evidence for face-bridging hydrogen atoms. J. Am. Chem. Soc. **98**(15), 4687–4689 (1976)
56. R.D. Adams, Y. Kan, Q. Zhang, M.B. Hall, E. Trufan, Bonding and reactivity in the electronically unsaturated hydrogen-bridged dimer $[Ru_3(CO)_8(\mu_3\text{-CMe})(\mu\text{-H})_2(\mu_3\text{-H})]_2$. Organometallics **31**(1), 50–53 (2012)
57. M.J. Ingleson, M.F. Mahon, P.R. Raithby, A.S. Weller, $[(^iPr_3P)_6Rh_6H_{12}]^{2+}$: a high-hydride content octahedron that bridges the gap between late and early transition metal clusters. J. Am. Chem. Soc. **126**(15), 4784–4785 (2004)
58. S.K. Brayshaw, M.J. Ingleson, J.C. Green, P.R. Raithby, G. Kociok-Köhn, J.S. McIndoe, A.S. Weller, Holding onto lots of hydrogen: a 12-hydride rhodium cluster that reversibly adds two molecules of H_2. Angew. Chem. Int. Ed. **44**(42), 6875–6878 (2005)
59. R.D. Adams, B. Captain, Hydrogen activation by unsaturated mixed-metal cluster complexes: new directions. Angew. Chem. Int. Ed. **47**(2), 252–257 (2008)
60. R.D. Adams, B. Captain, L. Zhu, Facile activation of hydrogen by an unsaturated platinum–osmium cluster complex. J. Am. Chem. Soc. **129**(9), 2454–2455 (2007)
61. R.D. Adams, B. Captain, A highly unsaturated platinum–rhenium cluster complex that adds an unusually large amount of hydrogen. Angew. Chem. Int. Ed. **44**(17), 2531–2533 (2005)
62. R.D. Adams, B. Captain, C. Beddie, M.B. Hall, Photoreversible multiple additions of hydrogen to a highly unsaturated platinum–rhenium cluster complex. J. Am. Chem. Soc. **129**(4), 986–1000 (2007)

63. R.D. Adams, B. Captain, Unusual structures and reactivity of mixed metal cluster complexes containing the palladium/platinum Tri-t-butylphosphine grouping. Acc. Chem. Res. **42**(3), 409–418 (2009)
64. J.F. Harrod, A.J. Chalk, Homogeneous catalysis. III. Isomerization of deuterio olefins by group VIII metal complexes. J. Am. Chem. Soc. **88**(15), 3491–3497 (1966)
65. R.D. Adams, T.S. Barnard, Z. Li, W. Wu, J. Yamamoto, Catalytic hydrogenation of diphenylacetylene by a layer-segregated platinum-ruthenium cluster complex. J. Am. Chem. Soc. **116**(20), 9103–9113 (1994)
66. A. Volbeda, L. Martin, C. Cavazza, M. Matho, B. Faber, W. Roseboom, S.J. Albracht, E. Garcin, M. Rousset, J. Fontecilla-Camps, Structural differences between the ready and unready oxidized states of [NiFe] hydrogenases. JBIC **10**(3), 239–249 (2005)
67. E. Garcin, X. Vernede, E.C. Hatchikian, A. Volbeda, M. Frey, J.C. Fontecilla-Camps, The crystal structure of a reduced [NiFeSe] hydrogenase provides an image of the activated catalytic center. Structure **7**(5), 557–566 (1999)
68. A. Volbeda, E. Garcin, C. Piras, A.L. de Lacey, V.M. Fernandez, E.C. Hatchikian, M. Frey, J.C. Fontecilla-Camps, Structure of the [NiFe] hydrogenase active site: evidence for biologically uncommon Fe ligands. J. Am. Chem. Soc. **118**(51), 12989–12996 (1996)
69. H. Ogata, Y. Mizoguchi, N. Mizuno, K. Miki, S.-I. Adachi, N. Yasuoka, T. Yagi, O. Yamauchi, S. Hirota, Y. Higuchi, Structural studies of the carbon monoxide complex of [NiFe]hydrogenase from Desulfovibrio vulgaris Miyazaki F: suggestion for the initial activation site for dihydrogen. J. Am. Chem. Soc. **124**(39), 11628–11635 (2002)
70. Y. Montet, P. Amara, A. Volbeda, X. Vernede, E.C. Hatchikian, M.J. Field, M. Frey, J.C. Fontecilla-Camps, Gas access to the active site of Ni-Fe hydrogenases probed by X-ray crystallography and molecular dynamics. Nat. Struct. Mol. Biol. **4**(7), 523–526 (1997)
71. P.E.M. Siegbahn, J.W. Tye, M.B. Hall, Computational studies of [NiFe] and [FeFe] hydrogenases. Chem. Rev. **107**(10), 4414–4435 (2007)
72. M. Bruschi, M. Tiberti, A. Guerra, L. De Gioia, Disclosure of key stereoelectronic factors for efficient H_2 binding and cleavage in the active site of [NiFe]-hydrogenases. J. Am. Chem. Soc. **136**(5), 1803–1814 (2014)
73. W. Lubitz, H. Ogata, O. Rüdiger, E. Reijerse, Hydrogenases. Chem. Rev. **114**(8), 4081–4148 (2014)
74. M. Brecht, M. van Gastel, T. Buhrke, B. Friedrich, W. Lubitz, Direct detection of a hydrogen ligand in the [NiFe] center of the regulatory H_2-sensing hydrogenase from *Ralstonia eutropha* in its reduced state by HYSCORE and ENDOR spectroscopy. J. Am. Chem. Soc. **125**(43), 13075–13083 (2003)
75. J.P. Whitehead, R.J. Gurbiel, C. Bagyinka, B.M. Hoffman, M.J. Maroney, The hydrogen binding site in hydrogenase: 35-GHz ENDOR and XAS studies of the nickel-C (reduced and active form) and the Ni-L photoproduct. J. Am. Chem. Soc. **115**(13), 5629–5635 (1993)
76. C. Tard, C.J. Pickett, Structural and functional analogues of the active sites of the [Fe]-, [NiFe]-, and [FeFe]-hydrogenases. Chem. Rev. **109**(6), 2245–2274 (2009)
77. Y. Ohki, K. Tatsumi, Thiolate-bridged iron–nickel models for the active site of [NiFe] hydrogenase. Eur. J. Inorg. Chem. **2011**(7), 973–985 (2011)
78. F. Gloaguen, T.B. Rauchfuss, Small molecule mimics of hydrogenases: hydrides and redox. Chem. Soc. Rev. **38**(1), 100–108 (2009)
79. J.M. Camara, T.B. Rauchfuss, Combining acid–base, redox and substrate binding functionalities to give a complete model for the [FeFe]-hydrogenase. Nat. Chem. **4**(1), 26–30 (2012)
80. M. Ichikawa, Metal cluster compounds as molecular precursors for tailored metal catalysts, in *Advances in Catalysis*, ed. by D.D. Eley, H. P., B.W. Paul, vol 38 (Academic, New York, 1992), pp. 283–400
81. D.W. Goodman, J.E. Houston, Catalysis: new perspectives from surface science. Science **236** (4800), 403–409 (1987)
82. J. Xiao, R.J. Puddephatt, Pt-Re clusters and bimetallic catalysts. Coord. Chem. Rev. **143**, 457–500 (1995)

83. M.J. Dees, V. Ponec, On the influence of sulfur on the platinum/iridium bimetallic catalysts in n-hexane/hydrogen reactions. J. Catal. **115**(2), 347–355 (1989)
84. R.W. Rice, K. Lu, Comparison of platinum and platinum-iridium catalysts for heptane reforming at different pressures. J. Catal. **77**(1), 104–117 (1982)
85. J.C. Rasser, W.H. Beindorff, J.J.F. Scholten, Characterization and performance of platinum-iridium reforming catalysts. J. Catal. **59**(2), 211–222 (1979)
86. J.H. Sinfelt, Bifunctional catalysis, in *Advances in Chemical Engineering*, ed. by T.B. Drew, J. W. H. T. V., R.C. Giles, vol 5 (Academic, New York, 1964), pp. 37–74
87. J. Schwank, Bimetallic catalysts: discoveries, concepts, and applications. By John H. Sinfelt, John Wiley & Sons, 1983. XI+164 pp. AlChE J. **31**(8), 1405 (1985)
88. J.H. Sinfelt, G.H. Via, Dispersion and structure of platinum-iridium catalysts. J. Catal. **56**(1), 1–11 (1979)
89. B.D. Chandler, A.B. Schabel, C.F. Blanford, L.H. Pignolet, Preparation and characterization of supported bimetallic Pt–Au particle catalysts from molecular cluster and chloride salt precursors. J. Catal. **187**(2), 367–384 (1999)
90. B.D. Chandler, A.B. Schabel, L.H. Pignolet, Preparation and characterization of supported bimetallic Pt–Au and Pt–Cu catalysts from bimetallic molecular precursors. J. Catal. **193**(2), 186–198 (2000)
91. F. Schüth, K. Unger, Precipitation and coprecipitation, in *Preparation of Solid Catalysts* (Wiley-VCH Verlag GmbH, Weinheim, 2008), pp. 60–84
92. S. Tan, X. Sun, C.T. Williams, In situ ATR-IR study of prochiral 2-methyl-2-pentenoic acid adsorption on Al2O3 and Pd/Al2O3. PCCP **13**(43), 19573–19579 (2011)
93. G. Chen, S. Tan, W.J. Koros, C.W. Jones, Metal organic frameworks for selective adsorption of t-Butyl mercaptan from natural gas. Energy Fuel **29**(5), 3312–3321 (2015)
94. Chapter 7: Preparation and characterization of metal and alloy catalysts, in *Stud. Surf. Sci. Catal.*, vol. 95, ed. by P. Vladimir, C. B. Geoffrey (Elsevier, 1995), pp. 299–391
95. L. Mond, C. Langer, F. Quincke, L.-Action of carbon monoxide on nickel. J. Chem. Soc. Trans. **57**, 749–753 (1890)
96. A.K. Smith, J.M. Basset, Transition metal cluster complexes as catalysts. A review. J. Mol. Catal. **2**(4), 229–241 (1977)
97. J.M. Thomas, B.F.G. Johnson, R. Raja, G. Sankar, P.A. Midgley, High-performance nanocatalysts for single-step hydrogenations. Acc. Chem. Res. **36**(1), 20–30 (2003)
98. O.S. Alexeev, B.C. Gates, Supported bimetallic cluster catalysts. Ind. Eng. Chem. Res. **42**(8), 1571–1587 (2003)
99. E.G. Mednikov, S.A. Ivanov, I.V. Slovokhotova, L.F. Dahl, Nanosized $[Pd_{52}(CO)_{36}(PEt_3)_{14}]$ and $[Pd_{66}(CO)_{45}(PEt_3)_{16}]$ clusters based on a hypothetical Pd38 vertex-truncated $\nu 3$ octahedron. Angew. Chem. Int. Ed. **44**(42), 6848–6854 (2005)
100. N.T. Tran, D.R. Powell, L.F. Dahl, Nanosized $Pd_{145}(CO)_x(PEt_3)_{30}$ containing a capped three-shell 145-atom metal-core geometry of pseudo icosahedral symmetry. Angew. Chem. Int. Ed. **39**(22), 4121–4125 (2000)
101. S. Zacchini, Using metal carbonyl clusters to develop a molecular approach towards metal nanoparticles. Eur. J. Inorg. Chem. **2011**(27), 4125–4145 (2011)
102. R.D. Adams, J.E. Babin, M. Tasi, J.G. Wang, Catalyst design. The activation of a trinuclear metal cluster complex by metal atom substitution. Organometallics **7**(3), 755–764 (1988)
103. M. Castiglioni, R. Giordano, E. Sappa, Phosphine-substituted and phosphido-bridged metal clusters in homogeneous catalysis. J. Organomet. Chem. **342**(1), 111–127 (1988)
104. M. Castiglioni, R. Giordano, E. Sappa, Homogeneous catalytic hydrogenation and isomerization of linear and cyclic monoenes and dienes in the presence of the heterometallic cluster $(\eta^5\text{-}C_5H_5)NiRu_3(\mu\text{-}H)_3(CO)_9$. J. Organomet. Chem. **319**(2), 167–181 (1987)
105. B.D. Dombek, Synergistic behavior of homogeneous ruthenium-rhodium catalysts for hydrogenation of carbon monoxide. Organometallics **4**(10), 1707–1712 (1985)
106. P. Buchwalter, J. Rosé, P. Braunstein, Multimetallic catalysis based on heterometallic complexes and clusters. Chem. Rev. **115**(1), 28–126 (2015)

107. R. Raja, S. Hermans, D. Shephard, B.F.G. Johnson, R. Raja, G. Sankar, S. Bromley, J. Meurig Thomas, Preparation and characterisation of a highly active bimetallic (Pd-Ru) nanoparticle heterogeneous catalyst[dagger]. Chem. Commun. (16), 1571–1572 (1999)
108. T. Ekou, A. Vicente, G. Lafaye, C. Especel, P. Marecot, Bimetallic Rh-Ge and Pt-Ge catalysts supported on TiO2 for citral hydrogenation: II. Catalytic properties. Appl. Catal. A Gen. **314** (1), 73–80 (2006)
109. G. Lafaye, C. Micheaud-Especel, C. Montassier, P. Marecot, Characterization of bimetallic rhodium-germanium catalysts prepared by surface redox reaction. Appl. Catal. A Gen. **230** (1–2), 19–30 (2002)
110. G. Jacobs, L. Williams, U. Graham, G.A. Thomas, D.E. Sparks, B.H. Davis, Low temperature water–gas shift: in situ DRIFTS-reaction study of ceria surface area on the evolution of formates on Pt/CeO2 fuel processing catalysts for fuel cell applications. Appl. Catal. A Gen. **252**(1), 107–118 (2003)
111. R. Burch, Platinum-tin reforming catalysts: I. The oxidation state of tin and the interaction between platinum and tin. J. Catal. **71**(2), 348–359 (1981)
112. R. Burch, L.C. Garla, Platinum-tin reforming catalysts. J. Catal. **71**(2), 360–372 (1981)
113. T. Fujikawa, F.H. Ribeiro, G.A. Somorjai, The effect of Sn on the reactions ofn-Hexane and cyclohexane over polycrystalline Pt foils. J. Catal. **178**(1), 58–65 (1998)
114. Y.-K. Park, F.H. Ribeiro, G.A. Somorjai, The effect of potassium and tin on the hydrogenation of ethylene and dehydrogenation of cyclohexane over Pt(111). J. Catal. **178**(1), 66–75 (1998)
115. R.D. Cortright, J.A. Dumesic, Microcalorimetric, spectroscopic, and kinetic studies of silica supported Pt and Pt/Sn catalysts for isobutane dehydrogenation. J. Catal. **148**(2), 771–778 (1994)
116. F. Epron, C. Carnevillier, P. Marécot, Catalytic properties in n-heptane reforming of Pt–Sn and Pt–Ir–Sn/Al2O3 catalysts prepared by surface redox reaction. Appl. Catal. A Gen. **295**(2), 157–169 (2005)
117. G.W. Huber, J.W. Shabaker, J.A. Dumesic, Raney Ni-Sn catalyst for H_2 production from biomass-derived hydrocarbons. Science **300**(5628), 2075–2077 (2003)
118. R.D. Cortright, J.M. Hill, J.A. Dumesic, Selective dehydrogenation of isobutane over supported Pt/Sn catalysts. Catal. Today **55**(3), 213–223 (2000)
119. S. Hermans, R. Raja, J.M. Thomas, B.F.G. Johnson, G. Sankar, D. Gleeson, Solvent-free, low-temperature, selective hydrogenation of polyenes using a bimetallic nanoparticle Ru–Sn catalyst. Angew. Chem. Int. Ed. **40**(7), 1211–1215 (2001)
120. B.F.G. Johnson, S.A. Raynor, D.B. Brown, D.S. Shephard, T. Mashmeyer, J.M. Thomas, S. Hermans, R. Raja, G. Sankar, New catalysts for clean technology. J. Mol. Catal. A Chem. **182–183**, 89–97 (2002)
121. D. Dumitriu, R. Bârjega, L. Frunza, D. Macovei, T. Hu, Y. Xie, V.I. Pârvulescu, S. Kaliaguine, BiOx clusters occluded in a ZSM-5 matrix: preparation, characterization, and catalytic behavior in liquid-phase oxidation of hydrocarbons. J. Catal. **219**(2), 337–351 (2003)
122. G. Qian, D. Ji, G. Lu, R. Zhao, Y. Qi, J. Suo, Bismuth-containing MCM-41: synthesis, characterization, and catalytic behavior in liquid-phase oxidation of cyclohexane. J. Catal. **232**(2), 378–385 (2005)
123. R.K. Grasselli, Selective oxidation and ammoxidation of olefins by heterogeneous catalysis. J. Chem. Educ. **63**(3), 216 (1986)
124. R. Raja, R.D. Adams, D.A. Blom, W.C. Pearl, E. Gianotti, J.M. Thomas, New catalytic liquid-phase ammoxidation approach to the preparation of niacin (vitamin B3). Langmuir **25**(13), 7200–7204 (2009)
125. R.D. Adams, M. Chen, G. Elpitiya, M.E. Potter, R. Raja, Iridium–bismuth cluster complexes yield bimetallic nano-catalysts for the direct oxidation of 3-picoline to niacin. ACS Catal. **3** (12), 3106–3110 (2013)
126. B. Li, H. Zhang, L. Huynh, C. Diverchy, S. Hermans, M. Devillers, E.V. Dikarev, Bismuth–palladium heterometallic carboxylate as a single-source precursor for the carbon-supported Pd–Bi/C catalysts. Inorg. Chem. **48**(13), 6152–6158 (2009)

127. M. Guidotti, V.D. Santo, A. Gallo, E. Gianotti, G. Peli, R. Psaro, L. Sordelli, Catalytic dehydrogenation of propane over cluster-derived Ir–Sn/SiO2 catalysts. Catal. Lett. **112**(1–2), 89–95 (2006)
128. J.W. Shabaker, D.A. Simonetti, R.D. Cortright, J.A. Dumesic, Sn-modified Ni catalysts for aqueous-phase reforming: characterization and deactivation studies. J. Catal. **231**(1), 67–76 (2005)
129. F.M. Dautzenberg, J.N. Helle, P. Biloen, W.M.H. Sachtler, Conversion of n-hexane over monofunctional supported and unsupported PtSn catalysts. J. Catal. **63**(1), 119–128 (1980)
130. P. Biloen, J.N. Helle, H. Verbeek, F.M. Dautzenberg, W.M.H. Sachtler, The role of rhenium and sulfur in platinum-based hydrocarbon-conversion catalysts. J. Catal. **63**(1), 112–118 (1980)
131. A.B. Goel, P.E. Throckmorton, R.A. Grimm, Homogeneous palladium catalyzed oxidations: a novel, highly effective bimetallic palladium lead acetate complex useful in benzylic acyloxylation of alkyl aromatics. Inorg. Chim. Acta **117**(1), L15–L17 (1986)
132. M.S. Holt, W.L. Wilson, J.H. Nelson, Transition metal-tin chemistry. Chem. Rev. **89**(1), 11–49 (1989)
133. R.D. Adams, D.A. Blom, B. Captain, R. Raja, J.M. Thomas, E. Trufan, Toward less dependence on platinum group metal catalysts: the merits of utilizing tin. Langmuir **24**(17), 9223–9226 (2008)

Hydrogen Separation Membranes of Polymeric Materials

3

Xiayun Huang, Haiqing Yao, and Zhengdong Cheng

Abstract

The increased requirement of a clean and efficient green energy source promotes the development of hydrogen-based economy. In order to lower the cost of manufacturing, the future development of the next generation of hydrogen separation membrane is necessary. This chapter summarized the hydrogen separation membrane technology, the membrane separation mechanism, the polymer material selection and membrane structure design, current industrial market and separation modules, as well as the future development of the next generation hydrogen separation membrane.

Author Contribution: All authors are contributing equally on the conceiving and outlook of the development of hydrogen separation polymer membrane. X. Huang complies the current research on polymer membrane, material development as well as industrial development. H. Yao contributes to principles of hydrogen separation membrane, membrane fabrication technique, and modules and system configuration. The editors, S. Bashir and J. Liu reviewed this chapter.

X. Huang (✉)
Department of Macromolecular Science, Fudan University, Shanghai, China

The State Key Laboratory of Molecular Engineering of Polymers, Fudan University, Shanghai, China

Artie McFerrin Department of Chemical Engineering, Texas A&M University, College Station, USA
e-mail: huangxiayun@fudan.edu.cn

H. Yao
Kaneka US Material Center, Kaneka Americas Holding, Inc., College Station, USA

Z. Cheng
Department of Macromolecular Science, Fudan University, Shanghai, China

Department of Materials Science and Engineering, Texas A&M University, College Station, USA

Mary Kay O'Connor Process Safety Center, Artie McFerrin Department of Chemical Engineering, Texas A&M University, College Station, USA
e-mail: zcheng@tamu.edu

Y.-P. Chen et al. (eds.), *Nanostructured Materials for Next-Generation Energy Storage and Conversion*, DOI 10.1007/978-3-662-53514-1_3

Abbreviations

α	Selectivity
μ	Permeability
6FDA	4,4′-(Hexafluoroisopropylidene) diphthalic anhydride
CA	Cellulose acetate
CMS	Carbon molecular sieve
CNT	Carbon nanotube
DOE	Department of energy
EC	Ethyl cellulose
EERC	Energy and environmental research center
IGCC	Integrated gasification combined cycles
MMM	Mixed matrix membrane
MOF	Metal organic frameworks
NCHT	National center for hydrogen technology
PBI	Polybenzimidazole
Pd	Palladium
PDA	1,3-Diaminopropane
PDMS	Poly(dimethyal siloxane)
PEI	Polyetherimide
PEMFC	Proton exchange membrane fuel cells
PEO	Poly(ethylene oxide)
PES	Polyethersulfone
PI	Polyimide
PIM	Polymer intrinsic microporosity
PMP	Polymethylpentene
PPO	Poly(phenylene oxide)
PS	Polystyrene
PSA	Pressure swing adsorption
PSF	Polysulfone
PVA	Polyvinyl alcohol
PVAm	Polyvinylamine
RTI	Research triangle institute
T_g	Glass transition temperature

Contents

3.1 Overview of Hydrogen Separation Membrane Technology

Due to increased carbon dioxide emissions, the requirement for a clean and efficient energy source is more acute, prompting the development of hydrogen-based economy. The advantages of such an approach are regeneration of less wasteful by-products and extended use of petroleum for plastics, drugs, and other commodities instead of heat or transport. If the hydrogen economy approaches 20% of total energy, efforts are required to generate the substantial amounts necessary for usage by the most efficient route possible to generate with high purity, low cost, to collect and to store hydrogen by the most cost effective means possible [1]. Hydrogen resources possess a high energy density compared with hydrocarbon-based resources. Combustion residual from hydrogen is only clean water. However, many issues in hydrogen production, delivery, and storage in an economic and safe way limit the growth of hydrogen energy uses. Energy conversion devices for hydrogen, such as fuel cell systems, have been developed for both mobile and stationary applications. A successful hydrogen resource should satisfy the production, delivery, and storage issues. Under the increasingly urgent environmental, economic, and political pressures from present fossil fuel, we must solve the many scientific and technological problems that exist in the present state of hydrogen production, separation, and storage. Especially, separation of hydrogen from other undesirable gases is an important step in the hydrogen production process.

In theory, hydrogen separation is an entropy decrease process, and as a result, it cannot happen spontaneously without consumption of energy [2]. The requirement for separation and purification technologies includes purity and productivity, which are directly related to processing costs. Currently, hydrogen can be purified through several techniques, such as cryogenic distillation, pressure swing adsorption (PSA), and membrane separation. While cryogenic distillation and PSA processes are commercially available, they are generally not cost effective and quite energetically demanding. Membrane separation, as the third method, is currently considered to be the most promising method because it can provide an attractive alternative to cryogenic distillation and PSA in terms of the purity and scale of production. Membrane gas separation processes do not require phase change or an extra thermal regeneration process, so they have a potential of energy efficiency competitive with other separation processes. Membrane gas separation processes also require relatively small footprints, which reduce the operation site requirements. Therefore, membrane separation processes consume less energy and have the possibility for continuous and ease of operation.

"Membrane" here is defined as the barrier that permits selective gas from a gas mixture to transport through. It is selective because some components can diffuse

through it much easier than others. In the past 50 years, the rapid membrane development for gas separation drives the hydrogen separation membrane application to two most popular critical processes [3]. One is the hydrogen recovery from off-gases in the ammonia industry starting from 1979. Another one is the hydrogen separation from syngas in the electronic industry in the second half of the 1990s [3]. Currently, pilot project and advance technology collectively enable other application of those separation membranes as the heart of the process.

There are different kinds of hydrogen selective membranes, and each of them has its own operating range (Table 3.1) in terms of operating temperature, flow composition (selectivity and flux), contamination mechanism, and the transportation mechanism. In general, the hydrogen selection membranes can be categorized into four types based on the membrane material: polymer, carbon, metallic, and ceramic membranes [4]. The latter three are called inorganic membranes. Also, it could further be divided into porous and nonporous (dense) membranes based on the geometry inside the membrane [1]. The membrane characteristics are summarized in Table 3.1 with operational hydrogen separation performance of those types of membrane. Compared with polymer membranes, inorganic membranes have such advantages as high thermal, chemical and mechanical stabilities, less plasticization, and better control of pore size and pore distribution for the control of selectivity and permeability [5].

Once the membrane type (such as polymer, metallic, carbon, or ceramic) is selected, the membrane module was another factor taking into account for the considerations of efficiency, membrane deterioration, manufacturability, maintainability, operability, as well as the operations cost [3]. Typically, the membrane modules can be divided into two main categories: flat and tubular. Based on flat membrane geometries, it includes plate-and-frame and spiral-wound modules. For the tubular geometry, it has tubular, capillary, and hollow-fiber modules. Those modules can be combined in multiple as a whole and can be combined in various ways.

Among the different types of hydrogen separation membrane, polymer membranes still dominate in the traditional gas separation market [1]. Consequently, polymeric membranes have a wide range of application due to ease to process as well as the relatively low cost. The idea to study the membrane for a variety of gas separation started at early 1950s [12]. It is due to the desired energy consideration, such as oxygen separation from air, helium gas separation from natural gas, and the hydrogen separation from produced petroleum gas [12]. In the late 1970s, Dupont [12] started manufacturing of first generation small diameter hollow fibrous membrane for viable gas separation. At that time, the manufacture efficiency was hard to be improved for the economically sustainable gas separation. This manufacture shortfall was later overcome by Monsanto [10] in 1980 to produce the asymmetric polysulfone silicone rubber hollow fibrous membrane for hydrogen separation from ammonia purge gases. This technology was quickly applied to the spiral-wound cellulose acetate membranes, which was developed by Separex (Honeywell's UOP) [11] and Cynara (Natco) [13] and carbon molecular sieve (CMS, Kvaerner) [13] (summarized in Table 3.2). The membrane has the better performance due to its high resistance to the hydrocarbon impurities. In 1983, one Japanese company, Ube [9], introduced a new type of polymer, polyimide membrane, which has the best thermo

Table 3.1 Properties of hydrogen separation membranes [1, 3, 4, 6–8]

Factors	Dense polymer	Microporous ceramic	Porous carbon	Dense metallic	Dense ceramic
Temperature (°C)	<100	200–600	500–900	300–600	600–900
H_2 Selectivity	Low	Moderate	Low	Very high	Very high
Strength	Medium	Strong	Low	Strong	Strong
H_2 Flux	Low	High	Moderate	High	Moderate
Known poisoning issues	HCl, SO_x, CO_2	–	Organics	H_2S, HCl, CO	H_2S
Stability issues	Swelling, compaction, mechanical strength	Stability in water	Brittle, oxidizing	Phase transition	Stability in CO_2
Costs	Low	High	High	Medium	High
Lifetime	Short	Long	Long	Long	Long
Example material	PI, PBI	Silica, alumina, zirconia,	Carbon	Palladium alloys, Pd-Cu, Pd-Au	Proton conducting ceramics
Transport mechanism	Solution/diffusion	Molecular Sieving	Surface Diffusion, Molecular Sieving	Solution/Diffusion	Solution/ Diffusion (Proton Conduction)
Development	Commercialized by air products, Linde, BOC, air liquid	Prototype tubular silica membranes available up to 90 cm^2	Small membrane modules commercial	Commercial by Johnson Matthey, prototype membrane tubes available up to 60 cm^2	Small sample (cm^2) available for testing

Table 3.2 Development history of polymeric hydrogen separation membranes and the corresponding gas separation performance [1, 9–11]

Membrane	Manufacture	H_2/N_2	H_2/CO	H_2/CH_4
Polysulfone silicone rubber [10]	Monsanto	39	23	24
Cellulose acetate [11]	Separex, Cynara, GMS	33	21	26
Polyimide [9]	Ube	35.4	30	–

and solvent resistance performance at that moment. The polyimide membrane was commercialized for the Seibu Oil's Onoba City refinery application. Although polymer membrane can be used for the separation of nearly all gas mixtures, in refineries and petrochemical industry, the common separations being of H_2/N_2, H_2/CO and H_2/CH_4 mixtures [1, 9–11].

The scope of this chapter focuses on the discussion of polymeric membranes as well as the polymer-hybrid porous membranes for the hydrogen separation application. Starting from separation mechanism of membrane, we focus on the separation mechanism and separation performance evaluation of polymer membrane in Sect. 3.2. Section 3.3 reviews the molecular design and application development of polymeric matrix for the hydrogen selection or hydrogen rejection depends on the functions of the separation mechanism. The relevant commercialized polymer separation membranes are also summarized in Sect. 3.3. In Sect. 3.4, the relevant industry designs for the hydrogen separation are included with the various types of polymer membranes. The challenge and recent development of the next generation of the polymeric hydrogen separation membrane is discussed in Sect. 3.5.

3.2 Principles of Hydrogen Separation Membrane

As mentioned before, the materials for hydrogen separation membrane span the entire periodic table and include metallic alloys, inorganic oxides, organic polymers, and composites. They are classified as follows: metallic (pure metals and alloys), inorganics (including ceramics, oxides, and zeolites), carbons, polymers, and composites. Due to their inherent chemical, mechanical, and thermal properties, each class of membranes offers its own unique pros and cons to H_2 separation [4, 14, 15]. To understand their performance as separation membrane, the main principles and important performance characteristics for gas separation membrane are described below.

3.2.1 Gas Separation Mechanism

There are five gas separation mechanisms (as shown in Fig. 3.1): (1) Knudson diffusion, (2) surface diffusion, (3) capillary condensation, (4) molecular sieving, and (5) solution diffusion [4, 6, 16].

Knudson diffusion (Fig. 3.1a) occurs when the pore size diameter in the membrane is smaller than the mean free path (average distance between collisions) of the

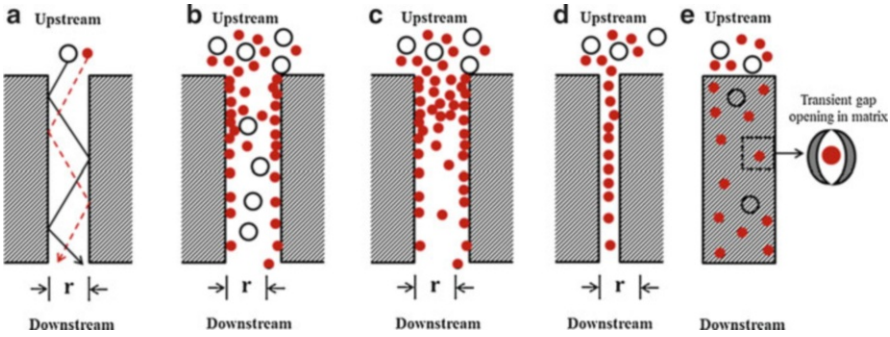

Fig. 3.1 Transport mechanisms in membranes: (**a**) Knudsen diffusion, (**b**) surface diffusion, (**c**) capillary condensation, (**d**) molecular sieving, and (**e**) solution diffusion [4, 17]

gas being separated. The Knudsen number K_n is defined as the ratio of the mean free path of the gas molecules (λ, nm) to the pore radius (R, nm) [16].

$$K_n = \lambda / R \tag{3.1}$$

For a specific gas, the free path is fixed. A larger pore size (relative to the mean free path of the gas molecules) leads to a smaller Knudsen number, hence lowers selectivity (α). When Knudsen values are < 1, the pore size in the membrane is larger than the mean free path of the gas molecules. In this case, the dominant transport mechanism is the viscous flow and nonselective separation occurs. From practical applications point of view, gas separation membranes only based on Knudsen diffusion mechanism are not commercially attractive due to their low selectivity.

Surface diffusion (Fig. 3.1b) occurs in two steps: (1) gas molecules are adsorbed on the pore walls of the membrane, and (2) adsorbed molecules migrate along the surface of the wall and pass through the membrane. This type of diffusion can occur in conjunction with Knudsen diffusion. Surface diffusion increases the permeability and selectivity for these gases that can be strongly adsorbed to the pore walls. During the diffusion, the gas absorption reduces the effective pore diameter. Consequently, transport of nonadsorbing gas molecules is reduced and selectivity for the adsorbed gas is increased.

Capillary condensation (Fig. 3.1c) happens when a condensed phase (partially) fills the pores. When the pores are fully filled with condensed phase, only the components soluble in the condensed phase can permeate through the membrane. Permeability and selectivity are generally high for capillary condensation.

Molecular sieving (Fig. 3.1d) operates on a size-exclusion principle. If pore diameter becomes sufficiently small (in the range of 3.0 – 5.2 Å), molecular sieving can be used to separate molecules with different kinetic diameters and only small gas molecules can pass through the membrane.

The solution diffusion mechanism (Fig. 3.1e) is the most commonly used model to explain gas transport through dense membranes. A gas molecule or atom adsorbed

on one side of the membrane permeates through the membrane and desorbs on the other side of the membrane. This separation mechanism is based on both solubility and mobility of gas molecule in the membrane barrier.

In some membranes, molecules can diffuse through the membrane by more than one mechanism. For example, combined mechanisms of Knudsen diffusion and surface diffusion occur in porous stainless steel. The contribution of these mechanisms in one specific material increases its overall separation performance. Generally, gas diffuses through porous membranes through the first four types of diffusion mechanisms, and for dense membranes, like dense polymer and palladium (Pd) based membranes, solution diffusion mechanism is dominated. Palladium-based membranes for gas separation have been commercialized. The solution-diffusion separations mechanism is based on both solubility and mobility of H^+ in Pd thin film [16]. There are three steps of hydrogen transport through Pd [17]: (1) dissociation of H^+ ions and electrons from chemisorbed H_2 on membrane surface, (2) diffusion of the H^+ ions through the membrane, and (3) re-association of the H^+ ions into H_2 molecules and desorption from the membrane.

3.2.2 Gas Separation Mechanism for Polymer Membrane

This section focuses specifically on polymer membranes for the separation of H_2, so the separation mechanism of polymeric membranes will be discussed in detail in this section. Polymeric membranes can be classified into glassy and rubbery polymeric membranes. When the operational temperature is lowered than its glass transition temperature (T_g, K), the polymer behaves as a rigid glass. Under this circumstance, the fractional free-volume in polymer decreases, and large-scale co-operative movements of the polymer backbone are restricted due to the limited space. When an amorphous polymer is kept above its T_g, the polymer is in a rubbery state. Due to transient voids between highly mobile polymer chains, it presents a relatively large amount of free-volume.

Compared with rubbery polymer membrane, glassy polymers are more feasible to be commercialized because of their high gas selectivity and good mechanical properties [18]. For glassy polymers, gas molecules with smaller diameter are more permeable than larger size molecules. The selectivity comes from the differences in molecular dimension. The fraction of free volume is an important parameter for glassy polymers. The amount of free volume (up to 20%) could be increased by some posttreatment methods, like a rapid cooling or a quick removal of the solvent. These voids generated from the above methods are not interconnected. Glassy polymers with a medium to high free-volume are usually utilized to produce membranes because they have enough voids to assist the transport of gas through membrane.

Polymers with large free volume have very porous structures so that diffusion occurs by the first four mechanisms as mentioned above, which depend on the sizes

of membrane pore and gas molecules. In Knudsen diffusion, the separation selectivity comes from the different retention times of diffusing gases. Gas molecules with smaller size collide more frequently with the pore walls than other gas molecules [19]. In surface diffusion, gas molecules adsorb to the pore walls and then move from one site to the next under a decreasing concentration gradient [4, 20]. Capillary condensation happens under very specific conditions when gas molecules condense within a pore to generate capillary forces. Only components soluble in the condensed phase can permeate through the membrane [21]. Finally, the molecular sieving occurs under a circumstance when the sizes of gas molecules and the pore are sufficiently close [22].

In the case of dense polymer membranes, gas transport occurs through the solution diffusion mechanism. But different with dense metal, H_2 molecules could not be dissociated into H^+ ions. There are no continuous passages for gas to pass through the membrane for dense polymer. The main force is the penetrant-scale transient gaps generated by the thermally agitated motion of chain segments in the polymer matrix. Therefore, gas could diffuse from the upstream to the downstream of the membrane through these transient gaps (schematically summarized in Fig. 3.1). The diffusing gas molecules undergo random jumps in the polymer membrane, but due to the concentration gradient between the upstream side and the downstream side, a diffusion flux transports toward the downstream side [17]. One of the advantages of dense polymer membranes is that the variation in the chemical nature of the polymer could allow for the control of the relative solubility and diffusion of different gases.

3.2.3 Gas Separation Performance Evaluation

Permeability and selectivity are the two most important performance characteristics for gas separation membranes [4, 23]. Permeability is the rate that gas molecule permeates through a membrane. The permeability under a solution-diffusion mechanism is a product of diffusion and selectivity, which is described as

$$P = S \times D \tag{3.2}$$

where P, S, and D are permeability ($cm^2 \cdot s \cdot$ cm-Hg), solubility (kg/L), and diffusivity ($mol/m^2 \cdot s$) coefficients, respectively. Solubility is correlated to the chemical interaction between gas molecules and the polymer matrix, whereas diffusion is related to the amount of free volume in polymers and the size of gas molecules.

Selectivity ($kmol \cdot m \cdot m^{-2} \cdot s^{-1} \cdot kPa^{-1}$) is defined as the flux per unit pressure difference between upstream and downstream sides, which is used to characterize the separating ability of a given membrane [4, 6]. Selectivity is a key parameter to determine the purity of hydrogen gas after separation. Ideal selectivity is considered as the ratio of permeability coefficients of the gas molecules.

$$\alpha_{i/j} = \frac{P_i}{P_j} = \frac{S_i}{S_j} \cdot \frac{D_i}{D_j} \tag{3.3}$$

where $\alpha_{i/j}$ is an ideal selectivity in a gas mixture of i and j [23–25].

Both permeability and selectivity are related to solubility and diffusion of the gas molecules in the membrane. Solubility is a thermodynamic factor that occurs when gas molecules adsorb onto the membrane, whereas diffusion is a kinetic factor that is correlated with the spatial extents of random motion of chain segments in a polymer matrix [24]. Solubility and diffusion are also activated energy processes, so they are frequently affected by the temperature. Polymer types determine the affinity between gas molecules and polymer matrix, which makes difference in solubility. Therefore, when developing new membrane materials, solubility and diffusivity coefficients are two key parameters to be considered.

As discussed in Sect. 3.2.2, there are two types of polymers: glassy and rubbery. Polymer membranes also can be classified into two types of gas separation membranes: sorption-selective and diffusion-selective [26]. Diffusion-selective membranes are usually glassy polymer membranes. The membrane performance can be improved by the gas diffusivity, which is influenced by the amount of free volume and the chain rigidity [27, 28]. Glassy polymers including cellulose acetate (CA), polyimide (PI), and polysulfone (PSF) are traditional gas separation membranes that have been widely used over the past three decades [17, 18, 25]. Those polymers have a small amount of free volume. Therefore, they have low gas permeability, but high selectivity. However, one disadvantage of glassy polymers is plasticization, which decreases the process efficiency and gas selectivity at high pressure [29].

Sorption-selective membranes are usually rubbery polymer membranes. The membrane performance can be improved by enhancing the gas solubility. Rubbery polymers have high chemical affinity with gas molecules due to the flexible chain motion in the rubbery state [30, 31]. Poly(ethylene oxide) (PEO)-based polymers, poly(dimethyl siloxane) (PDMS), polyvinylamine (PVAm), poly(amide-6-b-ethylene oxide) (Pebax®), and polyvinyl alcohol (PVA) are representative examples of sorption-selective membranes [32–35]. However, for small gas separation, most rubbery polymer membranes showed lower gas separation performances than glassy polymer membranes [36, 37]. Various modification methods have been researched to prevent the plasticization effect on rubbery polymer membranes, such as crosslinking and blending [38, 39].

Generally, glassy membranes have relatively high selectivity and low permeability, whereas rubbery membranes have high permeability but low selectivity. This trade-off relationship of gas separation membranes between gas permeability and selectivity has been well defined. Most commercial gas separation membranes are produced from low permeability polymers with reasonable selectivity. This trade-off relationship is mainly due to permeation efficiency. High permeability membranes usually possess either many sorption sites or diffusive pathways, where other gases can also transport through. Therefore, such membrane offers either poor gas selectivity or efficiency [36, 37].

3.3 Polymer Materials and Membrane Structure

The polymeric materials serve as the hydrogen separation membrane materials, the layered materials to separate hydrogen molecules from other gas molecules, such as N_2, CO_2 or CH_4 [37]. As stated in Sect. 3.2, it appears to have the trade-off limit between selectivity and permeability for the polymer membrane. Permeability here determines the productivity of the membrane while the selectivity contributes to the separation efficiency. Generally speaking, the membrane with high selectivity always tends to have a very low permeability. Those gas separation properties also depend on the membrane thickness with homogenous or heterogeneous as well as dense or porous structure. The membrane can be dense film or porous film, including microporous (pore size <2 nm), mesoporous (pore size in between 2 nm and 50 nm), and macroporous (pore size >50 nm) [40]. The membranes can be neutral or charged to transport the hydrogen molecules in a passive or active way. Moreover, the separation can be conducted under different gradient as the driving force, such as concentration pressure, chemical potential, electrical field, or magnetic field.

Except for the excellent gas separation performance, the membrane manufacture itself should also meet the following requirement. First, it should be easy to process with less cost. Second, the material should be chemically and physically stable, such as good mechanical property, thermal and chemical resistance and the plasticization tolerance as well as physical aging resistance to ensure the proper membrane robustness and life time [13]. At the same time, the cost-effective manufacture should also be considered for the industry application.

In those properties, the chemistry and structure of the membrane are the decisive factors. Ideally, the hydrogen separation membranes are expected to be defect-free in large scale, have great thermal, chemical, mechanical robustness, and high selectivity at high permeability (top right corner of Fig. 3.2). Although there are hundreds of polymer and membrane structures have been investigated as the candidates of hydrogen separation membrane, only few systems have been commercialized (summarized in Fig. 3.2). Robeson et al. [36, 37] illustrated this trade-off limit in selectivity and permeability of the polymeric membrane systems – the upper boundary in Fig. 3.2. The upper boundary has been greatly improved from 1991 to 2008 [36, 37], but still has a long path for the investigation towards the top right corner (desired high selectivity and high permeability as a whole).

In this section, we focus on the selection of the polymer material as well as the membrane structures to enable those desired properties. The chemical structure of polymer in one way decided the hydrogen separation performance and relevant robustness factors. The chemical modification and crosslinking were introduced to the membrane to tune the free volume, which significantly influence the hydrogen separation performance for the dense glassy polymer. Moreover, composition and microstructure of the membrane are also important factors to modulate the separation performance. Other than the free volume in the dense rigid polymer membrane, pore size can be tuned by other strategies, such as fibrous structure, gradient porosity, the hybrid mixed matrix membrane with porous filler, as well as the polymer intrinsic microporosity based on molecular free volume design.

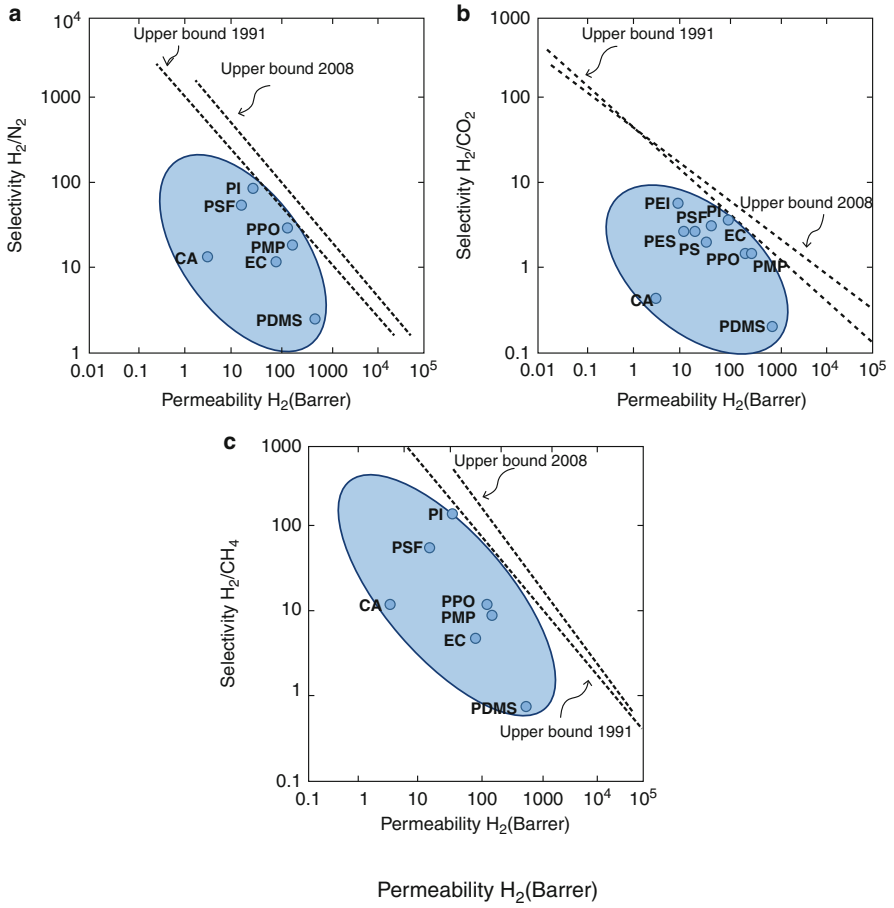

Fig. 3.2 Upper bound plot: selected hydrogen selectivity versus permeability of commercial polymer dense membrane for the industrial gas pairs. (**a**) H_2/N_2; (**b**) H_2/CO_2; and (**c**) H_2/CH_4 [36, 37]. *PI* polyimide, *PSF* polysulfone, *PPO* poly(phenylene oxide), *PMP* polymethylpentene, *CA* cellulose acetate, *EC* ethyl cellulose, *PDMS* polydimethylsiloxane, *PEI* polyetherimide, *PS* polystyrene, *PES* polyethersulfone (Reproduced from Refs. [36, 37] with permission from Elsevier)

3.3.1 Polymeric Membrane Material for Hydrogen Separation

The interactions between membrane and gas molecules that penetrate the membrane determine the separation performance. Kundsen diffusion and solution diffusion are the dominated mechanism for those interactions (discussed in Sect. 3.2) [1, 3, 4, 6, 7]. Specifically, for the polymer membrane, it can be further divided into glassy (rigid) polymeric membrane and rubbery (elastic) polymeric membranes. The distinction is based on the hydrogen separation testing temperature relative to the glass transition temperature (T_g) of the polymer. In general, the operating temperatures for polymer membranes are nearly 100 °C (373 K). When the operating temperature is above T_g,

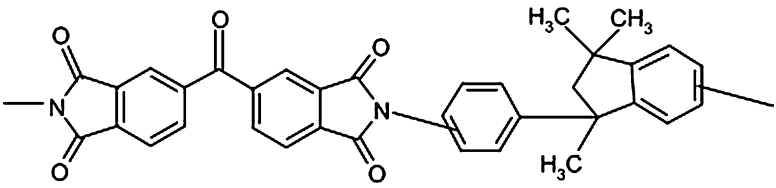

Fig. 3.3 Chemical Structure of Matrimid 5218 [46] (Reproduced from Ref. [46] with permission from Elsevier)

the membrane is rubbery, whereas when the operating temperature is below T_g, the membrane becomes glass [41]. The glassy dense membranes are rigid, which have the higher selectivity and lower flux, while the rubber-like elastic dense membrane has the higher flux but lower selectivity [3]. The high selectivity of the rigid polymer is due to the small free volume and lower flexibility of that rigid polymer chain in comparison with rubber polymers. It separates the molecules based on the size (size selective) and favors the small molecules to pass through it. The rubbery polymer, however, is highly flexible. It has a large amount of free volume [41] and shows high permeability, and the selectivity is influenced by the difference in the condensability of the type of gas molecules. In general, it prefers to reject the small molecule and permeable through the large hydrocarbons.

For the molecular design of the polymeric material, how to reach the desired separation performance is a critical technical parameter. The most highly permeable polymers normally have rigid, twisted molecular backbones that provide a number of free volume-microvoids [42]. The material should be relevantly robust and easily processable. Currently, the main polymers used in hydrogen separation are based on polymers of cellulose acetate (CA), ester (PE), sulfone (PSF), imide (PI), benzimidazole (PBI), and etherimide (PEI), and other arrangements [7, 36, 37]. In this section, we focus on two most popular polymers, PI and PBI, in the recent hydrogen separation membrane research. They have a similar conjugated backbone and are synthesized by condensation polymerization [43, 44]. However, the gas separation property is different from each other due to the stacking conformation [45]. Taking the idea from it, we take the chemical modification and structure design into the consideration to tune the gas separation behavior and relative robustness for a desired research.

3.3.1.1 Polyimide (PI)

Aromatic polyimide [43, 44] is an example of rigid glassy polymers, which was synthesized by the condensation polymerization of di-anhydrides and diamines. It has a strong thermal/mechanical property and excellent chemical resistance at the elevated temperature [23]. Matrimid 5218 (structure shown in Fig. 3.3) is a type of commercially available polyimide, developed by Ciba-Geigy, which has high gas permeability/selectivity, high thermal/mechanical stability, and solvent resistance at high temperatures [46]. Several other commercially available aromatic polyimides can also be considered as the candidate materials, such as Kapton (by DuPont),

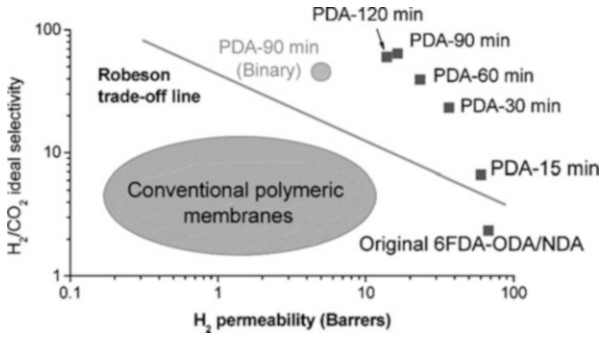

Fig. 3.4 Robeson upper bound plot. Selected hydrogen selectivity versus permeability of commercial dense polymeric membrane, co-poly(4,4′-diphenylene oxide/1,5-naphthalene-2,2′-bis (3,4-dicarboxylphenyl)hexafluoropropanediimide (6FDA-ODA/NDA) [36, 37, 44, 45]. The membrane surface modified with 1,3-diaminopropane (*PDA*) hit across the Robeson upper bounded limit and has the better hydrogen separation performance (Reproduced from Ref. [44] with permission from American Chemical Society)

IP-2080 (Dow Chemical), Ultem (General Electic), and LARC-TPI (Mitsui-Toatsu Chemicals) [47].

However, polyimides polymerized based on 4,4′-(hexafluoroisopropylidene) diphthalic anhydride (6FDA) suffer from a poor intrinsic H_2/CO_2 selectivity. Moreover, the solubility of CO_2 plasticizes the membrane to even worse scenario. Over decades, the modification of the 6FDA-based polyimide backbone is the most important research task to improve the gas selectivity. For example, a post-treatment (cross-linking) easily modulated the amount of free volume by simply selecting the size and spatial effect of the cross-linker [48]. However, this procedure was time-consuming; hence, an updated procedure has been introduced to induce cross-linking but with lesser steps [48]. The fluorine-containing polyimide, such as $–C(CF_3)_2$, improves the gas separation performance and still possesses excellent thermal and mechanical performance [48]. Low et al. [44] investigated the di-amino modified co-polyimide, co-poly(4,4′-diphenylene oxide/1,5-naphthalene-2,2′-bis(3,4-dicarboxylphenyl)hexafluoropropanediimide, (6FDA-ODA/NDA) on the H_2/CO_2 gas separation performance (summarized in history performance chart in Fig. 3.4). The diamino modified co-polyimide has a larger free volume and correspondingly increase the H_2/CO_2 permeability and selectivity. 1,3-Diaminopropane (PDA) was the most efficient surface modification reagent to increase the H_2/CO_2 separation performance (co-polyimide with PDA modification for 90 min for example) to across the Robeson trade-off line, which has a much better separation efficiency than 6-FDA-ODA/NDA co-polyimide.

3.3.1.2 Polybenzimidazole (PBI)

Polybenzimidazole (PBI) is a class of heterocylic polymer, which is similar to the aromatic polyimides. PBI systems possess extremely high thermal stability and excellent chemical resistance and moisture resistance [45, 49]. Moreover, it is easy

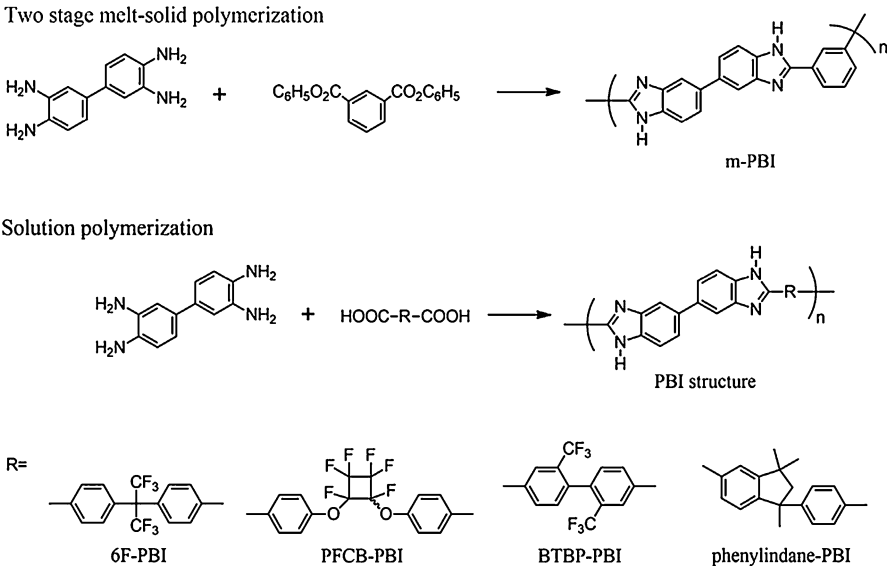

Fig. 3.5 Solid and solvent based polymerization of PBI derivatives [45] (Reproduced from Ref. [45] with permission from Elsevier)

to fabricate PBI bulk material into fibers and membranes with an outstanding stabilities [45, 49, 50]. PBI is a particularly interesting material for hydrogen separation because of the characteristics of this polymer. PBI itself is a rigid glassy thermoplastic with an extreme high glass transition temperature (T_g = 427 °C, 700 K) and does not hydrolyze. Polybenzimidazole materials are also resistant to common chemical agents, have high strength and structural stability, and are efficient at moving water due to the imidazole based side groups, which are capable of behaving as proton donors or proton acceptors, depending on the environmental pH. All these attributes make PBI based membranes thermo-mechanically robust with excellent selectivity and separation and are widely studied as a fuel cell proton exchange membrane. These properties also make PBI a great candidate for the hydrogen separation membrane among the glassy thermoplastics. The starting monomers are poly(2,2′-(*m*-phenylene)-5,5′-bibenzimidazole, *m*-PBI) condensed by a two-stage melt-solid polymerization (synthetically summarized in Fig. 3.5) [51]. The polymer was casted to a 4 μm thick membrane and it is found the H_2/CO_2 separation performance increased at a high temperature [51] and intersected the upper boundary of the Robeson plot as summarized as Fig. 3.1 [45]. Kumbharkar et al. [52] synthesized those *m*-PBI material via solution polycondensation processes for the asymmetric hollow fiber membrane and measured the performance at even wider temperature range from 100 °C to 400 °C. Similarly, it yielded a high selectivity for H_2/CO_2 separation with elevated performance, which was considered as a candidate for high temperature gas separation [52].

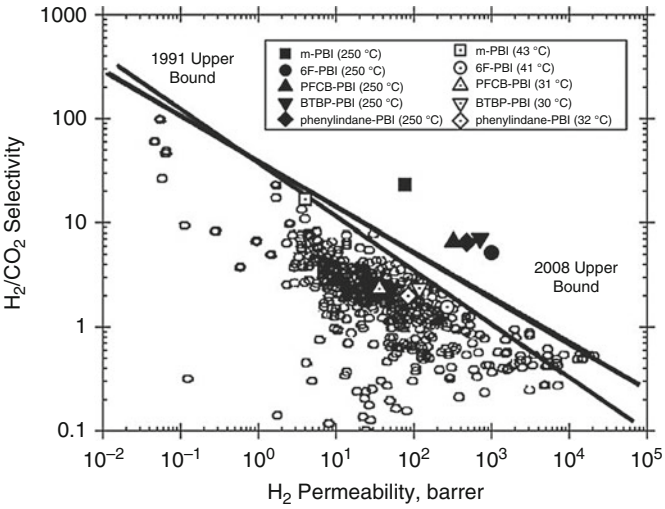

Fig. 3.6 Robeson upper bound plot. Selected hydrogen selectivity versus permeability of commercial polymer dense membrane and PBI for carbon dioxide [36, 37, 45] (Reproduced from Ref. [45] with permission from Elsevier)

However, at low temperature, *m*-PBI exhibited low H_2 permeability, which was attributed to the small free volume of *m*-PBI, resulting from the π−π stacking and strong H-bonding interaction [53, 54]. In order to improve the H_2 permeability and maintain high H_2/CO_2 selectivity, molecular structure modification is needed to modulate the macromolecular chain packing efficiency and free volume architecture within such kind of glassy polymer [54]. Polyimide-based polymers were optimized for gas permeability and selectivity [55, 56]. Li et al. [45] synthesized PBI-based polymers with different kinds of dicarboxylic acid monomer (schematic shown in Fig. 3.5) with either brush structure or with spatial configuration to increase the fractional free volume. Those structures demonstrated high localized mobility at high temperature, due to the polymer side groups adopting a bent configuration [45]. Although the thermal stability decreased due to the less compact packing, such as π−π stacking and strong H-bonding interaction, the mechanical properties of the polymer remained while conformational changes of the side groups enable the pore volume to "open up" for enhanced H_2 permeability (see in Fig. 3.6, up to 997.2 barrer compared with 76.81 barrer for *m*-PBI at 250 °C) [45] [Note: 1 Barrer = 10^{-11} (cm^3 O_2) cm cm^{-2} s^{-1} $mmHg^{-1}$, where cm^3 represents the molar quantity standardized against molecular oxygen, cm the thickness of the material, and cm^{-2} the reciprocal of the surface area of that material at standard temperature (°C) and pressure (mmHg)].

Hosseini et al. [46] blended the *m*-PBI and Matrimid (one type of commercial PI) together to form the homogenous blended membrane. The blended membrane was miscible at the molecular level and each component interacted with each other by

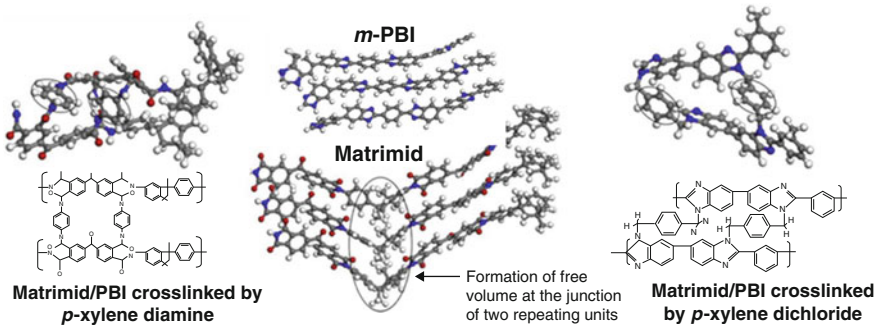

Fig. 3.7 (**a**) Molecular simulation of free volumes in the molecular structure of PBI monomer (structure of p-xylene diamine monomer and low energy conformation) [45]; (**b**) mPBI (*top*) and Matrimid [46] (*bottom*) membrane, and (**c**) PBI-Matrimid blended membrane with p-xylene dichloride monomer [46] The blended membrane has more compacted structure than PBI-Matrimid due to the small free volume induced by the hydrogen bonding. The spatial effect of the different rigid small molecules cross-linkers provides the variable in the free volume in this case (Reproduced from Refs. [45, 46] with permission from Elsevier)

H-bonding (schematic shown in Fig. 3.7). Therefore, the incorporation of PBI improves the gas separation performance which is limited by the Matrimid rigid structure. The PBI polymer modulates the chain packing density and hindrance in segmental mobility in the PBI-Matrimid blended system to improve the permeability/selectivity performance. Polymer cross-linking opens the free volume but restricts segmental mobility of the polymer chains in the membrane, which in turn increases the permeability but still keep the excellent selectivity ($\sim\alpha = 26$ for H_2/CO_2 selectivity).

3.3.2 Hydrogen Separation Membrane Structure

PBI polymers are model structures to investigate permeability in porous polymer film except for the dense polymeric formulations, where permeability is low. As discussed in Sect. 3.2, the transportation mechanisms are completely different for dense polymer membranes and porous polymer membranes. In dense polymer membranes, transport follows solution/diffusion mechanism. However, the porous membrane is diffusion dependent, which significantly depends on the pore size as well as the size of the gas molecules.

3.3.2.1 Dense Membrane

When nonporous dense polymeric membrane is used for the gas separation, the gases are separated due to the solubility and diffusion in the polymer materials, called as solution/diffusion transport mechanism (discussed in Sect. 3.2). In this case, the glassy polymer is more effective for gas separation. Gas molecules penetrate and move inside the polymer chain due to the formation of local gaps

in the chain due to the thermal motion of rigid polymer backbone. Free volume defined as the fraction of the volume that is not occupied by the conformational constraints of the polymer chain plays a major role in determining gas separation efficiency [41]. Within the free volume, transient gaps are formed, which accommodate the small gas molecules (small hydrogen molecules in our case) transportation [41].

3.3.2.2 Porous Membrane

Another approach to improve the hydrogen separation capacity of polymer membranes is to increase the gas-membrane interaction surface area with porosity. The porous film for the hydrogen separation follows the Kundsen diffusion (dimensionless unit) when it was lower than the limit of viscous flow. The flux is much higher than that of the dense membrane. However, the separation efficiency is moderate [4].

One widespread commercial membrane is the hollow fiber membrane for the hydrogen separation. The hydrogen selectivity seems to be acceptable (170 for H_2/CH_4 and 6.75 for H_2/CO_2) [57]. Moreover, thin dense polymer films have been coated on the porous medium to form an asymmetric multilayer film for the selected separation performance [58].

3.3.2.3 Hybrid Microporous Membrane

In order to across the limit of the Robeson plot and "trade-off line," high H_2 permeability is necessary. The blending of polymer systems with high performance components in different aspects is an approach that has been shown to be successful in crossing the Robeson threshold [59], by tailoring the molecular design of the copolymers as well as special interactions (hydrogen bonding) with each other in the membrane system. As discussed in Sect. 3.2, the inorganic membranes provide a better permeability and selectivity performance than polymer membranes. One potential method to improve the separation performance is to include the inorganic/organic fillers, such as carbon molecular sieves (CMS), mesoporous carbon, carbon nanotube, zeolite, mesoporous silica, and metal organic frameworks (MOFs), into polymer matrix to prepare the mixed matrix hybrid composite membrane [7, 60]. Moreover, the polymer intrinsic microporosity, developed in 2004 [61, 62], combined the concept of molecular design of dense rigid membrane as well as the microporous structure, such as MOF to achieve the interconnected microporous membrane structures and to tune the free volume for gas separation performance.

Mixed Matrix Membrane

Mixed matrix membrane (MMM) consists of an organic polymer matrix and the inorganic/organic fillers [60]. The selective fillers, metal organic frameworks (MOFs), for example, are integrated into the polymeric matrix to form a hybrid membrane structure. An appropriate selection of inorganic filler, the polymer matrix, as well as the elimination of interfacial adhesion are the three most important factors in the development of the defect -free hybrid membrane with high permeability and

selectivity [63]. However, performances of mixed matrix membrane are not always the sum of the intrinsic properties of each individual component. The interaction of inorganic filler and polymer matrix and the morphology of the membrane significantly influence the overall membrane properties. In those factors, the major challenges are the homogeneity of the inorganic filler dispersed within the polymer matrix [64]. Due to the heterogeneous density of the composite and interfacial adhesion between the filler and polymeric matrix, agglomeration, sedimentation, and the formation of the interfacial voids [64, 65] can occur, which cause pinholes to be created in the structure. These pinholes are nonselective defects and collectively decrease both the mechanical strength and gas permeation/separation performance of the membrane [66]. If the inorganic fillers is fabricated to a small size and dispersed with high interfacial area adhesion, a thinner mixed matrix membrane can be fabricated for long life-time gas separation with similar performance to CMS systems [65].

Polymer Intrinsic Microporosity

Polymer intrinsic microporosities (PIMs), developed initially by Budd and McKeown et al. [61, 62], are successive network structures with interconnected intermolecular voids due to the rigidity of the element macromolecules. Similar to the conjugated polymer discussed in Sect. 3.3.1, polymer intrinsic microporosity (structures schematically shown in Fig. 3.8) has a more complex, rigid, and contorted molecular backbone, which restricts the rotation. Polymer intrinsic microporosity has controllable free volume, which can be high with the local structures behaving as the micropores (pores with the dimension lower than 2 nm) allowing for efficient gas permeability [67–69]. The interconnected microporosity system behaves in a similar fashion to pore structured molecular sieves (such as observed in MOFs or zeolite systems). High selectivity of separation of H_2 over N_2 and CH_4 was observed, placing PIM systems in the Robeson upper bound line (Robeson plot summarized in Fig. 3.9) [70].

3.4 Industrial Application of Hydrogen Separation Polymer Membrane

Previous sections have discussed the relevance of polymer membranes in the separation of hydrogen and how separation performance can be enhanced through alterations of polymer properties. This section will briefly introduce the design elements of a practical separation membrane system for industrial application. The hydrogen separation industry must deal with various feed streams depending on the method of hydrogen production. Compared with other hydrogen separation techniques, one important advantage of membranes separation approach is its versatility. A great number of variables can be controlled to achieve the optimal design and separation. However, this versatility also means it is difficult to provide an in-depth

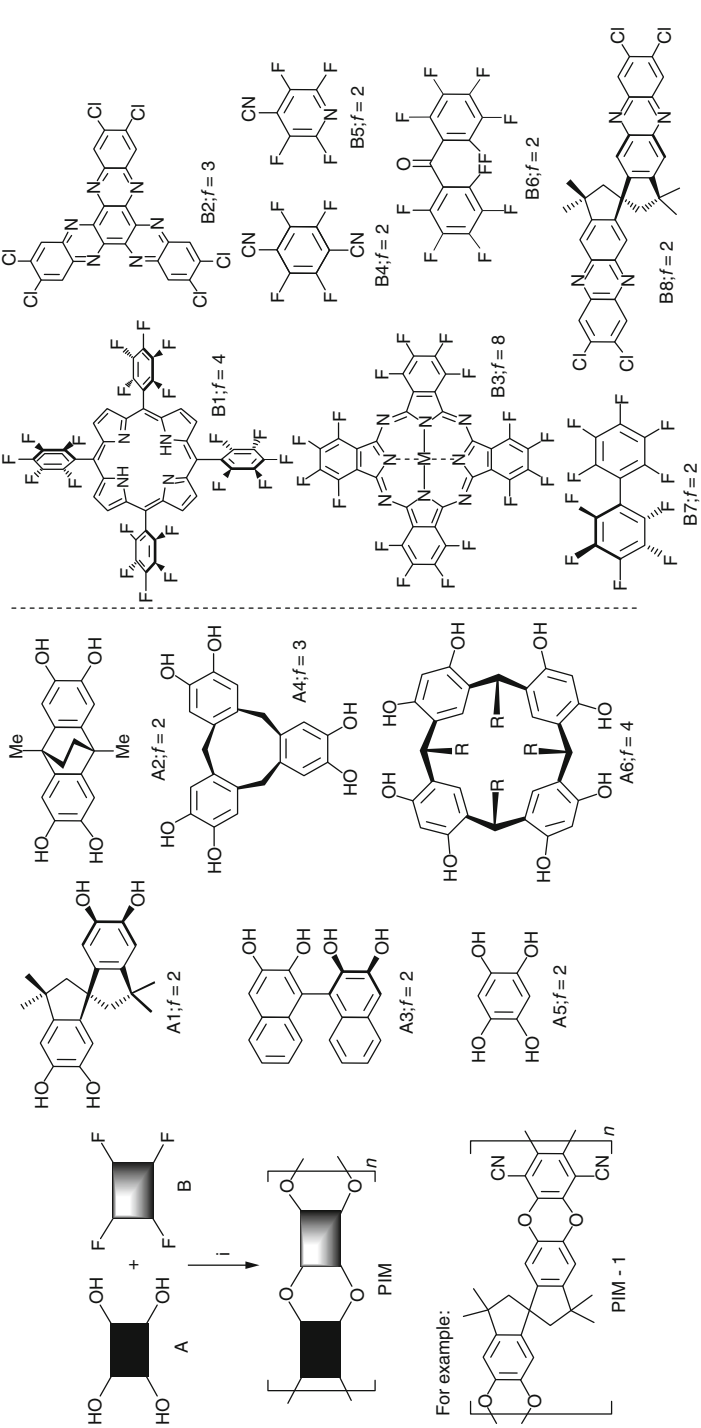

Fig. 3.8 Structures of monomers and the synthesis of polymer intrinsic microporosity membrane synthesis [7, 61, 71–73] (Reproduced from Ref. [72] with permission from Royal Society of Chemistry)

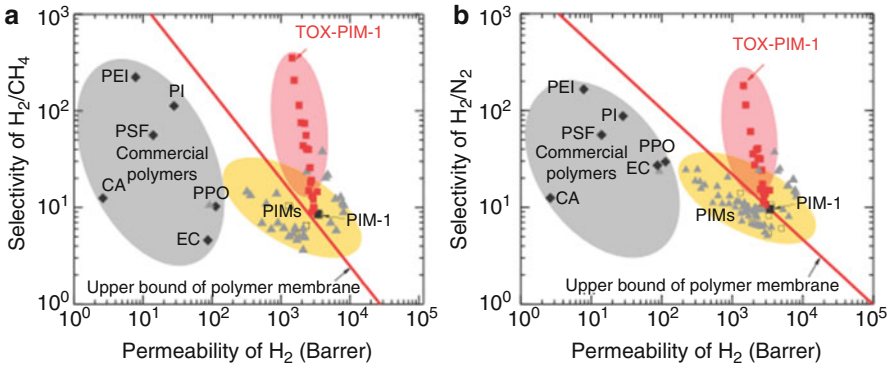

Fig. 3.9 Selectivity versus permeability of PIM-1 and TOX-PIM-1 membranes compared with Robeson upper bound plot and commercialized polymer membrane [70] (Reproduced from Ref. [70] with permission from Nature Publishing Group)

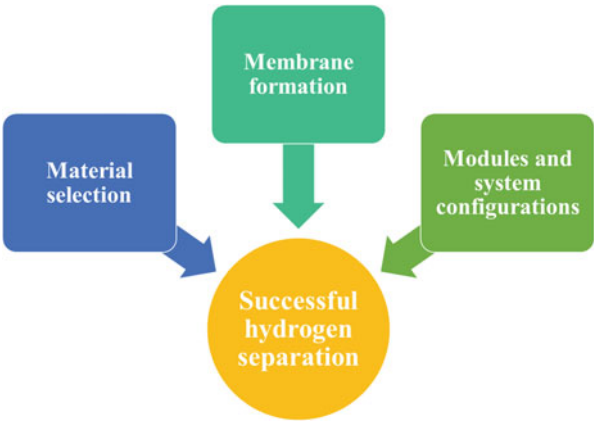

Fig. 3.10 Three supporting areas controlling successful membrane-based gas separation [17]

membrane system design database. Therefore, this section attempts not to give a complete overview about membrane system design, but merely some key insights into the membrane design process. To design a successful system for hydrogen separation, three supporting areas must be integrated together: material selection, membrane formation, and modules and system configurations (summarized using a block diagram in Fig. 3.10).

3.4.1 Current Industrial Development

To scale-up for industrial bulk separation and application, it requires initial system testing of "candidate" membranes in the laboratory using standard gas mixtures. Once the candidate membrane demonstrates robustness, selectivity, and stability, it is

Table 3.3 Summary of hydrogen separation behavior of commercial polymeric membranes [6, 18]

Hydrogen purification	Application	Polymer composition	Supplier
H_2/Hydrocarbon	Refinery H_2 recovery	Polysulfone	Air Products
H_2/CO	Syngas ratio adjustment	Polyimide, polyaramide	Air Liquid
H_2/N_2	Ammonia purge gas	Polyimide, polyaramide	Ube, Praxair

further evaluated using hydrogen-rich syngas produced in coal gasification systems. This step is to ensure that the membrane systems are effective in the presence of gas sources typically found in commercial applications. Table 3.3 summarizes the current typical commercialized polymer membrane for the hydrogen separation for different separation industries. Due to cost-effective considerations, most of the designed polymers and hybrid membranes so far have not been commercialized yet.

The development of membrane gas separation technique has slowly but steadily increased over the last century [29]. Since 1980, membrane gas separation has become a competitive separation technique with the implementation of a serial production of commercial polymeric membrane. In 2002, it was estimated that the market scale of membrane gas separation technique in the year of 2020 will grow four-fold relative to year 2000 [29]. It is anticipated that membrane gas separation technology will play an increasing role in reducing the costs of industrial processes and environmental emissions [18], especially in the present scenario of diminished global hydrocarbon reservoirs. Even if these reserves do not diminish, using membranes for hydrogen separation and hydrogen for generation of electricity or transport will lower carbon dioxide emissions and enable petroleum to be utilized in manufacturing of commodities.

Hydrogen separation was one of the first large-scale commercial applications of gas separation membrane technology in the early 1970s. Commercialized Permea (Permea, Inc) hollow-fiber prism system (Monsanto Company, currently owned by Air Products and Chemicals, Inc) was targeted for the recycling of hydrogen from ammonia purge gases. It was the first demonstration of the feasibility of membrane separation technology as a viable approach in bulk manufacturing [18, 25, 74]. Hydrogen recovery from refinery streams in the petrochemical industry is another emerging manufacturing field for the membrane separation industry. It is anticipated that membrane separation approaches can meet the increased demand of hydrogen separation to meet current and future environmental regulations, regarding greenhouse emissions. One example of hydrogen recovery is from high pressure purge gas of a hydrotreater, where a stream of hydrogen is passed over a catalyst to remove other components [18, 25, 74]. A lower investment cost than pressure swing adsorption (PSA) or cryogenic separation was estimated by Spillman for the hydrogen recovery from refinery off gas by polyimide (PI) membranes invested by Ube [18, 25, 74]. Since then, capital prices of membrane have dropped and the separation performances have been improved.

To drive future development, the cost of implementation has to be reduced; this total cost of ownership may be met through development of novel cost-effective membrane for industrial manufacturing using hydrogen as an energy carrier.

A number of consortia have cooperated in the development of novel cost-effective membrane in addition to the development of benchmarks to assess membrane performance and policy. The consortia includes the US department of energy (DOE), energy and environmental research center (EERC), national center for hydrogen technology (NCHT), and RTI (formerly research triangle institute) International [75].

The initial collaboration demo was done by the EERC and NCHT. They planned to design the reactor based on commercialized product for hydrogen separation membrane and then compare with several candidate membranes developed through funding from the DOE. This work is still on-going and no comparative performance data have been released. Currently, EERC-NCHT has designed and manufactured multiple bench-scale and pilot-scale gasification system to simulate the syngas for industrial-scale gas separation test. The gasification systems have the capability to gasify biomass, coal, and other solid/liquid feedstock, etc. In their designs, each system can be coupled with the "warm-gas clean-up train" to reduce contamination to the level suitable for the gas separation based on the commercialized separation membranes, in the form of a preseparation. Moreover, the "warm-gas clean-up train" enables the hydrogen separation performance to be evaluated at elevated temperatures without additional temperature control system. In the advanced design, the hydrogen membrane can be inserted to any position in the clean-up train to simulate different operation conditions. If needed, a small slipstream of the syngas from any gasification system can be pulled for the specific hydrogen separation testing [75]. RTI International is another institute, having the in-house expertise of gas separation membrane synthesis, characterization, and testing [75]. Membrane permeation testing facilities at RTI allow for both bench-scale and pilot scale testing for gas separation performance (selectivity and/or permeability) of membrane type and structure (polymeric or inorganic membranes; and dense or porous membranes), as well as membrane modules over a wide range of operating conditions (pressure, temperature, and gas environment). Moreover, RTI International's membrane testing facilities also allow for the determination of the long-term effect (lifetime) on the separation performance under the real gas separation environment. The range of test conditions includes: (1) multicomponent gas mixtures at extreme conditions (high pressures up to 1,500 Pa (11.2 mmHg) as well as the high temperatures up to 350 °C, 623 K) (2) separation performance under containments (toxic and corrosive gases, such as CO, H_2S, CO_2, SO_2, and humidified gas mixtures) [75].

3.4.2 Membrane Fabrication Technique

Among metals, ceramics, polymers, and composites, polymers are the dominant materials to be used to fabricate large scale applications due to their easy processability, good mechanical property, and capability to form an asymmetrical structure [23, 24]. Various polymeric membrane modules such as polyimides (PI), cellulose acetate (CA), and poly(phenylene oxide) (PPO) have been commercialized.

The main aim is to modify the material by means of construction techniques to obtain a membrane structure with morphology suitable for a specific separation. The chemical nature of the polymers determines the separation principle applied, the preparation techniques employed, and the membrane system obtained. This section will present the most popular manufacturing techniques for polymeric separation membranes. The manufacturing techniques for other materials have been presented in several other reviews [16, 24]. There are mainly four construction techniques for polymeric membranes: phase inversion, coating, sintering, and stretching methods [16].

Phase inversion is the most popular method to prepare polymer membrane [16]. This method can be used to prepare both porous and dense membranes. During preparation procedure, the polymer phase changes from liquid state into solid state, at the same time, a membrane is created. The phase inversion technique includes solvent evaporation, immersion precipitation, precipitation from the vapor phase, and thermal precipitation. Among them, immersion precipitation is the most frequently used method to prepare the phase inversion membranes [16].

Coating methods are always used to prepare dense polymeric membranes. A number of coating procedures in use are plasma polymerization, dip coating, in situ polymerization, and interfacial polymerization. Due to the low fluxes for dense membranes, membrane thickness needs to be minimized during the preparation procedure. The membranes are usually supported by a porous sublayer to attain structural strength for reduced membrane thicknesses.

Sintering is a process to form a membrane through compression and sintering powders at elevated temperature. This technique is suitable for organic and inorganic materials, especially materials with very high mechanical, thermal, and chemical stabilities. Pores will generate through the sintering process because of the irregular shapes of the particles. The pore sizes of the membrane normally range from 0.1 to 10 μm in diameter. The lower limit of the pore size is determined by the minimum particle size. The polymeric membranes obtained from this method always have a low porosity, generally in the order of 10–20%.

Stretching method can achieve the higher porosities, up to 90%. This technique is primarily suitable for manufacturing semi-crystalline polymeric materials. This technique involves extension of an extruded film in a direction of perpendicular to the extrusion direction. It will result in a porous structure with pore sizes in the range from 0.1 to 3 μm in diameter.

3.4.3 Modules and System Configuration

Ideally, membranes work as molecular scale filters to produce a pure permeate gas A and a nonpermeate gas B from a gas mixture of A and B [76]. For the case of hydrogen separation membrane, gas A will be hydrogen gas while gas B as the

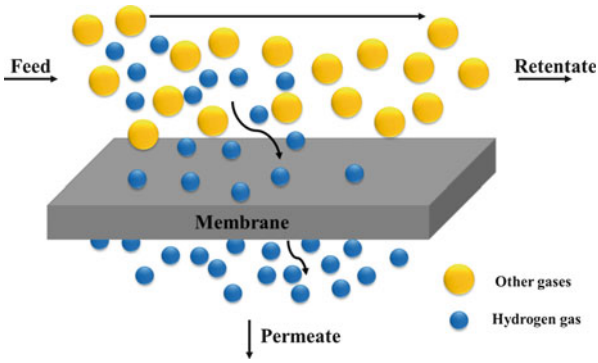

Fig. 3.11 Membrane separation system [76]. The hydrogen gases (*blue*) permeate through the membrane, while other gases (*yellow*) do not (Reproduced from Ref. [76] with permission from Elsevier)

mixture gases except hydrogen gas (*An illustration of hydrogen and other gas separation is shown in* Fig. 3.11). However, in reality, membrane cannot approach a separation efficiency of 100% through permeation. Therefore, more complex operational systems are necessary to achieve high purity separation, and as such a single pass cannot yield selectivity of unit between A and B. The optimum membrane separation's performance, i.e., a high throughput (defined as permeability) and a high product purity (defined as selectivity), can only be achieved by process conditions suitable to the membrane material and the feedstock. Therefore, in real applications, special design of the membrane systems is needed to be housed in a cassette, known as the module. To design a suitable membrane module, factors, such as manufacturability, operability, efficiency, maintainability, membrane deterioration, and costs, are needed to take into account [25, 77].

Currently, there are two types of membrane configurations for module design: flat and tubular. Flat-type membrane module includes the spiral-wound modules and plate-and-frame. Tubular-type membrane modules include capillary, tubular, and hollow fiber modules. A module shape selection depends on various factors, i.e., cost, pressure, temperature, etc. A detailed explanation about these modules has been reviewed by Kluiters [16]. A special feature for polymeric gas separation membranes is their easy processability into hollow fiber membranes. Hollow fiber modules contain thousands of fibers and have high membrane area. These features make hollow fiber modules attractive for large-scale industrial applications. This high membrane area also leads to cost efficient production and high productivity [78].

If hydrogen production is carried out inside a membrane module, the whole system is called a membrane reactor. For reactions to occur in a membrane module, catalysts are needed to be added inside the membrane reactor. This design results from the ability of membranes to selectively permeate species from equilibrium reactions. Membranes can selectively take away reaction products and shift the equilibrium to the product side. Adding the reaction to the module will complicate the module design, may result in substantial composition changes, and influence membrane operation.

3.5 Summary and Next Generation Hydrogen Separation Membrane

In the co-production of fuels, hydrogen produced during coal gasification requires storage; thus, hydrogen storage plays an important role in the future energy grid. Moreover, hydrogen production technology is considered as "green" where no carbon dioxide is generated upon use of hydrogen gas; however, hydrogen production is an energy-intensive process and is expensive due to the requirement of high purity, requiring pretreatment and separation modules and heat for gasification. In order to lower the cost of manufacturing, future development of the next generation hydrogen separation membranes should consider the following aspects.

In the case of developing membranes with excellent separation performance and long durability, a number of parameters need to be considered such as mechanism to remove feed-stock contaminates, good thermal and mechanical properties of the membrane, and resistance of the membrane to oxidation or reduction to prolong its lifetime of operation. The cost of manufacturing should also consider new less energy intensive processing: less material consumption and faster processing times. One example of less energy intensive processing is the manufacturing of multilayered (nanometer) thin film coatings applied on porous support with reduced material and manufacturing costs and improved membrane thermal properties [79–86]. Moreover, optimizing the surface chemistry of the film or membrane can enable additional functionalities to be introduced, such as color change to indicate end-of-life or tolerance to heavy metals.

Over the past 40 years, substantial studies on polymer membrane materials have been carried out to improve their performances. Consequently, both permeability and selectivity have been improved compared with the first generation materials [18, 87]. Current membrane performance is limited by the trade-off between permeability (μ) and selectivity (α), which is graphically represented as the "Robeson upper bound" in the μ versus α plot [36]. Glassy polymers lose separation performance quicker than other types of inorganic and metallic membranes. In the presence of even trace amount of hydrocarbons, the selective skin layer was plasticized by the acidic gases (such as CO_2) so that the gas separation performance decreased versus usage time. Physical aging occurred in the polymer as the result of slow and gradual loss of unrelaxed extra free volume under their glass transition temperature towards the equilibrium state under relaxation. The aging is more severe for the thin film membrane than bulk material and causes a generalized decrease in permeability. The swelling and mechanical/thermal stability issues for the polymer membrane can be solved through cross-linking. However, the cross-linking of polymer membrane has lower permeability than the untreated one. Here, polymers with enhanced selectivity were demonstrated by mixed matrix membrane (MMM) and polymer intrinsic microporosity membrane (PIMs) systems [58]. The development of new materials will also help to have a better understanding of the transport mechanism of gases at a molecular level. For example, computer simulation, especially molecular dynamics simulation, enables analyses of the molecular structure of polymer and the diffusion process of gas molecule through the membrane [88, 89]. Qualitative

information about relationship between structural properties and transport mechanisms could be obtained, which will guide further redesign [89]. The performance limitations are summarized by the Robeson [36] plot, where performance should place the candidate membrane in the upper quadrant of the α/μ plot. It has been realized that the increase in intermolecular and intramolecular free volume and polymer chain stiffness are the factors to improve gas separation performance using void bound theory for polymeric membrane systems [18]. Other systems, which may attain high selectivity and permeability, are based upon carbon nanotubes (CNTs) [90] or metal organic-frameworks (MOFs), which can be considered as excellent hybrid materials for the polymeric matrix.

The next generation of hydrogen separation membrane is also expected to be evaluated at both the bench-scale and the pilot-scale gasification unit, benchmarked by the consortia policy group of DOE, EERC-NCHT and RTI International as well as the academia and industrial collaborators. Moreover, candidate membranes must satisfy operational conditions pertinent in refineries and integrated gasification combined cycles (IGCCs) that may subject the membrane to extreme conditions, such as high temperature and pressure. In addition, the separation feed containing hydrogen may not be in liquid form or partially dissolved in solvents which are highly oxidizing or reducing, unlike hydrogen feeds used in traditional separation techniques [3]. In this chapter, only gas separation performance of gas phase interaction on both sides was considered; thus, practical considerations of IGCC systems using nontraditional hydrogen streams should also be factored-in when designing membrane systems for separation of hydrogen gas from various feed sources [91].

Membranes for hydrogen separation have a renewed research interest, due to the wider usage of hydrogen as an energy carrier. Gas separation membranes, especially hydrogen separation membranes, have the significant importance due to the potential application in several growing processes related to the hydrogen economy (summarized in Table 3.3) [1]. One primary polymer based relevant technology is the proton exchange polymeric membrane for the proton exchange membrane fuel cells (PEMFC), which utilize chemical energy in the form of hydrogen to electrical energy and water [Anode: $H_2 \rightarrow 2H^+ + 2\bar{e}$; Cathode: $H_2 + ½O_2 \rightarrow H_2O$; Overall: $H_2 + ½O_2 \rightarrow H_2O$]. In this catalytic process, no CO_x, NO_x, or SO_z are generated (where $x = 1–2$ and $z = 2–3$ and hydrocarbons) unlike conventional combustion engines [92]. If the source feed is methane or gasification of coal, then carbon dioxide will be produced, at parts-per-million (ppm) concentrations, water and electricity [93]. Examples of the redox reactions for molten carbonate fuel cells and solid oxide fuel cells are shown: at anode $CO_3^{2-} + H_2 \rightarrow CO_2 + 2\bar{e}$; at cathode $CO_2 + ½O_2 + 2\bar{e} \rightarrow CO_3^{2-}$; overall $H_2 + ½O_2 \rightarrow H_2O$ for molten carbonate fuel cell; at anode: $CO + O^{2-} \rightarrow CO_2 + 2\bar{e}$ or $H_2 + O^{2-} \rightarrow H_2O$ or $C_xH_{2x} + 2 + xH_2O \rightarrow xCO + (x + 2)H_2$; at cathode: $O_2 + 4\bar{e} \rightarrow 2O^{2-}$; overall: $2H_2 + O_2 \rightarrow 2H_2O$ for solid-oxide fuel cell where CO in the reformate gas is oxidized to CO_2 at the anode for solid oxide fuel cell, or released CO_2 from steam methane reforming [$CH_4 + H_2O \leftrightarrow CO + 3H_2$ and $CO + H_2O$ $CO_2 + H_2$ in the presence of Cu or Fe based catalyst] [94]. However, to scale up fuel cell usage for energy production using

hydrogen as a source requires industrial level of hydrogen production as well as hydrogen separation techniques [95].

Acknowledgments Manuel Marquez and technical scientists at YNano LLC are duly acknowledged by X. Huang for their support of her research. Dr. Masaya Kotaki and Kaneka US Material Center are also acknowledged by X. Huang and H. Yao in support of this book chapter.

References

1. J.D. Perry, K. Nagai, W.J. Koros, Polymer membranes for hydrogen separations. MRS Bull. **31**, 745–749 (2006)
2. F.G. Kerry, *Industrial Gas Handbook: Gas Separation and Purification* (CRC Press, Boca Raton, 2006)
3. S.C.A. Kluiters, *Status Review on Membrane System for Hydrogen Separation* (Energy Center of Netherlands, Petten, 2004)
4. N.W. Ockwig, T.M. Nenoff, Membranes for hydrogen separation. Chem. Rev. **107**, 4078–4110 (2007)
5. H. Shiga, K. Shinda, K. Hagiwara, A. Tsutsumi, M. Sakurai, K. Yoshida, E. Bilgen, Large-scale hydrogen production from biogas. Int. J. Hydrog. Energy **23**, 631–640 (1998)
6. S. Adhikari, S. Fernando, Hydrogen membrane separation techniques. Ind. Eng. Chem. Res. **45**, 875–881 (2006)
7. X.Y. Chen, H. Vinh-Thang, A.A. Ramirez, D. Rodrigue, S. Kaliaguine, Membrane gas separation technologies for biogas upgrading. RSC Adv. **5**, 24399–24448 (2015)
8. J.W. Phair, S.P.S. Badwal, Materials for separation membranes in hydrogen and oxygen production and future power generation. Sci. Technol. Adv. Mater. **7**, 792–805 (2006)
9. H. Makino, Y. Kusuki, H. Yoshida, A. Nakamaura, Process for preparing aromatic polyimide semipermeable membranes. U.S. Patent 4,378,324, 1983
10. J. M. S. Henis, M. K. Tripodi, Multicomponent membranes for gas separation, 1980
11. W.J. Schell, C.D. Houston, Spiral-wound permeators for purification and recovery. Chem. Eng. Prog. **78**, 33–37 (1982)
12. S. Weller, W.A. Steiner, Engineering aspects of separation of gases – fractional permeation through membranes. Chem. Eng. Prog. **46**, 585–590 (1950)
13. L. M. Gandia, G. Arzamendi, P. M. Dieguez, Renewable Hydrogen Technologies, Production, Purification, Storage, Applications and Safety (Elsevier, Oxford, 2013)
14. L. Hu, R. Benitez, S. Basu, I. Karaman, M. Radovic, Processing and characterization of porous Ti2AlC with controlled porosity and pore size. Acta Mater. **60**, 6266–6277 (2012)
15. L. Hu, C.-A. Wang, Effect of sintering temperature on compressive strength of porous yttria-stabilized zirconia ceramics. Ceram. Int. **36**, 1697–1701 (2010)
16. S.C.A. Kluiters, *Status Review on Membrane Systems for Hydrogen Separation* (Energy Center of Netherlands, Petten, 2004)
17. W.J. Koros, G.K. Fleming, Membrane-based gas separation. J. Membr. Sci. **83**, 1–80 (1993)
18. P. Bernardo, E. Drioli, G. Golemme, Membrane gas separation: a review/state of the art. Ind. Eng. Chem. Res. **48**, 4638–4663 (2009)
19. M. Knudsen, *The Kinetic Theory of Gases: Some Modern Aspects* (Wiley, New York, 1934)
20. S.T. Hwang, K. Kammerme, Surface diffusion in microporous media. Can. J. Chem. Eng. **44**, 82 (1966)
21. K.H. Lee, S.T. Hwang, The transportation of condensable vapors through a microporous vycor glass membrane. J. Colloid Interface Sci. **110**, 544–555 (1986)

22. J.S. Masaryk, R.M. Fulrath, Diffusivity of helium in fused silica. J. Chem. Phys. **59**, 1198–1202 (1973)
23. S. Kim, Y.M. Lee, Rigid and microporous polymers for gas separation membranes. Prog. Polym. Sci. **43**, 1–32 (2015)
24. M. Mulder, *Basic Principles of Membrane Technology* (Kluwer, Dordrecht, 1996)
25. R.W. Baker, *Separation Technology and Applications* (Wiley, West Sussex, 2004)
26. Y. Yampolskii, I. Pinnau, I.B. Freeman, *Materials Science of Membranes for Gas and Vapor Separation* (Wiley, Chichester, 2006)
27. A.W. Thornton, K.M. Nairn, A.J. Hill, J.M. Hill, New relation between diffusion and free volume: I. Predicting gas diffusion. J. Membr. Sci. **338**, 29–37 (2009)
28. J.G. Wijmans, R.W. Baker, The solution-diffusion model – a review. J. Membr. Sci. **107**, 1–21 (1995)
29. R.W. Baker, Future directions of membrane gas separation technology. Ind. Eng. Chem. Res. **41**, 1393–1411 (2002)
30. L.H. Sperling, *Introduction to Physical Polymer Science*, 4th edn. (Wiley, Hoboken, 2006)
31. H.R. Allcock, F.W. Lampe, J.E. Mark, *Contemporary Polymer Science* (Pearson Prentice Hall, Upper Saddle River, 2003)
32. I. Pinnau, Z.J. He, Pure- and mixed-gas permeation properties of polydimethylsiloxane for hydrocarbon/methane and hydrocarbon/hydrogen separation. J. Membr. Sci. **244**, 227–233 (2004)
33. T.C. Merkel, B.D. Freeman, R.J. Spontak, Z. He, I. Pinnau, P. Meakin, A.J. Hill, Ultrapermeable, reverse-selective nanocomposite membranes. Science **296**, 519–522 (2002)
34. A. Hussain, M.-B. Hagg, A feasibility study of CO_2 capture from flue gas by a facilitated transport membrane. J. Membr. Sci. **359**, 140–148 (2010)
35. J.H. Kim, Y.M. Lee, Gas permeation properties of poly(amide-6-b-ethylene oxide)-silica hybrid membranes. J. Membr. Sci. **193**, 209–225 (2001)
36. L.M. Robeson, Correlation of separation factor versus permeability for polymeric membranes. J. Membr. Sci. **62**, 165–185 (1991)
37. L.M. Robeson, The upper bound revisited. J. Membr. Sci. **320**, 390–400 (2008)
38. L. Deng, M.-B. Hagg, Swelling behavior and gas permeation performance of PVAm/PVA blend FSC membrane. J. Membr. Sci. **363**, 295–301 (2010)
39. A. Car, C. Stropnik, W. Yave, K.V. Peinemann, Pebax (R)/polyethylene glycol blend thin film composite membranes for CO_2 separation: performance with mixed gases. Sep. Purif. Technol. **62**, 110–117 (2008)
40. J.J. Rouquerol, D. Avnir, C.W. Fairbridge, D.H. Everett, J.M. Haynes, H. Pernicone, J.D.F. Ramsay, S.K.W. Sing, J.J. Unger, Recommendations for the characterization of porous solids. Pure Appl. Chem. **66**, 1739–1758 (1994)
41. P.C. Hiemenz, T.P. Lodge, *Polymer Chemistry*, 2nd edn. (CRC Press, Boca Raton, 2007)
42. P.M. Budd, N.B. McKeown, High permeable polymers for gas separation membranes. Polym. Chem. **1**, 63–68 (2010)
43. S. Shishatskiy, C. Nistor, M. Popa, S.P. Nunes, K.V. Peinemann, Polyimide asymmetric membranes for hydrogen separation: influence of formation conditions on gas transport properties. Adv. Eng. Mater. **8**, 390–397 (2006)
44. B.T. Low, Y. Xiao, T.S. Chung, Y. Liu, Simultaneous occurrence of chemical grafting, crosslinking, and etching on the surface of polyimide membranes and their impact on H_2/CO_2 separation. Macromolecules **41**, 1297–1309 (2008)
45. X. Li, R.P. Singh, K.W. Dudeck, K.A. Berchtold, B.C. Benicewicz, Influence of polybenzimidazole main chain structure on H_2/CO_2 separation at elevated temperatures. J. Membr. Sci. **461**, 59–68 (2014)
46. S.S. Hosseini, M.M. Teoh, T.S. Chung, Hydrogen separation and purification in membranes of miscible polymer blends with interpenetration networks. Polymer **49**, 1594–1603 (2008)

47. A.A. Tracton, *Coatings Materials and Surface Coatings* (CRC Press/Taylor & Francis Group, Boca Raton, 2006)
48. C. Cao, T. Chung, Y. Liu, R. Wang, K.P. Pramoda, Chemical cross-linking modification of 6FDA-2,6-DAT hollow fiber membranes for natural gas separation. J. Membr. Sci. **216**, 257–268 (2003)
49. X. Huang, H. Cao, Z. Shi, H. Xu, J. Fang, J. Yin, Q. Pan, A study on mineralization behavior of amino-terminated hyperbranched polybenzimidazole membranes. J. Mater. Sci. Mater. Med. **21**, 1829–1835 (2010)
50. H. Vogel, C.S. Marvel, Polybenzimidazoles, New thermally stable polymers. J. Polym. Sci. **50**, 511–539 (1961)
51. D.R. Pesiri, B. Jorgensen, R.C. Dye, Thermal optimization of polybenzimidazole meniscus membranes for the separation of hydrogen, methane, and carbon dioxide. J. Membr. Sci. **218**, 11–18 (2003)
52. S.C. Kumbharkar, Y. Liu, K. Li, High performance polybenzimidazole based asymmetric hollow fibre membranes for H_2/CO_2 separation. J. Membr. Sci. **375**, 231–240 (2011)
53. S.C. Kumbharkar, P.B. Karadkar, U.K. Kharul, Enhancement of gas permeation properties of polybenzimidazoles by systematic structure architecture. J. Membr. Sci. **286**, 161–169 (2006)
54. S.C. Kumbharkar, U.K. Kharul, Investigation of gas permeation properties of systematically modified polybenzimidazoles by N-substitution. J. Membr. Sci. **357**, 134–142 (2010)
55. J.D. Wind, D.R. Paul, W.J. Koros, Natural gas permeation in polyimide membranes. J. Membr. Sci. **228**, 227–236 (2004)
56. Y. Liu, R. Wang, T.-S. Chung, Chemical cross-linking modification of polyimide membranes for gas separation. J. Membr. Sci. **189**, 231–239 (2001)
57. N.N. Li, A.G. Fane, W.S.W. Ho, T. Matsuura, *Advanced Membrane Technology and Applications* (Wiley, Hoboken, 2008)
58. W.J. Koros, R. Mahajan, Pushing the limits on possibilities for large scale gas separation: which strategies? J. Membr. Sci. **175**, 181–196 (2000)
59. H.A. Mannan, H. Mukhtar, T. Murugesan, R. Nasir, D.F. Mohshim, A. Mushtaq, Recent applications of polymer blends in gas separation membranes. Chem. Eng. Technol. **36**, 1838–1846 (2013)
60. S.P. Nunes, K.V. Peinemann, *Membrane Technology in the Chemical Industry*, 2nd edn. (Wiley-VCH, Weinheim, 2001)
61. N. McKeown, P. Budd, Exploitation of intrinsic microporosity in polymer-based materials. Macromolecules **43**, 5163–5176 (2010)
62. M. Carta, R. Malpass-Evans, M. Croad, Y. Rogan, J.C. Jansen, P. Bernardo, F. Bazzarelli, N.B. McKeown, An efficient polymer molecular sieve for membrane gas separation. Science **339**, 303–307 (2013)
63. N. Jusoh, Y.F. Yeong, K.K. Lau, M.S. Azmi, Membranes for gas separation current development and challenges. Appl. Mech. Mater. **773–774**, 1085–1090 (2015)
64. Y. Zhang, J. Sunarso, S. Liu, R. Wang, Current status and development of membranes for CO_2/CH_4 separation: a review. Int. J. Green Gas Con. **12**, 84–107 (2013)
65. S.B. Tantekin-Ersolmaz, C. Ataly-Oral, M. Tather, A. Erdem-Senatalar, B. Schoeman, J. Sterte, Effect of zeolite particle size on the performance of polymer-zeolite mixed matrix membranes. J. Membr. Sci. **175**, 285–288 (2000)
66. T.S. Chung, L.Y. Jiang, Y. Li, S. Kulprathipanja, Mixded matrix membranes (MMMs) comprising organic polymers with dispersed inorganic fillers for gas separation. Prog. Polym. Sci. **32**, 483–507 (2007)
67. P.M. Budd, B.S. Ghanem, S. Makhseed, N.B. McKeown, K.J. Msayib, C.E. Tattershall, Polymers of intrinsic microporosity (PIMs): robust, solution-processable, organic nanoporous materials. Chem. Commun. **10**, 230–231 (2004)

68. P.M. Budd, K.J. Msayib, C.E. Tattershall, B.S. Ghanem, K.J. Reynolds, N.B. McKeown, D. Fritsch, Gas separation membranes from polymers of intrinsic microporosity. J. Membr. Sci. **251**, 263–269 (2005)
69. N.B. McKeown, P.M. Budd, K.J. Msayib, B.S. Ghanem, H.J. Kingston, C.E. Tattershall, S. Makhseed, K.J. Reynolds, D. Fritsch, Polymers of intrinsic microporosity (PIMs): bridging the void between microporous and polymeric materials. Chem. Eur. J. **11**, 2610–2620 (2005)
70. Q. Song, S. Cao, R.H. Pritchard, B. Ghalei, S.A. Al-Muhtaseb, E.M. Terentjev, A.K. Cheetham, E. Sivaniah, Controlled thermal oxidation crosslinking of polymer of intrinsic microporosity towards tunable molecular sieve membranes. Nat. Commun. **5**, 4811–4813 (2014)
71. P. Budd, N. McKeown, D. Fritsch, Polymers of intrinsic microporosity (PIMs): high free volume polymers for membrane applications. Macromol. Symp. **245**, 403–405 (2006)
72. N. McKeown, P. Budd, Polymers of intrinsic microporosity (PIMs): organic materials for membrane separations, heterogeneous catalysis and hydrogen storage. Chem. Soc. Rev. **35**, 675–683 (2006)
73. B. Ghanem, N. McKeown, P. Budd, D. Fritsch, Polymers of intrinsic microporosity derived from bis(phenazyl) monomers. Macromolecules **41**, 1640–1646 (2008)
74. R.W. Spillmann, T.E. Cooley, Economic considerations in membrane gas separation process design (1998)
75. M. Lesemann, *Membrane Separation Technologies* (RTI International, Research Triangle Park, 2015)
76. F. Gallucci, E. Fernandez, P. Corengia, M.V.S. Annaland, Recent advances on membranes and membrane reactors for hydrogen production. Chem. Eng. Sci. **92**, 40–66 (2013)
77. M. Ulbricht, Advanced functional polymer membranes. Polymer **47**, 2217–2262 (2006)
78. H. Strathmann, Membrane separation processes: current relevance and future opportunities. AICHE J. **47**, 1077–1087 (2001)
79. X. Huang, N.S. Zacharia, Functional polyelectrolyte multilayer assemblies for surfaces with controlled wetting behavior. J. Appl. Polym. Sci. **132**, 42767 (2015)
80. Y. Gu, X. Huang, C.G. Wiener, B.D. Vogt, N.S. Zacharia, Large-scale solvent driven actuation of polyelectrolyte multilayers based on modulation of dynamic secondary interactions. ACS Appl. Mater. Interfaces **7**, 1848–1858 (2015)
81. X. Huang, N.S. Zacharia, Facile assembly enhanced spontaneous fluorescent response of Ag^{+} ion containing polyelectrolyte multilayer films. ACS Macro Lett. **3**, 1092–1095 (2014)
82. X. Huang, M.J. Bolen, N.S. Zacharia, Silver nanoparticle aided self-healing of polyelectrolyte multilayers. Phys. Chem. Chem. Phys. **16**, 10267–10273 (2014)
83. X. Huang, Assembly and physico-chemical properties of polyelectrolyte multilayer films co-assembled with guest species (2014)
84. X. Huang, N.S. Zacharia, Surfactant co-assembly and ion exchange to modulate polyelectrolyte multilayer wettability. Soft Matter **9**, 7735–7742 (2013)
85. X. Huang, A.B. Schubert, J.D. Chrisman, N.S. Zacharia, Formation and tunable disassembly of polyelectrolyte–Cu^{2+} layer-by-layer complex film. Langmuir **29**, 12959–12968 (2013)
86. X. Huang, J.D. Chrisman, N.S. Zacharia, Omniphobic slippery coatings based on lubricant-infused porous polyelectrolyte multilayers. ACS Macro Lett. **2**, 826–829 (2013)
87. S.A. Stern, Polymers for gas separations – the next decade. J. Membr. Sci. **94**, 1–65 (1994)
88. D. Hofmann, M. Heuchel, Y. Yampolskii, V. Khotimskii, V. Shantarovich, Free volume distributions in ultrahigh and lower free volume polymers: comparison between molecular modeling and positron lifetime studies. Macromolecules **35**, 2129–2140 (2002)
89. D. Hofmann, J. Ulbrich, D. Fritsch, D. Paul, Molecular modelling simulation of gas transport in amorphous polyimide and poly(amide imide) membrane materials. Polymer **37**, 4773–4785 (1996)

90. H. Yao, C.-C. Chu, H.-J. Sue, R. Nishimura, Electrically conductive superhydrophobic octadecylamine-functionalized multiwall carbon nanotube films. Carbon **53**, 366–373 (2013)
91. A.T. Atimtay, Cleaner energy production with integrated gasification combined cycle systems and use of metal oxide sorbents for H_2S cleanup from coal gas. Clean Products Process **2**(4), 197–208 (2001)
92. P. Costamagna, S. Supramaniam, Quantum jumps in the PEMFC science and technology from the 1960s to the year 2000: part II. Engineering, technology development and application aspects. J. Power Sources **156**, 251–269 (2001)
93. S. Sá, J.M. Sousa, M. Adélio, Methanol steam reforming in a dual-bed membrane reactor for producing PEMFC grade hydrogen. Catal. Today **156**, 254–260 (2010)
94. S. Ahmed, M. Krumpelt, Hydrogen from hydrocarbon fuels for fuel cells. Int. J. Hydrog. Energy **26**, 291–301 (2001)
95. C.K. Dyer, Fuel cells for portable applications. J. Power Sources **106**, 31–34 (2002)

Hydrogen Storage Technologies

4

Dervis Emre Demirocak

Abstract

Hydrogen is considered as one of the promising alternative fuels to replace oil, but its storage remains to be a significant challenge. The main hydrogen storage technologies can be broadly classified as physical, chemical, and hybrid methods. The physical methods rely on compression and liquefaction of hydrogen, and currently compressed hydrogen storage is the most mature technology that is commercially available. The chemical methods utilize materials to store hydrogen, and hydrogen can be extracted by reversible (on-board regenerable) or irreversible (off-board regenerable) chemical reactions depending on the type of material. The hybrid methods take advantage of both physical and chemical storage methods. The most prominent hybrid method is the cryo-adsorption hydrogen storage which utilizes physisorption-based porous materials. In this chapter, all of the main hydrogen storage technologies are discussed in detail along with their limitations and advantages.

Contents

Author Contributions: I wrote this chapter without assistance from anyone else.

D.E. Demirocak (✉)
Department of Mechanical and Industrial Engineering, Texas A&M University-Kingsville, Kingsville, USA
e-mail: dervis.demirocak@tamuk.edu

Y.-P. Chen et al. (eds.), *Nanostructured Materials for Next-Generation Energy Storage and Conversion*, DOI 10.1007/978-3-662-53514-1_4

4.1 Hydrogen as a Fuel

4.1.1 Introduction

Global energy demand continues to rise mainly due to emerging economies (non-Organization for Economic Co-operation and Development (OECD) countries), and as of 2015, more than 80% of the worldwide energy demand is supplied from fossil fuel sources; in addition, the likelihood of continued reliance on fossil fuels will continue to be the primary source of energy in foreseeable future [1]. Excessive utilization of fossil fuels is responsible for many of the usage problems modern society facing today such as depletion of fossil fuels, global warming, environmental pollution, and energy security [2–5].

According to Hubbert's peak theory, production of a finite source (i.e., fossil fuels) follows a bell shaped curve. In other words, fossil fuel production from a certain reservoir will increase exponentially initially after its discovery, then production rate will decrease and reach a peak point, and then production rate will continuously decrease until the fossil fuel is depleted in the reservoir or it becomes economically unfeasible to extract [6]. Therefore, it is certain that oil as well as all other fossil fuels will be depleted sometime in the future. Oil, owing to its excessive use in transportation sector, is the most critical energy source humankind relies upon, and according to forecasts, oil is the one that is expected to be depleted well before the end of twenty-first century [7, 8].

Oil economy is large in percent-size, and any significant change in oil economy may take many decades before it is fully realized; therefore, it is imperative to act now to find cleaner alternatives to oil now than as opposed to later. Although depletion of oil is an important issue that needs to be addressed in near term, global warming is much more pressing problem that needs to be addressed urgently. Global warming is the increase in earth's temperature mainly due to anthropogenic CO_2 emissions caused by excessive fossil fuel use (i.e., transportation and power generation) [3]. Some of the adverse effects of global warming are sea level rise and extreme weather which in turn can cause colossal social and environmental changes worldwide [9]. The most important aspect of global warming is it is a time-sensitive problem, and to prevent irreversible changes to earth's atmosphere effective measures need to put in place immediately.

Environmental pollution associated with oil such as air pollution and oil spills is a also serious problem that needs to be addressed. Combustion of hydrocarbons in mobile platforms emits particulates, NO_x, CO_x, (where X = 1 or 2), SO_y (where y = 2 or 3), and benzene which are harmful to human health. Air pollution is especially problematic in densely populated areas. On the other hand, large-scale oil spills can have decades long devastating effects in aquatic life and surrounding communities [10].

The last but not the least important issue associated with the excessive use of fossil fuels is the energy security. Oil reserves are mostly located in the unstable regions of the world. As a result, from time to time oil supply is disrupted, and oil importing countries face the risk of not meeting their oil demand. The disruptions in oil supply of a country can have serious economic, political, and social consequences. Many of the countries built their own national reserves (short term energy security) or have policies in place to move away from oil in future (long term energy security) [4].

From the foregoing discussion, it is clear that alternative fuels to oil are required to save the planet earth and to reduce the risks associated with excessive fossil fuel (i.e., oil) use. Oil-derived fuels have been extensively used in mobile applications due to their high energy density. Therefore, replacing oil is a formidable task because oil is one of the most gravimetrically and volumetrically energy dense fuels known to humankind.

Hydrogen is considered as one of the strong candidates to replace oil in mobile applications. Hydrogen is an energy carrier not an energy source like oil, meaning hydrogen is not directly available on earth, but needs to be produced using other sources. Currently, significant portion of hydrogen is produced from methane via steam methane reforming (SMR) process. One of the other methods of hydrogen production is water electrolysis; if electricity produced by renewable energy technologies is used in this process, it is possible to produce hydrogen from renewable energy sources completely. Once hydrogen is produced, it needs to be transported to the end user or distribution facility, and finally, hydrogen needs to be stored for later use. These three phases – production, transportation and storage of hydrogen – altogether are called hydrogen economy. In the following section, hydrogen economy will be explained in more detail, and its pros and cons will be discussed.

4.1.2 Hydrogen Economy

Hydrogen economy is proposed as an alternative energy system to oil economy back in 1970s. The rationale behind the hydrogen economy is that hydrogen does not emit any carbon, nitrogen, or sulfur oxides (only H_2O is emitted) when utilized in an internal combustion engine or in a fuel cell as opposed to utilizing hydrocarbons in an internal combustion engine. However, hydrogen production must be supplied from renewable energy sources to combat global warming and other environmental issues as discussed in the Introduction.

Fig. 4.1 Hydrogen economy

Hydrogen economy is comprised of three parts as shown in Fig. 4.1 [11]. Hydrogen is mostly produced by SMR process which is the most efficient (83%) and cost effective (0.75 $/kg of hydrogen) option today [12]. On the other hand, renewable energy-based production methods (i.e., photocatalytic water splitting has a 10–14% efficiency and costs 4.98 $/kg of hydrogen) are not yet competitive with SMR [12]. The main issues with hydrogen production are: (i) it is an energy-intensive process and (ii) it must be based on renewable energy sources instead of SMR process to make a real contribution to environmental problems.

Transportation of hydrogen requires an extensive distribution network; hydrogen can be transported by pipelines, tube trailers, and cylinders in gaseous form as well as by cryogenic tanks in liquid form [13]. Hydrogen has a high energy capacity, but has a low energy density. Compression and liquefaction can increase energy density, but they are costly processes. For instance, almost one third of hydrogen's lower heating value is required to liquefy hydrogen [14]. Therefore, transportation medium either gaseous or liquid must be selected based on cost effectiveness, safety, and end use storage technology. In any case, the hydrogen distribution cost is estimated to be 15 times more expensive than liquid hydrocarbon fuels [15].

From the foregoing discussion, it is clear that the hydrogen economy suffers from high costs associated with the production and transportation steps; however, the main obstacle in realizing hydrogen economy is the hydrogen storage step. As of now, there is no hydrogen storage technology that can satisfy the Department of Energy (DOE) 2020 target benchmarks [16]. The main hydrogen storage technologies are (i) compressed hydrogen storage, (ii) liquefied hydrogen storage, (iii) solid-state hydrogen storage, and (iv) chemical hydrogen storage. Among these, compressed hydrogen storage technology is the most mature technology. All these technologies will be discussed in detail in Sect. 4.3. Hydrogen Storage Technologies.

Hydrogen economy is criticized due to significant energy losses involved in each step presented in Fig. 4.1 [17]. Considering a hydrogen fuel cell car, hydrogen needs to be produced using electricity generated from renewable energy sources, then hydrogen needs to be delivered to the end users, and finally hydrogen is converted back to electricity by a fuel cell. Due to additional conversion stages involved, overall efficiency of hydrogen economy is considerably lower than the electron economy [18]. Biofuels and electricity (i.e., battery storage) are the main alternatives to hydrogen [19].

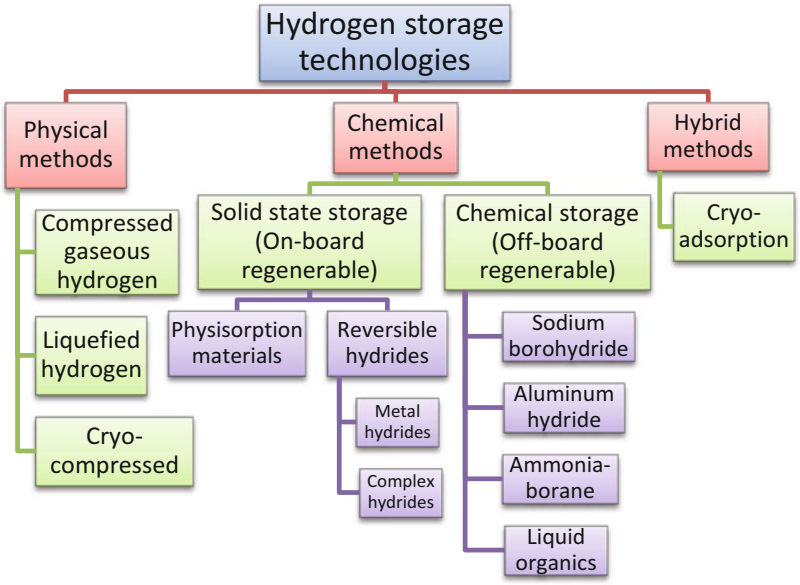

Fig. 4.2 Hydrogen storage technologies

4.2 Hydrogen Storage

4.2.1 Classification of Hydrogen Storage Technologies

Hydrogen storage technologies can be broadly classified into three main categories: (1) physical methods, (2) chemical methods (also called materials based hydrogen storage), and (3) hybrid methods as shown in Fig. 4.2. Physical methods are compressed gaseous hydrogen, liquefied hydrogen, and cryo-compressed hydrogen. Chemical methods are solid-state storage (on-board regenerable) and chemical storage (off-board regenerable). Hybrid method of storage is cryo-adsorption and makes use of both physical and chemical methods.

In physical methods of hydrogen storage, hydrogen does not interact with the storage media; however, in chemical methods of hydrogen storage, hydrogen interacts with the storage media via strong covalent/ionic bonds or via weak van der Waals forces (i.e., hydrogen is chemically bound to a storage material). Chemical methods always include a hydrogen storage material to store hydrogen.

Chemical methods drew significant attention since 2000s due to drawbacks of physical methods. Chemical methods classified into two: (i) solid-state storage and (ii) chemical storage. The primary distinction between solid state (i.e., reversible hydrides and porous materials[1]) and chemical storage (i.e., ammonia-borane, liquid

[1]Porous materials and physisorption materials are used interchangeably throughout the text.

organics, etc.) is solid-state materials can be regenerated on-board simply by charging with hydrogen, whereas chemical storage materials need to be regenerated off-board in centralized facilities [20]. On-board regenerable materials are visualized as the key element for the market penetration of fuel cell vehicles [21].

Cryo-adsorption is a hybrid (physical-chemical) method and takes advantage of compressed, liquefied, and physisorption materials-based hydrogen storage technologies.

4.2.2 US Department of Energy Targets for Hydrogen Storage Systems for Light Duty Vehicles

The summary of the DOE targets for hydrogen storage systems for light duty vehicles is given in Table 4.1 [22]. The most stringent DOE targets are gravimetric and volumetric capacities. In addition, operational cycle life (i.e., reversibility), system fill time (i.e., fast kinetics), and fuel purity are problematic for certain materials (i.e., complex hydrides). The DOE targets presented in Table 4.1 are for the system level hydrogen storage system; therefore, in addition to storage materials' weight, the balance of the plant elements such as storage tank, valves, tubing, control system also need to be accounted for. As a rule of thumb, the material's gravimetric storage capacity should be at least two times the system level targets to achieve the DOE system level targets [23].

In the most recent DOE targets, gravimetric hydrogen storage capacity of system is given in units of kg H_2/kg system as Table 4.1. In previous versions of the DOE targets, gravimetric hydrogen storage capacity of system was expressed in wt.%, and vast majority of the works in the literature continue to report gravimetric hydrogen storage capacity in wt.% which is defined as:

$$\text{wt}\% = \frac{\text{mass of stored hydrogen in system}}{\text{mass of system} + \text{mass of stored hydrogen}} \times 100\% \tag{4.1}$$

If system includes a hydrogen storage material (i.e., chemical methods of hydrogen storage), mass of the hydrogen storage material should be added to mass of the

Table 4.1 US DOE hydrogen storage targets for on-board hydrogen storage systems for light duty vehicles [22]

Storage parameter	Units	2020	Ultimate
System gravimetric capacity	kg H_2/kg system	0.055	0.075
System volumetric capacity	kg H_2/L system	0.040	0.070
Operating ambient temperature	°C	−40/60 (sun)	−40/60 (sun)
Min/max delivery temperature	°C	−40/85	−40/85
Operational cycle life	cycles	1500	1500
Well to power plant efficiency	%	60	60
System fill time (5 kg H_2)	min	3.3	2.5
Fuel purity	% H_2	99.7% (dry basis)	
Loss of useable H_2	(g/h)/kg H_2 stored	0.05	0.05

Table 4.2 Current status of the hydrogen storage technologies [24]

Hydrogen storage method		Gravimetric capacity (wt.%)	Volumetric capacity (g/L)
Physical storage	Compressed (350 bar)	2.8–3.8	16–18
	Compressed (700 bar)	2.6–4.4	19–25
	Liquid	4.8–6.8	31–39
Chemical storage	Complex hydride	1.9–2.5	16–28
	Carbon (porous)	2.9–3.1	13–15
	Chemical hydride	2.6–3.5	22–29
Hybrid storage	Cryo-compressed	5.0–5.8	28–38
Targets	2020	5.2	40
	Ultimate	7.0	70

system. Both units of gravimetric hydrogen storage capacity (i.e., kg H_2/kg system and wt.%) are used throughout this chapter.

4.2.3 Current Status of Hydrogen Storage Technologies

Current status of the hydrogen storage technologies are summarized in Table 4.2. As seen from Table 4.2, hydrogen storage capacity of various technologies spans from 1.9 to 6.8 wt.% (gravimetric capacity) and 13–39 g/L (volumetric capacity). Physical methods of hydrogen storage outperform chemical methods of hydrogen storage. Gravimetric capacity targets are harder to achieve than the volumetric capacity targets as seen from Table 4.2.

Solid-state storage materials have the lowest storage capacity. Complex hydrides can only store 1.9–2.5 wt.% of hydrogen. C-sorbent (activated carbon sorbent) is a physisorption material, and it can store around 3 wt.% of hydrogen. Chemical storage materials (i.e., chemical hydrides in Table 4.2) perform slightly better than solid-state storage materials. Chemical hydrides can store 2.6–3.5 wt.% of hydrogen. By using compressed hydrogen storage tank at 70 MPa, up to 4.5 wt.% of hydrogen can be stored. Two of the best technologies are liquefied hydrogen and cryo-compressed hydrogen in terms of gravimetric storage capacity.

4.3 Hydrogen Storage Technologies

4.3.1 Physical Methods of Hydrogen Storage

4.3.1.1 Compressed Gaseous Hydrogen Storage

Storing hydrogen in compressed form is the most convenient storage method. Typically, hydrogen is stored in steel cylinder tanks at 15–20 MPa; however, by using steel cylinders, only 1.5 wt.% and 10–12 kg/m^3 gravimetric and volumetric densities can be reached, respectively [25]. Higher pressures are required to achieve

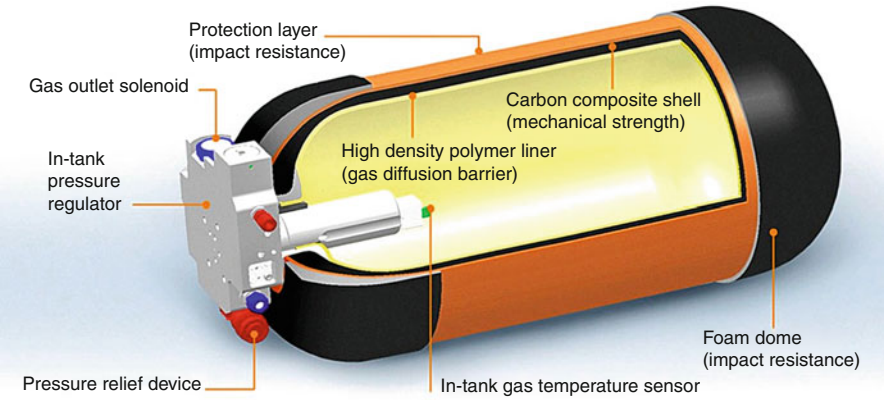

Fig. 4.3 Quantum Technologies type IV (refers to using composite liner material as opposed to a metallic liner in type III tank) compressed gaseous hydrogen storage tank [27] (Reprinted from Ref. [27] with permission from Journal of Power Sources. Copyright Elsevier)

the DOE targets of 5.5 kg H_2/kg system (~5.2 wt.%) and 40 kg/m^3 for 2020 (see Table 4.1). Increasing hydrogen pressure in a steel storage tank is not a solution since increasing pressure also requires increasing the shell thickness of steel tank. Going from 15–20 MPa to 70 MPa in a steel tank, gravimetric hydrogen storage capacity actually decreases [25]. Therefore, lighter storage tank materials are necessary to achieve the DOE targets.

The state of the art compressed gaseous hydrogen tanks are carbon fiber reinforced composite tanks as shown in Fig. 4.3. They are developed for two different pressure levels, 35 and 70 MPa. To satisfy end user expectations, typical hydrogen fueled vehicle should have a range of 300 miles on par with gasoline/diesel powered vehicles. This requires 4–7 kg of hydrogen to be stored onboard depending on the vehicle size [14].

The main components of a storage tank are as follows:

Liner: Hydrogen due to its very small size can permeate easily through many materials. Primarily for safety reasons, hydrogen permeation from the storage tank must be eliminated, and liner prevents permeation of hydrogen. High-density polymeric materials are adopted as liner due to their light weight as compared to metallic liner materials.

Shell: Shell is the load-bearing component of a storage tank. State-of-the-art storage tanks are made of carbon fiber reinforced composite shells to withstand high pressures and to meet the DOE targets. Carbon fiber's superior mechanical properties and low density make it possible to obtain higher hydrogen storage capacities; however, carbon fiber is the most costly part (i.e., ~65% of the system cost) of the compressed gaseous hydrogen storage system [26]. Due to its significance on overall system cost, research programs were developed to reduce the cost of carbon fiber production.

Protection layer: The outermost shell of the storage tank is the protection layer. This component is included for impact resistance.

Balance of plant: The other essential components are pressure regulator, pressure relief device, pressure sensors, temperature sensor, vehicle electrical interface connector, vehicle interface bracket, vent line ports, refueling port, fill line check valve, and stone shield.

General considerations: One liter of liquid hydrogen will occupy 780 L of gas at normal pressure and temperature. Hydrogen has a boiling temperature at 1 atm of 20.2 K, although this is related to pressure of compressed gas, for example, a boiling temperature of 13.K at 70 mbar or 33 K at 12.7 bar. Hydrogen has a heat of evaporation of 445 J/g; thus, 1 W of heat will evaporate 115 mL/h of liquid (5 times greater than liquid nitrogen), although its viscosity ($\eta = 140$ micro-poises) is 70 times smaller than that of water.

The density at a given temperature (T) and pressure (P) is given by:

$$\rho = \mathrm{M(g)}/22,400 \times \mathrm{P(Pa)}/1 \times 10^5 \times 273.15/\mathrm{T\ (K)\ \ in\ \ (g/cm^3)} \tag{4.2}$$

$$\mathrm{V_2(L) = P_1(atm)V_1/P_2/\xi,} \tag{4.3}$$

For example, 50 L × 150 atm/1 atm = 7500/ξ, 7500/862 = 10.7 L for N_2 at NTP, where NTP is T = 293 K, P = 1 atm, where ξ is compression factor and is 11,984 L for H_2, 604 L for Ar, 6030 L for He, 861 L for O_2, and 650 L for liquefied natural gas (LNG)). 1 L of liquefied gas would occupy about 800 L at NTP for most gases. Examples are 1 L (N_2) = 700 L gas at NTP, 1 L (O_2) = 800 L gas at NTP,1 L (H_2) = 780 L gas at NTP,1 L (He) = 1350 L gas at NTP, 1 L (Ar) = 784 L gas at NTP, and 1 L (He) = 750 L gas at NTP triple point. Therefore, gas compressibility and boiling rate are important considerations in design and implementation of cryo-storage.

Technical assessments on 35 and 70 MPa storage tanks showed that both type of tanks fall short of satisfying the ultimate DOE targets. It is worthy to note that 35 MPa (5.5 wt.%) system has a higher gravimetric capacity than the 70 MPa system (5.2 wt.%); however, 70 MPa system (17.6 kg/m^3) has a significantly higher volumetric capacity than the 35 MPa system (26.3 kg/m^3) [26].

One of the drawbacks of the compressed gaseous hydrogen storage is the amount of compression work. Required compression work to reach 35 and 70 MPa of hydrogen pressure is 12 and 15% of the lower heating value of hydrogen, respectively. Compression work becomes less and less significant as the pressure increases as shown in Fig. 4.4. During compression, hydrogen tank needs to be cooled down to keep temperature and pressure at safe levels as well as to fill as much hydrogen as possible. Cooling process will also add to the energy penalty. Considering the energy penalty of both compression and cooling, it was estimated that the cost of compression would be higher than the cost of liquefaction of hydrogen [28].

It is also important to mention that compressed gaseous hydrogen storage technologies refer to storing hydrogen at room temperature (i.e., 300 K). There are other

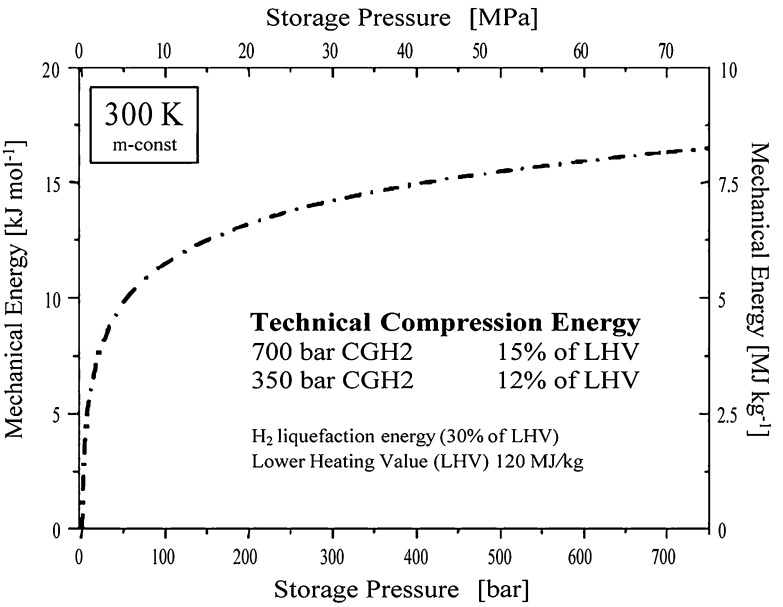

Fig. 4.4 Hydrogen compression work as a function of pressure [14] (Reprinted with permission from Ref. [14]. Copyright Royal Society of Chemistry)

technologies (i.e., cryo-compressed) that keep hydrogen at cryogenic temperatures and high pressures to attain higher storage capacity.

Automotive industry considers the gaseous storage as being the most practical option despite its shortcomings, and it is the only technology that is adopted commercially (i.e., Toyota Mirai) thus far [29].

4.3.1.2 Liquefied Hydrogen Storage

The other physical storage method is the liquefied hydrogen storage. As shown in Table 4.2, using this method high gravimetric and volumetric density can be achieved. Liquefied hydrogen storage tank pressure is much lower (<1 MPa) compared to compressed hydrogen storage (i.e., 35 or 70 MPa) which eliminates high costs associated with the load bearing carbon fiber reinforced composite material used in compressed hydrogen storage. On the other hand, liquefaction energy penalty and boil-off losses are the drawbacks of this storage method.

A typical liquid hydrogen storage tank and its various components as well as vacuum super insulation are shown in Fig. 4.5. Hydrogen storage tanks are double-walled vessels with insulation in between vessels. Due to significant temperature difference between ambient (300 K) and liquid hydrogen (20 K), the inner vessel is insulated with multilayer insulation (i.e., also called vacuum super insulation) comprised of alternating layers of metal foil and padding material (i.e., glass wool) to minimize heat gain from ambient. The design of a multilayer insulation is shown in Fig. 4.5 b. The space in between vessels is also evacuated to enhance the

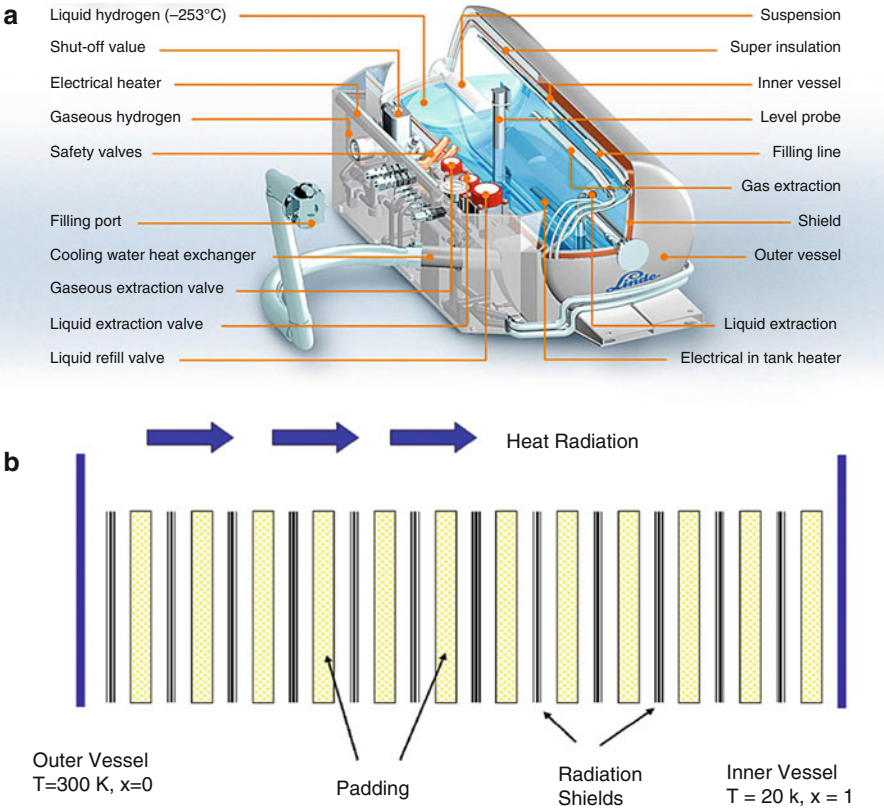

Fig. 4.5 (**a**) Liquid hydrogen tank design by Linde and (**b**) the vacuum super insulation [27] (Reprinted from Ref. [27] with permission from Journal of Power Sources. Copyright Elsevier)

effectiveness of insulation [30]. The most critical component in a liquid hydrogen tank is the insulation. All heat transfer modes (i.e., conduction, convection, and radiation) need to be considered in designing a tank, but conduction and radiation are more critical. Conduction occurs through pipes, ports, and mountings, and radiation heat transfer is effective between ambient and liquid hydrogen.

Another important aspect in thermal design of a liquid hydrogen tank is shape of the tank. To minimize heat flow, surface to volume ratio needs to be minimized, and this can be best achieved by cylindrical tanks. On the other hand, cylindrical tanks take up too much space in current vehicle designs (i.e., same problem also valid for compressed gaseous hydrogen storage). Therefore, conformable tanks are preferable in certain cases; however, conformable tanks usually show poorer thermal performance as compared to cylindrical tanks. In addition, manufacturing of conformable tanks is more labor intensive; hence, they are more costly [27].

It is impossible to eliminate all the heat input to the liquid hydrogen tank even with vacuum super insulation; therefore, hydrogen inside the tank evaporates due to

heat input constantly, and as a result, pressure inside the tank continuously increases. Once hydrogen pressure inside the tank reaches around 1 MPa, any excess hydrogen needs to be vented to the atmosphere, catalytically burned, or captured [14]. This excess hydrogen that is not utilized by the vehicle is called boil-off losses. The time period in between parking the vehicle to the venting process is called "dormancy." Longer dormancy periods are preferred, due to longer dwell times and lesser loss through adiabatic or isothermal processes. The state-of-the-art tank designs have a dormancy period of 3 days; in addition, dormancy can be further improved by applying innovative cooling methods [30].

Liquefied hydrogen storage shows one of the best gravimetric and volumetric storage densities among other storage methods. However, liquefaction cost of hydrogen is significant, 30% of the lower heating value of hydrogen, as shown in Fig. 4.4. When considered in combination with boil-off losses, overall cost of liquid hydrogen storage can easily surpass the cost of gaseous hydrogen storage. Currently, liquid hydrogen storage is only attractive for short-term storage (i.e., space applications) due to aforementioned limitations.

4.3.1.3 Cryo-Compressed Hydrogen Storage

Cryo-compressed hydrogen storage is based on storing hydrogen at high pressures and cryogenic temperatures (i.e., <77 K). Cryo-compression overcomes the most critical drawbacks of compressed and liquefied hydrogen storage technologies. One of the shortcomings of the compressed hydrogen storage is the low gravimetric and volumetric density of hydrogen even at high pressures (i.e., 70 MPa). By cooling hydrogen to cryogenic temperatures at high pressure, energy density can be improved while avoiding the high energy penalty associated with liquefaction. Considering liquefied hydrogen storage, boil-off loss of hydrogen is an important issue (see Sect. 4.1.2). Liquid hydrogen tanks are low pressure tanks, and maximum operating pressure is around 1 MPa; hence, liquid hydrogen tanks has a dormancy period of couple of days at max. By using high pressure capable cryogenic tanks, dormancy period can be increased significantly. In addition, heat transfer into the tank becomes less critical because evaporated hydrogen can be stored in the high pressure tank longer. Finally, cryo-compressed tank can be charged with liquid hydrogen, cryo-compressed hydrogen, or hydrogen in a two phase region. This flexibility makes them suitable for different needs; for instance, if driving range is more important than cost, liquid hydrogen can be used [31].

According to technical assessments, cryo-compressed hydrogen storage can meet the DOE targets of gravimetric and volumetric densities, and dormancy, but falls short of reaching manufacturing costs and well-to-wheel efficiency [32].

Cryo-compression hydrogen storage shows one of the highest gravimetric and volumetric densities among the current technologies (see Table 4.2). In addition, it significantly reduces, if not eliminates, boil-off losses which is an important shortcoming of the liquefied hydrogen storage. Therefore, cryo-compression hydrogen storage is considered as a promising hydrogen storage technology.

4.3.2 Chemical Methods of Hydrogen Storage

From the foregoing discussion, it is clear that physical methods of hydrogen storage (i.e., compressed and liquid hydrogen storage) have considerable limitations which resulted in worldwide search for better methods of hydrogen storage. Until 2000s, research efforts on chemical methods of hydrogen storage were very limited and mostly concentrated on metal hydrides. In the early 2000s, along with the increased awareness on environmental problems discussed in the *Introduction* section, hydrogen storage research has gained significant momentum.

Chemical methods of hydrogen storage (also called materials based hydrogen storage) are based on the interaction of hydrogen with the storage media (i.e., hydrogen storage materials) as opposed to physical methods of hydrogen storage in which there is no interaction between hydrogen and the storage media. These interactions can be weak (i.e., van der Waal forces) or strong (i.e., ionic and covalent bonds) or moderate (i.e., Kubas interaction) in strength [33]. The strength of the interactions dictates the operating conditions (charging/discharging temperature, pressure, etc.) of the hydrogen storage method.

Theoretically, hydrogen can be stored within certain materials much more efficiently as compared to compressed or liquefied hydrogen storage. For instance, gravimetric and volumetric densities of $LiBH_4$, a complex hydride, are 18.4 wt.% and 121 kg/m^3, respectively [34].

It is very important to note that, unless otherwise stated, all the gravimetric and volumetric densities that are given in chemical methods of hydrogen storage sections in this chapter (as well as in vast majority of the literature) indicate the storage capacity of the hydrogen storage material only. However, the DOE targets for hydrogen storage (see Table 4.1) are given for system level storage capacity. Materials-based storage capacity does not take into account balance of the plant components such as storage tank, safety features, and heating/cooling equipment. As a rule of thumb, hydrogen storage capacity of the system would be maximum half of the storage capacity of the material [23].

Chemical methods of hydrogen storage can be divided into two: (i) solid-state storage (on-board regenerable) and (ii) chemical storage (off-board regenerable). The main distinction in between these two are chemical storage materials have unfavorable kinetics or thermodynamics or both; therefore, they need to be regenerated off-board, whereas solid-state storage materials can be recharged by hydrogen on-board a vehicle. On-board regeneration is favorable over off-board regeneration because on-board regeneration is more practical and less costly. On-board regenerable materials can be directly charged with hydrogen without any other intermediate step. Off-board regeneration requires spent fuel to be processed in a central facility; this would add to the overall cost of the fuel as well as makes overall fuel cycle more complex.

4.3.2.1 Solid-State Hydrogen Storage (On-board Regenerable Materials)

The solid-state hydrogen storage materials can be broadly divided into two based on the strength of the interaction between hydrogen and the storage material, namely,

(i) reversible hydrides (based on strong interactions) and (ii) physisorption materials (based on weak interactions). Reversible hydrides can be further divided into two as metal hydrides and complex hydrides.

The research on hydrogen storage materials that can be regenerated on-board is mostly concentrated on complex hydrides [35] and porous materials [36] which comprise a significant portion of solid-state hydrogen storage materials. The complex hydrides have relatively high hydrogen storage capacity (i.e., high gravimetric and volumetric densities); however, they suffer from high operating temperatures, sluggish kinetics and reversibility [28]. On the other hand, physisorption-based porous materials have fast kinetics and complete reversibility; however, they can only store significant amount of hydrogen at cryogenic temperatures (i.e., 77 K) due to the weak interaction of hydrogen with the porous material matrix (i.e., low adsorption enthalpy) at or near room temperature (i.e., 300 K) [14].

Reversible Hydrides

Metal Hydrides

Metal hydrides, AB_5–type alloys (i.e., $LaNi_5$) and AB_2–type alloys (i.e., $ZrMn_2$), are relatively old classes of reversible hydrides that date back to 1960s [37]. Extensively studied metal hydrides are presented in Table 4.3. Metal hydrides form by dissociation of the hydrogen molecule on the metal surface and the subsequent migration of the hydrogen atoms to the crystal lattice [38]. AB_5 and AB_2 type metal hydrides are also called intermetallic hydrides since hydrogen atoms are located at the interstitial crystal lattice sites of the metal hydride. Major drawbacks of the metal hydrides are their low gravimetric density (i.e., $LaNi_5H_6$), high operating temperature (i.e., MgH_2), and high cost of rare earth metals (i.e., lanthanum (La)) and titanium (Ti). Since AB_5 and AB_2 type metal hydrides usually have low gravimetric densities (1–2 wt.%), they are not suitable for mobile applications; however, due to their good reversibility and favorable operating conditions, they can be useful in stationary applications [38]. Among the metal hydrides, MgH_2 attracted significant attention due to its high gravimetric capacity (7.6 wt.%). The chemical bond in MgH_2 shows both ionic and covalent character; therefore, MgH_2 has a quite high operating temperature (see Table 4.3) [39]. The studies on MgH_2 concentrated on lowering desorption temperature and enhancing kinetics by destabilization via different metal oxides and transition metals (i.e., Nb_2O_5, V_2O_5, Ti, Fe) [40, 41].

Table 4.3 Extensively studied metal hydrides [42]

Metals	Hydrides	Capacity (wt.%)	Temperature for 1 bar H_2 (°C)
$LaNi_5$	$LaNi_5H_6$	1.37	12
FeTi	$FeTiH_2$	1.89	−8
Mg_2Ni	Mg_2NiH_4	3.59	255
$ZrMn_2$	$ZrMn_2H_2$	1.77	440
Mg	MgH_2	7.60	279

Complex Hydrides

The complex hydrides were brought to the attention of the hydrogen storage community by the prominent work of Bogdanovic et al. on Ti-doped $NaAlH_4$ [43]. They showed that by adding a small amount of Ti (i.e., 2 mol%), the $NaAlH_4$ complex hydride system can be regenerated reversibly by applying hydrogen pressure. Elemental hydride MgH_2 has a theoretical storage capacity of 7.6 wt.% and a desorption temperature around 300 °C as shown in Table 4.3. Attaining a higher gravimetric storage capacity is only possible by incorporating metals lighter than Mg, such as Li and Na. Therefore, research efforts concentrated on light metal complex hydrides during the last decade. The bonding in complex hydrides shows both ionic and covalent character. For instance, in $LiNH_2$, the N–H bond in the (NH_2)- anion shows mainly covalent character [35], whereas the Li–N bond shows a mixed ionic and covalent character [44]. Complex hydrides have high theoretical gravimetric densities: $NaAlH_4$ (7.5 wt.%) [43], $LiAlH_4$ (10.6 wt.%) [45], $LiBH_4$ (18.4 wt.%) [46], and Li_3N (11.5 wt.%) [47]. However, their reversible gravimetric capacities are around 4–5 wt.% under practical operating temperatures and pressures [48]. The reversible capacities of the most studied complex hydride systems are $LiAlH_4$ (3–5 wt.%, 150–200 °C) [45], $NaAlH_4$ (3–5 wt.%, 120–150 °C) [49], $LiNH_2$–MgH_2/LiH (4–6 wt.%, 200–250 °C) [50, 51], and $LiBH_4$–$LiNH_2$–MgH_2 (4–8 wt.%, 200–280 °C) [52]. Studies on complex hydrides have mainly focused on destabilization and overcoming the reversibility, sluggish kinetics, and toxic/poisonous gas emission issues [48, 53–55].

Porous Materials

Porous materials (also called high surface area and physisorption based materials in the literature) [56, 57] include a wide range of organic and inorganic materials with ordered (i.e., zeolites) and amorphous (i.e., activated carbon) structures [58–60]. Porous materials have a wide range of applications in purification [61], ion exchange [59], separation [62], catalysis [63], gas storage [56], drug delivery [64], and biomaterials [65]. Porous materials can be classified according to their pore dimensions. According to the International Union of Pure and Applied Chemistry, pores are divided into three categories based on their diameters; micropores (<2 nm), mesopores (2–50 nm), and macropores (>50 nm) [66].

Development of novel high surface area porous materials such as metal organic frameworks (MOFs) [58], covalent organic frameworks (COFs) [67], templated carbons [68], porous aromatic frameworks (PAFs) [69], hypercrosslinked polymers [70], polymers of intrinsic porosity (PIMs) [71], and conjugated microporous polymers (CMPs) [72] in the last decade resulted in extensive research efforts on gas storage applications of these materials [56].

Porous materials have been extensively studied due to their fast sorption kinetics, reversibility, and promising gravimetric storage capacity. Storage of hydrogen in high surface area porous materials is realized by the interaction of hydrogen with porous material surface via physisorption (i.e., adsorption) which is based on weak van der Waals forces [73]. Due to weak intermolecular forces (i.e., <6 kJ/mol) [74] involved in physisorption of hydrogen, porous materials can only achieve significant

hydrogen uptake at cryogenic temperatures (i.e., 77 K). Their hydrogen storage capacity at room temperature is usually less than 1 wt.% at moderate pressures (i.e., 100 atm) [36, 75].

The most important parameters that determine porous materials' hydrogen storage capacity are surface area, pore volume, pore size, and adsorption enthalpy [76, 77]. The adsorption enthalpy of porous materials is low (<6 kJ/mol) [74] and needs to be improved (20–40 kJ/mol) [78] for significant hydrogen uptake at room temperature. The tuning of the adsorption enthalpy and/or improving hydrogen uptake at room temperature can be realized via multiple modification methods such as optimizing pore size [76], enhancing specific surface area, and doping with impurity atoms (B, N, alkali/transition metals) [79–81]. Therefore, studies concentrated on enhancing the adsorption enthalpy (i.e., creating open metal sites in MOFs) [82], maximizing surface area [83], and fine tuning pore size dimensions of porous materials [84].

4.3.2.2 Chemical Hydrogen Storage (Off-board Regenerable Materials)

Chemical hydrogen storage term in this chapter is used to define materials that cannot be regenerated easily on-board due to unfavorable thermodynamics or kinetics or both. Another term frequently used in the literature is the "chemical hydrides" to define same class of materials. As the "chemical hydrides" name implies, some of the chemical hydrogen storage materials such as sodium borohydride ($NaBH_4$) and aluminum hydride (AlH_3) belong to hydrides group; however, considering their difficulty of regenerability, they are not included under reversible hydrides discussed in Sect. Complex Hydrides.

The most promising and well-studied chemical hydrogen storage materials are $NaBH_4$ [85], AlH_3 [86], ammonia-borane ($NH_3 \cdot BH_3$ or simply AB) [87], and liquid organic hydrogen carriers such as cyclohexane-benzene [88, 89]. These materials will be discussed in more detail in the following sections.

In addition, ammonia (NH_3) [90], alcohols (i.e., methanol), and hydrocarbons [20] can be considered as chemical hydrogen storage materials. The common problem with these energy carries is that their production is mostly based on fossil fuels; hence, they do not provide a long-term sustainable solution.

Sodium Borohydride

Sodium borohydride ($NaBH_4$) releases hydrogen via hydrolysis reaction according to following reaction path, and half of the hydrogen comes from water:

$$NaBH_4 + 2H_2O \rightarrow NaBO_2 + 4H_2 \tag{4.4}$$

$NaBH_4$ has a 10.8 wt.% hydrogen storage capacity theoretically; however, in practical operating conditions, much lower storage capacities were reported (2.9–7.5 wt.%) [85]. There are two main issues associated with $NaBH_4$–H_2O system are: first, the low solubility of $NaBH_4$ and $NaBO_2$ in water which requires significant amount of excess water to be stored on-board, and second, the slow reaction rate of hydrogen generation which requires catalyst to increase the rate of reaction;

however, durability of the catalysts over the long-term usage leads to degradation in performance. Due to these reasons, DOE recommended these systems not be employed as aqueous solutions of $NaBH_4$ for hydrogen storage [85].

Aluminum Hydride

Aluminum hydride (AlH_3) has a 10.1 wt.% and 148 kg/m^3 gravimetric and volumetric hydrogen storage capacities, respectively. AlH_3 releases hydrogen with small amount of heat input (~7 kJ/mol) according to the following endothermic reaction: [91]

$$AlH_3 \rightarrow Al + \frac{3}{2}H_2 \tag{4.5}$$

The reaction rate can be controlled by manipulating the crystallite size, and smaller crystallites show faster decomposition of AlH_3, hence, resulting in faster hydrogen delivery.

The main challenge of AlH_3 is the regeneration; direct regeneration of AlH_3 from Al and H_2 requires significant pressures (~700 MPa) at room temperature. Alternative paths for regeneration of AlH_3 are ethereal reaction with $LiAlH_4$ and $AlCl_3$, and electrochemical hydrogenation [91].

Ammonia-Borane

Ammonia-borane (AB) is a nonflammable and nonexplosive white crystalline solid with a theoretical gravimetric hydrogen storage capacity of 19.6 wt.% [87]. Hydrogen in AB can be extracted via many different routes such as thermolysis with or without the presence of metal catalysts or additives, hydrolysis, and decomposition of AB in liquids such as ionic liquids or organic solvents [92]. Only thermolysis and hydrolysis will be discussed briefly (see Eqs. 4.6, 4.7, and 4.8):

$$nNH_3BH_3(s) \rightarrow nNH_3BH_3 \tag{4.6}$$

$$nNH_3BH_3(l) \rightarrow [NH_2BH_2]_n(s) \rightarrow [NHBH]_n(s) + nH_2(g) \tag{4.7}$$

$$[NHBH]_n(s) \rightarrow [NB]_n(s) + nH_2(g) \tag{4.8}$$

The onset temperature of AB thermal decomposition is 70 °C and peaks around 110 °C (1 mol of AB yields ~1.1 mol H_2). Upon decomposition, byproduct polyaminoborane ($[NH_2BH_2]_n$) is formed. Further heating to 200 °C releases additional hydrogen (~1 mol H_2) stored in polyaminoborane [93]. Thermal decomposition of AB may release trace amounts of borazine and ammonia which are detrimental to the operation of a proton exchange membrane fuel cell and needs to be eliminated or captured [55]. Another issue of thermolysis of AB is the induction period before hydrogen release; for instance, AB starts to release significant amounts of hydrogen only after 3 h at a temperature of 85 °C [93]. To overcome this problem, AB can be mixed with ionic liquids [94] or can be incorporated into

porous materials (i.e., mesoporous silica) [95]. However, both of these approaches add dead weight to the system and hence, lowers the system's overall hydrogen storage capacity.

Hydrolysis of AB is a pH-dependent process. In basic or neutral solutions, aqueous AB is very stable; however, when aqueous AB comes in contact with an acidic solution, hydrolysis commences instantaneously, and the reaction rate is high. In a real-world application, hydrogen should be available on demand; therefore, aqueous AB can be kept separately, and AB can be brought in contact with an acidic solution to generate hydrogen when needed. One of the challenges of hydrolytic pathway for AB is the formation of very stable borate (B–O) compounds. Therefore, regeneration of AB from borate products is an energy-intensive process and a formidable economical challenge. A similar regeneration problem is also a characteristic of the $NaBH_4$–H_2O system discussed before [96].

Liquid Organic Hydrogen Carriers

Liquid organic hydrogen carriers (LOHC) are energy carriers that can be loaded and unloaded with hydrogen in a cyclic fashion [89]. Handling liquid as opposed to solid as a hydrogen carrier has significant engineering advantages. First, it can be transported easily to end users using existing infrastructures. Second, in a vehicle, it can be pumped in required quantities to the reaction chamber where it is converted to heat. This way, there is no need to heat whole hydrogen storage material to release small quantities of hydrogen [88].

Some of the LOHC that have been studied are cyclohexane-benzene and N-ethylcarbazole [88, 89]. Typical LOHC has a theoretical hydrogen storage capacity of 6–8 wt.% which is relatively low considering other chemical hydrogen storage materials (i.e., AB has a 19.6 wt.% capacity). LOHC is relatively less studied area of hydrogen storage. Therefore, to better understand their potential more work needs to be done, especially on toxicity, thermal stability, safety, and large-scale production/regeneration methods of LOHC [88, 89].

4.3.3 Hybrid Methods of Hydrogen Storage

Hybrid methods of hydrogen storage make use of two or more different physical and chemical methods of hydrogen storage technologies (see Fig. 4.2) to overcome the shortcomings of each individually. The main hybrid method of hydrogen storage is cryo-adsorption. Cryo-adsorption is a physical-chemical method of hydrogen storage and takes advantage of compressed, liquefied, and physisorption materials-based hydrogen storage technologies.

4.3.3.1 Cryo-Adsorption Hydrogen Storage

Cryo-adsorption hydrogen storage is based on storing hydrogen in a physisorption-based (i.e., porous) material at cryogenic temperatures and high pressures. System's hydrogen storage capacity is closely related to the adsorption properties the porous

material. Surface area, pore volume, and heat of adsorption are critical to maximize the storage capacity of cryo-adsorption systems [77].

Cryo-adsorption performance of different porous materials such as activated carbon [97], zeolite [98], and MOFs [99] has been investigated. Using a porous material instead of an empty tank at the same pressure and temperature increases the hydrogen storage capacity considerably. For instance, MOF-210 has an excess[2] hydrogen storage capacity of 86 mg/g (~8 wt.%) and total[3] hydrogen storage capacity of 176 mg/g (~15 wt.%) [99]. More than half of the hydrogen storage capacity is due to MOF-210.

High pressure hydrogen storage capacities of porous materials given in the literature are the difference between saturation and the zero pressure. In real-world applications, one needs to consider practical operating conditions to better understand the actual hydrogen storage capacity of the system. For instance, gas pressure inside the tank can never be zero because fuel cells operate at pressures around 0.2–0.3 MPa [100]. Therefore, some of the hydrogen will always remain in the tank. This problem can be minimized by temperature swing, which is increasing the temperature of the tank using heat to desorb as much hydrogen as possible [97].

4.4 Challenges of Hydrogen Storage Technologies

The most significant challenges for the main hydrogen storage technologies are as summarized below.

Compressed hydrogen storage: High energy penalty due to compression. Up to 15% of hydrogen's lower heating value is required for compression. High pressure storage tank is manufactured from woven carbon nanofibers which is very costly.

Liquefied hydrogen storage: Liquefaction of hydrogen demands very high energy; around 30% of the hydrogen's lower heating value is required for liquefaction. Liquid hydrogen (20 K) tank must be super insulated to minimize heat gain from the surroundings (300 K). However, it is impossible to eliminate all heat gain by insulation, as a result some of the hydrogen boils-off from the vent of the tank regularly to keep the pressure inside the hydrogen tank at a safe level. This poses a great problem especially if a vehicle is not driven regularly.

Solid-state hydrogen storage: There are two main technologies under solid-state hydrogen storage; reversible hydrides and physisorption materials. *Physisorption materials* can only store significant amount of hydrogen at cryogenic

[2]Excess capacity is the capacity excluding compressed gaseous hydrogen at that temperature. In other words, excess capacity is the amount of hydrogen stored because of the presence of the porous material.

[3]Total hydrogen storage capacity reported here does not include the weight of the tank or any other balance of the plant components.

temperatures (77 K); therefore, during charging storage tank needs to be cooled, and this process adds an energy penalty though not as severe as liquefaction of hydrogen. *Reversible hydrides* usually require high temperatures (>100 °C) during charging onboard to enhance kinetics. Heating of the storage tank adds a significant energy penalty. In addition, reversible hydrides suffer from degradation over cycles. Moreover, during hydrogen discharging from reversible hydrides, it is possible that some toxic gases (i.e., NH_3) may be emitted concomitantly. These toxic gases, even at trace levels, can be detrimental to the operation of a fuel cell.

Chemical hydrogen storage: The main issue with chemical hydrogen storage materials is the off-board regeneration requirement. Due to unfavorable kinetics, thermodynamics, or both, these materials need to be regenerated off-board at central facilities, and regeneration is a costly process.

4.5 Summary

It is no question that modern society has been greatly benefiting from exploiting fossil fuels since the beginning of the industrial era. However, this almost perfect primary energy source (high energy density, easy to store, etc.) is a finite energy source. More importantly, excessive fossil fuel use causes various environmental problems such as global warming due to undue anthropogenic CO_2 emissions. Therefore, it is clear that society needs to find environmentally benign alternatives to fossil fuels to move towards low-carbon economy.

Transportation sector worldwide heavily relies on oil which is expected to be depleted well before the end of twenty-first century. The CO_2 emissions from mobile platforms are considered as distributed CO_2 sources, and there is no proven technology that can be installed on-board vehicles to capture CO_2 economically. Therefore, in mid future, the best approach to alleviate global warming and to prevent the depletion of oil is to replace oil with an environmentally friendly energy source or carrier. Among many alternatives for a sustainable energy carrier, hydrogen is considered to be a promising candidate. Hydrogen is a carbon free energy source, and when burned in internal combustion engines or converted to electricity in fuel cells, it only emits water to the environment.

Hydrogen economy is a system, similar to oil economy, including production, transportation, and storage of hydrogen. Currently, majority of hydrogen is produced by steam methane reformation process. It is necessary to produce hydrogen from renewable sources such as wind or photovoltaic (PV) powered water electrolysis. Transportation of hydrogen also poses significant challenges; most important one is the requirement of an extensive distribution network which would be costly. The last step in hydrogen economy is hydrogen storage. Hydrogen storage is considered as a bottleneck in hydrogen economy. Many countries in the world in collaboration with the automotive industry set targets for a hydrogen storage system for vehicular applications. The most stringent targets are gravimetric and volumetric hydrogen storage capacities, as a result, most often times different hydrogen storage

technologies are compared just based on energy density regardless of cost, operating temperature or efficiency.

The main hydrogen storage technologies are compressed, liquefied, solid-state, and chemical hydrogen storage technologies. Compressed and liquefied hydrogen storage technologies are physical methods of storage, whereas solid-state and chemical hydrogen storage technologies are chemical methods of hydrogen storage. The main distinction in between physical and chemical methods is in physical methods hydrogen does not interact with the storage media, whereas in chemical methods hydrogen interacts with the storage media.

Compressed and liquefied hydrogen storage can be considered as the conventional methods of hydrogen storage. These technologies have been in use for many decades. For gaseous storage, to increase the storage density, high pressure (i.e., 70 MPa) tanks have been developed; in addition, low-cost carbon fiber manufacturing methods were developed to bring down the tank costs. For liquefied storage, boil-off losses were minimized by incorporating vacuum super insulation; in addition, dormancy period of liquid hydrogen has been extended by developing novel cooling technologies. Despite all the efforts, neither compressed nor liquefied hydrogen storage meets all the DOE targets for hydrogen storage. However, compressed gaseous hydrogen storage is considered as the most mature technology among all others, and it is the only one that has been commercialized (i.e., Toyota Mirai) so far.

Starting from 2000s, the majority of the research efforts in hydrogen storage area has been concentrated on solid-state (on-board regenerable) and chemical (off-board regenerable) hydrogen storage technologies due to shortcomings of compressed and liquefied hydrogen storage. Solid-state storage attracted more attention compared to chemical storage because on-board regenerability is a desirable property to reduce the costs associated with the regeneration of spent fuel in chemical storage.

Solid-state storage materials are divided into two: reversible hydrides and physisorption (porous) materials. Reversible hydrides require relatively high temperatures to operate, and they suffer from reversibility issues. Porous materials operate at cryogenic temperatures to store significant amount of hydrogen, and their drawback is the cost associated with cooling. The major challenge in solid-state storage materials, other than having low energy density, is to bring the operating temperature closer to room temperature to avoid heating (i.e., complex hydrides) and cooling (i.e., porous materials) costs. Chemical hydrogen storage materials release hydrogen by processes like hydrolysis (i.e., $NaBH_4$) or thermolysis (i.e., $NH_3 \cdot BH_3$). After hydrogen is released, by-products (i.e., spent fuel) are too stable to be regenerated on-board simply charging by hydrogen. The main drawback of this class of materials is the cost and complexity associated with the regeneration of spent fuel.

In conclusion, in this chapter, the main hydrogen storage technologies and materials are introduced, and their advantages and disadvantages are discussed in detail. The quest for finding a benign fuel alternative to oil is still in progress, and hydrogen is one of the best options available as of now. More basic research and demonstration projects are required to advance the hydrogen storage field forward.

Market penetration of hydrogen storage technologies in near future is closely tied to the development of improved hydrogen storage materials.

Acknowledgment The author acknowledges the support from the College of Engineering at the Texas A&M University – Kingsville.

References

1. Anonymous, BP Energy Outlook 2035 (2015)
2. G. Maggio, G. Cacciola, When will oil, natural gas, and coal peak? Fuel **98**, 111–123 (2012)
3. J. Houghton, Global warming. Rep. Prog. Phys. **68**, 1343–1403 (2005)
4. M. Asif, T. Muneer, Energy supply, its demand and security issues for developed and emerging economies. Renew. Sust. Energ. Rev. **11**, 1388–1413 (2007)
5. F. Barbir, T. Veziroğlu, H. Plass, Environmental damage due to fossil fuels use. Int. J. Hydrog. Energy **15**, 739–749 (1990)
6. M.K. Hubbert, Nuclear energy and the fossil fuel, in *Drilling and production practice* (American Petroleum Institute, Washington, DC, 1956)
7. R. Agrawal, N.R. Singh, F.H. Ribeiro, W.N. Delgass, Sustainable fuel for the transportation sector. Proc. Natl. Acad. Sci. **104**, 4828–4833 (2007)
8. R.A. Kerr, Peak oil production may already be here. Science **331**, 1510–1511 (2011)
9. J.P. Bruce, H.-S. Yi, E.F. Haites, *Climate change 1995: Economic and social dimensions of climate change: Contribution of Working Group III to the second assessment report of the Intergovernmental Panel on Climate Change* (Cambridge University Press, Cambridge, 1996)
10. I.A. Mendelssohn, G.L. Andersen, D.M. Baltz, R.H. Caffey, K.R. Carman, J.W. Fleeger, S.B. Joye, Q. Lin, E. Maltby, E.B. Overton, Oil impacts on coastal wetlands: implications for the Mississippi River Delta ecosystem after the Deepwater Horizon oil spill. Bioscience **62**, 562–574 (2012)
11. G.W. Crabtree, M.S. Dresselhaus, M.V. Buchanan, The hydrogen economy. Phys. Today **57**, 39–44 (2004)
12. H.F. Abbas, W.W. Daud, Hydrogen production by methane decomposition: a review. Int. J. Hydrog. Energy **35**, 1160–1190 (2010)
13. R. Gerboni, E. Salvador, Hydrogen transportation systems: elements of risk analysis. Energy **34**, 2223–2229 (2009)
14. M. Felderhoff, C. Weidenthaler, R. von Helmolt, U. Eberle, Hydrogen storage: the remaining scientific and technological challenges. Phys. Chem. Chem. Phys. **9**, 2643–2653 (2007)
15. W. Lattin, V. Utgikar, Transition to hydrogen economy in the United States: a 2006 status report. Int. J. Hydrog. Energy **32**, 3230–3237 (2007)
16. Anonymous, Technical system targets: onboard hydrogen storage for light-duty fuel cell vehicles. http://energy.gov/eere/fuelcells/doe-technical-targets-onboard-hydrogen-storage-light-duty-vehicles. Accessed 3 Mar 2016
17. U. Bossel, B. Eliasson, G. Taylor, The future of the hydrogen economy: bright or bleak? Cogener. Distrib. Gener. J **18**, 29–70 (2003)
18. R. Shinnar, The hydrogen economy, fuel cells, and electric cars. Technol. Soc. **25**, 455–476 (2003)
19. K.G. Hoyer, E. Holden, Alternative fuels and sustainable mobility: is the future road paved by biofuels, electricity or hydrogen? Int. J. Altern. Propuls. **1**, 352–368 (2007)
20. U. Eberle, M. Felderhoff, F. Schueth, Chemical and physical solutions for hydrogen storage. Angew. Chem. Int. Ed. **48**, 6608–6630 (2009)
21. S.G. Chalk, J.F. Miller, Key challenges and recent progress in batteries, fuel cells, and hydrogen storage for clean energy systems. J. Power Sources **159**, 73–80 (2006)

22. Anonymous, US Department of Energy, Office of Energy Efficiency and Renewable Energy, and The FreedomCAR and Fuel Partnership. Targets for onboard hydrogen storage systems for light-duty vehicles (2009)
23. C. Read, G. Thomas, G. Ordaz, S. Satyapal, US Department of Energy's system targets for on-board vehicular hydrogen storage. Mater. Matters **2**, 3–5 (2007)
24. Anonymous, Status of hydrogen storage technologies. http://energy.gov/eere/fuelcells/status-hydrogen-storage-technologies. Accessed 3 Mar 2016
25. B.P. Tarasov, M.V. Lototskii, V.A. Yartys, Problem of hydrogen storage and prospective uses of hydrides for hydrogen accumulation. Russ. J. Gen. Chem. **77**, 694–711 (2007)
26. T. Hua, R. Ahluwalia, J.-K. Peng, M. Kromer, S. Lasher, K. McKenney, K. Law, J. Sinha, Technical assessment of compressed hydrogen storage tank systems for automotive applications. Int. J. Hydrog. Energy **36**, 3037–3049 (2011)
27. R. von Helmolt, U. Eberle, Fuel cell vehicles: status 2007. J. Power Sources **165**, 833–843 (2007)
28. L. Zhou, Progress and problems in hydrogen storage methods. Renew. Sust. Energ. Rev. **9**, 395–408 (2005)
29. C.W. Hamilton, R.T. Baker, A. Staubitz, I. Manners, B–N compounds for chemical hydrogen storage. Chem. Soc. Rev. **38**, 279–293 (2009)
30. J. Wolf, Liquid-hydrogen technology for vehicles. MRS Bull. **27**, 684–687 (2002)
31. S.M. Aceves, F. Espinosa-Loza, E. Ledesma-Orozco, T.O. Ross, A.H. Weisberg, T.C. Brunner, O. Kircher, High-density automotive hydrogen storage with cryogenic capable pressure vessels. Int. J. Hydrog. Energy **35**, 1219–1226 (2010)
32. R. Ahluwalia, T. Hua, J.-K. Peng, S. Lasher, K. McKenney, J. Sinha, M. Gardiner, Technical assessment of cryo-compressed hydrogen storage tank systems for automotive applications. Int. J. Hydrog. Energy **35**, 4171–4184 (2010)
33. T.K. Hoang, D.M. Antonelli, Exploiting the Kubas interaction in the design of hydrogen storage materials. Adv. Mater. **21**, 1787–1800 (2009)
34. A. Züttel, S. Rentsch, P. Fischer, P. Wenger, P. Sudan, P. Mauron, C. Emmenegger, Hydrogen storage properties of LiBH 4. J. Alloys Compd. **356**, 515–520 (2003)
35. I. Jain, P. Jain, A. Jain, Novel hydrogen storage materials: a review of lightweight complex hydrides. J. Alloys Compd. **503**, 303–339 (2010)
36. K.M. Thomas, Hydrogen adsorption and storage on porous materials. Catal. Today **120**, 389–398 (2007)
37. A. Zaluska, L. Zaluski, J. Ström-Olsen, Structure, catalysis and atomic reactions on the nano-scale: a systematic approach to metal hydrides for hydrogen storage. Appl. Phys. A **72**, 157–165 (2001)
38. D. Chandra, J.J. Reilly, R. Chellappa, Metal hydrides for vehicular applications: the state of the art. J. Miner. **58**, 26–32 (2006)
39. T. Noritake, M. Aoki, S. Towata, Y. Seno, Y. Hirose, E. Nishibori, M. Takata, M. Sakata, Chemical bonding of hydrogen in MgH_2. Appl. Phys. Lett. **81**, 2008–2010 (2002)
40. W. Oelerich, T. Klassen, R. Bormann, Metal oxides as catalysts for improved hydrogen sorption in nanocrystalline Mg-based materials. J. Alloys Compd. **315**, 237–242 (2001)
41. G. Liang, J. Huot, S. Boily, A. Van Neste, R. Schulz, Catalytic effect of transition metals on hydrogen sorption in nanocrystalline ball milled MgH_2–Tm (Tm = Ti, V, Mn, Fe and Ni) systems. J. Alloys Compd. **292**, 247–252 (1999)
42. G. Principi, F. Agresti, A. Maddalena, S.L. Russo, The problem of solid state hydrogen storage. Energy **34**, 2087–2091 (2009)
43. B. Bogdanović, M. Schwickardi, Ti-doped alkali metal aluminium hydrides as potential novel reversible hydrogen storage materials. J. Alloys Compd. **253**, 1–9 (1997)
44. Y. Song, Z. Guo, Electronic structure, stability and bonding of the Li-NH hydrogen storage system. Phys. Rev. B **74**, 195120 (2006)
45. J. Chen, N. Kuriyama, Q. Xu, H.T. Takeshita, T. Sakai, Reversible hydrogen storage via titanium-catalyzed $LiAlH_4$ and Li_3AlH_6. J. Phys. Chem. B **105**, 11214–11220 (2001)

46. S.-I. Orimo, Y. Nakamori, G. Kitahara, K. Miwa, N. Ohba, S.-I. Towata, A. Züttel, Dehydriding and rehydriding reactions of $LiBH_4$. J. Alloys Compd. **404**, 427–430 (2005)
47. P. Chen, Z. Xiong, J. Luo, J. Lin, K.L. Tan, Interaction of hydrogen with metal nitrides and imides. Nature **420**, 302–304 (2002)
48. B. Sakintuna, F. Lamari-Darkrim, M. Hirscher, Metal hydride materials for solid hydrogen storage: a review. Int. J. Hydrog. Energy **32**, 1121–1140 (2007)
49. M. Resan, M.D. Hampton, J.K. Lomness, D.K. Slattery, Effects of various catalysts on hydrogen release and uptake characteristics of $LiAlH_4$. Int. J. Hydrog. Energy **30**, 1413–1416 (2005)
50. W. Luo, ($LiNH_2$–MgH_2): a viable hydrogen storage system. J. Alloys Compd. **381**, 284–287 (2004)
51. Y. Nakamori, S.-I. Orimo, Destabilization of Li-based complex hydrides. J. Alloys Compd. **370**, 271–275 (2004)
52. A. Sudik, J. Yang, D. Halliday, C. Wolverton, Hydrogen storage properties in $(LiNH_2)_2$-$LiBH_4$-(MgH_2) X mixtures (X = 0.0–1.0). J. Phys. Chem. C **112**, 4384–4390 (2008)
53. A. Borgschulte, E. Callini, B. Probst, A. Jain, S. Kato, O. Friedrichs, A. Remhof, M. Bielmann, A. Ramirez-Cuesta, A. Züttel, Impurity gas analysis of the decomposition of complex hydrides. J. Phys. Chem. C **115**, 17220–17226 (2011)
54. T. Ichikawa, N. Hanada, S. Isobe, H. Leng, H. Fujii, Mechanism of novel reaction from $LiNH_2$ and LiH to Li_2NH and H_2 as a promising hydrogen storage system. J. Phys. Chem. B **108**, 7887–7892 (2004)
55. D.E. Demirocak, S.S. Srinivasan, M.K. Ram, J.N. Kuhn, R. Muralidharan, X. Li, D.Y. Goswami, E.K. Stefanakos, Reversible hydrogen storage in the Li–Mg–N–H system–The effects of Ru doped single walled carbon nanotubes on NH_3 emission and kinetics. Int. J. Hydrog. Energy **38**, 10039–10049 (2013)
56. R.E. Morris, P.S. Wheatley, Gas storage in nanoporous materials. Angew. Chem. Int. Ed. **47**, 4966–4981 (2008)
57. M. Nijkamp, J. Raaymakers, A. Van Dillen, K. De Jong, Hydrogen storage using physisorption–materials demands. Appl. Phys. A **72**, 619–623 (2001)
58. J.L. Rowsell, O.M. Yaghi, Metal–organic frameworks: a new class of porous materials. Microporous Mesoporous Mater. **73**, 3–14 (2004)
59. M.E. Davis, Ordered porous materials for emerging applications. Nature **417**, 813–821 (2002)
60. H. Zhang, A.I. Cooper, Synthesis and applications of emulsion-templated porous materials. Soft Matter **1**, 107–113 (2005)
61. M. Toyoda, Y. Nanbu, T. Kito, M. Hiranob, M. Inagaki, Preparation and performance of anatase-loaded porous carbons for water purification. Desalination **159**, 273–282 (2003)
62. K. Nakanishi, N. Tanaka, Sol–gel with phase separation. Hierarchically porous materials optimized for high-performance liquid chromatography separations. Acc. Chem. Res. **40**, 863–873 (2007)
63. A. Corma, From microporous to mesoporous molecular sieve materials and their use in catalysis. Chem. Rev. **97**, 2373–2420 (1997)
64. P. Horcajada, C. Serre, M. Vallet-Regí, M. Sebban, F. Taulelle, G. Férey, Metal–organic frameworks as efficient materials for drug delivery. Angew. Chem. **118**, 6120–6124 (2006)
65. V. Karageorgiou, D. Kaplan, Porosity of 3D biomaterial scaffolds and osteogenesis. Biomaterials **26**, 5474–5491 (2005)
66. K. Ssing, D. Everett, R. Haul, L. Moscou, R. Pierotti, J. Rouquerol, T. Siemieniewsks, Reporting physisorption data for gas/solid system. Pure Appl. Chem. **57**, 603–619 (1985)
67. S.S. Han, H. Furukawa, O.M. Yaghi, W.A. Goddard Iii, Covalent organic frameworks as exceptional hydrogen storage materials. J. Am. Chem. Soc. **130**, 11580–11581 (2008)
68. Z. Yang, Y. Xia, R. Mokaya, Enhanced hydrogen storage capacity of high surface area zeolite-like carbon materials. J. Am. Chem. Soc. **129**, 1673–1679 (2007)
69. T. Ben, H. Ren, S. Ma, D. Cao, J. Lan, X. Jing, W. Wang, J. Xu, F. Deng, J.M. Simmons, Targeted synthesis of a porous aromatic framework with high stability and exceptionally high surface area. Angew. Chem. **121**, 9621–9624 (2009)

70. J. Germain, J. Hradil, J.M. Fréchet, F. Svec, High surface area nanoporous polymers for reversible hydrogen storage. Chem. Mater. **18**, 4430–4435 (2006)
71. N.B. McKeown, P.M. Budd, Polymers of intrinsic microporosity (PIMs): organic materials for membrane separations, heterogeneous catalysis and hydrogen storage. Chem. Soc. Rev. **35**, 675–683 (2006)
72. J.-X. Jiang, F. Su, A. Trewin, C.D. Wood, H. Niu, J.T. Jones, Y.Z. Khimyak, A.I. Cooper, Synthetic control of the pore dimension and surface area in conjugated microporous polymer and copolymer networks. J. Am. Chem. Soc. **130**, 7710–7720 (2008)
73. M. Rzepka, P. Lamp, M. De la Casa-Lillo, Physisorption of hydrogen on microporous carbon and carbon nanotubes. J. Phys. Chem. B **102**, 10894–10898 (1998)
74. B. Schmitz, U. Müller, N. Trukhan, M. Schubert, G. Férey, M. Hirscher, Heat of adsorption for hydrogen in microporous high-surface-area materials. ChemPhysChem **9**, 2181–2184 (2008)
75. H. Kajiura, S. Tsutsui, K. Kadono, M. Kakuta, M. Ata, Y. Murakami, Hydrogen storage capacity of commercially available carbon materials at room temperature. Appl. Phys. Lett. **82**, 1105–1107 (2003)
76. S.K. Bhatia, A.L. Myers, Optimum conditions for adsorptive storage. Langmuir **22**, 1688–1700 (2006)
77. H. Frost, T. Düren, R.Q. Snurr, Effects of surface area, free volume, and heat of adsorption on hydrogen uptake in metal-organic frameworks. J. Phys. Chem. B **110**, 9565–9570 (2006)
78. S.-H. Jhi, J. Ihm, Developing high-capacity hydrogen storage materials via quantum simulations. MRS Bull. **36**, 198–204 (2011)
79. T.M. Chung, Y. Jeong, Q. Chen, A. Kleinhammes, Y. Wu, Synthesis of microporous boron-substituted carbon (B/C) materials using polymeric precursors for hydrogen physisorption. J. Am. Chem. Soc. **130**, 6668–6669 (2008)
80. S.S. Han, W.A. Goddard, Lithium-doped metal-organic frameworks for reversible H_2 storage at ambient temperature. J. Am. Chem. Soc. **129**, 8422–8423 (2007)
81. Y. Li, R.T. Yang, Significantly enhanced hydrogen storage in metal-organic frameworks via spillover. J. Am. Chem. Soc. **128**, 726–727 (2006)
82. W. Zhou, H. Wu, T. Yildirim, Enhanced H_2 adsorption in isostructural metal–organic frameworks with open metal sites: strong dependence of the binding strength on metal ions. J. Am. Chem. Soc. **130**, 15268–15269 (2008)
83. O.K. Farha, I. Eryazici, N.C. Jeong, B.G. Hauser, C.E. Wilmer, A.A. Sarjeant, R.Q. Snurr, S.T. Nguyen, A.O. Yazaydın, J.T. Hupp, Metal–organic framework materials with ultrahigh surface areas: is the sky the limit? J. Am. Chem. Soc. **134**, 15016–15021 (2012)
84. J.L. Rowsell, O.M. Yaghi, Strategies for hydrogen storage in metal–organic frameworks. Angew. Chem. Int. Ed. **44**, 4670–4679 (2005)
85. U.B. Demirci, O. Akdim, J. Andrieux, J. Hannauer, R. Chamoun, P. Miele, Sodium borohydride hydrolysis as hydrogen generator: issues, state of the art and applicability upstream from a fuel cell. Fuel Cells **10**, 335–350 (2010)
86. J. Graetz, J. Reilly, V. Yartys, J. Maehlen, B. Bulychev, V. Antonov, B. Tarasov, I. Gabis, Aluminum hydride as a hydrogen and energy storage material: past, present and future. J. Alloys Compd. **509**, S517–S528 (2011)
87. A. Staubitz, A.P. Robertson, I. Manners, Ammonia-borane and related compounds as dihydrogen sources. Chem. Rev. **110**, 4079–4124 (2010)
88. R.H. Crabtree, Hydrogen storage in liquid organic heterocycles. Energy Environ. Sci. **1**, 134–138 (2008)
89. D. Teichmann, W. Arlt, P. Wasserscheid, R. Freymann, A future energy supply based on liquid organic hydrogen carriers (LOHC). Energy Environ. Sci. **4**, 2767–2773 (2011)
90. A. Klerke, C.H. Christensen, J.K. Nørskov, T. Vegge, Ammonia for hydrogen storage: challenges and opportunities. J. Mater. Chem. **18**, 2304–2310 (2008)
91. J. Graetz, New approaches to hydrogen storage. Chem. Soc. Rev. **38**, 73–82 (2009)

92. Z. Huang, T. Autrey, Boron–nitrogen–hydrogen (BNH) compounds: recent developments in hydrogen storage, applications in hydrogenation and catalysis, and new syntheses. Energy Environ. Sci. **5**, 9257–9268 (2012)
93. B. Peng, J. Chen, Ammonia borane as an efficient and lightweight hydrogen storage medium. Energy Environ. Sci. **1**, 479–483 (2008)
94. M.E. Bluhm, M.G. Bradley, R. Butterick, U. Kusari, L.G. Sneddon, Amineborane-based chemical hydrogen storage: enhanced ammonia borane dehydrogenation in ionic liquids. J. Am. Chem. Soc. **128**, 7748–7749 (2006)
95. A. Gutowska, L. Li, Y. Shin, C.M. Wang, X.S. Li, J.C. Linehan, R.S. Smith, B.D. Kay, B. Schmid, W. Shaw, Nanoscaffold mediates hydrogen release and the reactivity of ammonia borane. Angew. Chem. Int. Ed. **44**, 3578–3582 (2005)
96. F.H. Stephens, V. Pons, R.T. Baker, Ammonia–borane: the hydrogen source par excellence? Dalton Trans. (25), 2613–2626 (2007)
97. R. Ahluwalia, J. Peng, Automotive hydrogen storage system using cryo-adsorption on activated carbon. Int. J. Hydrog. Energy **34**, 5476–5487 (2009)
98. J. Li, E. Wu, J. Song, F. Xiao, C. Geng, Cryoadsorption of hydrogen on divalent cation-exchanged X-zeolites. Int. J. Hydrog. Energy **34**, 5458–5465 (2009)
99. M. Hirscher, Hydrogen storage by cryoadsorption in ultrahigh-porosity metal-organic frameworks. Angew. Chem. Int. Ed. **50**, 581–582 (2011)
100. L. Wang, A. Husar, T. Zhou, H. Liu, A parametric study of PEM fuel cell performances. Int. J. Hydrog. Energy **28**, 1263–1272 (2003)

Hydrogen Storage in Metal-Organic Frameworks

5

Lanfang Zou and Hong-Cai Zhou

Abstract

In the past two decades, metal-organic frameworks (MOFs), constructed with coordination bonds between organic linkers and inorganic metal clusters, have become a burgeoning field of research and a great potential candidate for hydrogen storage due to their exceptional high porosity, high crystallinity, uniform yet tunable pore size and pore shape, great structural diversity, and various kinds of hydrogen occupation sites. Here, some technical elements are introduced in tailoring MOFs as hydrogen storage resins, including syntax, synthesis, fabrication, evaluation, and benchmark testing. As way of example, MOFs constructed by carboxylate, azolate or mixed linkers, are discussed in the context of hydrogen storage. Last but not least, the postsynthetic modifications on MOF materials to increase the hydrogen storage capacities will be carefully illustrated.

Abbreviations

AC	Activated carbon
BDC	Beneze-1,4-dicarboxylate

Author Contribution: This chapter was conceived and written by Lanfang Zou under the supervision of Prof. Hong-Cai Zhou. Dr. S. Bashir and Dr. J. Liu helped with the revision.

L. Zou
Department of Chemistry, Texas A&M University, College Station, USA
e-mail: lanfang.zou@chem.tamu.edu

H.-C. Zhou (✉)
Center for Electrochemical Systems and Hydrogen Research, Texas A&M University, College Station, USA

Department of Chemistry, Texas A&M University, College Station, USA

Department of Materials Science and Engineering, Texas A&M University, College Station, USA
e-mail: zhou@chem.tamu.edu

Y.-P. Chen et al. (eds.), *Nanostructured Materials for Next-Generation Energy Storage and Conversion*, DOI 10.1007/978-3-662-53514-1_5

BET	Brunauer–Emmett–Teller
BTB	4,4′,4″-benzene-1,3,5-triyl-tribenzoate ligand
BTC	Benzene-1,3,5-tricarboxylate
BTT	1,3,5-benzenetristetrazolate
BTTri	1,3,5-tris(1H-1,2,3-triazol-5-yl)benzene
DEF	*N,N*-diethylformamide
DMA	*N,N*-dimethylacetamide
DMF	*N,N*-dimethylformamide
GCMC	Grand Canomical Monte Carlo simulation
HKUST	Hong Kong University of Science and Technology
IRMOF	Isoreticular metal-organic framework
IUPAC	International Union of Pure and Applied Chemistry
MBB	Molecular building block
MIL	Material from Institute Lavoisier
MOF	Metal-organic framework
SBB	Super molecular building block
UMCM	University of Michigan Crystalline Material
ZIF	Zeolitic imidazole framework

Contents

5.1 Introduction

The concerns of energy resource consumption from fossil fuel use, related to global warming, has gained momentum to develop sustainable energy carriers such as hydrogen gas (H_2). The energy density of hydrogen is much higher than that of petroleum such as gasoline and the combustion of hydrogen emits no carbon dioxide (CO_2). However, the application of H_2 as fuel in transportation would be limited if there is not

an effective storage technology due to its volatile nature. The currently used liquid fuels, such as gasoline and diesel, can be easily stored in simple tanks at ambient condition. A gaseous fuel, such as hydrogen poses a real challenge because up to 13 kg of hydrogen would be consumed per trip of 450 km driven, suggesting safe hydrogen storage and transport technologies are critical in the twenty-first century. In general, hydrogen can be stored in through compression or entrapped. The former by liquefaction or isothermal compression and the latter by storage in solid porous materials [1–4]. Based on the interaction strength between the hydrogen molecules and the framework, the storage methods usually can be divided into two categories: chemisorption and physisorption.

According to the International Union of Pure and Applied Chemistry (IUPAC), chemisorption is defined as "the adsorption that results from strong interactions, such as chemical bond formation between the hydrogen and the material." The physisorption is the "adsorption in which the nonchemical bonding force involved is van der Waals forces, which do not involve a significant change in the electronic orbital patterns of the species involved." In physisorbed materials, hydrogen molecules are normally adsorbed on the pores' surface of the materials. Since the interaction energy is very low and no activation energy is needed, the physisorption processes are usually reversible. The H_2 adsorption inside the porous materials such as metal-organic frameworks, porous carbons [5, 6], organic polymers [7, 8], and zeolites [9, 10] belongs to this category. Much research has been focused on the synthesis of highly porous materials with enhanced interactions with hydrogen.

In the past few decades, metal-organic frameworks (MOFs) [11–21], constructed with coordination bonds between organic linkers and inorganic metal clusters, have become a burgeoning field of research and a great potential candidate for hydrogen storage due to their exceptional high porosity, high crystallinity, uniform yet tunable pore size and pore shape, great diversity, and various kinds of hydrogen occupation sites. The US Department of Energy (DOE) 2017 target for a hydrogen storage system is set at "5.5 weight-percent gravimetric capacity, 40 g L^{-1} of volumetric capacity at an operating temperature of −40 to 60 °C under a maximum delivery pressure of 100 bar" [22]. It is very important to be aware that the targets are for an entire system, so the performance of the storage material must be even better in order to account for the storage container as well as temperature regulating apparatus. In 2003, the initial H_2 storage data, a remarkable 4.5 wt% at 77 K and 1 atm, was demonstrated by MOF-5, which was synthesized by Zn ionic salt and beneze-1,4-dicarboxylate (BDC) ligand [20]. The maximum H_2 uptake in MOF-5 varied from 1.3 to 5.2 wt% at 77 K depending on fabrication and activation parameters. Since then, numerous reports of porous MOFs with different topologies and porosities have demonstrated relatively high H_2 storage. Coupled with measurements of porosity, some understanding of many factors that affect the hydrogen uptake by porous MOFs has been developed.

A number of monographs have been devoted to meta-organic frameworks (MOFs) fabrication, activation, and use as hydrogen storage materials [18, 23–34]. Here, some technical elements are introduced in tailoring MOFs as hydrogen storage resins, including syntax, synthesis, fabrication, evaluation, and benchmark testing. As way of example, MOFs constructed by carboxylate, azolate, or mixed linkers are discussed in the context of hydrogen storage. Last but not least,

the postsynthetic modifications on MOF materials to increase the hydrogen storage capacities will be carefully illustrated [22, 29, 35–38].

5.2 Syntax Used for Hydrogen Storage

As it is already mentioned in the introduction, there is a great need to standardize definitions and terminologies before we explore the hydrogen storage in MOFs.

5.2.1 Adsorption or Absorption

Adsorption (Fig. 5.1a) refers the adhesion of atoms, ions, or molecules to a surface, while absorption (Fig. 5.1b) is a physical or chemical process in which atoms, ions, or molecules permeation through the bulk volume of the materials and incorporated into the internal structure of the adsorbent. From the figure, it can be seen that the adsorption requires a large surface area to be effective.

5.2.2 Chemisorption and Physisorption

Chemisorption is a process which involves a chemical reaction between the surface and the adsorbate, while new chemical bonds are generated at the adsorbent surface. Usually, chemisorption only occurs in a monolayer on the surface. Physisorption, also called physical adsorption, is a process in which the force involved are the weak intermolecular van der Waals forces. The physisorption is normally multilayer adsorption, which highly depends on the temperature and pressure. There is no hard boundary between the physisorption and the chemisorption and the H-H bond is treated as a distinction. If the H-H bond is destroyed in the sorbed state, then it is considered chemisorption; otherwise, it is a physisorption phenomenon. In general, the binding energy threshold is about 0.5 eV per adsorbed species to differentiate the process of physisorption and chemisorption.

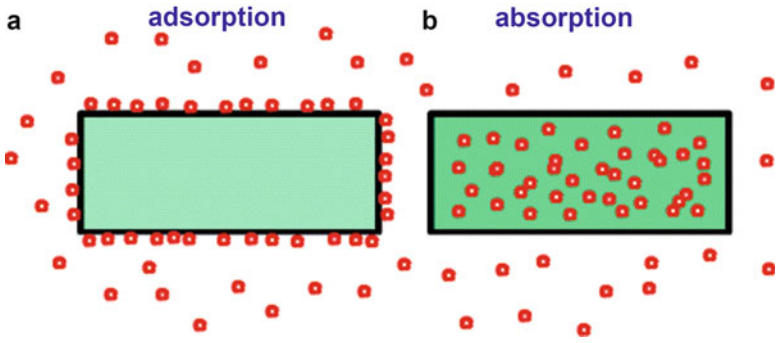

Fig. 5.1 A simplified schematic of adsorption versus absorption.

5.2.3 Langmuir Surface Area and BET Surface Area

Porous materials can be classified by their pore sizes into three categories: macroporous (>500 Å), mesoporous (20–500 Å), and microporous (<20 Å). The microporous materials can be further classified as: ultramicroporous (<7 Å) or supermicroporous (8–20 Å). Most MOFs reported so far are microporous materials, while the development of the mesoporous MOFs bursts out recently.

The Langmuir adsorption model (Fig. 5.2a), in which only a monolayer of gas molecules is allowed to adsorb onto the surface, explains adsorption by assuming the adsorbate behaves like ideal gas under isothermal conditions. In the Langmuir model, the following assumptions are proposed specifically for the simplest situation: the adsorption of a single adsorbate onto a series of equivalent sites on the surface.

1. The surface containing the adsorbing sites is homogeneous, which is a perfectly flat plane with no corrugations.
2. The gas molecule adsorbs into an immobile state.
3. All adsorbing sites are equivalent.
4. Each site can hold at most one molecule (monolayer coverage only).
5. There are no interactions between adsorbates on adjacent sites.

The Brunauer, Emmett, and Teller (BET) theory was developed by Stephen Brunauer, Paul Emmett, and Edward Teller, and they published a paper about the "physical adsorption of gas molecules on a solid surface" in 1938. This BET theory is an extension of the Langmuir theory. The BET model is in which multiple layers of gas may be adsorbed to the surface (Fig. 5.2b). For a given nitrogen isotherm, the BET model will always predict a smaller surface area than the Langmuir model. The BET theory extended the Langmuir theory to incorporate multilayer adsorption, where the:

1. Gas molecules physically adsorb in infinite layers.
2. The layers are noninteracting.
3. The Langmuir model is valid for each independent layer.

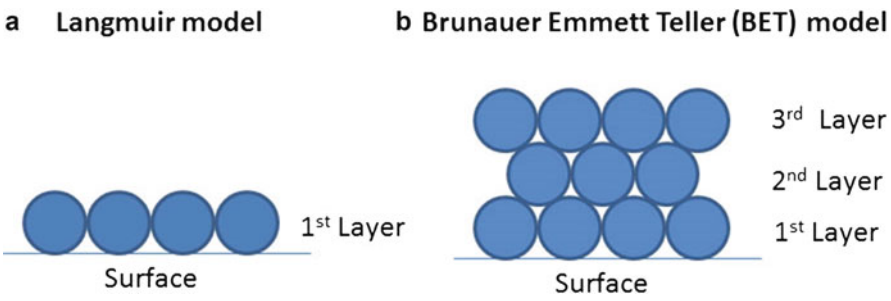

Fig. 5.2 A one-dimensional representation of the process involving adsorption of hydrogen molecule onto a surface, (**a**) Langmuir model monolayer adsorption, or (**b**) Brunauer–Emmett–Teller (BET) multilayer adsorption

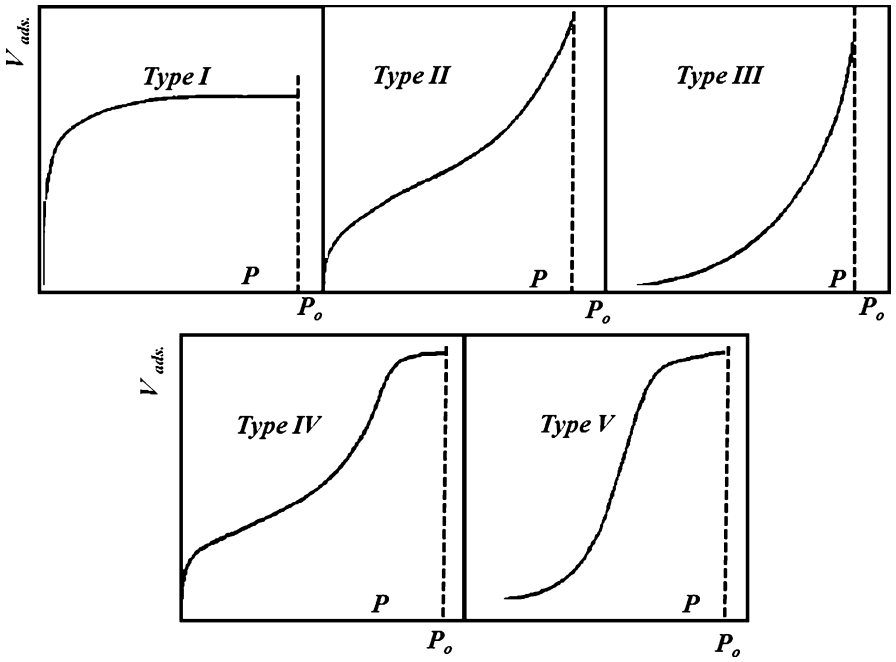

Fig. 5.3 The type I-V isotherm plots the gas volume adsorbed as pressure increases (where P_o stands for saturation pressure) (Reproduced with permission of Ref. [39]. Copyright © 1940 American Chemical Society)

In the analysis of surface coverage, nitrogen gas is commonly used due to its high purity, gas inertness, low cost (compared to helium), and the strong interactions with most solids. Liquid nitrogen temperature (77 K) is usually employed when measuring the nitrogen uptake due to the weak interactions between gaseous and solid phases to achieve detectable amounts of adsorption. The data collected are displayed in the form of an isotherm, which plots the amount of nitrogen adsorbed as a function of the relative pressure. There are five types of adsorption isotherms possible [39].

Type I isotherm: Type I isotherm is a pseudo-Langmuir isotherm (Fig. 5.3). Microporous materials with pore diameters less than 20 Å usually have this type of isotherm. This isotherm depicts monolayer adsorption, which can be readily explained by the Langmuir isotherms.

Type II isotherm: A type II isotherm (Fig. 5.3) has a different profile from that obtained from a single layer Langmuir model. At low pressure (concentration), material micropores are filled with gas molecules, such as nitrogen gas. The plateau region represents the formation of the monolayer. At higher pressure, multilayer adsorption occurs and continues until condensation due to capillary forces occurs.

Type III isotherm: A type III isotherm (Fig. 5.3) shows the formation of a multilayer. Since there is no asymptote observed in the curve, no monolayer is formed, but BET is not applicable.

Type IV isotherm: A type IV isotherm (Fig. 5.3) occurs when capillary condensation occurs. At the lower pressures, it shows the formation of a monolayer followed by a formation of multilayers at higher pressure regions. Mesoporous materials with pore diameters between 20 and 500 Å have this type of isotherm.

Type V isotherm: Type V isotherms (Fig. 5.3) are very similar to type IV isotherms but are not applicable to BET model.

In both Type IV and V isotherms, phenomenon of capillary condensation of gas can be seen.

When using the BET model to calculate the surface area, special care needs to be taken since the calculation results highly depend on the selected pressure region [40]. The Grand Canomical Monte Carlo (GCMC) simulation has been developed to calculate the BET surface area using the nitrogen isotherm, and the results have already been confirmed by comparing with the experimental results [41]. In addition, the difference between the Langmuir surface area and the BET surface area becomes smaller if the MOFs have a larger crystal density. In other words, when the void volume increases, the difference between the Langmuir and BET surface area becomes significant.

5.2.4 Excess and Total Adsorption Amount of Hydrogen

The hydrogen uptake is usually represented as the excess or total adsorption amount. The excess adsorption is the difference between the gas phase hydrogen which would be presented in the equal volume of the adsorbed phase with and without the adsorbent [42]. As we all know, the hydrogen gas density increases as pressure increases. Hence, the excess adsorption would reach saturation at high pressure and then decrease. So we can conclude that at lower pressures, the excess and total adsorption amounts are very close. The total adsorption of hydrogen can be calculated from the excess adsorption isotherm and the total skeletal volume of the adsorbents [43].

The total amount of adsorbed gas can be expressed as follows [44–46].

$$N(\text{total}) = N(\text{excess}) + d(\text{gas}) * V(\text{pore}) \tag{5.1}$$

where N(total) is the total adsorption (mg g^{-1}), N(excess) is the excess adsorption (mg g^{-1}) which is the quantity measured, d(gas) is the compressed gas at a given temperature, and pressure in g cm^{-3} and V_{pore} is the volume of pores.

Generally, hydrogen adsorption capacities in MOFs can also be represented in wt%, which can be expressed as:

$$\text{wt}\% = \frac{\text{mass (hydrogen)}}{\text{mass (sample)} + \text{mass (hydrogen)}} \tag{5.2}$$

5.2.5 Isosteric Heat of the Hydrogen Adsorption

For all the materials, the hydrogen uptake capabilities decrease with the increase of temperature. The strength of this decrease as well as the hydrogen uptake capability at low pressure is mainly governed by the heat of adsorption. Typically, the isosteric heat of hydrogen adsorption can be calculated from the adsorption isotherms measured at two independent temperatures, for example, 77 K (liquid nitrogen temperature) and 87 K (liquid argon temperature), respectively [28, 47–50]. The isosteric heat of hydrogen adsorption is one of the key thermodynamic variables for the design of a practical hydrogen adsorption samples. However, the small temperature range leads to a very high uncertainty when the heat of adsorption is calculated. Only a few publications presented the isosteric heat of adsorption with higher accuracy from several isotherms measured at various temperatures.

5.3 Engineering Novel MOFs for Hydrogen Storage

Metal-organic frameworks (MOFs) have been fabricated using hydrothermal or solvothermal conditions. The hydrothermal synthetic conditions use water as the solvent, while the solvothermal conditions use high boiling point organic solvent, such as *N,N*-dimethylformamide (DMF), *N,N*-diethylformamide (DEF), *N,N*-dimethylacetamide (DMA). Normally, both inorganic metal salts and organic linkers are dissolved in solvents and placed in sealed vials to produce MOFs at high temperature, generally ranging from 60 to 180 °C. Modulating agents, which can balance the association/dissociation of the coordination bonds, are another very important factor in the MOF synthesis, especially for the formation of the crystalline MOFs starting from high valent metal ions. Sometimes, mixed solvents are utilized to control the reaction polarity, the solubility of the starting materials, as well as the rate of the product recrystallization, so that highly crystalline products can be formed. For example, solvents with low boiling point could be added in order to facilitate the product formation during the synthesis. Every MOF is unique and the synthetic conditions usually vary a different MOF materials.

The assembly process of MOFs combines merits of various inorganic metal ions or clusters and designable organic linkers, which offers large structural topologies and diversified porosity properties. For the coordinating atoms in the organic linkers, they can be oxygen, nitrogen, and sometimes mixed coordinated atoms in one linker. For the geometry, the organic linkers can be linear, trigonal, tetragonal, and so on. For the connectivity, the organic linkers can be two connected, three connected, four connected, and sometimes, even six or eight connected. The varieties of the organic linkers provide lots of chances to synthesize novel MOF materials. Starting from the organic linkers, we can classify the MOF materials into three categories: MOFs based on carboxylate linkers, MOFs based on azolate linkers, and MOFs based on mixed linkers. These three categories of MOFs are discussed in the following sections.

5.3.1 MOFs Based on Carboxylate Linkers

Organic carboxylate linkers are the most commonly reported ligands used to synthesize MOFs with exceptional high surface area. Various metal ions, such as Zn, Cu, Mn, Co, Cr, Ni, Al, and lanthanide metals, have been utilized in the synthesis of MOFs. The structures, functionalization, and the hydrogen storage capabilities of several MOFs will be demonstrated in this chapter.

In 2003, the first hydrogen sorption properties using MOF material (Fig. 5.4), MOF-5, were reported by Yaghi's group [20]. MOF-5 are constructed with inorganic four connected Zn clusters and organic linkers, benzene-1,4-dicarboxylate (BDC), [20] with a cubic three-dimensional extended porous structure [43]. Due to the isolated linkers, which are accessible from all sides to the gas molecules, such a structure is ideal for hydrogen storage. An extraordinarily high apparent surface area (about 2000 $m^2\ g^{-1}$ equivalent to the area of a regular football field) was observed due to the scaffolding-like nature of MOF-5. At 77 K and 0.7 bar, 4.5 weight-percent (wt%) hydrogen absorption was observed using MOF-5 as absorbent and later revised maximum hydrogen capacity of 4.5–5.2 wt% at 77 K and 50 bar for MOF-5 [33] that has been confirmed independently [51–53].

The hydrogen uptake varied as a function of pore size and degree of ionic or electrostatic forces through formulation of Zn-MOF-5 variants. Here, the metal center and inorganic linkers were fixed, but the organic ligand varied and the maximum hydrogen uptake increased with surface area. Among them, MOF-177 (Fig. 5.5), which is synthesized with Zn_4 inorganic cluster and 4,4′,4″-benzene-1,3,5-triyl-tribenzoate (BTB) ligand (Fig. 5.5b), has the highest apparent surface area

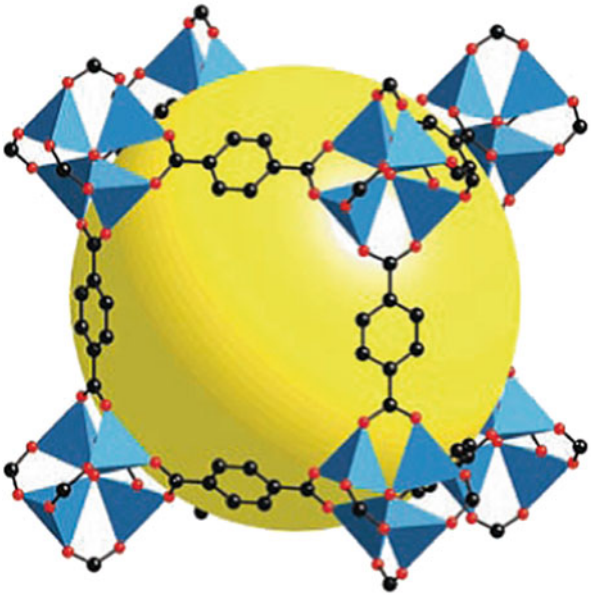

Fig. 5.4 Single-crystal X-ray structure of MOF-5 illustrated for a single cube fragment of their respective cubic three-dimensional extended structure. On each of the corners is a cluster of an oxygen-centered zinc tetrahedron that is bridged by six carboxylates of an organic linker. The *large yellow spheres* represent the largest sphere that would fit in the cavities without touching the van der Waals atoms of the frameworks (Reproduced with permission of Ref. [43]. Copyright © 2007 American Chemical Society)

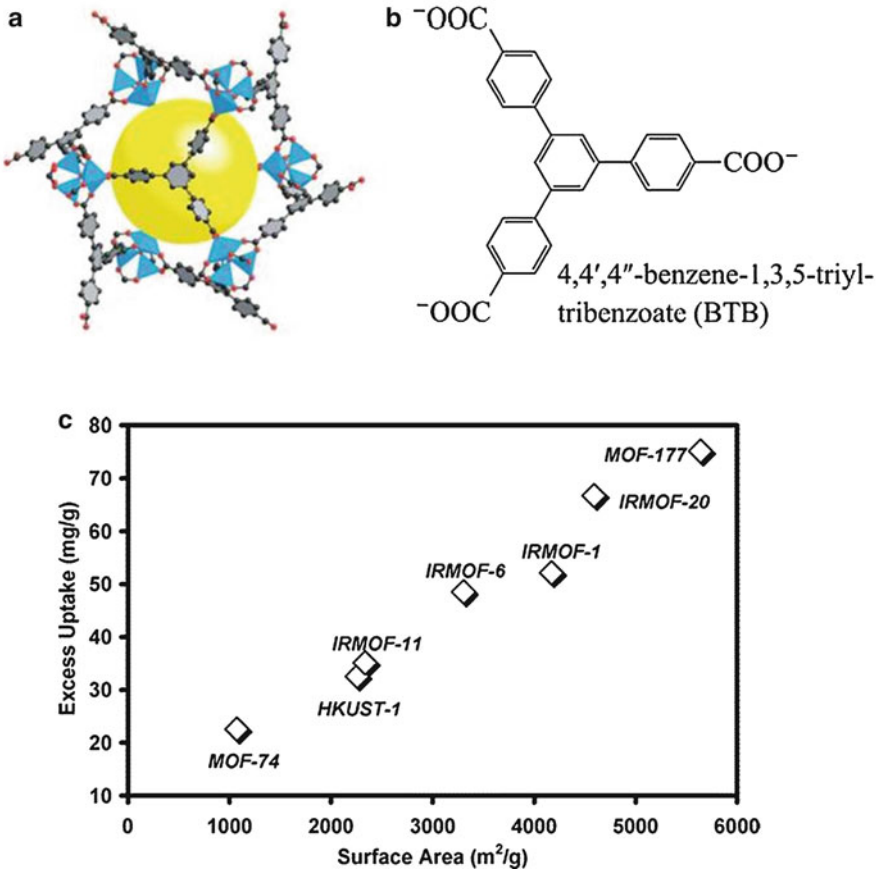

Fig. 5.5 (**a**) Single crystal structure of MOF-177; (**b**) The synthetic ligand for MOF-177, BTB; (**c**) Saturation H_2 uptake plotted against Langmuir surface area (Reproduced with permission of Ref. [51]. Copyright © 2006 American Chemical Society)

of 4746 $m^2\ g^{-1}$. Indeed, its hydrogen uptake is the highest (7.5 wt% at 77 K and 70 bar) [51, 53].

The Sabo group demonstrated the effect of Pd in MOF-5 on hydrogen adsorption [54]. After being incorporated with Pd in MOF-5, the surface area was anticipated to be decreased. However, the hydrogen capacity was found to be 1.86 wt% at 77 K and 1 bar, while the hydrogen adsorption is only 1.15 wt% at 77 K and 1 bar before the Pd impregnation. The enhanced storage capacity can be ascribed to dissociation of hydrogen molecules causing a primary spillover at the Pd catalyst and meantime MOF-5 acting as a secondary spillover receptor. This would increase the isosteric heat of hydrogen adsorption, which improves the hydrogen adsorption capacity.

Hong Kong University of Science and Technology MOF-1 (HKUST-1) is the firstly-reported Cu MOF [55] (Fig. 5.6), which is composed of copper paddlewheel clusters and trigonal benzene-1,3,5-tricarboxylate (BTC) linker. HKUST-1 is a face-

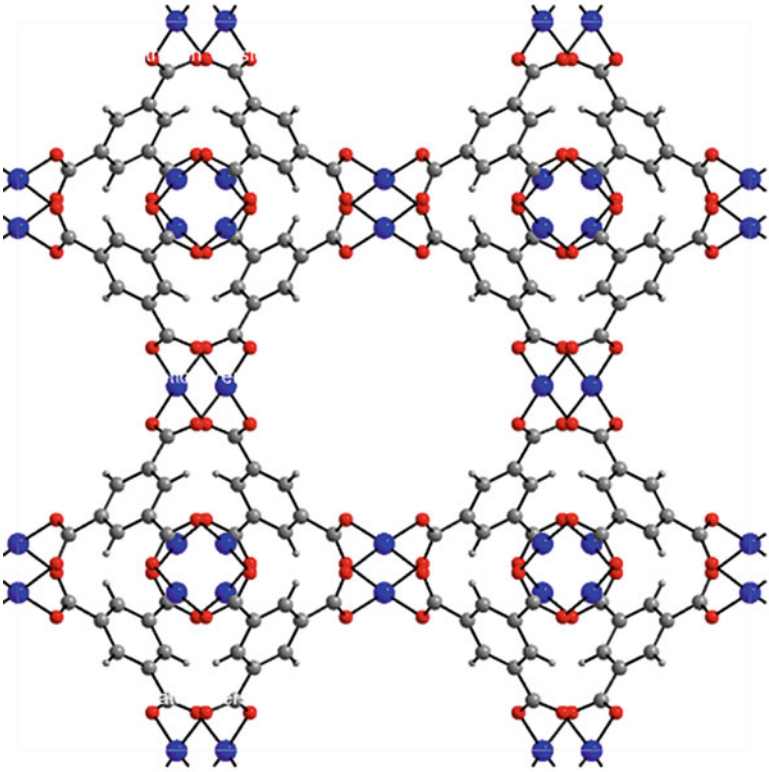

Fig. 5.6 Single crystal X-ray structure of HKUST-1 (copper is denoted as a color in *blue*, oxygen in *red* and carbon in *gray*)

centered cubic crystal with a BET surface area of about 1500 $m^2\ g^{-1}$. The advantage of HKUST-1 compared with MOF-5 is that it has open metal sites, which are occupied with the weakly coordinated solvent molecules. These solvent molecules can be removed, leading to an increase in the local interaction energy of hydrogen molecules. This observation can be confirmed with the isosteric heat ($q_{st,}$ 3.8-5.2 kJ mol^{-1}) of hydrogen adsorption in HKUST-1, which is about 1.0–2.0 kJ mol^{-1} larger compared with that of MOF-5. Accordingly, the hydrogen uptake of HKUST-1 is almost double that of MOF-5 at low pressures [52, 56]. However, at high pressures, MOF-5 has a much higher hydrogen adsorption capacity compared with HKUST-1, which indicates that the hydrogen adsorbed capacity at low pressures strongly depends on the binding affinity of H_2 to the frameworks, while the amount adsorbed at higher pressures is mainly determined by the surface area of the framework [57].

Several Cr- and Al-based MOFs have also been evaluated for the hydrogen adsorption. Material from Institute Lavoisier MOF-53 (MIL-53) is composed of trivalent metal ions (Cr/Al/Sc/Fe) and BDC ligands (Fig. 5.7) [58, 59]. MIL-53 is

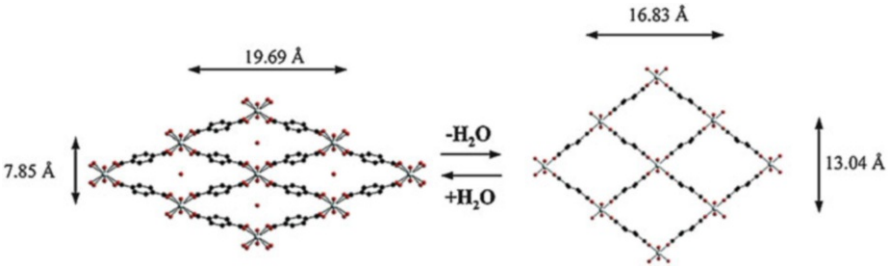

Fig. 5.7 Representation of the structure of MIL-53 showing the breathing effect due to the removal of water molecules: hydrated (*left*) and anhydrous form (*right*). The anhydrous form of MIL-53 was tested for the hydrogen adsorption experiment (Reproduced with permission of Ref. [59]. Copyright © 2002 American Chemical Society)

highly porous and shows both high chemical and high thermal stability. It exhibits one-dimensional channel filled with free disordered solvent molecules. When the free molecules are removed, the pore size of MIL-53(Cr) decreased from 13.04 Å to 7.85 Å, indicating very high breathing effect. It was found that the transition between the hydrated form and the anhydrous solid is fully reversible. The MIL-53(Cr) showed a maximal hydrogen capacity of 3.1 wt% at 77 K and 16 bar, whereas MIL-53(Al) exhibited the capacity of 3.8 wt%.

Furthermore, the hydrogen adsorption using Cr-based MIL-100 and MIL-101 as adsorbents was carefully examined by the Férey group (Fig. 5.8) [26, 60–62]. MIL-100 was composed of trimeric chromium (III) octahedral clusters and the BTC ligand. MIL-100 has two types of cages in its structure: The smaller cage is delimited by twelve pentagonal faces and the larger by sixteen faces, which include twelve pentagonal and four hexagonal faces. The accessible diameters of the two cages are 25 Å and 29 Å, respectively. The MIL-100 had a Langmuir surface area of 2700 $m^2\ g^{-1}$ and a maximum hydrogen uptake of 3.28 wt% at 77 K and 26.5 bar. MIL-101 was built up from the same trimeric chromium (III) octahedral clusters and BDC linkers. MIL-101 also has two types of cages with accessible diameters of 29 Å and 34 Å, respectively. However, additional treatment is required for MIL-101 to remove most of the BDC ligands in the pores [20]. The Langmuir surface area of MIL-101 is 5500 $m^2\ g^{-1}$ and the hydrogen adsorption capacity can reach to 6.1 wt% at 77 K and 80 bar. This higher hydrogen adsorption capacity of MIL-101 could be ascribed to its high adsorption heat (9.3–10.0 kJ mol^{-1} at low coverage), which arose from the strong adsorption affinity between the unsaturated metal sites and hydrogen molecules.

In addition, Zhou group developed a general synthetic method, which is derived from the rationalization of the MOF growth from both a kinetic and a thermodynamic perspective, to synthesize 34 large single crystals of iron-containing MOFs (Fig. 5.9) [63]. Among them, PCN-250 was constructed with 6-connected (Fe_2M) building blocks and a rectangular tetratopic linker. Interestingly, anther framework isomer of PCN-250, PCN-250′ was synthesized under a different synthetic condition. Along one axis, the ligands constructing the same cube in PCN-250 adopt

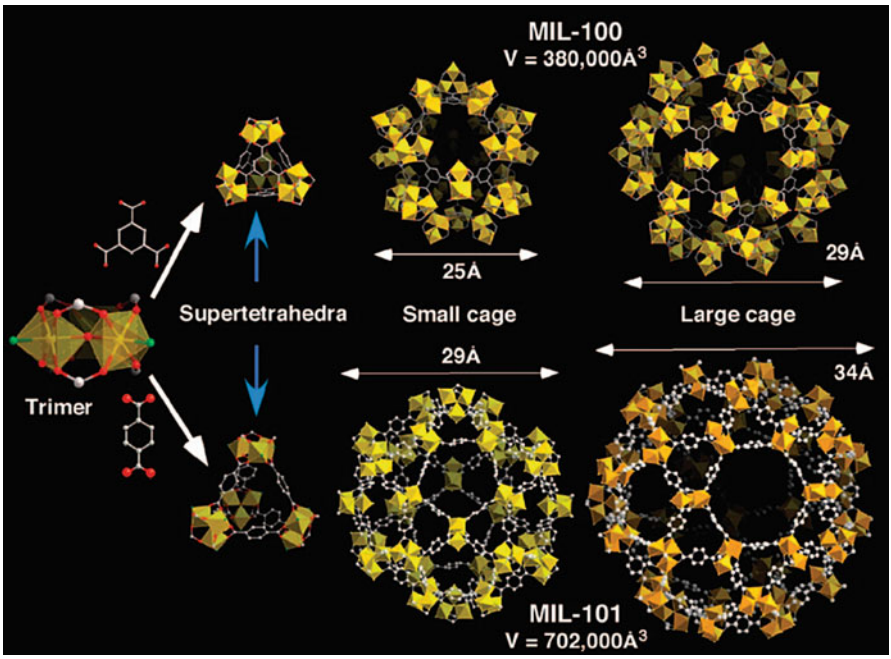

Fig. 5.8 Schematic view of the porous solids MIL-100 and MIL-101. *Left*: Trimers of chromium octahedra which assemble with either BTC (MIL-100) or BDC (MIL-101) to form the hybrid supertetrahedra; *Center*: Hybrid supertetrahedra; *Right*: Cages of MIL-100 and MIL-101 [62] (Reproduced with permission of Ref. [62]. Copyright © 2008 American Chemical Society)

mirror configurations and are alternatively arranged while in PCN-250′, ligands adopt the same configuration in the one cube and mirror configuration in the adjacent cubes along any axis. PCN-250 shows a record high H_2 uptake of 3.07 wt% and 28 g L^{-1} at 1.2 bar and 77 K. Also, PCN-250 exhibits one of the highest total H_2 volumetric uptake of 60 g L^{-1} at 40 bar and 77 K. The high uptakes of H_2 can be attributed to suitable size of the cages in PCN-250 and the well-dispersed and highly charged open metal sites. Moreover, PCN-250 can be maintained stable in water for more than six months.

5.3.2 MOFs Based on Azolate Linkers

All the aforementioned MOFs are using oxygen as the coordinated atom, the coordinated atom can also be nitrogen. Lots of heterocyclic ligands have been successfully used in the synthesis of the porous MOF materials, including imidazole, triazole, pyrazole, and tetrazole.

Among them, zeolitic imidazole frameworks (ZIFs) are a special category of MOFs constructed with organic imidazolate linkers and the tetrahedrally coordinated zinc/cobalt clusters. Various ZIFs have been well documented and they usually have

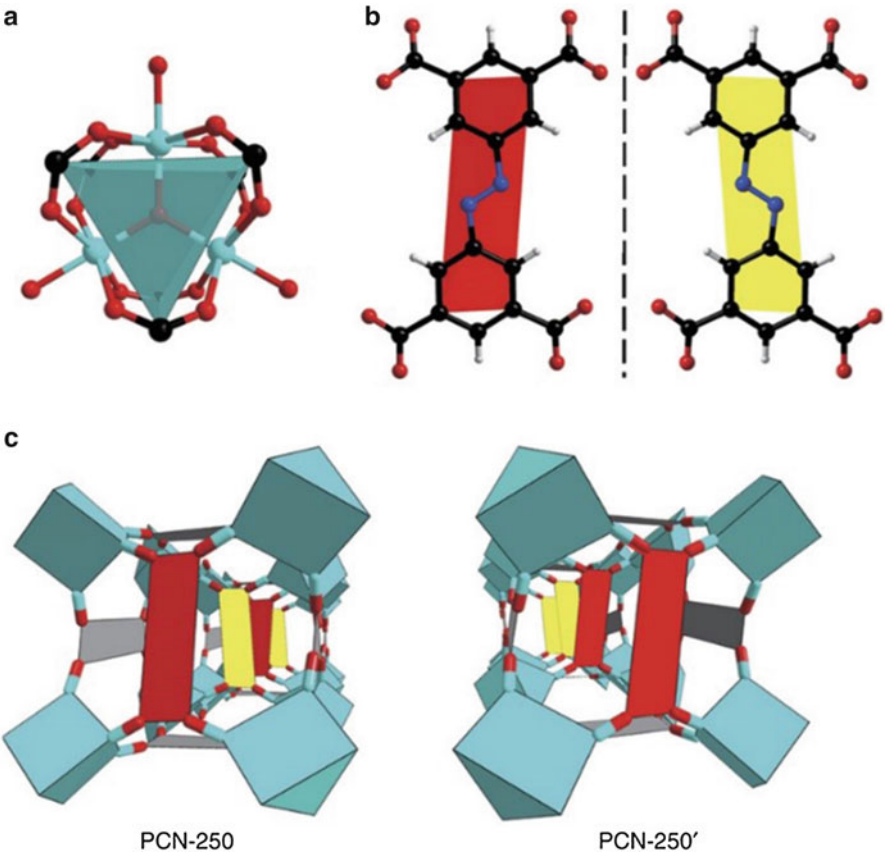

Fig. 5.9 Structures of PCN-250 and PCN-250′ (Reproduced with permission of Ref. [63]. Copyright © 2014 Nature Publishing Group)

exceptional high chemical, thermal, and water stability, which enable great promise for real industrial hydrogen adsorption [21, 64]. For example, ZIF-8 (Fig. 5.10), constructed with six-ring ZnN_4 clusters and MeIM (2-methylimidazolate), is a prototypical ZIF compound with a sodalite zeolite-type structure. The excess hydrogen adsorption capacity of ZIF-8 is 3.1 wt% at 77 K and 30 bar [64–67]. To our surprise, both of the two strongest adsorption sites are associated with organic linkers, instead of metal clusters, which is in strong contrast with carboxylates-based MOFs. This discovery is very important and it will lead to the right direction to optimize this class of ZIF materials for hydrogen adsorption.

Recently, the Long group reported a copper framework, Cu-BTTri starting from the trizaolate linker, 1,3,5-tris(1H-1,2,3-triazol-5-yl)benzene (BTTri, Fig. 5.11) [68]. Cu-BTTri has a sodalite structure, which consists of BTTri linked $[Cu_4Cl]$ square clusters in which each copper center has a terminal solvent molecules directed toward the interior of the large pore. After activation, the framework has exposed

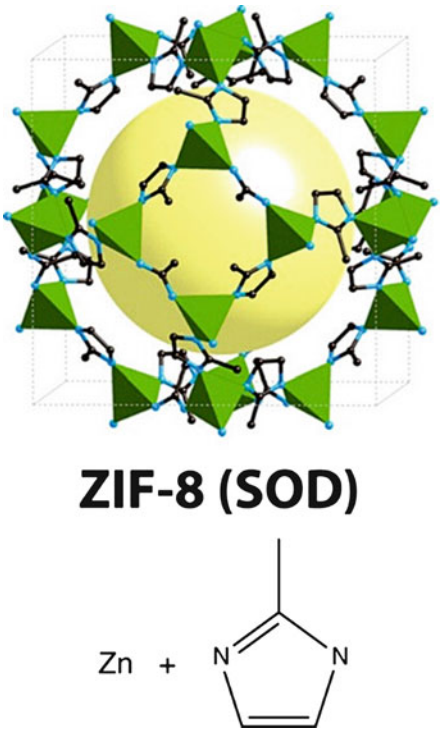

Fig. 5.10 Imidazolate linker, structure, and network topology of ZIF-8. *Yellow sphere* represents the free volume in the frameworks (Reproduced with permission of Ref. [67]. Copyright © 2007 American Chemical Society)

copper metal sites, which can enhance the interactions between the hydrogen molecules and the framework. The BET surface area of CuBTTri is 1770 $m^2\ g^{-1}$ and the H_2 uptake capacity is 1.2 wt% at 1.2 bar and 77 K. Moreover, Cu-BTTri exhibits a really high thermal stability of up to 270 °C and exceptional stability in air, boiling water, and even acidic media.

Long et al. synthesized another new Mn-based MOF by using the tritopic tetrazolate ligand, BTT (1,3,5-benzenetristetrazolate) (Fig. 5.12) [28]. This framework showed a high nitrogen surface area of up to 2100 $m^2\ g^{-1}$. The framework contained coordinately unsaturated Mn sites, which have a strong hydrogen binding. So the isosteric heat of hydrogen adsorption at zero surface coverage is 10.1 kJ mol^{-1}. As a result, the high hydrogen adsorption heat gives rise to the high total hydrogen uptake (6.9 wt% at 77 K and 90 bar). Surprisingly, since the hydrogen adsorption did not reach to the saturation yet at 90 bar, the hydrogen adsorption is anticipated to further increase with pressure.

5.3.3 MOFs Based on Mixed Linkers

Mixed ligand coordination systems have also been taken advantage of to explore their hydrogen storage potential. Although it becomes increasingly difficult to design materials that contain two different metal-binding functionalities, frameworks with

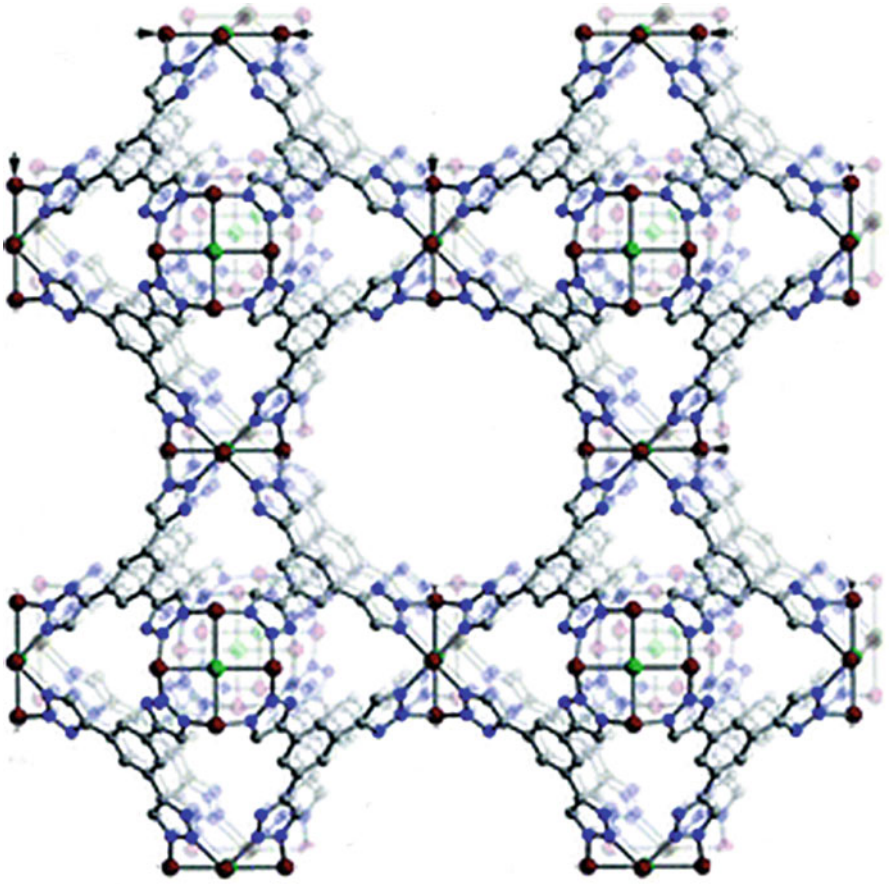

Fig. 5.11 A portion of the structure of the sodalite-type framework of Cu-BTTri. *Purple* is Cu, *green* is Cl, *gray* is C, and *blue* is N, respectively; framework H atoms are omitted for clarity (Reproduced with permission of Ref. [68]. Copyright © 2009 American Chemical Society)

impressive hydrogen storage properties have been demonstrated using this strategy. This is a novel approach for the bottom-up assembly of hierarchical building blocks: simple molecular building blocks (MBBs) and the resultant super molecular building blocks (SBBs) to build highly coordinated nets. Indeed, $Cu(TZI)_3$ was synthesized from the solvothermal reaction between 5-tetrazolylisophthalic acid (H_3TZI) and Cu salt in a DMF/ethanol solution (Fig. 5.13) [69]. H_3TZI possesses two carboxylate groups and a tetrazolate ring. In this structure, the carboxylate groups serve to construct the famous paddlewheel building unit, while the tetrazolate groups to form a triangular cluster. In this triangular cluster, each copper ion exhibits two empty coordination sites, which presumably have a higher affinity with hydrogen

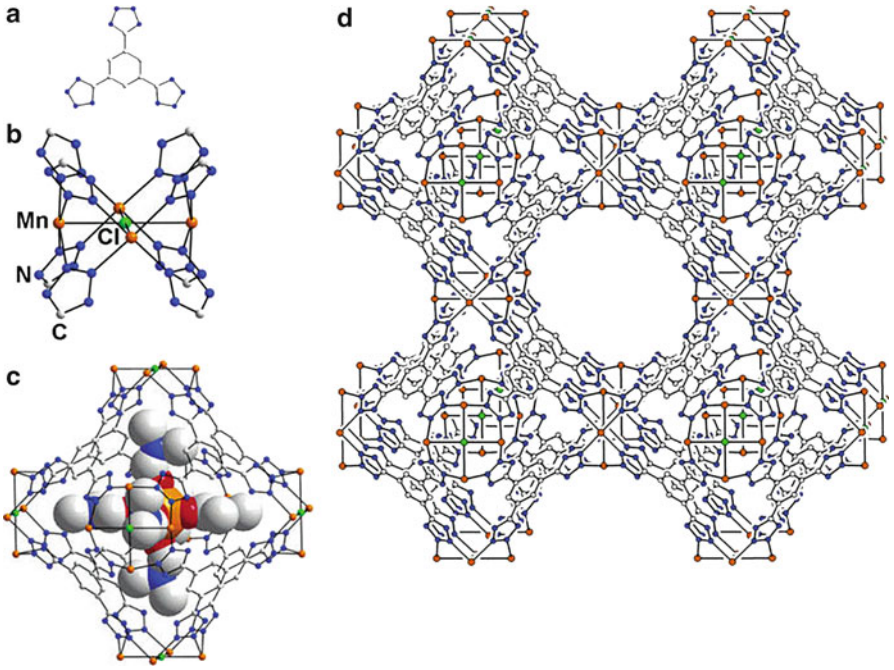

Fig. 5.12 Portions of the crystal structure: (**a**) chemical structure of the ligand H_3BTT, (**b**) a square-planar Mn_4Cl cluster connected by eight tetrazolate linkers, (**c**) a sodalite cage-like unit, and (**d**) a cube of eight such units sharing square Mn_4Cl faces (Reproduced with permission of Ref. [28]. Copyright © 2006 American Chemical Society)

molecules and hence enhance the isosteric heat of adsorption. As expected, the isosteric heat of adsorption is 9.5 kJ mol^{-1} while the H_2 uptake is 2.4 wt% at 1 bar and 77 K. Similar approach may reduce the serendipity associated with this method and could potentially lead to particularly complex, but well-engineered and effective hydrogen storage materials.

5.4 Postsynthetic Modification of MOFs to Improve the Hydrogen Storage Capability

Postsynthetic modification of MOFs is a widely used powerful strategy to change the functional properties of MOF materials, such as the surface area, pore size, and pore volume, and to synthesize novel MOFs, which cannot or hardly be achieved using the direct synthetic method. Moreover, specific functional groups can be incorporated into the frameworks to change their chemical properties or provide strong interaction sites for hydrogen without losing their crystallinity.

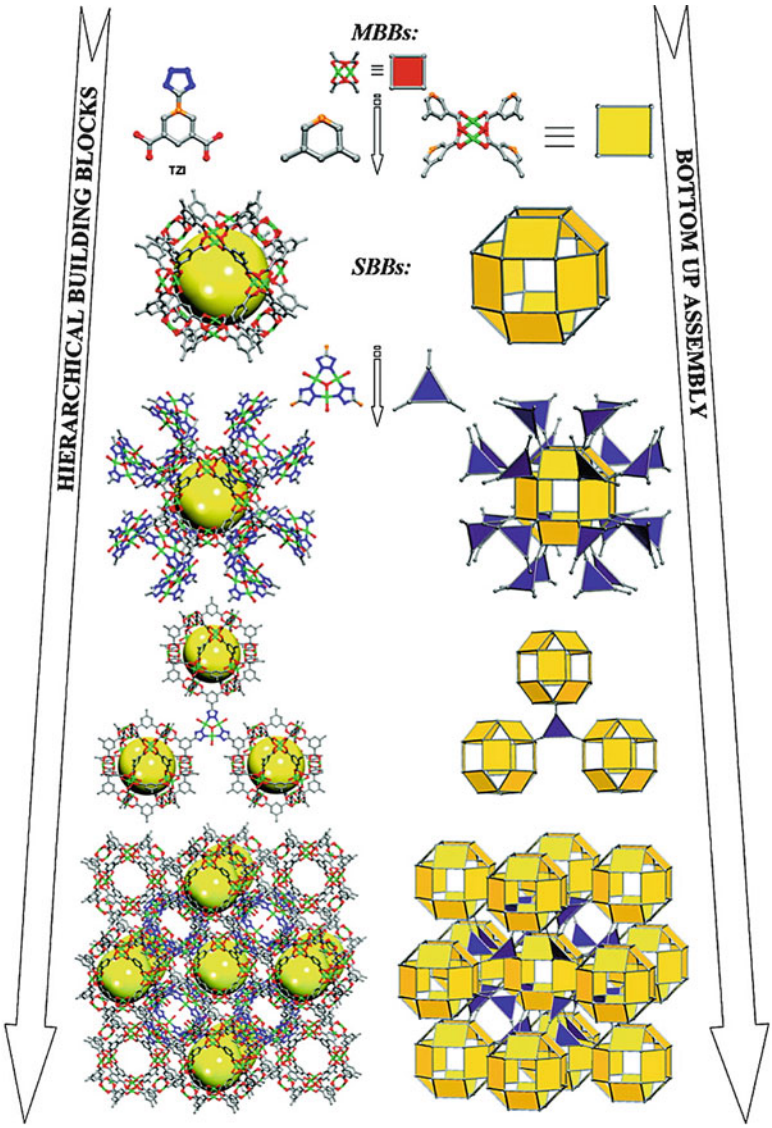

Fig. 5.13 (*Left*) Select fragments from the crystal structure. C = gray, N = blue, O = red, Cu = green; the 5-position of the 1,3-BDC ligand is highlighted in *orange*; the *yellow spheres* indicate the cavity of truncated cuboctahedra; some spheres, all solvent molecules, and all hydrogen atoms have been omitted for clarity. (*Right*) Schematic showing the corresponding strategy from MBBs to SBBs to MOFs (Reproduced with permission of Ref. [69]. Copyright © 2008 American Chemical Society)

5.4.1 Postmodification of the Inorganic Clusters

Modification of the inorganic clusters is less common compared with the post-synthetic modification of the organic linkers. The Zhou group also developed the postsynthetic metathesis and oxidation (PSMO) strategy to synthesize novel MOF materials [70–72]. Starting with the labile Mg-MOFs, they firstly used Fe (II) and Cr (II) to exchange with the Mg cations in the MOFs so that the exchange process is accelerated and the overall structure can be preserved. Then, the intermediate Fe (II)- and Cr (II)- MOFs can be oxidized in the air to form the ultra-water-stable Fe (III)- and Cr (III) MOFs while maintaining the single crystallinity. Significantly, the single crystalline MOFs that contain high valence metals, especially Cr(III), were very rare until this work.

The Férey group reported amine-grafting at open metal sites in MIL-101(Cr) [73]. By replacing coordinated water molecules with ethylene diamine, diethylenetriamine, or 3-aminopropyltrialkoxysilane, the effective BET surface area is anticipated to be reduced. But the powder X-ray diffraction (PXRD) patterns are well indexed with each other, which confirms that the crystallinity before and after postsynthetic modification is well maintained. Then metal complexes, such as $[PdCl_4]^{2-}$, $[PtCl_6]^{2-}$ or $[AuCl_4]^{-}$, were incorporated into the MOF materials. They were reduced to afford nanoparticles around 2–4 nm in size, which could increase the hydrogen storage ability as confirmed by several reports [30, 74].

In another report, Hupp and his co-workers reported that the H_2 storage capacity of MOFs can be increased by the postsynthetic modification of the open metal sites with a pyridine ligand [75]. A careful investigation reveals that the MOFs' internal surface area, pore volume, and ability to absorb molecular hydrogen can be modulated by postsynthetic modification. However, it should be noted that the hydrogen uptake capacity decreases significantly as compared to the frameworks with open metal sites.

Suh and his co-workers demonstrated that the gas adsorption properties can be changed by postsynthetic replace coordinated water molecules with bidendate organic linkers (Fig. 5.14) [76]. Firstly, they synthesized a porous MOF, SNU-30, by the solvothermal reaction, which has open metal sites coordinated by water molecules. Then linker 3,6-di(4-pyridyl)-1,2,4,5-tetrazine (bpta, Fig. 5.14a) was postsynthetically inserted between two paddlewheel-shaped zinc clusters to afford the single crystalline SNU-31SC, which divided the channels into smaller pores, enabling efficient gas movement. Moreover, the inserted bpta linkers can be removed by immersing the SUN-31SC in *N,N*-diethylformamide (DEF), and at the same time, the crystallinity was well maintained upon modification. The BET surface area of SNU-30 measured from the N_2 isotherm was 704 $m^2\ g^{-1}$. At 1 bar and 77 K, the H_2 uptake of SNU-30 reached to 1.42 wt% and the isosteric hydrogen adsorption heat for SNU-30 ranges from 8.12 to 7.27 kJ mol^{-1}. In addition, an excess of hydrogen uptake of SNU-30 reaches to 2.75 wt%, while the total uptake

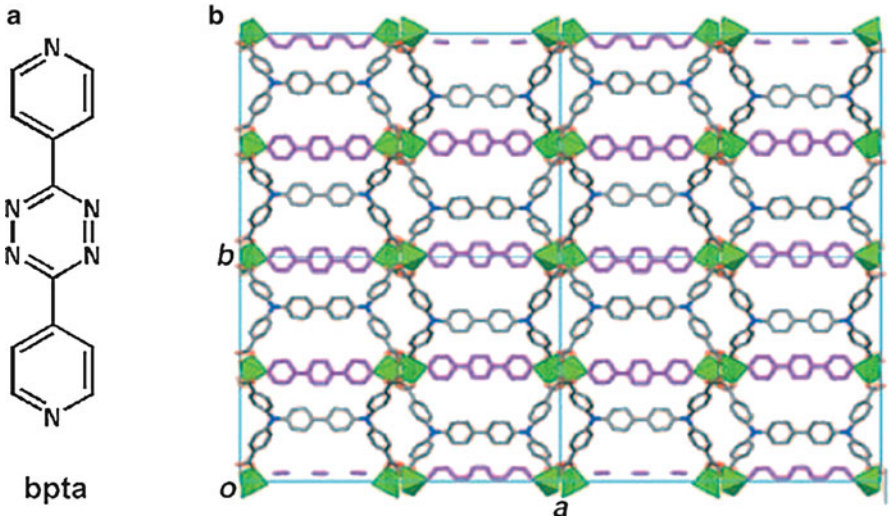

Fig. 5.14 (**a**) The chemical structure of ligand, bpta; (**b**) The X-ray crystal structure of SNU-31 SC. Views seen on the *ab* plane. Color scheme: Zn = green, C = gray, O = red, N = blue, bpta linker = pink (Reproduced with permission of Ref. [76]. Copyright © 2010 WILEY-VCH Verlag GmbH & Co. KGaA, Weinheim)

reaches to 3.27 wt% at 61 bar and 77 K. Interestingly, the postsynthetically modified framework did not adsorb H_2, N_2, O_2, CH_4 but selectively adsorbed CO_2.

5.4.2 Postmodification of the Organic Linkers

The hydrogen uptake capacity of MOFs can also be modulated by postmodification of organic linkers, which have been successfully demonstrated by the Cohen group (Fig. 5.15) by incorporating of phenyl groups into the frameworks [77]. The MOFs connected with NH_2 functionalized ligand, NH_2-MOFs, which include isoreticular metal-organic framework 3 (IRMOF-3), 1,4-diazabicyclo[2.2.2]octane scaffold MOF 1 (DMOF-1), and University of Michigan Crystalline Material-1 (UMCM-1). UMCM-1-NH_2 can react with anhydrides or isocyanates to form amide groups. The pore volume, pore size, and the surface area of the MOFs will be changed by this postsynthetic modification. At the same time, this modification will alter the isosteric heat of the hydrogen adsorption and the hydrogen uptake capacities. The hydrogen storage capacities of IRMOF-3-AMPh (where AMPh is the benzoic anhydride substituent), IRMOF-3-URPh (where URPh is the isocyanate substituent), and UMCM-1-AMPh increased up to 1.73 wt%, 1.54 wt%, and 1.54 wt%, respectively, at 77 K and 1 atm. In comparison, IRMOF-3 and UMCM-1-NH_2 only demonstrated the hydrogen uptake as 1.51 wt% and 1.35 wt%, respectively. Moreover, the isosteric heats of hydrogen adsorption in MOFs having aromatic ring substituents were higher compared with those with alkyl chain substituents. These results suggest that the

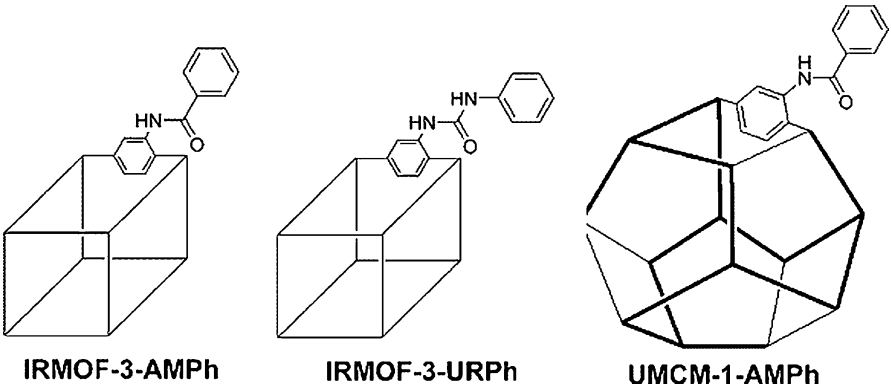

Fig. 5.15 Schematic representation of the three modified MOFs of IRMOF-3-AMPh, IRMOF-3-URPh, and UMCM-1-AMPh (Reproduced with permission of Ref. [77]. Copyright © 2010 WILEY-VCH Verlag GmbH & Co. KGaA, Weinheim)

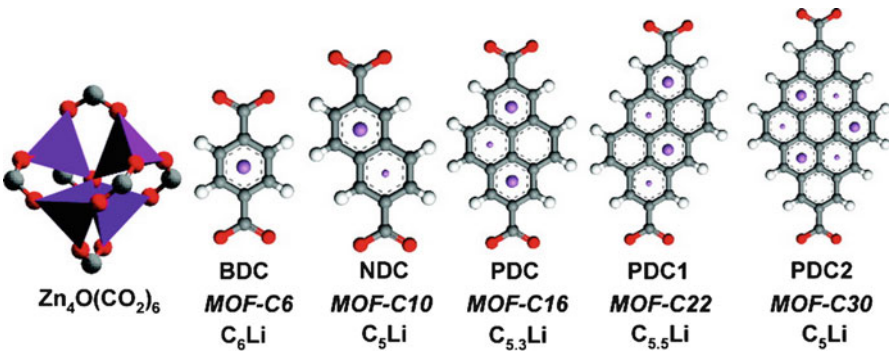

Fig. 5.16 Li-doped MOFs. In each case, the zinc cluster couples to six aromatic linkers through the O-C-O common to each linker. These MOFs are named according to the number of aromatic carbon atoms. The large violet atoms in the linkers represent Li atoms above the linkers while small violet Li atoms lie below the linkers. The C*x*Li ratio considers only aromatic carbon atoms [78] (Reproduced with permission of Ref. [78]. Copyright © 2007 American Chemical Society)

optimal interaction geometry between the MOF and H_2 is that the H_2 molecules are located at the centers of the phenyl rings in the ligand.

Recently, the effect of lithium (Li) on hydrogen adsorption properties of MOFs has already been thoroughly explored by several theoretical research groups, such as the grand canonical ensemble Monte Carlo (GCMC) simulations [78–81]. The GCMC simulations have been validated by the fact that the simulated results by GCMC match very well with the experimental data for the hydrogen storage in MOFs without Li. Then the GCMC technique was utilized to simulate five Li-doped MOFs (Fig. 5.16). Simulation results suggest that the Li atoms are preferred to bind to the center of the aromatic rings with Li atoms on adjacent aromatic rings on the opposite sides, as we can see from Fig. 5.16. More importantly, the high electron

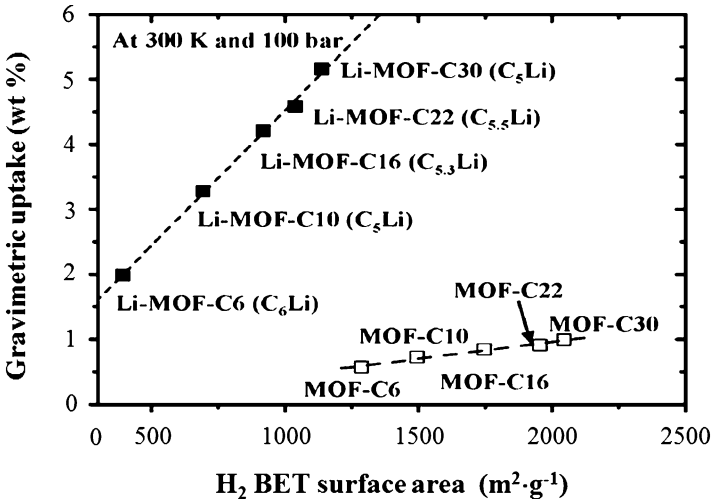

Fig. 5.17 Gravimetric H_2 uptake at 300 K and 100 bar plotted against the H_2 BET surface area for MOF without Li and Li-MOF systems. This demonstrates that both surface area and the ratio of Li to C are important for the higher performance in hydrogen uptake [78] (Reproduced with permission of Ref. [78]. Copyright © 2007, American Chemical Society)

affinity of the aromatic rings can create positive Li sites, leading to a very strong binding affinity between H_2 and MOFs. From their results, the hydrogen uptake of Li-MOF-C30, in which the molar ratio of C/Li is 5, would reach to 3.89 wt% at 20 bar and 300 K and 4.56 wt% at 50 bar and 300 K, which exhibits the highest storage capacity for hydrogen at room temperature to-date. In contrast, the hydrogen uptakes for the MOF-C30 before doping Li were only 0.25 wt% at 300 K and 20 bar and 0.56 wt% at 300 K and 50 bar, respectively. From the results, we can conclude that doping Li on MOFs is a very critical strategy to enhance hydrogen uptake at room temperature [82].

Hydrogen uptake increased with increasing surface area (Fig. 5.17), where the hydrogen BET surface area was determined using hydrogen adsorption isotherms for Li-doped MOF at 300 K compared to the un-doped MOF at 77 K, using rigid rotor model for hydrogen diameter of 0.351 nm. For both MOF systems without Li and Li-doped, there is a linear correspondence of H_2 uptake with the H_2 BET surface area. It was also found that the slope increased with increasing ratio of Li to C. The data confirmed that the Li concentration is the driving force for increasing H_2 uptake capacity at ambient temperature.

The promoting effect of Li on H_2 adsorption on MOFs was confirmed by Mulfort and Hupp groups (Fig. 5.18) [83, 84]. They doped Li on a special Zn MOFs and the hydrogen uptakes before and after the Li doping was found to be 0.93 wt% and 1.63 wt% at 77 K and 1 bar, respectively. After being doped with Li, the Zn-MOF nearly doubled the hydrogen capacity. Notably, the striking increase in H_2 uptake cannot be solely attributed to strong interactions between H_2 and Li. Instead, it is

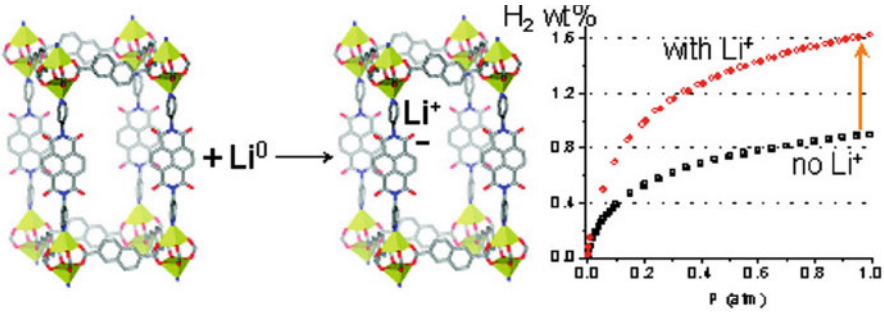

Fig. 5.18 *Left*: The chemically reduction of Zn MOF in the solid state by lithium metal; *Right*: the comparison of the hydrogen uptake before and after the lithium reduction (Reproduced with permission of Ref. [84]. Copyright © 2007 American Chemical Society)

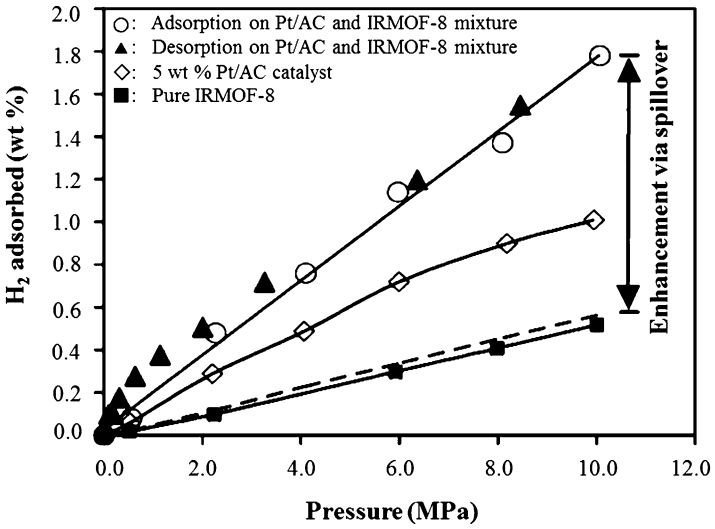

Fig. 5.19 High-pressure hydrogen isotherms at 298 K for pure IRMOF-8 (■), 5 wt% Pt/AC catalyst (◇), a mixture of Pt/AC and IRMOF-8: adsorption (○), desorption (▲) [85] (Reproduced with permission of Ref. [85]. Copyright © 2006 American Chemical Society)

most likely augmented by the increased ligand polarizability and framework displacement effects.

5.4.3 Post Modification of MOFs by Doping Catalysts

Li and Yang groups have successfully demonstrated that the hydrogen uptake capacities in MOFs would greatly increase by doping Pt/AC (activated carbon) catalyst into MOF materials (Fig. 5.19) [85]. For spillover experiments, the active

carbon was the primary receptor for hydrogen spillover and MOFs are the secondary spillover receptor. The hydrogen molecules are adsorbed rapidly on the Pt catalyst and then dissociated into hydrogen atoms. Then the hydrogen atoms would diffuse into the active carbon and then to the MOF surface. The H_2 uptake on pure IRMOF-8 was ~0.5 wt% at 298 K and 100 bar. In a Pt/AC and IRMOF-8 physical mixture (at 1:9 weight ratio), the hydrogen adsorption amount was increased to 1.8 wt% under the same conditions [86]. In addition, if Pt/AC and IR-MOF-8 are well-connected by more carbon bridges, the hydrogen uptake can reach to 4 wt% at 298 K and 100 bar, which is the highest experimental hydrogen uptake capacity reported for MOFs at ambient temperature. And there is no apparent saturation even at 100 bar, suggesting that a further increase in hydrogen uptake capacity can be reached at higher pressures. The isosteric heat of the hydrogen adsorption ranged between 20 and 23 kJ mol^{-1}, which can be ascribed to that the hydrogen atoms have a much stronger binding ability to both the inorganic metal clusters and the organic linkers compared with molecular hydrogen. Similar results were also obtained by using the combination of Pt/AC catalyst with other MOFs, including MOF-5, MOF-177, covalent organic-framework 1 (COF-1), HKUST-1, and MIL-101 [87].

5.5 Summary

MOFs with defined crystalline structures, extremely high surface areas, and very high pore volumes can be regarded as good candidate materials for hydrogen storage. MOFs usually exhibit excellent performance for hydrogen adsorption at very low temperatures, such as 77 K and 87 K. However, it is still a great challenge to store hydrogen at ambient temperature, which can be ascribed to the relatively weak interactions between molecular hydrogen and MOFs. To achieve high H_2 storage capacity in a MOF at ambient temperature, the MOF should possess not only a very high surface area but also a high isosteric heat of H_2 adsorption.

Acknowledgment This work is supported by the Center for Gas Separations Relevant to Clean Energy Technologies, an Energy Frontier Research Center funded by the U.S. Department of Energy (DOE), Office of Science, Office of Basic Energy Sciences under Award Number DE-SC0001015. This work is also supported as part of the Hydrogen and Fuel Cell Program under Award Number DE-EE-0007049.

References

1. L. Schlapbach, A. Zuttel, Hydrogen-storage materials for mobile applications. Nature **414** (6861), 353–358 (2001)
2. M. Fichtner, Nanotechnological aspects in materials for hydrogen storage. Adv. Eng. Mater. **7** (6), 443–455 (2005)
3. S.-i. Orimo, Y. Nakamori, J.R. Eliseo, A. Züttel, C.M. Jensen, Complex hydrides for hydrogen storage. Chem. Rev. **107**(10), 4111–4132 (2007)
4. Y.H. Hu, E. Ruckenstein, High reversible hydrogen capacity of $LiNH_2/Li_3N$ mixtures. Ind. Eng. Chem. Res. **44**(5), 1510–1513 (2005)

5. H.-M. Cheng, Q.-H. Yang, C. Liu, Hydrogen storage in carbon nanotubes. Carbon **39**(10), 1447–1454 (2001)
6. R.H. Baughman, A.A. Zakhidov, W.A. de Heer, Carbon nanotubes – the route toward applications. Science **297**(5582), 787–792 (2002)
7. J. Germain, J.M.J. Fréchet, F. Svec, Nanoporous polymers for hydrogen storage. Small **5**(10), 1098–1111 (2009)
8. L. Zou, D. Feng, T.-F. Liu, Y.-P. Chen, S. Fordham, S. Yuan, J. Tian, H.-C. Zhou, Facile one-pot synthesis of porphyrin based porous polymer networks (PPNs) as biomimetic catalysts. Chem. Commun. **51**(19), 4005–4008 (2015)
9. J. Weitkamp, M. Fritz, S. Ernst, Zeolites as media for hydrogen storage. Int. J. Hydrog. Energy **20**(12), 967–970 (1995)
10. J. Dong, X. Wang, H. Xu, Q. Zhao, J. Li, Hydrogen storage in several microporous zeolites. Int. J. Hydrog. Energy **32**(18), 4998–5004 (2007)
11. H.-C. Zhou, J.R. Long, O.M. Yaghi, Introduction to metal–organic frameworks. Chem. Rev. **112**(2), 673–674 (2012)
12. A. Carne, C. Carbonell, I. Imaz, D. Maspoch, Nanoscale metal-organic materials. Chem. Soc. Rev. **40**(1), 291–305 (2011)
13. A.U. Czaja, N. Trukhan, U. Muller, Industrial applications of metal-organic frameworks. Chem. Soc. Rev. **38**(5), 1284–1293 (2009)
14. T.-F. Liu, D. Feng, Y.-P. Chen, L. Zou, M. Bosch, S. Yuan, Z. Wei, S. Fordham, K. Wang, H.-C. Zhou, Topology-guided design and syntheses of highly stable mesoporous porphyrinic zirconium metal–organic frameworks with high surface area. J. Am. Chem. Soc. **137**(1), 413–419 (2015)
15. D. Liu, T.-F. Liu, Y.-P. Chen, L. Zou, D. Feng, K. Wang, Q. Zhang, S. Yuan, C. Zhong, H.-C. Zhou, A reversible crystallinity-preserving phase transition in metal–organic frameworks: discovery, mechanistic studies, and potential applications. J. Am. Chem. Soc. **137**(24), 7740–7746 (2015)
16. S. Yuan, T.-F. Liu, D. Feng, J. Tian, K. Wang, J. Qin, Q. Zhang, Y.-P. Chen, M. Bosch, L. Zou, S.J. Teat, S.J. Dalgarno, H.-C. Zhou, A single crystalline porphyrinic titanium metal-organic framework. Chem. Sci. **6**(7), 3926–3930 (2015)
17. H.W. Langmi, J. Ren, B. North, M. Mathe, D. Bessarabov, Hydrogen storage in metal-organic frameworks: a review. Electrochim. Acta **128**, 368–392 (2014)
18. L.J. Murray, M. Dinca, J.R. Long, Hydrogen storage in metal-organic frameworks. Chem. Soc. Rev. **38**(5), 1294–1314 (2009)
19. J. Goldsmith, A.G. Wong-Foy, M.J. Cafarella, D.J. Siegel, Theoretical limits of hydrogen storage in metal–organic frameworks: opportunities and trade-offs. Chem. Mater. **25**(16), 3373–3382 (2013)
20. N.L. Rosi, J. Eckert, M. Eddaoudi, D.T. Vodak, J. Kim, M. O'Keeffe, O.M. Yaghi, Hydrogen storage in microporous metal-organic frameworks. Science **300**(5622), 1127–1129 (2003)
21. D. Zhao, D. Yuan, H.-C. Zhou, The current status of hydrogen storage in metal-organic frameworks. Energy Environ. Sci. **1**(2), 222–235 (2008)
22. M.P. Suh, H.J. Park, T.K. Prasad, D.-W. Lim, Hydrogen storage in metal–organic frameworks. Chem. Rev. **112**(2), 782–835 (2012)
23. M. Dincă, J.R. Long, Hydrogen storage in microporous metal–organic frameworks with exposed metal sites. Angew. Chem. Int. Ed. **47**(36), 6766–6779 (2008)
24. S.S. Han, J.L. Mendoza-Cortes, W.A. Goddard Iii, Recent advances on simulation and theory of hydrogen storage in metal-organic frameworks and covalent organic frameworks. Chem. Soc. Rev. **38**(5), 1460–1476 (2009)
25. J. Ren, H.W. Langmi, B.C. North, M. Mathe, Review on processing of metal–organic framework (MOF) materials towards system integration for hydrogen storage. Int. J. Energy Res. **39**(5), 607–620 (2015)
26. M. Latroche, S. Surblé, C. Serre, C. Mellot-Draznieks, P.L. Llewellyn, J.-H. Lee, J.-S. Chang, S.H. Jhung, G. Férey, Hydrogen storage in the giant-pore metal–organic frameworks MIL-100 and MIL-101. Angew. Chem. Int. Ed. **45**(48), 8227–8231 (2006)

27. B. Kesanli, Y. Cui, M.R. Smith, E.W. Bittner, B.C. Bockrath, W. Lin, Highly interpenetrated metal–organic frameworks for hydrogen storage. Angew. Chem. Int. Ed. **44**(1), 72–75 (2005)
28. M. Dincă, A. Dailly, Y. Liu, C.M. Brown, D.A. Neumann, J.R. Long, Hydrogen storage in a microporous metal – organic framework with exposed Mn^{2+} coordination sites. J. Am. Chem. Soc. **128**(51), 16876–16883 (2006)
29. J.L.C. Rowsell, O.M. Yaghi, Strategies for hydrogen storage in metal–organic frameworks. Angew. Chem. Int. Ed. **44**(30), 4670–4679 (2005)
30. Y.E. Cheon, M.P. Suh, Enhanced hydrogen storage by palladium nanoparticles fabricated in a redox-active metal–organic framework. Angew. Chem. Int. Ed. **48**(16), 2899–2903 (2009)
31. O.K. Farha, A. Özgür Yazaydın, I. Eryazici, C.D. Malliakas, B.G. Hauser, M.G. Kanatzidis, S.T. Nguyen, R.Q. Snurr, J.T. Hupp, De novo synthesis of a metal–organic framework material featuring ultrahigh surface area and gas storage capacities. Nat. Chem. **2**(11), 944–948 (2010)
32. L. Pan, M.B. Sander, X. Huang, J. Li, M. Smith, E. Bittner, B. Bockrath, J.K. Johnson, Microporous metal organic materials: promising candidates as sorbents for hydrogen storage. J. Am. Chem. Soc. **126**(5), 1308–1309 (2004)
33. J.L.C. Rowsell, A.R. Millward, K.S. Park, O.M. Yaghi, Hydrogen sorption in functionalized metal – organic frameworks. J. Am. Chem. Soc. **126**(18), 5666–5667 (2004)
34. Y. Liu, J.F. Eubank, A.J. Cairns, J. Eckert, V.C. Kravtsov, R. Luebke, M. Eddaoudi, Assembly of metal–organic frameworks (MOFs) based on indium-trimer building blocks: a porous MOF with soc topology and high hydrogen storage. Angew. Chem. Int. Ed. **46**(18), 3278–3283 (2007)
35. Y.H. Hu, L. Zhang, Hydrogen storage in metal–organic frameworks. Adv. Mater. **22**(20), E117–E130 (2010)
36. J. Sculley, D. Yuan, H.-C. Zhou, The current status of hydrogen storage in metal-organic frameworks-updated. Energy Environ. Sci. **4**(8), 2721–2735 (2011)
37. S. Ma, H.-C. Zhou, Gas storage in porous metal-organic frameworks for clean energy applications. Chem. Commun. **46**(1), 44–53 (2010)
38. D.J. Collins, H.-C. Zhou, Hydrogen storage in metal-organic frameworks. J. Mater. Chem. **17**(30), 3154–3160 (2007)
39. S. Brunauer, L.S. Deming, W.E. Deming, E. Teller, On a theory of the van der Waals adsorption of gases. J. Am. Chem. Soc. **62**(7), 1723–1732 (1940)
40. T. Düren, F. Millange, G. Férey, K.S. Walton, R.Q. Snurr, Calculating geometric surface areas as a characterization tool for metal – organic frameworks. J. Phys. Chem. C **111**(42), 15350–15356 (2007)
41. K.S. Walton, R.Q. Snurr, Applicability of the BET method for determining surface areas of microporous metal – organic frameworks. J. Am. Chem. Soc. **129**(27), 8552–8556 (2007)
42. M.M.K. Salem, P. Braeuer, M.v. Szombathely, M. Heuchel, P. Harting, K. Quitzsch, M. Jaroniec, Thermodynamics of high-pressure adsorption of argon, nitrogen, and methane on microporous adsorbents. Langmuir **14**(12), 3376–3389 (1998)
43. S.S. Kaye, A. Dailly, O.M. Yaghi, J.R. Long, Impact of preparation and handling on the hydrogen storage properties of Zn_4O(1,4-benzenedicarboxylate)$_3$ (MOF-5). J. Am. Chem. Soc. **129**(46), 14176–14177 (2007)
44. H. Furukawa, M.A. Miller, O.M. Yaghi, Independent verification of the saturation hydrogen uptake in MOF-177 and establishment of a benchmark for hydrogen adsorption in metal-organic frameworks. J. Mater. Chem. **17**(30), 3197–3204 (2007)
45. S. Sircar, Gibbsian surface excess for gas adsorption revisited. Ind. Eng. Chem. Res. **38**(10), 3670–3682 (1999)
46. A. Myers, J. Calles, G. Calleja, Comparison of molecular simulation of adsorption with experiment. Adsorption **3**(2), 107–115 (1997)
47. L. Czepirski, J. JagieŁŁo, Virial-type thermal equation of gas – solid adsorption. Chem. Eng. Sci. **44**(4), 797–801 (1989)
48. K.V. Kumar, G. Charalambopoulou, M. Kainourgiakis, A. Gotzias, A. Stubos, T. Steriotis, The required level of isosteric heat for the adsorptive/storage delivery of H_2 in the UiO series of MOFs. RSC Adv. **4**(85), 44848–44851 (2014)

49. Y.-S. Bae, R.Q. Snurr, Optimal isosteric heat of adsorption for hydrogen storage and delivery using metal–organic frameworks. Microporous Mesoporous Mater. **132**(1–2), 300–303 (2010)
50. B. Schmitz, U. Müller, N. Trukhan, M. Schubert, G. Férey, M. Hirscher, Heat of adsorption for hydrogen in microporous high-surface-area materials. ChemPhysChem **9**(15), 2181–2184 (2008)
51. A.G. Wong-Foy, A.J. Matzger, O.M. Yaghi, Exceptional H_2 saturation uptake in microporous metal – organic frameworks. J. Am. Chem. Soc. **128**(11), 3494–3495 (2006)
52. B. Panella, M. Hirscher, H. Pütter, U. Müller, Hydrogen adsorption in metal–organic frameworks: Cu-MOFs and Zn-MOFs compared. Adv. Funct. Mater. **16**(4), 520–524 (2006)
53. A. Dailly, J.J. Vajo, C.C. Ahn, Saturation of hydrogen sorption in Zn benzenedicarboxylate and Zn naphthalenedicarboxylate. J. Phys. Chem. B **110**(3), 1099–1101 (2006)
54. M. Sabo, A. Henschel, H. Frode, E. Klemm, S. Kaskel, Solution infiltration of palladium into MOF-5: synthesis, physisorption and catalytic properties. J. Mater. Chem. **17**(36), 3827–3832 (2007)
55. S.S.-Y. Chui, S.M.-F. Lo, J.P.H. Charmant, A.G. Orpen, I.D. Williams, A chemically functionalizable nanoporous material $[Cu_3(TMA)_2(H_2O)_3]_n$. Science **283**(5405), 1148–1150 (1999)
56. S.R. Batten, R. Robson, Interpenetrating nets: ordered, periodic entanglement. Angew. Chem. Int. Ed. **37**(11), 1460–1494 (1998)
57. H. Frost, T. Düren, R.Q. Snurr, Effects of surface area, free volume, and heat of adsorption on hydrogen uptake in metal – organic frameworks. J. Phys. Chem. B **110**(19), 9565–9570 (2006)
58. G. Ferey, M. Latroche, C. Serre, F. Millange, T. Loiseau, A. Percheron-Guegan, Hydrogen adsorption in the nanoporous metal-benzenedicarboxylate $M(OH)(O_2C\text{-}C_6H_4\text{-}CO_2)$ ($M = Al^{3+}$, Cr^{3+}), MIL-53. Chem. Commun. **24**, 2976–2977 (2003)
59. C. Serre, F. Millange, C. Thouvenot, M. Noguès, G. Marsolier, D. Louër, G. Férey, Very large breathing effect in the first nanoporous chromium(III)-based solids: MIL-53 or CrIII(OH)·$\{O_2C–C_6H_4–CO_2\}$·$\{HO_2C–C_6H_4–CO_2H\}_x$·H_2O_y. J. Am. Chem. Soc. **124**(45), 13519–13526 (2002)
60. G. Férey, C. Mellot-Draznieks, C. Serre, F. Millange, J. Dutour, S. Surblé, I. Margiolaki, A chromium terephthalate-based solid with unusually large pore volumes and surface area. Science **309**(5743), 2040–2042 (2005)
61. G. Férey, C. Serre, C. Mellot-Draznieks, F. Millange, S. Surblé, J. Dutour, I. Margiolaki, A hybrid solid with giant pores prepared by a combination of targeted chemistry, simulation, and powder diffraction. Angew. Chem. Int. Ed. **43**(46), 6296–6301 (2004)
62. P.L. Llewellyn, S. Bourrelly, C. Serre, A. Vimont, M. Daturi, L. Hamon, G. De Weireld, J.-S. Chang, D.-Y. Hong, Y. Kyu Hwang, S. Hwa Jhung, G. Férey, High uptakes of CO_2 and CH_4 in mesoporous metal – organic frameworks MIL-100 and MIL-101. Langmuir **24**(14), 7245–7250 (2008)
63. D. Feng, K. Wang, Z. Wei, Y.-P. Chen, C.M. Simon, R.K. Arvapally, R.L. Martin, M. Bosch, T.-F. Liu, S. Fordham, D. Yuan, M.A. Omary, M. Haranczyk, B. Smit, H.-C. Zhou, Kinetically tuned dimensional augmentation as a versatile synthetic route towards robust metal–organic frameworks. Nat. Commun. **5**, 5723 (2014)
64. A. Phan, C.J. Doonan, F.J. Uribe-Romo, C.B. Knobler, M. O'Keeffe, O.M. Yaghi, Synthesis, structure, and carbon dioxide capture properties of zeolitic imidazolate frameworks. Acc. Chem. Res. **43**(1), 58–67 (2010)
65. H. Wu, W. Zhou, T. Yildirim, Hydrogen storage in a prototypical zeolitic imidazolate framework-8. J. Am. Chem. Soc. **129**(17), 5314–5315 (2007)
66. K.S. Park, Z. Ni, A.P. Côté, J.Y. Choi, R. Huang, F.J. Uribe-Romo, H.K. Chae, M. O'Keeffe, O.M. Yaghi, Exceptional chemical and thermal stability of zeolitic imidazolate frameworks. Proc. Natl. Acad. Sci. **103**(27), 10186–10191 (2006)
67. A.U. Ortiz, A. Boutin, A.H. Fuchs, F.-X. Coudert, Investigating the pressure-induced amorphization of zeolitic imidazolate framework ZIF-8: mechanical instability due to shear mode softening. J. Phys. Chem. Lett. **4**(11), 1861–1865 (2013)
68. A. Demessence, D.M. D'Alessandro, M.L. Foo, J.R. Long, Strong CO_2 binding in a water-stable, triazolate-bridged metal – organic framework functionalized with ethylenediamine. J. Am. Chem. Soc. **131**(25), 8784–8786 (2009)

69. F. Nouar, J.F. Eubank, T. Bousquet, L. Wojtas, M.J. Zaworotko, M. Eddaoudi, Supermolecular Building Blocks (SBBs) for the design and synthesis of highly porous metal-organic frameworks. J. Am. Chem. Soc. **130**(6), 1833–1835 (2008)
70. T.-F. Liu, L. Zou, D. Feng, Y.-P. Chen, S. Fordham, X. Wang, Y. Liu, H.-C. Zhou, Stepwise synthesis of robust metal–organic frameworks via postsynthetic metathesis and oxidation of metal nodes in a single-crystal to single-crystal transformation. J. Am. Chem. Soc. **136**(22), 7813–7816 (2014)
71. L. Zou, D. Feng, T.-F. Liu, Y.-P. Chen, S. Yuan, K. Wang, X. Wang, S. Fordham, H.-C. Zhou, A versatile synthetic route for the preparation of titanium metal-organic frameworks. Chem. Sci. **7**(2), 1063–1069 (2016)
72. X. Lian, D. Feng, Y.-P. Chen, T.-F. Liu, X. Wang, H.-C. Zhou, The preparation of an ultrastable mesoporous Cr(iii)-MOF via reductive labilization. Chem. Sci. **6**(12), 7044–7048 (2015)
73. Y.K. Hwang, D.-Y. Hong, J.-S. Chang, S.H. Jhung, Y.-K. Seo, J. Kim, A. Vimont, M. Daturi, C. Serre, G. Férey, Amine grafting on coordinatively unsaturated metal centers of MOFs: consequences for catalysis and metal encapsulation. Angew. Chem. Int. Ed. **47**(22), 4144–4148 (2008)
74. M. Meilikhov, K. Yusenko, D. Esken, S. Turner, G. Van Tendeloo, R.A. Fischer, Metals@MOFs – loading MOFs with metal nanoparticles for hybrid functions. Eur. J. Inorg. Chem. **2010**(24), 3701–3714 (2010)
75. O.K. Farha, K.L. Mulfort, J.T. Hupp, An example of node-based postassembly elaboration of a hydrogen-sorbing, metal – organic framework material. Inorg. Chem. **47**(22), 10223–10225 (2008)
76. H.J. Park, Y.E. Cheon, M.P. Suh, Post-synthetic reversible incorporation of organic linkers into porous metal–organic frameworks through single-crystal-to-single-crystal transformations and modification of gas-sorption properties. Chem. Eur. J. **16**(38), 11662–11669 (2010)
77. Z. Wang, K.K. Tanabe, S.M. Cohen, Tuning hydrogen sorption properties of metal–organic frameworks by postsynthetic covalent modification. Chem. Eur. J. **16**(1), 212–217 (2010)
78. S.S. Han, W.A. Goddard, Lithium-doped metal-organic frameworks for reversible H2 storage at ambient temperature. J. Am. Chem. Soc. **129**(27), 8422–8423 (2007)
79. A. Mavrandonakis, E. Tylianakis, A.K. Stubos, G.E. Froudakis, Why Li doping in MOFs enhances H_2 storage capacity? A multi-scale theoretical study. J. Phys. Chem. C **112**(18), 7290–7294 (2008)
80. G. Férey, F. Millange, M. Morcrette, C. Serre, M.-L. Doublet, J.-M. Grenèche, J.-M. Tarascon, Mixed-valence Li/Fe-based metal–organic frameworks with both reversible redox and sorption properties. Angew. Chem. Int. Ed. **46**(18), 3259–3263 (2007)
81. Y. Zhang, L.G. Scanlon, M.A. Rottmayer, P.B. Balbuena, Computational investigation of adsorption of molecular hydrogen on lithium-doped corannulene. J. Phys. Chem. B **110**(45), 22532–22541 (2006)
82. A. Blomqvist, C.M. Araújo, P. Srepusharawoot, R. Ahuja, Li-decorated metal–organic framework 5: a route to achieving a suitable hydrogen storage medium. Proc. Natl. Acad. Sci. **104**(51), 20173–20176 (2007)
83. K.L. Mulfort, J.T. Hupp, Alkali metal cation effects on hydrogen uptake and binding in metal-organic frameworks. Inorg. Chem. **47**(18), 7936–7938 (2008)
84. K.L. Mulfort, J.T. Hupp, Chemical reduction of metal – organic framework materials as a method to enhance gas uptake and binding. J. Am. Chem. Soc. **129**(31), 9604–9605 (2007)
85. Y. Li, R.T. Yang, Significantly enhanced hydrogen storage in metal – organic frameworks via spillover. J. Am. Chem. Soc. **128**(3), 726–727 (2006)
86. Y. Li, R.T. Yang, Hydrogen storage in metal – organic frameworks by bridged hydrogen spillover. J. Am. Chem. Soc. **128**(25), 8136–8137 (2006)
87. Y. Li, R.T. Yang, Gas adsorption and storage in metal – organic framework MOF-177. Langmuir **23**(26), 12937–12944 (2007)

Porous Carbons for Hydrogen Storage

6

Mathieu Bosch and Hong-Cai Zhou

Abstract

Porous carbon-based materials are promising candidates as adsorbents to increase the gravimetric and volumetric uptake of hydrogen at cryogenic temperatures and moderate pressures. In most cases, this uptake increases linearly with surface area, but strategies to increase uptake beyond that predicted by this "chahine rule," to increase surface area, and to otherwise improve these materials are discussed.

Acronyms

AC	Activated carbon
BDC	1,4-benzene dicarboxylic acid, or Terephthalic Acid
BET	Brunauer–Emmett–Teller
BTC	1,3,5-benzenetricarboxylate
CDC	Carbide-derived carbon
CNT	Carbon nanotubes
COD	bis(1,5-cycloocatdiene)
COP	Covalent organic polymer

Author Contribution: This chapter was written by Mathieu Bosch and rewritten and revised by H.-C. Zhou.

M. Bosch
Department of Chemistry, Texas A&M University, College Station, USA
e-mail: mathieu.bosch@chem.tamu.edu

H.-C. Zhou (✉)
Center for Electrochemical Systems and Hydrogen Research, Texas A&M University, College Station, USA

Department of Chemistry, Texas A&M University, College Station, USA

Department of Materials Science and Engineering, Texas A&M University, College Station, USA
e-mail: zhou@chem.tamu.edu

Y.-P. Chen et al. (eds.), *Nanostructured Materials for Next-Generation Energy Storage and Conversion*, DOI 10.1007/978-3-662-53514-1_6

CVD	Chemical vapor deposition
DBA	Benzene-1,3-diboronic acid
DMF	Dimethylformamide
FESEM	Field-emission scanning electron microscopy
GO	Graphene oxide
GOF	Graphene oxide framework
HCPM	Hierarchically porous carbon monolith
HMS	Hexagonal mesoporous silica
IRMOF	Isoreticular metal-organic framework
K	Kelvin
LC	Liquid crystalline or liquid crystal
MDC	MOF-derived carbons
MOF	Metal-organic framework
MS	Mesoporous silica
MWCNT	Multiwalled carbon nanotubes
nm	Nanometer
NPC	Nanoporous carbon
NPC	Nanoporous carbon
PAF	Porous aromatic framework
PIM	Polymer of intrinsic microporosity
PPN	Porous polymer network
PXRD	Powder X-ray diffraction
SCXRD	Single-crystal X-ray diffraction
SSA	Specific surface area
SWCNT	Single-walled carbon nanotubes
TEM	Transmission electron microscopy
wt%	Weight percent
XRD	X-ray diffraction
ZTC	Zeolite templated carbon

Contents

6.1 Introduction

In this chapter, we will summarize recent progress in the storage of hydrogen gas in porous carbon-based materials through physical or chemical interactions. The class of materials is diverse and consists of porous polymer networks (PPNs), porous organic polymers (POPs), graphene oxide frameworks (GOFs), activated carbons (ACs), metal-organic framework (MOF), derived carbons (MDCs), and other carbon nanomaterials. Recent advancements in preparation of these porous materials with ultrahigh surface areas make them viable candidates for hydrogen storage, especially at low temperatures ($T < 123$ K; $P > 25$ bar) where the weak intermolecular forces inherent to all physisorption phenomena, such as adsorption of hydrogen, can dominate. This approach to hydrogen storage promises high gravimetric hydrogen uptake, distinct to cryogenic storage approach ($\leq$123 K), which require cooling with nitrogen (77 K) or argon (87 K) and a resultant insulation capsule. Room temperature ($\geq$123 K) interactions occur because the adsorption forces of the hydrogen to the pockets, surfaces, and functional groups are carefully chosen to maximize intermolecular forces between the hydrogen molecules and material. Thus, it is essential to maximize the adsorption enthalpy of any porous material for hydrogen storage, because for the use of these materials to be economical requires cooling temperature close to room temperature to avoid additional costs in materials and weight. For this reason, special consideration will be given in this overview to attempt to increase the adsorption enthalpy of hydrogen in engineered porous materials at higher than cryogenic temperatures.

These materials are engineered to meet the current US Department of Energy (DOE) 2020 performance targets for hydrogen storage materials, namely, materials that can store 5.5 weight-percent (wt%) of hydrogen for the gravimetric target, 0.040 kg hydrogen/L for the volumetric target, and at $333/kg stored hydrogen capacity for the cost target. It should be noted that this target is for the complete storage system "including the tank, storage media, safety system, valves, regulators, piping, mounting brackets, insulation, added cooling capacity, and any other balance-of-plant components," not just the porous material, so the material must have a significantly higher capacity. This DOE benchmark essentially excludes all organic synthesis requiring many steps or resulting in low yields, or use of anything other than low-cost bulk commodities. This is where porous polymers may have an advantage over materials such as metal-organic frameworks (MOFs) or metal-hydride based materials that require expensive components, whereas carbon-based polymers can potentially be synthesized at a much lower cost, depending on the synthesis steps chosen, once the methodology has been perfected.

6.2 Adsorptive Hydrogen Storage

6.2.1 The Chahine Rule

Most of these materials have a total hydrogen storage capacity that linearly scales to their surface area, based on the physisorption interactions. Experimentally, it was found that most materials with optimum pore size of 7 Å stored about 2 wt% H_2 per

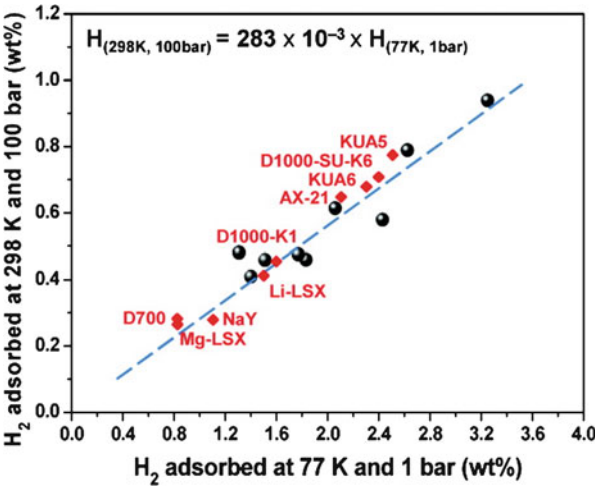

Fig. 6.1 A linear relationship between hydrogen uptake at 77 K, 1 bar, and 298 K, 100 bars [3] (Reprinted with permission from Ref. [3]. Copyright 2012 American Chemical Society)

gram of material per 1000 m^2/g surface area at 77 K. At higher temperature, this storage dropped to 0.35 wt% per 1000 m^2/g surface area at 120 bar pressure at 298 K, which was not greatly influenced by an increase in pressure, for example, almost trebling the pressure, gave a new storage value of 0.45 wt% per 1000 m^2/g surface area at 300 bar hydrogen pressure. This phenomenon is known as the "Chahine rule" [1]. It should be noted that this rule is only applied to materials that have pores appropriate to the size of hydrogen in the low Ångström range (Å). Porous materials with large open pores (≥10 Å) and a high surface area (≥6000 m^2/g) as measured by nitrogen (N_2) adsorption (77 K) may not have as high H_2 uptake as calculated, as H_2 may not condense into these pores as easily as N_2. Current porosity materials areas in the range of 4000–7000 m^2/g surface area [2], less than what is required to meet the 2020 DOE targets using physisorption at room temperature alone using porous materials. Most research focuses on materials with high hydrogen gas (H_2) uptake at 77 K. As some of these materials reach hydrogen sorption saturation or near saturation at 77 K at high pressure, while none reach saturation at (293 K) room temperature. Therefore, an intermediate temperature may be suited to sorption, higher than cryogenic temperatures but lower than room temperature.

In general, hydrogen uptake at 77 K and 1 bar (100,000 Pa ≈ 750.06 Torr or mmHg) was found to be linearly related to the hydrogen uptake at 298 K and 100 bars in porous adsorbents (Fig. 6.1 for plot of adsorption versus temperature) with uptake occurring mostly in extremely small micropores, under either (77 K or 298 K) set of conditions [3]. This occurred across many different types of adsorbents, as long as those adsorbents were primarily microporous in morphology. In contrast, the adsorbents with larger pores had relatively high uptakes at 77 K, but showed small uptakes, below 0.5 wt% at 298 K and 100 bars pressure. Clearly, hydrogen is able to be adsorbed into larger pores but only at low temperature. However, the porous materials with the highest overall surface area also have relatively larger pores and are not suitable for hydrogen adsorption at higher

temperatures. To improve hydrogen adsorption at higher temperatures, materials must be designed with maximum pore volume and surface area, but also pore size optimized to hydrogen uptake at the temperature and pressure allowed. A material with optimal hydrogen uptake at 77 K and 1 bar is not likely to be the best material at 77 K at 100 bars or 298 K and 100 bars of pressure. Under the conditions in Fig. 6.1, only pores below 1 nm diameter contribute significantly to hydrogen uptake, unlike at 77 K and 100 bars where hydrogen can adsorb efficiently into larger pores [3].

6.2.2 Deliverable (or Working) Capacity

Deliverable capacity is the difference in hydrogen uptake between a low- and high-pressure (e.g., 1–100 bars) environment and is more important than total capacity for most hydrogen storage applications. Depending on the material used, some amount of hydrogen will remain in the material at a low pressure – and unless the material is re-activated by heat, vacuum, or some other input of energy to remove it – which cannot be used as a fuel source. In this manner, the deliverable capacity is less than total capacity and is a more practical consideration. An analysis of isotherms at different pressure levels can yield information on adsorption capacity, but materials with high total uptake at very low pressure may not yield a practical deliverable capacity.

6.2.3 BET Surface Area

The Brunauer–Emmett–Teller (BET) method can overestimate the surface area of highly microporous materials, due to quasi-capillary condensation occurring at a P/P_0 range of 0.1–0.3 (where P and P_0 are the equilibrium and the saturation pressure of adsorbates at the temperature of adsorption) although analysis applied below this region is expected to give valid results [4]. This is of critical importance for hydrogen sorbents, which often have very small pore sizes. At a temperature below the critical temperature, many molecular species may condense into a liquid form inside the pores. This phenomenon occurs normally in type II and type IV of the pressure-temperature isotherms. But in materials with microporous pockets that have very high affinity for N_2, adsorption occurs at a very low pressure, lower than the isotherm calibration, giving rise to a higher standard error.

The BET calculations can further overestimate the surface area of materials that have pores 1 nm or larger, “due to the overlap of pore-filling and formation of monolayer- consisting of these two types of pores.” [5] The BET surface area calculations attempt to estimate the monolayer loading, where low-pressure pore-filling nitrogen adsorption is “counted” as monolayer-formation adsorption and used to determine the surface area. For example, for graphene-slit pores, a diameter of 13.2 Å drastically overestimates surface area due to inclusion of second-layer molecules in the monolayer regime (see Fig. 6.2 for conceptual model of hydrogen adsorption) where H_2 uptakes are also susceptible to experimental error if appropriate control and checks in the experimental setup are not properly implemented [6].

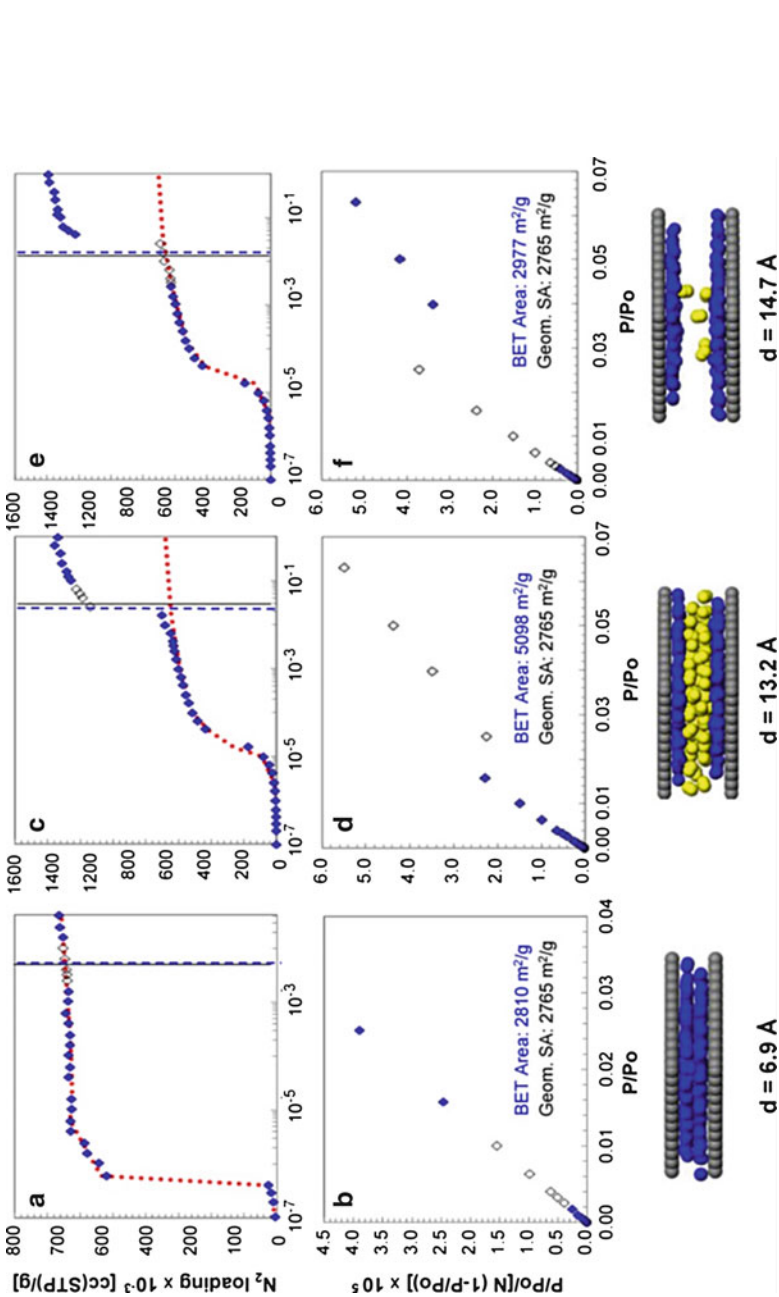

Fig. 6.2 Even when all BET consistency criteria are applied, calculated surface area can differ dramatically from calculated "true" nitrogen accessible surface area in certain types of pores (Reprinted with permission from Ref. [5] (a). Copyright 2015 American Chemical Society)

In general, the porosity or uptake behavior of a material cannot be described adequately by one or two parameters. Complete porosity data would include multiple gas loading isotherms at a variety of temperatures and as pressure ranging from zero until saturation is reached, if possible. "BET surface areas should always be given with the range used for analysis." [7] In most cases, this is not the case, and hence BET surface areas must always be assumed to be provisional. In all cases, BET surface area results are less informative than complete H_2 (or other gas of interest) and N_2 uptake isotherms, which should be examined for isotherm type, total uptake values, and saturation.

6.3 Porous Carbons with High Hydrogen Uptake

6.3.1 Activated Carbons

The theoretical maximum hydrogen adsorbed per surface area in a monolayer on the pore surfaces on a porous material is 2.28 wt% per 1000 m^2/g, assuming a surface density identical to liquid hydrogen. At 77 K, various activated carbons and single-walled carbon nanotubes (SWCNTs) of various dimensions exhibit a surface area that is quasi-proportional to surface area, as determined from the gradient. An analysis of the plot reveals an average adsorption per surface area of 1.91 mass% per 1000 m^2/g, analogous to 84% surface coverage. At room temperature, this coverage was only 0.23 mass% per 1000 m^2/g or 10% [1]. These materials did not show changes in hydrogen adsorption between SWCNTs and conventionally produced activated carbons. The best conventionally prepared activated carbons have surface areas lower than MOFs, leading to a further development of high surface area materials based on porous carbon (Fig. 6.3).

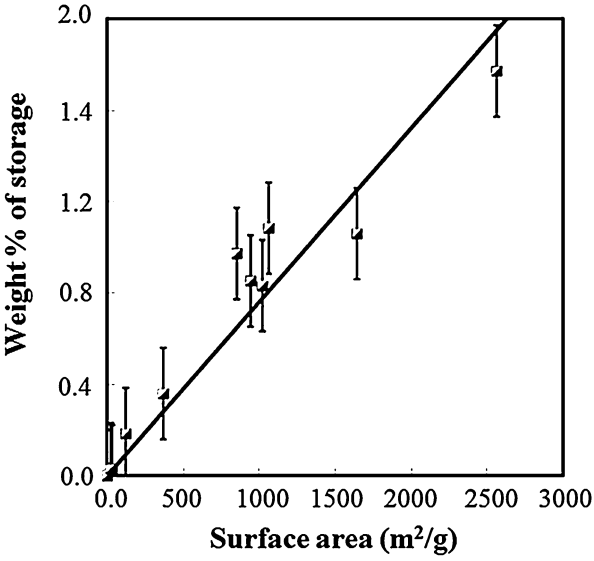

Fig. 6.3 Weight % storage of activated carbons versus surface area at 77 K. The best fit *line* for the experimental values roughly describes the Chahine rule (Reprinted with permission from Ref. [1]. Copyright 2005 Elsevier Ltd)

In general, carbon materials may be activated and made porous through "chemical activation" by reactive liquids, solids, or solvated species that can oxidize and remove some of the carbon at high temperature in an inert gas or through "physical activation" with gasses or gas mixtures. The precise method of activation, in addition to the carbon feedstock, can influence the porosity, pore size distribution, and degree of graphitization or oxidization of the resulting porous carbon [8]. Direct physical activation in the air tends to result in mesopore formation and surface area of only 700 m^2/g [9], unsuitable for hydrogen storage. However, when already porous titanium carbide (TiC)-derived carbon was further activated in carbon dioxide (CO_2), a surface area of 3100 m^2/g was achieved [10]. In general, chemical activation is more expensive than physical due to the additional cost of the activating chemical, but results in higher surface area materials with greater control of porosity with narrow pore size distribution [10, 11].

A highly porous activated carbon was prepared by the further activation of commercially available activated carbon through impregnation of the carbon with potassium hydroxide (KOH), slowly heating to 750 °C under argon atmosphere and washing with hydrochloric acid (HCl) and water consequently [12]. Oxidation of the carbon with KOH affords as one of the products potassium carbonate (K_2CO_3), which breaks down into potassium oxide (K_2O) and CO_2 [13]. With a ratio of 5 g of KOH to 1 g of activated carbon used, a carbon with a surface area of 3190 m^2/g was produced, compared to the 1585 m^2/g of the carbon before additional activation. This material had an H_2 uptake of 7.08 wt% at 77 K and 20 bars, only slightly less than the theoretical maximum value of 7.27 wt% at that surface area (assuming an adsorbed monolayer and the density of liquid hydrogen). The authors showed some evidence that the hydrogen uptake per surface area, which is usually about 2 wt% H_2 per gram of material per 1000 m^2/g surface area at 77 K was as according to the Chahine rule, where increases in the R value of graphitic porous carbons led to an increase in hydrogen uptake. The R value is an empirical parameter relating to the ratio of the 002 Bragg peak to the background in powder X-ray diffraction (PXRD) pattern. A large R value corresponds to more ordered, parallel single graphitic layers in most instances.

It was found that in the KOH-activated carbons, R values were close to 1 (no 002 peak present), lower than the values of other activated carbons, indicating randomly oriented graphene sheets [12, 14]. R-value increases with edge orientation of the sheets within the pores, as sheet edges provide higher adsorption enthalpy [15]. However, these KOH-activated carbons still had the highest overall wt% uptake of hydrogen, as the increased surface area and micropore volume was a more important factor at cryogenic temperatures where condensation into less-optimized larger micropores may have taken place.

Potassium hydroxide activation is a well-documented technique to attempt to achieve greater surface area and hydrogen uptake in porous carbons. This higher surface area is due to the microporous nature of the materials produced as opposed to larger pores from other activation methods [16]. For example, use of the technique on hemp stem as a carbon feedstock afforded carbon with BET surface area of 3241 m^2/g and 3.28 wt% H_2 uptake at 77 K and 1 bar pressure, at higher pressure, and cryogenic temperature mesopores morphology was reported [17]. Potassium

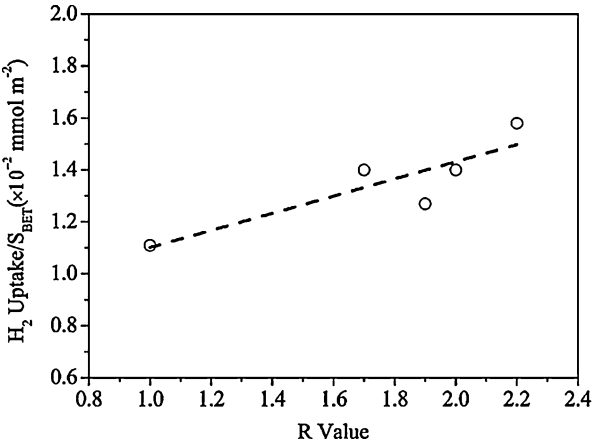

Fig. 6.4 H_2 uptake/surface area vs R value (Reprinted with permission from Ref. [12]. Copyright 2009 American Chemical Society)

hydroxide-activated carbons derived from various commercially available fungi reported a maximum BET surface area of 2526 m^2/g and hydrogen uptake of 2.4 wt% at 77 K and 1 bar pressure [18]. Chitosan-derived activated carbons (ACs) further activated with KOH achieved a BET surface area of up to 3066 m^2/g and hydrogen adsorption of 2.95 wt% at 77 K and 1 bar and 5.61 wt% at 77 K and 4 MPa (40 bars) [19]. Materials with poly(vinylidene chloride), carbonized and KOH activated, were found to have a hydrogen uptake of 4.85 wt% at 77 K and 20 bars, with 2.43 wt% at 77 K and 1 bar [20] (Fig. 6.4).

Zinc chloride ($ZnCl_2$) or phosphoric acids (H_3PO_4) are common chemical activation reagents [16] which upon treatment produce distinct pore size distributions between 0.5 and 2.5 nm in activated carbons. Impregnation of feedstock with homogenously distributed amounts of $ZnCl_2$ followed by pyrolysis results in porous carbon "monoliths" that have evenly distributed and sized pores with sizes controlled by the amount of Zn added, with a total volume of micropores around the same as the volume of the salt originally added. Removal of the salt by washing physically creates the pores, and the high temperature removes functional groups from the feedstock and bonds the surrounding carbon atoms to allow the carbon to retain the pores in its structure instead of collapsing. In contrast, H_3PO_4 activation results in a wider pore size distribution, and at high acid concentration, the volume of the porosity is higher than the volume of the acid, indicating that chemical reaction between the feedstock and the phosphoric acid takes place. Overall, as seen in Fig. 6.5, the highest reported BET surface area among conventionally produced activated carbons was found with KOH activation process.

6.3.2 Porous Graphene-Based Materials

Graphite oxide (GO), a form of graphite that is modified with oxide defects upon its surface, has attracted much interest both as a precursor material for graphene and

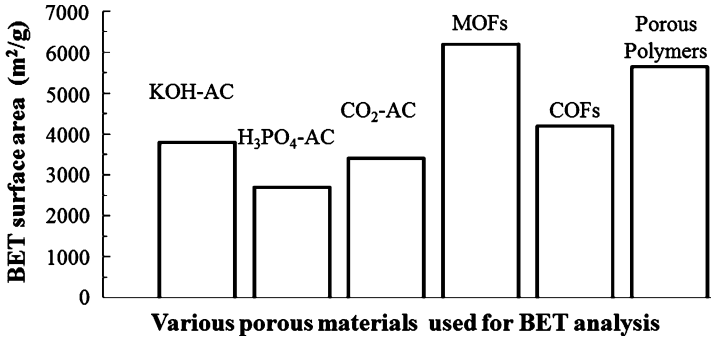

Fig. 6.5 Highest reported surface areas for various porous materials as of 2014

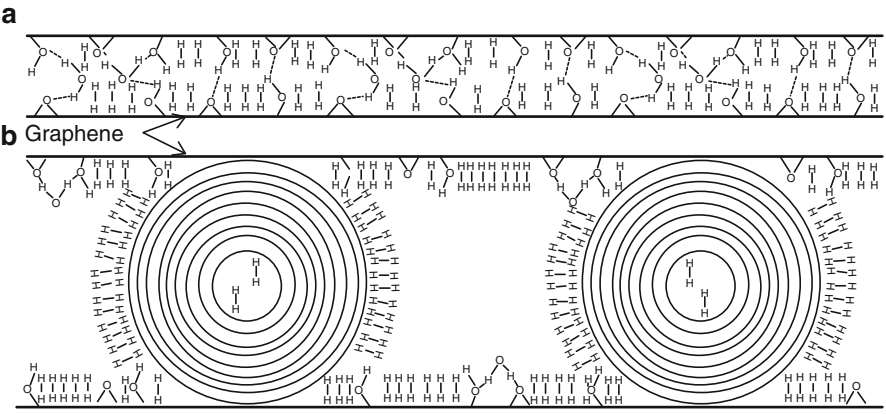

Fig. 6.6 Graphene oxide/multiwalled carbon nanotube structure (Reprinted with permission from Ref. [23]. Copyright 2012 Wiley Co)

other advanced materials due to its electrical and optical properties [21]. These sheets are readily produced by oxidizing graphite and can be suspended and processed in water [22]. The hydroxyl and other functional groups produced can then be functionalized in various ways to increase hydrogen uptake. Theoretically, high uptakes can be achieved in structures such as a graphene oxide/carbon nanotube pillared material. This may have been realized in graphene oxide/multiwalled carbon nanotube (MWCNTs) materials as shown in Fig. 6.6.

This graphene oxide/MWCNT material was reported to have a hydrogen uptake of 2.6 wt% at room temperature and 50 atm (50.6 bar) pressure [23]. The researchers suggest that the liquid crystal synthesis route produces highly ordered structures with more well-defined and controllable pore size. The enhanced structure and pore size results in an increase of the uptake, just as their LC-GO dispersions were reported to have 1.4 wt% uptake at room temperature, as opposed to the 0.2 wt% reported for

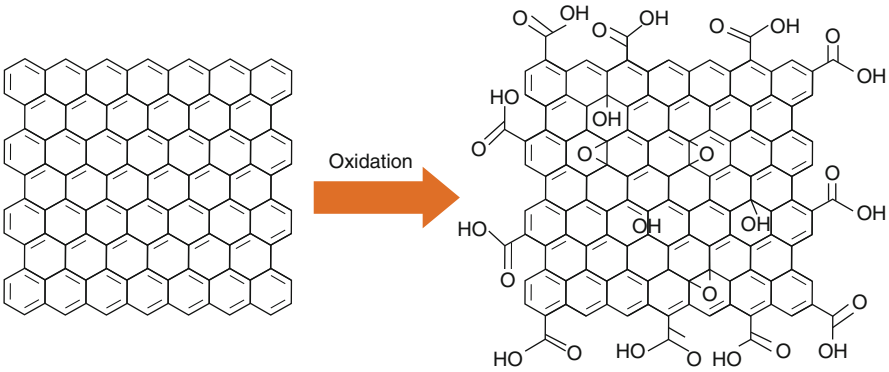

Fig. 6.7 Example structures of graphitic carbon sheets and graphene oxide (GO) (Reprinted with permission from Ref. [22]. Copyright 2012 Elsevier Ltd)

GO prepared by other groups. However, this material had slow adsorption kinetics, taking 60 min to reach full capacity of gas uptake, with no additional information regarding the materials surface area. It seems likely that the hydrogen uptake is correlated with both the surface area and the heat of adsorption of hydrogen to the material, which is influenced by the material type, the pore size, and shape [24].

In another example, random hydroxyl groups of GO, similar to those shown below in Fig. 6.7, were functionalized with benzene-1,3-diboronic acid (DBA) [21]. As one GO sheet is functionalized on one side of the linker, another is functionalized on the opposite side. This functionalization process theoretically connects many layers of GO sheets into disordered graphene oxide frameworks (GOFs).

However, these materials were found to undergo swelling in polar solvents, which would not be compatible with such a rigidly linked structure. Further investigation indicated two likely outcomes either DBA molecules attached on only one side, or the GO sheets were separated by self-reacted DBA molecules (Fig. 6.8a shows cross-section with DBA molecules as linkers). Optimization of synthesis conditions produced material with the specific surface area of about 1000 m^2/g. Since many of these materials follow the Chahine rule for hydrogen uptake, further development is likely to increase hydrogen storage capacities. Even materials that have high adsorption enthalpy and deviate from the Chahine rule must retain very high pore volume and overall porosity to be able to meet DOE targets [8].

As the DOE targets appear to be reachable by physisorption materials under cryogenic conditions due to the limited heat of adsorption of hydrogen to carbon materials. Tailored synthesis of materials with controlled pore sizes above those recommended for maximizing total hydrogen uptake in physisorption materials must be attempted in addition to chemical activation or metal doping to increase hydrogen binding energy as a means to meet the DOE target. To increase H_2 uptake at ambient conditions, including temperature and pressure, simulation studies have

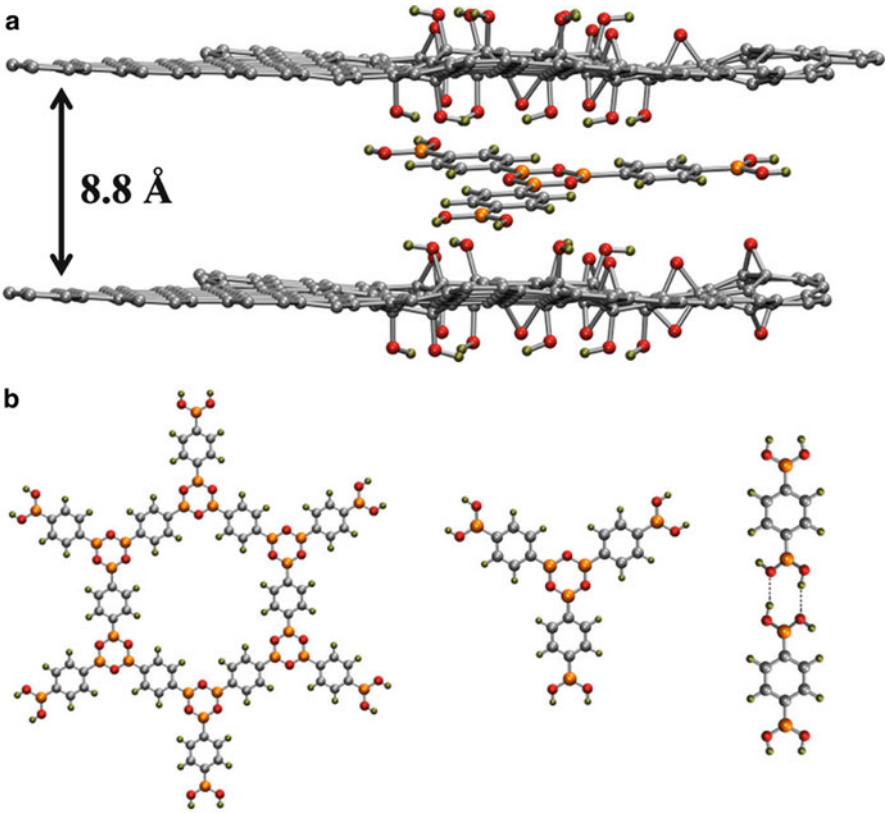

Fig. 6.8 Graphene oxide sheets separated by DBA dimers, trimers, or larger polymeric units (Reprinted with permission from Ref. [21]. Copyright 2015 American Chemical Society)

demonstrated that higher heat of adsorption than what is produce by small pores is required [25]. This "energy deficient" may be met if porous materials are designed with pores optimized for hydrogen sorption at a higher than cryogenic temperatures, while still allowing efficient hydrogen saturation of its pores.

An example of this strategy realized by a graphene scaffold material was made more porous through both KOH activation and hydrogen annealing, which removed oxygen moieties and broadened pores [26]. In this material, BET surface area determined to be 3400 m^2/g and the material exhibited a saturated H_2 uptake of 7.5 wt% at 77 K, while nonsaturated hydrogen uptake was 1.25 wt% at 296 K. The nonsaturated uptake was 4.2 wt% at 120 bar pressure at 193 K, the temperature of solid CO_2. This report also showed that hydrogen weight-percent (wt%) versus specific surface area of many porous carbons followed the Chahine Rule (summarized in Fig. 6.9).

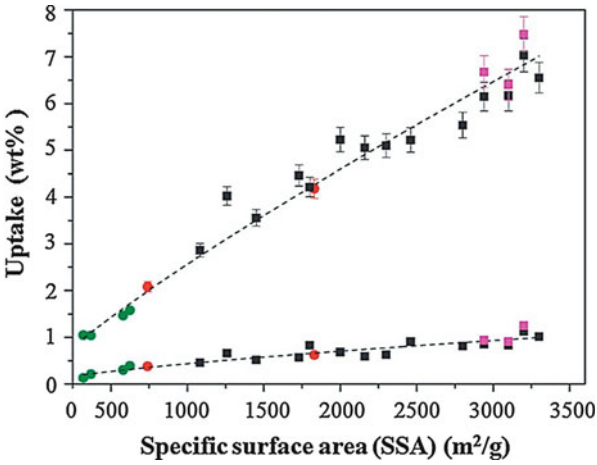

Fig. 6.9 The Chahine rule illustrated for many porous carbons at different temperatures. It follows logically and has been demonstrated in a few experiments that porous carbons using physisorption should follow a Chahine line in between the two temperatures at an intermediate temperature [26] (Reprinted with permission from Ref. [26]. Copyright 2015 Royal Society of Chemistry)

6.3.3 MOF-Derived Porous Carbons

Some of the highest surface areas to be measured among porous carbons are found among MOF-derived carbons (MDCs) [27]. Here, high-surface area MOFs are synthesized, sometimes with metals or functional groups specific to the application such as catalysis. Then, the MOF is calcined, or carbonized, subjected to extremely high temperatures sufficient to quickly remove the metals from the structure while somewhat preserving the preexisting pore size and shape [28]. However, the behavior and products of calcination of MOFs made from different metals can vary because the metals and metal oxide clusters can have very different melting points.

For example, in one study, porous carbons resulted from isoreticular metal-organic framework 1 (IRMOF-1, MOF-5, the structure has Zn_4O nodes with 1,4-benzodicarboxylic acid as struts between the nodes) had higher porosity overall than ones produced by calcination of chromium-based MOFs, as, according to the study, the Cr-based porous carbons had pores clogged with chromium oxides and carbides while the Zn oxides and carbides were removable from the crystalline structure. Carbonization of MOFs is done by slow heating under inert gas to prevent oxidization of carbon to carbides or metal to metal oxides. It was found that zinc was not present in the carbonized samples based on MOF-5 while chromium-based MOFs had residual metal still present. Depending on the ligand and metal used, nonporous or even porous metal oxides can be the end-product [29]. Chromium-MOF-based porous carbons were observed by powder X-ray diffraction (PXRD), which contained chromium carbide and oxide at various synthesis temperatures, and were treated further with HF or HCl to remove residual chromium. This treatment was unsuccessful as confirmed by differential thermal analysis (TGA) and a drastic lowering of measured surface area, as opposed to the increase in surface area of Zn-MOF based carbon from 835 to 2393 m^2/g was observed. The preliminary result

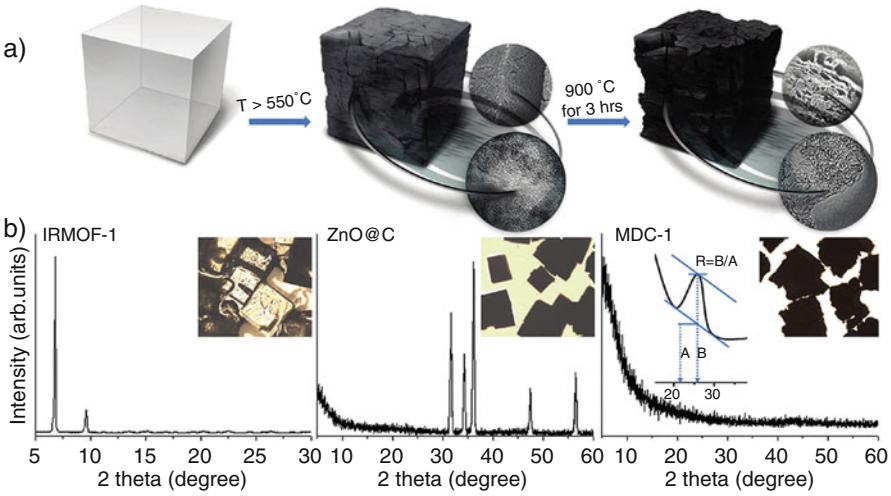

Fig. 6.10 Carbonization of MOF-5(IRMOF-1) to MDC-1 [27] (Reprinted with permission from Ref. [27]. Copyright 2012 American Chemical Society)

also indicates that MOFs based on metals with low melting and boiling points, such as zinc, may be more appropriate for development of new MDCs (Fig. 6.10).

MOF-derived carbons (MDCs) in general can store more hydrogen per surface area than standard MOFs, when their pore sizes are smaller than the corresponding MOFs. MDCs also usually retain overall high porosity. This is because structures containing large and open pores, such as mesopores, are not as suitable for hydrogen adsorption as materials with high micropore density. It is possible that structures with hierarchically sized pores may have a higher hydrogen uptake at higher pressures. This is because ultramicropores (extremely small pores with a size similar to that of the hydrogen molecules) may become saturated at low temperature and high pressure, even though those pores are more appropriate to hydrogen sorption at higher temperature [27]. In general, both ultramicropores and extremely high total pore volume are required for high gas uptake.

An MDC derived (modified) from a Zn-BTC MOF achieved a surface area of up to 1671 m^2/g [30]. The unmodified MOF was unsuitable for H_2 storage, due to its mesoporous nature. Carbonization of an MOF based on aluminum (Al) and 1,4-naphthalene-dicarboxlate afforded a porous carbon with a surface area of 5500 m^2/g, which was confirmed by 10 repeated syntheses and measurements [31]. The carbonization was carried out at 800 °C under inert gas, followed by removal of remaining Al species with HF. This material did, however, have a wide pore size distribution of between 1 and 5 nm. Graphitization and collapse of the surface area occurred at 900 °C or above, and the material retained approximately 65% of its pore volume after compression at 10 MPa for 10 min. In another study, a metal-organic xerogel was prepared and carbonized, resulting in a BET surface area of 3770 m^2/g [32].

Interestingly, a "foam-like" porous structure was observed in a carbonized Zn-MOF that was synthesized using a nitro-functionalized ligand. Rapid removal and gasification of these functional groups during carbonization result in a unique microstructure with many large macropores, which are formed by removal of the Zn products through postcarbonization washing [33]. Though this material is not suitable for hydrogen storage, it is a key example of how ligand choice can drastically affect the character of the resulting porosity in MOF carbonization.

In another study, an MDC with high surface area and pore volume, 3000 m^2/g and 5.45 cm^3/g, respectively, was synthesized through the direct carbonization of IRMOF-1 immersed in dimethylformamide (DMF). The rapid removal of the DMF molecules introduced large pores into the MDC without destroying the microporosity. Interestingly, pyrolysis of the activated, solvent-free IRMOF-1 produced an MDC with a surface area of 3110 m^2/g, but a total N_2 uptake of only 1720 cm^3/g at 1 bar pressure and 77 K. The MDC derived from DMF-infused IRMOF-1 had a BET surface area of 2980 m^2/g, but a total N_2 uptake of 3526 cm^3/g. As seen in Fig. 6.11, the introduction of large mesopores by this carbonization method lowered the surface area, but drastically raised the pore volume and overall porosity [34]. This is further example of how BET surface area is not a complete measure of the total porosity of a material and also of how the type of porosity can be drastically altered by synthesis conditions.

In some cases, MOFs act as templating agents for other carbon sources in addition to being the carbon source themselves, similar to the use of solvents above. This can produce templated ACs with higher surface areas than those of the original MOFs. One example of this approach is use of isoreticular metal-organic framework-3 (RMOF-3, $[Zn_4O(NH_2\text{-}BDC)_3] \cdot x$DMF, NH_2BDC = 2-amino-1,4-benzene-di-carboxylate) was used with various quantities of sucrose ($C_{12}H_{22}O_{11}$), heated to promote uptake of sucrose into the pores, and pyrolyzed in an inert atmosphere (such as Ar) at 900 °C for 6 h [35]. The sample was washed with dilute HCl and then with a binary mixture of water/ethanol, followed by removal of remaining Zn species. A surprising observation was that the BET surface areas varied among samples based on sucrose loading, as shown in Table 6.1. The number in each sample name refers to the milligrams of sucrose used in each pyrolysis. Field-emission scanning electron microscopy (FESEM), transmission electron microscopy (TEM), PXRD, and Raman spectroscopy analyses all showed different morphologies in each sample. In functional nanoporous carbon (NPC)-300, hydrogen uptake of 2.45 wt% at 77 K and 1 bar pressure was observed which was much higher than the unmodified MOF. This was attributed to the modified structure having a higher microporosity than the unmodified parent MOF. This is another example of how guest solvent or other small molecules introduced into an MOF before pyrolysis can drastically affect the properties of the final MOF-derived carbon.

The morphology of the MDCs produced can be further influenced by other experimental parameters such as carbonization temperature, ligand, and solvent used or temperature of reaction. For example, materials of institute Lavoisier (MIL) framework with aluminum metal [MIL(Al)] was fabricated with aluminum and oxygen (Al_3O_2) nodes with btc acid supporting struts between the nodes Al_3O

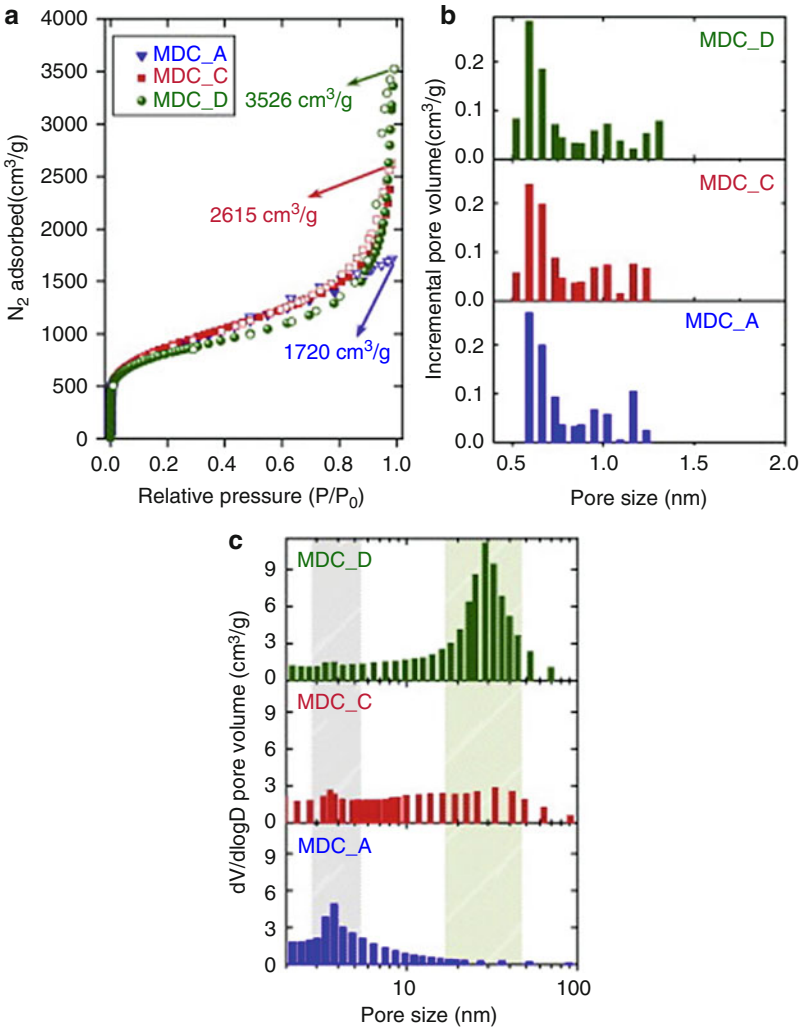

Fig. 6.11 The porosity of IRMOF-1 derived MDC carbonized solvent-free (*blue*) versus in chloroform (*red*) or DMF (*green*) (Reprinted with permission from Ref. [34]. Copyright 2014 Elsevier Ltd)

$(OH)(H_2O)_2(btc)_2 \cdot nH_2O$ (btc = 1,3,5-benzenetricarboxylate) and was carbonized at 800 °C under argon to produce an MDC [36]. This MDC required HF washing to remove residual aluminum oxide (Al_3O_2) species. Upon removal of Al_3O_2, hollow octahedral carbon shells were produced, with outer morphology mimicking that of the source MOF and micro- and mesoporosity in the shell. Large interconnected (50 nm) nanochannels in the center of the particles were shown by TEM (in Fig. 6.12,

Table 6.1 Textural parameters of the resultant functional nanoporous carbon (NPC) samples

Sample	S_{BET} (m^2/g)[a]	S_{Lang} (m^2/g)[b]	S_{micro} (m^2/g)[c]	S_{meso} (m^2/g)[d]	S_{meso}/S_{micro}	V_t (cm^3/g)[e]	V_{micro} (cm^3/g)[f]	V_{meso} (cm^3/g)[g]	$V_{meso/micro}$ (cm^3/g)
Sucrose	258	391	117	141	1.2	0.17	0.08	0.09	1.125
NPC-0	392	581	299	93	0.31	0.409	0.36	0.049	0.136
NPC-150	1022	1567	898	124	0.13	0.65	0.58	0.07	0.121
NPC-300	3120	4031	2987	133	0.03	1.93	1.89	0.04	0.024
NPC-500	1761	2687	1692	69	0.04	0.74	0.58	0.16	0.103
NPC-1000	1077	1622	994	83	0.08	0.435	0.245	0.19	0.175

Reprinted with permission from Ref. [35]. Copyright 2015 Elsevier Ltd

[a] S_{BET} is the BET-specific surface area

[b] S_{Lang} is the Langmuir-specific surface area

[c] S_{micro} is the *t*-plot-specific micropore surface area calculated from the N_2 adsorption–desorption isotherm

[d] S_{meso} is the specific mesopore surface area estimated by subtracting S_{micro} from S_{BET}

[e] V_t is the total specific pore volume determined by using the adsorption branch of the N_2 isotherm at $P/P_0 = 0.99$

[f] V_{micro} is the specific micropore volume calculated by a non-local density functional theory (NLDFT) method

[g] V_{meso} is the specific micropore volume calculated by subtracting V_{micro} from V_t

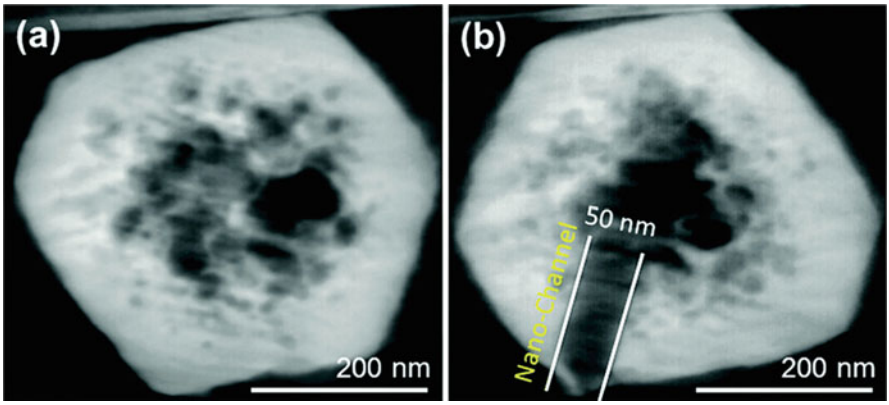

Fig. 6.12 MDC cage particles with massive voids in the center of porous carbon shells (Reprinted with permission from Ref. [36]. Copyright 2014 Elsevier Ltd)

the nanochannels are marked by vertical lines). The BET surface area of 1711 m^2/g, hydrogen uptake of 1.5 wt% at 77 K and 1 atm (1.01 bar) pressure and pore size distribution collectively indicated that this material possessed hierarchical micro-, meso-, and macropores. This would make it less suitable for pure hydrogen storage, but it is additional example of how metal and activating agent choice can control the nature of the pores produced.

6.3.4 Doped Porous Carbons

Lithium-atom-doped graphene sheets were shown in grand canonical Monte Carlo simulation to possess a maximum hydrogen adsorption of 6.5 wt% at room temperature and 20 bar pressure. The model is based on the assumption that if one atom of lithium is present per carbon and the sheets are separated by 10 Å, the interactions would yield between 5% and 7% adsorption. However, such a structure has proved synthetically inaccessible [25]. Other simulations predicted a hydrogen uptake of up to 16 wt% in graphenes with adsorbed lithium or boron (Fig. 6.13 is a graphical illustration of the various simulations) [25]. In general, high adsorption enthalpy, surface area, and pore volume that is accessible to about 2 layers of hydrogen are optimal for room temperature hydrogen storage meeting targets. However, physisorption of hydrogen onto graphitic carbon does not produce the required adsorption enthalpy, necessitating cryogenic temperatures for high uptake in most materials. One way to increase the adsorption enthalpy is to administer metal ions or particles into the pores of the carbon, due to the Kubas interaction between the hydrogen sigma bonding or antibonding orbitals with the d-orbitals of transition metals, or the polarization of the H_2 molecules by the charged metals [37].

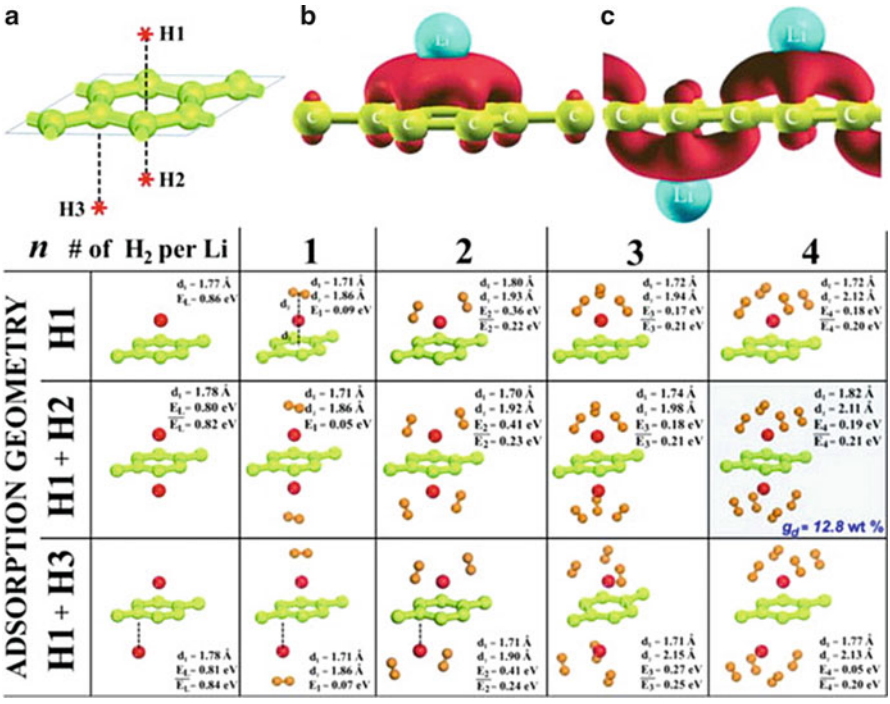

Fig. 6.13 (**a**) Simulated hydrogen adsorption sites in Li-doped graphenes. (**b**) Li's charge accumulation when adsorbed to site H1. (**c**) Li's charge accumulation when adsorbed to H1 and H3. (Reprinted with permission from [25]. Copyright 2015 Elsevier Ltd).

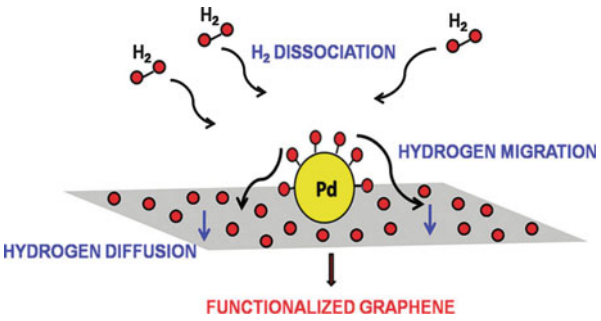

Fig. 6.14 Hydrogen spillover from metal nanoparticles to graphitic porous carbons (Reprinted with permission from Ref. [39]. Copyright 2011 American Chemical Society)

Metal-nanoparticles doped hierarchically porous carbon monoliths (Ni-HCPMs) were demonstrated to have hydrogen uptakes well in excess of what would be predicted by the Chahine rule, with 4.29 wt% H_2 uptake at 77 K and 5 bar pressure while possessing only 620 m^2/g surface area [38]. This is because of the hydrogen spillover effect, where chemisorption of H_2 molecules on metal nanoparticles is followed by dissociation of the hydrogen into isolated atoms bonded to the nanoparticle, which can then migrate to the graphitic activated carbon surfaces near the nanoparticles [39]. This drastic increase in the adsorption enthalpy would also increase uptake at higher temperatures (Fig. 6.14).

Carbon monoliths were prepared by suspending a nickel salt in a polymeric precursor solution of phenol, formaldehyde, NaOH, water, and pluronic P123 (E21P67E21) and F127 (E98P67E98) co-block polymers (where E is ethylene glycol monomer and P is propylene glycol). The above precursor was then heated at 100 °C for 18 h to produce a polymeric monolith, which was then pyrolyzed and made porous under nitrogen at 600 °C with slow heating. The prepared HCPM was pyrolyzed in the same fashion except without nickel and showed a surface area of 688 m^2/g, but hydrogen uptake of 1.44 wt%, helping to show the efficacy of the spillover effect, which was enhanced by using nickel nanoparticles directly within micropores. It is possible that similar materials may be fabricated starting from porous materials with the higher surface area, which may have performance criteria capable of meeting the 2020 DOE targets. The previous example is an illustration of how pyrolysis and carbonization can make even nonporous materials into porous carbons, though templating from already porous materials tend to result in higher surface areas. Templating from nonporous Zn MOFs, for example, resulted in maximum surface area of 1278 m^2/g in one study [40] (Fig. 6.15).

Nitrogen-doped (7 wt%) graphenes holding 20 wt% of Palladium (Pd) nanoparticles were shown to have hydrogen uptake of 1.9 wt% at 298 K and 20 bar pressure, even with a low surface area of 146.4 m^2/g. This was enhanced by 48.1% by a spillover mechanism as estimated by the uptake of the nanoparticles alone under identical conditions [41]. Nitrogen doping may have increased uptake due to enhanced interaction between the nitrogen-doped graphene and the metal nanoparticles. Graphene doped with nickel boron nanoalloys through reduction showed hydrogen uptake of 2.81 wt% at 77 K and 1.06 bar pressure through

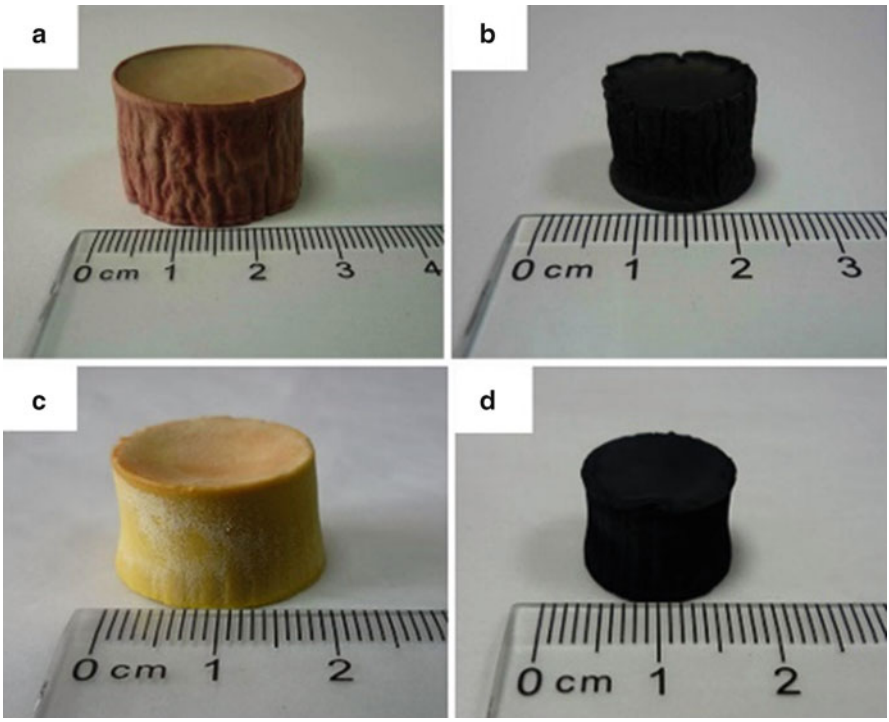

Fig. 6.15 Porous carbon monoliths prepared from polymer blocks (Reprinted with permission from Ref. [38]. Copyright 2015 Springer)

spillover enhancement [42]. Another graphene with a low surface area of 272 m^2/g was doped with nickel boride (Ni-B) was shown to have 4.4 wt% hydrogen uptake at 77 K and 1.06 bar, as seen in Fig. 6.16 [43]. For the doping process, solutions of graphene oxide (GO) and nickel acetate ($C_4H_{14}NiO_8$) were reduced with sodium borohydride ($NaBH_4$).

A carbon foam similar to graphene oxide was prepared, but with a higher oxide and defect concentration. The GO surface was doped with nanoparticles of an alloy of palladium (Pd) and mercury (Hg) with the formula Pd_4Hg. It was reported to have 4.6 wt% hydrogen uptake at 298 K at 20 bars [44]. However, due to the spillover mechanism of the storage, the adsorption or induction time was extremely long to achieve maximum uptake, and the uptake was not as high on other cycles. As shown in Fig. 6.17, measurements were made after a 1500 min equilibrium, with the first isothermal point being determined at a 15 min interval, subsequent points were determined at 15–40 min and the plots showed a very high wt% hydrogen uptake. It was hypothesized that if all cycles had been set to 1500 min induction time, uptake would have been identical. Attempts to reproduce the same results were successful only once, with other attempts producing materials with maximum 2 wt% uptake, with retained enhancement after doping. The isotherm also showed that a deliverable

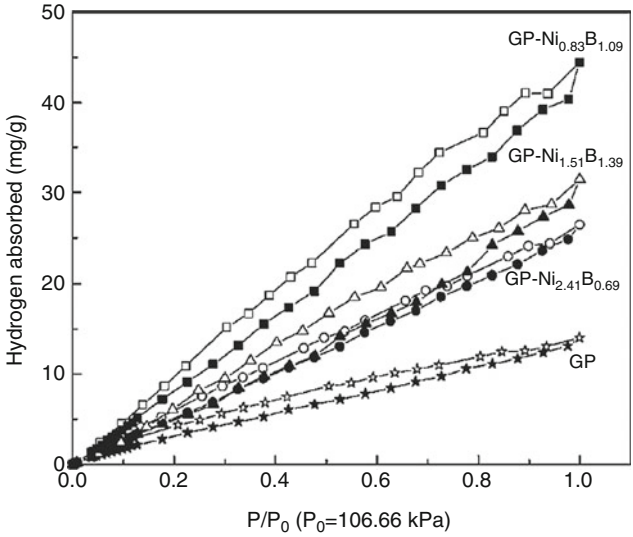

Fig. 6.16 Hydrogen uptake of Ni-B-doped graphenes at 77 K. *Closed symbols* refers to adsorption, *open symbol* refers to desorption (Reprinted with permission from Ref. [43]. Copyright 2010 Royal Society of Chemistry)

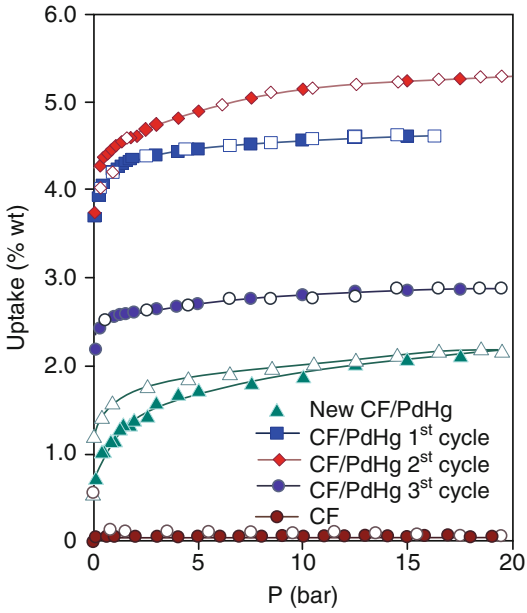

Fig. 6.17 Hydrogen uptakes among Pd_4Mg-CF composite varying wildly based on cycle induction time (Reprinted with permission from Ref. [44]. Copyright 2011 Royal Society of Chemistry)

hydrogen capacity of uptake between, for example, 10 bar and 20 bars pressure would be extremely low as a vacuum is necessary to desorb the hydrogen taken up through spillover. This mechanism will be explored further below.

6.3.5 Zeolite-Templated Carbons

Zeolite-templated carbons (ZTCs) are prepared by filling a zeolite structure with polymer feedstock such as propylene through a method such as chemical vapor deposition (CVD), heating to fill all pores with polymer, and final removal of the zeolite with HF or another etching agent [45]. Zeolite beta (e.g., CB850h) has demonstrated hydrogen uptake of 6.9 wt% at 77 K and 20 bars pressure. This sample was prepared from zeolite β templates and was subject to the zeolite/carbon composite obtained after the CVD step to further heat treatment under nitrogen flow for 3 h [46]. At room temperature, one ZTC preparation showed an hydrogen uptake which was proportional to their specific surface areas until 10 MPa (100 bar) pressure. However, above that pressure, having an appropriate pore size of 1.2 nm diameter seemed more important, in terms of H_2 uptake. This may be due to the condensation or multilayer adsorption of H_2 occurring in those pores at high pressure, resulting in enhanced adsorption enthalpy within the pores. Another ZTC preparation had a BET surface area of 3370 m^2/g and a hydrogen uptake of 2.2 wt% at high pressure. This reported uptake was greater than corresponding measurements using activated carbons with the similar surface area but uncontrolled pore size and shape. Hydrogen spillover was also demonstrated by an increase in capacity after Pt nanoparticle loading. This is an example of how ZTCs with the similar surface area can exhibit higher hydrogen uptake at high temperatures and low pressures. This is because their enthalpy of adsorption to hydrogen is raised after loading of metal nanoparticles. Material pore design can also raise heats of adsorption somewhat without nanoparticles, but this study also serves as evidence that DOE targets are likely to be unontainable at room temperature through pure physisorption processes.

In another study, a physical composite of MIL-101, composed of chromium and terephthalic acid (BDC), was formed by adding ZTC to the synthesis conditions of MIL-101 metal-organic framework, resulting in crystals of MIL-101 grown in and around the ZTC particles [47]. Poly crystalline X-ray diffraction spectroscopy confirmed peaks in the composite corresponding to both structures. Slight increases in surface area and hydrogen uptake were seen from either ZTC or MIL-101 materials. The nitrogen isotherm had higher uptake in the low-pressure region due to additional micropores and hysteresis in the high-pressure region consistent with newly formed mesopores. The pore size distribution showed a new unimodal pore size as opposed to the bimodal pore size of MIL-101. The surface area of MIL-101(Cr) was 2552 m^2/g and H_2 uptake was 1.91 wt% at 77 K and 1 bar pressure, ZTC was 2577 m^2/g and 2.39 wt%, and the hybrid composite was measured to have a surface area of 2957 m^2/g and 2.55 wt%. The finding of mesoporosity due to the new isotherm shape is not consistent with the narrow pore size distribution found, and the higher uptake may be primarily due to new pores

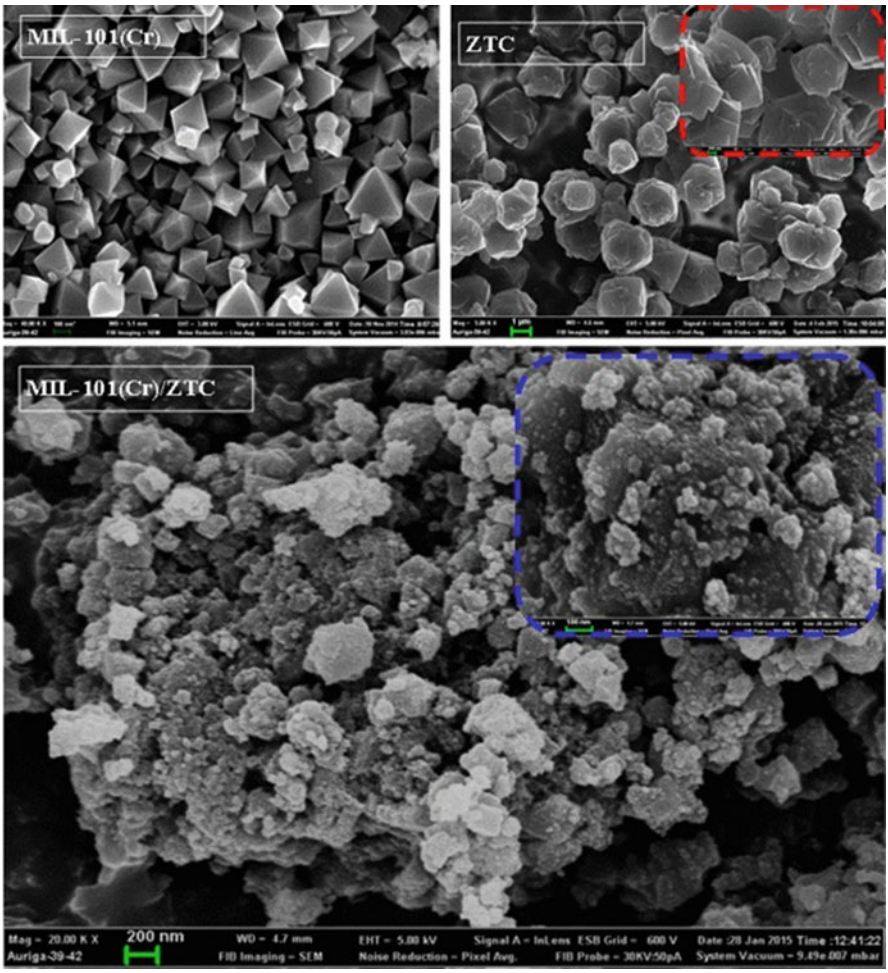

Fig. 6.18 SEM Images of ZTC, MIL-101, and the composite (Reprinted with permission from [47]. Copyright 2015 Springer

formed between the ZTC and the MIL-101 grown on and around the nodes. Such pores could physically increase the porosity and uptake of the material when compared to crystals or polymer pieces that are physically separated by distances which do not enhance sorption process due to smaller pores which allow more layers of adsorbate to interact with each other (a phenomenon not accounted by BET theory) (Fig. 6.18).

Other ZTCs were hydrogen uptake as improved through postsynthetically impregnating them with 2–5 nm Pd nanoparticles. This impregnation was accomplished through a CO_2 supercritical mediated hydrogenation and reduction of a precursor. After Pd was added, the surface area went down from 2045 m^2/g to

1390 m^2/g, while the H_2 uptake went from 4.9 wt% at 77 K and 20 bars pressure to 4.7–5.3 wt%, indicating a higher heat of adsorption for hydrogen uptake, as the material has a similar gravimetric uptake despite lower porosity [48]. A Pd loading of 0.4 wt% optimized for H_2 uptake is summarized in Fig. 6.19, which depicts the relationship between uptake and percent metal loading. This procedure demonstrated the hydrogen spillover effect, demonstrating that a precursor of much higher intrinsic porosity would be required for optimal application. Hypothetically a material with mesopores structure could be filled with slightly smaller nanoparticles, which would then promote hydrogen spillover into now-optimal pore sizes.

Hydrogen spillover in Pt-loaded ZTCs was studied more extensively, where they investigated both endothermic and exothermic process in addition to speciation, summarized in Fig. 6.20) [49]. It was found that processes increasing spillover

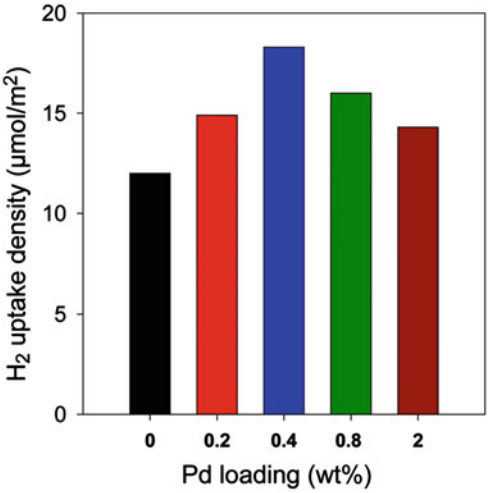

Fig. 6.19 Pd loading versus H_2 uptake in Pd-doped ZTCs (Reprinted with permission from Ref. [48]. Copyright 2013 American Chemical Society)

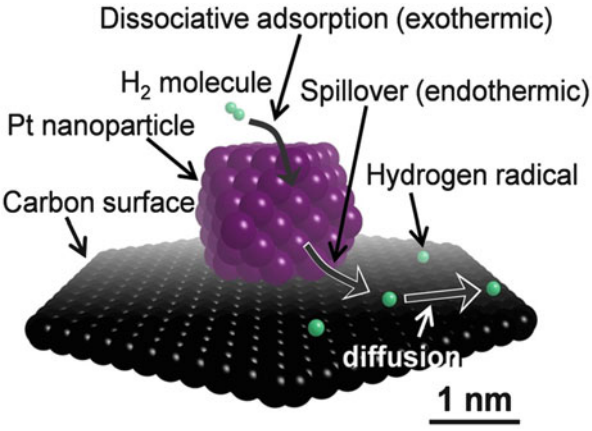

Fig. 6.20 Hydrogen spillover in Pt-loaded ZTCs (Reprinted with permission from Ref. [49]. Copyright 2014 American Chemical Society)

occurred at increased temperature and pressure, making nanoparticle loading an especially promising method for improving hydrogen uptake at higher temperatures. An appropriately prepared ZTC alone had a surface area of greater than 3000 m^2/g and pore size of 1.2 nm, resulting in hydrogen storage capacity of 2.2 wt% at 34 MPa (340 bar) pressure and room temperature. Mixing the prepared ZTC with Pt nanocolloidal suspension resulted in uptake of 3.23 wt% of Pt into the carbon, without loading optimization. The BET surface area was found to decrease to 3060 m^2/g from 3220 m^2/g. The PXRD confirmed the presence of ZTC and Pt nanoparticle, as both species partly ordered and crystalline, due to the ZTC being broad template, and Pt being much smaller in size relative to the ZTC.

The study found that the dissociated hydrogen radicals, migrating throughout the ZTC surface, enabled the release of the spillover only after a degas cycle at 423 K for 6 h to recover the chemisorbed hydrogen radicals. This spillover storage increases at higher temperature, as the diffusion of the particles onto the carbon is endothermic, which is promoted at higher temperatures. The total hydrogen uptake was not reported, although the reported hydrogen uptake for unmodified ZTC was 2.2 wt%. The lower than anticipated uptake for the modified material may be due to the high loading of Pt nanoparticles. Collectively, this study showed that dissociative spillover would produce an increase in hydrogen uptake that is not easily reversible, making it unsuitable for hydrogen storage applications unless long adsorption and desorption times and harsh experimental conditions necessary for desorption can be remedied. The spillover-based chemisorption of hydrogen radicals appears to have unfavorable desorption kinetics, making facile recovery much more difficult [44, 50]. This approach for hydrogen uptake is similar to chemical and other chemisorption-based hydrogen storage methods which exhibit very high uptake, but also very unfavorable desorption kinetics and thermodynamics requiring long desorption times, lower temperatures, or other harsh treatment conditions that make the overall procedure too expensive for practical DOE applications [25].

Materials with hexagonal mesoporous silica (HMS) were also used as a template to produce a porous carbon with a BET surface area of 2644 m^2/g. Here the carbon was decorated with nickel during the synthesis to increase hydrogen uptake. Resol-type resin ($HOCH_2$-ArOH, where Ar are different polyphenols) was used as the carbon source after glucose ($C_6H_{12}O_6$) and sucrose ($C_{12}H_{22}O_{11}$) sources were found to produce carbons with a BET surface area of 1100 m^2/g. Nickel-decorated materials had a loss of surface area to 1326 m^2/g and of mesoporosity, suggesting nickel nanoparticles filled many mesopores. Room temperature hydrogen uptake was 0.53 wt% at 20 bars pressure with no saturation shown in the isotherm for a carbon with a moderate amount of nickel, which was the highest as expected due to a balance between increased sorption and a loss of porosity due to the nickel. It was hypothesized that large Ni nanoparticle size caused an enhancement in hydrogen uptake, although this measured enhancement was less than calculated, suggesting that smaller nickel nanoparticles might be more effective in terms of improved hydrogen uptake [51].

6.3.6 Carbide-Derived Carbons

Carbide-derived carbons (CDCs) [52] usually have specific surface areas from 1000 to 2000 m^2/g and have been used for hydrogen uptake [53]. A molybdenum carbide-derived carbon was heated, exposed to chlorine gas, heated under an Ar purge, and then hydrogen annealed at 600 °C. The BET surface area of this modified CDC was 2520 m^2/g at 800 °C, with a pore size distribution between 2 and 4 nm, although there was pores with wider diameter, which was not suitable for hydrogen adsorption. An uptake that was 20% higher was found in the a CDC material, produced at 600 °C during chlorination, that had two-third of the total pore volume of the more porous carbon materials, as its larger pores increased its total porosity but lowered its hydrogen uptake at 77 K and 35 bar pressure. This is an evidence that in general, large pores degrade hydrogen uptake under many conditions, acting only as "wasted space" that does not adsorb hydrogen, unless either the heat of adsorption is increased through another mechanism, or extreme conditions such as 77 K and 100 bar pressure are adopted [54].

Porous CDCs, which were "super activated" by chemically activating them with KOH, reached 2800 m^2/g BET surface area, with a retention of microporosity, and an increase of the hydrogen uptake from 3.8 wt% to 6.2 wt% at 77 K and 20 bar pressure [55]. This observation was found to be partially due to the porous carbons becoming more functionalized with surface oxygen moieties after oxidation by the KOH. One study demonstrated an uptake of 2.7 wt% at 77 K and 1 bar pressure, indicating higher affinity of hydrogen for this material, as shown in Fig. 6.21, where the super activated materials have H_2 uptake deviated above the nominal Chahine plot.

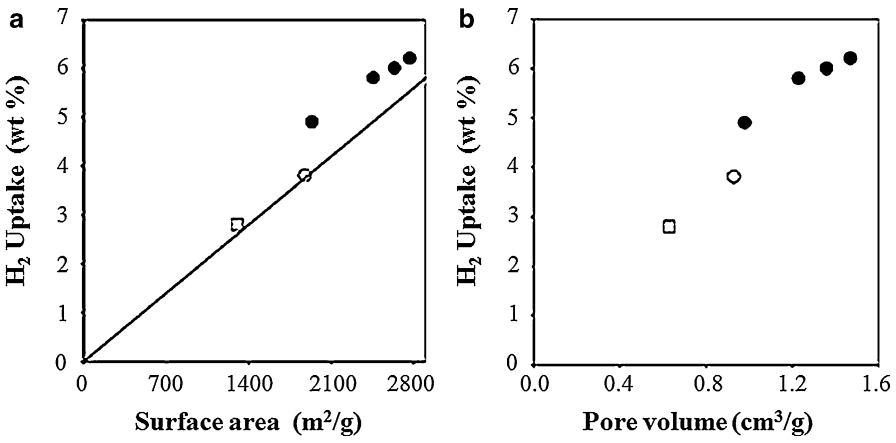

Fig. 6.21 Chahine plot of H_2 uptake versus porosity of Zr-CDCs (*clear symbols*) and super activated CDCs (*black circles*) (Reprinted with permission from Ref. [55]. Copyright 2009 Royal Society of Chemistry)

6.3.7 Porous Polymer Networks

Porous polymer networks (PPNs) are polymers of intrinsic microporosity (PIMs), due to the geometry, symmetry, and rigidity of their monomers or other linking units [56]. The porous aromatic framework-1 (PAF-1) was synthesized from tetrakis (4-bromophenyl)methane through a Yamamoto homo-coupling [57]. The PAF-1 material exhibited a BET surface area of 5600 m^2/g and a hydrogen uptake of 10.7 wt% at 77 K and 48 bar pressure. This high hydrogen uptake may be due to the "activation" of polymer supports under relatively mild conditions that merely remove guest molecules as opposed to reacting with species within the material as chemical or physical activation does. The PAF-1 structure needed only to be placed in a vacuum at 200 °C for the uptake measurements. Highly stable porous polymer networks-4 (PPN-4, schematically shown in Fig. 6.22) was based on the approach used for the fabrication of PAF-1. The material was synthesized by an Yamamoto homo-coupling of tetrakis(4-bromophenyl)silane under reaction conditions designed to slow polymerization [56]. This fabricated material had a BET surface area of 6461 m^2/g, which was the highest reported among all porous materials with a hydrogen uptake of 8.34 wt% at 77 K and 55 bars of pressure. Additionally, the H_2 deliverable or working capacity of PPN-4 was approximately 5.5 wt% 1.5 bar pressure at 77 K and was higher than other comparable materials at that time and currently and remains one of the highest hydrogen storage materials.

This above example demonstrates that if the pore size can be carefully adjusted for gas capture, high uptake is feasible in meeting the DOE targets for hydrogen storage using porous materials. When the pore size is below 1 nm, hydrogen uptake (measured at 1 bar and 77 or 298 K) may also increase [3]. Therefore, to design materials with the highest uptake at these conditions, it is imperative to maximize the density of small micropores and minimize any pores above that size. However, to produce a higher deliverable capacity at a given temperature, uptake near and below 1 bar, and thus small micropores, must be minimized, while larger pores which have size and shape appropriate to saturate with hydrogen near whatever maximum pressure is allowed by a particular system must be maximized, assuming no increase of heat of adsorption due to metal doping or other techniques.

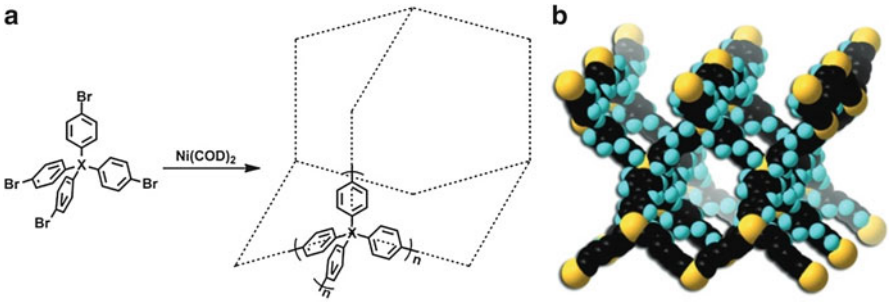

Fig. 6.22 PPN-4 (**a**) synthesis route and (**b**) idealized structure (Reprinted with permission fromRef. [56]. Copyright 2011 John Wiley and Sons)

However, PAF-1 and PPN-4 discussed above had a shortcoming preventing practical application, due to the expensive coupling reagent $Ni(COD)_2$ (where COD is bis(1,5-cyclooctadiene) necessary for the Yamamoto homo-coupling during the synthesis step [58]. The DOE target cost is $333/kg stored hydrogen capacity; thus, any porous material adopted for hydrogen storage applications will have to be synthesized in large quantities, using cheap precursors. Many other porous polymers such as porous poly(triazines) have been prepared and have hydrogen uptake of 1.44 wt% at 77 K and 1 bar pressure [59]. Another triazine-based PPN, TPC-1, showed 1.02 wt % uptake at 77 K and 1 bar pressure. A wide variety of covalent organic polymers (COPs) were synthesized by the polymerization of a tetrahedral and C4-, C3-, or C2-symmetrical linking unit, producing porous polymers of up to 3624 m^2/g [60].

The demonstration of the hydrogen storing capacity of PPN-4 has been adopted for gas capture of CO_2 or CH_4, catalysis, separations, or other applications, indicating this synthetic approach is flexible and can be used towards hydrogen capture. To our knowledge, no directly synthesized and vacuum-activated porous polymers have yet been reported with hydrogen uptake performance unambiguously exceeding PAF-1 or PPN-4 [61]. However, PAF-1 was synthesized, carbonized under high temperature, then chemically activated with KOH [62]. This K-PAF-1-750 had improved H_2 uptake at 1 bar pressure and 77 K of 3.06 wt%, but at higher pressures the hydrogen uptake was slightly reduced (though the CO_2 and CH_4 uptakes increased.) This is consistent with a decrease in mesoporosity and an increase in microporosity as confirmed by pore volume analysis, despite much lower surface area (2926 m^2/g) and total pore volume is summarized in Fig. 6.23 which is a plot of pore volumes at different curation temperatures.

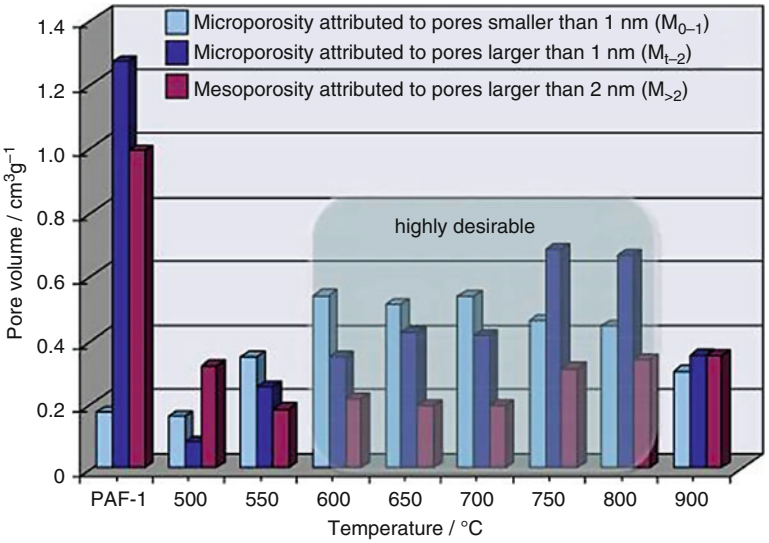

Fig. 6.23 Pore volume analysis of PAF-1 versus K-PAFs KOH-activated at different temperatures (Reprinted with permission from Ref. [62]. Copyright 2013 Nature Publishing Group)

6.4 Summary

In the design of porous materials for hydrogen storage, carbon-based porous materials have many advantages, such as intrinsically low molecular weight, high gravimetric porosity, excellent stability, and in some cases low fabrication costs. However, advanced hydrogen sorbents have several challenges to overcome in order to meet the DOE targets, particularly at high temperatures. Because of the low heat of adsorption inherent to hydrogen physisorption, materials with very small pores, either 1 nm or less; or materials with lower pore density must be utilized at low temperatures (77 K) making them unsuitable as materials which meet the DOE target. On the other hand, materials that are engineered to increase the heat of adsorption to hydrogen promoting hydrogen spillover have their own set of challenges which must be overcome. It is possible that DOE targets can be met with materials that have extremely high microporosity and pore volume, kept at low temperature but above 77 K and high pressures (40 bar pressure); however, technical challenges remain in the engineering of sorbent materials to meet the benchmarks in terms of capacity and cost.

Acknowledgment Mathieu Bosch was supported by the Texas Space Grant and the Texas A&M Graduate Merit Fellowship. We would also like to acknowledge U.S. Department of Energy award number DE-EE0007049.

References

1. B. Panella, M. Hirscher, S. Roth, Hydrogen adsorption in different carbon nanostructures. Carbon **43**(10), 2209–2214 (2005)
2. O.K. Farha, I. Eryazici, N.C. Jeong, B.G. Hauser, C.E. Wilmer, A.A. Sarjeant, R.Q. Snurr, S.T. Nguyen, A.Ö. Yazaydın, J.T. Hupp, Metal–organic framework materials with ultrahigh surface areas: is the sky the limit? J. Am. Chem. Soc. **134**(36), 15016–15021 (2012)
3. S.J. Yang, J.H. Im, H. Nishihara, H. Jung, K. Lee, T. Kyotani, C.R. Park, General relationship between hydrogen adsorption capacities at 77 and 298 K and pore characteristics of the porous adsorbents. J. Phys. Chem. C **116**(19), 10529–10540 (2012)
4. K. Kaneko, C. Ishii, M. Ruike, H. Kuwabara, Origin of superhigh surface-area and microcrystalline graphitic structures of activated carbons. Carbon **30**(7), 1075–1088 (1992)
5. (a) D.A. Gómez-Gualdrón, P.Z. Moghadam, J.T. Hupp, O.K. Farha, R.Q. Snurr, Application of consistency criteria to calculate BET areas of micro- and mesoporous metal–organic frameworks. J. Am. Chem. Soc. **100**, 100–101 (2015); (b) T.C. Wang, W. Bury, D.A. Gómez-Gualdrón, N.A. Vermeulen, J.E. Mondloch, P. Deria, K. Zhang, P.Z. Moghadam, A.A. Sarjeant, R.Q. Snurr, J.F. Stoddart, J.T. Hupp, O.K. Farha, Ultrahigh surface area zirconium MOFs and insights into the applicability of the BET theory. J. Am. Chem. Soc. **137**(10), 3585–3591 (2015)
6. D.E. Demirocak, S.S. Srinivasan, M.K. Ram, D.Y. Goswami, E.K. Stefanakos, Volumetric hydrogen sorption measurements – uncertainty error analysis and the importance of thermal equilibration time. Int. J. Hydrogen Energy **38**(3), 1469–1477 (2013)
7. T. Duren, F. Millange, G. Ferey, K.S. Walton, R.Q. Snurr, Calculating geometric surface areas as a characterization tool for metal-organic frameworks. J. Phys. Chem. C **111**(42), 15350–15356 (2007)

8. M. Sevilla, R. Mokaya, Energy storage applications of activated carbons: Supercapacitors and hydrogen storage. Energy Environ. Sci. **7**(4), 1250–1280 (2014)
9. B. Feng, S.K. Bhatia, Variation of the pore structure of coal chars during gasification. Carbon **41** (3), 507–523 (2003)
10. S. Osswald, C. Portet, Y. Gogotsi, G. Laudisio, J.P. Singer, J.E. Fischer, V.V. Sokolov, J.A. Kukushkina, A.E. Kravchik, Porosity control in nanoporous carbide-derived carbon by oxidation in air and carbon dioxide. J. Solid State Chem. **182**(7), 1733–1741 (2009)
11. (a) I. Cabria, M.J. Lopez, J.A. Alonso, The optimum average nanopore size for hydrogen storage in carbon nanoporous materials. Carbon **45**(13), 2649–2658 (2007); (b) M. Sevilla, P. Valle-Vigon, A.B. Fuertes, N-doped polypyrrole-based porous carbons for CO_2 capture. Adv. Funct. Mater. **21**(14), 2781–2787 (2011)
12. H.L. Wang, Q.M. Gao, J. Hu, High hydrogen storage capacity of porous carbons prepared by using activated carbon. J. Am. Chem. Soc. **131**(20), 7016–7022 (2009)
13. S.J. Yang, H. Jung, T. Kim, C.R. Park, Recent advances in hydrogen storage technologies based on nanoporous carbon materials. Progr. Nat. Sci. Mater. Int. **22**(6), 631–638 (2012)
14. (a) Y. Liu, J.S. Xue, T. Zheng, J.R. Dahn, Mechanism of lithium insertion in hard carbons prepared by pyrolysis of epoxy resins. Carbon **34**(2), 193–200 (1996); (b) V. Subramanian, C. Luo, A.M. Stephan, K.S. Nahm, S. Thomas, B. Wei, Supercapacitors from activated carbon derived from banana fibers. J. Phys. Chem. C **111**(20), 7527–7531 (2007)
15. D. Qu, Investigation of hydrogen physisorption active sites on the surface of porous carbonaceous materials. Chem. Eur. J. **14**(3), 1040–1046 (2008)
16. M. Molina-Sabio, F. Rodriguez-Reinoso, Role of chemical activation in the development of carbon porosity. Colloid Surf. A **241**(1–3), 15–25 (2004)
17. R. Yang, G. Liu, M. Li, J. Zhang, X. Hao, Preparation and N_2, CO_2 and H_2 adsorption of super activated carbon derived from biomass source hemp (Cannabis sativa L.) stem. Microporous Mesoporous Mater. **158**, 108–116 (2012)
18. J. Wang, I. Senkovska, S. Kaskel, Q. Liu, Chemically activated fungi-based porous carbons for hydrogen storage. Carbon **75**, 372–380 (2014)
19. I. Wróbel-Iwaniec, N. Díez, G. Gryglewicz, Chitosan-based highly activated carbons for hydrogen storage. Int. J. Hydrogen Energy **40**(17), 5788–5796 (2015)
20. J. Cai, J. Qi, C. Yang, X. Zhao, Poly(vinylidene chloride)-based carbon with ultrahigh microporosity and outstanding performance for CH_4 and H_2 storage and CO_2 capture. ACS Appl. Mater. Interfaces **6**(5), 3703–3711 (2014)
21. G. Mercier, A. Klechikov, M. Hedenström, D. Johnels, I.A. Baburin, G. Seifert, R. Mysyk, A.V. Talyzin, Porous graphene oxide/diboronic acid materials structure and hydrogen sorption. J. Phys. Chem. C **119**(49), 27179–27191 (2015)
22. D. Krishnan, F. Kim, J. Luo, R. Cruz-Silva, L.J. Cote, H.D. Jang, J. Huang, Energetic graphene oxide: challenges and opportunities. Nano Today **7**(2), 137–152 (2012)
23. S.H. Aboutalebi, S. Aminorroaya-Yamini, I. Nevirkovets, K. Konstantinov, H.K. Liu, Enhanced hydrogen storage in graphene oxide-MWCNTs composite at room temperature. Adv. Energy Mater. **2**(12), 1439–1446 (2012)
24. G. Srinivas, Y.W. Zhu, R. Piner, N. Skipper, M. Ellerby, R. Ruoff, Synthesis of graphene-like nanosheets and their hydrogen adsorption capacity. Carbon **48**(3), 630–635 (2010)
25. S. Gadipelli, Z.X. Guo, Graphene-based materials: synthesis and gas sorption, storage and separation. Prog. Mater. Sci. **69**, 1–60 (2015)
26. A. Klechikov, G. Mercier, T. Sharifi, I.A. Baburin, G. Seifert, A.V. Talyzin, Hydrogen storage in high surface area graphene scaffolds. Chem. Commun. **51**(83), 15280–15283 (2015)
27. S.J. Yang, T. Kim, J.H. Im, Y.S. Kim, K. Lee, H. Jung, C.R. Park, MOF-derived hierarchically porous carbon with exceptional porosity and hydrogen storage capacity. Chem. Mater. **24**(3), 464–470 (2012)
28. T. Segakweng, N. Musyoka, J. Ren, P. Crouse, H. Langmi, Comparison of MOF-5- and Cr-MOF-derived carbons for hydrogen storage application. Res. Chem. Intermed. **1–11** (2015)

29. T.K. Kim, K.J. Lee, J.Y. Cheon, J.H. Lee, S.H. Joo, H.R. Moon, Nanoporous metal oxides with tunable and nanocrystalline frameworks via conversion of metal–organic frameworks. J. Am. Chem. Soc. **135**(24), 8940–8946 (2013)
30. W.Q. Wang, D.Q. Yuan, Mesoporous carbon originated from non-permanent porous MOFs for gas storage and CO_2/CH_4 separation. Sci. Rep-Uk **4** (2014)
31. M. Hu, J. Reboul, S. Furukawa, N.L. Torad, Q. Ji, P. Srinivasu, K. Ariga, S. Kitagawa, Y. Yamauchi, Direct carbonization of al-based porous coordination polymer for synthesis of nanoporous carbon. J. Am. Chem. Soc. **134**(6), 2864–2867 (2012)
32. W. Xia, B. Qiu, D. Xia, R. Zou, Facile preparation of hierarchically porous carbons from metal-organic gels and their application in energy storage. Sci. Rep-Uk **2013**, 3 (1935)
33. K. Kongpatpanich, S. Horike, Y. Fujiwara, N. Ogiwara, H. Nishihara, S. Kitagawa, Formation of foam-like microstructural carbon material by carbonization of porous coordination polymers through a ligand-assisted foaming process. Chem-Eur. J. **21**(38), 13278–13283 (2015)
34. S.J. Yang, T. Kim, K. Lee, Y.S. Kim, J. Yoon, C.R. Park, Solvent evaporation mediated preparation of hierarchically porous metal organic framework-derived carbon with controllable and accessible large-scale porosity. Carbon **71**, 294–302 (2014)
35. K. Jayaramulu, K.K.R. Datta, K. Shiva, A.J. Bhattacharyya, M. Eswaramoorthy, T.K. Maji, Controlled synthesis of tunable nanoporous carbons for gas storage and supercapacitor application. Microporous Mesoporous Mater. **206**, 127–135 (2015)
36. A. Aijaz, J.-K. Sun, P. Pachfule, T. Uchida, Q. Xu, From a metal-organic framework to hierarchical high surface-area hollow octahedral carbon cages. Chem. Commun. **51**(73), 13945–13948 (2015)
37. G.J. Kubas, Metal-dihydrogen and sigma-bond coordination: the consummate extension of the Dewar-Chatt-Duncanson model for metal-olefin bonding. J. Organomet. Chem. **635**(1–2), 37–68 (2001)
38. Y.R. Liu, D. Li, B.P. Lin, Y. Sun, X.Q. Zhang, H. Yang, Hydrothermal synthesis of Ni-doped hierarchically porous carbon monoliths for hydrogen storage. J. Porous. Mater. **22**(6), 1417–1422 (2015)
39. V.B. Parambhath, R. Nagar, K. Sethupathi, S. Ramaprabhu, Investigation of spillover mechanism in palladium decorated hydrogen exfoliated functionalized graphene. J. Phys. Chem. C **115**(31), 15679–15685 (2011)
40. H.B. Aiyappa, P. Pachfule, R. Banerjee, S. Kurungot, Porous carbons from nonporous MOFs: influence of ligand characteristics on intrinsic properties of end carbon. Cryst. Growth Des. **13** (10), 4195–4199 (2013)
41. B.P. Vinayan, K. Sethupathi, S. Ramaprabhu, Facile synthesis of triangular shaped palladium nanoparticles decorated nitrogen doped graphene and their catalytic study for renewable energy applications. Int. J. Hydrogen Energy **38**(5), 2240–2250 (2013)
42. Y. Wang, J. Liu, K. Wang, T. Chen, X. Tan, C.M. Li, Hydrogen storage in Ni–B nanoalloy-doped 2D graphene. Int. J. Hydrogen Energ **36**(20), 12950–12954 (2011)
43. Y. Wang, C.X. Guo, X. Wang, C. Guan, H. Yang, K. Wang, C.M. Li, Hydrogen storage in a Ni-B nanoalloy-doped three-dimensional graphene material. Energy Environ. Sci. **4**(1), 195–200 (2011)
44. G.M. Psofogiannakis, T.A. Steriotis, A.B. Bourlinos, E.P. Kouvelos, G.C. Charalambopoulou, A.K. Stubos, G.E. Froudakis, Enhanced hydrogen storage by spillover on metal-doped carbon foam: an experimental and computational study. Nanoscale **3**(3), 933–936 (2011)
45. H. Nishihara, P.-X. Hou, L.-X. Li, M. Ito, M. Uchiyama, T. Kaburagi, A. Ikura, J. Katamura, T. Kawarada, K. Mizuuchi, T. Kyotani, High-pressure hydrogen storage in zeolite-templated carbon. J. Phys. Chem. C **113**(8), 3189–3196 (2009)
46. Z.X. Yang, Y.D. Xia, R. Mokaya, Enhanced hydrogen storage capacity of high surface area zeolite-like carbon materials. J. Am. Chem. Soc. **129**(6), 1673–1679 (2007)
47. N. Musyoka, J. Ren, P. Annamalai, H. Langmi, B. North, M. Mathe, D. Bessarabov, Synthesis of a hybrid MIL-101(Cr)/ZTC composite for hydrogen storage applications. Res. Chem. Intermed. **1–9** (2015)

48. E. Masika, R.A. Bourne, T.W. Chamberlain, R. Mokaya, Supercritical CO_2 mediated incorporation of pd onto templated carbons: a route to optimizing the pd particle size and hydrogen uptake density. ACS Appl. Mater. Interfaces **5**(12), 5639–5647 (2013)
49. H. Nishihara, S. Ittisanronnachai, H. Itoi, L.-X. Li, K. Suzuki, U. Nagashima, H. Ogawa, T. Kyotani, M. Ito, Experimental and theoretical studies of hydrogen/deuterium spillover on pt-loaded zeolite-templated carbon. J. Phys. Chem. C **118**(18), 9551–9559 (2014)
50. (a) Q. Zhou, C. Wang, Z. Fu, L. Yuan, X. Yang, Y. Tang, H. Zhang, Hydrogen adsorption on palladium anchored defected graphene with B-doping: a theoretical study. Int. J. Hydrogen Energy **40**(6), 2473–2483 (2015); (b) L. Wang, J.A.J. Lachawiec, R.T. Yang, Nanostructured adsorbents for hydrogen storage at ambient temperature: high-pressure measurements and factors influencing hydrogen spillover. RSC Adv. **3**(46), 23935–23952 (2013)
51. J. Shi, W. Li, D. Li, Synthesis, nickel decoration, and hydrogen adsorption of silica-templated mesoporous carbon material with high surface area. J. Phys. Chem. C **119**(41), 23430–23435 (2015)
52. (a) G. Yushin, R. Dash, J. Jagiello, J.E. Fischer, Y. Gogotsi, Carbide-derived carbons: effect of pore size on hydrogen uptake and heat of adsorption. Adv. Funct. Mater. **16**(17), 2288–2293 (2006); (b) Y. Gogotsi, R.K. Dash, G. Yushin, T. Yildirim, G. Laudisio, J.E. Fischer, Tailoring of nanoscale porosity in carbide-derived carbons for hydrogen storage. J. Am. Chem. Soc. **127** (46), 16006–16007 (2005)
53. H.S. Kim, J.P. Singer, Y. Gogotsi, J.E. Fischer, Molybdenum carbide-derived carbon for hydrogen storage. Microporous Mesoporous Mater. **120**(3), 267–271 (2009)
54. S.-H. Yeon, I. Knoke, Y. Gogotsi, J.E. Fischer, Enhanced volumetric hydrogen and methane storage capacity of monolithic carbide-derived carbon. Microporous Mesoporous Mater. **131** (1–3), 423–428 (2010)
55. M. Sevilla, R. Foulston, R. Mokaya, Superactivated carbide-derived carbons with high hydrogen storage capacity. Energ Environ Sci **3**(2), 223–227 (2010)
56. D. Yuan, W. Lu, D. Zhao, H.-C. Zhou, Highly stable porous polymer networks with exceptionally high gas-uptake capacities. Adv. Mater. **23**(32), 3723–3725 (2011)
57. T. Ben, H. Ren, S. Ma, D. Cao, J. Lan, X. Jing, W. Wang, J. Xu, F. Deng, J.M. Simmons, S. Qiu, G. Zhu, Targeted synthesis of a porous aromatic framework with high stability and exceptionally high surface area. Angew. Chem. Int. Ed. **48**(50), 9457–9460 (2009)
58. L.B. Sun, A.G. Li, X.D. Liu, X.Q. Liu, D.W. Feng, W.G. Lu, D.Q. Yuan, H.C. Zhou, Facile fabrication of cost-effective porous polymer networks for highly selective CO_2 capture. J. Mater. Chem. A **3**(7), 3252–3256 (2015)
59. S. Wu, Y. Liu, G. Yu, J. Guan, C. Pan, Y. Du, X. Xiong, Z. Wang, Facile preparation of dibenzoheterocycle-functional nanoporous polymeric networks with high gas uptake capacities. Macromolecules **47**(9), 2875–2882 (2014)
60. Z. Xiang, R. Mercado, J.M. Huck, H. Wang, Z. Guo, W. Wang, D. Cao, M. Haranczyk, B. Smit, Systematic tuning and multifunctionalization of covalent organic polymers for enhanced carbon capture. J. Am. Chem. Soc. **137**(41), 13301–13307 (2015)
61. W.G. Lu, Z.W. Wei, D.Q. Yuan, J. Tian, S. Fordham, H.C. Zhou, Rational design and synthesis of porous polymer networks: toward high surface area. Chem. Mater. **26**(15), 4589–4597 (2014)
62. Y. Li, T. Ben, B. Zhang, Y. Fu, S. Qiu, Ultrahigh gas storage both at low and high pressures in KOH-activated carbonized porous aromatic frameworks. Sci. Rep-Uk **3**, 2420 (2013)

Strategies for Hydrogen Storage in Porous Organic Polymers

7

Weigang Lu

Abstract

Gas storage by using porous materials has been a hot research topic in recent years. In this review, we highlight advances in porous organic polymers for their hydrogen storage applications.

Contents

Author Contribution: Dr. W. Lu conceived and wrote this chapter solely.

W. Lu (✉)
Research and Technology Transfer Office, Fayetteville State University, Fayetteville, NC, USA
e-mail: wlu1@uncfsu.edu

Y.-P. Chen et al. (eds.), *Nanostructured Materials for Next-Generation Energy Storage and Conversion*, DOI 10.1007/978-3-662-53514-1_7

7.1 Introduction

The percentage of greenhouse-gas emissions into the atmosphere attributed to anthropological activities has increased faster this century than the last century [1]. This is largely due to consumption of petroleum to meet current energy demands. Numerous studies have shown that combustion of carbon-based materials in air results in the production of carbon dioxide (CO_2). The interaction between CO_2 and visible to far-red light leads to increased retention of the longer wavelengths, which contribute towards a rise in global temperature [2]. Comparison of CO_2 levels from the past three hundred years suggests that certain regions will get warmer and others colder (global warming) and this redistribution of temperature will drastically affect the entire planet [3]. Different weather models share the following themes that the ice shelves will melt raising river water levels that will impact on wild life habitat, fish populations, and usable land for humans [4]. Regions that get hotter will experience faster water evaporation leading to a shortage of salt-free water for growth of crops, which further promote likelihood of starvation and disease [5]. Global weather models also predict that a reduction of CO_2 emission will retard or delay global warming projections [6] by using clean and alternative energy resources to replace fossil fuels in transportation, heating and generation of raw resources [7]. Among several potential candidates, hydrogen gas stands out because it generates water as an byproduct and has the highest energy density per unit mass of any known fuel, its heat of combustion is almost tripled that of gasoline (120 MJ/kg vs. 44.5 MJ/kg) [8]. However, it has a relatively low energy per unit volume at ambient temperature because of its low density, which is proportional to its molecular mass; therefore, the development of advanced storage methods to greatly increase its volumetric energy density is required for its applications such as powering small vehicles. US home vehicles account for approximately 17% of the total CO_2 emissions and substitution of petroleum by hydrogen would reduce the CO_2 emissions by more than 1% globally [9].

To date, storage of hydrogen is either at high pressure as a gas or at low temperature as a liquid. The former requires high-pressure tanks (350–700 bar or 5000–10,000 psi tank pressure) [10] to achieve a reasonable volumetric energy density. However, safety concerns are always big issues associated with high pressure gas storage; the latter requires keeping the storage system at cryogenic temperatures because of the extremely low boiling point of hydrogen gas (−252.8 °C at 1 atm). The cryogenic storage on vehicles necessitates a considerable amount of energy consumption to maintain the cryogenic temperatures. It is worth pointing out that hydrogen storage under cryo-compressed conditions is so far the only technology that meets 2015 US Department of Energy (DOE) targets for both volumetric and gravimetric capacities [11].

Recent studies have also suggested that porous materials are suitable candidates to address both safety and cost issues [12]. Some of them exhibit high and reversible adsorption-desorption of hydrogen under operable conditions, for example, at close-to-ambient temperature and relatively safe pressures (less than 100 bar) in the gas form. In this scenario, sorbents interact with hydrogen molecules through weak van

der Waals forces, often referred to as physisorption [13]. On the opposite side end of the spectrum, sorbents interact with hydrogen molecules through significant chemical bonding, often referred to as chemisorption [14]. The difference between physisorption and chemisorption can be viewed primarily in their binding energies with chemisorption involving much more energy to release the bound hydrogen gas [15]. If a system requires many times of gas storage and delivery, moderate binding energies (heats of adsorption) are highly desired to maximize the overall energy efficiency. Therefore, from a practical application point of view, porous materials based on physisorption are more suited for this kind of application, as porous materials based on chemisorption will necessitate a considerable amount extra energy to release the adsorbed hydrogen gas [16–19].

Historically, activated carbons [20] and zeolites [21] porous materials were used in a variety of applications including catalysis because of their low-cost and microporosity (pore diameter less than 0.2 nm) [22]. However, activated carbons can reach relatively high surface area, but is difficult to tune the pore structures to specific sizes; on the other hand, zeolites have ordered structures, but have low surface area. An ideal material would have tunable pore and high surface area, leading to development of organic and inorganic materials for gas storage [17].

Recent advancements in two new type of porous materials, metal–organic frameworks (MOFs) [19] and porous organic polymers (POPs) [23], have shown exciting results related to the increasing density of stored hydrogen gas under moderate conditions, primarily because of their unprecedented high surface areas and fine-tuned pore structures. These advanced porous materials have the technical potential to meet the 2015 US DOE hydrogen storage targets with sorbent-based materials.

Over the past two decades, MOFs have demonstrated the potential to be used as materials in catalysis or storage due to their three-dimensional structure, which can be tuned (pore volume, pore density, and lattice dimensions) using organic linkers as a framework scaffold and a catalytic center through coordinative metals or metal clusters. Through the appropriate combination of metal and organic linker, the generated MOF has chemical and catalytic properties for catalysis, separation, gas capture, and/or storage [24].

POPs have also been demonstrated as materials with exceptionally high surface area and promising potential applications in gas storage and separation [25]. POPs are composed predominantly of carbon, boron, oxygen, and nitrogen that are connected through covalent bonds as opposed to coordination bonds as in MOFs. The major advantages of POPs over other porous materials are exceptional porosity, ultra-high surface area, and generally superior physicochemical stability, the combination of which enables an enormous scope of postsynthetic modifications to introduce specific chemical functionalities [26]. POPs can generally be subjected to standard wet chemical reaction conditions without significant degradation of the framework or loss of porosity [27].

Whether or not the polymeric product can reach high crystallinity is largely dependent on the bond reversibility. Crystalline POPs are formed through reversible covalent bonding, which have the potential to correct the defects; therefore, they can reach high crystallinity in the same way that crystalline MOFs are formed.

Covalent organic frameworks (COFs) is a prominent example of crystalline POPs. COPs have high thermal stabilities (over 400 °C), and they are usually constructed through reversible condensation reactions, some of them exhibit high surface areas and interesting gas storage capacities, for example, the surface area for COF-102 and COF-103 are 3472 and 4650 m^2/g, respectively, and both of them show promising gas storage capacities [28, 29]. On the other hand, amorphous POPs are usually formed through irreversible coupling/substitution reactions, generally producing less/none ordered structures, which are associated with wide pore size distributions. As a result, it is very difficult to determine the structures of amorphous POPs; however, a model can be built based on the geometric combination of monomer/monomers, with that gas sorption behavior and pore size can be calculated. In combination of the experimental data, we should be able to approximate the real structures of the products and the degree of interpenetration, if there is any [30].

Due to the strength of irreversible covalent bonding, amorphous POPs usually exhibit exceptional physiochemical stability and tolerance toward wet chemical reaction conditions, which often breaks down the crystalline POPs, MOFs, and others constructed with either coordination bonding or reversible condensation reactions [31, 32], Many organic reactions have been utilized for making amorphous POPs with multitopic monomer/monomers, and the obtained polymers were named without a standard convention, For example, McKeown et al., generated POPs with micropores, called polymers with intrinsic microporosity (PIMs) [33–35], that exhibit similar behavior to the traditional microporous materials, such as activated carbons [37]. Cooper et al., generated microporosity with conjugated microporous polymers (CMPs), which are synthesized through coupling reactions such as Sonogashira-Hagihara coupling, show high surface area, microporosity, and chemical resistance [36–39]. Most recently, this approach was advanced by Ben using a Yamamoto homo-coupling reaction with a tetrahedral monomers; they were able to synthesize porous aromatic framework (PAF-1); [40]. This material has an exceptionally high Langmuir surface area of 7100 m^2/g and exhibits excellent hydrogen storage capacity (7.0 wt%) at 77 K and 48 bar. On top of that, PAF-1 shows extraordinarily physicochemical stability. Here, we review the current state of hydrogen storage in amorphous POPs, with a particular emphasis on strategies for further improving the hydrogen storage capacity of these materials.

7.2 Key Challenges for Porous Materials in Hydrogen Storage

For sorbent-based storage materials, current research has been focusing on optimizing the material's pore size, pore volume, and surface area, as well as material densification in the belief that these strategies will help improve the hydrogen binding energies, therefore, the hydrogen gravimetric and volumetric capacities.

7.2.1 Surface Area

Hydrogen storage technology is critical for next-generation energy conversion devices such as proton exchange membrane fuel cells. For practical applications in transportation, hydrogen storage system should reach gravimetric capacity of 0.055 kg H_2/kg system and volumetric capacity of 0.040 kg H_2/L system at a cost of \$400/kg H_2 stored according to the performance targets set by US DOE for 2017 [11]. No current technology meets all of these goals. Compared with chemical or metal hydride-based approaches, sorption-based technology has the advantages of (a) low parasitic energy consumption for desorption, (b) fast kinetics for storage and delivery, and (c) light material for high gravimetric and reasonable volumetric storage capacity. Porous materials with high surface area can reach reasonable high storage capacity for hydrogen. The main challenge, however, is its limited capacity under close-to-ambient conditions.

The theoretical calculation by Chahine and Benard drew the conclusion that gas adsorption at cryogenic temperatures on carbon-based porous materials is largely dependent on the surface area. In general, the hydrogen uptake by sorbents at liquid nitrogen temperature follows the so-called Chahine rule (CR), that is, the excess gravimetric capacity increases proportionally at the rate of 1 weight-percent (wt%) for every 500 m^2/g Brunauer, Emmett and Teller (BET)-specific surface area [41, 42]. Porous materials based on physisorption, including MOFs, POPs, activated carbons, et al., follow the Chahine rule very well [43–45]. The physisorptive hydrogen uptake is well proportional to surface area (Fig. 7.1) at cryogenic temperature (<= 123 K).

Excessive increase of surface area, however, leads to the reduction of sorbent's density, therefore the volumetric storage capacity. Studies show that the volumetric capacity peaks near the BET surface area of 3000 m^2/g, suggesting a ceiling of 6 wt% gravimetric capacity if the sorbent follows CR strictly. To achieve DOE's 2017 gravimetric and volumetric capacity goals simultaneously, the new adsorbent must exceed this CR limitation, which we will discuss in heat of adsorption.

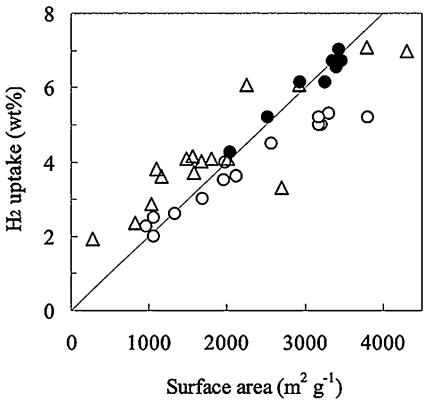

Fig. 7.1 A comparison of the hydrogen uptake capacity vs. surface area for activated carbons (○, ●) and MOFs (Δ). The *solid line* corresponds to the Chahine rule) (i.e., 1 wt% sorption per 500 m^2/g) (Reproduced with permission from Ref. [44]. Copyright © 1940 American Chemical Society)

7.2.2 Pore Size Distribution

Microporosity in porous materials in which physisorption and van der Waals forces dominate the adsorption process is generally believed to be the most useful in terms of high pressure hydrogen storage. It is consistent with the theoretical calculations and experimental results. Cabria et al. calculated the optimum average pore size for hydrogen storage in carbonaceous materials based on a thermodynamical model in slitpores [46]. The model predicts that the nanopore widths should be at least 5.6 Å in order to reach the US DOE hydrogen volumetric and gravimetric storage targets for 2010 at low temperatures and pressures [47]. Another prediction, which is apparently more interesting, is that the nanopore widths should be around 6 Å to reach the DOE 2010 volumetric target at 300 K and at least 10 MPa [48].

More specific but deviated predictions have been made by Geng et al. [49]. By utilizing SEM, HRTEM, and N_2-sorption characterization technologies, they carefully examined the morphologies and pore structures of a series of high-surface-area carbon materials. Porous carbons should show different pore size distribution and specific surface area because of their different synthetic procedures. Therefore, the high-pressure hydrogen uptake performance was analyzed using standard Pressure-Composition-Temperature apparatus and the structure (pore size)-property (hydrogen storage) relationship was studied. The results indicate that the most effective pores for hydrogen storage are largely dependent on the storage pressure. Ultramicropores (0.65–0.85 nm) was the most desired for hydrogen uptake at 1 bar and 77 K, and micropores (0.85–2 nm) would be more useful for hydrogen storage at higher pressure at 77 K. However, the authors found that the effects of pore size on hydrogen storage were very weak at room temperature, whereas surface area and pore volume would be more important under the condition [49]. It has been demonstrated that high surface area and high pore volume are positively proportional to the gravimetric uptake at low temperature, though unlikely for volumetric uptake, since porous materials with high surface area and large pore volume usually possess relatively low density, which will be rendered into a compromise for volumetric uptake [50].

A commonly accepted microporous materials pore size is 7 Å mostly, as the diameter to enable maximal hydrogen storage capacity at room temperature, based on the assumption that a 7 Å slit-shaped pore could accommodate two layers of hydrogen molecules, one on each opposite wall, with the maximized van der Waals potential, considering the 2.89 Å kinetic diameter of hydrogen molecule [51]. At 77 K, however, a third layer of hydrogen molecules in between these two on the opposite wall becomes possible and favorable, and the ideal pore size for maximum volumetric hydrogen storage at 100 bar is predicted to be 10 Å [52].

Most of MOFs reported, however, have distances between their opposite walls larger than 7 Å, which is not the most effective for the adsorption of hydrogen [53]. For example, the distance between phenylene in MOF-5's spherical pore is 15 Å in diameter; therefore, there would be an unused void volume at the center of these pores, which would compromise the volumetric packing density if the adsorption of hydrogen is monolayered [54]. To increase this hydrogen storage in MOFs,

smaller pores are necessary. This could be done by the use of shorter organic linkers, or through framework catenation to achieve a reduction of the pore diameter [55]. In some cases, it has been proven to a viable strategy for improving hydrogen capacity. For example, in a series of porous metal–organic frameworks based on linking zinc oxide clusters, the interwoven IRMOF-11 material showed the highest hydrogen storage capacity at 77 K; [56] two fourfold interpenetrated MOFs of cubic topology, synthesized by Kesanli et al., exhibit significant hydrogen storage (~1 wt%) at room temperature and over 40 bar [57]. The results indicate that large surface area and pore volume are not the only parameter for the hydrogen storage materials; building interpenetrated network might be a new approach for efficient hydrogen storage materials [58]. The interaction between hydrogen molecules and the frameworks is strengthened by multiple contact sites due to interpenetration; such sites would have higher hydrogen binding energy, therefore, beneficial to hydrogen storage at room temperature; however, interpenetration brings down the surface area, therefore, and a balance should be carefully considered between surface area and interpenetration if this direction is pursued [59].

7.2.3 Heat of Adsorption

Gravimetric adsorption capacity is highly correlated with surface area, which dictates the geometric design criteria for hydrogen storage materials to maximize surface area while retaining a high microporosity. We have discussed that one of the advantages of using porous materials as a hydrogen storage medium is that hydrogen molecules retain its molecular form throughout the adsorption and desorption cycle with minimal release energy. Unfortunately, relatively weak binding energy is also one of the primary disadvantages when compared to high binding energy in chemical bonding in metal hydrides; as a result, the storage capacity reduces significantly as temperature increases for POPs.

Currently, one of the research focuses is to increase the hydrogen adsorption enthalpy (binding energy), through different approaches, although nonstrategies thus far meet the DOE target goals.

The enthalpy for hydrogen storage materials based on physisorption is typically in the range of 5–10 kJ/mol [60]. In general enthalpy of adsorption for chemisorption is much more than that of physisorption. It is important to clarify that, for sorption, the term “enthalpy” is not a single valued quantity, although it is often referenced in this manner [61]. This value will generally be at its highest as the initial molecule adsorbs onto the strongest binding site without the influence from the neighboring adsorbed gas molecules. Therefore, for hydrogen adsorption, the isosteric enthalpy is expected to decay monotonically [62].

Two primary criteria determine a sorbent’s hydrogen storage capacity: surface area and adsorption enthalpy. Progress has been made in generating solid hydrogen storage materials with exceedingly high surface area and moderate to excellent stability; these materials include activated carbons, carbon nanostructures, zeolites, POPs, and MOFs. Although some of these materials have been shown to have

capacities higher than DOE's ultimate technical goals at cryogenic temperatures (such as NU-100 [63] and MOF-210 [64], with excess gravimetric capacity of 9.05 wt% and 7.92 wt% at 77 K, respectively), their hydrogen uptake quickly drops to insignificant levels (typically less than 1 wt%) at ambient temperatures. This is due to low hydrogen affinity as reflected by a moderate adsorption enthalpy (less than 7 kJ/mol in most cases). Although materials with adsorption enthalpy around 10 kJ/mol have been prepared, they typically have insufficient surface area and thus take up insignificant amount of hydrogen at room temperature [65]. If the material's hydrogen-adsorption enthalpy can be improved to 15~20 kJ/mol while maintaining a high surface area [66, 67], high uptake of hydrogen at room temperature can be achieved.

In short, optimizing the material's pore size and surface area, as well as increasing the hydrogen binding energy are key criteria to enhancing material storage capabilities. For storage in automobiles, volumetric capacity is another important parameter to consider.

7.3 Advantages of POPs Over MOFs

MOF materials have exhibited high surface area, tunable pore size, and stability under standard operating conditions [68–70]. POP-based materials have potential advantages to meet all technical parameters required for hydrogen storage, although amorphous and difficult to characterize with broad pore size distribution that need further refinement before wide-scale use.

7.3.1 Potential to Reach Higher Surface Area

MOF development has enabled their use in a number of divergent fields [71–73]. This wide usage is in the flexibility of connecting the active metal center to linkers, which can be strained, flexible, and contain large pores or small pores with ultra-high surface area limit for solid porous materials; NU-110E is the first one surpassed the 7000 m^2/g BET surface area [74], nevertheless, POP has the potential for higher surface area. This is because MOFs are coordinate structures where the metal centers serve as anchors and do not create pores for storage, whereas in an organic covalent system, tetravalent carbon can serve as an anchor and part of pore structure. The metal clusters in MOFs are coordinated to organic linkers to form one-, two-, or three-dimensional structures that can be porous; however, the metal clusters which are an ensemble of bound atoms are polynuclear compounds that contain two or more metals linked by metal-metal bonds to each other and coordinate bonds to the linkers such as pyridines or carboxylates (Lewis base, if donate a pair of nonbonding electrons) as the exclusive or predominant ligand [75]. High valent metal clusters may be used due to their stability, for example, trinuclear iron cluster, tetranuclear manganese cluster, and hexa or octanuclear zirconium clusters tend to have a high number of metal atoms which take volume

but do not generate pore spacing for storage. The simulated structures of POPs use one single atom to replace the bulky metal cluster. If POP polymerization is executed perfectly, the resulting POP materials will have much higher surface area since it eliminates the metal cluster.

7.3.2 Excellent Physicochemical Stability

A huge number of porous MOF materials have been reported in the literatures. However, the low chemical stability of most MOFs hinders them from practical applications under extreme conditions because of the relative susceptibility of coordination bonds. On the other hand, porous organic polymers (POPs), though amorphous, are low cost precursors, allow for easy processing, and contain robust covalent bonds, leading to these materials with exceptionally high chemical stability. Therefore, POP materials can survive the vigorous postsynthetic treatment either required to thoroughly empty the voids in the framework or to introduce functionalities [76–80]. For example, PPN-6 (PAF-1) was subjected to sulfonation and neutralization to incorporate lithium cations. The extremely harsh acidic and basic conditions along the synthesis attest to the superior chemical stability of all carbon network that is absent in most other porous materials. Although the experimental BET surface area dropped as a result of the modifications, the H_2 adsorption enthalpy was enhanced by 47%, consistent with theoretical calculations. The further reveal in terms of stability is that the sulfonate-grafted materials showed no loss of surface area or decrease in CO_2-uptake capacity after being boiled in water for 6 h (Fig. 7.2) [79].

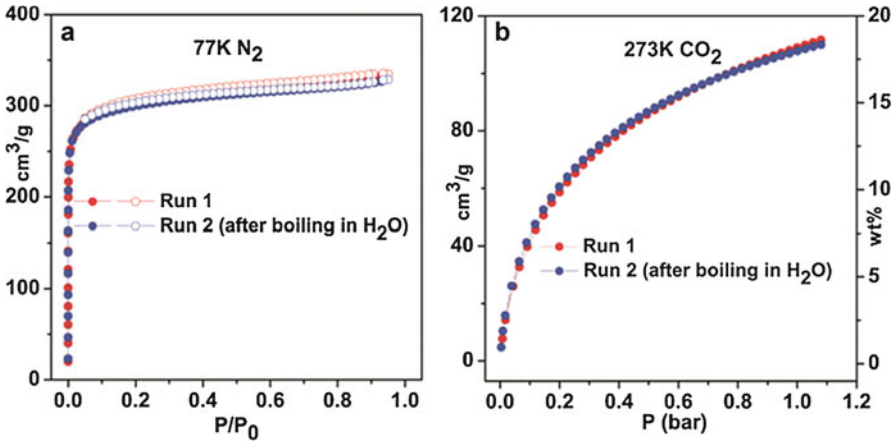

Fig. 7.2 (**a**) N_2 adsorption (b)/desorption (O) isotherms of PPN-6-SO_3Li at 77 K. (**b**) Gravimetric CO_2 adsorption curves for PPN-6-SO_3Li at 273 K. Run 2 employed material regenerated after run 1 by boiling in water for 6 h (Reproduced with permission from Ref. [79]. Copyright © 2011 American Chemical Society)

7.4 Strategies to Improve Hydrogen Storage Capacity in POPs

7.4.1 Rational Design to Achieve High Surface Area

Compared to traditional porous materials, such as zeolites and activated carbons, POPs have the potential for more flexible and rational design through control of the architecture and functionalization of the pores [81]. Recently, the surface area reached new high in porous organic polymer via Yamamoto homo-coupling. By using tetrahedral monomer tetrakis(4-bromophenyl)methane, PAF-1 (porous aromatic framework) was synthesized with a BET surface area of 5600 m^2/g (Fig. 7.3); [82] PAF-1 combines high physicochemical stability with the potential synthetic diversification offered by organic polymers. A simulated structure was built by using a model for amorphous silica as a template, the calculated surface area from this simulation by using a probe radius of 1.82 Å compare well with the experimentally determined surface areas for PAF-1 consistent with predicted calculations using structural analogies with similar phases or with materials containing silicon or germanium may assist in understanding networks such as PAF-1 that are based on tetrahedral linkers [83]. Indeed, porous polymer network (PPN-4), used tetrakis(4-bromophenyl)silane instead, was synthesized with a BET surface area of 6461 m^2/g, which translated into excellent gas storage capacities [84].

Closer examination reveals several parameters to achieve high surface area in POPs.

7.4.1.1 Size of Monomer

Ideally, the strategy to maximize surface area is to use long linkers, which, however, likely lead to interpenetrated structures, the framework that would otherwise collapse upon guest removal. Although interpenetration has been shown to experimentally stabilize the structure, it is not practicable for increasing absolute surface area. Analysis of geometric accessible surface areas for the interpenetrated structure indicates that they have a much lower surface than the non-interpenetrated structure [85, 86].

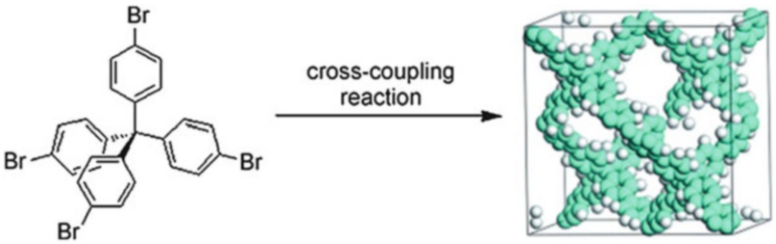

Fig. 7.3 Synthesis of the microporous polymer network PAF-1 by a Yamamoto coupling reaction (Reproduced with permission from Ref. [82]. Copyright © 2009 WILEY-VCH Verlag GmbH & Co. KGaA, Weinheim)

7.4.1.2 Geometry of Monomer

Most POPs are synthesized through kinetically dominated process, and it is widely accepted that the monomeric components generally govern the formation of network geometry. Linear monomers tend to form one dimensional polymer chains, likewise, monomers with trigonal planar geometry tend to form two dimensional polymer sheets, and three dimensional building units have the tendency to form three dimensional frameworks if head to head polymerization is applied. From the architecture point of view, tetrahedral monomers can form three dimensional frameworks with diamondoid topology, which is imposed by the monomers themselves, and it provides widely open and interconnected pores to efficiently prevent the formation of "dead space". [87]

7.4.1.3 Efficiency of Polymerization

Linear polymers usually can be achieved with high extents of polymerization partly because the polymers themselves are soluble in reaction solutions, which allow active sites to have better chances to collide and react. Unlike linear polymers, in which all of the repeating units are surrounded and therefore solvated by solvents, three-dimensional polymers tend to precipitate at much earlier stage probably due to the less effective interaction between solutes and solvents. Once precipitated, the polymer propagation is virtually terminated because the chances of effective collision between the active centers on the precipitate and monomers in the solution will be greatly reduced.

To achieve efficient gas adsorption through high surface area, degrees of three-dimensional complete polymerization are reduced to increase surface area past 10,000 m^2/g benchmark. One approach to achieve that is to apply highly efficient reactions, such as Eglinton homo-coupling [87], or the Yamamoto homo-coupling [88], or Azide-Alkyne "Click Chemistry" [89] or any facile coupling giving a high yield. These reactions can help instant elimination of unreacted termini at the monomers and formation of three-dimensional frameworks in thousands of degree before the polymer particles repeatedly collide, stick, and then break apart from the solution [90].

Zhou et al. have previously reported the synthesis of porous polymer network (PPN-1) with tetrakis(4-ethynylphenyl)methane (TEPM) through oxidative Eglinton coupling of terminal alkynes [87]. The as-synthesized PPN-1 significantly shrinked after guest solvent removal, clearly indicating the framework was partially collapsed due to the pressure differential. Later on, they reported a smaller tetrahedral monomer with terminal alkynes, 3,3′,5,5′-tetraethynyl-2,2′,4,4′,6,6′-hexamethyl-1,1′-biphenyl (THMB) [91].The distance from the center of monomer to the terminal alkyne carbon reduced from ~7.0 Å in TEPM to ~5.5 Å in THMB, which leads to the significant decrease of simulated unit cell parameters. Although monomer based on biphenyl ring is not perfectly tetrahedral, the 2,2′,6,6′-substituents can be introduced to lock the two phenyl rings into a nearly perpendicular position; therefore, a slightly distort diamond cage can be formed. By introducing tetrahedral monomers using biphenyl as backbone, a series of porous polymer networks (PPNs) have been synthesized and characterized (Fig. 7.4). Among them, PPN-13 shows BET surface

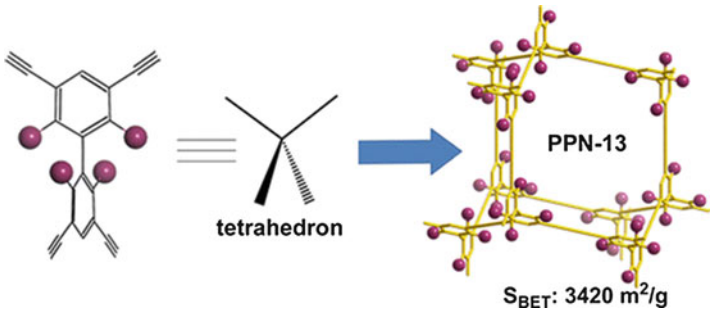

Fig. 7.4 Illustration of building tetrahedral monomer and polymerization by an Eglinton coupling reaction (Reproduced with permission from Ref. [91]. Copyright © 2014 American Chemical Society)

area of 3420 m^2/g, the total H_2-uptake capacity is 52 mg/g at 40 bar and 77 K, and the total CH_4-uptake capacity is 179 mg/g at 65 bar and 298 K. The introduction of methyl or methoxy groups at 2, 2′, 6, and 6′ positions locks two phenyl rings into perpendicular conformation and imposes the formation of three dimensional frameworks with diamondoid topology, therefore, provides widely open and interconnected pores to efficiently prevent the formation of "dead space". [91]

7.4.2 Improving Heat of Adsorption by Metal Insertion

Heat of adsorption is one of the previously overlook features in hydrogen storage materials. Here is dilemma, if this value is too high, as in metal hydrides where heats of adsorption are usually reported at around 100 kJ/mol, enormous amount energy would be required to on both hydrogen release and recharging; if this value is too low, as in the case of porous materials based on physisorption, where heats of adsorption are usually reported in the range of 5–10 kJ/mol, cryogenic cooling has to be used to keep the hydrogen inside the material and to have sufficient amount of storage capacity, which would also require large amount of extra energy. Overall, physisorption of hydrogen on porous materials shows promising properties such as high gravimetric storage, fast adsorption, and desorption kinetics.

Since the adsorption is dominated by weak van der Walls forces, high-surface-area possess very high hydrogen physisorption at cryogenic temperature, but their adsorption capacities at room temperature are rather limited due to the limited adsorption enthalpy. This is because the 5–10 kJ/mol binding enthalpies are too weak to hold the hydrogen to the surface under room temperature. For example, an enthalpy for hydrogen in the range of 15–20 kJ/mol is calculated to be suitable for hydrogen storage at room temperature, if the interaction between the material and hydrogen molecule can be strengthen. Most of the theoretical calculations are using MOF as a baseline model, probably because MOF has uniformed structure. It has been reported the adsorption of Li atoms on organic linker of MOF-5 improves the

hydrogen storage capacity [92]. If each organic linker is able to bind two Li atoms through an ionic interaction, each Li can bind up to three hydrogen molecules around itself with a binding energy of 12 kJ/mol, which is much higher than that of pure MOF-5. In the ideal situation, in which all Li sites are saturated, the storage capacity amounts to 4.3 wt% of hydrogen at 78 K and 1 bar as opposed to 1.3 wt% for the undoped MOF-5 [92].

A grand canonical Monte Carlo simulation showed that Li-doped pillared graphene can bind reversibly up to 6.5 mass% of hydrogen at 20 bar and room temperature [93], which is close to the DOE target. A similar ab initio simulation in MOF showed that doping of MOF-C30 with atomically dispersed alkali-metal leads to gravimetric hydrogen uptake of 6.0 wt% at −30 °C and 100 bar, reaching the 2010 Department of Energy target (6.0 wt% in the temperature ranges of −30 to 80 °C and pressures ≤100 bar) [94]. Even at room temperature, Li-MOF-30 leads to 5.2 wt% at 100 bar. This suggests that the doping of MOF with electropositive metals is a promising strategy for practical hydrogen storage [95].

Recently, experimental investigations also showed that H_2 uptake of the MOFs can be improved by introduction of Li^+ ions into MOF systems. For instance, an Li-doped MOF, which was prepared with lithium metal in dimethylformamide (DMF) as solvent, was reported to exhibit nearly double the hydrogen uptake compared with an undoped MOF (1.63 wt% and 0.93 wt%, respectively) at 77 K and 1 atm [96]. Additionally, the isosteric heat of adsorption, a measure of the interaction strength between hydrogen molecule and the material, is substantially greater for Li-doped MOF than MOF itself over the entire loading range [97]. Another Li-doped MOF, which was prepared by reaction of lithium diisopropylamide (LDA) on the MOF structure with pendant hydroxy groups. The low-pressure hydrogen adsorption isotherms at 77 K were measured. The adsorbed amount of hydrogen corresponds to 0.50 and 1.7 wt% at 1 bar for undoped and doped MOF, respectively. The hydrogen uptake after Li doping was increased by approximately 1.2 wt% [98].

The impact of Li^+ ion doping on hydrogen sorption was also reflected on the isosteric heat of adsorption. The values for Li-doped range from 11.6 to 6.4 kJ/mol, compared to the values from 5.8 to 4.4 kJ/mol for undoped one [98], consistent with theoretical calculations [99, 100]. The experimental data on Li-doped porous organic polymers have been much less than metal organic frameworks.

A porous polymer network (PPN) grafted with sulfonic acid (PPN-6-SO_3H) and its lithium salt (PPN-6-SO_3Li) exhibit significant increases in isosteric heats of hydrogen adsorption [79]. The extremely harsh acidic and basic conditions post-synthesis methodologies confirm their superior chemical stability of porous organic polymers that is absent in most other porous materials. Although the experimental BET surface area dropped as a result of the modifications, the H_2 adsorption enthalpy was enhanced by 47% [79]. Li et al. first synthesized a porous organic polymers (conjugated microporous polymers, CMP) by Pd^{II}/Cu^{I}-catalyzed homocoupling polymerization. Then CMP was doped with Li by immersing the CMP in a solution of the naphthalene anion radical salt in THF. They found that the storage capacity for one Li-CMP structure for hydrogen at 1 bar and 77 K is 6.1 wt%, which is one of the

highest reported to date for physisorption materials such as MOFs carbon nanotubes under the same conditions [101]. Also the isosteric heat of adsorption of Li-CMP was much improved in the whole adsorption range, especially in the higher hydrogen loading [101]. We anticipate further progress on the hydrogen storage results at higher pressures and temperatures of CMPs (Fig. 7.5).

Current experimental data and theoretical calculations are not consistent quantitatively, but are qualitatively. Cation doping has focused on lithium. The maximum of each attached lithium atom or ion can hold is two hydrogen molecules. Only very few reported that the Li-doped porous organic polymers could potentially reach the proposed heat of adsorption range (15–20 kJ/mol). Due to the greater valency of transition metal, the DOE target for heat of adsorption may be met with an unsaturated transition metal center with multiple hydrogen binding sites (up to five site per metal center) to enhance hydrogen affinity through Kubas-type interactions [102]. Generating unsaturated transition metal center inside a solid support material has not been systematically explored. Hypothetically this approach has the advantage to increase hydrogen uptake through affinity stacking. Multiple molecules are expected to be bound per metal. The single attachment of metal ions through the anchor to the material will ensure a homogeneous immobilization of the metal. Due to the small size of the metal, they will have minimal impact on the preoptimized porosity and surface area but will impact the volumetric uptake positively. A disadvantage of this approach is the synthetic procedure for transition metal incorporation which is more difficult compared to that of lithium, especially for the removal of coordinated solvent molecules to expose the metal center. For example, lithiation and metal exchange followed will generate the material containing metal sites with five potential hydrogen-binding sites per metal. The charge on the metal ion will be balanced by noncoordinating ligands such as PF_6^-, and the metal center will be stabilized within a solid porous environment (Fig. 7.6).

7.4.3 Capacity Improvement Through Material Engineering

Material engineering is an integrate part of sorbent development which directly impacts the overall storage performance. For automotive applications, volumetric and gravimetric capacities are equally important. In general, high surface area sorbents have low packing density and therefore low volumetric capacity. At packing density of 0.8 g/cm^3, the volumetric capacity can reach ~0.05 kg H_2/L with only 6 wt% gravimetric capacity. Enhancing the packing density through compression or binding techniques will also significantly improve the thermal conductivity. The heat transfer in POPs is through inefficient particle percolation or gas conduction. By pelletizing the POP powder under pressure, the particle contact hence the thermal conductivity will be substantially improved. Moreover, their thermal conductivities could also be greatly improved by blending with better heat-conducting materials

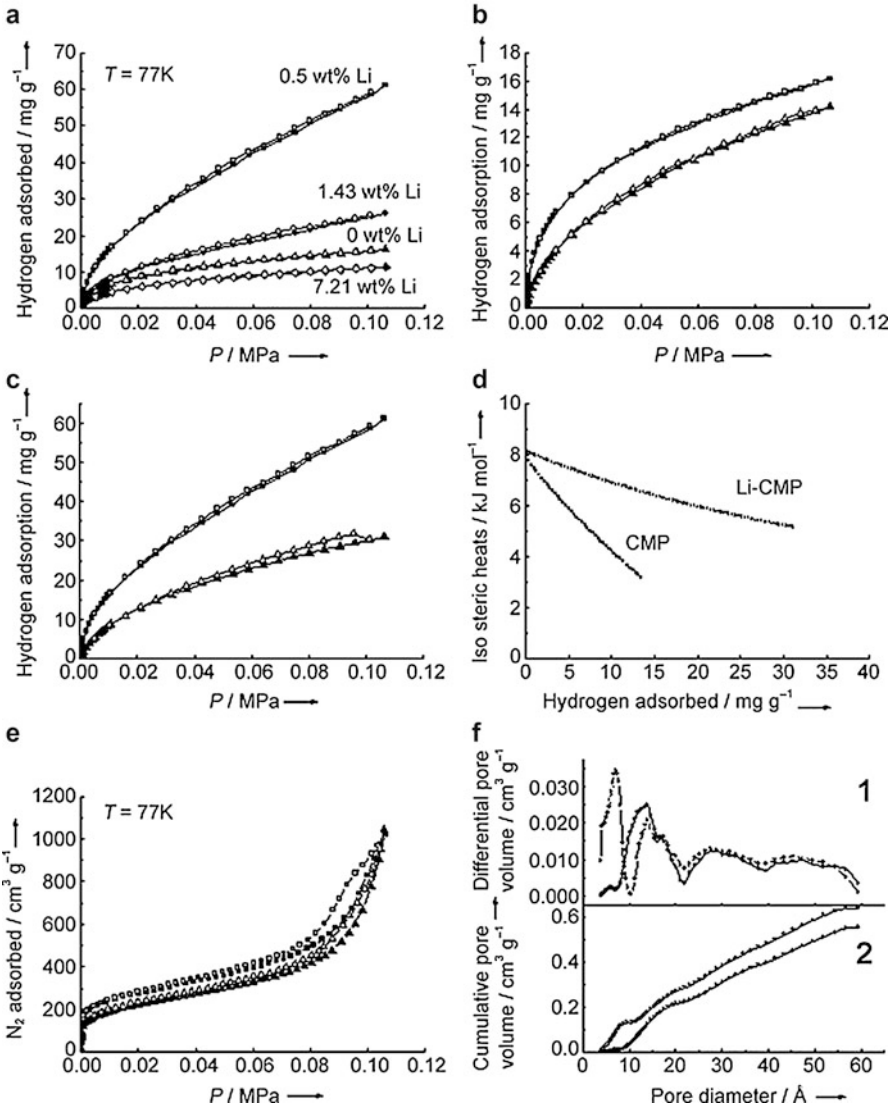

Fig. 7.5 (**a**) Hydrogen adsorption (*filled* symbols) and desorption (*empty* symbols) isotherms of the Li-CMPs with various Li contents at 77 K. (**b**) Hydrogen adsorption and desorption isotherms of the CMP at 77 K and 87 K. (**c**) Hydrogen adsorption and desorption isotherms of the Li-CMP (0.5 wt% Li). (**d**) Isosteric heats of hydrogen adsorption of CMP and Li-CMP (0.5 wt% Li). (**pi**) Nitrogen adsorption and desorption isotherms measured for CMP and Li-CMP at 77 K. (f) Pore-size distribution (1) and cumulative pore volume (2) curves of CMP and Li-CMP (Reproduced with permission from Ref. [101]. Copyright © 2010 WILEY-VCH Verlag GmbH & Co. KGaA, Weinheim)

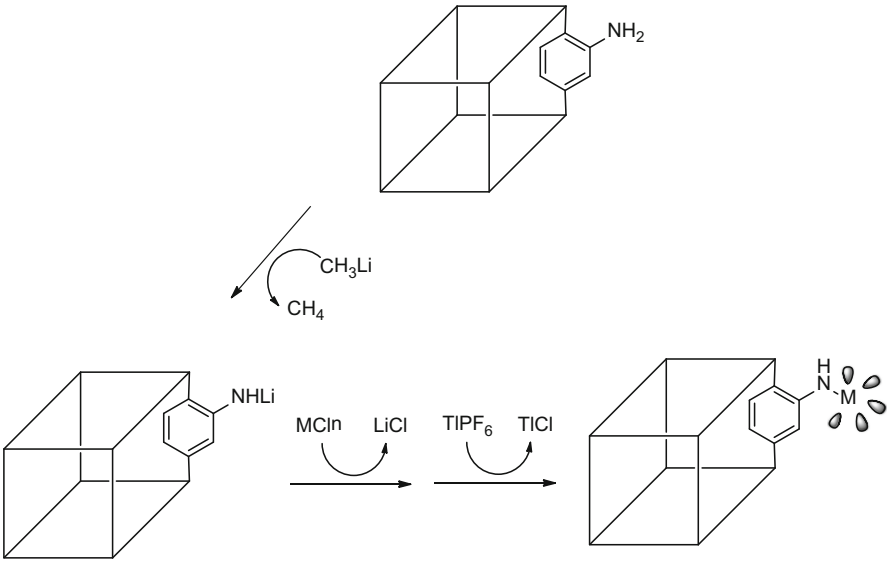

Fig. 7.6 An illustration of incorporation of high valance metal

such as carbon-based additives. A disadvantage of this approach is the loss of total storage capacity if the blended additive has a substantially lower capacity.

MOF is generally considered as soft and brittle. Individual MOF crystallites are randomly stacked in powder form. Under compression, the voids between the crystallites will collapse, followed by the destruction of the crystallites [103]. POP, although less ordered in structure, do not have these structural instabilities, are easier to process into materials, and can be made to be flexible due to their organic polymer composition. For example, after compressed at 17,000 psi, the densified PPN-4 exhibit improved total volumetric methane uptake compared to the powder.

7.5 Summary

The DOE has reduced the on-board hydrogen storage targets recently; nevertheless, these targets still pose a formidable challenge to researchers who are interested and working on hydrogen storage using MOF or POP-based materials. These materials also have the potential to significantly reduce the required storage pressure, increase gravimetric and volumetric capacity, and reduce cost.

Despite some promising results in hydrogen storage, the weak interaction between hydrogen molecule and the porous materials at ambient temperatures remains the main hurdle for its practical applications. One approach to overcome this hurdle is to use metal-to-pore with a strong and constant heat of adsorption and large enough surface area. Such microporous organic materials can be generated using POPs at ambient temperatures. This target can be achieved if theoretical

models can be improved and novel coupling methodologies introduced, some of which were reviewed in this chapter.

References

1. E.A. Rosa, T. Dietz, Human drivers of national greenhouse-gas emissions. Nat. Clim. Chang. **2**(8), 581–586 (2012)
2. J.T. Houghton, B.A. Callander, *Climate Change 1992* (Cambridge University Press, Cambridge, 1992), pp. 5–13
3. N. Oreskes, The scientific consensus on climate change. Science **306**(5702), 1686–1686 (2004)
4. R.H. Moss et al., The next generation of scenarios for climate change research and assessment. Nature **463**(7282), 747–756 (2010)
5. F. Giorgi, L.O. Mearns, Approaches to the simulation of regional climate change: a review. Rev. Geophys. **29**(2), 191–216 (1991)
6. M. Meinshausen et al., Greenhouse-gas emission targets for limiting global warming to 2 C. Nature **458**(7242), 1158–1162 (2009)
7. A.M. Omer, Energy, environment and sustainable development. Renew. Sust. Energ. Rev. **12**(9), 2265–2300 (2008)
8. D. Zhao, D. Yuan, H.-C. Zhou, The current status of hydrogen storage in metal-organic frameworks. Energy Environ. Sci. **1**(2), 222–235 (2008)
9. I. Meyer, M. Leimbach, C.C. Jaeger, International passenger transport and climate change: a sector analysis in car demand and associated CO_2 emissions from 2000 to 2050. Energy Policy **35**(12), 6332–6345 (2007)
10. M. Zieliński, R. Wojcieszak, S. Monteverdi, M. Mercy, M.M. Bettahar, Hydrogen storage in nickel catalysts supported on activated carbon. Int. J. Hydrog. Energy **32**(8), 1024–1032 (2007)
11. S. Satyapal et al., The US Department of Energy's National Hydrogen Storage Project: progress towards meeting hydrogen-powered vehicle requirements. Catal. Today **120**(3), 246–256 (2007)
12. K.M. Thomas, Hydrogen adsorption and storage on porous materials. Catal. Today **120**(3), 389–398 (2007)
13. M.G. Nijkamp et al., Hydrogen storage using physisorption–materials demands. Appl. Phys. A **72**(5), 619–623 (2001)
14. P. Jena, Materials for hydrogen storage: past, present, and future. J. Phys. Chem. Lett. **2**(3), 206–211 (2011)
15. A. Züttel, Materials for hydrogen storage. Mater. Today **6**(9), 24–33 (2003)
16. J. Yang, A. Sudik, C. Wolverton, D.J. Siegel, High capacity hydrogen storage materials: attributes for automotive applications and techniques for materials discovery. Chem. Soc. Rev. **39**(2), 656–675 (2010)
17. T.A. Makal, J.-R. Li, W. Lu, H.-C. Zhou, Methane storage in advanced porous materials. Chem. Soc. Rev. **41**(23), 7761–7779 (2012)
18. M. Bastos-Neto, C. Patzschke, M. Lange, J. Mollmer, A. Moller, S. Fichtner, C. Schrage, D. Lassig, J. Lincke, R. Staudt, H. Krautscheid, R. Glaser, Assessment of hydrogen storage by physisorption in porous materials. Energy Environ. Sci. **5**(8), 8294–8303 (2012)
19. L.J. Murray, M. Dinca, J.R. Long, Hydrogen storage in metal-organic frameworks. Chem. Soc. Rev. **38**(5), 1294–1314 (2009)
20. M.A. De la Casa-Lillo et al., Hydrogen storage in activated carbons and activated carbon fibers. J. Phys. Chem. B **106**(42), 10930–10934 (2002)
21. J. Weitkamp, M. Fritz, S. Ernst, Zeolites as media for hydrogen storage. Int. J. Hydrog. Energy **20**(12), 967–970 (1995)

22. X.S. Zhao, Q. Ma, G.Q. Lu, VOC removal: comparison of MCM-41 with hydrophobic zeolites and activated carbon. Energy Fuel **12**(6), 1051–1054 (1998)
23. C.D. Wood et al., Hydrogen storage in microporous hypercrosslinked organic polymer networks. Chem. Mater. **19**(8), 2034–2048 (2007)
24. W. Lu, Z. Wei, Z.-Y. Gu, T.-F. Liu, J. Park, J. Park, J. Tian, M. Zhang, Q. Zhang, T. Gentle Iii, M. Bosch, H.-C. Zhou, Tuning the structure and function of metal-organic frameworks via linker design. Chem. Soc. Rev. **43**(16), 5561–5593 (2014)
25. P. Kaur, J.T. Hupp, S.T. Nguyen, Porous organic polymers in catalysis: opportunities and challenges. ACS Catal. **1**(7), 819–835 (2011)
26. Y. Zhang, S.N. Riduan, Functional porous organic polymers for heterogeneous catalysis. Chem. Soc. Rev. **41**(6), 2083–2094 (2012)
27. A. Modak et al., Porphyrin based porous organic polymers: novel synthetic strategy and exceptionally high CO_2 adsorption capacity. Chem. Commun. **48**(2), 248–250 (2012)
28. H.M. El-Kaderi, J.R. Hunt, J.L. Mendoza-Cortés, A.P. Côté, R.E. Taylor, M. O'Keeffe, O.M. Yaghi, Designed synthesis of 3D covalent organic frameworks. Science **316**(5822), 268–272 (2007)
29. A.P. Côté, A.I. Benin, N.W. Ockwig, M. O'Keeffe, A.J. Matzger, O.M. Yaghi, Porous, crystalline, covalent organic frameworks. Science **310**(5751), 1166–1170 (2005)
30. P.J. Langley, J. Hulliger, Nanoporous and mesoporous organic structures: new openings for materials research. Chem. Soc. Rev. **28**(5), 279–291 (1999)
31. K.A. Cychosz, A.J. Matzger, Water stability of microporous coordination polymers and the adsorption of pharmaceuticals from water. Langmuir **26**(22), 17198–17202 (2010)
32. P.M. Schoenecker, C.G. Carson, H. Jasuja, C.J.J. Flemming, K.S. Walton, Effect of water adsorption on retention of structure and surface area of metal–organic frameworks. Ind. Eng. Chem. Res. **51**(18), 6513–6519 (2012)
33. N.B. McKeown, P.M. Budd, K.J. Msayib, B.S. Ghanem, H.J. Kingston, C.E. Tattershall, S. Makhseed, K.J. Reynolds, D. Fritsch, Polymers if intrinsic microporosity (PIMs). Chem.-Eur. J. **11**(9), 2610–2620 (2005)
34. P.M. Budd, B.S. Ghanem, S. Makhseed, N.B. McKeown, K.J. Msayib, C.E. Tattershall, Polymers of intrinsic microporosity (PIMs): robust, solution-processable, organic nanoporous materials. Chem. Commun. **2**, 230–231 (2004)
35. N.B. McKeown, P.M. Budd, Polymers of intrinsic microporosity (PIMs): organic materials for membrane separations, heterogeneous catalysis and hydrogen storage. Chem. Soc. Rev. **35**(8), 675–683 (2006)
36. J.X. Jiang, F.B. Su, A. Trewin, C.D. Wood, N.L. Campbell, H.J. Niu, C. Dickinson, A.Y. Ganin, M.J. Rosseinsky, Y.Z. Khimyak, A.I. Cooper, Conjugated microporous poly (aryleneethynylene) networks. Angew. Chem. Int. Ed. **46**(45), 8574–8578 (2007)
37. K. Gergova, N. Petrov, V. Minkova, A comparison of adsorption characteristics of various activated carbons. J. Chem. Technol. Biotechnol. **56**(1), 77–82 (1993)
38. J.X. Jiang, F. Su, A. Trewin, C.D. Wood, H. Niu, J.T.A. Jones, Y.Z. Khimyak, A.I. Cooper, Synthetic control of the pore dimension and surface area in conjugated microporous polymer and copolymer networks. J. Am. Chem. Soc. **130**(24), 7710–7720 (2008)
39. A.I. Cooper, Conjugated microporous polymers. Adv. Mater. **21**(12), 1291–1295 (2009)
40. T. Ben, H. Ren, S.Q. Ma, D.P. Cao, J.H. Lan, X.F. Jing, W.C. Wang, J. Xu, F. Deng, J.M. Simmons, S.L. Qiu, G.S. Zhu, Targeted synthesis of a porous aromatic framework with high stability and exceptionally high surface area. Angew. Chem. Int. Ed. **48**(50), 9457–9460 (2009)
41. P. Bénard, R. Chahine, Storage of hydrogen by physisorption on carbon and nanostructured materials. Scr. Mater. **56**(10), 803–808 (2007)
42. P. Bénard, R. Chahine, Modeling of adsorption storage of hydrogen on activated carbons. Int. J. Hydrog. Energy **26**(8), 849–855 (2001)
43. M.P. Suh, H.J. Park, T.K. Prasad, D.-W. Lim, Hydrogen storage in metal–organic frameworks. Chem. Rev. **112**(2), 782–835 (2012)

44. M. Sevilla, R. Mokaya, Energy storage applications of activated carbons: supercapacitors and hydrogen storage. Energy Environ. Sci. **7**(4), 1250–1280 (2014)
45. E. Poirier, R. Chahine, T.K. Bose, Hydrogen adsorption in carbon nanostructures. Int. J. Hydrog. Energy **26**(8), 831–835 (2001)
46. I. Cabria, M.J. López, J.A. Alonso, The optimum average nanopore size for hydrogen storage in carbon nanoporous materials. Carbon **45**(13), 2649–2658 (2007)
47. Y. Gogotsi et al., Importance of pore size in high-pressure hydrogen storage by porous carbons. Int. J. Hydrog. Energy **34**(15), 6314–6319 (2009)
48. I. Cabria, M.J. López, J.A. Alonso, Simulation of the hydrogen storage in nanoporous carbons with different pore shapes. Int. J. Hydrog. Energy **36**(17), 10748–10759 (2011)
49. Z. Geng, C. Zhang, D. Wang, X. Zhou, M. Cai, Pore size effects of nanoporous carbons with ultra-high surface area on high-pressure hydrogen storage. J. Energy Chem. **24**(1), 1–8 (2015)
50. F.D. Minuto et al., Liquid-like hydrogen in the micropores of commercial activated carbons. Int. J. Hydrog. Energy **40**(42), 14562–14572 (2015)
51. R. Ströbel et al., Hydrogen adsorption on carbon materials. J. Power Sources **84**(2), 221–224 (1999)
52. M. Rzepka, P. Lamp, M.A. de la Casa-Lillo, Physisorption of hydrogen on microporous carbon and carbon nanotubes. J. Phys. Chem. B **102**(52), 10894–10898 (1998)
53. B. Panella, M. Hirscher, Hydrogen physisorption in metal–organic porous crystals. Adv. Mater. **17**(5), 538–541 (2005)
54. N.L. Rosi, J. Eckert, M. Eddaoudi, D.T. Vodak, J. Kim, M. O'Keeffe, O.M. Yaghi, Hydrogen storage in microporous metal-organic frameworks. Science **300**(5622), 1127–1129 (2003)
55. J.L.C. Rowsell, O.M. Yaghi, Strategies for hydrogen storage in metal–organic frameworks. Angew. Chem. Int. Ed. **44**(30), 4670–4679 (2005)
56. J.L.C. Rowsell, A.R. Millward, K.S. Park, O.M. Yaghi, Hydrogen sorption in functionalized metal–organic frameworks. J. Am. Chem. Soc. **126**(18), 5666–5667 (2004)
57. B. Kesanli, Y. Cui, M.R. Smith, E.W. Bittner, B.C. Bockrath, W. Lin, Highly interpenetrated metal–organic frameworks for hydrogen storage. Angew. Chem. Int. Ed. **44**(1), 72–75 (2005)
58. L. Huang et al., Synthesis, morphology control, and properties of porous metal–organic coordination polymers. Microporous Mesoporous Mater. **58**(2), 105–114 (2003)
59. B. Chen et al., Hydrogen adsorption in an interpenetrated dynamic metal-organic framework. Inorg. Chem. **45**(15), 5718–5720 (2006)
60. A. Züttel, Hydrogen storage methods. Naturwissenschaften **91**(4), 157–172 (2004)
61. F. Rouquerol, J. Rouquerol, K.S.W. Sing, G. Maurin, P. Llewellyn, 1 – Introduction, in *Adsorption by Powders and Porous Solids*, ed. by F.R.R.S.W.S.L. Maurin, 2nd edn. (Academic, Oxford, 2014), pp. 1–24
62. N.T. Stetson, S. McWhorter, C.C. Ahn, 1 – Introduction to hydrogen storage, in *Compendium of Hydrogen Energy*, ed. by R.B.G.B.N. Veziroğlu (Woodhead Publishing, Cambridge, 2015), pp. 3–25
63. O.K. Farha, A. Özgür Yazaydın, I. Eryazici, C.D. Malliakas, B.G. Hauser, M.G. Kanatzidis, S.T. Nguyen, R.Q. Snurr, J.T. Hupp, De novo synthesis of a metal–organic framework material featuring ultrahigh surface area and gas storage capacities. Nat. Chem. **2**(11), 944–948 (2010)
64. H. Furukawa, N. Ko, Y.B. Go, N. Aratani, S.B. Choi, E. Choi, A.Ö. Yazaydin, R.Q. Snurr, M. O'Keeffe, J. Kim, O.M. Yaghi, Ultrahigh porosity in metal-organic frameworks. Science **329**(5990), 424–428 (2010)
65. J. Germain, J.M.J. Fréchet, F. Svec, Nanoporous polymers for hydrogen storage. Small **5.10**, 1098–1111 (2009)
66. Y.-S. Bae, R.Q. Snurr, Optimal isosteric heat of adsorption for hydrogen storage and delivery using metal–organic frameworks. Microporous Mesoporous Mater. **132**(1–2), 300–303 (2010)
67. S.K. Bhatia, A.L. Myers, Optimum conditions for adsorptive storage. Langmuir **22**(4), 1688–1700 (2006)
68. O.M. Yaghi, M. O'Keeffe, N.W. Ockwig, H.K. Chae, M. Eddaoudi, J. Kim, Reticular synthesis and the design of new materials. Nature **423**(6941), 705–714 (2003)

69. N.W. Ockwig, O. Delgado-Friedrichs, M. O'Keeffe, O.M. Yaghi, Reticular chemistry: occurrence and taxonomy of nets and grammar for the design of frameworks. Acc. Chem. Res. **38** (3), 176–182 (2005)
70. M. O'Keeffe, Design of MOFs and intellectual content in reticular chemistry: a personal view. Chem. Soc. Rev. **38**(5), 1215–1217 (2009)
71. D. Wu, F. Xu, B. Sun, R. Fu, H. He, K. Matyjaszewski, Design and preparation of porous polymers. Chem. Rev. **112**(7), 3959–4015 (2012)
72. R. Dawson, A.I. Cooper, D.J. Adams, Nanoporous organic polymer networks. Prog. Polym. Sci. **37**(4), 530–563 (2012)
73. H.-C. Zhou, J.R. Long, O.M. Yaghi, Introduction to metal–organic frameworks. Chem. Rev. **112**(2), 673–674 (2012)
74. O.K. Farha, I. Eryazici, N.C. Jeong, B.G. Hauser, C.E. Wilmer, A.A. Sarjeant, R.Q. Snurr, S.T. Nguyen, A.Ö. Yazaydın, J.T. Hupp, Metal–organic framework materials with ultrahigh surface areas: is the sky the limit? J. Am. Chem. Soc. **134**(36), 15016–15021 (2012)
75. N. Stock, S. Biswas, Synthesis of metal-organic frameworks (MOFs): routes to various MOF topologies, morphologies, and composites. Chem. Rev. **112**(2), 933–969 (2011)
76. W. Lu, W.M. Verdegaal, J. Yu, P.B. Balbuena, H.-K. Jeong, H.-C. Zhou, Building multiple adsorption sites in porous polymer networks for carbon capture applications. Energy Environ. Sci. **6**(12), 3559–3564 (2013)
77. W. Lu, J.P. Sculley, D. Yuan, R. Krishna, H.-C. Zhou, Carbon dioxide capture from air using amine-grafted porous polymer networks. J. Phys. Chem. C **117**(8), 4057–4061 (2013)
78. W. Lu, J.P. Sculley, D. Yuan, R. Krishna, Z. Wei, H.-C. Zhou, Polyamine-tethered porous polymer networks for carbon dioxide capture from flue gas. Angew. Chem. Int. Ed. **51**(30), 7480–7484 (2012)
79. W. Lu, D. Yuan, J. Sculley, D. Zhao, R. Krishna, H.-C. Zhou, Sulfonate-grafted porous polymer networks for preferential CO_2 adsorption at low pressure. J. Am. Chem. Soc. **133** (45), 18126–18129 (2011)
80. W. Lu, M. Bosch, D. Yuan, H.-C. Zhou, Cost-effective synthesis of amine-tethered porous materials for carbon capture. ChemSusChem **8**(3), 433–438 (2015)
81. W.-C. Xu et al., Investigation of hydrogen storage capacity of various carbon materials. Int. J. Hydrog. Energy **32**(13), 2504–2512 (2007)
82. T. Ben, H. Ren, S. Ma, D. Cao, J. Lan, X. Jing, W. Wang, J. Xu, F. Deng, J.M. Simmons, S. Qiu, G. Zhu, Targeted synthesis of a porous aromatic framework with high stability and exceptionally high surface area. Angew. Chem. Int. Ed. **48**(50), 9457–9460 (2009)
83. A. Trewin, A.I. Cooper, Porous organic polymers: distinction from disorder? Angew. Chem. Int. Ed. **49**(9), 1533–1535 (2010)
84. D. Yuan, W. Lu, D. Zhao, H.-C. Zhou, Highly stable porous polymer networks with exceptionally high gas-uptake capacities. Adv. Mater. **23**(32), 3723–3725 (2011)
85. B. Chen, M. Eddaoudi, S.T. Hyde, M. O'Keeffe, O.M. Yaghi, Interwoven metal-organic framework on a periodic minimal surface with extra-large pores. Science **291**(5506), 1021–1023 (2001)
86. J.K. Schnobrich, K. Koh, K.N. Sura, A.J. Matzger, A framework for predicting surface areas in microporous coordination polymers. Langmuir **26**(8), 5808–5814 (2010)
87. W. Lu, D. Yuan, D. Zhao, C.I. Schilling, O. Plietzsch, T. Muller, S. Bräse, J. Guenther, J. Blümel, R. Krishna, Z. Li, H.-C. Zhou, Porous polymer networks: synthesis, porosity, and applications in gas storage/separation. Chem. Mater. **22**(21), 5964–5972 (2010)
88. J. Schmidt, M. Werner, A. Thomas, Conjugated microporous polymer networks via Yamamoto polymerization. Macromolecules **42**(13), 4426–4429 (2009)
89. J.-F. Lutz, Z. Zarafshani, Efficient construction of therapeutics, bioconjugates, biomaterials and bioactive surfaces using azide–alkyne "click" chemistry. Adv. Drug Deliv. Rev. **60**(9), 958–970 (2008)
90. T. Muller, S. Bräse, Click chemistry finds its way into covalent porous organic materials. Angew. Chem. Int. Ed. **50**(50), 11844–11845 (2011)

91. W. Lu, Z. Wei, D. Yuan, J. Tian, S. Fordham, H.-C. Zhou, Rational design and synthesis of porous polymer networks: toward high surface area. Chem. Mater. **26**(15), 4589–4597 (2014)
92. A. Blomqvist, C.M. Araújo, P. Srepusharawoot, R. Ahuja, Li-decorated metal–organic framework 5: a route to achieving a suitable hydrogen storage medium. Proc. Natl. Acad. Sci. **104** (51), 20173–20176 (2007)
93. W.-Q. Deng, X. Xu, W.A. Goddard, New alkali doped pillared carbon materials designed to achieve practical reversible hydrogen storage for transportation. Phys. Rev. Lett. **92**(16), 166103 (2004)
94. J.J. Bozell, G.R. Petersen, Technology development for the production of biobased products from biorefinery carbohydrates – the US Department of Energy's "top 10" revisited. Green Chem. **12**(4), 539–554 (2010)
95. S.S. Han, W.A. Goddard, Lithium-doped metal-organic frameworks for reversible H_2 storage at ambient temperature. J. Am. Chem. Soc. **129**(27), 8422–8423 (2007)
96. K.L. Mulfort et al., Framework reduction and alkali-metal doping of a triply catenating metal – organic framework enhances and then diminishes H_2 uptake. Langmuir **25.1**, 503–508 (2008)
97. K.L. Mulfort, J.T. Hupp, Chemical reduction of metal–organic framework materials as a method to enhance gas uptake and binding. J. Am. Chem. Soc. **129**(31), 9604–9605 (2007)
98. D. Himsl, D. Wallacher, M. Hartmann, Improving the hydrogen-adsorption properties of a hydroxy-modified MIL-53(Al) structural analogue by lithium doping. Angew. Chem. Int. Ed. **48**(25), 4639–4642 (2009)
99. A. Mavrandonakis, E. Klontzas, E. Tylianakis, G.E. Froudakis, Enhancement of hydrogen adsorption in metal–organic frameworks by the incorporation of the sulfonate group and Li cations. A multiscale computational study. J. Am. Chem. Soc. **131**(37), 13410–13414 (2009)
100. A. Mavrandonakis, E. Tylianakis, A.K. Stubos, G.E. Froudakis, Why Li doping in MOFs enhances H_2 storage capacity? A multi-scale theoretical study. J. Phys. Chem. C **112**(18), 7290–7294 (2008)
101. A. Li, R.-F. Lu, Y. Wang, X. Wang, K.-L. Han, W.-Q. Deng, Lithium-doped conjugated microporous polymers for reversible hydrogen storage. Angew. Chem. Int. Ed. **49**(19), 3330–3333 (2010)
102. G. Kim et al., Crossover between multipole Coulomb and Kubas interactions in hydrogen adsorption on metal-graphene complexes. Phys. Rev. B **79.15**, 155437 (2009)
103. A.G. Slater, A.I. Cooper, Function-led design of new porous materials. Science 348(6238) (2015). doi:10.1126/science.aaa8075

Metal Hydrides used for Hydrogen Storage

8

Sesha S. Srinivasan and Dervis Emre Demirocak

Abstract

This chapter discusses about metal hydride technologies for on-board reversible hydrogen storage applications. The metal hydrides such as intermetallic alloys and solid solutions have interstitial vacancies where atomic hydrogen is absorbed via an exothermic reaction; however, by endothermic path, the metal hydride desorbs the hydrogen reversibly at ambient to moderate temperatures. In any case, the hydrogen storage capacity of interstitial metal hydrides is rather low (<2 wt%) due to limitation in the crystal structure and unit cell volume. In order to increase the hydrogen storage densities, transition metal assisted Mg-based hydrides and other nontransition metal complex hydrides have been reviewed as part of exploratory studies which have been aligned with the US Department of Energy 2020 technical targets. A number of useful characterization techniques (X-ray diffraction, scanning electron microscopy, energy dispersive spectroscopy, thermo gravimetric analysis, differential scanning calorimetry, Fourier transform infrared spectroscopy) and hydrogen storage property measurements (kinetics, pressure-composition isotherms, thermal programmed desorption, gas chromatography-mass spectrometry) have been employed for the investigation of some candidate materials.

Author Contribution: Both authors of this book chapter equally contributed in developing this book chapter and associated prior-art and results. The results and data provided in this chapter are original and not reproduced from any other publications.

S.S. Srinivasan (✉)
College of Innovation and Technology, Florida Polytechnic University, Lakeland, USA
e-mail: ssrinivasan@flpoly.org

D.E. Demirocak
Department of Mechanical and Industrial Engineering, Texas A&M University-Kingsville, Kingsville, USA
e-mail: dervis.demirocak@tamuk.edu

Y.-P. Chen et al. (eds.), *Nanostructured Materials for Next-Generation Energy Storage and Conversion*, DOI 10.1007/978-3-662-53514-1_8

Contents

8.1 Metal Hydrides Fundamentals

Hydrogen storage by metal hydrides comprises an intermetallic alloy phase that has the capability to absorb and hold hydrogen through chemical bondings [1]. An appropriate hydrogen storage matrix should have the capacity to absorb and release hydrogen without compromising the matrix structure. Metal hydrides are prepared by reaction between a metallic phase and hydrogen ($M_m^{\delta+} + H_2 \rightarrow [MH_x]^{\delta-}$ where m, x, $\delta = 1$, 2, 3) or covalent hydride formation $2\ LiAlH_4 + BeCl_2 \rightarrow 2\ AlH_3 + Li_2BeH_2Cl_2$ as opposed to an ionic hydride [$R(O)CH_3 + KH \rightarrow R(O)CH_2K + H_2$]. When exposed to hydrogen at certain pressures and temperatures, these phases absorb large quantities of hydrogen gas and form the corresponding metal hydrides. If this is the scenario, the hydrogen is distributed compactly throughout the intermetallic lattice. Metal hydrides represent an exciting process of hydrogen storage which is inherently safer than the compressed gas or liquid hydrogen storage. Additionally, some intermetallics (including metals and alloys) store hydrogen at a higher volume density than liquid hydrogen (see Table 8.1 below).

The qualities required to make these intermetallic alloys useful include the facility to absorb and release large amounts of hydrogen gas, many times without damaging the storage material and with good selectivity (only hydrogen absorption).

Table 8.1 Theoretical capacities of hydriding substances as hydrogen storage media

Medium	Hydrogen content, kg/kg	Hydrogen storage capacity, kg/L of vol.	Energy density, kJ/kg	Energy density, kJ/L of vol.
MgH_2	0.070	0.101	9,933	14,330
Mg_2NiH_4	0.0316	0.081	4,484	11,494
VH_2	0.0207		3,831	
$FeTiH_{1.95}$	0.0175	0.096	2,483	13,620
$TiFe_{0.7}Mn_{0.2}H_{1.9}$	0.0172	0.090	2,440	12,770
$LaNi_5H_{7.0}$	0.0137	0.089	1,944	12,630
$MmNi_5H_{6.5}$	0.0135	0.090	1,915	12,770
Liquid H_2	1.00	0.071	141,900	10,075
Gaseous H_2 (100 bar)	1.00	0.0083	141,900	1,170
Gaseous H_2 (200 bar)	1.00	0.0166	141,900	2,340
Gasoline	–	–	47,300	35,500

Moreover, suitable metal hydrides absorb and release hydrogen at rates that can be controlled by adjusting temperature and/or pressure.

As mentioned in ▶ Chap. 2, a typical relation of metal hydrides with hydrogen can be expressed in Eq. 8.1

$$M + \frac{x}{2}H_2 \leftrightarrow MH_x + \Delta H \tag{8.1}$$

where M represents the intermetallic matrix and H is hydrogen. The effect is reversible and the direction is determined by the pressure (and temperature) of the hydrogen gas. If the pressure is above a certain level (the equilibrium pressure), the effect proceeds to the right to form hydride, whereas below the equilibrium pressure, hydrogen is liberated and the intermetallic matrix returns to its original state. The equilibrium pressure, itself, depends upon temperature. It increases due to expansion with an increment in temperature (and vice versa). Note the hydride ion has a strong reducing potential [$H_2 + 2\bar{e} \leftrightarrow 2H^-$; $E^o = -2.25$ V] and chemically it is a Lewis base.

8.2 Classification of the Hydrides

In general, hydrides are classified according to the nature of the bonding of hydrogen to the host lattice such as covalent, saline or ionic, and metallic, all of these classes bearing different bonding characteristics [2]. Such a classification does not always clarify the characteristic features of the compound in question. For example, lithium hydride is classified as a saline hydride, where in reality it actually exhibits some covalent characteristics. The rare-earth hydrides are normally classified in the metallic hydride group, whereas they exhibit some characteristics similar to those of volatile and saline hydrides (e.g., high heat of formation).

8.2.1 Ionic Hydrides

Ionic hydrides are created by reaction between a strongly electro-positive alkali (or alkaline-earth) metal and hydrogen, which becomes strongly electronegative because of the electron transfer. Contrary to the covalent hydrides, the bonding in the ionic hydrides results from the strong electrostatic forces between the dissimilar charges of the two different ions. The ionic hydrides are usually crystalline and show high heat formation and high melting points. The ionic alkali and alkaline earth hydrides have a higher density than the pure alkali (45–75%) and alkaline-earth metals (20–25%) [3].

8.2.2 Covalent Hydrides

Covalent hydrides are found in the solid, liquid, or gaseous phases. The bonding between hydrogen and the other constituents is characterized by sharing of valence electrons on a relatively equal basis. In general, molecules with covalent bonding are not strongly attracted to each other. The lack of strong intermolecular forces yields a degree of volatility and a low melting point. Covalent hydrides are generally thermally unstable, and this instability goes up with increasing atomic weight of the nonhydrogen element(s). Typical covalent hydrides are carbon hydrides, boron hydrides, germanium hydrides, etc. Covalent hydrides normally exhibit low symmetric structures.

8.2.3 Metallic Hydrides

Metallic hydrides are normally formed by the transition metals, for example, ScH_2. They generally exhibit metallic characteristic properties such as high thermal and electrical conductivity, hardness, luster. Due to the wide homogeneity ranges adopted by metallic hydrides, they have occasionally been considered as solid solutions of hydrogen in the interstitials of metal, alloy, or intermetallic matrices.

8.3 Metal Hydride Formation

Hydrogen can be packed and stored in a solid state by forming metal hydride [4–12]. During the formation of the metal hydride, hydrogen molecules are dissociated into hydrogen atoms which insert themselves into interstitial spaces inside the lattice of intermetallic compounds and/or alloys (Fig. 8.1).

At a large distance from the metal surface, the energy difference between a hydrogen molecule and two separate hydrogen atoms is the dissociation energy ($H_2 \rightarrow 2H$, $E_D = 435.99\ kJ \cdot mol^{-1}$). The first attractive interaction of the hydrogen molecule approaching the metal surface is the Van der Waals force leading to the physisorbed state ($E_{Phys} \approx 10\ kJ \cdot mol^{-1}$) more or less one hydrogen molecule radius (≈0.2 nm) from the metal surface. Closer to the surface the hydrogen has to overcome an activation barrier in order to dissociate and create the hydrogen metal

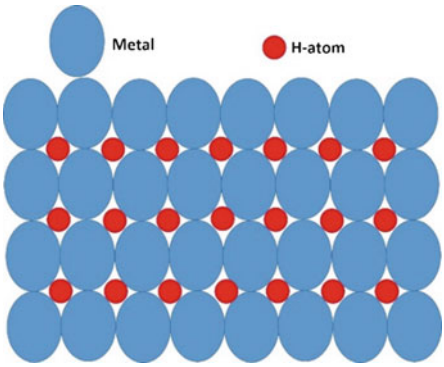

Fig. 8.1 Hydrogen in atomic form on interstitial lattice sites of an intermetallic alloy (Redrawn with permission from Ref. [13]. Copyright John Wiley & Sons)

bond. The height of the activation barrier depends on the surface elements involved. Hydrogen atoms sharing their electrons with the metal atoms at the surface are in the chemisorbed (C_{hem}) state ($E_{Chem} \approx 50$ kJ $\cdot$ mol^{-1} $\cdot$ H_2). The chemisorbed hydrogen atoms may have a high surface mobility, interact with each other, and form surface phases at considerably high coverage. In the following step, the chemisorbed hydrogen atoms can jump into the subsurface layer and finally diffuse to interstitial sites through the host metal lattice. An interstitial hydrogen atom contributes its electron to the band structure of the metal; this process is depicted in Fig. 8.1.

In an Van't Hoff equilibrium to concentration phase diagram, the first region representing the solid solution is also known as the α-phase, due to diffusion of gaseous hydrogen into the interstices; here the hydrogen concentration or its ratio to metal is small ($H/M < 0.1$) and hydrogen is exothermically dissolved in the metal. The metal lattice expands relative to the hydrogen concentration by approximately 2–3 Å^3 per hydrogen atom [14]. At greater hydrogen concentrations in the host metal ($H/M > 0.1$, calculated as equal to $K_sP^{½}$, where K_s is the Sievert constant, mol m^{-3} Pa$^{0.5}$ and P is the pressure, pa) a strong H-H interaction due to the lattice expansion becomes significant and the hydride phase (β-phase) nucleates and grows. The hydrogen concentration in the hydride phase is commonly found to be $H/M = 1$.

The volume expansion between the coexisting α- and the β-phase [15] corresponds in many cases 10–20% of the metal lattice. Therefore, at the phase boundary, large stresses are created that frequently lead to a decrepitation of brittle host metals including intermetallic compounds, resulting in a final hydride powder with a representative particle size of 10–100 μm.

8.4 Metal Hydride properties

8.4.1 Pressure–Composition–Temperature (PCT)

An idealized representation of pressure–concentration–temperature isotherms for α solid solution phase and β hydride phase is shown in Fig. 8.2. A plateau is observed on the pressure versus hydrogen/metal ratio for fixed temperature. When the reaction

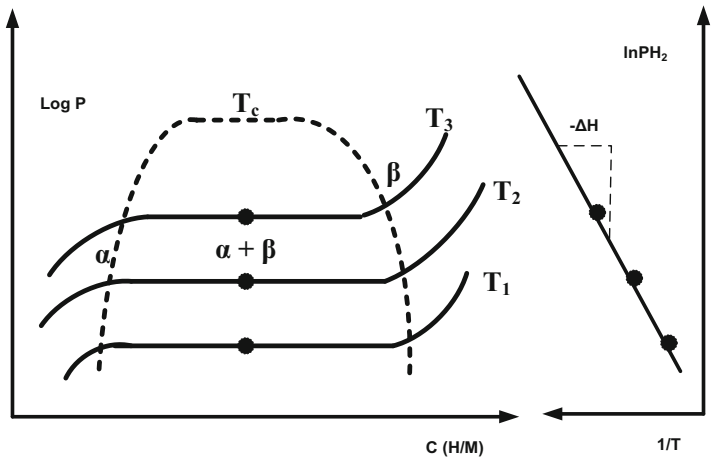

Fig. 8.2 Effect of temperature on the general features of the P-C isotherms (Reprinted with permission from Ref. [13]. Copyright John Wiley & Sons)

is complete, another sharp pressure rise is seen if more hydrogen is added. At a certain temperature, the plateau pressure reflects one point on a pressure–temperature (Van't Hoff) plot. The log of pressure versus reciprocal temperature is linear with a negative slope and is related to the heat of reaction (heat of hydriding); the plateau pressures must increase with temperature due to the linear relationship between pressure and temperature.

An increment in isothermal temperature causes the plateau pressure to increase and, at the same time, reduces the width of the plateau which represents the miscibility regime of the α- and β-phase. This narrowing process of the plateau with increasing of temperature continues until, eventually, at a certain "critical temperature," T_c, the plateau disappears totally, reducing the miscibility of the two phases to zero, and the α- phase converts continuously into the β-phase. The slope and length of the equilibrium plateau is of particular importance for hydrogen storage application; a flat plateau enables the reversible absorption and desorption of hydrogen from a metal simply by raising or lowering the surrounding hydrogen pressure above or below the plateau pressure.

The equilibrium pressure as a function of temperature is related to the changes ΔH and ΔS of enthalpy and entropy, in that order, by the Van't Hoff equation [16–18].

$$\ln\left[\frac{P(H_2)}{P^0}\right] = \frac{\Delta H}{RT} - \frac{\Delta S}{R} \tag{8.2}$$

where $P(H_2)$ is the hydrogen equilibrium pressure at α to β hydride phase conversion, determined from pressure–composition–temperature (PCT) isotherms; P° is the standard pressure (Pa), R is the ideal gas constant (8.314 m^3 Pa.mol^{-1} K^{-1}), and T is the absolute temperature (K). The enthalpy, ΔH, of hydride formation is an important parameter characterizing the alloy as a proper hydrogen absorber for various applications. In general, the difference in standard entropy (ΔS, J mol^{-1} K^{-1})

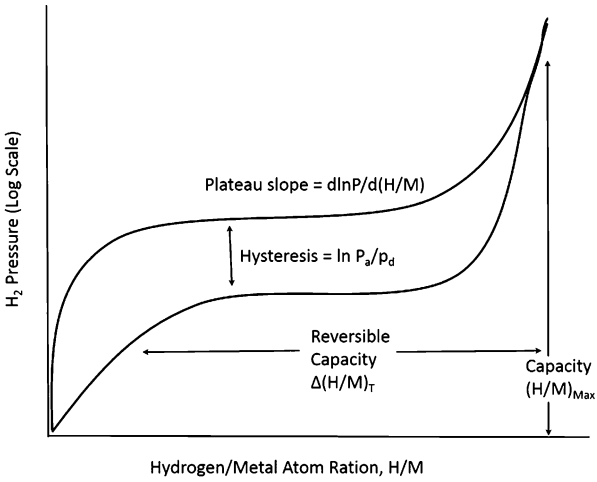

Fig. 8.3 Plateau pressure and hysteresis effect in a real metal hydride (Redrawn from Ref. [8]. Copyright Pergamon Press)

between a metal hydride alloy and its hydride is small and is on the order of 10 J mol^{-1} K^{-1}. The modification in entropy with hydride formation is mainly provided by the loss of the standard entropy of hydrogen gas (130.858 J · mol^{-1} · K^{-1} at 298 K), which means that ΔS can be assumed to be a constant and does not depend on the nature of the metal hydride alloy [2]. The knowledge of ΔH (kJ mol^{-1}) particularly is significant to the management of heat needed for practical engineering devices and is a fundamental measure of the M–H bond strength. The Van't Hoff plot (ln P vs 1/T) is a practical way to compare hydrides due to their thermal stabilities.

Most practical hydriding metals do not show perfectly flat plateau or zero hysteresis [19] due to defects in the lattice or disorder in the atomic arrangement which creates slightly different potential for crystallographically identical interstitial sites and the irreversible elastic after-effects [20]. Figure 8.3 represents real metal hydrides PCT plot including the mathematical and numerical definitions of hysteresis, plateau slope, and hydrogen storage capacity. In particular, there are a few ways to show the H-capacity. The reversible capacity, $\Delta(H/M)_r$, is defined as the plateau width, which can be considerably less than the maximum capacity, $(H/M)_{max}$. In practice, depending on available pressure and temperature ranges, engineering capacity is frequently somewhere between $\Delta(H/M)_r$ and $(H/M)_{max}$. Hydrogen storage capacity can be shown in either atomic H/M ratio or weight percent. In calculating weight-percent (wt%), both H and M (not only M) are included in the denominator. Adding up, it is sometimes useful to express capacity in volumetric terms, for example, number of H atoms per unit volume.

8.4.2 Activation and Decrepitation

The process needed to hydride a metal for the first time and bring it up to maximum H-capacity and hydriding/dehydriding kinetics is called activation. The ease of

initial H_2-penetration depends on surface structures and barriers, such as dissociation, catalytic species, and oxide layers. A second stage of activation involves internal cracking of metal particles to amplify reaction surface area. This process is the self-pulverization of large metal particles into powder, a common phenomenon that comes about from a combination of a change in the hydriding volume and the brittle characteristic of hydriding alloys (especially when they contain some H in solution) [21]. The morphology of the decrepitated powder affects heat transfer as well as the tendency of powder migration into undesirable places like valve seats. A disadvantage is that most hydride powders have poor heat transfer coefficients and require engineering means for thermal enhancement, for example, by using Al foam, internal fins, etc. The morphology of the powder can have an effect on packing, which in turn can lead to internal gas impedance and container deformation.

8.4.3 Kinetics of Hydriding and Dehydriding

In order to keep the weight and volume of hydride small, it is very important to maintain short cycle times for loading and unloading hydrogen. Heat transfer has been shown to be the rate limiting process controlling hydrogen uptake or removal. This is the result of the low-conductivity of the finely divided powder and poor heat transfer between the particles and the container wall [21]. Hydrogen flow is not rapid enough to decrease these heat transfer resistances. Supper and coworkers [22] showed that it is just as important to improve both the heat transfer and the hydrogen flow to achieve high gas transfer. The most common method to evaluate the kinetics of a material is simply to measure the concentration of hydrogen absorbed or desorbed versus time, but there are some factors that could effect this measurement, such as quantity of sample, sample shape, porosity, thermal (bulk and grain-to-grain) conductivity, thermal contact with the sample holder, size distributions of particles, particle shape, applied hydrogen overpressure, and the purity of the gas.

8.4.4 Gaseous Impurity Resistance

There can be several types of damage and degradation of performance due to the alloy-impurity concentrations [23]. (1) Poisoning, where capacity is rapidly lost without a concurrent decrease of initial kinetics; (2) retardation, where kinetics are quickly lost without loss of ultimate capacity; (3) reaction, where the alloy is slowly corroded; (4) innocuous, where there is no surface damage, but there can be pseudo-kinetic decreases due to inert gas blanketing, an interparticle gas diffusion problem. Damages from poisoning and retardation are for the most part recoverable in contrast to reaction damages that are usually unrecoverable.

8.4.5 Cyclic Stability, Alloy Cost, and Safety

This property is referred to the repeatability of the hydride/dehydride process and widely varies for different alloys or compounds [24]. Alloys and intermetallic compounds are normally metastable relative to disproportionation, the tendency to break up metallurgically to form stable, not easily reversible hydrides. Even if very pure H_2 is used, disproportion can occur with a resultant loss of reversible capacity. The alloys cost has been influenced by several factors, which include raw materials cost, melting and annealing costs, and metallurgical complexities the degree of PCT precision required for the specific application. Safety usually centers on pyrophoricity, the tendency for a hydride powder to burn when suddenly exposed to air, such as an accidental tank rupture. But the term can also include toxicity that results from accidental ingestion or inhalation.

8.5 Metal Hydride Families

An overview of hydrogen storage alloys has been discussed from the solid-gas reaction point of view [14]. There are a number of important properties that must be considered in metal hydride storage. Some of the most important ones are: (a) ease of activation, (b) heat transfer rate, (c) kinetics of hydriding and dehydriding, (d) resistance to gaseous impurities, (e) cyclic stability, (f) safety, and (g) weight and cost. Although metal hydrides can theoretically store large amounts of hydrogen in a safe and compact way, the practical gravimetric hydrogen density is limited to <3 mass%. It is still a challenge to explore the properties of lightweight metal and complex hydrides. Hydrogen is a highly reactive element and has been found to form hydrides and solid solutions with thousands of metals and alloys [14]. A hydride "family tree" of the elements, alloys, and complexes is shown in Fig. 8.4.

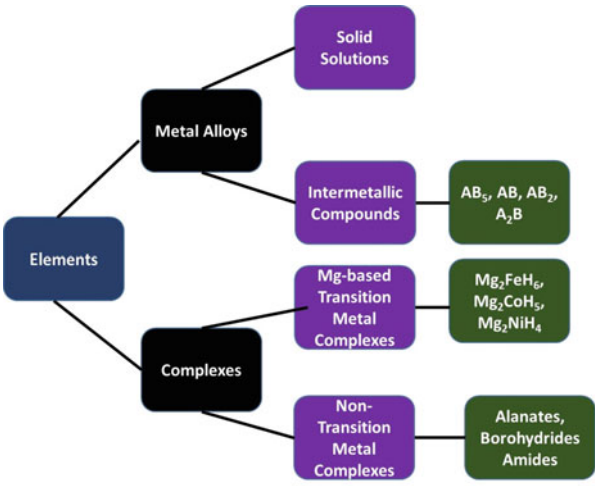

Fig. 8.4 Family tree of the elements, alloys, and complexes

8.5.1 Elements

The majority of the 91 natural elements below hydrogen in the periodic table will form hydrides such as, VH_2, NaH, LaH_2, ZrH_2 under appropriate conditions. Unfortunately the PCT properties are not very suitable for the 1–10 atm, 0–100 °C range used for practical hydrogen storage. Only vanadium (V) is in the range and there has been extensive study of solid solutions of V and other metals. Palladium (Pd) has been used for over 100 years for H-storage, but it is very costly, it does not absorb much H, and it requires heating temperatures above 100 °C to release atomic hydrogen.

8.5.2 Alloys

To prepare useful reversible hydrides, strong hydride-forming elements A are combined with weak hydriding elements B to form alloys (especially intermetallic compounds) that have the desired intermediate thermodynamic affinities for hydrogen. A good example of this characteristic is the combination of La (forming LaH_2 with 25 °C, $P_d = 3 \times 10^{-29}$ atm and $\Delta H_f = -208$ kJ·mol^{-1} H_2) with Ni (NiH, 25 °C, $P_d = 3{,}400$ atm, $\Delta H_f = -8.8$ kJ mol^{-1} H_2) to form the intermetallic compound $LaNi_5$ ($LaNi_5H_6$, 25 °C, $P_d = 1.6$ atm, $\Delta H_f = -30.9$ kJ mol^{-1} H_2). This ability to "interpolate" between the extremes of elemental hydriding behavior opened the door to the modern world of reversible hydrides.

8.5.3 AB_5 Intermetallic Compounds

The AB_5 family has an exceptional versatility because many different elemental species can be substituted (at least partially) into the A and B lattice sites. A-elements tend to be one or more of the lanthanides (elements 57–71; less familiar elements are named), calcium (Ca), or other elements such as yttrium (Y), zirconium (Zr). The B-elements are based on Ni with many other possible substitutional elements such as Co, Al, manganese (Mn), Fe, Cu, tin (Sn), Si, Ti. Modern commercial AB_5 hydriding alloys are for the most part based on the use of the lanthanide mixture or "mixed metal" (mischmetal, Mm = cerium (Ce) + lanthanum (La) + neodymium (Nd) + praseodymium (Pr)) for the A site and Ni + Al + Mn + Co+, etc., on the B-site.

Hydrogen storage capacity is less than 1.3 wt% on the plateau basis. Alloy raw material cost is high, at least by comparison to other systems (AB_2 and AB) that are discussed below; the AB_5 alloys are easy to activate, hardly requiring any heating. They decrepitate (an inclusion within a crystal disintegrates upon heating at a specific temperature, T_{dec}) on the 1st H/D cycle to fine powder which is mildly pyrophoric (liable to ignite spontaneously) if suddenly exposed to air, a well-known property that must be included in safety considerations. Both easy activation and pyrophoricity indicate the AB_5 alloys do not form defensive oxide layers. Intrinsic kinetics of the AB_5 alloys is generally very good.

8.5.4 AB_2 Intermetallic Compounds

Like the AB_5 compounds, the AB_2 intermetallics represent a large and versatile group of hydriding materials with good PCT properties at ambient temperature. The A-elements are often from the IVA group (Ti, Zr, hafnium, (Hf)) and/or rare earth series (elements 57–71). The B-elements can be a variety of transition or non-transition metals with somewhat of a preference for atomic numbers 23–26 (V, Cr, Mn, Fe). A large variety of substitutions are possible for both A- and B-elements, thus providing a high degree of fine tuning of PCT properties.

The decisive advantages with regard to hydrogen storage and related thermal applications are high hydrogen capacity, ease of activation, very rapid rates of absorption and desorption, long cycling life, and low cost of materials. The main disadvantages for hydrogen storage are high ΔH values (moderate stabilities of hydrides). These properties make these compounds good for hydrogen compression applications. An excellent example is $ZrMn_2$ that contents 3.6 atoms of hydrogen and $\Delta H = -53.0$ kJ mol^{-1} H_2, showing a high hydrogen content and a high T_{dec}, related to the high ΔH [25]. The high T_{dec} and the high hydrogen content make this compound good for hydrogen compression.

Method of preparing an alloy of zirconium and manganese suitable for storing hydrogen consists of two steps [26]: making an intimate mixture of Zr and Mn in correct stoichiometric ratio and heating the sample between 900 °C and 1,150 °C. The intimate mixture is done using a straightforward, repeatable, and inexpensive procedure, ball milling under H_2 atmosphere. The annealing was applied for 10 h in a helium atmosphere at 1,100 °C.

Figure 8.5 demonstrates the representative X-ray diffraction profiles of Zr-Mn mixtures subjected to ball milling and subsequent annealing. The Zr-Mn mixtures ball milled for two different milling duration (10 h and 24 h) exhibit identical X-ray patterns with a diffraction peak from the (411) Mn lattice plane. However, for the case of 24 h ball milled and annealed sample at 1,100 °C, in addition to Mn reflections, peaks correspond to $ZrMn_2$ and ZrO_2 are indexed with the increasing crystallinity. Ball mill induced nanocrystallization and subsequent annealing at high temperature, thus improves the formation of $ZrMn_2$ intermetallic phase.

8.5.5 AB Intermetallic Compounds

The first example of a reversible intermetallic hydride was demonstrated with the AB compound, ZrNi by Libowitz in 1957 [27]. The hydride $ZrNiH_3$ has a 1 atm desorption temperature of about 300 °C, too high for hydrogen storage applications but suitable for hydrogen compression. These intermetallic alloys show good volumetric and gravimetric reversible H-capacities, competitive with the best of the AB_5 and AB_2 systems. Activation is pretty slow and hard for the ZrNi-based alloys, requiring a day or more at high (50+ atm) pressures for total activation to be achieved. The passive oxide films that can form on ZrNi (and its derivatives) do not result in a high degree of sensitivity to gaseous impurities in the H_2 used; hence,

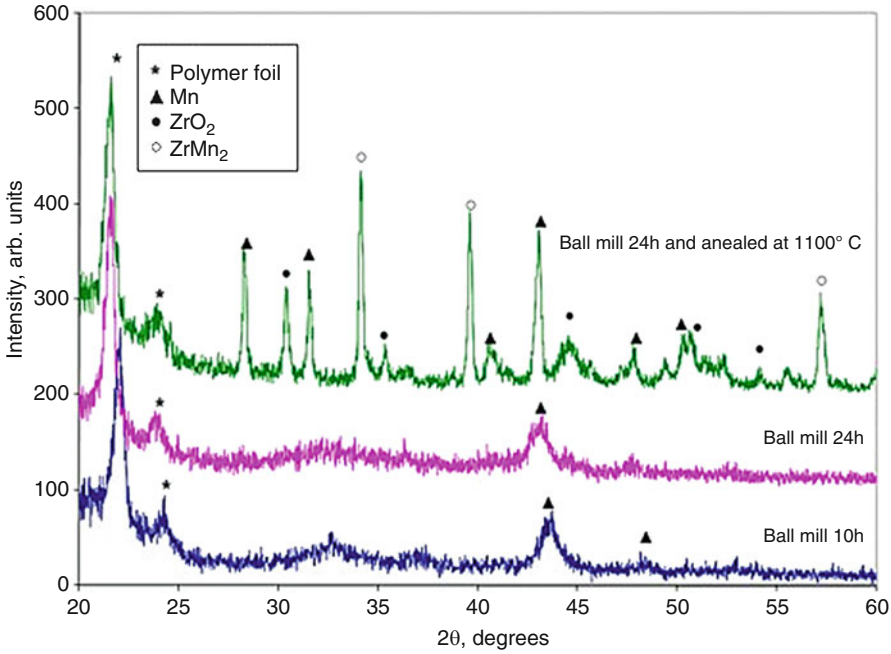

Fig. 8.5 XRD spectra of $ZrMn_2$ alloy, ball milled and annealed at 1,100 °C

these alloys are resistant to impurities. Cyclic stability of the lower plateau is great, but the upper plateau tends to drift higher with H/D cycling.

8.5.6 A_2B Intermetallic Compounds

A is typically of the Group IVA elements Ti, Zr, or Hf and B is a transition metal, typically Ni. Another family is based on Mg_2Ni [28]. Unfortunately, the A_2Bs offer little in the 0–100 °C, 1–10 atm range, in terms of hydrogen storage. They are definitely more stable. H-capacity and cost properties of Mg_2Ni are attractive, but desorption temperatures are too elevated for most applications. Mg_2Ni is not very amenable to modification of PCT properties by ternary and higher-order substitutions. Various attempts to lower desorption temperatures have not been successful.

8.5.7 Other Intermetallic Compounds

In addition to the AB_5, AB_2, AB, and A_2B intermetallic compounds discussed above, various other families of intermetallics have been shown capable of reversible

hydriding/dehydriding reactions [29, 30]. Examples include AB_3, A_2B_7, A_6B_{23}, A_2B_{17}, A_3B, and others. Most structures involve long-period AB_5 and AB_2 stacking sequences and are thus crystallographically related to these two classic families. Most have narrow plateaux with long sloping upper legs (e.g., gadolinium triiron, ($GdFe_3$)) or multiple plateau (e.g., $NdCo_3$ or Pr_2Ni_7).

8.5.8 Mg-Based Hydrides

When the mass of the metal or alloy is taken into account, the metal hydride gravimetric storage density is comparable to storage of pressurized hydrogen. The best achievable gravimetric storage density is about 0.07 kg of H_2/kg of metal, for a high temperature hydride such as MgH_2 as shown in Table 8.1 which gives a comparison of some hydriding substances with liquid hydrogen, gaseous hydrogen, and gasoline [31, 32]. It can effectively store hydrogen due to its thermodynamic stability; however, reaction kinetics are too slow and the decomposition temperature is high, approximately at 330 °C. A possible way to achieve Mg like storage capacity but with reversible hydrogenation characteristics is to form composites with Mg as one of the components. The other component may be one of the known hydrogen storage intermetallic alloys [33].

Different approaches to improve the reaction kinetics of MgH_2 have been taken, including the mechanical milling. The mechanical milling of a hydrogen absorbing compound, in this case MgH_2, under hydrogen pressure leads to hydrogen uptake and defects and changes in the surface [34–37]; however, the attention is more focused on the effective reduction of the desorption temperature by ball milling [38–42]. Experiments have taken place in order to catalytically improve MgH_2 kinetics with Nb_2O_5 [43, 44]. More studies involve the addition of small amounts of Ti, V, Mn, Fe, Ni mechanically milled with MgH_2 reporting good results [45–49]. A recent approach is the use of magnesium nickel alloys for hydrogen storage systems [50–52], the presence of nickel improves the hydriding and dehydriding rates. An important feature of the metallic hydrides is the high volumetric density of the hydrogen atoms present in the host lattice as shown in Fig. 8.6 [53].

The highest theoretical volumetric hydrogen density known today is 150 $kg \cdot m^{-3}$ for Mg_2FeH_6 and $Al(BH_4)_3$. The Mg_2FeH_6 hydride belongs to the family of Mg-transition metal complex hydrides with $[FeH_6]^{4-}$ octahedral surrounded by Mg atoms in cubic configuration [54]. Interestingly, iron does not form intermetallic compounds with Mg, but it readily combines with hydrogen and Mg to form ternary hydride Mg_2FeH_6 according to the reactions:

$$2Mg + Fe + 3H_2 \leftrightarrow Mg_2FeH_6 \tag{8.3}$$

$$2MgH_2 + Fe + H_2 \leftrightarrow Mg_2FeH_6 \tag{8.4}$$

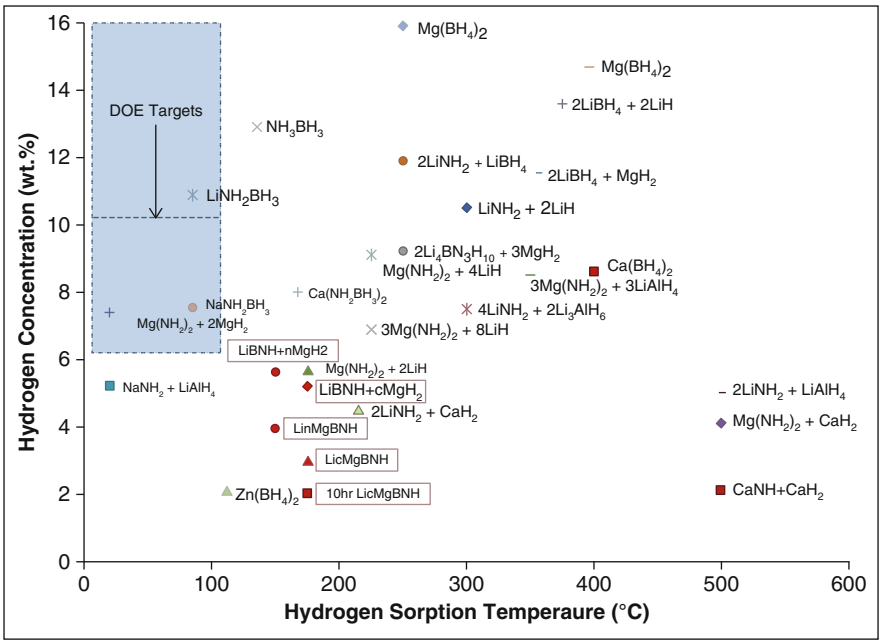

Fig. 8.6 Volumetric and gravimetric hydrogen densities of various hydrogen storage systems

8.6 Metal Hydrides Synthesis and Characterization Equipment

All sample handling was carried out in a glove box under a nitrogen filled atmosphere to reduce the oxygen and moisture level down to <1 part-per-million (ppm). The mixtures in the present investigation were mechanically milled in a high-energy Fritsch (Cranberry Township, PA) pulverisette planetary mono mill P6 using a stainless steel balls and bowl (80 mL) sealed with a viton O-ring. The ball to powder weight ratio and milling speed are optimized to 20:1 and 300 revolutions-per-minute (rpm), respectively. Milling duration and other milling parameters have been varied depending on the sample property to optimized hydrogen storage material. After ball milling, the as-synthesized compounds were transferred from the milling bowl into respective sample holders in the glove box for further characterization measurements.

In the heat flow and weight loss analysis, samples were loaded in aluminum and alumina pans, respectively, in the nitrogen gas filled glove box. The measurements have been performed using a differential scanning calorimeter (DSC) Q10 (aluminum pan) and a stepwise differential thermolysis (SDT Q600 with alumina pan) model from TA Instruments (New Castle, DE). The thermal measurements were analyzed using an Advantage Software v5.5.20 (Universal Analysis software tool, TA Instrument).

Powder X-ray diffraction (PXRD) patterns were collected on a Philips X'pert diffractometer with $CuK_{\alpha 1}$ radiation of $\lambda = 1.54056$ Å (PANalytical, Westborough MA). The incident and diffraction slit widths used for the measurements are 1° and 2°, respectively. The collimating mask of 10 mm was used throughout the analysis. Phase identification and particle size calculation has been carried out using PANalytical X'pert Highscore software, version 1.0e. The samples were protected from air and moisture by wrapping it with thin foil, which shows diffraction peaks in the 2θ range of 21–28°.

The B-H bond stretch of the complex metal hydride samples was compared and analyzed via a Perkin-Elmer One Fourier transform infrared spectroscopy (FT-IR) spectrometer. The isothermal volumetric sorption measurements have been carried out by Hy-Energy's PCT equipment (now a subsidiary of SETARAM, Hillsborough, NJ). The volume calibration without and with sample was performed at a constant temperature with accuracy of ±1 °C. The dehydrogenation and rehydrogenation parameters such as pressure and temperature have been optimized for the efficient hydrogen storage characteristics. During sorption, the sample temperature and applied pressure were monitored and recorded by a Lab View software program. The analysis of the measurements such as full absorption/desorption kinetics, cycle life, and PCT was carried out using Hy-Analysis macros in the Igor program (WaveMetrics, Inc., Nimbus, Portland, OR).

The microstructures of the samples in the different stages were observed by Hitachi S800 scanning electron microscope (SEM), and local phase composition was determined in the energy dispersive X-ray spectrometry (EDS) mode using the same instrument (Hitachi High Technologies America, Inc., Dallas, TX). A fixed working distance of 5 mm and a voltage of 20 kV were used. Genesis software (EDAX Inc, Mahwah, NJ) was used to analyze the SEM images and EDS mappings.

Temperature programmed desorption (TPD) technique was carried out by Quantachrome Instruments Autosorb-1 equipment (Boynton Beach, FL). The carrier gases used for the TPD and temperature-programmed reduction (TPR) measurement were nitrogen and argon:hydrogen (95%):(5%) v/v premixed gases, respectively. The thermal desorption/reduction profiles were recorded and analyzed using TPRWin PC software (Quantachrome Instruments). The thermal decomposition behaviors of the hydride samples were examined by a gas chromatography mass spectrometry (GC-MS) triple quadrupole (320-MS GC/MS, Agilent Technologies, Santa Clara, CA) upon heating up to 150 °C with a heating rate of 5 °C/min under a helium flow.

8.6.1 Synthesis Techniques

8.6.1.1 High Energy Ball Mill (BM)

The objectives of the ball milling process include particle size reduction, mixing or blending, and particle shape changes. The most common mill used for these purposes has been a planetary ball mill; a bowl sits on a grinding platform and rotates in

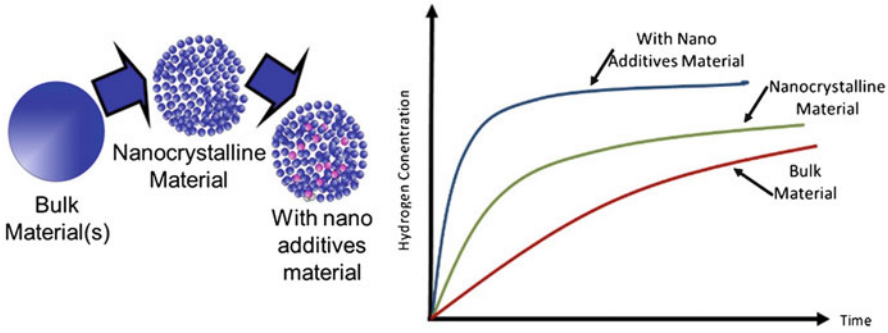

Fig. 8.7 Scheme and hydrogen sorption kinetics of nanocrystalline transformation and catalyst doping of bulk material via high energy ball milling method

a direction opposite to the direction of the base fixture. In planetary action, centrifugal forces alternately add and subtract. The grinding balls roll halfway around the bowls and then are thrown across the bowls, impacting on the opposite walls at high speed. Grinding is further intensified by interaction of the balls and sample. Planetary action gives up to 10 g acceleration. The schematic cross-section diagram of the planetary ball mill principle is illustrated elsewhere [55]. In the planetary mono mill pulverisette 6, grinding bowls rotate around their own axes while also orbiting around a central axis reaching a speed up to 650 rpm [56]. As a result, forces are exerted on the grinding balls and the materials which are constantly changing direction and amount. Optimum grinding ball movements are obtained due to design of geometry and transmission ratios.

The high-energy ball-milling process is becoming a necessary (pre)treatment tool for a successful solid-state preparation of hydrogen storage materials. An increase in the active nanostructured surface of the crystallites and an improvement in the contact between catalyst and hydrogen storage materials in the solid phase stand out among the most important factors for achieving fast kinetics of hydrogen transformations as represented in the schematic Fig. 8.7 [57]. Another important factor in the success of this instrument is its economy; it is an in-expensive and rapid process when compared with other synthesizing methods such induction melting, quenching, sintering, etc.

8.6.1.2 Nitrogen Filled Glove Box (Dry Box)

All the metal/complex hydride samples and the sample holder preparation for the analytical tools were carried out in a nitrogen atmosphere glove box manufactured by Innovative Technology Inc (Amesbury, MA). The oxygen and moisture level inside the box are controlled and lowered to the order of <1 ppm by continuously purging with nitrogen gas. A glove box is a sealed container that is designed to allow workers to manipulate objects that are in an inert atmosphere. Built into the sides of the glove box are two gloves with which workers can perform tasks inside the box without breaking the seal or allowing potential damage to the workers' hands.

The principal components of the glove box used are: (i) gloves that are usually sized large (8 in.) so that anyone can get their hands in, (ii) vacuum pump, (iii) electronic sensors that monitor oxygen and water content, (iv) two chambers, called the antechambers or ports that are used for insertion or removal of objects that are handled in the glove box. Each antechamber has two doors, one that can be opened only from the inside of the box and one that can be opened only from the outside. The antechamber can be evacuated with a pump or filled with nitrogen gas; (v) the gauge controls, they control the upper and lower pressure limits inside the glove box, if the pressure in the box gets too high, the controller automatically opens a valve to the vacuum pump to relieve the excess pressure and prevent the gloves from blowing off, likewise, if the pressure is too low, the controller fills the box with nitrogen; (vi) the pedatrol, it is a foot pedal that allows workers to manually adjust the pressure inside the glove box; and finally (vii) the purification system with automatic valves that maintains the inside atmosphere less than 1 ppm level of O_2 and H_2O, respectively [58]. The incoming purging nitrogen gas passes through a molecular sieve which continuously absorbs the contaminants to keep the glove box dry. The schematic diagram of the system one glove box can be found in Innovative Technologies company website [58].

8.6.1.3 Solvent Purification System

The principal objective of the solvent purification system is to remove water and oxygen in order to produce dry, deoxygenated, and high-purity solvents on demand. Solvents like pentane, hexane, isopropanol, tetrahydrofuran (THF), ether, and toluene are purified in "Pure Solv 400-5-MD" equipment, manufactured by Innovative Technology Inc. (Amesbury, MA); in this system, a purification grade solvent is pushed from its storage container under low nitrogen pressure through two stainless steel columns containing activated alumina and copper. Trace amounts of water and oxygen are removed producing dry, deoxygenated solvent. The processed solvent is drained into in a storage flask where it can be dispensed, under nitrogen, using standard syringe techniques.

8.6.1.4 Annealing (Tube Furnace) System

After the ball milling process, some compounds such as AB, AB_2 (see next section) lose their crystallinity due to the high energy ball collisions against the sample powder. With a proper heating process, the crystal structure of these compounds can be recovered. Figure 8.8 shows the schematic diagram and the real annealing system used. The main component of this heating system is the tube furnace, manufactured by Thermolyne (Thermo Scientific, Waltham, MA); it can reach temperatures in the range of 100 and 1,200 °C.

The operation of the annealing system above is as follows: the sample is pelletized in a press at 10–20 tons and loaded in a ceramic boat inside the glove box to prevent oxidation. The boat is introduced in a mullite tube which has a melting point of 1,680 °C. After inserting the mullite tube with the sample in the tube furnace, a vacuum/helium purge cycle is done in three alternative cycles, to avoid oxygen/moisture inside the tube and in the lines. This cycling process is manually operated,

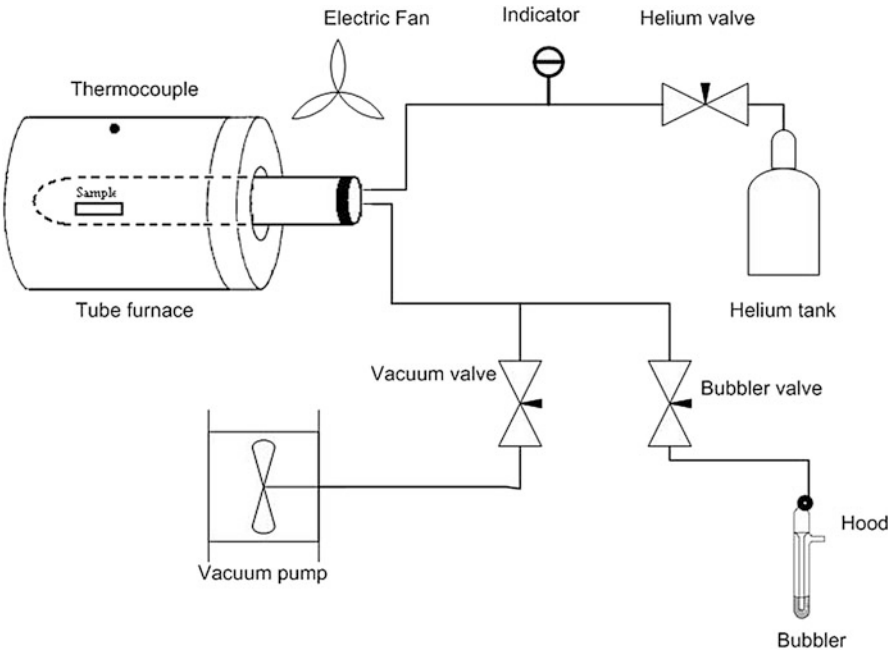

Fig. 8.8 Schematic diagram of the annealing arrangement developed by the authors for the synthesis of AB_2 or other metal hydride systems

first the helium and bubbler valves remain closed and the vacuum valve opened. After 15 min of evacuation, the vacuum valve is closed and the helium valve is opened; when the indicator shows no negative pressure, the bubbler valve is opened; the helium flush is continued for 15 min. Finally after that the two valves are turned to close position and the vacuum valve is opened again. In the annealing process, the vacuum pump and the valve are turned off, the helium and bubbler valves are opened, and the tube furnace is turned on to start heating. The electric fan is used to prevent melting of the rubber stopper.

8.6.2 Characterization Techniques

8.6.2.1 Differential Scanning Calorimetry (DSC)

This thermo-analytical tool measures the difference in the amount of heat required to increase the temperature of a sample and an inert reference as a function of time and temperature. The specific Q10-P differential scanning calorimeter (DSC) manufactured by TA instruments (New Castle, DE) consists of two sealed pans, one is the sample pan and the other is the reference pan (which is generally an empty standard pan) inside a helium filled chamber at 50 pounds-per-square-inch (psi) gas pressure. The heat flow difference between the two pans is monitored while they are

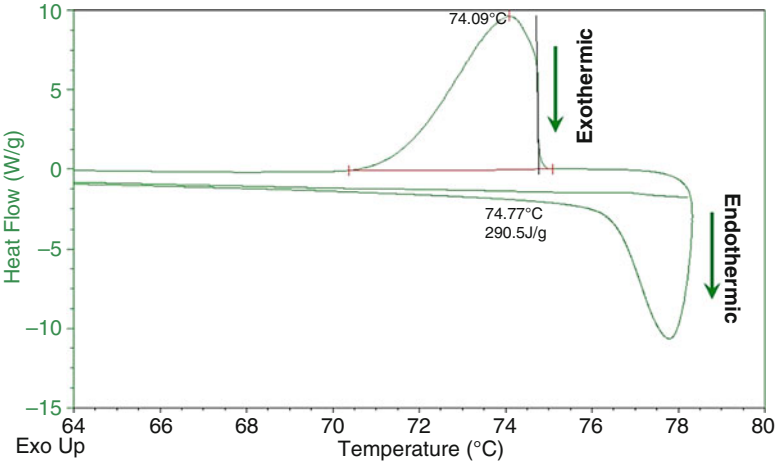

Fig. 8.9 DSC heat flow measurements both endothermic and exothermic reaction of Ba $(OH)_2.8H_2O$ phase change materials [60]

heated, or cooled, uniformly. This can be done at a constant temperature (isothermally) or by changing the temperature at a constant rate [59].

The basic principle in this technique is that when the sample undergoes a physical transformation such as a phase transition, more (or less) heat will need to flow to it than the reference to maintain both the reference pan and the sample pan at the same temperature. The process can be exothermic or endothermic depending whether more or less heat flows to the sample. Endothermic heat flows into the sample as a result of either warming or some endothermic process (glass transition, melting, evaporation, etc.) and exothermic heat flows out if the sample as a result of either cooling or some exothermic process (crystallization, oxidation, etc.). An example DSC profile of barium hydroxide octahydrate phase change material is illustrated in Fig. 8.9.

8.6.2.2 Thermogravimetric Analysis (TGA)

Thermogravimetric analysis uses heat to force reactions and physical changes in the materials under investigation. TGA measures the amount and rate of change in the weight of a material due to dehydration, decomposition, and oxidation as a function of temperature or time in a controlled atmosphere. Characteristic thermogravimetric curves occur for specific materials due to unique sequences of physicochemical reactions occurring over specific temperature ranges and heating rates. The specific TGA used is the Q600 series; it provides a true simultaneous (SDT) measurement of weight change (TGA) and heat flow (DSC) on the same sample. A matched Platinum/Platinum-Rhodium thermocouple pair embedded in the ceramic beams provides direct sample [61], reference, and differential temperature measurement, and a dual balance mechanism gives an accurate weight loss/gain measurement. The balance operates on a null-balance principle. At the zero position, equal amounts of

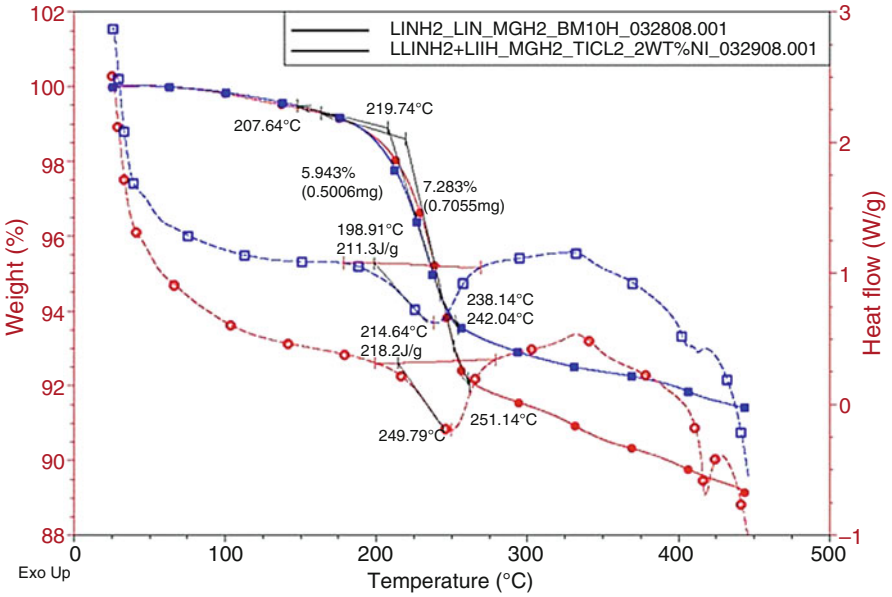

Fig. 8.10 SDT weight and heat analysis profiles of complex hydrides without and with additives of nanocatalysts such as Ti and Ni [63]

light shine on the two photodiodes. If the balance moves out of the null position, an unequal amount of light shines on the two photodiodes. Current then is applied to the meter movement to return the balance to the zero position. The amount of current applied is proportional to the weight loss or gain [62]. The SDT profile of lithium amide-magnesium hydride complex hydride ball milled and without and with catalysis shows weight loss of about 7.28% at the endothermic transition temperature of approximately 250 °C as shown in Fig. 8.10.

8.6.2.3 X-Ray Diffractrometer (XRD)

X-ray powder diffraction (XRD) is an efficient analytical technique used to characterize and identify unknown crystalline materials. Monochromatic X-rays are used to determine the interplanar spacings of the unknown materials. X-rays are electromagnetic radiation similar to light, but with a much shorter wavelength. They are produced when electrically charged particles of sufficient energy are decelerated. In an X-ray tube, the high voltage maintained across the electrodes draws electrons toward a metal target (the anode). X-rays are produced at the point of impact and radiate in all directions.

With this technique, the samples are analyzed as powders with grains in random orientations to insure that all crystallographic directions are "sampled" by the beam. The basic principle of operation of the XRD spectrometer is based on Bragg's law. When the Bragg conditions for constructive interference are obtained, a "reflection" is produced, and the relative peak height is generally proportional to the number of

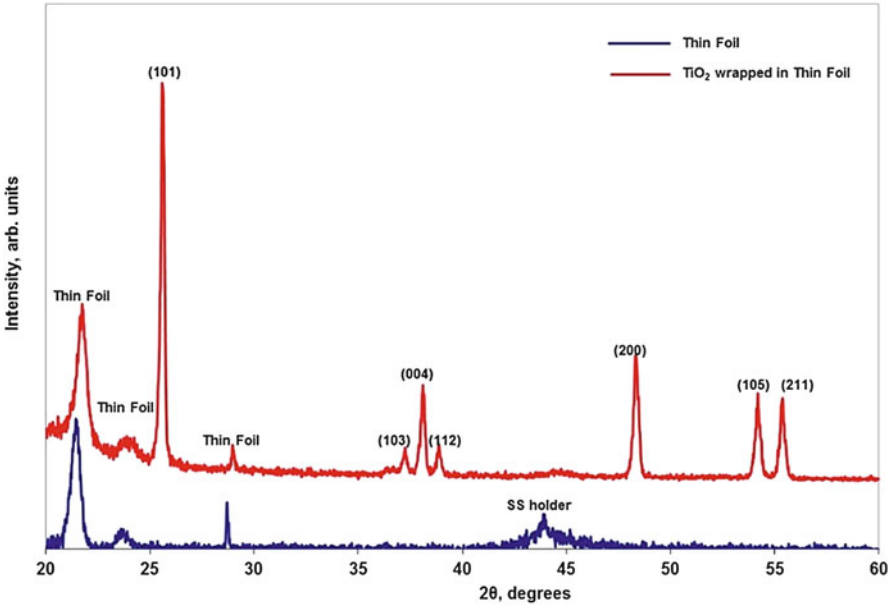

Fig. 8.11 X-ray diffraction spectrum of sol-gel based TiO_2 nanoparticles [64]

grains in a preferred orientation. The basic geometry of an X-ray diffractometer has a source of monochromatic radiation and an X-ray detector situated on the circumference of a graduated circle centered on the powder specimen. The detector and specimen holder are mechanically coupled with a goniometer so that a rotation of the detector through 2θ degrees occurs in conjunction with the rotation of the specimen through θ degrees, a fixed 2:1 ratio. Divergent slits, located between the X-ray source and the specimen, and between the specimen and the detector, limit scattered (nondiffracted) radiation, reduce background noise, and collimate the radiation. Figure 8.11 represents a characteristic XRD spectrum of TiO_2 nanoparticles as synthesized via sol-gel process as a catalysts to dope with the metal hydrides.

8.6.2.4 Scanning Electron Microscope (SEM)

The scanning electron microscope (SEM) is a type of microscope capable of producing high resolution images of a sample surface using electrons rather than light to form an image. Electron microscopy takes advantage of the wave nature of rapidly moving electrons. Where visible light has wavelengths from 4,000 to 7,000 Å, electrons accelerated to 10,000 keV have wavelengths of 0.12 Å. Optical microscopes have their resolution limited by the diffraction of light to about 1,000 diameters magnification. The Hitachi S800 scanning electron microscope in the present study is limited to magnifications of around 3,000,000×.

The SEM uses the secondary electrons when a focused electron beam is incident on the specimen to form the image. The secondary electron signal provides

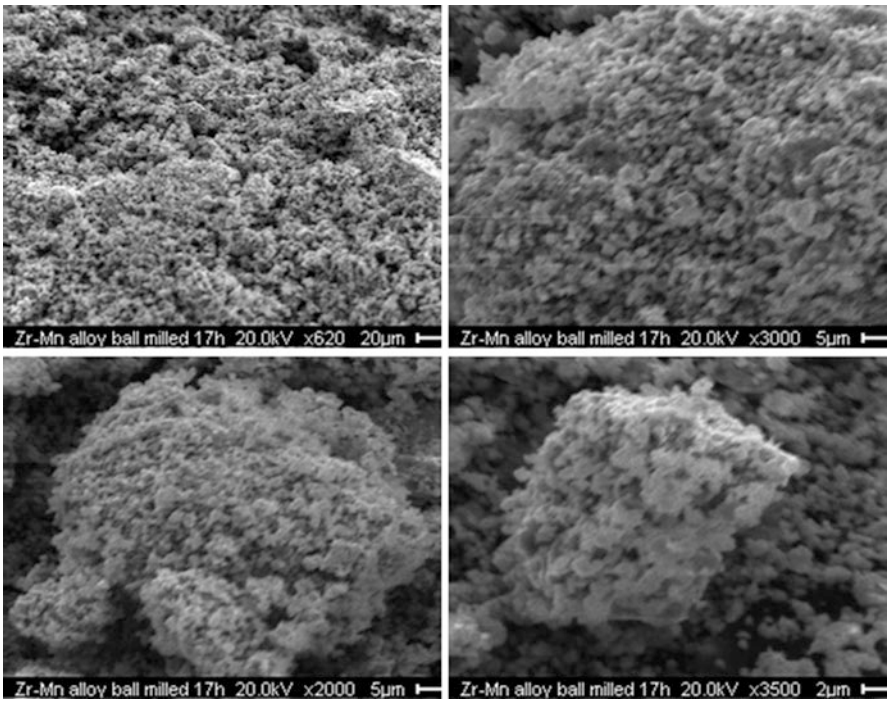

Fig. 8.12 Scanning electron micrographs of $ZrMn_2$ metal hydride at different magnifications (500X, 2000X, 3000X, 3500X) [67]

information about the surface of a specimen. Since secondary electrons do not diffuse much inside the specimen, they are most suitable for observing fine structure of the specimen surface. Electrons from a filament in an electron gun are beamed at the specimen inside a vacuum chamber. That beam is collimated by electromagnetic condenser lenses, focused by an objective lens and then swept across the specimen at high speed. The secondary electrons are detected by a scintillation material that produces flashes of light from the electrons. The light flashes are then detected and amplified by a photomultiplier tube [65, 66]. Figure 8.12 depicts the surface morphology of zirconium-manganese ($ZrMn_2$)-type metal hydride alloys at different magnifications [67].

8.6.2.5 Energy Dispersive X-Ray Spectroscopy (EDS)

Another important signal that can be analyzed by the Hitachi S800 SEM, when the electron beam- specimen interaction occurs is the X-ray emission. EDS identifies the elemental composition of materials imaged in a scanning electron microscope (SEM) for all elements with an atomic number greater than boron (B). Most elements are detected at concentrations of order 0.1% excluding hydrogen. When the electron beam of the SEM hits the sample surface, it generates X-ray fluorescence from the atoms in its path. The energy of each X-ray photon is characteristic of the element

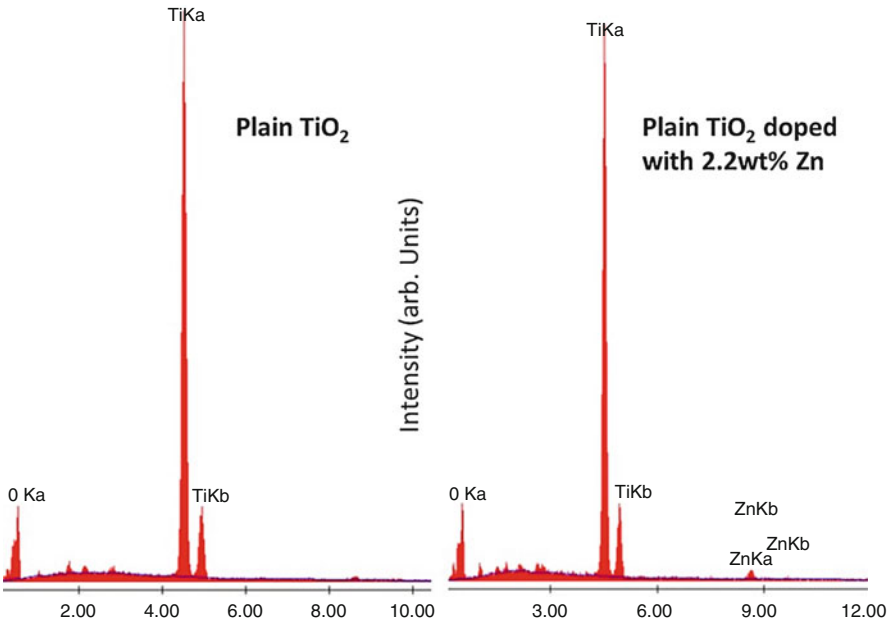

Fig. 8.13 EDS spectra of pristine and Zn-doped TiO_2 nanoparticles [68]

which produced it. The EDS microanalysis system collects the X-rays, sorts and plots them by energy, and automatically identifies and labels the elements responsible for the peaks in this energy distribution. The liquid nitrogen cooled detector is used to capture and map the X-ray counts continuously. Typical EDS showing the Kα and Kβ spectral lines of elements is pictured in Fig. 8.13.

8.6.2.6 Pressure Composition Temperature (PCT) Apparatus

The instrument used is the PCTPro-2000 manufactured by Hy-Energy, USA (SETARAM, Hillsborough, NJ). It is an automated Sieverts type instrument for measuring gas absorption/desorption properties of materials designed mainly for hydrogen storage and metal hydride applications. Important measurements that can be done with this instrument are PCT, gas sorption kinetics, heat-of-formation, cycle-life kinetics, cycle-life PCT, volume calibration, and packing density measurements. In the Sieverts technique, a calibrated reference volume at a constant temperature is filled with gas to a measured pressure and then opened to the sample chamber, and the gas uptake by the sample is calculated from the change in the gas pressure in the system. Hydrogen uptake is represented by the hydrogen-to-host atomic ratio, H/X, by analogy with the hydrogen-to-metal ratio for a metal, H/M. Similarly, the gas release by the sample is measured from the gas pressure difference in the system. A helium bottle (purity 99.9999%l He-6P) is used for calibrating the volume and for purging air from the line. In this Sieverts type [67] apparatus, to measure the volumetric hydrogen sorption, two gas reservoirs have

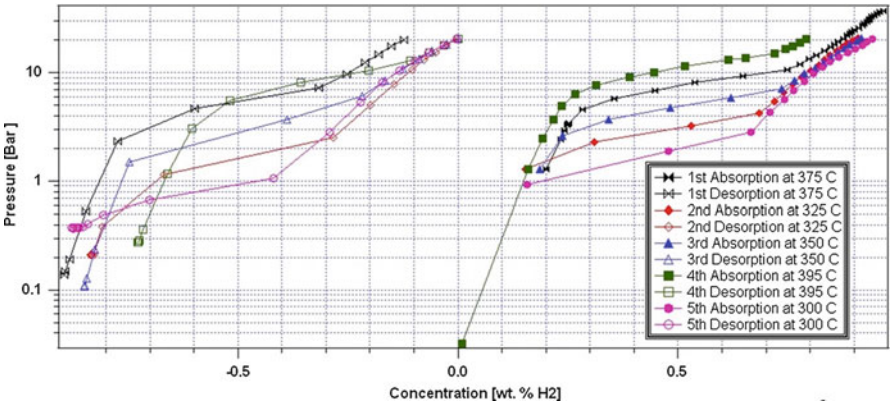

Fig. 8.14 Hydrogen absorption and desorption PCT of Zr70Ni30 MH [68]

been used with known and calibrated tank volumes. An example PCT isotherm showing α, β, and α + β (equilibrium) phases of Zr70Ni30 metal hydrides recorded in using our Sieverts system is shown in Fig. 8.14.

8.6.2.7 Thermal Programmed Desorption or Reaction (TPD/TPR)

The rate of hydrogen absorption (reaction) of a metal hydride sample is function of temperature as shown in the metal hydrides chapter. The temperature at which the maximum rate is observed is characteristic of the metal hydride, the metal and its interaction with the hydrogen gas. Temperature programmed reaction (TPR) is a technique in which the amount of reaction is monitored as a function of temperature. The temperature is raised in a linear fashion so that a suitable detection system can record a characteristic reaction profile or fingerprint of the sample being tested. The monitoring is done with a high sensitivity thermal conductivity detector (TCD).

In an analogous manner, gases that were previously absorbed during chemisorption process can be desorbed by ramping again the temperature to sufficiently high values to break the chemical bonds holding the gas molecules (or atoms); again the TCD signal is proportional to the quantity of molecules desorbed as thermal energy overcomes the binding energy. This type of experiment is called temperature programmed desorption (TPD).

The sample between two quartz wool pieces is purged with nitrogen in order to avoid oxygen in the sample and inside the lines. Then for the TPR measurement, a mixture of 95% argon and 5% hydrogen flows over the sample with a temperature ramping, a monitoring process is conducted recording the amount of hydrogen absorbed based on the signal in the B TCD detector filament and compared with the A TCD filament. For the TPD measurement, the hydrogen mixture is replaced by nitrogen and the TCD is changed to TPD option [69]. TPD profile of lithium-aluminum hydride milled for 2 h is shown in Fig. 8.15. It is clear that the hydrogen decomposition occurs at different temperatures from each of individual compounds such as $LiAlH_4$ and MgH_2 [70].

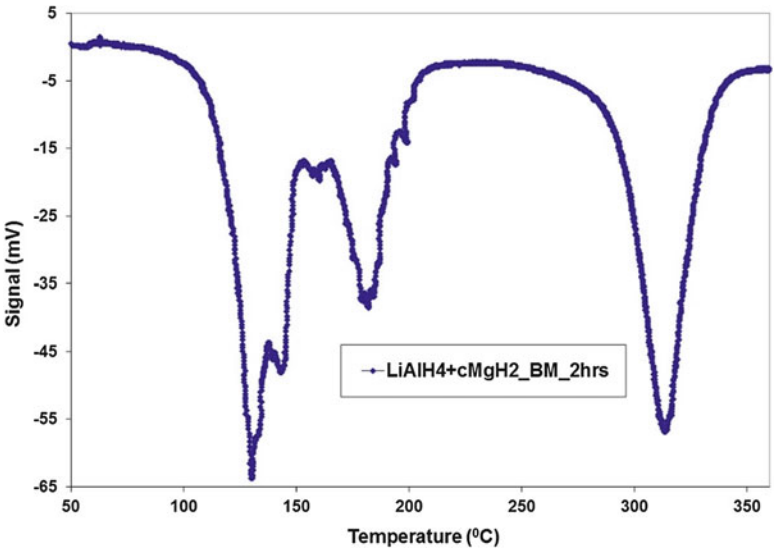

Fig. 8.15 Thermal programmed desorption profile for the decomposition of Li-Al-Mg-H complex metal hydrides [68]

8.6.2.8 Fourier Transform Infrared Spectrometer (FT-IR)

Infrared (IR) spectroscopy is a chemical analytical technique, which measures the infrared intensity versus wavelength of light. Based upon the wavenumber, infrared light can be categorized as far infrared ($4 \sim 400$ cm^{-1}), mid infrared ($400 \sim 4{,}000$ cm^{-1}), and near infrared ($4{,}000 \sim 14{,}000$ cm^{-1}). Infrared spectroscopy detects the vibration characteristics of chemical functional groups in a sample. When an infrared light interacts with the matter, chemical bonds will stretch, contract, and bend. As a result, a chemical functional group tends to absorb infrared radiation in a specific wavenumber (frequency) range regardless of the structure of the rest of the molecule.

In a Fourier transform infrared spectrometer [71], the light passes through an interferometer which creates constructive and destructive interference pattern of two light beams, the recombined beam passes through the sample. The sample absorbs all the different wavelength characteristics of its spectrum, and this subtracts specific wavelengths from the interferometer. The detector now reports variation in energy versus time for all wavelengths simultaneously. A laser beam is superimposed to provide a reference for the instrument operation. Determining these frequencies allows identification of the sample's chemical environment, since chemical functional groups are known to absorb radiation at specific frequencies. The intensity of the absorption is related to the concentration of the component. Intensity and frequency of sample absorption are depicted in a two-dimensional plot called a spectrum. Intensity is generally reported in terms of percent transmittance, the fraction of the light that passes through it. Typical FTIR spectra of polyaniline nanofiber before and after subjected to hydrogen sorption is plotted in Fig. 8.16.

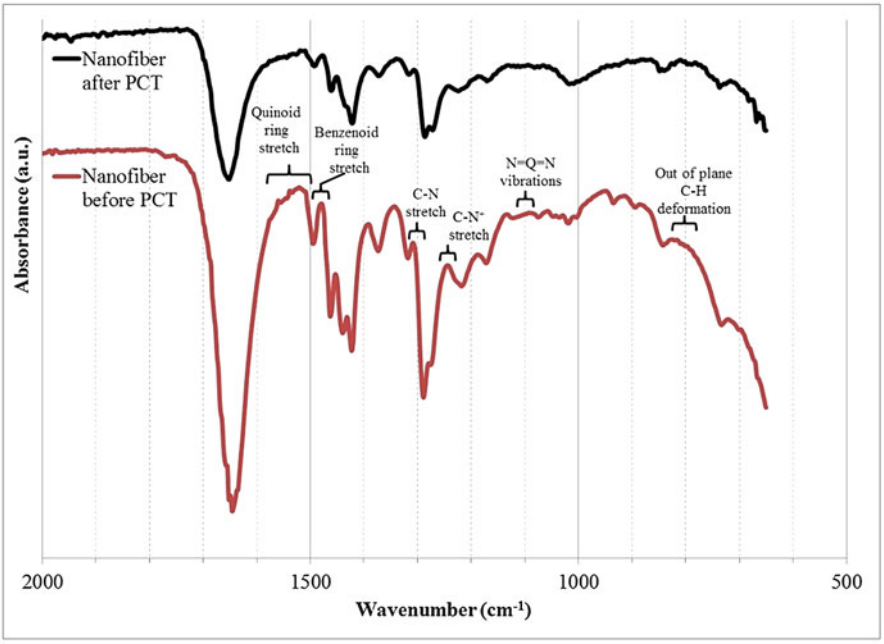

Fig. 8.16 Fourier Transform Infrared Spectra of polyaniline hydrogen sorption

From this figure, it is discernable that the C-H and C-N bonding stretches and bending modes are unaltered; however, their intensity of transmittance was reduced, which may be due to hydrogen passivation [72].

8.6.2.9 Gas Chromatography and Mass Spectroscopy (GC-MS)

Two techniques are combined to form a single method of analyzing mixtures of chemicals or evolving gas. Gas chromatography separates the components of a mixture and mass spectroscopy characterizes each of the components individually. By combining the two techniques, the qualitatively and quantitatively composition of a solution containing a number of chemicals can be known.

Gas chromatography is a chemical analysis instrument for separating chemicals in a complex hydride sample. A gas chromatograph uses a flow-through narrow tube known as a column, through which different chemical constituents of a sample pass in a gas stream known as the mobile phase at different rates depending on their various chemical and physical properties and their interaction with a specific column filling, called the stationary phase. As chemicals exit the end of the column, they are detected and identified electronically, those that interact faster will exit (elute from) the column first. The function of the stationary phase in the column is to separate different components, causing each one to exit the column at a different time

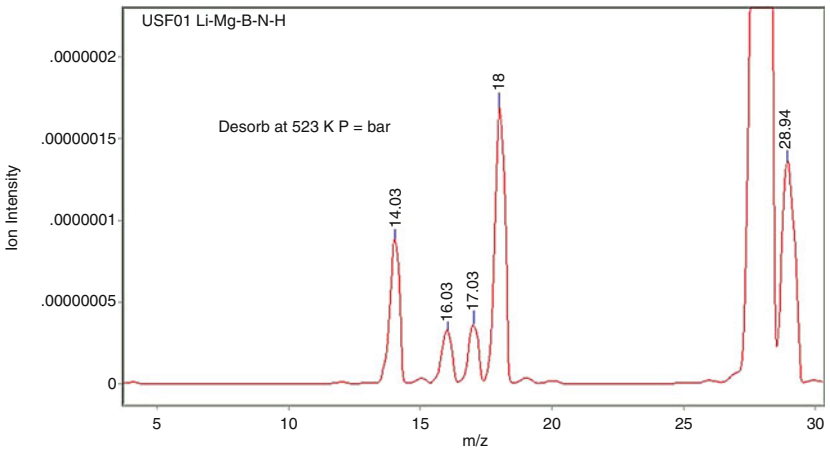

Fig. 8.17 Mass spectrometry profiles of H_2 decomposition from Li-B-N-H

(retention time). Changing the carrier gas flow rate and the temperature can alter the retention time.

As the individual compounds exit from the GC column, they enter the electron ionization (mass spectroscopy) detector. There, they are bombarded with a stream of electrons causing them to break apart into fragments. These fragments can be large or small pieces of the original molecules. The positive fragments which are produced (cations and radical cations) are accelerated in a vacuum through a quadrupole ion analyzer and are sorted on the basis of mass-to-charge (m/z) ratio. Since the bulk of the ions produced in the mass spectrometer carry a unit positive charge, the value m/z is equivalent to the molecular weight of the fragment [73]. Figure 8.17 represents the mass-spectrometer analysis of lithium borohydride-lithium amide-magnesium hydride complexes and it exhibited no signatures of diborane or amino-borane compounds during the thermal decomposition [74].

8.7 Summary

In summary, metal hydrides are classified based on the amount of hydrogen localized in the lattice of their structure. For example, AB_5 type intermetallic compounds (for example $LaNi_5$) can store 6 hydrogen atoms per metal formula when compared to 2 H atoms per metal in AB systems (e.g., FeTi). Moreover, the magnesium transition metal hydrides has very high hydrogen volumetric density of >150 kg/m^3 and gravimetric capacity of >5 wt% at higher temperatures and moderate pressures.

It is to be concluded that metal hydrides have versatile applications in stationary and mobile (automotive applications), in hydrogen permeable sensors, a combination of diesel engine and electric *gen*erator *set*up (GEN-SET), proton exchange membrane (PEM) fuel cells, tritium adsorption in nuclear reactors, heat pumps, refrigeration and isotopic separation, etc.

Acknowledgments Authors wish to acknowledge their respective institutions (Florida Polytechnic University and Texas A&M University, Kingsville) for research support. Financial support from Florida Energy Systems Consortium (FESC) is gratefully acknowledged.

References

1. J.H.N. van Vucht, F.A. Kuipers, H.C.A.M. Bruning, Reversible room-temperature absorption of large quantities of hydrogen by intermetallic compounds. Phillips Res. Rep. **25**, 133 (1970)
2. Z.P. Li, B.H. Liu, K. Arai, N. Morigazaki, S. Suda, Protide compounds in hydrogen storage systems. J. Alloys Compd. **356–357**, 469–474 (2003)
3. P. Vajeeston, Theoretical modeling of hydrides. Dissertation presented for the degree of Doctor Scientiarum, University of Oslo (2004)
4. G.G. Libowitz, A. Maeland, Hydrides, Volume 3, Non-metallic Compounds – 1, 1979, Ist Repr; ISBN 0-444-85215-8, page 299; in *Handbook on the Physics and Chemistry of Rare Earths*, vol. 28, ed. by K.A. Gschneidner, Jr. and L. Eyring, ISBN 978-0-444-50346-6, (Elsevier Science B.V., 2000)
5. Y. Fukai, *The Metal-Hydrogen System, Basic Bulk Properties*, 1st edn. (Springer, Berlin/Heidelberg, 1993)
6. W.M. Muller, J.P. Blackledge, G.G. Libowitz, *Metal Hydrides* (Academic, New York/London, 1968)
7. B.L. Shaw, *Inorganic Hydrides* (Pergamon Press, Oxford, 1967)
8. G.D. Sandrock, The metallurgy and production of rechargeable hydrides, in *Hydrides for Energy Storage*, ed. by A.F. Anderson, A.J. Maeland (Pergamon, Oxford, 1978), p. 353
9. J.J. Reilly, Metal hydrides as hydrogen storage media and their applications, in *Hydrogen: Its Technology and Implications*, ed. by K.E. Cox, K.D. Williamson Jr., vol II (CRC, Cleveland, 1977), pp. 13–48
10. L. Schlapbach, A. Seller, F. Stucki, H.C. Siegman, Surface effects and foundation of metal hydrides. J. Less Common Met. **T3**, 145 (1980)
11. K.J. Gross, Intermetallic "materials for hydrogen storage". Ph.D. Thesis, University of Fribourg, Switzerland (1998)
12. S.S. Sai Raman, Hydrogen storage materials. Ph.D. Thesis, Banaras Hindu University, Varanasi (2000)
13. E.K. Stefanakos, D.Y. Goswami, S.S. Srinivasan, J. Wolan, *Hydrogen Energy*. John Wiley & Sons series in Environmentally Conscious Power Generation, Edited by Myer Kutz, 4, (2007) 165–206, ISBN: 978-0-471-73911-1
14. G. Sandrock, A panoramic overview of hydrogen storage alloys from a gas reaction point of view. J. Alloys Compd. **293–295**, 877–888 (1999)
15. S. Bliznakov, E. Lefterova, L. Bozukov, A. Popov, P. Andreev, Techniques for characterization of hydrogen absorbtion/desorbtion in metal hydride alloys, in *Proceedings of the International Workshop: Advanced Techniques for Energy Sources Investigation and Testing*, Sofia (2005)
16. L. Schlapbach, I. Anderson, J.P. Bruger, Hydrogen in metals, in *Electronic and Magnetic Properties of Metals and Ceramics Part II*, ed. by K.H. Jurgen Buschow, vol 3B (VCH, Weinheim, 1994), p. 271

17. M. Yamaguchi, E. Akiba, Ternary hydrides, in *Electronic and Magnetic Properties of Metals and Ceramics Part II*, ed. by K.H. Jurgen Buschow, vol 3 (VCH, Weinheim, 1994), p. 333
18. J. Huot, Hydrogen in metals, in *Proceedings of the NATO Advanced Study Institute on New Trends in Intercalation Compounds, Sozopol, Bulgaria*, ed. by C. Julien, J.P. Pereira-Ramos, A. Momchilov, vol 61, p. 109, Springer-Science+Business Media B.V., ISBN 978-1-4020-0595-4k; ISBN 978-94-010-0389-6 (eBook); doi:10.1007978-94-010-0389-6.
19. T.B. Flanagan, W.A. Oates, Some thermodynamic aspects of metal hydrogen systems. J. Alloys Compd. **404–406**, 16–23 (2005)
20. M. Sastri, B. Vismanathan, S. Srinivasa, *Metal Hydrides* (Narosa publishing house, New Delhi, 1998). 5, 10
21. M. Groll, H.-P. Klein, Metal hydride technology with special emphasis on thermodynamic machines. Institut für Kernenergetik und Energiesysteme (IKE), Universität Stuttgart (2002)
22. M. Ram Gopal, S. Srinivasa Murthy, Prediction of metal hydride heat transformer performance based on heat transfer and reaction kinetics. Ind. Eng. Chem. Res. **34**, 2305–2313 (1995)
23. G.D. Sandrock, P.D. Goodell, Cyclic life of metal hydrides with impure hydrogen: overview and engineering considerations. J. Less Common Mat. **104**(1), 159–173 (1984)
24. M. Wanner, G. Friedlmeier, G. Hoffmann, M. Groll, Thermodynamic and structural changes of various intermetallic compounds during extended cycling in closed systems, in *International Symposium on Metal-Hydrogen Systems*, Les Diablerets (1996)
25. G. Thomas, G. Sandrock, Hydride Information Center, online posting: http://hydpark.ca.sandia.gov (2006)
26. I.I. Bulyk, Y.B. Basaraba, A.M. Trostianchyn, Features of the HDDR process in ZrT_2 (T = Cr, Mn, Fe, Co) compounds. J. Alloys Compd. **367**, 283–288 (2004)
27. G.G. Libowitz, H.F. Hayes, R. Thomas, The system zirconium-nickel and hydrogen. J. Chem. Phys. **27**, 514 (1957)
28. A. Maddalena, M. Petris, P. Palade, S. Sartori, G. Principi, E. Settimo, B. Molinas, S. Lo Russo, Study of Mg-based materials to be used in a functional solid state hydrogen reservoir for vehicular applications. Int. J. Hydrog. Energy **31**(14), 2097–2103 (2006)
29. G. Sandrock, State-of-the-art review of hydrogen storage in reversible metal hydrides for military fuel cell applications. Final Report for ONR (2005)
30. G. Sandrock, *Hydrogen energy system – production and utilization of hydrogen and future aspects* (Kluwer, Dordrecht, 1995), p. 135
31. T.N. Veziroglu, Hydrogen technology for energy needs of human settlements. Int. J. Hydrog. Energy **12**(2), 99–129 (1987)
32. W. Grochala, P. Edwards, Thermal decomposition of the non-interstitial hydrides for the storage and production of hydrogen. Chem. Rev. **104**, 1283–11315 (2004)
33. S.S. Sai Raman, O.N. Srivastava, Hydrogenation behavior of the new composite storage mateirals Mg-xwt% CFMmNi5. J. Alloys Compd. **241**, 167–174 (1996)
34. Y. Chen, J.S. Willams, Formation of metal hydrides by mechanical alloying. J. Alloys Compd. **217**, 181 (1995)
35. P. Tessier, H. Enoki, M. Bououdina, E. Akida, J. Alloys Compd. **268**, 285 (1998)
36. J. Huot, E. Akiba, T. Takada, Mechanical alloying of Mg-Ni compounds under hydrogen and inert atmosphere. J. Alloys Compd. **231**, 815 (1995)
37. A. Zaluska, L. Zaluski, J. Strom-Olsen, Nanocrystalline magnesium for hydrogen storage. J. Alloys Compd. **288**, 217 (1999)
38. F.C. Gennari, F.J. Castro, G.J. Urretavizcaya, Hydrogen desorption behavior from magnesium hydrides synthesized by mechanical alloying. J. Alloys Compd. **321**, 46 (2001)
39. L. Zaluski, A. Zaluska, P. Tessier, J.O. Strom Olsen, R. Schulz, Effects of relaxation on hydrogen absorption in Fe-Ti produced by ball milling. J. Alloys Compd. **227**, 53–57 (1995)
40. G. Liang, S. Boily, J. Huot, A. Van Neste, R.J. Schulz, Hydrogen absorption properties of LaNi5 composite. J. Alloys Compd. **268**, 302–3027 (1998a)
41. G. Liang, S. Boily, J. Huot, A. Van Neste, R. Schulz, Mechanical alloying and hydrogen absorption properties of the Mg-Ni system. J. Alloys Compd. **267**, 302–306 (1998b)

42. K.J. Gross, P. Spatz, A. Zuttel, L.J. Schlapbach, Mechanically milled Mg composites for hydrogen storage – The transition to a steady state compositions. J. Alloys Compd. **240**, 206–213 (1996)
43. G. Barkhordarian, T. Klassen, R. Bormann, Fast hydrogen sorption kinetics of nanocrystalline Mg using Nb_2O_5 as catalyst. Scr. Mater. **49**, 213 (2003)
44. G. Barkhordarian, T. Klassen, R. Bormann, Effect of Nb_2O_5 content on hydrogen reaction kinetics of Mg. J. Alloys Compd. **364**, 242 (2004)
45. G. Liang, J. Huot, S. Boily, A. Van Neste, R.J. Schulz, Hydrogen storage properties of the mechanically milled MgH_2-V nanocomposite. J. Alloys Compd. **291**, 295–299 (1999a)
46. G. Liang, J. Huot, S. Boily, A. Van Neste, R.J. Schulz, Catalytic effect of transition metals on hydrogen sorption in nanocrystalline ball milled MgH_2-Tm (Tm=Ti, V, Mn, Fe and Ni) system. J. Alloys Compd. **292**, 247–252 (1999b)
47. G. Liang, J. Huot, S. Boily, R.J. Schulz, Hydrogen desorption kinetics of a mechanically milled MgH_2+5at% F nanocomposite. J. Alloys Compd. **305**, 239–245 (2000)
48. Z. Dehouche, R. Djaozandry, J. Huot, S. Boily, J. Goyette, T.K. Bose, R.J. Schulz, Influence of cycling on the thermodynamic and structure properties of nanocrystalline magnesium based hydride. J. Alloys Compd. **305**, 264–271 (2000)
49. J. Huot, J.F. Pelletier, G. Liang, M. Sutton, R.J. Schulz, Structure of nanocomposite metal hydrides. J. Alloys Compd. **330–332**, 727–731 (2002)
50. J.J. Reilly, G.D. Sandrock, Hydrogen storage in metal hydrides. Sci. Am. **242**, 98 (1980)
51. D.L. Douglass, The formation and dissociation of magnesium alloy hydrides and their use for fuel storage in the hydrogen car. Metall. Mater. Trans. A **6A**, 2179 (1975)
52. D. Cooper, C.Y. Wu, D. Yasensky, D. Butt, M. Cai, Hydrogen storage characteristics of nickel nanoparticle coated magnesium prepared by dry particle coating. KONA **23**, 139–151 (2005)
53. A. Zuttel, P. Wenger, S. Rentsch, P. Sudan, P. Mauron, C. Emmenegger, $LiBH_4$ a new hydrogen storage mateiral. J. Power Sources **118**, 1 (2003)
54. J.J. Didisheim, P. Zolliker, K. Yvon, P. Fischer, J. Schefer, M. Gubelmann, A. Williams, Dimanesium iron (II) hydride, Mg_2FeH_6 containing octahedral $[FeH_6]^{4-}$ anions. Inorg. Chem. **23**, 1953 (1984)
55. The Glassware Gallery, Planetary ball milling, online posting: www.ilpi.com/inorganic/glassware/ballmill.html
56. Fritsch "Pulverisette manual." www.fritsch.de/data/prospekte/e_pulverisette6.pdf
57. C. Suryanarayana, M. Dekker, Mechanical alloying and milling. Adv. Mater. **17**, 2893–2894 (2005)
58. Innovative Technology, System one glovebox, online posting: www.gloveboxes.com
59. TA Instrument Website, DSC tutorial, online posting: www.tainstruments.com
60. S. Srinivasan, Y. Goswami, E. Stefanakos, DSC studies of $Ba(OH)_2.8H_2O$ as a phase changed materials. Unpublished results (2009)
61. TA Instrument Website, SDT tutorial, online posting: www.tainstruments.com
62. Fisk University, Simultaneous differential scanning calorimetry & thermogravimetric analysis statistical review of world energy, online posting: www.fisk.edu (2005)
63. S. Srinivasan, Lithium amide-magnesium hydride complex hydrides. Unpublished results (2006)
64. J. Wade, An investigation of TiO_2-$ZnFe_2O_4$ nanocomposites for visible light photocatalysis. Master Dissertation, University of South Florida (2005)
65. New Mexico tech, FESEM types of signals, online posting: http://infohost.nmt.edu/~maximino/fesem_types_of_signals.htm
66. ETH Zürich Website, SEM technology, online posting: www.microscopy.ethz.ch/sem.htm
67. D. Escobar, Investigation of ZrNi, $ZrMn_2$ $Zn(BH_4)_2$ metal/complex hydrides for hydrogen storage. Masters Dissertation, University of South Florida (2007)
68. B.M. Clemens, GCEP technical report 2006, online posting: http://gcep.stanford.edu (2006)
69. Quantachrome Instruments Website, Autosorb1-C Chemisorption – Physisorption Analyzer manual. Online posting: www.quantachrome.com

70. A. Vitetoe, M. Jurczyk, S. Srinivasan, A. Kumar, E. Stefanakos, Destabilization of lithium aluminum hydride for hydrogen storage. NSF REU Workshop Poster Presentation, University of South Florida (2008)
71. Keck Interdisciplinary Surface Science Center, Fourier transform infrared spectroscopy (FT-IR), online posting: www.nuance.northwestern.edu (2005)
72. M. Niemann, Development of novel nanostructures and complex hydrides for hydrogen storage. Ph.D. Dissertation, University of South Florida (2009)
73. University of Arizona, Department of Chemistry, Introduction to mass spectrometry, online posting: http://www.chem.arizona.edu/massspec
74. S. Srinivasan, Mass spectrometry studies of Li-B-N-H decomposition. Unpublished results (2009)

Characterization of H_2 Adsorption Sites: Where Are the Hydrogens Stored in the Materials?

9

Ying-Pin Chen and Hong-Cai Zhou

Abstract

The most significant parameters such as pore size and binding energy need to be quantified to design advanced absorbents and improve their hydrogen uptake. The in situ and ex situ examination of hydrogen storage materials is helpful to provide the information with hydrogen favorable sites. The most common techniques to probe hydrogen molecules are:

- ***Neutron powder diffraction*** (NPD)
- ***Inelastic neutron scattering*** (INS)
- ***Variable temperature Infrared spectroscopy***
- ***Solid-state nuclear magnetic resonance*** (SSNMR)

In this chapter, several examples demonstrated how the hydrogen molecules store in the host materials. Knowing which structural characteristics contribute to hydrogen uptake became the design guidance because the effective moieties can be added by elegant synthetic methods. Scientists can introduce strong functional groups, modify the weak interacting parts, or tailor the structural geometry in the

Author Contribution: The chapter context was mainly compiled by Y.-P. Chen under the supervision of Dr. H.-C. Zhou. The introduction part, chemical expression, and the revision of other subsections were reviewed by Dr. J. Liu and Dr. S. Bashir.

Y.-P. Chen
Department of Materials Science and Engineering, Texas A&M University, College Station, USA
e-mail: ying-pin.chen@chem.tamu.edu

H.-C. Zhou (✉)
Center for Electrochemical Systems and Hydrogen Research, Texas A&M University, College Station, USA

Department of Chemistry, Texas A&M University, College Station, USA

Department of Materials Science and Engineering, Texas A&M University, College Station, USA
e-mail: zhou@chem.tamu.edu

Y.-P. Chen et al. (eds.), *Nanostructured Materials for Next-Generation Energy Storage and Conversion*, DOI 10.1007/978-3-662-53514-1_9

candidate materials based on the analysis results of material–H_2 interactions. ***Ligand elongation, interpenetration, impregnation, mixed-ligand, as well as introduction of open metal sites and charged frameworks*** were proposed to enhance H_2 uptake in the storage materials.

Contents

9.1 Characterization of Material–H_2 Interactions

Hydrogen as an energy carrier is one option as a clean alternative to fossil fuels, and technological development for its use is the focus of the current chapter. Hydrogen gas (H_2) is extremely volatile, as indicated a low volumetric energy density for on-board uses. The goal therefore is to design storage materials that can supply hydrogen at a density higher than liquid hydrogen [1]. For H_2 storage applications, a wide variety of adsorbents have been tested for their ability to adsorb and desorb hydrogen. However, simply meeting the US Department of Energy (DOE) storage density target is only the first step in wide scale use of H_2 as an energy carrier stored within adsorbents. Other parameters such as fast kinetics, good reversibility, and low heat load treatments to adsorb/desorb hydrogen under ambient conditions are necessary for practical situations.

Gas storage is not simple diffusion into pores, but use of electrostatic, ionic forces to trap and release hydrogen gas. One of the thermodynamic parameters is binding energy. Energies less than 10 kJ/mol require the hydrogen molecules have lower kinetic energy, achieved by use of cryogenic temperature ($T < 123$ K), or the gases be coalesced, achieved through compression. In contrast, if the binding energy is too high, (>30 kJ/mol) additional thermal treatment is required to assist in the release of hydrogen from the

materials. Using, $\Delta G = \Delta H - T\ \Delta S = 0$, where ΔH is the binding energy of the adsorption system, and ΔS is the entropy of the surrounding hydrogen, suitable values can be calculated and are estimated to 131 J/K · mol at 298 K/1 atm [2]. The ideal binding energy is estimated to be approximately 40 kJ/mol at ambient conditions.

The most significant parameters in design of absorbent need to be quantified, such as pore volume, binding energy, and binding and release kinetics. The in situ and ex situ examination of hydrogen storage materials in the absence and presence of hydrogen is required to obtain the appropriate kinetics and chemical stability information. The techniques span the field of spectroscopy, microscopy, mass spectrometry, and electrochemistry. The most common techniques to probe H_2 molecules are *neutron powder diffraction (NPD), inelastic neutron scattering (INS), infrared spectroscopy (IR),* and *solid-state nuclear magnetic resonance (SSNMR)* used to probe H_2 active sites and/or the corresponding binding energy on the host materials. The acquired information may not be complete due to different natures of the interactions between the hydrogens and the host materials. Based on those complementary characterization results, materials can be tuned to increase the H_2 uptake. The strategies employed to increase uptake, control kinetics and stability are discussed in subsequent sections; however, detailed theory and analysis are beyond the scope of this chapter and the reader is guided to the literature section for specific research details or reviews on a single area.

9.2 Neutron Powder Diffraction

9.2.1 Comparison Between Neutron and X-ray Diffraction

Neutron powder diffraction (NPD) is one of the common tools to probe H element in the host matrix. The analytical method of neutron diffraction is quite similar to that of X-ray diffraction (XRD), in terms of its operational principles. The fundamental difference between these two techniques is the way the beam is scattered by matter. Neutrons interact with atomic nuclei, while X-rays disturb the electron clouds of the samples [3]. X-ray diffraction produces stronger interference signals since X-ray scattering is proportional to the square of atomic number (Z^2), while scattering from a neutrons shows little systematic tendency with Z (Fig. 9.1a).

Moreover, neutron diffraction is able to distinguish elements from one another and isotopes (such as hydrogen, H and deuterium, D) on account of the difference of the scattering cross section (see Fig. 9.1 note) [3]. The scattering cross section is related to the spin state of the combined nuclei in that element. Also because of the property of spins, neutrons are sensitive to probe magnetic moment of atoms, opening a wide scope to study magnetic materials [6].

As complementary measures, powder XRD (PXRD) and NPD have different sensitivities for different elements. Lighter atoms are generally more detectable by neutron diffraction than by X-ray diffraction (Fig. 9.1b). Especially, the nuclei ^1H and ^2H (deuterium, D) are strong scatters for neutrons. This greater scattering power

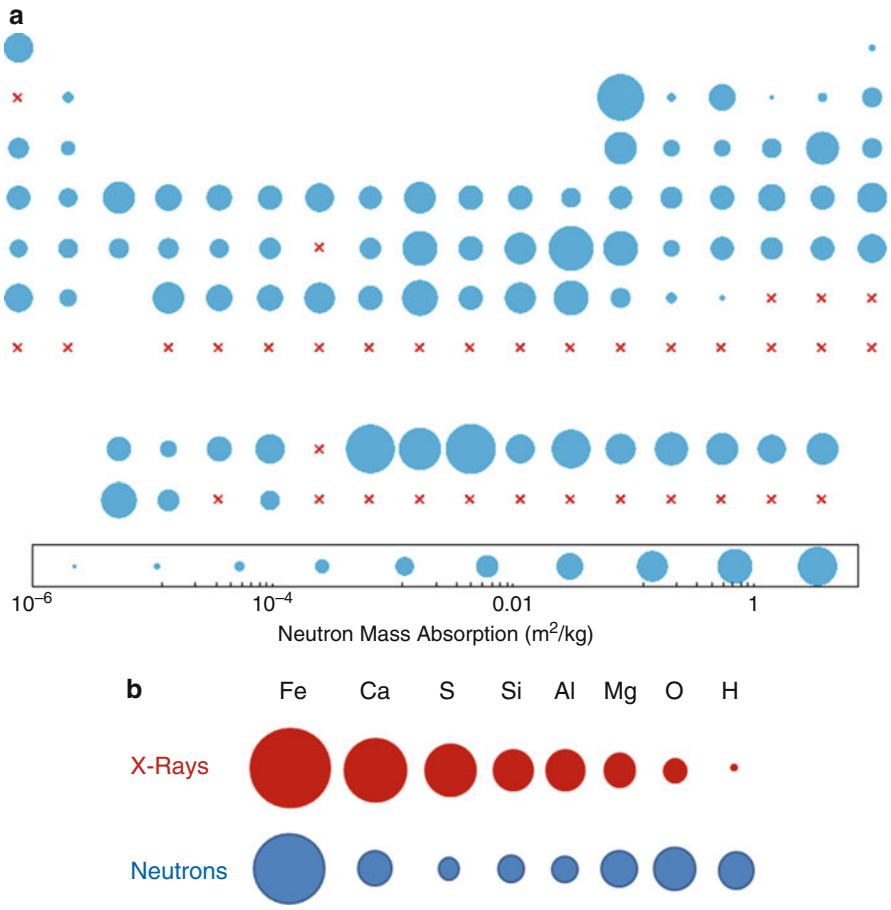

Fig. 9.1 (**a**) Neutron scattering cross sections in periodic table. (**b**) Comparison between cross sections of X-rays and neutrons for selected elements. The values of neutron scattering lengths and cross sections of all the elements and their isotopes were tabled in the Ref. [4]. [Note 1] Cross section is measured in barns (1 barn = 10^{-28} m^2). If neutrons hit this area, neutrons are scattered isotropically. [Note 2] The coherent scattering lengths for the elements H and D are -3.74×10^{-13} cm and $6.67 \cdot 10^{-13}$ cm, respectively. The incoherent scattering lengths for the elements H and D are 25.18×10^{-13} cm and 3.99×10^{-13} cm, respectively [5]. The negative sign for the scattering length of H stands for that the neutron wavefunction is out of phase with respect to the incident neutron wavefunction

means that the atomic position and the thermal motions of hydrogen or deuterium in the host material can be detected by NPD. The observation for H element or H_2 molecules is not possible by using PXRD measurements. Table 9.1 summarizes the major advantages and drawbacks of the NPD.

Neutrons are located in the center of the nuclei and are electrically neutral. Therefore, neutrons can penetrate and travel larger distance through most materials than charged particles. Compared with 99% per millimeter for X-rays, the

Table 9.1 Advantages and disadvantages of NPD

Advantages	Disadvantages
Sensitive to light elements/isotopes	High costs for maintenance (billions)
Probe magnetic materials	Low fluxes compared to synchrotrons
High penetration	Relatively large amounts of samples
Low absorption	Relatively large single crystals
Wide range of wavelengths (Å ~ μm)	
High signal-to-noise ratio	
Absence of radiation damage	
Information for structure/dynamics	

attenuation of a neutron beam is only 1% per millimeter in aluminum [5]. Once deep penetration happens, however, it means neutrons are weakly scattered. While synchrotron-based X-ray can emit 10^{18} photons/s·mm^2, available neutron sources can only produce 10^4 neutrons/s·mm^2 [5].

The characterization of H_2 adsorption sites is carried out by NPD to examine desolvated samples at low temperature and/or under a hydrogen loading pressure, from which the precise spatial resolution of hydrogen molecules is obtained. However, H atoms possess large incoherent scattering cross section (see note in Fig. 9.1) in neutron diffraction experiments, leading to uncertainties in positional identification. This positional uncertainty can be lowered by using deuterium (D_2) or HD, a substituent to minimize the signal background arising from the hydrogen's large incoherent scattering cross section [7]. Because H_2 and its isotope D_2 have similar chemical interactions but differ only in their isotopic mass, NPD studies on D_2 should shed light on the behavior of H_2 in the same host materials.

The NPD patterns (Fig. 9.2) of the guest-free framework and those patterns with various D_2-loadings are both required to achieve the difference maps (Fig. 9.3a). Using the guest-free framework as the model, Fourier difference method is performed to find the scattering-length density for the missing D_2 molecules in the guest-free model. Consequently, the exact D_2 adsorption positions and the corresponding occupancy can be refined, in a similar manner to PXRD analysis. Furthermore, the adsorption preference and the relative binding energies for those sites can be ascertained using information derived from NPD scattering. In the following two cases, the H_2/D_2 adsorption sites and the H_2/D_2 molecular arrangements in several well-known porous media were extracted by using NPD method.

9.2.2 Hydrogen/Deuterium Adsorption Sites in Crystalline Materials

Adsorption Sites Adjacent to Uncoordinated Metal Centers

An example of NPD study of hydrogen binding materials is the binding of deuterium (D_2) sorption process in copper benzene-1,3,5-benzenetricarboxylate metal-organic framework (MOF) system (HKUST-1, Cu-BTC, Fig. 9.3a). The preference of the

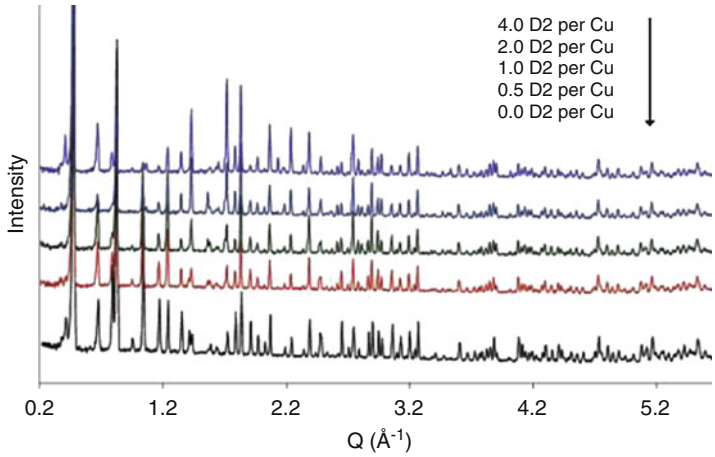

Fig. 9.2 NPD patterns collected for a classic metal-organic framework, HKUST-1. The patterns sampled on a guest-free framework and those with various D_2-loadings (Reproduced with permission from Ref. [8]. Copyright © 2006 American Chemical Society)

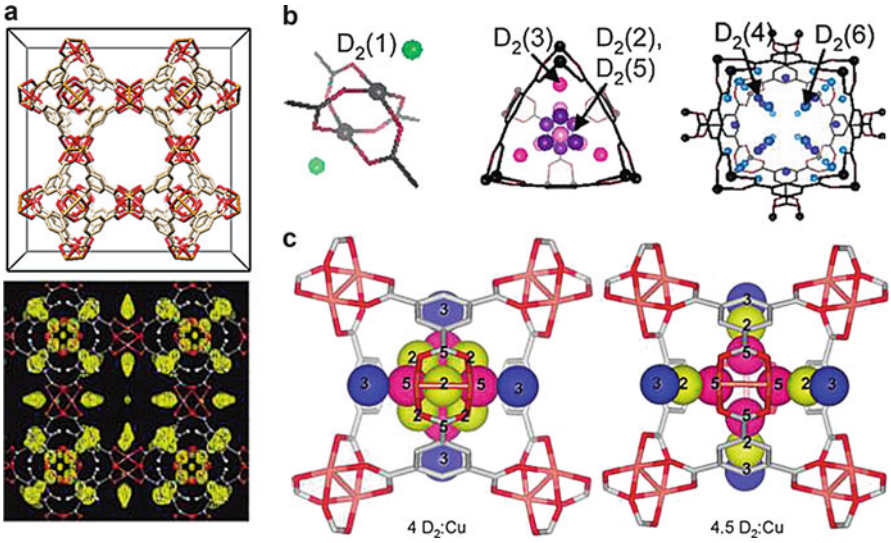

Fig. 9.3 (**a**) The structure of HKUST-1 and the real-space Fourier-difference map; (**b**) D_2 active sites in HKUST-1: site 1 is the axial Cu sites; sites 2, 3, and 5 viewed along [111] in the small octahedral pores; and sites 4 and 6 viewed along [100] in the large cuboctahedral cages (Reproduced with permission from Refs [8, 9].. Copyright © 2006/2011 American Chemical Society)

adsorption sites in HKUST-1 can be analyzed by monitoring the occupancy of each site as a function of D_2 loading. In the in situ diffraction experiments, well-known dosing volumes of D_2 were loaded into a capillary line packed with crystalline samples at 77 K. The NPD patterns were diffracted and collected at 3.5 K from D_2-loaded samples with various D_2/unit ratios (Fig. 9.2).

Interpreted by Fourier difference maps, it revealed that the most favorable site, $D_2(1)$, is located 2.39 Å away from the unsaturated axial sites of the dinuclear Cu centers and that the filling sequence is progressively from $D_2(2)$ to $D_2(6)$ (Fig. 9.3b) [8, 9]. The analysis also suggested that the *uncoordinated metal centers (UMCs)* play a primary role in hydrogen adsorption due to Coulomb-type electrostatic interactions arising from charge overlap of H_2-σ and metal-*d* orbitals [10]. Higher concentration of D_2 loadings helped the identification of the next adsorption positions. It showed that the minor adsorption sites are sequentially occupied from the small octahedral cages, the cage windows, and then to the large cages. It can be noted that in the small octahedral cage (Fig. 9.3c), the D_2 molecular distribution was highly concentration-dependent even in such limited space, which was deemed a compromise between D_2-D_2 and D_2-framework interactions. In the isostructural Cr-BTC, however, the uncoordinated Cr (II) site is not the most favorable site at initial D_2 loadings. This is a very rare example. The filling order from UMCs to cage windows is applicable until an elongation of Cr-Cr binding is observed at higher coverages [11].

The strong correlation between UMCs and enhanced hydrogen surface density was also displayed in MOF-74 that possesses highest exposed metal density [12] and in NOTT-112 that has exposed Cu(II) sites in the cuboctahedral cages [13]. In MOF-74, exposed Zn (II) sites are the first sites of D_2 binding with a distance of 2.6 Å (the position 1 labeled in Fig. 9.4c). The second and third adsorption sites are, respectively, located above a triangle of oxygen atoms and near a benzene ring. In NOTT-112, the Cu-D_2 binding length is 2.23 Å.

Besides those carboxylate-based MOFs, a series of azolate-based MOFs constructed with M(II) (M = Mn, Fe, Cu) and tritopic trazolate ligands (BTT^{3-},1,3,5-benzenetris-tetrazolate) were studied because of their record-high adsorption heat of −11.9 kJ/mol for Mn-BTT, −12.9 kJ/mol for Fe-BTT, and −10.4 kJ/mol for Cu-BTT [18]. The NPD analysis was employed to find out what kind of interactions is responsible for this high enthalpy. As expected, the result revealed that the first D_2 adsorption site is adjacent to the unsaturated Mn (II) centers with a distance of 2.27 Å. The second site is inside a bowl-shaped cavity above the chloride anion with a van der Waals contact of 3.47 Å (the same positions I and II in Fig. 9.4d) [19].

Adsorption Sites Near Organic Linkers

Yildirim *et al.* had adopted the same method to identify the H_2/D_2 adsorption sites in ZIF-8 (Zn (II) ions coordinated by four imidazolate rings) [14], because of its high chemical stability and diverse zeolite-type topologies. Differing from MOFs mentioned above, ZIF-8 possesses no UMCs but features ZnN_4 tetrahedra in the structure. Surprisingly, the primary H_2-ZIF-8 interactions are present near the C = C double bonds of the *imidazolate organic linkers* (Fig. 9.4b), rather than near the ZnN_4 tetrahedra. MOF MIL-53 (Cr) also displays strong adsorption sites that are

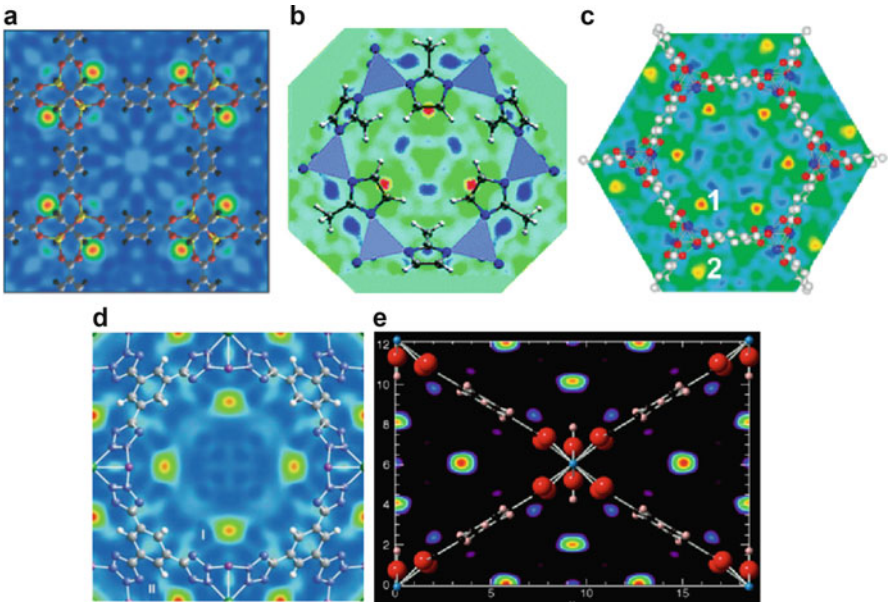

Fig. 9.4 The real-space Fourier-difference scattering-length density superimposed with structures of (**a**) MOF-5, (**b**) ZIF-8, (**c**) MOF-74, (**d**) Cu-BTT, and (**e**) MIL-53(Al). The maps show the primary H_2 adsorption sites are located at (**a**, **c**, **d**) exposed metal clusters, or near (**b**) C = C bonds of the imidazolate organic linkers (*red-yellow* regions) (Reproduced with permission from Refs [12, 14–17]. Copyright © 2008/2007/2014 American Chemical Society; Copyright © 2005 American Physical Society; Copyright © 2007 WILEY-VCH)

located at sharp and blunt corners constructed by the organic linkers, but not near the Cr-O clusters (the same positions in Fig. 9.4e) [20]. These results suggested that modifying organic linkers may be an effective strategy to increase H_2 uptake.

Adsorption Sites in a Cage

The rare earth metal-organic framework, $Y(BTC)(H_2O)\cdot 4.3H_2O$ (BTC: 1,3,5-benzene tricarboxylate), was investigated for the H_2 adsorption sites [21]. This MOF was found to possess several distinct sites in the pores instead of UMCs. The most primary H_2 adsorption site is closer to the BTC linkers: 3.7 Å from the benzene rings and 4.27 Å from the exposed Y^{3+} ions. The second site is positioned in the pores: 3.6 Å from the benzene ring and 3.9 Å from the exposed Y^{3+} ions. The other two weak adsorption sites are only present at high H_2 loading levels. Overall, it pointed out that the cages with pore size about 6 Å have stronger van der Waals force than the interaction with metal ions. On the other hand, first-principle simulations on several paddle-wheel containing MOFs also demonstrated that the structural confinement effect can enhance the H_2 uptake on weak adsorption sites near the narrowest windows and small cavities ranging from 5.3 Å to 8.5 Å [22]. The calculated and experimental results concluded that for H_2 uptake improvement an

optimal pore size for H_2-framework interaction is ~6 Å, as opposed to the exposed metal sites. The analysis suggests that constructing pore size of 6 Å should enhance H_2 capacity in MOFs.

9.2.3 Observation of Hydrogen/Deuterium Interlinked Clusters

Hydrogen confinement in materials has usually been concerned for two reasons. First in the area of fundamental physical phenomenon of super-fluid confined in porous materials, which suppresses H_2 bulk freezing point (13.8 K), and second in practical application, where H_2 storage capacity in porous materials has been applied in isotope separation and catalysis [23].

In addition to identifying the adsorption positions, NPD analysis is a powerful technique to observe the packing structure of guest molecules in a confinement space. In the system of $D_2/AlPO_4$-5 [7], it has been found that the diffraction pattern of the empty $AlPO_4$-5 zeolite is greatly modified after D_2 loading. With Rietveld refinement, the structure of confined D_2 molecules in $AlPO_4$-5 possesses a chain of hexagonal "tetramers" with a super-cell of $a = b = 3.62$ Å, $c = 16.7$ Å (Fig. 9.5). The D_2 tetramers show a commensurate effect to sorption sites when the guest molecular size matches the inner surface characteristics, such as chemical nature, framework topology, inner surface periodicity, and electric field [7]. The D_2 molecular arrangement is in close correlation with the D_2 uptake determined by sorption isotherm measurements.

The similar H_2/D_2 molecular clusters are also formed in metal-organic frameworks. National Institute for Standards and Technology Center for Neutron Research (NIST) has made a number of studies on H_2 adsorption studies with NPD technique. With Rietveld refinements, four adsorption sites were obtained from the Fourier difference maps in MOF-5 (Fig 9.4a). The primary adsorption sites were located at the center of the three ZnO_3 triangular faces of the tetrahedral Zn_4O cluster, while the secondary adsorption sites were at the top of the ZnO_3 triangles. The third one was

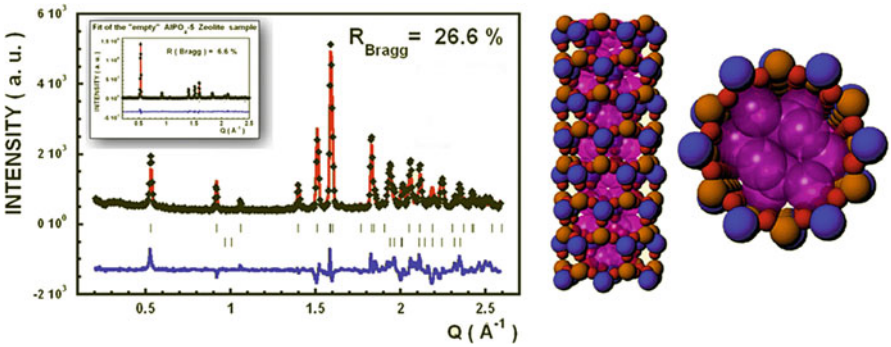

Fig. 9.5 Rietveld refinement of the neutron diffraction pattern measured for D_2 confined phase in the $AlPO_4$-5 zeolite and *hcp* "tetramer" chain (*purple*) (Reproduced with permission from Ref. [7]. Copyright © 2007 Elsevier Inc.)

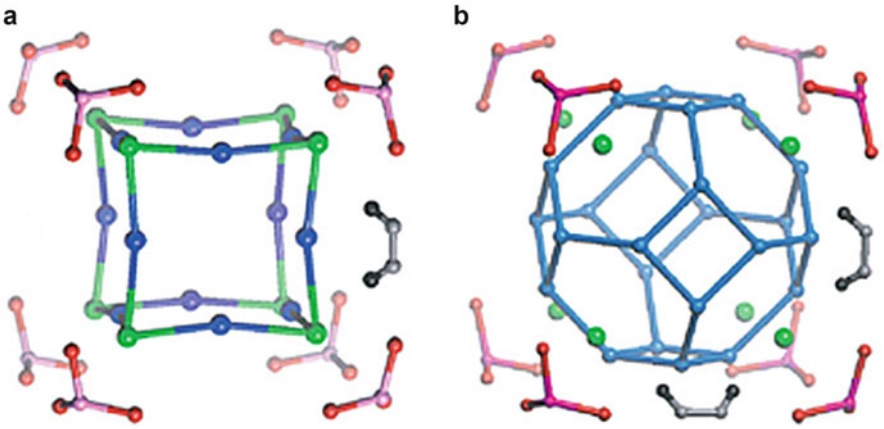

Fig. 9.6 Different D_2 nanocages (constructed by *blue* and *green spheres*) in MOF-5 obtain (**a**) 34 D_2 and (**b**) 46 D_2 per unit loading, respectively (Reproduced with permission from Ref. [15]. Copyright © 2005 American Physical Society)

located above two oxygen ions, and the fourth one was the top of the aromatic rings. It demonstrated that the metal-oxide nodes are the key positions for the H_2 uptake of 6.8 wt% in the MOF-5.

Interestingly, it was further found that under the condition of low temperature and high concentration, D_2 molecule neighbored each other with a distance of 3.0 Å, which is shorter than the intermolecular H_2—H_2 distance observed in the solid H_2. The same phenomenon was also seen in ZIF-8 [14] and MOF-74 [12]. These findings suggest a different efficient packing of up to 11.0 wt% H_2 uptake in MOF-5 compared to liquid and solid H_2. (The Department of Energy has determined hydrogen storage density of 5.5 wt% for the realization of fuel-cells to replace petroleum-fueled vehicles.) Additionally, these D_2 molecules construct interlinked molecular nanocages with distinguishable topologies upon different D_2 loadings (Fig. 9.6). It indicates that MOF lattices can be employed as a template to build artificial hydrogen nanoclusters, which might possess unique quantum natures and confinement effects [15]. As a future perspective, it points out a direction for this important theoretical research.

9.3 Inelastic Neutron Scattering

9.3.1 Introduction to Inelastic Neutron Scattering

Classification of Neutron Scattering

Neutron scattering types (Fig. 9.7), including elastic and inelastic scattering, are determined by the speed of the neutrons (whether fast or thermal), the nucleus it strikes, and its neutron cross section. In the first case, we discussed the diffraction (Fig. 9.8a); in the second case, we illustrated using spectroscopy (Fig. 9.8b). Elastic

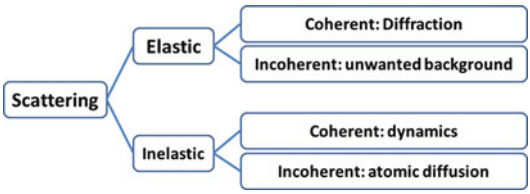

Fig. 9.7 The classification of neutron scattering

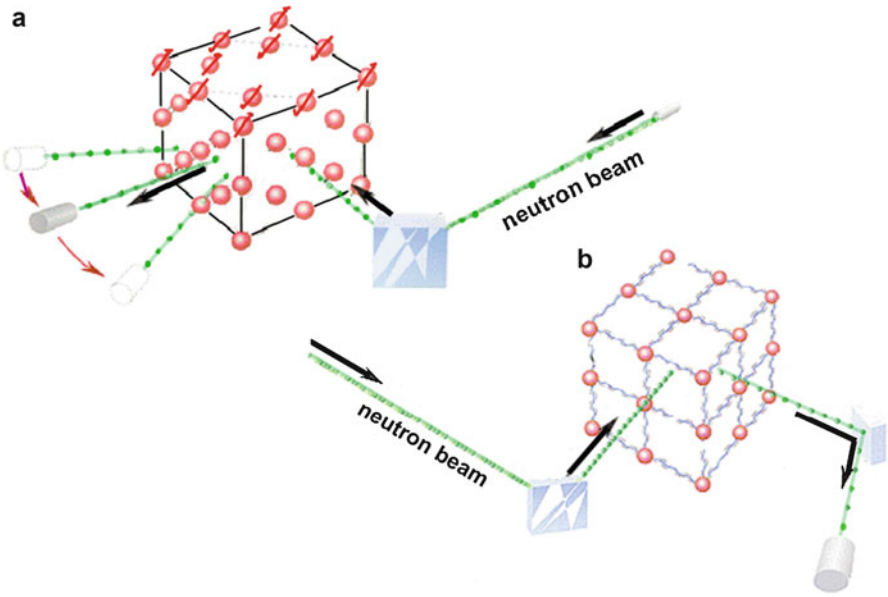

Fig. 9.8 (**a**) Elastic neutron scattering: when the neutrons interact with the atoms in the crystal, the neutrons change their original direction without losing energy, which is recorded by the detector. (**b**) Inelastic neutron scattering: when the neutrons penetrate through the material, they absorb or emit energy from phonons (e.g., atomic oscillations in the material)

neutron scattering does not involve energy change upon neutron collision; it usually gives one form of diffraction providing structural information. However, inelastic neutron scattering (INS) does involve change of energy upon collision, and the technique can offer vibrational spectra obtained from the process of neutron thermalization [24]. If the energy change is negligible compared to the incident energy, then quasielastic scattering occurs.

A variety of neutron scattering instruments has arisen (Table 9.2) with sufficient scattered intensity to determine the structural details in the materials. For example, neutron diffraction has been utilized to determine atomic arrangements, while inelastic neutron scattering has been for vibrational spectroscopy. Small-Angle Neutron Scattering (SANS) has been utilized to study polymers or colloids, while reflectometry has been utilized for layered structures [5]. In this section, we will

Table 9.2 Various types of neutron scattering experiments

Name	Energy change	Basic process	Information
Diffraction	Elastic	Coherent	Structure
SANS	Elastic	Coherent	Big picture (to provide information of the structure of various substances at a mesoscopic scale of about 1–100 nm)
Reflectometry	Elastic	Coherent	Depth structure
QENS	Quasielastic	Incoherent	Diffusion, dynamics [17]
NSE (spin echo)	Quasielastic	Incoherent	NMR time scale
Backscattering	Inelastic	Coherent/ incoherent	–
Vibrational	Inelastic	Coherent/ incoherent	–
Neutron compton	Inelastic	–	H/D wave functions

Reproduced with permission from Ref. [24]. Copyright © 2006 Elsevier B.V.
[Note 1] Coherent scattering: there is a phase relationship among the scattered neutrons. Coherent cross section represents average scattering, produces interference, and thus provides structure information
[Note 2] Incoherent scattering: there is no phase relationship due to different scattering length of different atoms. Incoherent cross section represents standard deviation in scattering

focus on how inelastic neutron scattering (INS) technique characterizes H_2 molecules in the host materials.

Working Principle of Inelastic Scattering

Atoms in a crystal lattice are usually analogous to coupled pendulums connected with springs. When an atom (pendulum) is displaced from its "official" position due to thermal energy (external force), the binding force (spring) that couples the atoms (pendulum) will cause the neighboring atoms (adjacent pendulum) to oscillate, accordingly [5]. The whole effect represents a wave-like motion in three dimensions, which can be described by a superposition of waves of various frequencies and wavelengths. This vibrational wave in a crystalline lattice is known as phonons, which have a quantized energy *hv;* (v, the frequency of atomic motion, Hz). The frequency of the phonon is determined by the atom masses (amu) and the binding forces (kJ/mol or eV).

As mentioned above, when neutrons go through the crystalline lattice, they absorb or emit a quantized energy *hv* from phonons and thus gain or lose energy (if energy was not lost, this could constitute elastic collisions). If the thermal neutrons have the energy falling in the meV range, scattering by a phonon will result in a considerable fractional energy change to be accurately observed in INS spectra [5].

In the case that none of the scattering from the host structure is changed in peak positions, H_2/D_2 molecules will be regarded to be trapped in the structure without causing structural changes. During the INS measurements, a blank spectrum and a

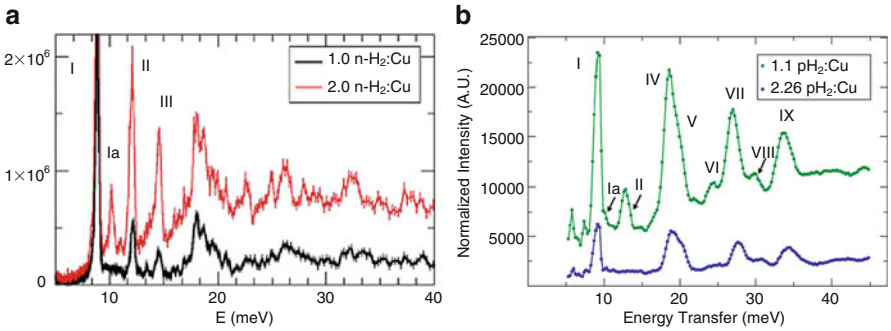

Fig. 9.9 INS spectra of H_2 adsorbed in HKUST-1 after subtraction of the H_2-free framework spectra as measured on the (**a**) QENS spectrometer and (**b**) filter-analyzer neutron spectrometer (FANS). Note that Data set collected from different instruments measure different trajectories in momentum transfer, Q. QENS measures the scattering function, S(Q, ω) and FANS measures intensities proportional to the densities-of-states (Reproduced with permission from Ref. [25]. Copyright © 2009 IOP Publishing. All rights reserved)

spectrum on a sample with various amounts of H_2/D_2 are both recorded (usually around 15 K). If the background scattered from the blank host structure is removed, the additional scatterings can be attributed to H_2/D_2 adsorption (Fig. 9.9). Hence, the INS analysis has discovered the fine details of H_2/D_2 adsorption in numerous porous materials, such as zeolites, metal-organic frameworks, phosphates [26], prussian blue analogs [27], and Buckminsterfullerene (C_{60}). We will focus on two practical examples to demonstrate how INS methods are capable of providing such information later on. Peaks with the highest rotational barrier to the positions near metal clusters are first annotated [1]. However, only the INS adsorption band cannot be assigned to specific positions. A model is acquired to propose peak assignments for INS spectra and to calculate the adsorption energy for a given site [28].

Besides the peak positions, peak profiles keep a clue to the microstructure and the constitution way [29]. INS can provide information on the long- and short-range correlations in adsorbed systems. The D_2 scattering consists of sharp diffraction peaks and a broad background. The sharp diffraction peaks reflect the adsorbed D_2 with long-range translational correlations. The broad structureless scattering is proposed to be resulted from short-range correlations of a liquid phase or diffuse scattering arising from randomly occupied adsorption sites, large zero-point motion or orientational disorder of the adsorbates [30]. The diffuse scattering will not be discussed in this chapter.

9.3.2 Hydrogen/Deuterium Filling Orders and Binding Energy

We take the zeolite 13X (Na_{86} $[(AlO_2)_{86}(SiO_2)_{106}]$•$H_2O$) as our first example to demonstrate INS's probe ability of H_2/D_2 infusion. This material possesses 25-Å face-centered cubic structure with an alumino-silicate backbone, 12-Å-diameter

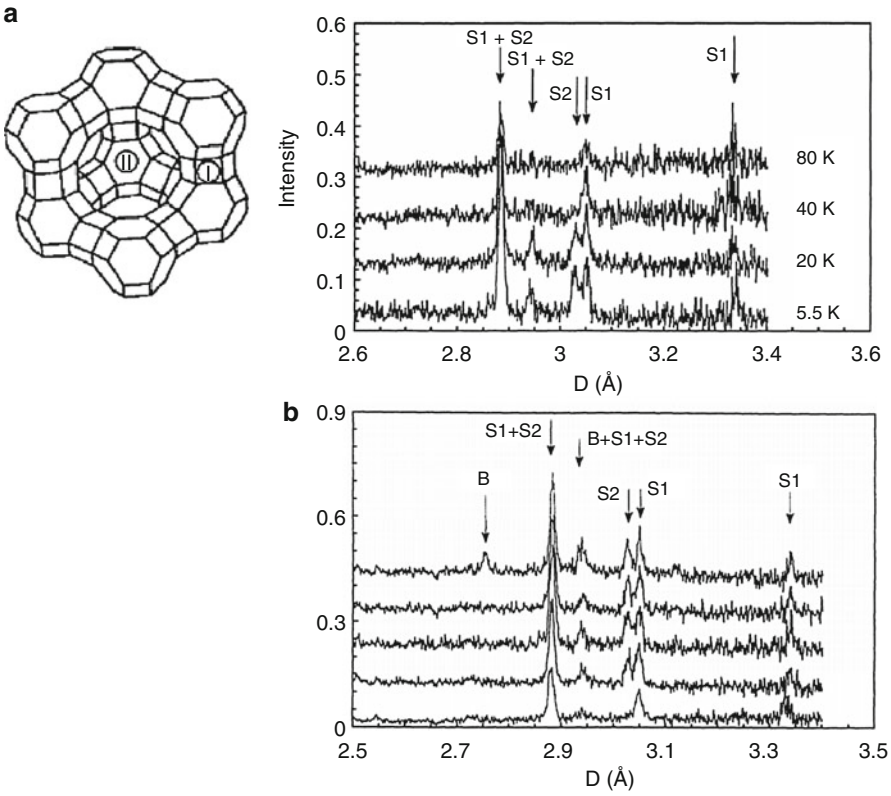

Fig. 9.10 (**a**) Scattering from D_2 adsorbed in zeolite 13X at temperatures of 5.5, 20, 40, and 80 K with the empty zeolite scattering removed. (**b**) Scattering at 5.5 K with various D_2 loadings of 0.705, 0.893, 1.024, 1.252, and 1.264 *l* atm from bottom to top (Reproduced with permission from Ref. [30]. Copyright © 1994 American Physical Society)

pores, and 9-Å-diameter channels. In the INS measurement, the adsorption states of D_2 in zeolite 13X were monitored at temperatures ranging from 5.5 K to 80 K with a variety of gas loadings (Fig. 9.10) [30]. Unlike NPD, all spectroscopy technique including INS cannot directly provide positional information for bound H_2 molecules. This *variable temperature INS* experiment, nevertheless, is straightforward to estimate the relative binding strength for each site in porous materials.

At lower temperatures (ranging from 5.5 K to 20 K), diffraction peaks associated with both the S1 and S2 sites are present. However, it is not possible to identify the absolute positions merely based on the data from Fig. 9.10. Upon heating to 40 K (see Fig. 9.10a), the peaks associated with the S2 sites disappeared, indicating that the binding energy of S2 sites is on the order of 40 K. While the reflections associated with the S2 peak are absent at 40 K, the reflections associated with the S1 peaks are still present at 40 K but reduce the intensity at 80 K. This suggests that the binding energy of S1 sites is higher than the order of 80 K. Therefore, it can be classified as two

energy-defined positions within the structure, interpreted as D_2 molecules captured by the first and the second adsorption sites sequentially. After the two adsorption sites are saturated with more D_2 loadings (Fig. 9.10b), a bulk phase, labeled as B, is interpreted as bulk D_2 either on the surface or between the grains of the zeolite [30]. The peaks located at 2.76, 2.94, and 3.13 Å match the peaks scattered from the hexagonal structure of D_2, which is supposed to be outside the zeolite cavities.

Although VT-INS analyses for simple zeolite structures are relatively straightforward due to their symmetries and chemical compositions, the analyses can also be performed on complex systems, such as metal-organic frameworks. Three distinct INS peaks among more than seven peaks in the spectra were assigned to three binding sites in HKUST-1, which are progressively populated [31]. The peak I, II, and III were indicative of the D_2 located at the UMCs, in the small octahedral cags, and near the cage windows, respectively [31]. The peak III is also identified as a free-rotor in larger cavities [25]. Peaks at higher energy regions might be related to D_2 attached to the UMCs at low loadings but become more complicated upon D_2 increasing. With a help of hindsight, the postulation can be verified by the NPD studies in the Sect. 9.2.2. In another case of single-walled carbon nanotubes, a complicated interaction was found between the H_2 and the nanotubes with orientation dependence [32].

9.3.3 Minute Difference in Binding Sites in Reticular Structures

INS analysis has also been used to characterize the H_2 binding sites in other metal-organic frameworks. Based on the geometrically tailorable nature of MOFs, a series of iso-reticular MOF-5 [33], and a family of functionalized MOF-74(M) isomers [34] were systematically investigated. As a sensitive probe, INS spectrum on each material provides an excellent opportunity to see the detailed chemical differences between these iso-reticular structures.

In the IRMOF series (formed from Zn_4O nodes with various linear ligands), the structures were chemically similar but displayed H_2 uptake: 5.0 molecules for IRMOF-1, 6.9 molecules for IRMOF-8 and 9.3 molecules for IRMOF-11 per formula unit at 1 atm [35]. At a loading level of four hydrogen molecules per metal node, the INS measurement showed that chemical environments of the adsorption sites are quite different for the three IRMOFs. More than two peaks present in the INS spectra are regarded to be the transitions associated with more than two bonding sites. The main peaks located at 10.3 meV and 12.1 meV were assigned to the H_2 adsorption site I and II (see Fig. 9.11), which are the 0–1 rotational transition listed in Table 9.3. The energy barrier for the rotation of H_2 adsorbed on sites I and II was 1.7 and 1.0 kJ/mol and supposed to be responsible for the H_2 uptake [36].

The result indicated that the number of rings in the organic moiety plays a role in H_2 adsorption capacity besides the metal sites. The organic linkers are not only able to determine pore sizes, but may also alter the electron distribution between the metal nodes and the linkers. Based on the NPD studies on MOF-5 (Fig. 9.4a), the

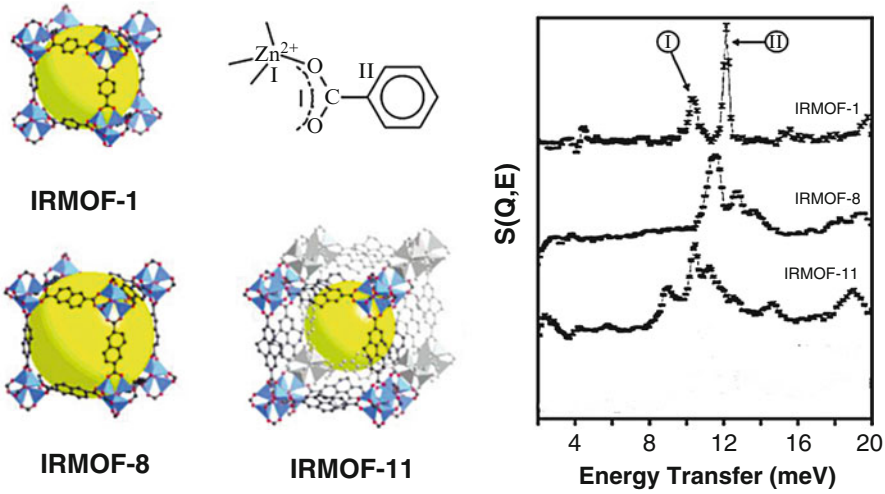

Fig. 9.11 The series of iso-reticular MOFs: IRMOF-1 (known as MOF-5), IRMOF-8, IRMOF-11 analyzed by INS method. Note that IRMOF-11 consisted of two interwoven frameworks, one shown in gray-scale. The *yellow spheres* represent the large pore of each structure (Reproduced with permission from Ref. [33]. Copyright © 2005 American Chemical Society)

Table 9.3 Model calculation (the method described in Ref. [28]) and proposed peak assignment for INS data above

Materials	Sites	Transition energy (meV)			Potential barrier (kcal/mol)
		0–1	0–2	1–2	
IRMOF-1	I	**10.3**	17.5	7.5	0.42
	II	**12.1**	15.5	4.4	0.24
	III	12.5	15.8	3.4[a]	0.19
	IV	13.3	15.4	2.1[a]	0.13
IRMOF-8	I	10.8	17.2[a]	6.4[a]	0.36
	II	11.5	16.6	5.1[a]	0.29
	III	12.8	15.7	3	0.17
	IV	14.4	14.9	0.5[a]	0.03
	Zn^{2+}defect	8.1	19.7[a]	11.6[a]	0.66
IRMOF-11	I	8.9	18.9	10	0.56
	II	10.5	17.4	7[a]	0.39
	III	11.2	16.9	5.7	0.32
	IV	13.8	15.2	1.4[a]	0.08

Reproduced with permission from Ref. [33]. Copyright © 2005 American Chemical Society
[a]Expected but not observed

primary H_2 adsorption sites are located near Zn_4O clusters and the carboxylate groups. Therefore, the H_2 binding sites around the metal clusters and the carboxylate groups might be affected by the electrophilic/electrophobic nature of the organic linkers.

The similar conclusion was also drawn in the system of M_2(*m*-dobdc) [M = Mg, Mn, Fe, Co, Ni; *m*-dobdc^{4-} = 4,6-dioxido-1,3-benzenedicarboxylate], which is a *meta*-functionalized version of their well-known isomers MOF-74 [34]. The symmetry of the ligand field of the *m*-dobdc linker is altered, thus increasing the H_2 binding enthalpy of 0.4 ~ 1.5 kJ/mol compared to M_2(dobdc). Such enthalpy increase was attributed to how electronic difference in the frameworks changes the interactions of the adsorption sites (open metal sites in this example) with hydrogens.

9.4 Infrared Spectroscopy

9.4.1 IR Response to Free and Trapped Hydrogen Molecules

Infrared spectroscopy is another useful technique to see if H_2 molecules are trapped in the host materials. The perturbation induced on the H_2 molecule by surface active sites brings about the onset of IR activity of the target dihydrogen and a redshift of the H-H stretching mode (unperturbed v(H-H) mode at 4161.1 and 4155.2 cm^{-1} for *para*- and *ortho*-H_2, respectively, as reference [37]). Simply speaking, the free H_2 molecules are infrared (IR) inactive, while the adsorbed H_2 molecules become active. This is because one molecule must have a dipole moment to act as an antenna that can interact with the photon [38]. The free homonuclear H_2 has no permanent dipole moment to absorb photons, thus being infrared inactive. In contrast, hydrogen's IR activity appears through interactions with the host materials.

The isosteric heat of adsorption is an average measure of all adsorption sites at low H_2 loadings, which is unlikely to differentiate the isosteric heat of individual adsorption sites. But the IR technique (as well as INS) can tell the interaction difference with a site-specific manner even though they have very similar interaction energies. When the surroundings induce H-H bond to be polarized and then interact with incident photons, the H-H stretching mode is shifted to a lower frequency [39]. The information of frequency shift (Δv) accordingly suggests different binding energy of the specific sites.

On the other hand, the atoms in host frameworks are not static. The perturbations of hosts, or the combination bands present in the H_2 stretching range, also respond to the guest incorporation. Because this effect might lead to mis-assignments, the first necessary step to quantify the degree of perturbation of the host materials is to examine the IR spectra using different probing gases, such as He or D_2 at various loading pressures [29]. The hydrogen stretch vibrational region for some materials is at 4000–5000 cm^{-1}, whereas the stretch frequency of *ortho*-D_2 is at 2983 cm^{-1}. Hence, deuterium is a perfect reference to obtain a clean background and to remove interference from host-induced absorption bands (>4000 cm^{-1}) [29]. After H_2 incorporated, we can conclude the newborn features unrelated to hosts' combination band spectrum are unambiguously assigned to the perturbed H-H stretch of H_2 molecules adsorbed in the host materials.

9.4.2 Indirect Structural Information and Selected Reference

The following is a practical example demonstrating variable-temperature infrared spectroscopy used to probe the H_2-framework interactions. It reported that a series of IR spectra was recorded with the increasing hydrogen equilibrium pressure in MOF-5 [36]. In the MOF-5 system, two doublets, at 4088–4093 cm^{-1} and 4175–4181 cm^{-1}, were the characteristic of the IR peaks attributed to framework overtones (v(CO) vibrations and v(CC) of benzene ring modes). After H_2 loading with increasing equilibrium pressure, the above bands were broadened and shifted as shown in Fig. 9.12a. It was noticed that new sharp peaks resulting from those adsorbed H_2 were increased at 4110–4150 cm^{-1} interval. The small red shifts of all the vibrational transitions of H_2 indicated that H_2 did not undergo dissociative adsorption or directly interact with exposed Zn (II).

At low pressures, the two peaks at 4112 and 4121 cm^{-1} were expected for *ortho*-H_2 and *para*-H_2 adsorbed on a well-defined site. This doublet was also observed in H_2/HKUST-1 system at 4097 and 4090 cm^{-1} and assigned to *ortho*-H_2 and *para*-H_2 as well [41]. The $\Delta v = 9\ cm^{-1}$ is sufficient to tell the difference between *ortho*-H_2 and *para*-H_2 in IR spectra. While the equilibrium pressure was increased, the peak at 4121 cm^{-1} turned to be broad and a new band centered at 4130 cm^{-1} boosted. This feature was characterized by $\Delta v = -31\ cm^{-1}$, indicating a dominant occupation at the sites with lower adsorption energy. Other satellite bands present on the left and right side of the main band (curve 17) were considered to be liquefied H_2.

Infrared spectroscopy is unable to directly identify the H_2 positions in the host materials. To assign the spectral features is difficult; other reference closely related structures and/or computational models (first principle/density functional theory,

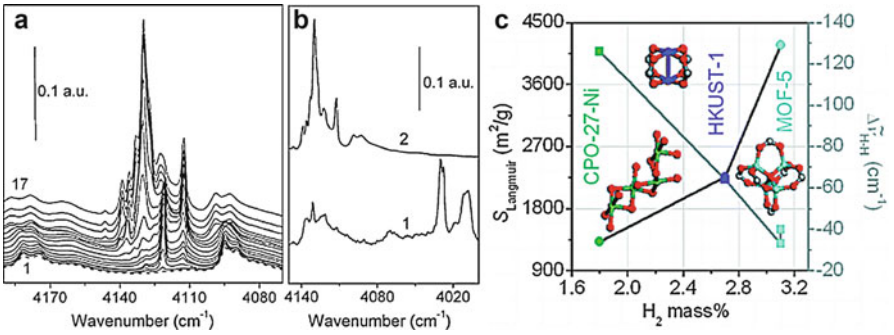

Fig. 9.12 (**a**) Pressure-dependent IR spectra of H_2 adsorbed on MOF-5 at 15 K in the presence of hydrogen. Curve 1, $<1{\cdot}10^{-7}$ bar; curve 17, 0.006 bar. The bottom dashed curve, corresponding to the empty MOF-5 spectrum. (**b**) Curve 1, IR spectrum of H_2 adsorbed on ZnO sample at 0.005 bar equilibrium pressure. Curve 2 is the curve 17 of (**a**). (**c**) Dependence of the Langmuir surface area ($S_{Langmuir}$, *circle*) on the adsorbed H_2 amounts at 77 K and 45 bar (volumetric values) for MOF-5, HKUST-1, and CPO-27-Ni (also known as MOF-74-Ni). The dependence of the H-H shift ($\Delta\nu$, *square*) on the hydrogen uptake is also depicted on the right-side axis (Reproduced with permission from Refs [36, 40]. Copyright © 2005/2008 American Chemical Society)

DFT) can help ascertain the involved sites responsible for the IR absorption. In MOF-5, the possible site is inaccessible Zn (II) of the Zn_4O clusters. The IR spectra of H_2 adsorbed on bulk ZnO (Fig. 9.12b) was thus selected as a comparison. It was observed that the two peaks at 4112 and 4121 cm^{-1} mentioned in H_2/MOF-5 system also fall in the same frequency region of H_2 adsorbed on OH groups of ZnO. This confirms that the H_2 molecules prefer to occupy the sites near the Zn clusters.

In spite of indirect position information, IR's probe ability for the H_2-material interaction is still powerful to study the correlation between adsorbed H_2 and different accessibility of the metal sites [40]. Three types of metal sites were selected in Fig. 9.12c: MOF-5 possesses unexposed Zn (II) sites; HKUST-1, exposed Cu (II) sites; and CPO-27-Ni, exposed Ni (II) sites, respectively. Not surprisingly, the attractive field built by these three metal clusters controls the H-H stretching frequency, leading to largest $\Delta v_{H\text{-}H}$ for exposed Ni (II) in CPO-27-Ni and smallest $\Delta v_{H\text{-}H}$ for inaccessible Zn (II) sites in MOF-5. However, the H_2 uptake exhibits an inverse dependence on the frequency shift (Δv), indicating the metal activity is not the most dominant factor in H_2 adsorption.

9.5 Solid-State Nuclear Magnetic Resonance

As shown in the previous three sections, NPD, INS, and IR techniques are frequently applied to characterize H_2 adsorption sites in host materials, particularly successful in zeolite/MOF adsorbents. On the other hand, the variable temperature solid-state nuclear magnetic resonance (SSNMR) is performed on the nuclei, not the neutrons or electrons, and commonly used to monitor the catalytic reactions. If the nuclei possessing a half-integer spin (i.e. 1/2, 3/2, 5/2, ^{13}C) or an integer spin (i.e. 1, 2, 3, ^{2}H, ^{14}N) interact with an external magnetic field, then the energy levels will split and thus absorb electromagnetic radiations. Such spin interactions construct the foundation of all the solid-state NMR characterizations. Chemical bonding between hosts and guests can usually result in anisotropic interactions between nuclei. The ^{2}H SSNMR line-shape analysis [42] has been conducted to probe the site-specific information of catalytic applications, such as the binding states of H_2/D_2 to transition metal atoms [43], H_2-D_2 exchange in a bio-system [44], and *para-/ortho*-H_2 probe [45].

In classical liquid-state NMR measurements, the anisotropic interactions are averaged to zero due to Brownian motion. Compared to the liquid-state counterparts, solid-state NMR spectra are substantially influenced by orientation-dependent interactions, primarily including chemical shift anisotropy (CSA) and dipolar coupling [46]. In their appearances of spectra, the solution-state NMR ones consist of sharp peaks arisen from average of anisotropic interactions, while solid-state NMR ones are broadened by orientation-dependent interactions (Fig. 9.13b, c). The broad line-shapes hide vast amount of information on detailed structures and dynamics; a number of special approaches, such as magic-angle spinning (MAS), cross polarization (CP), 2D NMR, are required to eliminate such broadening effect in solid state [46]. (Table 9.4)

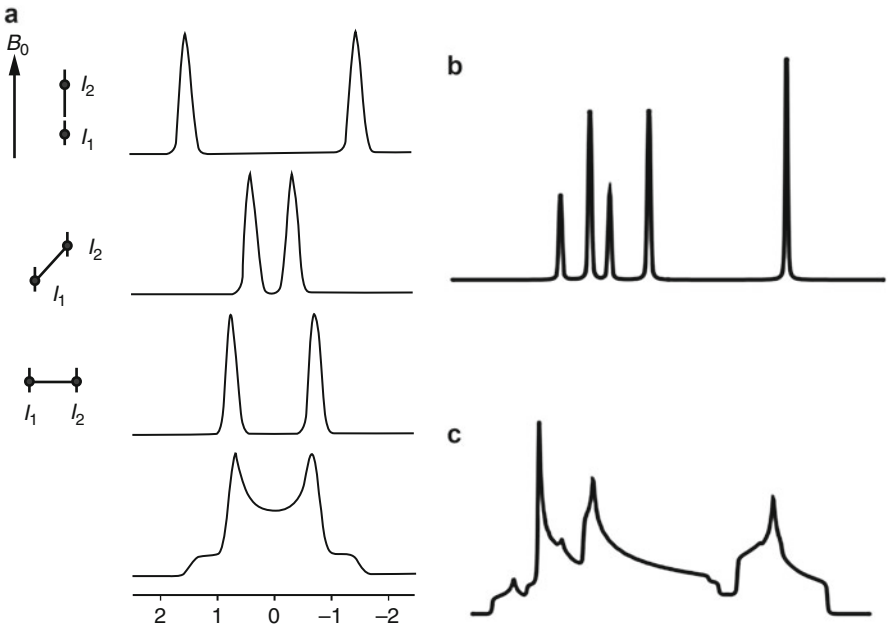

Fig. 9.13 (**a**) The bottom NMR spectrum is superposed by individual signals given by three orientations. *Line* shapes of (**b**) solution NMR and (**c**) solid-state NMR

Table 9.4 Comparison between solution and solid-state NMR

	Solution	Solid
Chemical shift anisotropy	Isotropic	Anisotropic
Dipole interactions	0.2 kHz	10 kHz
J-coupling	5–200 Hz	200Hz
Quadrupolar interaction	Average 0	Dominant (~MHz)
Rotational angle	0	54.7° or others
Rotational frequency	Hz	kHz, >35 kHz
Peak width	Sharp	Broad
Decoupling	low (5 W)	High (1000 W)
Operation	Routine	Skill

9.5.1 Hydrogen/Deuterium Bound to Transition Metal Clusters

Immobilization of a homogeneous catalyst into mesoporous supports has the advantages to separate, to recycle, and to minimize the metal traces (Ru, Rh, Pt), leading to lower costs in the reaction process [47]. Ruthenium (Ru) nanoparticles are very common to be catalysts in hydrogenation reactions. Ordered mesoporous silica is used as support media with pore sizes of 20–500 Å. Direct incorporation of Ru nanoparticles into such silica framework is able to be well dispersed, thus enhancing the catalytic applicability [48]. The variable temperature ^{2}H SSNMR has been exploited to characterize the H_2/D_2

interacting with Ru nanoparticles inside mesoporous silica, as suggested the catalytic mechanisms as in particular hydrogenation reactions [43].

The prominent interaction in ^2H SSNMR is the quadrupolar interaction. The changes of quadrupolar interactions induce changes of the line shape of SSNMR patterns. In the following example, these changes were caused by the various exchange forms of the deuterium ligands. As shown in Fig. 9.14a, the ^2H SSNMR experiments were performed in the temperature range of 25–300 K. The line-shape analyses of the spectra were deconvoluted into four subspectra with the quadrupolar interactions ($Q_{zz1} \sim Q_{zz4}$) shown in Table 9.5. The different components of the subspectra were assigned to different deuteron species: mobile D, -Ru_3-D, -Ru-D_2, -Ru-D, -O-D [43].

At these four temperatures, a Pake-like component of 180–200 kHz (Q_{zz1}) standing for the -O-D signal was always found. It indicated that the Ru nanoparticles activates the D-D bonds and then deuterates the -Si-O-H groups of the silica material, confirming ruthenium's catalytic activity to hydrogenation reactions.

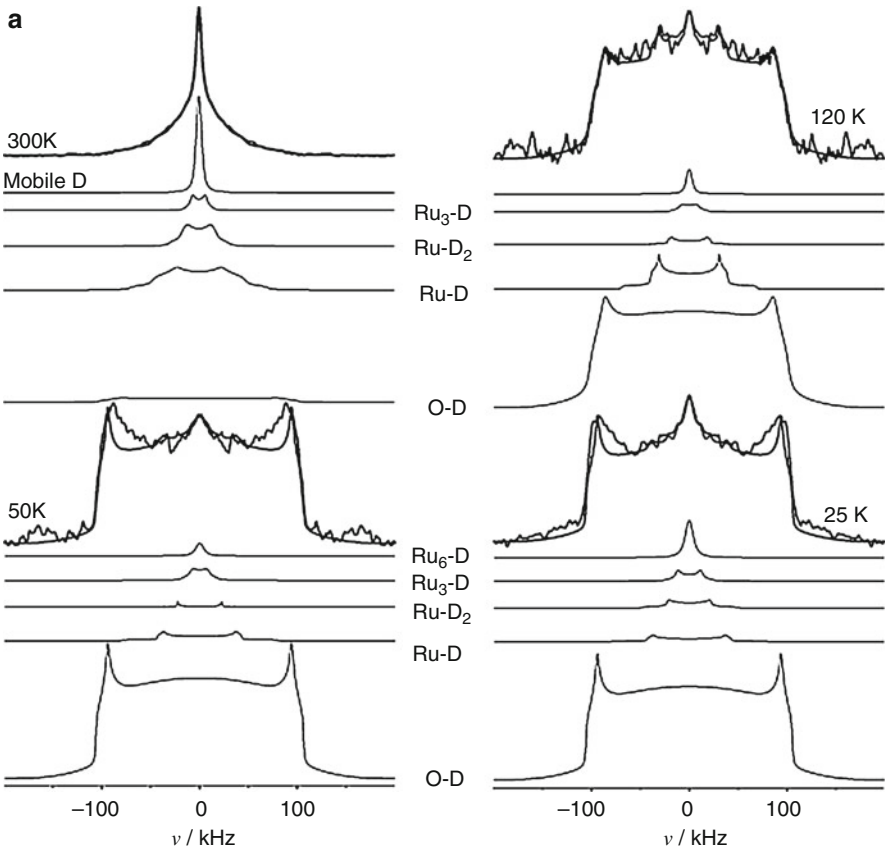

Fig. 9.14 (continued)

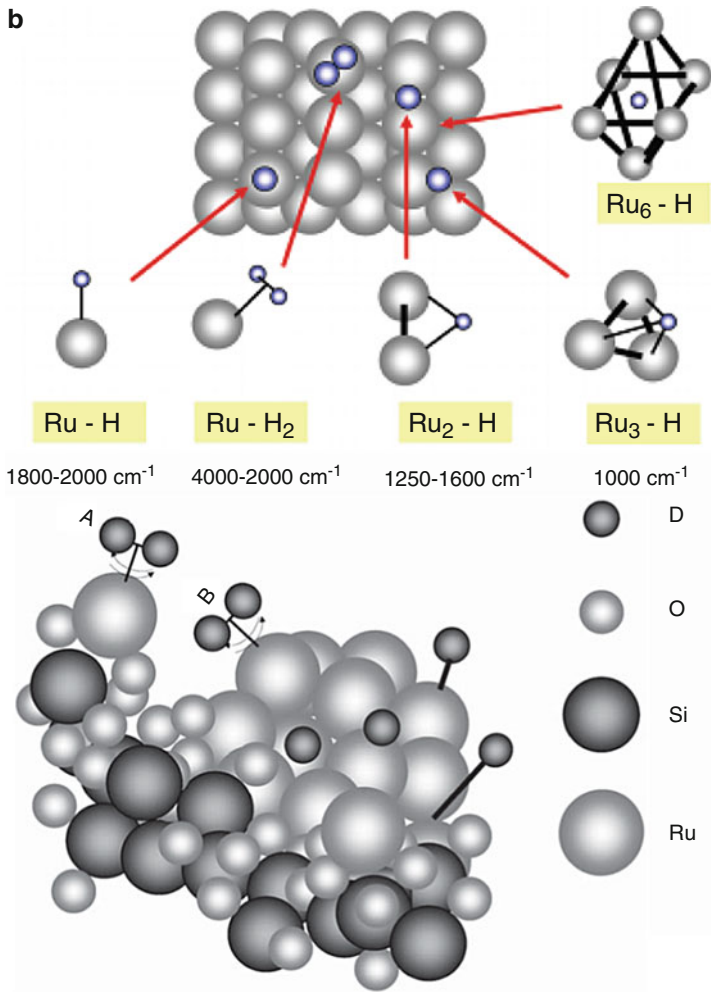

Fig. 9.14 (**a**) Solid-state 46.03 MHz ^{2}H-NMR spectra of the sample consisting of ruthenium nanoparticles embedded in neat SBA-3. The experimental spectra and their simulation are presented by the sum of the corresponding subspectra. (**b**) Model of deuterium/hydrogen–ruthenium bonding built from the NMR data in the left side. –OD deuterons are not shown for clarity (Reproduced with permission from Refs [43, 49]. Copyright © Elsevier Inc; Copyright © 2010 American Chemical Society)

Besides -Si-O-D deuterons, two types of deuterium atoms were revealed. One was dissociated type of deuterons (-Ru-D species) bound on top of Ru atoms, exhibiting quadrupolar tensor values of 56–90 kHz (Q_{zz2}). This Q_{zz2} component indicated the binding sites possess various binding strength due to the bond distances between Ru atoms and D atoms. The other type was a dihydrogen species –Ru-D_2 shown in the subspectra of 45 kHz (Q_{zz3}), attributing to fast rotational D_2 ligands at all temperatures. There were indications that the narrow Pake-like profiles at 25 K and 50 K (Q_{zz4}) are

Table 9.5 Parameters found by the line-shape analysis of ^{2}H-NMR spectra

T (K)	Signals	Q_{zz} (kHz)	Assignment
300	Q_{zz1}	180	O-D
	Q_{zz2}	70	Ru-D
	Q_{zz3}	30	Ru-D_2
	Q_{zz4}	14	Surface deuterium and/or Ru_3-D
120	Q_{zz1}	188	O-D
	Q_{zz2}	70	Ru-D
	Q_{zz3}	40	Ru-D_2
	Q_{zz4}	18	Surface deuterium and/or Ru_3-D
50	Q_{zz1}	200	O-D
	Q_{zz2}	80	Ru-D
	Q_{zz3}	45	Ru-D_2
	Q_{zz4}	18	Surface deuterium and/or Ru_3-D
25	Q_{zz1}	200	O-D
	Q_{zz2}	80	Ru-D
	Q_{zz3}	45	Ru-D_2
	Q_{zz4}	24	Surface deuterium and/or Ru_3-D

Reproduced with permission from Ref. [43]. Copyright © Elsevier Inc.
Q_{zz}: a measure for the strength of the quadrupolar interaction

related to threefold coordinated deuterons involved in surface diffusion (-Ru_3-D species) and octahedrally coordinated deuterons inside the Ru_6 octahedrons in the metallic ruthenium (-Ru_6-D species). Finally, the strong isotropic peak was more noticeable at 300 K than 120 K, which was assigned to a highly mobile D of the –Si-O-D groups.

Along with porous silica or Al_2O_3 membranes, Ru core shell MOF-5 (Ru@MOF-5) system was selected to study the surface chemistry by temperature-dependent ^{2}H SSNMR [50]. The measurements revealed that the caged Ru nanoparticles weakly interact with the MOF-5 support based on the highly mobile Ru-D species on the surface in contrast to colloidal Ru nanoparticles with similar sizes. Hence, it gave an idea that the mobile proton carriers for proton conductors can be controlled by the tunable host-guest interactions, which are heavily dependent on the nature of the microporous frameworks [51].

9.5.2 Probe of *para*- and *ortho*-Hydrogen

***Para*- and *ortho*-form of H_2**

Heisenberg predicted that hydrogen molecules consist of two distinct spin isomers: *para*-form (*p*-H_2) and *ortho*-form (*o*-H_2). Based on Pauli principle, the exchange of two indistinguishable fermions (e.g., two electrons or two protons in one H_2 molecule) must be restricted by wave function symmetry, resulting in the fact that the total wave function ($\Psi_{total} = \Psi_{rotation} \times \Psi_{spin}$) changes sign. Therefore, *para*-H_2 has an antiparallel spin ($\uparrow\downarrow$) with spin state of 0, which must be visualized as a

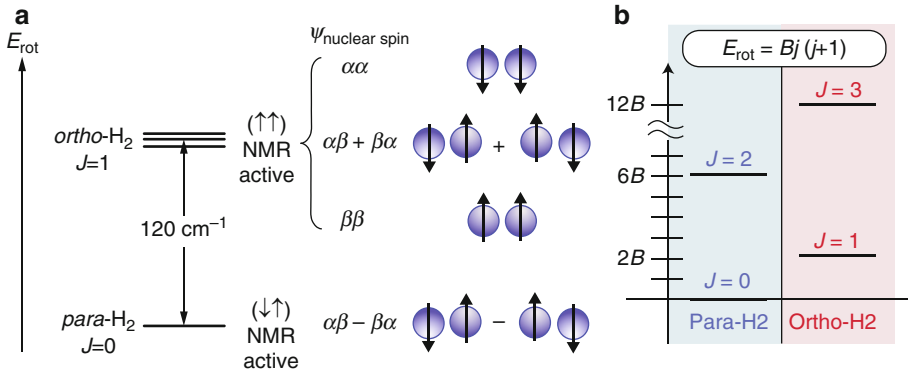

Fig. 9.15 (**a**) Energy diagram for the four lowest spin-rotational states of H_2. The Pauli principle requires that the lowest rotational state ($J = 0$, analogous to an atomic s-orbital) possesses a singlet nuclear spin state and that the first rotational state ($J = 1$, analogous to an atomic p-orbital) possesses a triplet nuclear spin state. *p*-H_2 is 120 cm^{-1} lower in energy than *o*-H_2. (**b**) Energy level diagram of the rotational motion of H_2. *Para*-H_2 (*ortho*-D_2) has even J, whereas *ortho*-H_2 (*para*-D_2) has odd J (Reproduced with permission from Refs. [45, 52]. Copyright © 2010 American Chemical Society; Copyright © 2011 Nature Publishing Group)

spherical rotating. *Ortho*-H_2 has a parallel spin (↑↑) with total nuclear spin of 1, which is visualized as rotating like a cartwheel [45]. Both species should be confined to different rotational states J to satisfy the acceptability of the wave functions: the *para*-H_2 characterized by even J while the *ortho*-H_2, odd J (Fig. 9.15b). At room temperature, normal H_2 (n-H_2) is a mixture of 25% in the *para* state and 75% in the *ortho* state. The conversion between the two states needs to be accelerated in the presence of a spin catalyst.

Considering the H_2 molecules as 3-dimensional quantum rotors, the energy levels (E_J) can be described as [53]

$$E_J = BJ(J+1)$$

where B is the rotational constant, taken to be 7.35 meV. Accordingly, the *rotational transition* from *para* form to *ortho* form ($J = 0 \rightarrow J = 1$) occurs at 14.7 meV in a free molecule [54]. Understandably, these two isomers bring about profound differences in their spectroscopic features.

In practice, the host's chemical environment can affect the guest's rotational transition, leading to a line shift from ideal 14.7 meV [39]. Anisotropic environments can lift the degeneracy of the triplet state $J = 1$ and split the 14.7 meV peak [53]. Infrared and INS spectroscopy, accordingly, are able to sensitively detect changes in the H-H interactions, in the vibrational frequency, in the rotational constant and in the conversion of *para*-/*ortho*-H_2 [25, 55, 56]. On the other hand, NMR only responds to paramagnetic *ortho*-H_2 but keeps silent to diamagnetic *para*-H_2 (Fig. 9.15a), because an NMR signals are produced by net nuclear spins not equal to zero.

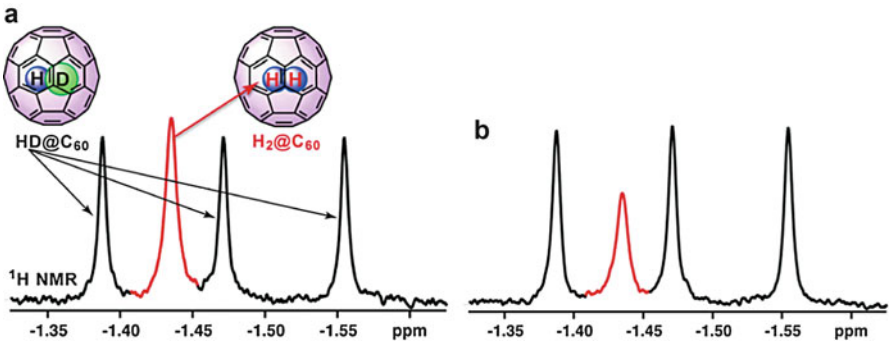

Fig. 9.16 Comparison of the ^{1}H NMR spectrum of a mixture of $H_2@C_{60}$ and $HD@C_{60}$ in 1,2-dichlorobenzene-d_4 before (**a**) and after (**b**) treatment with liquid O_2 (spin catalyst) at 77 K (Reproduced with permission from Ref. [45]. Copyright © 2010 American Chemical Society)

Probing the Interconversion Between the *ortho*- and *para*-H_2

C_{60} core shell with hydrogen gas system ($H_2@C_{60}$) has attracted attention because it simulates a model of a quantum rotor entrapped in a spherical box. This core shell system can be used as a model system to investigate the communication between the incarcerated H_2 and the external environment. Herein, ^{1}H NMR analysis was used to confirm the existence of the *ortho*- and *para*-H_2 and to monitor the interconversion between these two spin isomers incarcerated in a buckyball (p-$H_2@C_{60}$ and o-$H_2@C_{60}$) [45].

In this guest@host system, an internal standard compound, $HD@C_{60}$, was selected to improve the instrumental accuracy. To be an internal standard, the chemical shift has to be close to that of $H_2@C_{60}$, and the compound does not be affected at 77 K in the presence of spin catalysts. Because H and D are not identical particles, the rotational states of HD are not required to be locked in either even J or odd J (quantized energy levels in Fig. 9.15b) [55]. This complex does not need to obey the rules that H_2 must follow and then is not composed of two spin isomers. Hence, the ^{1}H NMR signals of $HD@C_{60}$ will not be affected in the presence of O_2 spin catalyst (Fig. 9.16). In contrast, it can be seen that the NMR signal of o-$H_2@C_{60}$ becomes weaker after the catalysis of O_2 [45].

9.6 Strategies Inspired from the Characterizations to Increase H_2 Uptake

Specific system targets in 2015 determined by the US Department of Energy (DOE) include the following: [57]

- 1.8 kWh/kg system (gravimetric 5.5 wt% hydrogen)
- 1.3 kWh/L system (volumetric 40 g hydrogen/L)
- $10/kWh ($333/kg stored hydrogen capacity)

The crystalline materials mentioned above may serve as pristine models for improvements of H_2 uptake capacity because of their customizable and designable natures. As a promising candidate, MOFs have exhibited the highest H_2 uptake among numerous physisorption porous solids. Several factors in these materials, such as surface area, free volume, and adsorption heat, have been thoroughly investigated over a wide range of pressures for increasing H_2 uptake. The H_2 uptake correlates with adsorption enthalpy at low pressure, with the surface area at intermediate pressure (30 bar) and with the free volume at high pressure (120 bar) [58]. These results have been confirmed from neutron powder diffraction (NPD), inelastic neutron scattering (INS), and infrared spectroscopy (IR), inspiring materials scientists to pursue new approaches to enhance H_2 storage performance [39, 59]. Hydrogen storage strategies can be divided into two main groups: (1) increase in surface area and tailoring pore geometry and (2) increase in isosteric heat of H_2 adsorption. In the following sections, both approaches in manipulating the H_2 uptake in the MOF family are discussed [1, 39, 60].

9.6.1 Increase in Surface Area and Tailoring Pore Geometry

9.6.1.1 Ligand Elongation

Although surface area and pore size are significant factors for high-pressure storage, MOF materials with high surface area and large pores easily suffer framework collapse and decomposition upon activation (solvent removal). Moreover, interpenetration might occur only if the pore space is large enough to accommodate another framework, reducing the porosity of the original single net. Accordingly, pore/surface enlargement by applying ligand extension is not a panacea for all MOFs to improve H_2 uptake.

It has been reported that (3,24)-connected networks are in the group where ligand elongation strategy effectively works [61], because it topologically incorporates mesocavities with microwindows to strengthen the frameworks. A iso-reticular series of (3,24) framework (PCN-6X series in Fig. 9.17) can be synthesized by using ligands with C_3 symmetry plus coplanar isophthalate moieties, as happens to keep the cuboctahedral building units unchanged [62]. The H_2 uptake at 90 bar and room temperature are 6.67 $mg \cdot g^{-1}$, 7.85 $mg \cdot g^{-1}$, and 10.1 $mg \cdot g^{-1}$ for PCN-61, PCN-66, and PCN-68, respectively. Among these three MOFs, PCN-68, which is constructed with the largest ligands (5,5′-((5′-(4-((3,5-dicarboxyphenyl)ethynyl) phenyl)-[1,1′:3′,1″]-terphenyl]-4,4″-diyl)-bis(ethyne-2,1-diyl)) diisophthalate (*ptei*), showed the highest maximum excess hydrogen capacity of 73.2 $mg \cdot g^{-1}$ (50 bar, 77 K). To be a successful demonstration of this strategy, PCN-68's performance is comparable with the record holder MOF-177, 75 $mg \cdot g^{-1}$ (69 bar) [63].

9.6.1.2 Catenation and Interpenetration

Based on the efforts of ligand elongation, pore sizes are tunable for a crystalline adsorbent with desired topologies. However, the larger pores do not always mean the better performance in H_2 uptake, especially at lower pressure. Since the pore center

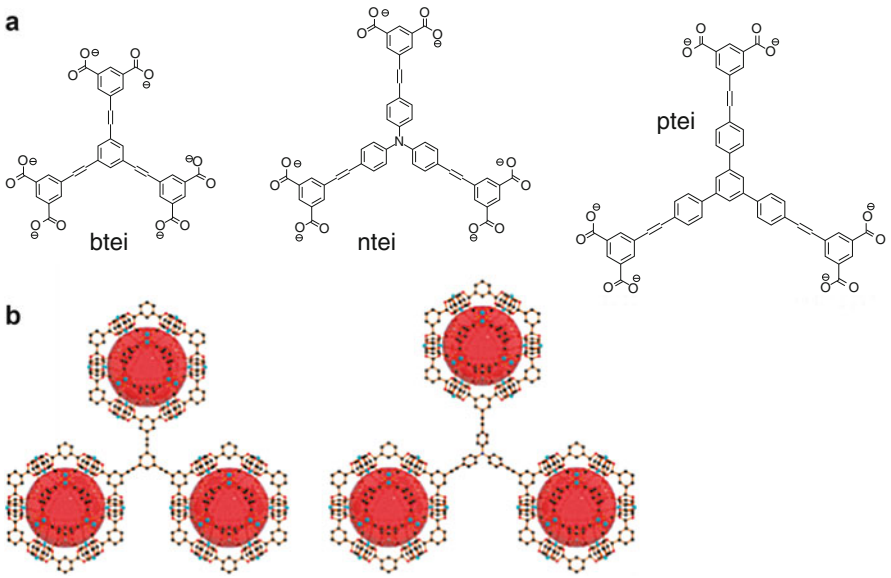

Fig. 9.17 (**a**) Ligands with C_3 symmetry and dendritic hexacarboxylate: (5,5-5″-(benzene-1,3,5-triyl-tris(biphenyl-4,4′-diyl)triisophthalate, *btei*, 5,5′,5″-(4,44′,4″-nitrilotris(benzene-4,1-diyl)tris (ethyne-2,1-diyl)triisoptthalate, *ntei*, (5,5′-((5′-(4-((3,5-dicarboxyphenyl)ethynyl)phenyl)-[1,1′:3′,1″]-terphenyl]-4,4″-diyl)-bis(ethyne-2,1-diyl)) diisophthalate, *ptei*. (**b**) Cuboctahedral cages as structural building units in (*left*) PCN-61 constructed with *btei*, and (*right*) PCN-66 constructed with *ntei*. (PCN-68, *ptei*, not shown here) (Reproduced with permission from Ref. [62]. Copyright © 2009 American Chemical Society)

does not offer any attractive force to H_2 molecules, the frameworks should possess small and interconnected pores to generate strong interactions between hosts and guests [64]. Catenation, the structural entanglement of two or more identical frameworks, is one possibility to restrict the free diameter of pores considerably (see the definition in Fig. 9.18).

A pair of framework-catenation isomers, the interpenetrated PCN-6 and non-interpenetrated PCN-6′, were both crystalized with the formula of Cu_3 $(TATB)_2$ (copper paddle-wheel units and 4,4′,4″-s-triazine- 2,4,6-triyltribenzoate (TATB)). The sorption data showed that after 50 °C activation PCN-6 adsorbed 1.74 wt% and PCN-6′ adsorbed 1.35 wt% at 1 bar and 77 K, respectively [65, 66]. The BET analyses indicated that interpenetrated version increased 41% in Langmuir surface area and 29% in gravimetric H_2 uptake. In another example, it was demonstrated that in the IRMOF series (structures in Fig. 9.11): IRMOF-1, -8, and -18, a simple cubic net, and IRMOF-11, interpenetrated nets, exhibited different mole-per-formulae-weight adsorbent of hydrogen. The interpenetrated IRMOF-11 was the best on a molar basis (9.3 H_2 per formula unit) at 77 K among the four compounds (5.0 H_2 for IRMOF-1, 6.9 H_2 for IRMOF-8, and 4.2 H_2 for IRMOF-18) [35, 67].

Even though the interpenetration strategy is successful in the above examples, it is unclear whether this approach will be successful in other MOF systems and at

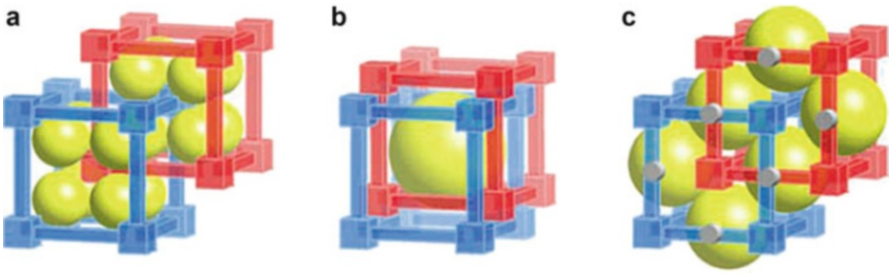

Fig. 9.18 (**a**) interpenetration, a maximal displacement occurs between the catenated frameworks. (**b**) interweaving, a minimal displacement occurs between the catenated frameworks. (**c**) The two frameworks are fixed by specific chemical groups represented by gray discs (Reproduced with permission from Ref. [59]. Copyright © 2005 WILEY-VCH Verlag GmbH & Co. KGaA, Weinheim)

ambient conditions. More challengingly, the interpenetrated frameworks cannot be sustained in the vacuum condition upon the activation process. Host-host interactions arise in the interweaving with closer contacts (Fig. 9.18b). Although mechanically rigidifying the framework by mutual reinforcement, interweaving might block the potential adsorption sites that are exposed to the pores. In order to prevent two frameworks from interweaving, specified chemical features are adorned at the midpoint of a linker and thus localize the distance between two interframeworks (Fig. 9.18c) [59].

9.6.1.3 Impregnation

In addition to inserting an additional framework into the pore space of the structures, impregnation of another nonvolatile adsorbate within huge pores might optimize the pore size and concurrently provide more adsorption sites. Similar to the interpenetration (Sect. 9.6.1.2), the imbedded adsorbates should possess appropriate sizes without blocking the existing adsorption sites. MOF-177 was selected as a right system where large molecular adsorbates such as C_{60} or dyes can be immobilized in [68]. Ionic-liquid@MIL-100(Al) was also found remarkable H_2 capacity [69]. Pd@HKUST-1 showed twice the H_2 storage capacity of the bare Pd nanoparticles, which are known as a H_2-storage metal [70].

Both approaches of interpenetration and impregnation can cause higher material density and thus decrease the gravimetric H_2 capacity. An optimized doping level must be found, making the increased mass from large molecular adsorbates compensated by the increased H_2 uptake.

9.6.1.4 Mixed Ligand System

It should be emphasized that not all designed structures with huge porosity or interpenetration can surely improve the H_2 uptake of the pristine structures. The ligand elongation strategy (Sect. 9.6.1.1) has a high threshold of synthetic skills to obtain the target organic ligands. Mixed ligand strategy detours such difficult synthetic routes. Differing from usual assembly of MOF materials, this method is

to construct a crystalline structure with two or more types of ligands. Understandably, it might create novel topologies which are impossible to achieve by using single type of ligands. With careful control of ligand molar ratio, synthesis temperature, and solvent, the new topological frameworks might possess right cage size and/or build an elegant force field to trap more H_2 molecules. Besides, mixed ligand strategy could avoid unexpected interpenetration and afford highly porous frameworks. For example, the MOF-205 and MOF-210 were crystalized with mixed BTB/NDC and BTE/BPDC, respectively, which showed exceptional high BET (Langmuir) surface areas 4460 (6170) and 6240 (10,400) $m^2 \cdot g^{-1}$. The MOF-210 exhibited the record-high excess H_2 uptake of 86 $mg \cdot g^{-1}$ at 77 K/56 bar and total H_2 uptake of 176 $mg \cdot g^{-1}$ at 77 K/80 bar [71].

9.6.2 Increase in Isosteric Heat of H_2 Adsorption

9.6.2.1 Exposed Metal Sites

As shown in Sect. 9.2.2, uncoordinated metal centers (UMCs) have been verified as one of the most attractive adsorption sites. In spite of the importance, it is still difficult to incorporate high concentration of exposed metal sites arbitrarily through self-assembly processes. Besides the conventional UMCs, a postsynthetic metalation method to introduce exposed metal sites into MOFs is to anchor isolated metal particles with chelating ligands.

This was demonstrated by adopting N,N'-phenyl-enebis (salicylideneimine) dicarboxylate as the equatorially chelating ligand [72]. Various UMCs such as Cu (II), Ni (II), or Co (II) can be entrapped in a square-planer geometry formed by two nitrogen and two oxygen atoms of the chelating ligand. In another example, $Zr_6O_4(OH)_4(bpydc)_6$, (bpydc: 2,2′- bipyridine-5,5′-dicarboxylate) featuring open 2,2′-bipyridine sites, can be metalated with Cu (I), Cu (II), Co (II), Fe (II), and Cr ions [73]. As a result, most metalated frameworks exhibited greater gravimetric H_2 uptake than the pristine material around 1 bar despite increased molecular weight.

9.6.2.2 Ionic Frameworks and Functionalization

It has been understood that four principle potentials contribute to H_2 physisorption in MOF materials, including van der Waals force, charge-quadrupole, induction, and polarization effects [64]. Particularly, polarization is enhanced in a charged framework. In-*soc*-MOF (In_3O nodes bridged to 5,5′-azobis(1,3-benzenedicarboxylate) struts) features a charged frameworks and contains nitrate counter anions, showing an impressive H_2 uptake of 2.5 wt% at 77 K and 1 atm [74]. The primary adsorption sites were identified as the nitrate ions, the In_3O nodes, and the nitrogen atoms of the azobenzenes, which is responsible for the predicted high adsorption heat of −8.5 kJ/mol. Other metal variants of *soc*-MOFs, such as Fe, Ga, Al-*soc*-MOF, were expected to take up more H_2 quantity because of their light weight of the metal nodes [74]. In addition to metal substitution for a charged MOF, the chemical substitution to linkers can tune the electrostatics of the metal ions [75]. The resulting anionic framework with polar amino-decorated linkers was discovered to reach 2.0 wt% of H_2 uptake

(223.9 cm^3/g) at 77 K and 1 atm. This effect can be explained that the negatively charged amide groups induce more positively charged metal ions, thus leading to higher isosteric heat of H_2 adsorption.

9.7 Summary

In this chapter, several characterization methods were introduced to observe H_2 molecules adsorbed in the host materials. These were:

- ***Neutron powder diffraction*** (NPD) is a powerful tool to directly observe H_2 adsorption positions as well as hydrogen molecular clusters in crystalline adsorbents, which is unlikely to do with X-ray diffraction method,
- ***Inelastic neutron scattering*** (INS) is capable of providing the information on relative binding energy for each well-defined adsorption site. If combining a computational modeling, the calculated enthalpy of each site in the materials can be properly assigned to the INS transitions shown in the spectra.
- ***Variable temperature Infrared spectroscopy*** (IR) is regarded as a supporting evidence to monitor the change in H_2-framework interactions by judging the frequency shifts. The free H_2 molecules are IR inactive while the adsorbed H_2 molecules become active. Comparing with a known reference, we can understand what the IR transitions probably mean in the studied materials.
- ***Solid-state nuclear magnetic resonance*** (SSNMR) has strong probe ability in catalytically hydrogenation reactions, rather than in characterization in H_2 adsorption. The changes of the line-shape of SSNMR patterns are resulted from the changes of quadrupolar interactions between D element and transition metals. If the experimental spectra can be decomposed into several subspectra, these different quadrupolar tensor values (Q_{zz}) will be assigned as different deuteron species, such as mobile D, -Ru_3-D, -Ru-D_2, -Ru-D, -O-D.

Spectral data analyzed by these techniques have enabled refinement in the synthetic or MOF fabrication approaches, such as ligand elongation, interpenetration/impregnation, mixed-ligand, as well as introduction of open metal sites, and were proposed to enhance H_2 uptake in the storage materials. It is noted that having high porosity and high adsorption enthalpy is a trade-off that should be considered to achieve the DOE target for on-board usage.

Acknowledgments Y.-P. Chen acknowledges the Center for Gas Separations Relevant to Clean Energy Technologies, an Energy Frontier Research Center funded by the U.S. Department of Energy (DOE), Office of Science, Office of Basic Energy Sciences under Award Number DE-SC0001015. Dr. H.-C. Zhou thanks the High-Capacity and Low-Cost Hydrogen-Storage Sorbents for Automotive Applications, funded by the U.S. Department of Energy (DOE) under Award Number DE-EE0007049.

References

1. L.J. Murray, M. Dinca, J.R. Long, Hydrogen storage in metal-organic frameworks. Chem. Soc. Rev. **38**(5), 1294–1314 (2009)
2. D.V. Schroeder, *An Introduction to Thermal Physics* (Addison Wesley Longman, New York, 2000)
3. W. Massa, *Crystal Structure Determination*, 2nd edn. (Springer, Berlin, 2004)
4. V.F. Sears, Neutron scattering lengths and cross sectioirn. Neutron News **3**(3), 26–37 (1992)
5. R. Pynn, Neutron scattering-A non-destructive microscope for seeing inside matter, in *Neutron Applications in Earth, Energy and Environmental Science* (Springer, New York, 2009)
6. A. Kumar, S.M. Yusuf, L. Keller, J.V. Yakhmi, Microscopic understanding of negative magnetization in Cu, Mn, and Fe based prussian blue analogues. Phys. Rev. Lett. **101**(20), 207206 (2008)
7. J.-P. Coulomb, N. Floquet, N. Dufau, P. Llewellyn, G. André, Structural and dynamic properties of confined hydrogen isotopes (H_2, HD, D_2) in model porous materials: silicalite-I, $AlPO_4$-N family (N = 5, 8, 11, 54) and MCM-41 ($\varnothing$ = 25 Å). Microporous Mesoporous Mater. **101** (1–2), 271–278 (2007)
8. V.K. Peterson, Y. Liu, C.M. Brown, C.J. Kepert, Neutron powder diffraction study of D_2 sorption in Cu_3(1,3,5-benzenetricarboxylate)$_2$. J. Am. Chem. Soc. **128**(49), 15578–15579 (2006)
9. V.K. Peterson, C.M. Brown, Y. Liu, C.J. Kepert, Structural study of D_2 within the trimodal pore system of a metal organic framework. J. Phys. Chem. C **115**(17), 8851–8857 (2011)
10. W. Zhou, T. Yildirim, Nature and tunability of enhanced hydrogen binding in metal–organic frameworks with exposed transition metal sites. J. Phys. Chem. C **112**(22), 8132–8135 (2008)
11. K. Sumida, J.-H. Her, M. Dincă, L.J. Murray, J.M. Schloss, C.J. Pierce, B.A. Thompson, S.A. FitzGerald, C.M. Brown, J.R. Long, Neutron scattering and spectroscopic studies of hydrogen adsorption in $Cr_3(BTC)_2$ – a metal–organic framework with exposed Cr^{2+} sites. J. Phys. Chem. C **115**(16), 8414–8421 (2011)
12. Y. Liu, H. Kabbour, C.M. Brown, D.A. Neumann, C.C. Ahn, Increasing the density of adsorbed hydrogen with coordinatively unsaturated metal centers in metal–organic frameworks. Langmuir **24**(9), 4772–4777 (2008)
13. Y. Yan, I. Telepeni, S. Yang, X. Lin, W. Kockelmann, A. Dailly, A.J. Blake, W. Lewis, G.S. Walker, D.R. Allan, S.A. Barnett, N.R. Champness, M. Schröder, Metal–organic polyhedral frameworks: high H_2 adsorption capacities and neutron powder diffraction studies. J. Am. Chem. Soc. **132**(12), 4092–4094 (2010)
14. H. Wu, W. Zhou, T. Yildirim, Hydrogen storage in a prototypical zeolitic imidazolate framework-8. J. Am. Chem. Soc. **129**(17), 5314–5315 (2007)
15. T. Yildirim, M. Hartman, Direct observation of hydrogen adsorption sites and nanocage formation in metal-organic frameworks. Phys. Rev. Lett. **95**(21), 215504 (2005)
16. M. Dincă, W.S. Han, Y. Liu, A. Dailly, C.M. Brown, J.R. Long, Observation of Cu^{2+}–H_2 interactions in a fully desolvated sodalite-type metal–organic framework. Angew. Chem. Int. Ed. **46**(9), 1419–1422 (2007)
17. R.A. Pollock, J.-H. Her, C.M. Brown, Y. Liu, A. Dailly, Kinetic trapping of D_2 in MIL-53(Al) observed using neutron scattering. J. Phys. Chem. C **118**(31), 18197–18206 (2014)
18. K. Sumida, D. Stück, L. Mino, J.-D. Chai, E.D. Bloch, O. Zavorotynska, L.J. Murray, M. Dincă, S. Chavan, S. Bordiga, M. Head-Gordon, J.R. Long, Impact of metal and anion substitutions on the hydrogen storage properties of M-BTT metal–organic frameworks. J. Am. Chem. Soc. **135** (3), 1083–1091 (2013)
19. M. Dincă, A. Dailly, Y. Liu, C.M. Brown, D.A. Neumann, J.R. Long, Hydrogen storage in a microporous metal–organic framework with exposed Mn^{2+} coordination sites. J. Am. Chem. Soc. **128**(51), 16876–16883 (2006)

20. F.M. Mulder, B. Assfour, J. Huot, T.J. Dingemans, M. Wagemaker, A.J. Ramirez-Cuesta, Hydrogen in the metal–organic framework Cr MIL-53. J. Phys. Chem. C **114**(23), 10648–10655 (2010)
21. J. Luo, H. Xu, Y. Liu, Y. Zhao, L.L. Daemen, C. Brown, T.V. Timofeeva, S. Ma, H.-C. Zhou, Hydrogen adsorption in a highly stable porous rare-earth metal-organic framework: sorption properties and neutron diffraction studies. J. Am. Chem. Soc. **130**(30), 9626–9627 (2008)
22. D.A. Gomez, A.F. Combariza, G. Sastre, Confinement effects in the hydrogen adsorption on paddle wheel containing metal-organic frameworks. PCCP **14**(7), 2508–2517 (2012)
23. H. Fu, F. Trouw, P.E. Sokol, A quasi-elastic and inelastic neutron scattering study of H_2 in zeolite. J. Low Temp. Phys. **116**(3-4), 149–165 (1999)
24. B.S. Hudson, Vibrational spectroscopy using inelastic neutron scattering: Overview and outlook. Vib. Spectrosc. **42**(1), 25–32 (2006)
25. M.B. Craig, L. Yun, Y. Taner, K.P. Vanessa, J.K. Cameron, Hydrogen adsorption in HKUST-1: a combined inelastic neutron scattering and first-principles study. Nanotechnology **20**(20), 204025 (2009)
26. P.M. Forster, J. Eckert, J.-S. Chang, S.-E. Park, G. Férey, A.K. Cheetham, Hydrogen adsorption in nanoporous nickel(II) phosphates. J. Am. Chem. Soc. **125**(5), 1309–1312 (2003)
27. M.R. Hartman, V.K. Peterson, Y. Liu, S.S. Kaye, J.R. Long, Neutron diffraction and neutron vibrational spectroscopy studies of hydrogen adsorption in the prussian blue analogue $Cu_3[Co(CN)_6]_2$. Chem. Mater. **18**(14), 3221–3224 (2006)
28. J.M. Nicol, J. Eckert, J. Howard, Dynamics of molecular hydrogen adsorbed in CoNa-A zeolite. J. Phys. Chem. **92**(25), 7117–7121 (1988)
29. N. Nijem, J.-F. Veyan, L. Kong, K. Li, S. Pramanik, Y. Zhao, J. Li, D. Langreth, Y.J. Chabal, Interaction of molecular hydrogen with microporous metal organic framework materials at room temperature. J. Am. Chem. Soc. **132**(5), 1654–1664 (2010)
30. M.P. Fang, P.E. Sokol, Y. Wang, Structure of D_2 in zeolite. Phys. Rev. B **50**(17), 12291–12296 (1994)
31. Y. Liu, C.M. Brown, D.A. Neumann, V.K. Peterson, C.J. Kepert, Inelastic neutron scattering of H_2 adsorbed in HKUST-1. J. Alloys Compd. **446–447**, 385–388 (2007)
32. D.G. Narehood, M.K. Kostov, P.C. Eklund, M.W. Cole, P.E. Sokol, Deep inelastic neutron scattering of H_2 in single-walled carbon nanotubes. Phys. Rev. B **65**(23), 233401 (2002)
33. J.L.C. Rowsell, J. Eckert, O.M. Yaghi, Characterization of H_2 binding sites in prototypical metal–organic frameworks by inelastic neutron scattering. J. Am. Chem. Soc. **127**(42), 14904–14910 (2005)
34. M.T. Kapelewski, S.J. Geier, M.R. Hudson, D. Stück, J.A. Mason, J.N. Nelson, D.J. Xiao, Z. Hulvey, E. Gilmour, S.A. FitzGerald, M. Head-Gordon, C.M. Brown, J.R. Long, M_2(m-dobdc) (M = Mg, Mn, Fe, Co, Ni) metal–organic frameworks exhibiting increased charge density and enhanced H_2 binding at the open metal sites. J. Am. Chem. Soc. **136**(34), 12119–12129 (2014)
35. J.L.C. Rowsell, A.R. Millward, K.S. Park, O.M. Yaghi, Hydrogen sorption in functionalized metal–organic frameworks. J. Am. Chem. Soc. **126**(18), 5666–5667 (2004)
36. S. Bordiga, J.G. Vitillo, G. Ricchiardi, L. Regli, D. Cocina, A. Zecchina, B. Arstad, M. Bjørgen, J. Hafizovic, K.P. Lillerud, Interaction of hydrogen with MOF-5. J. Phys. Chem. B **109**(39), 18237–18242 (2005)
37. A. Zecchina, C. Otero Arean, G. Turnes Palomino, F. Geobaldo, C. Lamberti, G. Spoto, S. Bordiga, The vibrational spectroscopy of H_2, N_2, CO and NO adsorbed on the titanosilicate molecular sieve ETS-10. PCCP **1**(7), 1649–1657 (1999)
38. S.A. FitzGerald, H.O.H. Churchill, P.M. Korngut, C.B. Simmons, Y.E. Strangas, Low-temperature infrared spectroscopy of H_2 in crystalline C_{60}. Phys. Rev. B **73**(15), 155409 (2006)
39. M.P. Suh, H.J. Park, T.K. Prasad, D.-W. Lim, Hydrogen storage in metal–organic frameworks. Chem. Rev. **112**(2), 782–835 (2012)

40. J.G. Vitillo, L. Regli, S. Chavan, G. Ricchiardi, G. Spoto, P.D.C. Dietzel, S. Bordiga, A. Zecchina, Role of exposed metal sites in hydrogen storage in MOFs. J. Am. Chem. Soc. **130**(26), 8386–8396 (2008)
41. S. Bordiga, L. Regli, F. Bonino, E. Groppo, C. Lamberti, B. Xiao, P.S. Wheatley, R.E. Morris, A. Zecchina, Adsorption properties of HKUST-1 toward hydrogen and other small molecules monitored by IR. PCCP **9**(21), 2676–2685 (2007)
42. E.R.D. Azevedo, T.J. Bonagamba, Molecular dynamics and local molecular conformation in solid materials studied by nuclear magnetic resonance. Braz. J. Phys. **36**, 61–74 (2006)
43. B. Walaszek, X. Yeping, A. Adamczyk, H. Breitzke, K. Pelzer, H.-H. Limbach, J. Huang, H. Li, G. Buntkowsky, ^{2}H-solid-state-NMR study of hydrogen adsorbed on catalytically active ruthenium coated mesoporous silica materials. Solid State Nucl. Magn. Reson. **35**(3), 164–171 (2009)
44. M. Cotten, R. Fu, T.A. Cross, Solid-state NMR and hydrogen-deuterium exchange in a bilayer-solubilized peptide: structural and mechanistic implications. Biophys. J. **76**(3), 1179–1189 (1999)
45. N.J. Turro, J.Y.C. Chen, E. Sartori, M. Ruzzi, A. Marti, R. Lawler, S. Jockusch, J. López-Gejo, K. Komatsu, Y. Murata, The spin chemistry and magnetic resonance of $H_2@C_{60}$. From the pauli principle to trapping a long lived nuclear excited spin state inside a buckyball. Acc. Chem. Res. **43**(2), 335–345 (2010)
46. S.E. Ashbrook, S. Sneddon, New methods and applications in solid-state NMR spectroscopy of quadrupolar nuclei. J. Am. Chem. Soc. **136**(44), 15440–15456 (2014)
47. M. Heitbaum, F. Glorius, I. Escher, Asymmetric heterogeneous catalysis. Angew. Chem. Int. Ed. **45**(29), 4732–4762 (2006)
48. N.T. Whilton, B. Berton, L. Bronstein, H.-P. Hentze, M. Antonietti, Organized functionalization of mesoporous silica supports using prefabricated metal–polymer modules. Adv. Mater. **11**(12), 1014–1018 (1999)
49. T. Gutmann, B. Walaszek, X. Yeping, M. Wächtler, I. del Rosal, A. Grünberg, R. Poteau, R. Axet, G. Lavigne, B. Chaudret, H.-H. Limbach, G. Buntkowsky, Hydrido-ruthenium cluster complexes as models for reactive surface hydrogen species of ruthenium nanoparticles. solid-state ^{2}H NMR and quantum chemical calculations. J. Am. Chem. Soc. **132**(33), 11759–11767 (2010)
50. F. Schröder, D. Esken, M. Cokoja, M.W.E. van den Berg, O.I. Lebedev, G. Van Tendeloo, B. Walaszek, G. Buntkowsky, H.-H. Limbach, B. Chaudret, R.A. Fischer, Ruthenium nanoparticles inside porous $[Zn_4O(bdc)_3]$ by hydrogenolysis of adsorbed [Ru(cod)(cot)]: a solid-state reference system for surfactant-stabilized ruthenium colloids. J. Am. Chem. Soc. **130**(19), 6119–6130 (2008)
51. S. Bureekaew, S. Horike, M. Higuchi, M. Mizuno, T. Kawamura, D. Tanaka, N. Yanai, S. Kitagawa, One-dimensional imidazole aggregate in aluminium porous coordination polymers with high proton conductivity. Nat. Mater. **8**(10), 831–836 (2009)
52. T. Sugimoto, K. Fukutani, Electric-field-induced nuclear-spin flips mediated by enhanced spin-orbit coupling. Nat. Phys. **7**(4), 307–310 (2011)
53. W.L. Queen, E.D. Bloch, C.M. Brown, M.R. Hudson, J.A. Mason, L.J. Murray, A.J. Ramirez-Cuesta, V.K. Peterson, J.R. Long, Hydrogen adsorption in the metal-organic frameworks Fe_2(dobdc) and $Fe_2(O_2)$(dobdc). Dalton Trans. **41**(14), 4180–4187 (2012)
54. D.G. Narehood, N. Grube, R.M. Dimeo, D.W. Brown, P.E. Sokol, Inelastic neutron scattering of H_2 in xerogel. J. Low Temp. Phys. **132**(3-4), 223–237 (2003)
55. S. Mamone, J.Y.C. Chen, R. Bhattacharyya, M.H. Levitt, R.G. Lawler, A.J. Horsewill, T. Rõõm, Z. Bačić, N.J. Turro, Theory and spectroscopy of an incarcerated quantum rotor: the infrared spectroscopy, inelastic neutron scattering and nuclear magnetic resonance of $H_2@C_{60}$ at cryogenic temperature. Coord. Chem. Rev. **255**(7–8), 938–948 (2011)
56. K. Sumida, S. Horike, S.S. Kaye, Z.R. Herm, W.L. Queen, C.M. Brown, F. Grandjean, G.J. Long, A. Dailly, J.R. Long, Hydrogen storage and carbon dioxide capture in an iron-based sodalite-type metal-organic framework (Fe-BTT) discovered via high-throughput methods. Chem. Sci. **1**(2), 184–191 (2010)

57. Hydrogen storage. http://energy.gov/eere/fuelcells/hydrogen-storage. Accessed 11 June.
58. H. Frost, T. Düren, R.Q. Snurr, Effects of surface area, free volume, and heat of adsorption on hydrogen uptake in metal–organic frameworks. J. Phys. Chem. B **110**(19), 9565–9570 (2006)
59. J.L.C. Rowsell, O.M. Yaghi, Strategies for Hydrogen storage in metal–organic frameworks. Angew. Chem. Int. Ed. **44**(30), 4670–4679 (2005)
60. H.W. Langmi, J. Ren, B. North, M. Mathe, D. Bessarabov, Hydrogen storage in metal-organic frameworks: a review. Electrochim. Acta **128**, 368–392 (2014)
61. D. Yuan, D. Zhao, D. Sun, H.-C. Zhou, An isoreticular series of metal–organic frameworks with dendritic hexacarboxylate ligands and exceptionally high gas-uptake capacity. Angew. Chem. Int. Ed. **49**(31), 5357–5361 (2010)
62. D. Zhao, D. Yuan, D. Sun, H.-C. Zhou, Stabilization of metal–organic frameworks with high surface areas by the incorporation of mesocavities with microwindows. J. Am. Chem. Soc. **131** (26), 9186–9188 (2009)
63. H. Furukawa, M.A. Miller, O.M. Yaghi, Independent verification of the saturation hydrogen uptake in MOF-177 and establishment of a benchmark for hydrogen adsorption in metal-organic frameworks. J. Mater. Chem. **17**(30), 3197–3204 (2007)
64. J.L. Belof, A.C. Stern, M. Eddaoudi, B. Space, On the mechanism of hydrogen storage in a metal–organic framework material. J. Am. Chem. Soc. **129**(49), 15202–15210 (2007)
65. D. Sun, S. Ma, Y. Ke, D.J. Collins, H.-C. Zhou, An interweaving MOF with high hydrogen uptake. J. Am. Chem. Soc. **128**(12), 3896–3897 (2006)
66. S. Ma, D. Sun, M. Ambrogio, J.A. Fillinger, S. Parkin, H.-C. Zhou, Framework-catenation isomerism in metal–organic frameworks and its impact on hydrogen uptake. J. Am. Chem. Soc. **129**(7), 1858–1859 (2007)
67. J.L.C. Rowsell, O.M. Yaghi, Effects of functionalization, catenation, and variation of the metal oxide and organic linking units on the low-pressure hydrogen adsorption properties of metal–organic frameworks. J. Am. Chem. Soc. **128**(4), 1304–1315 (2006)
68. H.K. Chae, D.Y. Siberio-Perez, J. Kim, Y. Go, M. Eddaoudi, A.J. Matzger, M. O'Keeffe, O.M. Yaghi, A route to high surface area, porosity and inclusion of large molecules in crystals. Nature **427**(6974), 523–527 (2004)
69. A. Aijaz, T. Akita, H. Yang, Q. Xu, From ionic-liquid@metal-organic framework composites to heteroatom-decorated large-surface area carbons: superior CO_2 and H_2 uptake. Chem. Commun. **50**(49), 6498–6501 (2014)
70. G. Li, H. Kobayashi, J.M. Taylor, R. Ikeda, Y. Kubota, K. Kato, M. Takata, T. Yamamoto, S. Toh, S. Matsumura, H. Kitagawa, Hydrogen storage in Pd nanocrystals covered with a metal–organic framework. Nat. Mater. **13**(8), 802–806 (2014)
71. H. Furukawa, N. Ko, Y.B. Go, N. Aratani, S.B. Choi, E. Choi, A.Ö. Yazaydin, R.Q. Snurr, M. O'Keeffe, J. Kim, O.M. Yaghi, Ultrahigh porosity in metal-organic frameworks. Science **329**(5990), 424–428 (2010)
72. R. Kitaura, G. Onoyama, H. Sakamoto, R. Matsuda, S.-I. Noro, S. Kitagawa, Immobilization of a metallo schiff base into a microporous coordination polymer. Angew. Chem. **116**(20), 2738–2741 (2004)
73. M.I. Gonzalez, E.D. Bloch, J.A. Mason, S.J. Teat, J.R. Long, Single-crystal-to-single-crystal metalation of a metal–organic framework: a route toward structurally well-defined catalysts. Inorg. Chem. **54**(6), 2995–3005 (2015)
74. T. Pham, K.A. Forrest, A. Hogan, B. Tudor, K. McLaughlin, J.L. Belof, J. Eckert, B. Space, Understanding hydrogen sorption in In-*soc*-MOF: a charged metal-organic framework with open-metal sites, narrow channels, and counterions. Cryst. Growth Des. **15**(3), 1460–1471 (2015)
75. T. Pham, K.A. Forrest, P. Nugent, Y. Belmabkhout, R. Luebke, M. Eddaoudi, M.J. Zaworotko, B. Space, Understanding hydrogen sorption in a metal–organic framework with open-metal sites and amide functional groups. J. Phys. Chem. C **117**(18), 9340–9354 (2013)

Hydrogen-driven Economy and Utilization 10

Sajid Bashir and Jingbo Louise Liu

Abstract

At present, the economy is dominated by carbon (coal, gasoline, petroleum) for generation of electricity and transport. These sections account for almost 56% of greenhouse emissions and contribute towards global warming. This realization that carbon dioxide leads to general increase in global temperatures was released from 1966 to the present day. Current awareness among the members of the general public policy makers and industrial captains has started a dialogue on transitioning from predominately carbon economy to hydrogen or electron (batteries) economy. This can be realized initially in the transport sector (26% of CO_2 emissions). The key problem is generation of sustainable hydrogen with zero or lower CO_2 emissions than current practice, which is geared towards industrial processes. A log fold increase in hydrogen production would be required from a diverse pool both fossil and renewable sources. Examples discussed include hydrogen production from biomass (glucose economy) through steam reformation (shown in Eq. 10.1), partial oxidation of hydrocarbon (Eq. 10.2), pyrolysis (Eq. 10.3), microbial (Eq. 10.4), and electrolysis (Eqs. 10.5a, 10.5b, and 10.5c).

$$2C_xH_y\,(g) + 2xH_2O\,(g) \rightarrow 2xCO\,(g) + (2x+y)H_2(g) \qquad (10.1)$$

Author Contribution: The first draft was written by Bashir except section 10.4 (Liu). The chapter was revised by both authors after reviewers comments and corrected by Bashir and uploaded by Liu. All figures supplied by Liu, except as noted.

S. Bashir (✉)
Department of Chemistry, Texas A&M University-Kingsville, Kingsville, USA
e-mail: br9@tamuk.edu

J.L. Liu
Department of Chemistry, Texas A&M University-Kingsville, Kingsville, USA

Department of Chemistry, Texas A&M University, College Station, USA
e-mail: jingbo.liu@tamuk.edu

Y.-P. Chen et al. (eds.), *Nanostructured Materials for Next-Generation Energy Storage and Conversion*, DOI 10.1007/978-3-662-53514-1_10

$$2C_xH_y\,(g)\ +\ xO_2\,(g)\ \rightarrow\ 2xCO\,(g)\ +\ yH_2(g) \tag{10.2}$$

$$2C_xH_y\,(g) +\ 2xC + yH_2\,(g) \rightarrow\ \text{hydrocarbon} \tag{10.3}$$

$$2H^+\,(aq)\ +\ 2e^- \rightarrow H_2(g) \tag{10.4}$$

$$\text{Anode reaction}:\ 4OH^-(aq) +\ 4e^- \rightarrow O_2(g) + 2H_2O(l) \tag{10.5a}$$

$$\text{Cathode reaction}:\ 2H_2O(l) +\ \ \rightarrow H_2(g) + 2OH^-(aq) + 4e^-(g) \tag{10.5b}$$

$$\text{Overall reaction}:\ 2H_2O(l) \rightarrow 2H_2(g) + O_2(g) \tag{10.5c}$$

The above processes could generate sufficient hydrogen to meet the needs of the transport sector, with hydrogen used as a fuel. Examples of hydrogen usage in this manner include: fuel cell powered automobiles either as hybrid (fuel cell – lithium ion batteries), plug-ins (Li-ion battery or hydrogen fuel cell vehicle with on-board storage. The function of the fuel cells such as proton exchange membrane fuel cells is to convert chemical energy to electrical energy spontaneously during electrochemical reactions (Eqs. 10.6a and 10.6b):

$$\text{Anode (hydrogen oxidation reaction, } HOR):\ 2H_2(g) \rightarrow 4H^+ + 4e^- \tag{10.6a}$$

$$\text{Cathode (oxygen reducion reaction, } ORR):\ 2O_2(g) + 4H^+ + 4e^- \rightarrow 4H_2O(l) \tag{10.6b}$$

While no single technology appears to be superior in all aspects, steam reformation and biomass gasification offer practical approaches to generate sufficient hydrogen to meet transportation needs in the near term. The steam reformation of natural gas coupled with CO_2 capture can offer a sustainable method, while gasification of biomass using supercritical chromatograph with catalyst offers another approach to generate sustainable hydrogen. In the mid-term, the electrolysis of water using off-peak grid electricity offers a pathway to generate hydrogen with negligible greenhouse emission. In the long term, the biogeneration of hydrogen and splitting of water using photo electrolysis or thermochemical pyrolysis are feasible avenues. The development of these technologies also needs policy makers to create a favorable legislature environment such as tax incentives for end-user or product generator and wider disseminations on the need to transition away from carbon, particularly for nations that do not have a native supply of coal, or petroleum.

Contents

10.1 Introduction of Hydrogen Economy

Hydrogen is a clean energy carrier (like electricity) made from diverse domestic resources such as renewable energy (solar, wind, geothermal), nuclear energy, and fossil energy (combined with carbon capture/sequestration). Hydrogen in the long term will simultaneously reduce dependence on foreign oil and emissions of greenhouse gases and carbon-derived pollutants. The US Federal government has several initiatives and programs aimed at alternate fuels such as the Energy Policy Act [1], Hydrogen Fuel Initiative (2003; cited in [2]), Energy Independence and Security Act [3], Energy Improvement and Extension Act (2008; cited by [4]), and American Recovery and Reinvestment Act (2009; cited by [5]), including Tax Relief Acts (2010, 2012, 2014, and 2016) [6], which give tax incentives for use of several alternative fuels. The Department of Energy (DOE) initiative called the Fuel Cell Technologies Program (funding decided by the Senate Appropriations Subcommittee on Energy and Water Development) has the goal of funding development of portable fuel cell technologies and on-board hydrogen storage/generation for automobiles with negligible carbon emissions. The 2003 hydrogen-fuel initiative under the DOE is now the Energy Hydrogen Program [7] and is a broad framework of expected developments initially identified by the previous secretary (Steven Chu). The 2015 DOE target can be met with compressed hydrogen powered automobiles. A broader plan is encapsulated in the Hydrogen Posture Plan [8], which expands the 2003 proposal to at least 2020 focused on the transportation sector using a number of viable technologies such as electric, hydrogen, or hybrid automobiles, trucks, and buses. The overall goal as defined by the Energy Policy Acts [9] to provide clean fuels (including biofuels and batteries) and lower the dependence on fossil fuels from overseas. This can only be accomplished through creation of policy, federal research grants, tax credits, workforce training and implementation of energy challenges,

technical milestones, deliverables, and implementation of early generation II, III prototypes on limited commercial basis. One example of this policy is gasoline hybrid electric vehicles or the hydrogen powered Honda Fuel Cell eXperimental (FCX) Clarity 4-door sedan, which is currently on a 3-year lease (at $600/month, Southern California as of April 2015 [10]). Honda anticipated the FCX will be rolled nation-wide in 2018. The original industrial revolution kicked off the petroleum economy principally through the use of coal and steam. Its refinement led today's petroleum [11] or carbon economy and currently there is an attempt to transition to a glucose/ethanol economy, which is anticipated will terminate to a hydrogen/nuclear fusion/electron economy [12]. The advantages of hydrogen as an energy carrier are elimination of carbon-based pollutants and greenhouse emission [13]. The challenges are on-board storage, safety, duration-per-tank, hydrogen distribution infrastructure, cost, and societal adoption of this new technology [14]. Technical challenges to developing cost-effective hydrogen technologies include lowering the cost of hydrogen production, delivery, storage, fuel cells, and end-user applications. Hydrogen systems require effective safety codes and standards, not only to ensure safe systems, but also to help define design standards for future hydrogen vehicles and infrastructure [15]. A number of industrial consortia have stated that hydrogen powered vehicles will be manufactured and offered to the public between 2015 and 2018 and will become widespread from 2018 to 2020 and onwards. The use of platinum catalyst per fuel cells (mg catalyst/stack) has dropped significantly between 2000 and 2010 to less than 30 g/stack and current on-board storage focus is compressed (~700 atm) hydrogen in composite cylinders rather than cryogenic storage [16]. Hydrogen re-fill stations cost approximately $4 million/station and the cost is expected to decline as more stations become available or there is a centralized distribution network [17]. Hydrogen production currently produces carbon dioxide, however electrolysis of water using wind power or solar can eliminate this issue by tapping into excess off-peak capacity of these renewable resources including the use of battery storage at approximately twice the production cost per kilogram for hydrogen relative to that produced using natural gas; however as electrolysis becomes more widespread using renewable energy sources the cost is expected to decline [18]. The most critical non-technical component is dissemination of why and how much rather than how. The average citizen understands the importance of clean soil, water and air and is able to grasp the concept of renewable resources; however may not see the need to transition to a more experimental and costly technology of electric, hybrid or hydrogen powered cars [19]. Here the industrial-scientific driven consortia need liaisons to advocate with local communities, state legislatures and federal agencies to education on the long-term benefits of a transition and also the awareness not to over sell the benefits. Today, the infrastructure does not exist; however, with a concerted effort it can exit nationwide, in a similar fashion to the carbon infrastructure which took almost 100 years to develop; the glucose/hydrogen economy is being developed within 25 years in comparison [2].

For the last 5 years, the editors have been functioning either as session moderators or symposium co-organizers at the annual American Chemical Society conferences and have observed as increased focus in renewable energy [20]. This is due to the

realization that diversity and reduction of greenhouses gas, such as carbon monoxide/carbon dioxide (CO_x), nitrogen monoxide/nitrogen dioxide (NO_x), and sulfur dioxide/sulfur trioxide (SO_x), lead to a sound economic and ecological state [21]. From the thermodynamic standpoint, energy or entropy is central to life and death [22]. Why is this textbook coming now? An acknowledgement that as the human population approaches 7 billion souls [23] and portable devices reaching 6.8 billion [24] and not counting other devices or automobiles, the demand for energy will increase [25]. More usage means more demand for energy either electrical or petrochemical [26]. An additional acknowledgment is that current fossil-fuel reserves may not be sufficient to meet demand [27]. And thirdly, hydrogen gas could use the current infrastructure with minimal modification and would not pose additional environmental burden [28]. Hydrogen is an attractive candidate as a natural gas replacement since it can be generated electrolytically from water in the form of a gas [29] or in the form of a liquid derived from ammonia [30], hydrazine [31], methanol [32], or liquefaction of coal [33]. Initial modeling data from Hubbert predicted that US oil production would peak between 1965 and 1970 and would decline thereafter [34]. From 1860 to 1970, almost 250 billion barrels of oils were extracted and usage has accelerated since, although not at a linear rate ([35], also see Fig. 10.1 for production profile and trends). If newer discoveries such as shale, tar-sands, and additional reserves are taken into account, the Hubbert curve in oil production will peak between 2010 and 2020 and then decline, favoring alternatives such as hydrogen [36]. Current electrical demand is around 20,000 TW and anticipated to rise above 20,000 TW by 2030 with addition of pure electric and plug-in hybrids to the grid [37].

The current usage-versus-time electrical profile has maxima at "peak times," with the addition of electric vehicles; the plot is expected to be flatter with lesser peaks, since the "intermediate load" will be filled by charging of these devices [38]. The end-result is an increase in base-load capacity requirement from a base of 50% reaching 95% of capacity to a constant requirement of 70% peaking at 90%, requiring feedstocks, which produce less environment effects, are portable, and can be stored [39]. Assuming energy consumption of 12,000 million tons of coal equivalent (Mtce), almost 7 Gton of CO_2 is produced, with the majority of resources being electricity or heat released with projected emissions to increase to 14 Gton of carbon by 2050 [40]. The approximate usage (in percent decades) is 40% electricity, 40% industrial, and 20% transport, with 10% of energy lost due to inefficiencies in the electric grid system [41]. From the net whole, approximately one third of energy is derived from oil [42]. The US Energy Information Administration (EIA) estimates that there are sufficient reserves of coal, and natural gas to meet US needs for 256 and 93 years, respectively, and world demand for crude oil for 25 years based on current crude oil reserves [43]. Most of these prediction models assume that the usage rate is fixed and that cost of extraction, and processing is also fixed, which is untrue when coal process are examined over the last 25 years [45]. These factors point to coal, natural gas, or hydrogen-based fuels as feedstocks or nuclear power stations to meet expected electrical demand [44]. Some of the physical characteristics for hydrogen and other fuels are summarized in Table 10.1, but in the most general sense, hydrogen yields one of the highest energy densities with no by-products except hydroxide radicals with hydrogen-producing water [46].

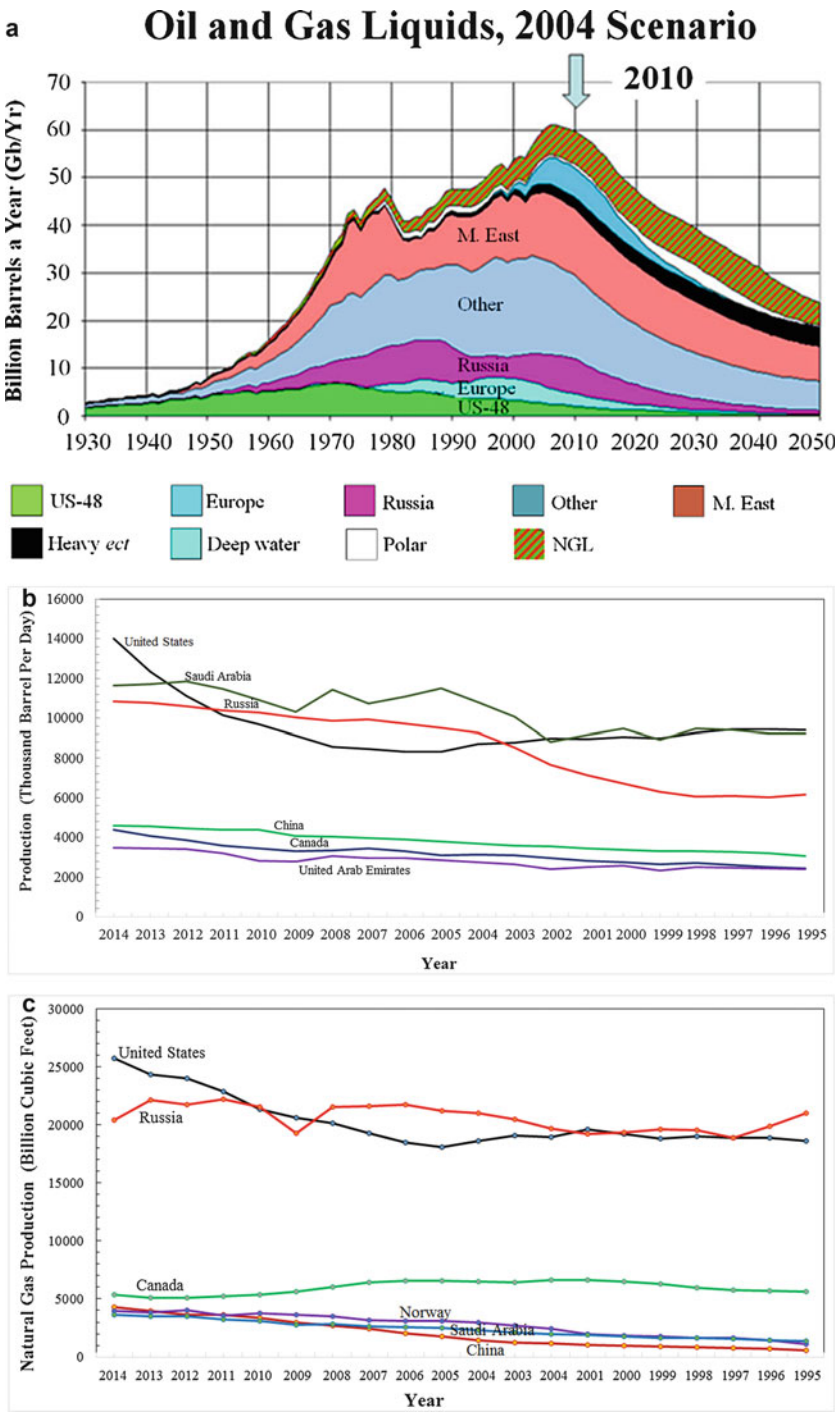

Fig. 10.1 (continued)

The above Table 10.1 and figures (Fig. 10.1a–c) also indicate that fossil fuel production (ignoring shale gas) will decline by 2040 and has remained constant over the last 20 years. If shale gas is included, natural gas and oil has increased in the USA, but it is unclear of whether this increase is long term or short term. Hydrogen is attractive since it has heating value greater than common fossil fuels, although its energy density is lesser than natural gas and gasoline (10–20 kg/L). To increase its storage density, hydrogen needs to be stored at high pressures, low temperatures, or within microporous particles. These procedures require advanced product development, adding to the infrastructure costs. The current system has two broad chemical networks: fossil fuels for generation of electricity and gasoline-based transport, and heating and chemical energy to sustain life. If only 20% of this segment was shifted to hydrogen (for generation of electricity or transport), carbon dioxide and acid rain emissions could be reduced. This is due to the absence of carbon or nitrogen in pure hydrogen, whose combustion will not result in generation of CO_2 and or NO_x. In addition, the fossil fuels could be used as precursors in the manufacturer of plastics or drugs. Another alternative is production of biofuels, which generate less CO_2 on a molar basis due to the lower content of carbon relative to gasoline or coal. Plants produce 1×10^9 calories annually enough to feed 9 billion people; however, if some plant use is diverted to production of biofuels and others to energy feedstocks, food for livestock or people will be lessened. This diversion has the potential to leave certain regions with insufficient food, which will be supplemented with processed food. In agriculture, oil and gasoline are also required to power the tools to plant, cultivate, extract, package, and export the food [49].

The expected shift is towards electrical, chemical, and hydrogen with the latter displacing to various degrees the current fossil fuel network. Ideally, electricity will be generated (Fig. 10.2 for current profile) using natural gas via hydrogen production with carbon sequestration of cogenerated CO_2 using short rotation crops, waste plant biomass that are unsuitable for distillation and/or fermentation to biofuels, with coal as a strategic backup or use in high power plants for electrical generation. Other sustainable resources such as solar, wind, geothermal, hydroelectric will also lessen the load on fossil fuels, but most are not compatible with the current fossil fuel based infrastructure. Lastly, while nuclear fission does not generate greenhouses gases, these power stations require fissionable materials such as uranium which needs to be extracted. The current estimates vary with the amount of available uranium with estimates centering around 20 Mton [50] leaving enough fuel to generation of electricity at current levels for between 85 and 300 years [51]. These estimates ignore compliance costs, increased cost of extraction, or extraction from seawater or use of fuel-recycling fast-breeder reactors instead of using low-enriched uranium in light-water reactors, which most likely would extend the availability and usage of

Fig. 10.1 (**a**) Schematic of world production of oil and gas peaked in 2010 (Reproduced with permission from htttp://www.peakoil.net/uhdsg/). (**b**) Total petroleum and other liquids production – 1995–2014 (Data obtained from http://www.eia.gov/beta/international). (**c**) Total dry natural gas production – 1995–2014 (Data obtained from http://www.eia.gov/beta/international)

Table 10.1 A summary of energy parameter

Parameter description	Approximate parameter value under STP for: (in MJ/Kg)	Parameter description	Approximate parameter value under STP for
Lower heating value	121 (H_2)	Specific heat (C_p)	14,000 J/kg K (20 °C, H_2)
Upper heating value	142 (H_2)	Gas density	0.1 kg/m^3 (H_2)
Lower heating value	50 MJ/Kg (CH_4); 23 (CH_3OH)	Liquid density	70 kg/m^3 (−252 °C, H_2)
Lower heating value	29 CH_3OCH_3; 45 (Gasoline)	Lower heating value	49 MJ/Kg (LPG); 17–24 MJ/Kg (Coal)

Sources: OECD/IEA Electricity Information [47], for coal; Australian Energy Consumption and Production, historical trends and projections, ABARE [48]
STP: T = 273 K, p = 1.013 bar; peta (P) = 1×10^{15} for example 1 PJ = 1×10^{15} J ~ 0.27 TWh ~ 0.03 Mtce (million metric tons coal equivalent) or 1 Mtce ~ 29.3 PJ and 1 TWh ~ 3.6 PJ ~ 0.123 Mtce. LPG: Liquefied Petroleum Gas and MJ = 1×10^6 J

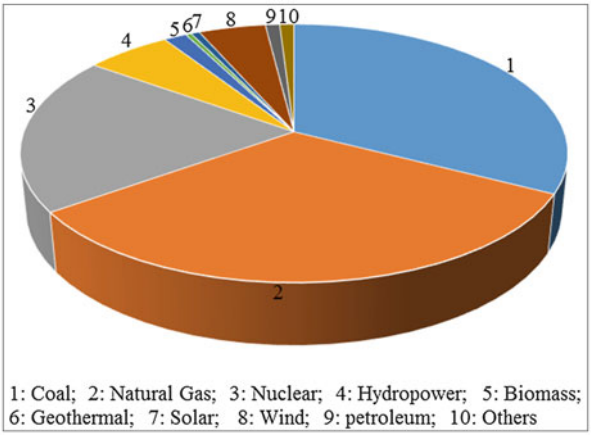

Fig. 10.2 Major energy sources and percent share of total US electricity generation in 2015 (Data obtained from http://www.eia.gov/beta/international)

nuclear fuels. The most favored scenario is in situ decentralized generation of hydrogen by electrolysis [52] using fuel cells with photovoltaic solar panels [53], wind [54] or biofuels [55] as hydrogen energy stations or hydrogen and electrical generation from integrated natural gas power stations that are centralized [56].

In 2015, the United States generated about four trillion kilowatt hours of electricity. About 67% of the electricity generated was from fossil fuels (coal, natural gas, and petroleum). This results in 30% emission of carbon dioxide or 2.06 Gton [57]. To mitigate the environmental pollution, hydrogen as an energy carrier provides a feasible avenue. To move towards hydrogen-driven economy, four general phases are summarized in Fig. 10.3.

The greatest impact of hydrogen as an energy carrier in the economy is in the transport and electricity sectors as a replacement of carbon-based fuel. In the

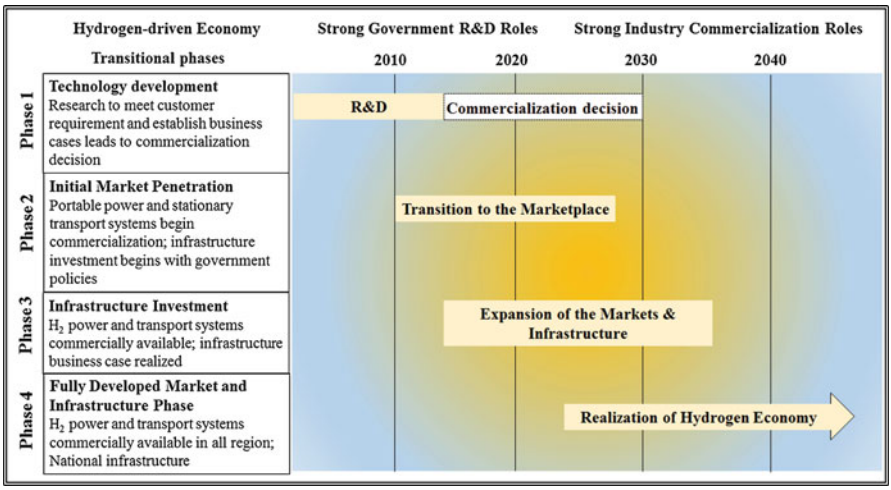

Fig. 10.3 Possible scenarios for hydrogen technology development and market transformation. (Reproduced with permission. Copyright © http://www.hydrogen.energy.gov)

transport sector, in addition to availability of hydrogen, automobile requires fuel cells as a replacement for internal combustion engine. Therefore, research is required to make these new technologies competitive with current diesel/gasoline engines. These hydrogen technologies also have to be economically comparable to current design. In the roadmap, this is the first phase where the replacement technologies will be developed and evaluated. In the second phase, these emerging technologies need to be certified as practical, economical, and safe to use. One example is cooperation between industry leaders, policy and law makers in designed the legal and commercial frameworks to implement these technologies. Specifically, the utility companies could be given tax incentives to develop cleaner power using hydrogen. In the phase three, as these technologies diffuse into the marketplace and home, new infrastructure will need to be created to meet capacity. A few examples are the development and rollout of hydrogen fill stations and at-point electricity for plug-in vehicles. In these cases, these technologies have to be commercially viable and within the reach of the average consumers. In the phase four, these maturing technologies will need to be accessible through the country instead of few pilot states for both portable and stationary applications with corresponding increase in hydrogen production using sustainable energies, such as solar or wind.

To foster new technologies, the industrial partners, consumers, and law makers need to set common standard. When there are competing industrial standards, the consumers often utilize technology based on expectations and support. This has been shown in other industries, when competing multimedia technologies, where are rolled out (Betamax vs. VHS; HD-DVD vs Blu-ray). In the previous case, the more successful technologies are adopted by the user where the ones which met user's requirements, even if there are technological inferior to the competing technology [58].

10.2 Properties of Hydrogen

All matter capable of forming chemical bonds has a nucleon consisting of a proton and neutrons with orbiting electrons. If the elements possess two eight or eighteen electrons, they are chemically inert; otherwise they will form ionic or covalent bonds to become stable. The most abundant isotope of hydrogen is protium, which has one proton, one electron, and zero neutrons. Protium will form a diatomic molecule through a covalent bond.

10.2.1 Covalent Diatomic Molecule

Since a diatomic molecule consists of two protons and protons possess spin, two possible arrangements are possible. The protons with the spin in the same direction can be described as the triplet state, also known as orthohydrogen, $1/\sqrt{2}$ [↑ + ↑ = 1; $I = 1$; $M_I = 1, 0, -1$, where I is the total angular momentum of a nucleus, also known as nuclear spin and M_I is the spin along the defined axis). On the other hand, if the protons have opposite spins ($1/\sqrt{2}$([↑-↓ = 0; $I = 0$; $M_I = 0$), they are defined as singlet state, known as parahydrogen [59].

Protons have a spin state of ½ ($E_J = 2$ J + 1, where J is the rotational quantum number), the total number of rotational states is fixed, for orthohydrogen (protons are parallel) adopts symmetric spin functions, yielding an odd value for J, whereas the parahydrogen (protons are antiparallel) adopts an antisymmetric spin function, yielding an even J value. Due to symmetry-imposed restriction on rotational states, para isomer has lower rotational energy than the ortho isomer, although the isomers exist in 3:1 ratio between ortho:para at standard temperature and pressure (normal form; [60]). The residual energy of normal hydrogen is expected to be greater than that for the parahydrogen, which is the dominant isomer at low temperatures. The conversion between the spin states can occur without a catalyst, but it is exothermic and slow. If the ferric oxide catalyst is used, the conversion to parahydrogen can occur [61] forming stable liquid parahydrogen at 20.28 K and 1–4 bar (Fig. 10.4).

The conditions for cryogenic hydrogen storage are different to compressed hydrogen (700 bar, 293 K; Fig. 10.5) or even cryo-compressed hydrogen (1000 bar, 33 K: The temperature of 33 K is the critical point of hydrogen, and if cooled below this temperature, hydrogen will exist as a liquid without boiling at atmospheric pressure (~1.01 bar)). One consideration of on-board hydrogen storage

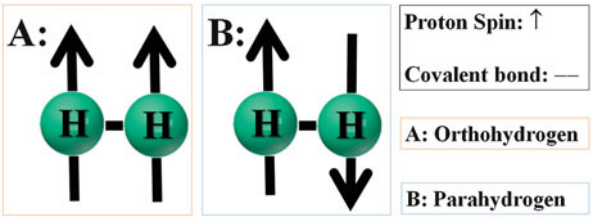

Fig. 10.4 The schematic demonstration of spin isomers of molecular hydrogen: (**a**) orthohydrogen and (**b**) parahydrogen

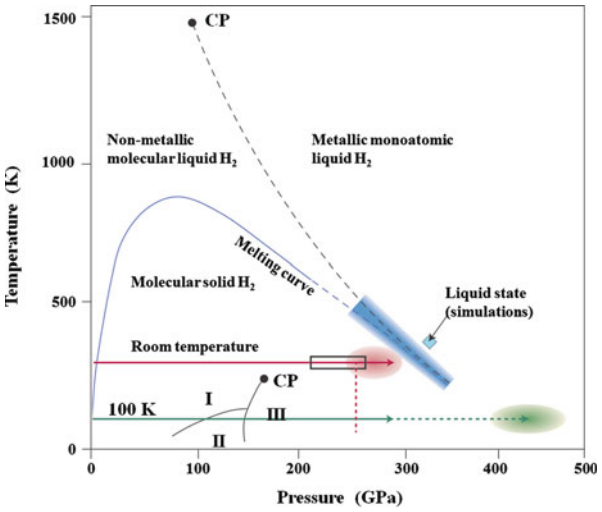

Fig. 10.5 Phase diagram of molecular hydrogen (Reproduced with permission from Jephcoat [66]. Copyright © NPG)

is itis gravimetric versus volumetric capacity since liquid hydrogen has lower energy density by volume than petroleum. Compressed hydrogen likewise has high energy density by mass and low density by volume, with liquefaction or compression imposing some energy loss (to cool or to compress) the gas, with metal organic framework (MOF-177; [62]) and cryo-compressed hydrogen [111] meeting the DOE 2005–2015 targets of 5.5 wt% H_2, for a working system [63]. The density of liquid hydrogen is only 70.99 g/L (at 20 K), a relative density of just 0.07. Although the specific energy is around twice that of other fuels, this gives it a remarkably low volumetric energy density, many fold lower. Cryo-compressed hydrogen will need to be stored in insulated tanks or cylinders that require pressurization and cooling unlike a regular gasoline tank, with a much higher leakage rate of 1% per day [64] with additional requirements not observed in gasoline powered automobiles [65].

10.3 Generation of Hydrogen

Hydrogen is an energy carrier, since it cannot be obtained directly like a fossil fuel, but produced from natural gas (Fig. 10.6), resulting in CO_2 emission. Hydrogen can also be produced through electrolysis without generation of CO_2, but electrolysis requires electricity, obtained using coal, which also generates CO_2. If hydrogen was produced by electrolysis where energy was provided from renewable sources, or biomass, near-zero CO_2 emissions would result, enabling hydrogen to be used for generation of electricity, in a hydrogen-dominated economy as opposed to a petroleum-dominated economy. In the long term, solar energy (electron economy) and biomass (glucose economy) can be used more directly to generate hydrogen, or using thermochemical cycles without emissions of greenhouse gases. The problems

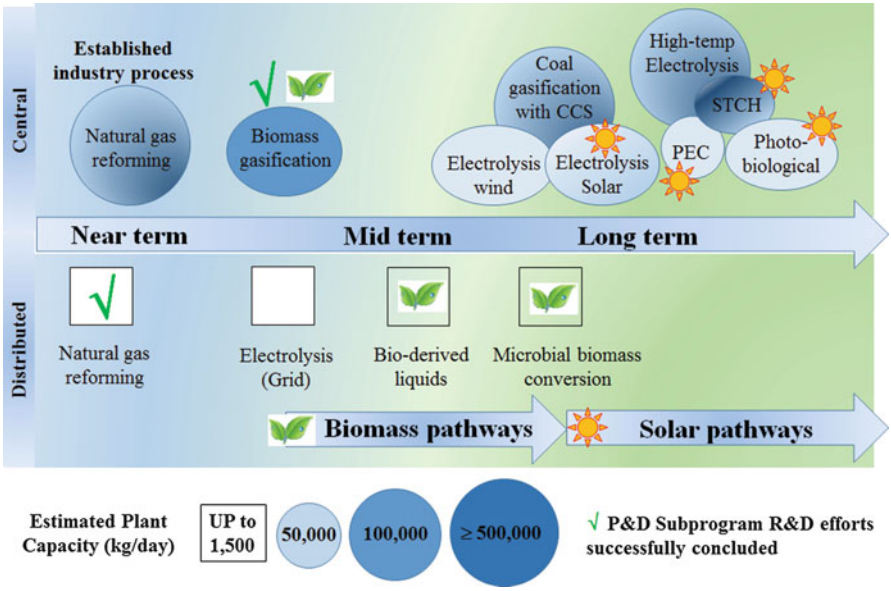

Fig. 10.6 Hydrogen production (Reproduced with permission from http://energy.gov/eere/fuelcells/hydrogen-resources)

for electrolysis or biomass are availability of affordable efficient catalysts with high conversion efficiencies. In electrolysis, a visible light catalyst can facilitate water splitting at 70–80% efficiency. These catalysts can be designed to be similar to catalyst in plants that are clusters based on manganese oxide ($[MnO]_4 + 2H_2O \rightarrow 4H^+ + 4\bar{e} + [MnO_{1.5}]_4$). Alternately, the catalysts can be based on iron and nickel clusters, which are used by microorganisms for hydrogen production. Thermochemical method to produce hydrogen can also be used, but requires separation at high temperatures using stable membranes. The current method of hydrogen production using steam reformation of natural gas would not solve the global warming problem, since a hydrogen-based economy would need at least a 10–15 fold increase in hydrogen gas production. Therefore, different approaches are required to meet the high capacity and mitigate emission.

Currently, the global hydrogen production is 48% from natural gas, 30% from oil, and 18% from coal; water electrolysis accounts for only 4% (Fig. 10.7). Hydrogen generation would need to increase from approximately 9 to 150 Mtons [67] to meet the high needs. The likelihood is that hydrogen will be produced using a mix of resources and approaches, from heat from nuclear reactors to or plant and steam reformation of natural gas. One possible approach is generation of hydrogen from supercritical water gasification using biomass. Other approaches, including thermochemical pyrolysis, tidal power, or wind, can also be employed. The potential approach is determined by initial start-up cost, environmental tax, and relative cost of hydrogen relative to that of gasoline (fixed at $1.00 per kg as a baseline). Current

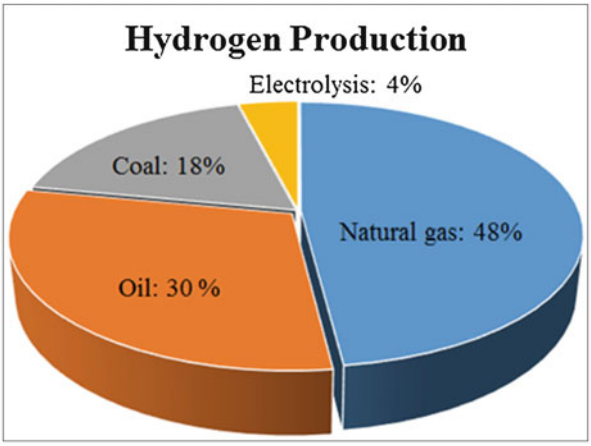

Fig. 10.7 Current hydrogen production using hydrocarbon feedstocks and electrolysis

analyses indicate that the expense to produce hydrogen from coal gasification is the most cost-effective ($1.03), followed by natural gas reformation or coal with CO_2 sequestration ($1.11), natural gas with CO_2 sequestration ($1.31), nuclear thermal splitting of water ($1.75), and biomass gasification ($4.98). It was found that electrolysis using wind energy ($7.14) could be offset by using ocean thermal energy conversion ($2.40) as attractive options in terms of using sustainable energy to generate hydrogen [68–70]. An older Pacific Northwest National Laboratory cost analysis gave slightly different results with coal gasification, yielding a cost similar to gallons of gasoline-equivalent (gge). Gasification of biomass was slightly more expensive at $1.90 gge; natural gas via steam reformation and steam from nuclear fission plants or wind were similar between $2.50–$3.00 gge, and solar being the most expensive ($9.50 gge). The DOE current estimates are that the average cost of hydrogen production varies from $2 to $4 gg. between now and 2020 [71].

The efficiency of the overall hydrogen production varied from methods to methods. It was found that the steam reformation being the most efficient (85%) method, followed by electrolysis (75%) and biomass gasification (50%) [72]. Since the cost of electricity is dependent on type of feedstock or usage of solar thermal systems or wind power, this estimated cost may be lowered. The realization of replacing gasoline in automobiles is not controversial; however, replacing gasoline with hydrogen from nonrenewable resources such as coal or natural gas is an issue for some policy makers, because up to five-fold more CO_2 can be produced per mole of hydrocarbon. Therefore, hydrogen should be produced through CO_2 sequestration incorporated with steam reformation to decrease CO_2 emission. Or hydrogen production can be transitioned to the renewable resources to increase overall efficiencies and decrease costs. Integration of off-peak electrical power in grid electrolysis and biomass conversion using supercritical water gasification are other potential approaches to lower the gallons of gasoline-equivalent costs. It should also be noted that infrastructure costs are not insignificant in production, storage, or transport of hydrogen due to its physical properties relative to natural gas.

10.3.1 Generation of Hydrogen from Water

Generation of hydrogen (Eq. 10.7) has from water is thermodynamically unfavorable and requires electrical or thermal energy ‡[values are rounded to the nearest decade] as can be seen from the equations of state [72]:

$$H_2O\ (l)\ H_2\ (g) + \frac{1}{2}O_2\ (g) \tag{10.7}$$

where $\Delta H^\circ = +240$ kJ/mol and $\Delta G^\circ = +230$ kJ/mol

The equilibrium K can be calculated by the following equations:

$$K_p = P_{H_2} \times P^{1/2}{}_{O_2} / P_{H_2O} \tag{10.8a}$$

$$K_p = \exp(^{-}\Delta G^o/_{RT}) \tag{10.8b}$$

From the above known values, we can determine $K_p = 4.0 \times 10^{-76}$ atm ½ and $C_p = 10$ kJ/mol*K with ΔG° decreasing with increasing temperature.

At 1980 K, $O_2 \leftrightarrow 2O$, $\Delta H^\circ = +250$ kJ/mol and $H_2 \leftrightarrow 2H$, $\Delta H^\circ = +220$ kJ/mol with the mole fraction of water being unit until approximately 2500 K and then dropping off with corresponding increases in H_2 which peak around 3300 K and H around 4000 K, which is not effective in terms of using hydrogen as an energy carrier, using $d\text{InK}/d\text{T} = \Delta H^\circ/RT^2$ [74]. Further, noting that $\Delta H^\circ < 0$, K is expected to decrease with increasing temperature, while $\Delta H^\circ > 0$, K is expected to increase with temperature, where $K = e^{(-\Delta G^\circ/RT)}$, where R is the universal gas constant (8.314 K*J/mol) and T = 298 K. Indicating that splitting of water at low temperature is nonspontaneous and at high temperature, six potential species can be generated (H_2O, O_2, O, H_2, H, and OH) ignoring issues of how the heat would be generated (coal, gas, or nuclear) and how these species would be separated [73]. Electrolysis of water (Fig. 10.8 and Eqs. 10.9a, 10.9b) will produce hydrogen and oxygen [75].

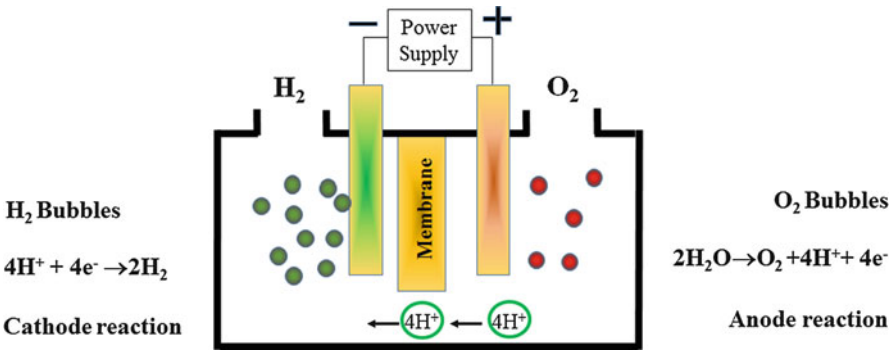

Fig. 10.8 Schematic demonstration of water electrolysis to produce hydrogen and oxygen

At the anode compartment, oxidation of H_2O occurs to produce O_2 gas ($E^\circ = 0.82$ V):

$$2H_2O\ (l)\ O_2(g) + 4H^+(aq) + 4e^- \tag{10.9a}$$

and at the cathode compartment, reduction of H_2O occurs to produce H_2 gas ($E^\circ = -0.41$ V):

$$4H^+(aq) + 4e^-\ 2H_2(g) \tag{10.9b}$$

From the above redox reaction, it can be seen that one mole of electrons (one Faraday) yield one-half of a mole of hydrogen and one-quarter mole of oxygen. At one ampere per second (one coulomb), 5 μmol H_2 and 2.5 μmol O_2 produce 5 kW h/m^3 H_2 at 60% efficiency. The voltage required to initiate electrolysis of hydrogen-one in water (^1H_2O) can be calculated using Nernst equation (Eq. 10.10).

$$E_{cell} = E^\circ_{cell} - \frac{RT}{nF} LnQ \tag{10.10}$$

where E_{cell} represents the cell potential; E°_{cell}, the cell potential at standard state; R, the ideal gas constant (0.08216 atm·L/mol·K); F, Faraday constant (96,485 C/mol), and n, the electron transferred during redox reaction. The chemical quotient, Q, depends on the redox reaction shown in Eq. 10.10. This value is a dimensionless value and depends on the temperature, concentration, and gas partial pressure.

If the reaction occurs at ambient condition (25 °C and 1 atm), the above Nernst equation can be simplified as the following (10.11):

$$E_{cell} = E^\circ_{cell} - \frac{0.0592V}{n} LogQ \tag{10.11}$$

From water electrolysis, the standard reduction potential for anode and cathode can be calculated using the Eqs. 10.12a and 10.12b.

$$E^\circ_{anode} = 1.229 - \frac{0.0592V}{n} LogQ \tag{10.12a}$$

$$E^\circ_{cathode} = -\frac{0.0592V}{n} LogQ \tag{10.12b}$$

The half cell potential can measured, ranging from 1.3 to 1.5 V according to the acidity (pH value) and amount of heat loss to the surroundings.

This required voltage is heavily influenced by other electrolytes, pH (due to formation of H_3O^+ and OH^-), and other radical species such as superoxide or ozone and gas/liquid interfacial chemistries [76]. In practical terms, over-potential is required to overcome the activation barriers and to drive the forward to overcome resistance of the circuit and cell, resulting in heating and evaporation of the electrolyte limiting the overall efficiency of the process [77].

$$\Delta H_{T,P} - \Delta H_{25^{\circ}C,\,1\,\mathrm{atm}} = \left(\Delta H_{T,P} - \Delta H_{T,\,1\,\mathrm{atm}}\right) - \left(\Delta H_{T,\,1\,\mathrm{atm}} - \Delta H_{25^{\circ}C,\,1\,\mathrm{atm}}\right) \tag{10.13a}$$

$$\Delta H_{T,P} - \Delta H_{T,\,1\,\mathrm{atm}} = \left(\Delta H_{T,P} - \Delta H_{T,\,1\,\mathrm{atm}}\right)_{\mathrm{H_2}} + \frac{1}{2}\left(\Delta H_{T,P} - \Delta H_{T,\,1\,\mathrm{atm}}\right)_{\mathrm{O_2}} - \left(\Delta H_{T,P} - \Delta H_{T,\,1\,\mathrm{atm}}\right)_{\mathrm{H_2O}} \tag{10.13b}$$

$$\Delta H_{T,P} - \Delta H_{T,\,1\,\mathrm{atm}} = \left(\Delta H_{T,P} - \Delta H_{T,\,1\,\mathrm{atm}}\right)_{\mathrm{H_2}} + \frac{1}{2}\left(\Delta H_{T,P} - \Delta H_{T,\,1\,\mathrm{atm}}\right)_{\mathrm{O_2}} - \left(\Delta H_{T,P} - \Delta H_{T,\,1\,\mathrm{atm}}\right)_{\mathrm{H_2O}} \tag{10.13c}$$

$$\Delta H_{T,\,1\,\mathrm{atm}} - \Delta H_{25^{\circ}C,\,1\,\mathrm{atm}} = \left(\Delta H_{T,\,1\,\mathrm{atm}} - \Delta H_{25^{\circ}C,\,1\,\mathrm{atm}}\right)_{\mathrm{H_2}} + \frac{1}{2}\left(\Delta H_{T,\,1\,\mathrm{atm}} - \Delta H_{25^{\circ}C,\,1\,\mathrm{atm}}\right)_{\mathrm{O_2}} - \left(\Delta H_{T,\,1\,\mathrm{atm}} - \Delta H_{25^{\circ}C,\,1\,\mathrm{atm}}\right)_{\mathrm{H_2O}} \tag{10.13d}$$

The last two expressions at nonstandard temperatures can be expressed as:

$$\Delta H^{\circ}\left(T_f\right) = \Delta H^{\circ}(T_i) + \sum_{H2} \int_{Ti}^{Tf} Cp^{\circ}(T)dT \tag{10.13e}$$

where T is temperature (K), *i* and *f* are initial or final, respectively, and $C^{\circ}_{p,H2}$ is the heat capacity of hydrogen, as a function of temperature (J mol^{-1} K^{-1}) and entropy would be estimated using a similar expression except $\frac{C^{\circ}_{p,H2(T)}}{T}dT$ is used instead of $C^{\circ}_{p,H2(T)}dT$ and ΔS° instead of ΔH° with the enthalpy voltage at T and P (volt, V) being equal to $\Delta H_{T,P}/nF$ and corresponding energy for electrolysis at T,P (V) being equal to $\Delta G_{T,P}/nF$ with n representing the number of electrons transferred, F the Faraday constant (96,500 C mol^{-1}) and at nonstandard temperature and pressure $H_{T,Pf}$- $H_{T,Pi} = \int_{Pi}^{Pf}\left(v - T\frac{\delta v}{\delta T}\right)dp$, where p is pressure, v is volume (m^3), and R is 0.8216 atm·L mol^{-1}·K^{-1} and the temperature/pressure boundary limits are approximately 273 K $< T_{i,f} <$ 1000 K and $0 < p_{i,f} <$ 1000 atm. The equilibrium plots follow Le Chatelier principle with an enthalpy [voltage (V) and electrolysis voltage (E)] versus temperature plot. At 1 atm, both V and E decrease with increasing temperature, with E decreasing at a faster rate. At 298 K and increasing pressure, the rate of E increases rapidly between 0 and 50 atm and continues to slowly rise, whereas enthalpy voltage, V, is constant or decreases at a slow rate. The relationship between enthalpy voltages (V) versus pressure (atm) is constant between 300 and 500 K, with electrolysis voltage (E) a rapid rise between 0 and 50 atm and a steady increase at increasing pressure [78]. Thus, direct electrolysis of water to hydrogen at

high pressure and lower temperatures for use in vehicles may not be practical; however, hydrogen storage and use in fuel cells coupled with supplemental fuel supplies, methane, solar, or gasoline would be feasible and practical. This approach enables petroleum to be used as a feed stock for generation of chemicals or pharmaceuticals instead of an energy carrier [79].

10.3.2 Steam Methane Reformation Coupled with CO_2 Sequestration

The above description also ignores the current method of hydrogen production from methane or natural gas (Eqs. 10.14a and 10.14b) using steam [80].

$$CH_4\ (g) + H_2O\ (g)\ CO(g) + \ 3H_2(g) \text{ at } 1100^\circ C \tag{10.14a}$$

$$CO(g) + H_2O\ (g)\ CO_2\ (g) + \ H_2(g) \text{ at } 350^\circ C \tag{10.14b}$$

Equation 10.14b occurs with the carbon dioxide being separated in a pressure swing adsorption process and stored in oceanic plum or lake, between 5.1 atm and greater from the triple point (5.1 atm and 216 K) to its critical point (73 atm and 304 K) along with the liquid-vapor critical point curve in its phase diagram [81]. The process generates considerable carbon dioxide, almost 14 kg-per-kg of hydrogen. If hydrogen is produced from coal gasification, carbon dioxide amounts will approximately be doubled [82]. Statoil is currently sequestering CO_2 in deep saline aquifers in the North Sea [83], and other companies are using it for enhanced oil recovery in the Gulf of Mexico appears the most synergistic in terms of operability and cost [84]. The environment cost of CO_2 storage or injection into deep water (3000 m or deeper), mines, or old wells over the next decade to century is undetermined, because the geochemistry is unknown over that time period [85]. In addition, the relationship between storage volume, geologic/biotic interfacial chemistries, and storage susceptibility to outgassing is unknown, as demonstrated in Cameroon [86]. At Lake Nyos maar CO_2 outgassing led to a number of deaths due to asphyxiation, which may occur if the mechanism is not understood and appropriate actions taken [87]. To minimize outgassing, CO_2 could be mineralized with limestone or carbonates, which would trap gaseous/liquid CO_2. The minerals, such as olivine (Mg_2SiO_4) and carbonates ($MgCO_3$, [89]) or hydrogen bicarbonates [88], can be used to trap CO_2, if stored in liquid form. The reaction is shown in Eq. 10.15 [90]:

$$CO_2\ (g) + H_2O\ (l) + CaCO_3\ (gs)\ 2HCO_3^-(aq) + Ca^{2+}\ (aq) \tag{10.15}$$

The resulting emulsion would have a pH between 3.0 and 4.6 and unlike liquid CO_2 with a lower specific gravity would be amenable to low depth (<800 m) oceanic storage [91]. To increase the specific gravity above that of seawater, CO_2 could be composited with carbon, enabling the composite to sink to the ocean floor as hydrates, akin to methane hydrates ($CO_2{\cdot}xH_2O$ where x is 6–8, [92]).

10.3.3 Generation of Hydrogen from Methane

Dissociation of methane from natural gas can produce hydrogen without CO_2 [93], requiring approximately 40 kJ/mol H_2, whereas enthalpy change of steam reformation is close to 65 kJ/mol H_2 (energy to the nearest half-decade) $CH_4 \rightarrow C + 2H_2$, $\Delta H^\circ = \sim 75$ kJ/mol at 1000 °C, due to high C-H bond energy ~ 440 kJ/mol. The decomposition temperature may be lowered through use of heterogeneous metal catalysis using nickel, iron, or other second-row transition metals, generating hydrogen and carbon in the form of nanotubes, filaments, or amorphous state such as carbon black [94]. The metal catalysts are susceptible to positioning particularly if the feedstock contains sulfur [95]. This is not the case with carbon-based catalyst, for example activated stratic carbon would produce hydrogen and catalytically deactivated carbon which could be regenerated using steam and CO_2. High surface area catalytically active carbon (such as carbon black or activated carbon) need not have an ordered structure, but would need active sites for methane decomposition [96]. Upscale production of hydrogen from carbon-based catalysts using catalytic decomposition of natural gas could be accomplished in the 50-ton/a day range. This would utilize activated carbon liquid bed reactor, with hydrogen acting as a fuel to generate heat and steam/CO_2 to reactivate the carbon catalyst and a semipermeable membrane for hydrogen-to-methane separation [97]. The methane or other natural gases can be decomposed in the liquid bed at <1000 °C at moderate pressures <20 atm. The partial decomposed products and by-products are passed through cyclone-mixers and heat exchangers and then separated with the unreacted natural gas recycled back to the bed reactor, alongside new catalytic carbon to replace the coarser carbon in the bed which has grown due to methane decomposition. This system requires less oxygen than partial oxidation or steam reformation due to the low endothermic properties of the decomposition [73]. The current industrial model is carbon-petroleum based with CO_2 as an unused toxic byproduct.

Currently, about 5% of natural gas is converted to H_2 using steam reformation. If catalytic decomposition of natural gas (methane) was increased to 50%, up to 40 million tons of carbon will be produced, which is in excess to what is currently used [98]. This excess carbon could be used as raw materials for construction, roads, electricity as carbon fuel cells or added to soil in the form of soil remediation. For example, carbon filaments/tubes are lighter than steel and have greater mechanical strength, but are more expensive to be produced. If hydrogen is produced using metal catalysts from methane decomposition, the likely cost would decrease and usage would increase, benefiting society in terms of lowering CO_2 and carbon emissions into the environment. In 2015, the worldwide production of crude steel, cement, and concrete was approximately 1.6, 4.1, and 2 billion tons, respectively [99, 100]. The usage of carbon-based products as concrete-substitutes, additives, supports, or feedstocks would lead to a further decrease of CO_2, since cement production leads CO_2 production roughly in 1:1 ratio [101]. Production of concrete accounts for between 5% and 8% of global CO_2 emission [102]; thus, hydrogen production from methane and subsequent usage in construction would have a synergistic effect on CO_2 reduction, if the carbon could be bound with asphalt tar or pitch as binding materials and heated to produce carbon composites [103].

10.3.4 Generation of Hydrogen from Microorganism

Although it is not expected to be a major source, algae and cyanobacteria can produce hydrogen from solar light with water as a cofactor and hydrogenase catalyst via a redox reaction shown in Eqs. 10.16a and 10.16b [104]:

$$H_2 + A_{ox}\ 2H^+ + A_{red}\ (\text{A}:\ \text{Electron acceptor}) \tag{10.16a}$$

$$2H^+ + D_{red}\ H_2 + D_{ox}\ (\text{A}:\ \text{Electron donor}) \tag{10.16b}$$

Methane can be produced anaerobically, shown in Eq. 10.17 [105]:

$$CO_2 + 4H_2\ CH_4 + 2H_2O \tag{10.17}$$

or through fermentation with methane acting as feedstocks for hydrogen generation [106] shown in Eq. 10.18.

$$CH_3COO^- + H^+\ CH_4 + CO_2 \tag{10.18}$$

While the efficiency of hydrogen production through microbial is less than 30%, these processes allow for generation of hydrogen under anaerobic conditions coupled with fuel cells for generation of electricity [107]. The generated hydrogen from any sources can be stored using microporous particles as resins [108], or in natural gas silos [109], depleted mines [110], or caverns in saline formations [111], depending on amount, and type of geologic formation.

10.4 Utilization of Hydrogen in Fuel Cells

Hydrogen can be used in different fields, such as metal production, ammonia, chemical pharmaceutical, food and beverage, petroleum fields, and glass and ceramics. The most immediate effect would be as a substitute of gasoline in automobiles and trucks, and once approach is to develop automobile with fuel cells for energy. Eventually hydrogen will join electricity as the major energy carrier, supplying every end-user energy need in the economy, including transportation, central and distributed electric power, portable power, and combined heat and power for buildings and industrial processes. But today, hydrogen fuel cell vehicles (FCVs) are currently in the preproduction stage of development, and the infrastructure to refuel hydrogen as fuel does not currently exist. The DOE Hydrogen and Fuel Cells Program is sponsoring a variety of projects to demonstrate the technical and economic feasibility of integrated hydrogen and fuel cell systems in real-world situations that are consistent with early transition strategies [112].

Hydrogen can be used in fuel cells to generate power during an electrochemical reaction rather than combustion, producing only water and heat as by-products. It can be used in cars, in houses, for portable power, and in many more applications.

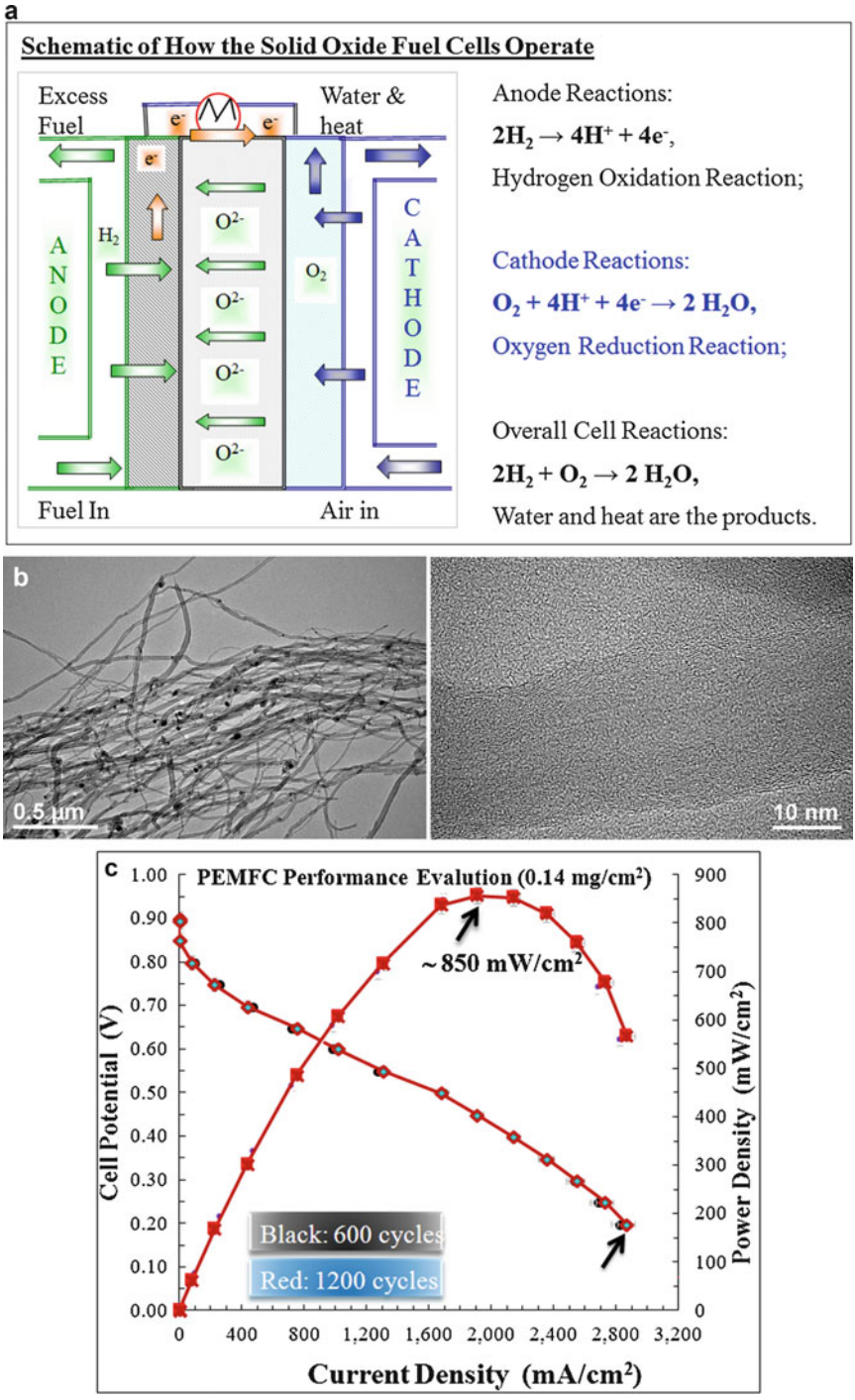

Fig. 10.9 (continued)

In automobiles, hydrogen would need to be stored, which is a major technical hurdle. In practical terms, hydrogen needs to be stored at a higher density than liquid requiring pressurization or cooling which increase the mass and cost of the "storage component" [113]. If hydrogen is stored chemically in the form of hydrides, these samples need to release the hydrogen quickly requiring weaker bonds. The problem with this approach lies in that the release of hydrogen is slow and requires high temperatures (300 °C) although lithium borohydride ($LiBH_4$) has high hydrogen content. Another example, lanthanum nickel hydride ($LaNi_xH_6$) has the potential to release hydrogen at lower temperatures; however, it has a low hydrogen mass percent and therefore would require more hydride, increasing the storage weight [114]. Hydrogen absorption on carbon, within zeolites or metal-organic frameworks (MOFs), may offer another approach. Here hydrogen is adsorbed onto the pores as a monolayer via van der Waal interactions with additional layers upon hydrogen. Ideally, multiple layers should be with the adsorbent, which is the case with structured zeolites and MOFs. In the latter, the metal atoms at the vertices serve as catalysts and the organic linkers as struts, which enable pores to be formed in which hydrogen is stored [115].

Once hydrogen is stored and then released, fuel cells are ideally suited to convert chemical energy to electrical energy in an exothermic redox reaction. As is known in thermodynamics, most systems which generate heat (associated with friction and movement of gears) are not efficient (22% for a gasoline powered engine, 45% for a diesel engine). One of the key advantages of fuel cells is that they are highly efficient, ranging from 60% to 85% (for system). The electric motors can reach 90% efficiency to couple chemical energy with kinetic energy, producing negligible carbon dioxide, nitrogen oxide, or sulfur oxide since carbon is not combusted. Therefore, greenhouse gas emissions, acid rain, and environmental pollutants can be lowered using fuel cells, assuming the hydrogen production step does not generate carbon dioxide [116]. The conventional engine can be modified to utilize hydrogen as a fuel in a manner similar to jet engines with almost no harmful emissions with improved efficiency. The option remains for hydrogen as fuel for airplanes and hydrogen to electricity to drive vehicles. Herein, the fuel cell transmits protons or oxygen across a conducting electrolyte between the electrodes to complete the electrical circuit between feedstocks (hydrogen or air or oxygen component), electrolytic proton conducting component, and metal electrode component to enable electron flow (Fig. 10.9a). Below technical and experimental details will be given for a proton exchange membrane fuel cell [117].

Fig. 10.9 (**a**) Schematic of a proton exchange membrane electrode assembly and associated components. (**b**) The TEM morphological analysis of Pt-functionalized aligned carbon nanotubes (*bottom panel* is the enlarged image). (**c**) The electrochemical performance of PEMFC device with H_2 as fuel and O_2 as oxidant (Reproduced with permission from Yuan et al. [124]. Copyright © Elsevier)

10.4.1 Use of Hydrogen in Proton Exchange Membrane Fuel Cells

Proton exchange membrane fuel cells (PEMFCs) are composed of membrane electrode assembly (MEA), including a polymeric membrane (commercially available Nafion 117 has been used in this study) in the center and an anode and a cathode at each side [118]. On the anode compartment, fuel supplies, such as hydrogen (H_2), are oxidized to proton (H^+), whereas, oxidants, such as oxygen (O_2), are reduced on the cathode side (Fig 10.9a; [119, 120]). The electrons travel from anode to cathode externally to provide direct current for stationary and portable application [121]. The H^+ ions are transferred from the anode through the Nafion electrolyte and react with the O_2 to form water at the cathode surface ($4H^+ + O_2 + 4e^- \rightarrow 2H_2O$, [122]).

PEMFCs provide direct electricity; however, problems remain with robustness and cell performance over longer durations of the catalyst such as carbon supported platinum (Pt) and its alloy. The cost of the catalyst is high and the catalyst has a propensity to easily be poisoned [123]. We demonstrated that the incorporation of aligned carbon nanotubes (ACNTs) decorated with Pt enables the electrode to increase its catalytic performance. This is due to rapid gas diffusion and chemisorption of the gas reactants. ACNT hydrophobicity also provides a new tool to prevent cathode flooding, resulting in long-term device stability [124]. To achieve the above goal, we focused on three key steps: aligned carbon nanotubes synthesis, nanostructural characterization, and electrochemical property test. The aligned carbon nanotubes are synthesized using chemical vapor deposition with a xylene-ferrocene solution as starting materials. Xylene is used as the carbon source and ferrocene as iron metal source to act as catalyst to promote nanotubes growth. The aligned carbon nanotubes were prepared using a two-stage furnace with temperature at 225 and 725 °C, respectively. The anodic and cathodic materials were then place on two sides of the commercially available Nafion membrane. Hot pressing technique was then used to fabricate the membrane electrode assembly (MEA) under temperature of 210 °C and pressure of 600 pound-forces per square inch gauge (pisg) for 5–10 min. The MEA was treated using boiling H_2SO_4 (0.5 M) and distilled water for 1–2 h, accordingly. The exchange ions from Na^+ to H^+ were used implemented to increase the ionic conductivity. The surface morphology, cross-sectional images, and the thickness of the aligned carbon nanotubes were determined using state-of-the-arts instrumentation. The single cell is attached to an Electrochem Inc. test stand to record the I-V polarization curves, which gives a measurement of the MEA's performance. The polarization curves were collected by potentiostatically cycling the voltage between 0.2 and 1 V.

Transmission electron microscopic (SEM) analyses indicated that MEA shows unique aligned structure of carbon nanotubes with Pt deposition on their surfaces (Fig. 10.9b), which allows the fast gas diffusion through cathodic materials and chemisorbed on the surface of the catalyst. This will ensure the mass transfer is not the rate limiting step to enhance MEA kinetics. The diameter of the aligned carbon nanotubes was found to vary from 20 to 50 nm and length from 10 to 30 μm according to the different growth time period. The Pt nanoparticles are uniformly distributed on the surface of tubes, whose size is ranged from 1 to 8 nm.

Table 10.2 The optical feature of aligned carbon nanotubes

Vibration mode	Raman shift (cm^{-1})	Origination
Radial breathing mode (RBM)	102.40–298.18	Radial expansion-contraction
D mode	1330.00	Structural defects and disorder-induced feature
G mode	1584.17	Planar vibrations of carbon atoms
M mode	1759.28 cm^{-1}	Overtones of the out-of-plane ($_oTO$) in graphite
G′ mode	2662.59	Overtone of the defect-induced D mode, involving "self-annihilating" pair of phonons

Raman spectroscopy was used to evaluate one-dimensional aligned carbon nanotubes. The spectra of the ACNT showed the orderly arranged structure of the aligned CNT. The one-dimension (1D) confinement contributes significantly to its unique optical and spectroscopic properties. The vibration mode and its associated frequency are listed in Table 10.2. Some satellites spectra were also seen due to the complexity of the MEA elemental composition and structure.

Previous to I-V polarization, the PEMFC was conditioned for 16 h to obtain stabilized kinetics. The flow rate for H_2 was controlled at 100 mL/min and the rate for O_2 at 300 mL/min. Cell temperature was maintained at 80 °C. It was found that the novelty of using aligned CNTs as cathodic catalyst allows improved performance due to rapid gas diffusion and chemisorption of the gas reactants. The hydrophobicity of the carbon tubes also helped to prevent cathode flooding, further resulting in long-term device stability. The current density (i_o) of the MEA is ranged from 2800 to 3200 mA/cm^2 when O_2 was used (Fig. 10.9c). At this condition, the MEA exhibits a maximum power density varying from 850 to 920 mW/cm^2. It was found that the open circuit voltage is measured to be 0.997 V. Generally, the PEMFC devices operate at about 67% of the maximum current density due to the ohmic loss and concentration loss. This ohmic loss is caused by the internal resistance loss and the concentration loss by the depletion of the reaction concentration.

In summary, chemical vapor deposition and a post-amphiphilic modification are feasible to produce Pt-functionalized aligned carbon nanotubes cathodic catalyst. The highly aligned nanotubes layers favor the gas diffusion, resulting enhanced power density. The single PEMFC displayed the maximum power density >850 mV/cm^2 using the O_2 as oxidant.

10.4.2 Use of Hydrogen in Solid Oxide Fuel Cells

Whereas protein exchange membrane fuel cells utilize a proton-conducting polymer membrane (typically Nafion) that contains the electrolyte operating at 80 °C, solid oxide fuel cells (SOFC) utilize a solid material, typically yttria-stabilized zirconia (YSZ), as the electrolyte and operate near 1000 °C. Similar chemistries occur, such as the anode [$2H_2 + 2O^{2-} \rightarrow 2H_2O + 4\bar{e}$; $H_2 \rightarrow 2H^+ + 2\bar{e}$ for PEM] and cathode [$O_2 + 4\bar{e} \rightarrow 2O^{2-}$; $½O_2 + 2H^+ + 2\bar{e} \rightarrow H_2O$ for PEM] to generate water [$2H_2 + O_2$

$\rightarrow 2H_2O$; $H_2 + ½O_2 \rightarrow H_2O$ for PEM]. In particular, failure to obtain a gas-tight seal between chambers is a severe problem, causing gas leakage and eventually destruction of the stacked cells. In addition, the interconnect material, lanthanum chromate, is particularly difficult to process because of chromium evaporation at high temperatures, which leads to poor densification. Therefore, there has been much attention on the development of cathode and electrolyte materials with long life-spans and high conductivities, allowing operation in the temperature range of 600–800 °C [125]. The $La_{1-x}Sr_xCo_{1-y}Fe_yO_{3-\delta}$ (LSCF) perovskites have been considered as the cathode materials for the SOFCs to replace the conventional $La_{1-x}Sr_xMnO_{3-\delta}$ (LSM) materials [126]. This is attributed to the one order higher catalytic activity of LSCF for oxygen reduction than that of LSM, especially of the A-site deficient $La_{0.58}Sr_{0.42}Co_{0.2}Fe_{0.8}O_{3-\delta}$ perovskite [127]. However, as the operating temperature of an SOFC is decreasing, a higher activity of oxygen reduction reaction (ORR) becomes increasingly important, and thus, the adding of metals into the cathode material to increase its ORR activity has been the subject of numerous studies; the metals, which have been studied, include platinum (Pt), palladium (Pd), silver (Ag), and copper (Cu) [128].

Traditionally, SOFC cathodes have been fabricated using ceramic-grade materials and sintering at relatively high temperatures, which lowers the surface area and would limit the exchange current density (i_0). To improve the i_0, the sol-gel (SG) method is becoming an increasingly popular route for the preparation of SOFC materials. While SG process gives time and energy saving advantages, the main benefit is the formation of highly porous structures, providing very high surface areas and triple phase boundary. This approach also allows the preparation of a mixture in solution, achieving homogeneity on the molecular scale in the solid product. Further, the composition of the oxide can easily be tailored by varying the ratios of the precursors in solution

To achieve conducting properties and longevity, by increasing the porosity, we produced Pt modified LSCF by sol method of fabrication and followed by nano-micro integration. Several state-of-the-art instrumental analyses were applied to determine the structure of the cathodic catalyst and its electrochemical performance. The LSCF sol-precursor was then screen-printed on the samarium doped ceria (SDC) electrolyte. Totally, five layers of LSCF cathode catalyst membrane (also called working electrode, WE) were applied to increase the porosity and TPB. High temperature XRD (Ultima IV, Rigaku Americas Corporation, Woodlands, Texas) was used to determine the crystalline phase and the lattice distortion of sol-derived Pt-LSCF electrode material. The facility is equipped with Cu target with the operating voltage of 40 kV and current of 30 mA. High temperature transmission electron JEOL 2010 TEM, (Microscopy and Imaging Center, TAMU-College station) equipped with Gatan heating stage by using silicon nitride support film, electron diffraction (ED), and Oxford INCA X-ray energy dispersive spectroscopy spectrometer (EDS) techniques was also employed to obtain Nanostructural information, crystalline phase and elemental composition of Pt-LSCF. The high-resolution TEM images were taken at a direct magnification of 600,000 magnitudes with the point resolution of 0.23 nm, and all image magnifications were calibrated with a

commercial cross-line grating replica and SiC single crystal lattice images. Cyclic voltammetry (at low and high polarization), electrochemical impedance spectroscopy (EIS) methods were employed to evaluate the ORR reactivity on the surface of the cathode composite. Pt gauze (coated with Pt black to increase the conducting surface area), attached to a Pt wire, was press-contacted to the working electrode (WE), counter electrode (CE), and reference electrode (RE) surfaces, respectively. Half-cell experiments were carried out over temperatures ranging from 400 °C to 700 °C in a vertical split-tube furnace. For ac impedance measurements, an analytical Solartron 1252A frequency response analyzer was coupled with the Solartron 1287 potentiostat. The frequency applied ranged from 100 kHz to 0.05 Hz and the measurements were carried out at the open circuit voltage (OCV), using a perturbation amplitude of 10 mV rms. The impedance measurements and fitting analysis were controlled with commercial software (ZPLOT).

High temperature X-ray diffraction (Fig. 10.10a) confirmed the formation of the perovskite structure with the expected tetragonal phase symmetry. The rietveld XRD quantification ensured the quantities of crystalline components in this multiphase mixture to avoid overlapping. Average crystallite sizes of SOFC ranged from 36.50 to 48.30 nm, and Pt samples are 5.46–13.68 nm, respectively. The size of Pt was tripled with the temperature increase; however, the LSCF increased by approximately 32.3% within the temperature range of 25–800 °C. From this study, it was found that the crystal growth will occur when the sintering temperature was above 900 °C.

The high temperature transmission electron microscopic images indicated that monodispersed and quasi-spherical particles were obtained. The morphology and crystallinity were found highly depending on the temperature changes (from ambient temperature, 500 °C, 600 °C, 700 °C, 800 °C, Fig. 10.10b). The selected -area electron-diffraction (SAED) analysis on LSCF cathode indicated that the ring patterns and single-crystal pattern (corresponding to the [110] lattice plane zone axis) resulted from a polycrystal and single crystal unit, suggesting formation of well-crystallized LSCF. After annealing at various temperatures, it can be seen that the LSCF particles diameter increased 36.50–48.30 nm. Although the heat-treatment causes particle growth unfavorable to the grain boundary, the lattice imperfection would be mitigated and impurities could be removed at high temperatures.

For comparison purposes, the postfactum IR compensated low-field and high-field cyclic voltammetry and electrochemical impedance spectroscopy were used to study ORR at cathodic materials (Fig. 10.10c). The half-cell operating temperatures were controlled fewer than 400–700 °C with increments of 50 °C. Based on the more reliable impedance and low field data, it is seen that the ORR is one order faster on the surface of colloidal-LSCF cathode than that on the commercial LSCF at 700 °C. Pt-modification was found to double the ORR kinetic due to the high porosity and large triple phase boundary of colloidal LSCF. Additionally, the high mixed ionic-electronic conductivity of LSCF (MIEC, [129]) is dictated by the need to retain an oxygen deficiency in the oxidizing atmosphere at the cathode. The mixed valence state (observed from the XPS data) also gives faster ORR reaction rate.

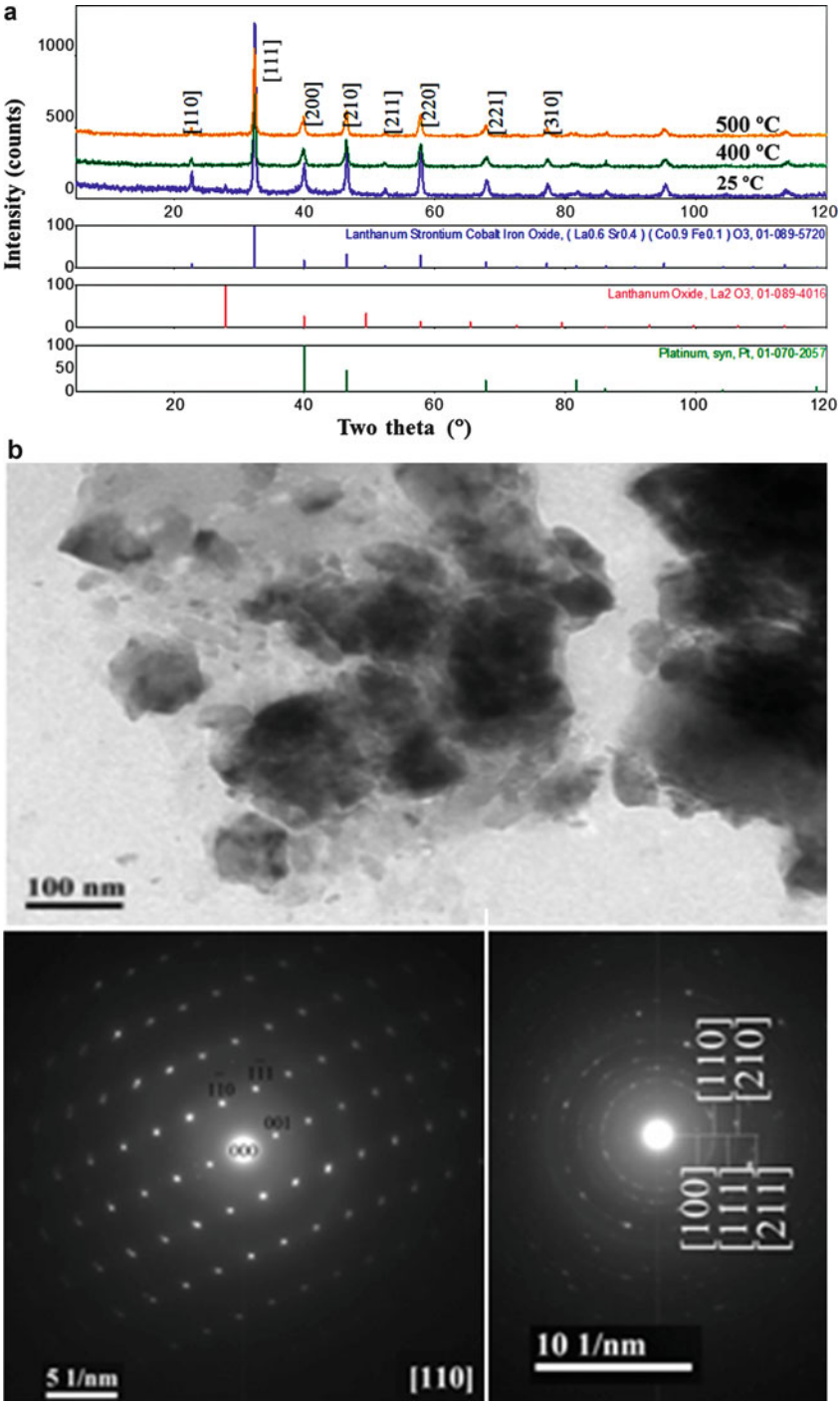

Fig. 10.10 (continued)

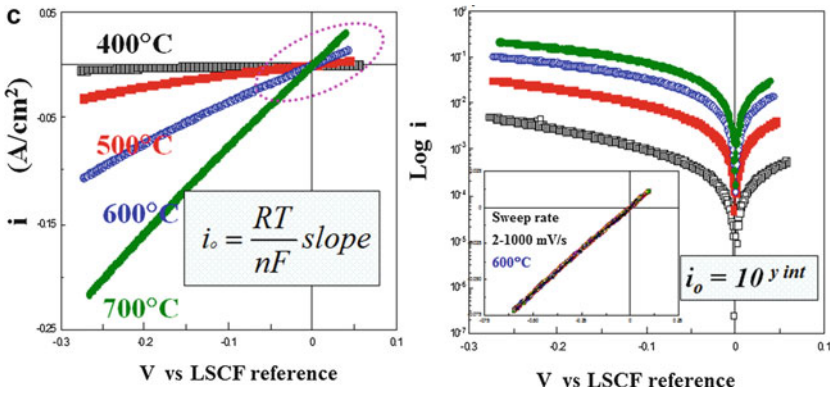

Fig. 10.10 (**a**) High temperature XRD analyses of LSCF cathodic catalyst, indicating the crystalline structure was maintained at tetragonal with particle size incremental increase (Image courtesy of Ms. Aya Takase from Rigaku Corporation). (**b**) High temperature TEM analyses of LSCF cathodic catalyst (Image courtesy of Dr. Zhiping Luo from Fayetteville State University), well-indexing with XRD data (selected data shown). (**c**) The ORR of LSCF cathode under various operating temperatures, the left panel showing the low field CV and right panel the high field CV data (Reproduced with permission from Liu et al. [130]. Copyright © Elsevier)

In summary, the colloidal chemistry is powerful method to prepare homogeneous perovskite-type materials. The $La_{0.6}Sr_{0.4}Co_{0.2}Fe_{0.8}O_{3-\delta}$ was found to be an active catalyst for oxygen reduction reaction (ORR). The high temperature XRD and TEM were used as complimentary approaches whereby in situ analyses were performed to evaluate the dynamic process of the phase formation and transition. The catalytic activity of oxygen reduction reaction on the LSCF cathodic compartment can be related to the readily accessible active sites (electrophilic surface oxygen species). This results from the specific composition and multiple oxidation states of the tertiary elements on of surface layer. The postmodification of LSCF using Pt nanoparticles was also found to be productive to advance the current density and power density at various half-cell operating temperatures.

10.4.3 Use of Hydrogen in Fuel Cell Vehicle

The above two technical sections demonstrate the feasibility of producing a fuel cell within a stack and thus the potential to manufacture a fuel cell based automobile. Since fuel cells can utilize any fuel containing hydrogen, automobiles using hydrogen gas will emit water and almost no harmful emissions (CO_x, NO_x, and SO_x) and their associated acids (carbonic, nitric, and sulfuric) emissions when interacting with water will also diminish.

A Look Inside: From the outside, a gasoline powered 4-door sedan will resemble a fuel cell powered 4-door sedan, where the gasoline fuel tank and combustion engine are replaced with a hydrogen storage system and electric motor (composed of fuel cells and battery), respectively. In a typical fuel cell vehicle (FCV, for example

Honda FCX), there are five key parts: power control unit, electric motor, fuel cell stack, high-output battery, and hydrogen storage tank (Fig. 10.11a). A reformer is included to connect the fuel cell to the fuel tank and inverter, AC/DC; DC/DC with H_2 purge system and exhaust. On the other hand, gasoline powered car would consist of petrol engine, alternator, differential transmission with battery ignition system, cooling, and exhaust. Some technology from gasoline vehicle could be incorporative into the hybrid one, such as regenerative braking or lane assist technology. In the interim, the hybrid vehicle may consist of a petrol-engine, connected to an electric motor, either in parallel or series configurations [131]. In the FCV, the power control unit is used to govern the flow of the electricity. The electric motor is used to propel the vehicle in a quiet, smooth, and efficient mode. In other words, the FCV is driven with less engine noise compared with the traditional gasoline powered vehicle. The fuel cell stack can convert chemical energy into the electricity during the chemical redox reaction. The electricity is normally direct current which can be used to power the electric motor. High-output battery enables the storage of energy generated from regenerative braking and provides supplemental power to the electric motor. The hydrogen storage tank is used to store hydrogen gas, which is compressed at high pressure to increase the energy density.

A Miniature Vehicle: A 1:320 ratio model car was tested (Honda Fit: Dr. Fuel cell car volume/volume) by Liu and her group. The catalysts (15 formulations, Fig. 10.11B-1) were used to improve water splitting, in future to increase the driving distance. Several of the nanocataysts were encapsulated using natural products. The metal ions or metal elements are iron, cerium, and other transitions metals as listed in the figure. The natural products were extracted from *Hygrophilia auriculata* (HA) and *Chlorophytum borvilianum* (CB). The cerium-doped titania was found to have with anatase crystalline phase. The catalysts were ranging from 2 to 10 nm (Fig. 10.11B-2). The detailed study on Fe_3O_4 and $Ce_xTi_{1-x}O_2$ (Fig. 10.11B-3) indicated that catalysts were well indexed and crystalline with ultrafine particles. The catalyst exhibits cubic structure. The Nobel (Pd or Pt) metals showed body centered cubic, while cerium (Ce), zinc (Zn), or gadolinium (Gd) metal oxide exhibit face-centered cubic structure. The iron exhibited a spinel structure which was well indexed with standard iron (II,III) oxide. Transmission electron microscopic analysis

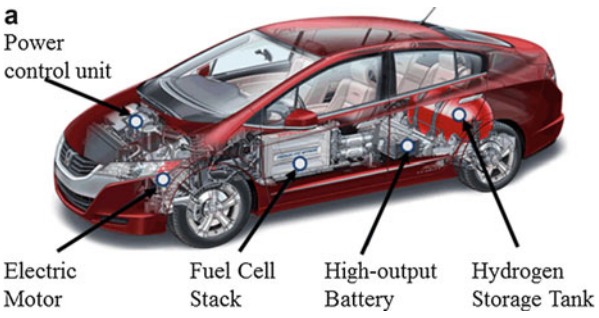

Fig. 10.11 (continued)

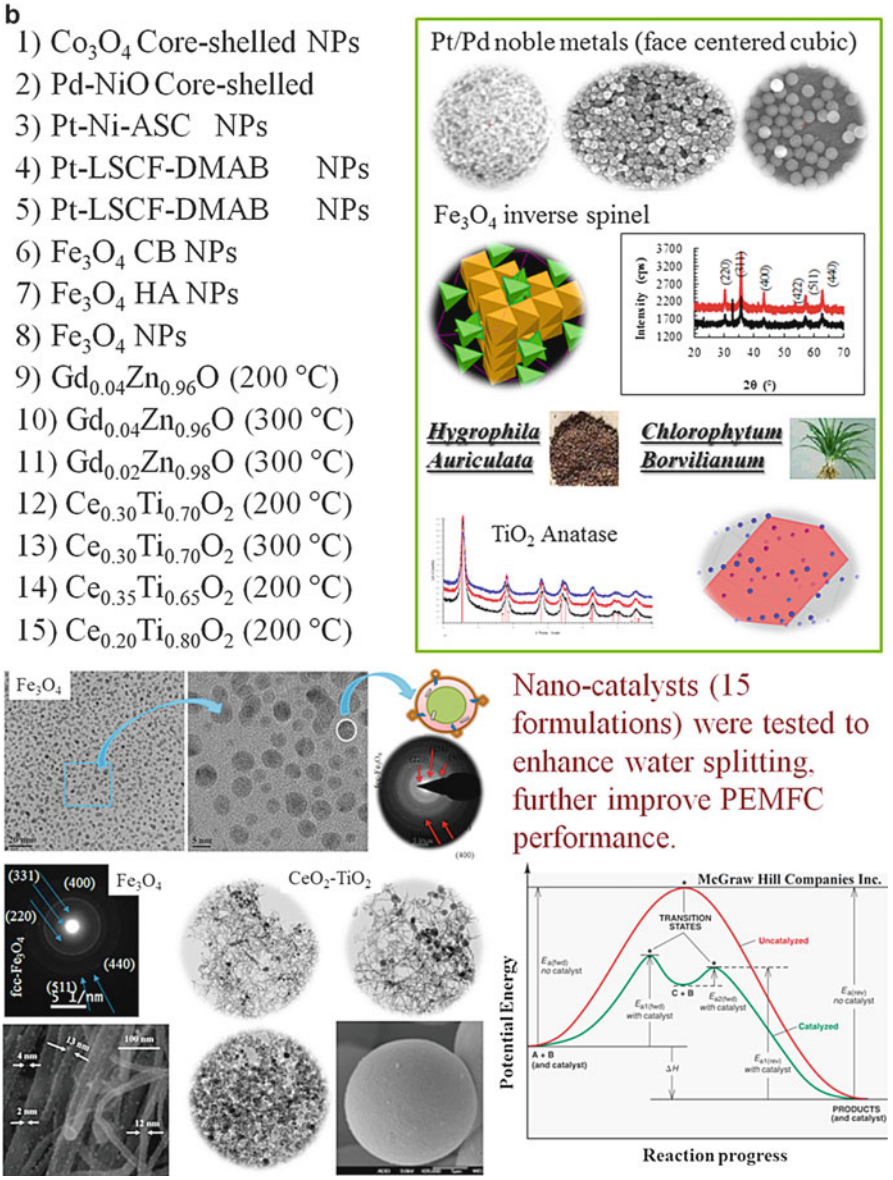

Fig. 10.11 (**a**) Schematic of Honda FCX Clarity (Reproduced with permission. Copyright © Honda USA). (**b**) **B1**: All catalysts were fabricated at temperatures under 100 °C unless specified; **B2**: The TEM and XRD analysis of the nanocatayst; **B3**: The characterizations of selected catalyst (iron oxide, ceria-titania) were further characterized using X-ray diffraction; and **B4**: The schematic of activation energy lowering using catalyst (**B-4**), further enhancing vehicle performance

Table 10.3 Performance of hydrogen model car with different formulations of cathode catalyst in PEMFC

H_2 Fuel cells driven vehicles performance w/nano-catalyst					
Nano-catalysts	Drive time (S)	Distance (m)	Velocity (m/s)	Time (s) to split H_2O	Voltage created (V)
*Control	125.2	35.2	0.269	108	1.40
*Co_3O_4	61.0	13.9	0.228	62.0	1.38
$Pd(OAc)_2$	158.0	42.4	0.268	67.4	1.42
*Pt-Ni-ASC 1:1:4	153.0	36.1	0.237	73.0	0.74
*Pt-LSCF 1:5:4 (DMAB)	138.0	30.2	0.219	96.0	0.74
*Pt-LSCF 1:1:4 (DMAB)	211.0	66.3	0.314	92.0	1.37
Fe_3O_4CB NPs 3:2 CB	260.0	67.1	0.257	70.0	1.03
Fe_3O_4 3:2 HA	80.0	25.0	0.313	76.0	1.38
Fe_3O_4 2:1 RT	No speed: reason to be determined			54.0	1.41
*$Gd_{0.02}Zn_{0.98}O$ 300 °C	194.0	57.2	0.295	44.0	1.24
*$Gd_{0.04}Zn_{0.96}O$ 200 °C	No speed: reason to be determined			52.7	1.39
*$Gd_{0.04}Zn_{0.96}O$ 300 °C				42.0	1.30
$Ce_{0.30}Ti_{0.70}O_2$ 300 °C	232.0	66.4	0.286	83.0	1.16
$Ce_{0.30}Ti_{0.70}O_2$ 200 °C	78.0	22.0	0.282	98.0	0.87
$Ce_{0.35}Ti_{0.65}O_2$ 200 °C	183.0	67.0	0.361	103.0	1.40
$Ce_{0.20}Ti_{0.80}O_2$ 200 °C	45.0	12.8	0.285	57.0	1.40
Control no nano-catalyst (NC) present	Most efficient NC		*Averages of different trails	30 mL H_2O, sources 12 V power	
Nano-catalyst: longest drive and greatest distance	Time least efficient NC: splitting and velocity		Nano-catalyst: best vehicle performance (velocity and distance)		

Systems marked with asterisk [*] were averaged over five runs; empirical formulae of catalyst is shown with reduction using dimethylamine borane (DMAB) and ascorbate (ASC) at room temperature (RT) or higher (temperature specified). The metals were also reduced using natural products derived from *Hygrophilia auriculata* (HA) and *Chlorophytum borvilianum* (CB) with metal salt: reducing agent: natural product ratio shown where it was not 1:1. The fuel cell voltage (V), total drive time (s), distance traveled (m), speed (m/s), and start-up time to generate sufficient hydrogen to gain momentum (s) was measured against a battery powered car as control

confirmed the crystalline nature of the catalysts to be ultrasmall in diameter (5 nm). The nanotubes (2–4 nm in diameter and about 25 μm in length) were used as a host for Pt catalyst. The metal ions were reduced with ascorbate (ASC) and dimethylamine borane (DMAB). By introducing a thin layer of gadolinium-doped zinc oxide or ceria-titania decorated lanthanum strontium cobalt ferrite (LSCF) composite cathode, the fuel cell resistivity was lowered. In general, these catalysts lower the activation energy barrier by creating a new pathway for chemical reaction. They facilitated water splitting to generate hydrogen and oxygen, which were used as fuel and oxidant to power the model automobile.

Eight formulations (Table 10.3) gave superior results than control (without addition of any catalyst). Among these catalysts, five formulations almost provided twice the distance of the control or gave higher velocities. The average from the

Table 10.4 Average performance of hydrogen model car with different formulations of cathode catalyst in FCV against solar powered car and with battery as control

Average	Control	Solar cells	12 Nano-catalysts	Top 5 nano-catalysts	$Gd_{0.02}Zn_{0.98}O$ 300 °C	$Ce_{0.35}Ti_{0.65}O_2$ 200 °C
Time (s)	125.2	19.6	149.4	216.0	194.0	183.0
Distance (m)	35.2	11.0 (fixed)	42.2	64.8	57.2	67.0
Velocity (m/s)	0.269	0.566	0.279	0.314	0.295	0.361

twelve nanocatalysts, and top five catalyst for parameters such as drive time (s), drive distance (m) and velocity (m/s) using battery as control and solar cell were compared with each other (Table 10.4). The cut-off distance was 11 m which was matched or exceed by all formulations which demonstrate that cathode composition affects performance to a much higher degree than generated voltage (above the electrolysis minimum, cf. Eq. 10.1) or velocity of vehicle.

Hybrid vehicles such as Honda (FCX Clarity, launched in 2007), which utilizes compressed hydrogen and generates 100 kW energy using a PEMFC stack, give comparable performance to diesel or gasoline powered comparable vehicles in endurance, ride comfort and safety. The FCX can drive up to 570 km on one tank of hydrogen. General Motors (GM) also released a model using compressed hydrogen (Provoq; launched in 2008; Barrett and Stubley, 2008 [132, 133], containing an 88 kW PEMFC and battery hybrid configuration with a drive range of 483 km. Since these automobiles operate on electricity, other modifications have been introduced into concept vehicles, which may become standard, such as photovoltaic (PV) roof for auxiliary power units. This PV roof can provide air conditioning when parked or extend the range of cars with a primary fuel cell. Other modifications include substitution of the hydraulic drive with an electric drive to replace oil as a lubricant. Alternatively, on-board storage of hydrogen can be supplemented by hydrogen generation through electrolysis or thermolysis. The hydrogen source can be also from flexible fuels such as biomass or reformed natural gas [134].

The conflict in the Middle East raised oil prices and the average US citizen felt the impact at the fuel pump. This increase in oil prices led consumers to purchase more fuel-efficient or electric vehicles. Auto manufactures met this challenge through increased research in fuel efficient and hybrid electric vehicles. From 2008, they also introduced an emerging hydrogen powered fuel cell cars. Toyota's Hybrid-Prius culminated these research efforts with an automobile utilizing a parallel configuration with a continuous variable transmission known as Estima Hybrid System (1997–2004). A modified configuration of the Prius was introduced in 2005 with a greater power supplies. This additional power enables a smoother ride by the electric drive train with the 500 V motor. Another enhancement includes a direct current to direct current converter with battery pack. The system composed of drive train, motor, and converter is known as Hybrid Synergy Drive [135]. These engineering upgrades reduce gasoline consumption and CO_2 emission, but do not eliminate them. Current configurations to produce cars with

zero CO_2 emissions focus on lithium-ion battery alone or in combination with proton exchange membrane fuel cells hybrid. The current major problem with H_2-PEMFC cars is availability of hydrogen and the gasoline-gallon equivalent (gge) cost is much greater. As stated above, several US automakers have released new models, such as Honda FCV Concept (2014), Hyundai ix35 (2014), Toyota Mirai FCV (2015), and Volkswagen:Golf SportWagen HyMotion (2014). Other manufactures proposed to release hydrogen powered models between 2017 and 18, suggesting a degree of maturity unmatched previously. However, more research is needed to optimize layout configuration, hydrogen storage, hydrogen accessibility, fuel supply, and gge cost. The current emphasis is placed on automobiles, since the transport sector accounts for 26% of total CO_2 emissions. Within the transport sectors, the automobiles and trucks occupy the largest fraction of the transportation emission. However, design of electric vehicle has also been applied to buses, tractors, golf carts, and folk-lifts [136]. Since the number of them is low, the impact is less than that of consumer cars or trucks.

10.4.4 Hydrogen Storage for Transport

The technologies to produce hydrogen are reforming natural gas, which reacts with water at high temperatures to produce hydrogen and CO_2, where the generated hydrogen needs to be stored. The US Department of Energy (DOE) initial benchmark was 11 wt% of hydrogen [137], enabling a round trip of 400 km without refilling. The storage cost ratio was \$67/kg H_2, which is lower than current costs for high pressure or cryogenic storage. One technology which may meet the twin DOE objectives (summarized in Fig. 10.12) is hydrogen storage and release using microporous particles in the form of metal organic frameworks [138]. The stored and then released hydrogen would be used in an internal combustion engine similar rather than current gasoline compression engines before transitioning to electric fuel cell based engines, with Li-ion battery providing sufficient voltage to activate the electric engine, with excess energy being recycled to charge the battery. The major reason for not having a direct transition between hydrogen storage and fuel cell based vehicles is the cost of the fuel cell of almost \$1500/kW [139]. In an analogous manner, fuel cells such as solid oxide fuel cells operating at 1000 °C could serve as power stacks in homes, for electrical and heat generation, at much higher operational efficiencies than coal based electricity (70% to 45%) with the feedstock being methane and later hydrogen [140]. The current limitations are cost orientated due to the almost $\times 5$ folder higher equipment and implementation costs compared to the current grid system that has been subsidized over the last century [141].

10.5 Renewable Framework, Path, and Policy

We have seen that the transport section accounts for approximately 26% of greenhouse emissions and generation of electricity 30% in 2014 [142]. We have demonstrated that transitioning gasoline and diesel automobiles to hydrogen (or battery or

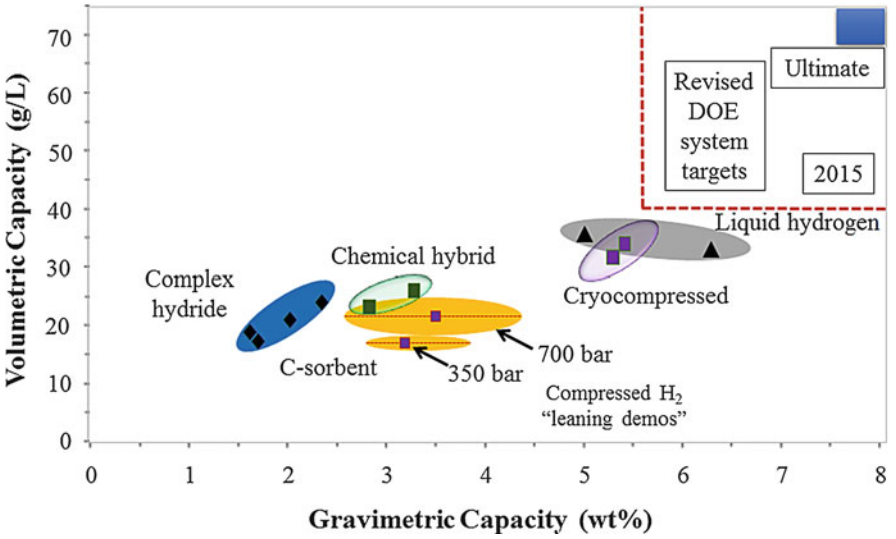

Fig. 10.12 Summary of storage capacity of hydrogen using complex hydrides, metal organic frameworks, and compression (Reproduced with permission from Ahluwalia et al. [112]. Copyright © Elsevier)

hybrid) would reduce emissions, which would make a societal impact. Hydrogen can also be used in stationary applications and below we will investigate impact of large scale hydrogen production to meet this transition on the environment. We have seen that impetus for auto-development came from three sources –consumers, legislatures, and technical expert – general auto managers on the feasibility and profitability of such projects. The rise in gasoline prices in 1973–1974 (1st gulf war and OPEC Oil embargo), 1978–1981 (Iran-Iraq conflict and war), 1988–1990 (regional tensions and invasion of Kuwait by Iraq), and 2007–2009 (US recession and collapse of housing market) increased the price from $2.05 (1972) a gallon to $3.57 (2008) a gallon. This price was adjusted for inflation to value of dollar in 2016, focusing the minds of consumers to more energy efficient cars and lowering sales of automobiles for those quarters [143]. Public awareness started in the early to mid-60s in the state of California regarding clear air and its associated health benefits. The awareness was acute in the city of Los Angeles, due to occurrences of smog, culminating in public opinion favoring cleaner air and less auto emissions by 1966. Congress passed the Clean Air Act Amendments in 1970, amending the 1963 law, which expanded the air pollution list for both stationary and mobile sources including enforcement. This necessitated automakers designing cars which meet these new tighter emission standards [144]. This standard was incorporated and tightened by the California Air Resources Board requiring 2% (1988) to 10% (2003) of automobiles sold in the state to have zero emissions [145]. Additionally in 1988 the United Nations established the Intergovernmental Panel on Climate Change (IPCC), with the first Assessment report released in 1990 showing emissions contributing to

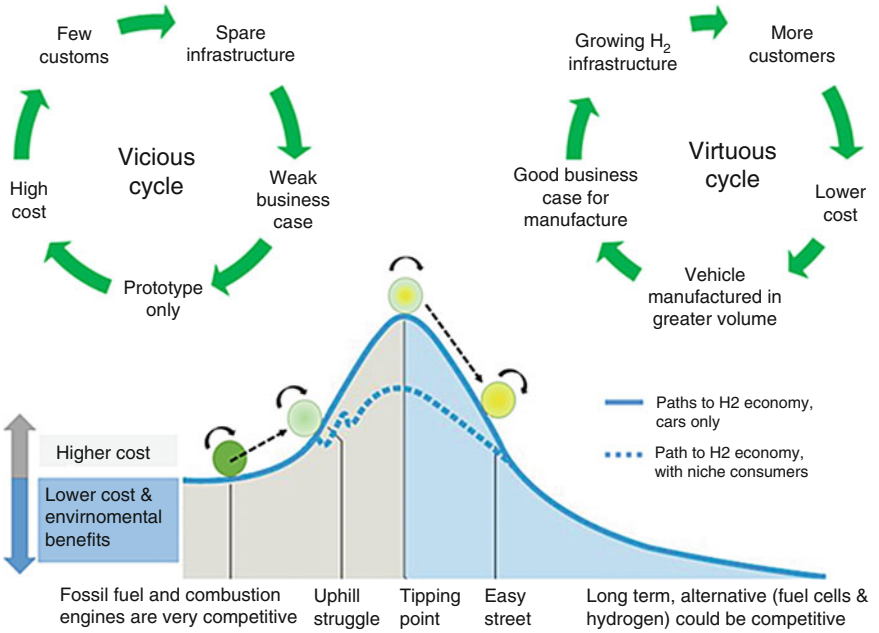

Fig. 10.13 Summary of "barriers" in implementing electric, hybrid, and FC based automobiles (Reproduced with permission from http://www.ika.rwth-aachen.de/r2h/index.php/Introduction_to_Hydrogen_and_Hydrogen_Communities.html)

global warming [146]. Lastly, advances in nickel metal hydride or lead acid, lithium-ion and sodium sulfur batteries, hybrid powertrains, and fuel cells [147] enable companies like Tesla to produce high performance lithium-ion electric sports car. The Toyota Prius was a hybrid gasoline-electric motors with nickel metal hydride (NiMH) battery pack (~274 V and a 12 V low voltage battery) or Toyota Prius electric vehicle with 4.4-kWh lithium-ion battery and electric motor and have sold in excess of 75,000 units in the USA in 2015 [148]. These various hurdles and setbacks are illustrated in Fig. 10.13 and also apply for stationary power generators such as coal-based power stations.

10.5.1 Environmental Remediation

The major advantage for hydrogen is that its usage from nonfossil fuels does not generate CO_2, and if generated through steam reformation, the by-products can be applied to further decrease the CO_2 pool, an ability terrestrial plants have through photosynthesis [150]. Plants are both CO_2 neutral or drawn down the pool depending on the ratio between respiration (releasing CO_2) and photosynthesis (using CO_2, [151]). For example, banana farmers have known that addition of

soot/ash or charcoal to soil enhances plant growth, due to increased soil aeration, nutrient, and water retention in addition to supporting symbiotic microorganisms facilitating increased biomass and CO_2 fixation [152]. A side benefit of addition of carbon by-products was the diminished use of inorganic fertilizers due to more efficient incorporation of organic carbon and its sustained release over a longer time period [153]. Ash and soot also have metal cations which promote cation exchange, pH balance, and root elongation. Soil can be modified using stratic carbon from methane could serve as a carbon source, CO_2-sink and a "foundation" for healthy root formation and would be cheaper than common inorganic fertilizers due to its large scale availability [154].

10.5.2 Biomass for Electrical Generation

The magnitude of this transition is to supply almost 40,000 TWh of electricity and 2.5 Gtce of heat, requiring a similar amount of hydrogen to be produced by 2050 [155]. The electrical energy required for electrolyzes to produce hydrogen could be supplied from hydroelectric, geothermal, and nuclear power stations without increasing the carbon dioxide. Other sustainable resources such as solar and wind power are excluded due to intermittent conditions. Biomass and fossil fuels are excluded, due to production of CO_2 as feedstocks for wide scale production of hydrogen [156]. From 2015 to 2050, the most likely scenario due to economics of large scale implementation of these sustainable technologies is continued use of coal reforming and natural gas for generation of electricity [157] bridged with biomass from corn, sugar cane, rapeseed, and sunflower including wood pulp (as biofuels and bio-gas, [158]) for the generation of hydrogen and/or electricity. Thus, biomass or the glucose economy [$C_6H_{10}O_5 + 7H_2O \rightarrow 12H_2 + 6CO_2$; $CO + H_2O \leftrightarrow CO_2 + H_2$ with zirconia catalyst (0.2–0.35 g or 1 M NaOH) in supercritical water (673–713 K; 30–35 MPa] yielding 5–25% hydrogen relative to no catalyst, indicating that biomass is carbon neutral (storage during photosynthesis and emission during pyrolysis or gasification) yielding hydrogen for electrical generation or feedstock for fuel cells [149].

10.5.3 Biogas for Electrical or Hydrogen Generation

Biogas (methane, [159]) or biofuel (methanol, [160]) can feed fuel cell to produce hydrogen from water to generate electricity. A fuel cell engine has the advantage of negligible CO_2 production as opposed to direct combustion of methanol alone or as a gasoline additive [161]. Alternatively, using water gas shift reaction, hydrogen could be produced from biomass directly for use as gasoline substitutes in transport and heat generation [162]. If biomass from lignin/cellulose is used instead of cereals, this would free up those crops as a food sink. Here biofuels could utilize the current liquid fuel infrastructure with minimal, overhead, although technical challenges remain [163].

10.5.4 Sulfur–Iodine Thermocycle for Hydrogen Generation

In the proceeding sections, it was demonstrated that although hydrogen generation from water is possible, it is technically difficult to achieve economically due to the high temperature required for lysis of water. One approach to minimize this high energy cost is through the use of thermochemical cycling to produce oxygen and hydrogen separately [164] using energy from solar [165] or nuclear sources [166]. For example, $2HI \rightarrow I_2 + H_2$, where I_2 is recycled at 450 °C and HI is generated from oxidation of sulfur dioxide to sulfuric acid, $I_2 + SO_2 + 2H_2O \rightarrow H_2SO_4 + 2HI$ at 120 °C with oxygen being generated in a likewise fashion from sulfuric acid. This approach would not generate any greenhouse gases [167], but would require an increase in solar collectors or nuclear power stations operating at higher temperatures to facilitate these reactions, using up uranium and generating radioactive waste by-products [168].

10.5.5 The Hydrogen Production, Storage, and Utilization

During the early eighteenth century in England, particularly in London, manufacturing was a local affair with basic tool, industrialization enabled fabrication, specialization, commoditization of processes, instrumentation, and standardization of products [169]. In lieu of a shift to the cities, the transport, banking, and housing infrastructures were built up. In the area of transport, the steam engine enabled water to be pumped from mines to power machinery to movement of locomotives, automobiles, and ships [170]. As a consequence of the rapid industrial heavy industry was unregulated and dumped waste by-products such as muriatic acid gas [$2\ NaCl + H_2SO_4 \rightarrow Na_2SO_4 + 2\ HCl$] in the production of soda ash with calcium sulfide and hydrogen chloride as waste by-products. The calcium sulfide decomposed to hydrogen sulfide [171]. The British Alkali Act 1863 and subsequent acts legislation of what major heavy industries, which not emit into the environment in great quantities such as smoke, grit dust, and fumes [172]. Poor enforcement of some aspects of this act led to the Great London Smog of 1952, in which between 4000 and 12,000 people died and over 100,000 made ill, and led to tougher enforcement and the new supplemental act, the Clean Air Act 1956, amended in 1968 [173]. Today we have the United Nations Framework Convention on Climate Change from 1992 and United Nations Framework Convention on Climate Change (UNFCCC) first round (Kyoto Protocol period I from) is complete [174]. The Kyoto Protocol period II (2012–2020) has not been implemented by a number of countries including the US and Canada [175]. Recently, the Paris Agreement, agreed in 2015 and to be signed in 2016, will enter become effective upon ratification by the top 55 greenhouse gas emitting countries to be implemented from 2020 [176]. The aim of the agreement is to limit the rise greenhouse gas based temperature rise to 1.5 °C. Much of the technical assessment is conducted by the UNs the Intergovernmental Panel on Climate Change (IPCC) which generate assessment reports triennially or hexennially [177]. The first assessment report was published in 1990, followed by an

supplement (1992), an second (1995), an third (2001), an fourth (2007), an fifth (2013), and an anticipated sixth assessment to be published around 2019 to continually review, revise, and predict current scientific literature related to global warming [178]. The current regulatory environment "tax" of around \$50 CO_2-per-ton serves as an economical driving force towards carbon-free energy carriers. If a transition from Fischer–Tropsch synthetic fuels to hydrogen energy carrier is enacted, technical developments need to be realized to cope with anticipated demand. Assuming a baseline transition from no H_2 (% 0, in 2015) to 33% by 2050 would require at least a 300 GW electrical and heat capacity using hydrogen [179] and fuel cell development, hydrogen storage, and electrical generation from lithium batteries and biofuels [180] to power cars. Cars which are powered by hydrogen alone would be expected to be developed in the next phase (from 2050 to 2100) beginning at the twenty-second century to meet current and future decline in CO_2 as outlined by the UNFCCC [181].

10.6 Hydrogen Economy from 2015 to 2050

Any discussion of hydrogen as a fuel source ought to couple greenhouse gases and CO_2 sequestration, since energy and global warming are linked [182]. Although hydrogen can be produced from salt water, a more practical method, currently employed is from natural gas or methane [183] with the resultant carbon by-products being recycled as building materials, in fuel cells, or as soil additives. Natural gas is proposed, since this would entail minimal changes to the current petroleum/natural gas infrastructure [184], with the projected longevity of natural gas being surpassed by coal and possibly uranium and methane can be derived from nonfossil sources [185]. In addition, the generate carbon by-products can be used direct carbon fuel cells. This has the multiple advantages that hydrogen combustion does not produce CO_2, the carbon by-products from methane steam reformation to generate H_2 can be used to generate electricity via fuel cells, as concrete substitutes and also as soil additives, all of which lower CO_2 usage [186]. Fossil fuels would be regulated to use in plastics, drugs, and other critical materials instead of energy production [187]. While the methane reserves from fossil fuels are limited, methane is also found in biogas [188], landfill [189], and methane hydrates [190]. In the coming decade, use of hydrogen will increase as an energy carrier substitute for fossil fuels. The route for hydrogen generation (summarized in Fig. 10.14) will impact the environment, due to the production of CO_2 either by steam reformation of methane and CO_2 sequestration or through catalytic decomposition of natural gas and usage of carbon by-products, which would further lower CO_2 generation through use as construction material substitutes, soil enhancers, or materials for fuel cells enabling the increase demand for energy to be met and also decreasing CO_2 production and usage [195].

One technology that is being considered and would be synergistic with hydrogen production from natural gas is fuel cells which generate electrical energy from chemical feedstocks [191]. The efficiency is related to the ratio between Gibbs

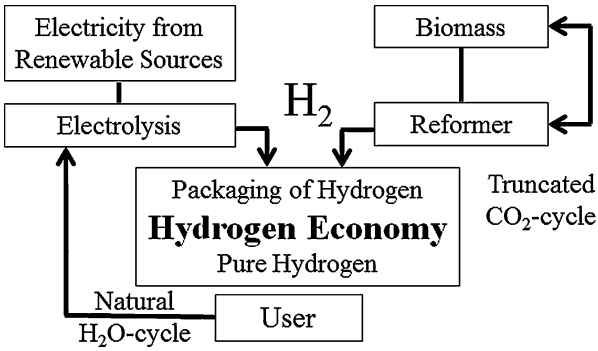

Fig. 10.14 Summary of components in hydrogen production to be used for generation of energy in the hydrogen economy (Reproduced with permission from http://www.oilcrash.com/articles/h2_eco.htm)

energy and enthalpy which are dependent upon the voltage-to-enthalpy difference between reactants and products, $\eta = \frac{nFE}{\Delta H}$, where η is the efficiency of the fuel cell (dimensionless or %), n the number of electrons in the chemical reaction, F the Faraday's constant (9.648 70 × 10^4 C/mol), E the voltage of the cell (V), and ΔH the enthalpy of the reaction (kJ/mol). The C(s) + O_2 (g) → CO_2 (g) potential ($E°$) is 1.02 V with entropy close to zero. Assuming η of 0.9 and V/V° of 0.8, the estimated efficiencies are close to 90% or higher [192] compared with hydrogen based fuel cells (E = 1.229 V and η ~ 80%), respectively [193, 194], with molten salts as electrolytes at intermediate temperatures around 800 °C [196]. Here, direct carbon fuel cells are utilized for stationary power generation [197] with hydrogen used as a fuel for portable power generation [198].

10.6.1 Hydrogen Distribution and Economics

The last technical issues are hydrogen distribution; here the natural gas network could be adapted to carry hydrogen. Since hydrogen volumetric density is lower than natural gas, the transport pipes would need to be retrofitted and a cheaper option than de novo fabrication of a new transport system [199]. In automobiles, weight and cost of hydrogen storage units limit their applications with metal organic framework, zeolites [200], and metal hydrides [201] being capable of storage hydrogen at around 8 wt% at 60 atm, meeting the department of energy objectives [202]. The ability of proton exchange membrane fuel cells to utilize the hydrogen and air (oxygen) to water and electricity is hindered by the high cost of these devices for large scale adaptation, $1500/kW [203], whereas a typical gasoline engine has an equivalent cost of $40/kW (summarized to the nearest decade, [204]). In addition, proton exchange membrane fuel cell employs a Nafion membrane as electrolytes to separate the anode and cathode operated at low temperatures (<100 °C) with platinum as a Nobel catalyst [205]. Any wide scale use would need to minimize the use of this metal either by increasing temperature to in excess of 100 °C [130, 206] or a

composite alloy with cobalt [207] or chromium [208] or nanotubes to reduce the percent metal used [124]. Higher temperatures would require newer temperature tolerant membrane, but the fuel cell could be integrated to allow for methanol reformation [209].

10.7 Conclusion: Realistic Expectations for Hydrogen as Energy Carrier: For Our Yesterdays, Today and Tomorrows

Hydrogen gas has potential as an energy carrier with near zero emissions upon reaction. If hydrogen is to replace coal for electricity generation and petroleum in automobiles for transport, production of hydrogen has to increase almost 10–15 fold and has to be sustainable [210]. In the short term, biomass (glucose economy) appears to meet the requirements of low greenhouse emission due to photosynthesis using CO_2 to synthesis glucose (sugars) which are released upon biomass gasification or pyrolysis, which appear to be on part with natural gas reforming methods in terms of cost [211]. Although hydrogen gas can be combusted as in rocket fuel, most likely use is as a feedstock for solid oxide fuel cells or proton exchange membrane fuel cells in hydrogen powered generation of electricity or transport. Fuel cells are attractive but are limited by the capacity of the feedstock (hydrogen), which needs to be stored at high densities such that automobiles can travel a distance similar to current gasoline powered costs with a similar cost per gallon [212]. Hydrogen storage is a hurdle since hydrogen has different physical properties to natural gas, the same infrastructure cannot be used, and for on-board storage sorption using metal organic frameworks or cryo-compression supplemented with metal hydrides appears to be the current and proposed modalities. The current bottleneck for portable uses is related to deployment and delivery and would require a hydrogen infrastructure similar to the ones for petroleum and natural gas (refill stations, underground storage silos, consumer marketplace) that currently is limited to California and New York [213]. The current framework of international cooperative agreements on research, federal policy on clean air, and tax incentives will move emerging technologies forward that utilize hydrogen. This development could facilitate technology transfer in new markets and positively impact on global deployment of allied technologies for production, storage, and efficient use of hydrogen towards a 10 terawatt supply with negligible emission of greenhouse gases, using a mix of carbon capture/carbon neutral of fossil fuels. The addition of renewable energy sources includes nuclear energy benefiting the citizens and the environment [214]. The most likely approach (yesterday and today) towards fuel is the use of fossil fuels with carbon capture and utilization of the captured carbon as a new feedstock. The carbon neutral biomass-based fuels and production of hydrogen from water using solar, geothermal, wind, and nuclear energy provide a different avenue for hydrogen production. In the near future, the thermochemical pyrolysis and electrolysis can be used to produce

hydrogen used in fuel cells for both stationary and portable energy as a sustainable hydrogen economy [215].

Acknowledgment The authors are grateful to the National Science Foundation, Center of Research Education in Science and Technology (HRD-0734850) and Major Research Instrumentation program at the Texas A&M University-Kingsville. The support from Department of Energy, the Office of Science and the Divisions of Educational Programs and Chemical Science and Engineering is also duly acknowledged. The Department of Education and R. Welch Foundation are also duly acknowledged for support undergraduate and graduate students to participate in fuel cell research. Acknowledgment is made to the Donors of the American Chemical Society Petroleum Research Fund for partial support of this research (shale gas storage and methane reforming). Authors are also thankful to the assistance and support from the fuel cell group members (Dr. D.-J. Liu) at Argonne National Laboratory. The use of TAMU Materials Characterization Facility and Dr. Liang and Dr. Young's suggestion and discussion are acknowledged.

References

1. Act, U. S., & Congress, U., Energy Policy Act of 1992. Pub L, 102–486; Act, U. S., & Congress, U. (2005). Energy policy act of 2005. Public Law **109**(58), 42 (1992)
2. J. Tollefson, Hydrogen vehicles: fuel of the future. Nature **464**(7293), 1262–1264 (2010)
3. E. Independence, Security Act of 2007. Public Law **110**(140), 19 (2007)
4. F. Sissined, *Energy Independence and Security Act of 2007: A Summary of Major Provisions* (Library of Congress, Congressional Research Service, Washington, DC, 2007)
5. Act, R., & Grant, W. A. American Recovery and Reinvestment Act of 2009 (2009)
6. Act of 2015. Pub S. Rept. 114–118 Tax relied extension Act of 2015
7. G. Thomas, Overview of storage development DOE hydrogen program. Sandia National Laboratories, 9 (2000)
8. M.E. Ros, M. Weeda, H. Jeeninga, Snapshots of hydrogen uptake in the future. Policy Studies, 2011–2080 (2012)
9. P.Z. Grossman, Energy shocks, crises and the policy process: a review of theory and application. Energy Policy **77**, 56–69 (2015)
10. C.S. Thomas, Automobile companies on FCEVs, in *Sustainable Transportation Options for the 21st Century and Beyond* (Springer International Publishing, Cham, 2015), pp. 109–111
11. S.A. Ciatti, Compression ignition engines–revolutionary technology that has civilized frontiers all over the globe from the industrial revolution into the twenty-first century. Front. Mech. Eng. **1**(5), 1–6 (2015)
12. A. Horvath, E. Rachlew, Nuclear power in the 21st century: challenges and possibilities. Ambio **45**(1), 38–49 (2016)
13. R.S. El-Emam, H. Ozcan, I. Dincer, Comparative cost evaluation of nuclear hydrogen production methods with the Hydrogen Economy Evaluation Program (HEEP). Int. J. Hydrog. Energy **40**(34), 11168–11177 (2015)
14. R.K. Ahluwalia, J.K. Peng, T.Q. Hua, Sorbent material property requirements for on-board hydrogen storage for automotive fuel cell systems. Int. J. Hydrog. Energy **40**(19), 6373–6390 (2015)
15. F. Montignac, V. Mousseau, D. Bouyssou, M.A. Aloulou, B. Rousval, S. Damart, An MCDA approach for evaluating hydrogen storage systems for future vehicles, in *Evaluation and Decision Models with Multiple Criteria* (Springer, Berlin/Heidelberg, 2015), pp. 501–532
16. S. Bakker, J. Farla, Electrification of the car–Will the momentum last? Introduction to the special issue. Environ. Innov. Soc. Trans. **14**, 1–4 (2015)
17. J. Alazemi, J. Andrews, Automotive hydrogen fuelling stations: an international review. Renew. Sust. Energ. Rev. **48**, 483–499 (2015)

18. S. Sharma, S.K. Ghoshal, Hydrogen the future transportation fuel: from production to applications. Renew. Sust. Energ. Rev. **43**, 1151–1158 (2015)
19. R. Bohnsack, A. Kolk, J. Pinkse, Catching recurring waves: low- emission vehicles, international policy developments and firm innovation strategies. Technol. Forecast. Soc. Chang. **98**, 71–87 (2015)
20. J. Liu, S. Bashir (2015), http://pubs.acs.org/doi/pdf/10.1021/bk-2015-1213.ot001. Accessed Apr 2016
21. W.D. Nordhaus, A review of the "Stern review on the economics of climate change". J. Econ. Lit. **45**, 686–702 (2007)
22. H. Ozawa, A. Ohmura, R.D. Lorenz, T. Pujol, The second law of thermodynamics and the global climate system: a review of the maximum entropy production principle. Rev. Geophys. **41**(4) (2003)
23. World Population Prospect (2015): the 2015 Revision, http://esa.un.org/unpd/wpp/. Accessed Apr 2016
24. Z.D. Boren (2014) http://www.independent.co.uk/life-style/gadgets-and-tech/news/there-are-officially-more-mobile-devices-than-people-in-the-world-9780518.html. Accessed Apr 2016
25. L. Suganthi, A.A. Samuel, Energy models for demand forecasting – a review. Renew. Sust. Energ. Rev. **16**(2), 1223–1240 (2012)
26. M.Z. Jacobson, Review of solutions to global warming, air pollution, and energy security. Energy Environ. Sci. **2**(2), 148–173 (2009)
27. N.A. Owen, O.R. Inderwildi, D.A. King, The status of conventional world oil reserves – hype or cause for concern? Energy Policy **38**(8), 4743–4749 (2010)
28. A. Midilli, M. Ay, I. Dincer, M.A. Rosen, On hydrogen and hydrogen energy strategies: I: current status and needs. Renew. Sust. Energ. Rev. **9**(3), 255–271 (2005)
29. G. Nicoletti, The hydrogen option for energy: a review of technical, environmental and economic aspects. Int. J. Hydrog. Energy **20**(10), 759–765 (1995)
30. J.C. Ganley, E.G. Seebauer, R.I. Masel, Porous anodic alumina microreactors for production of hydrogen from ammonia. AICHE J. **50**(4), 829–834 (2004)
31. S. Swinnen, V.S. Nguyen, M.T. Nguyen, Catalytic generation of molecular hydrogen from hydrazine using lithium and beryllium hydrides. Chem. Phys. Lett. **496**(1), 25–31 (2010)
32. P.J. De Wild, M.J.F.M. Verhaak, Catalytic production of hydrogen from methanol. Catal. Today **60**(1), 3–10 (2000)
33. R.C. Neavel, Liquefaction of coal in hydrogen-donor and non-donor vehicles. Fuel **55**(3), 237–242 (1976)
34. R.W. Bentley, Global oil & gas depletion: an overview. Energy Policy **30**(3), 189–205 (2002)
35. J.H. Gibbons, W.U. Chandler, Liquids and gases, the crux of the matter, in *Energy* (Springer US, New York, 1981), pp. 67–82
36. G.C. Watkins, Oil scarcity: what have the past three decades revealed? Energy Policy **34**(5), 508–514 (2006)
37. World Energy Outlook (2015), http://www.worldenergyoutlook.org/media/weowebsite/2015/WEO2015_ToC.pdf. Accessed Apr 2016
38. J. Widén, M. Lundh, I. Vassileva, E. Dahlquist, K. Ellegård, E. Wäckelgård, Constructing load profiles for household electricity and hot water from time-use data – modelling approach and validation. Energy Build. **41**(7), 753–768 (2009)
39. S.W. Hadley, A.A. Tsvetkova, Potential impacts of plug-in hybrid electric vehicles on regional power generation. Electr. J. **22**(10), 56–68 (2009)
40. S. Pacala, R. Socolow, Stabilization wedges: solving the climate problem for the next 50 years with current technologies. Science **305**(5686), 968–972 (2004)
41. A.E. Outlook, *Energy Information Administration* (Department of Energy, 2010), https://www.stb.dot.gov/stb/docs/RETAC/2010/March/EIA%20AEO%202010.pdf. Accessed Apr 2016
42. M. Finley, BP statistical review of world energy (2013), http://www.usaee.org/usaee2013/submissions/presentations/SR%202013%20US%20events.pdf. Accessed Apr 2016

43. EIA, Coal (2014), http://www.eia.gov/energyexplained/index.cfm?page=coal_reserves; gas http://www.eia.gov/tools/faqs/faq.cfm?id=58&t=8; and oil http://www.eia.gov/tools/faqs/faq.cfm?id=38&t=6. Accessed Apr 2016
44. T.N. Veziroglu, Hydrogen technology for energy needs of human settlements. Int. J. Hydrog. Energy **12**(2), 99–129 (1987)
45. EIA (2015) http://www.eia.gov/todayinenergy/detail.cfm?id=24472
46. T. Lazarides, T. McCormick, P. Du, G. Luo, B. Lindley, R. Eisenberg, Making hydrogen from water using a homogeneous system without noble metals. J. Am. Chem. Soc. **131**(26), 9192–9194 (2009)
47. OECD/IEA Electricity Information (2008), http://ny.whlib.ac.cn/pdf/Electricity_Information_2008_Edition.pdf. Accessed Apr 2016
48. ABARE Research Report (1999), http://data.daff.gov.au/data/warehouse/pe_abarebrs99000327/PC10536.pdf. Accessed Apr 2016
49. World Resource Report (2014), http://www.wri.org/our-work/project/world-resources-report. Accessed Apr 2016
50. OECD NEA & IAEA (2014), https://www.oecd-nea.org/ndd/pubs/2014/7209-uranium-2014.pdf. Accessed Apr 2016
51. S. Fetten, How long will the world's uranium supplies last? Scientific American, 9 Mar 2009
52. J. Ivy, *Summary of Electrolytic Hydrogen Production: Milestone Completion Report (No. NREL/MP-560-36734)* (National Renewable Energy Lab, Golden, 2004). Accessed Apr 2016
53. J.R. Bolton, Solar photoproduction of hydrogen: a review. Sol. Energy **57**(1), 37–50 (1996)
54. J.A. Turner, Sustainable hydrogen production. Science **305**(5686), 972–974 (2004)
55. D.B. Levin, L. Pitt, M. Love, Biohydrogen production: prospects and limitations to practical application. Int. J. Hydrog. Energy **29**(2), 173–185 (2004)
56. C.C. Cormos, Evaluation of energy integration aspects for IGCC-based hydrogen and electricity co-production with carbon capture and storage. Int. J. Hydrog. Energy **35**(14), 7485–7497 (2010)
57. United States Environmental Protection Agency, U.S. Greenhouse Gas Inventory Report: 1990–2014. https://www.epa.gov/ghgemissions/us-greenhouse-gas-inventory-report-1990-2014 (2016)
58. J.P. Christ, A.P. Slowak, Why Blu-ray vs. HD-DVD is not VHS vs. Betamax: the co-evolution of standard-setting consortia. Schriftenreihe des Promotionsschwerpunkts Globalisierung und Beschäftigung **29**, 1–34 (2010)
59. R.D. McCarty, J. Hord, H.M. Roder, *Selected Properties of Hydrogen (Engineering Design Data) (No. NBS-Mono-168)* (National Engineering Lab. (NBS), Boulder, 1981)
60. V.I. Tikhonov, A.A. Volkov, Separation of water into its ortho and para isomers. Science **296** (5577), 2363 (2002)
61. G.E. Schmauch, A.H. Singleton, Technical aspects of ortho- parahydrogen conversion. Indust. Eng. Chem. **56**(5), 20–31 (1964)
62. Y. Li, R.T. Yang, Gas adsorption and storage in metal-organic framework MOF-177. Langmuir **23**(26), 12937–12944 (2007)
63. T.Q. Hua, R.K. Ahluwalia, J.K. Peng, Technical assessment of compressed hydrogen storage tank systems for automotive applications (DOE has recently lowered the 2015 gravimetric total system target to only 5.5 total system wt%) (2014), http://energy.gov/sites/prod/files/2014/03/f9/compressedtank_storage.pdf. Accessed Apr 2016
64. G. Petitpas, P. Bénard, L.E. Klebanoff, J. Xiao, S. Aceves, A comparative analysis of the cryo-compression and cryo-adsorption hydrogen storage methods. Int. J. Hydrog. Energy **39**(20), 10564–10584 (2014)
65. T. Gnann, P. Plötz, A review of combined models for market diffusion of alternative fuel vehicles and their refueling infrastructure. Renew. Sust. Energ. Rev. **47**, 783–793 (2015)
66. A.P. Jephcoat, High-pressure physics: testing one's metal. Nat. Mater. **10**(12), 904–905 (2011)

67. W.C. Lattin, V.P. Utgikar, Transition to hydrogen economy in the United States: a 2006 status report. Int. J. Hydrog. Energy **32**(15), 3230–3237 (2007)
68. J.I. Levene, M.K. Mann, R.M. Margolis, A. Milbrandt, An analysis of hydrogen production from renewable electricity sources. Sol. Energy **81**(6), 773–780 (2007)
69. K. Christopher, R. Dimitrios, A review on exergy comparison of hydrogen production methods from renewable energy sources. Energy Environ. Sci. **5**(5), 6640–6651 (2012)
70. NREL (2014), http://www.nrel.gov/hydrogen/production_cost_analysis.html. Accessed Apr 2016
71. DOE (2007), http://energy.gov/sites/prod/files/2015/01/f19/11007_h2_threshold_costs.pdf. Accessed Apr 2016
72. S.K. Thengane, A. Hoadley, S. Bhattacharya, S. Mitra, S. Bandyopadhyay, Cost-benefit analysis of different hydrogen production technologies using AHP and Fuzzy AHP. Int. J. Hydrog. Energy **39**(28), 15293–15306 (2014)
73. N. Muradov, Z. Chen, F. Smith, Fossil hydrogen with reduced CO_2 emission: modeling thermocatalytic decomposition of methane in a fluidized bed of carbon particles. Int. J. Hydrog. Energy **30**(10), 1149–1158 (2005)
74. R.L. LeRoy, C.T. Bowen, D.J. LeRoy, The thermodynamics of aqueous water electrolysis. J. Electrochem. Soc. **127**(9), 1954–1962 (1980)
75. K. Onda, T. Kyakuno, K. Hattori, K. Ito, Prediction of production power for high-pressure hydrogen by high-pressure water electrolysis. J. Power Sources **132**(1), 64–70 (2004)
76. A. Ursua, L.M. Gandia, P. Sanchis, Hydrogen production from water electrolysis: current status and future trends. Proc. IEEE **100**(2), 410–426 (2012)
77. J.E. Funk, R.M. Reinstrom, Energy requirements in production of hydrogen from water. Indust. Eng. Chem. Process Design Dev. **5**(3), 336–342 (1966)
78. C.A. Schug, Operational characteristics of high-pressure, high- efficiency water-hydrogen-electrolysis. Int. J. Hydrog. Energy **23**(12), 1113–1120 (1998)
79. S. Licht, Solar water splitting to generate hydrogen fuel: photothermal electrochemical analysis. J. Phys. Chem. B **107**(18), 4253–4260 (2003)
80. A.P. Simpson, A.E. Lutz, Exergy analysis of hydrogen production via steam methane reforming. Int. J. Hydrog. Energy **32**(18), 4811–4820 (2007)
81. H.E.C. Swanenberg, Phase equilibria in carbonic systems, and their application to freezing studies of fluid inclusions. Contrib. Mineral. Petrol. **68**(3), 303–306 (1979)
82. P.L. Spath, M.K. Mann, *Life Cycle Assessment of Hydrogen Production via Natural Gas Steam Reforming* (National Renewable Energy Laboratory, Golden, 2000)
83. P. Audigane, I. Gaus, I. Czernichowski-Lauriol, K. Pruess, T. Xu, Two-dimensional reactive transport modeling of CO_2 injection in a saline aquifer at the Sleipner site, North Sea. Am. J. Sci. **307**(7), 974–1008 (2007)
84. K.S. Lackner, A guide to CO_2 sequestration. Science **300**(5626), 1677–1678 (2003)
85. H. Herzog, K. Caldeira, E. Adams, Carbon sequestration via direct injection. Encycl. Ocean Sci. **1**, 408–414 (2001)
86. J.P. Lockwood, M. Rubin, Origin and age of the Lake Nyos maar, Cameroon. J. Volcanol. Geotherm. Res. **39**(2–3), 117–124 (1989)
87. W.C. Evans, L.D. White, M.L. Tuttle, G.W. Kling, G. Tanyileke, R.L. Michel, Six years of change at Lake Nyos, Cameroon, yield clues to the past and cautions for the future. Geochem. J. **28**(3), 139–162 (1994)
88. A. Yamasaki, An overview of CO_2 mitigation options for global warming- emphasizing CO_2 sequestration options. J. Chem. Eng. Jpn **36**(4), 361–375 (2003)
89. H. Béarat, M.J. McKelvy, A.V. Chizmeshya, D. Gormley, R. Nunez, R.W. Carpenter, G.H. Wolf, Carbon sequestration via aqueous olivine mineral carbonation: role of passivating layer formation. Environ. Sci. Technol. **40**(15), 4802–4808 (2006)
90. M. Steinberg, Fossil fuel decarbonization technology for mitigating global warming. Int. J. Hydrog. Energy **24**(8), 771–777 (1999)

91. M.I. Hoffert, K. Caldeira, G. Benford, D.R. Criswell, C. Green, H. Herzog, H.D. Lightfoot, Advanced technology paths to global climate stability: energy for a greenhouse planet. Science **298**(5595), 981–987 (2002)
92. N.Z. Muradov, T.N. Veziroglu, "Green" path from fossil-based to hydrogen economy: an overview of carbon-neutral technologies. Int. J. Hydrog. Energy **33**(23), 6804–6839 (2008)
93. B.C. Steele, Fuel-cell technology: running on natural gas. Nature **400**(6745), 619–621 (1999)
94. L. Piao, Y. Li, J. Chen, L. Chang, J.Y. Lin, Methane decomposition to carbon nanotubes and hydrogen on an alumina supported nickel aerogel catalyst. Catal. Today **74**(1), 145–155 (2002)
95. P. Tang, Q. Zhu, Z. Wu, D. Ma, Methane activation: the past and future. Energy Environ. Sci. **7** (8), 2580–2591 (2014)
96. A.W. Weimer, J. Dahl, J. Tamburini, A. Lewandowski, R. Pitts, C. Bingham, P. Design, Thermal dissociation of methane using a solar coupled aerosol flow reactor. Proceedings of the 2001 DOE Hydrogen Program Review, NREL/CP-570-30535. (Apr. 2001). http://citeseerx.ist.psu.edu/viewdoc/download?doi=10.1.1.195.309&rep=rep1&type=pdf]
97. P.L. Spath, W.A. Amos, M.K. Mann, Process analysis work for the DOE hydrogen program-2001. In *Proceedings of the 2002 US DOE Hydrogen Program Review* (*2002*) NREL/CP-610-32405. (2002). https://www.eecbg.energy.gov/hydrogenandfuelcells/pdfs/32405b1.pdf
98. L. Fulcheri, Y. Schwob, From methane to hydrogen, carbon black and water. Int. J. Hydrog. Energy **20**(3), 197–202 (1995)
99. World Steel Association (2015), https://www.worldsteel.org/dms/internetDocumentList/bookshop/2015/World-Steel-in-Figures2015/document/World%20Steel%20in%20Figures%202015.pdf. Accessed Apr 2016
100. J.M. Crow, The concrete conundrum. Chemistry Word 62–66 (2008), http://www.rsc.org/images/Construction_tcm18-114530.pdf. Accessed Apr 2016
101. E. Fitzer, The future of carbon-carbon composites. Carbon **25**(2), 163–190 (1987)
102. E. Worrell, L. Price, N. Martin, C. Hendriks, L.O. Meida, Carbon dioxide emissions from the global cement industry. Annu. Rev. Energy Environ. **26**(1), 303–329 (2001)
103. U. Meier, Carbon fiber-reinforced polymers: modern materials in bridge engineering. Struct. Eng. Int. **2**(1), 7–12 (1992)
104. A. Le Goff, V. Artero, B. Jousselme, P.D. Tran, N. Guillet, R. Métayé, M. Fontecave, From hydrogenases to noble metal–free catalytic nanomaterials for H_2 production and uptake. Science **326**(5958), 1384–1387 (2009)
105. V.N. Gunaseelan, Anaerobic digestion of biomass for methane production: a review. Biomass Bioenergy **13**(1), 83–114 (1997)
106. K. Urbaniec, A. Friedl, D. Huisingh, P. Claassen, Hydrogen for a sustainable global economy. J. Clean. Prod. **18**, S1–S3 (2010)
107. F. Joensen, J.R. Rostrup-Nielsen, Conversion of hydrocarbons and alcohols for fuel cells. J. Power Sources **105**(2), 195–201 (2002)
108. N.L. Rosi, J. Eckert, M. Eddaoudi, D.T. Vodak, J. Kim, M. O'Keeffe, O.M. Yaghi, Hydrogen storage in microporous metal-organic frameworks. Science **300**(5622), 1127–1129 (2003)
109. A.S. Lord, *Overview of Geologic Storage of Natural Gas with an Emphasis on Assessing the Feasibility of Storing Hydrogen. SAND2009-5878* (Sandia National Laboratory, Albuquerque, 2009)
110. J.B. Taylor, J.E.A. Alderson, K.M. Kalyanam, A.B. Lyle, L.A. Phillips, Technical and economic assessment of methods for the storage of large quantities of hydrogen. Int. J. Hydrog. Energy **11**(1), 5–22 (1986)
111. A. Ozarslan, Large-scale hydrogen energy storage in salt caverns. Int. J. Hydrog. Energy **37** (19), 14265–14277 (2012)
112. R.K. Ahluwalia, T.Q. Hua, J.K. Peng, On-board and off-board performance of hydrogen storage options for light-duty vehicles. Int. J. Hydrog. Energy **37**(3), 2891–2910 (2012)
113. K. O'Malley, G. Ordaz, J. Adams, K. Randolph, C.C. Ahn, N.T. Stetson, Applied hydrogen storage research and development: a perspective from the US Department of Energy. J. Alloys Compd. **645**, S419–S422 (2015)

114. R.A. Huggins, Hydrogen storage, in *Energy Storage* (Springer International Publishing, Cham, 2016), pp. 95–118
115. Q. Lai, M. Paskevicius, D.A. Sheppard, C.E. Buckley, A.W. Thornton, M.R. Hill, Z. Guo, Hydrogen storage materials for mobile and stationary applications: current state of the art. ChemSusChem **8**(17), 2789–2825 (2015)
116. T. Kawada, Fuel cells for efficient use of energy, in *Topical Themes in Energy and Resources* (Springer Japan, Tokyo, 2015), pp. 59–74
117. A. Kraytsberg, Y. Ein-Eli, Review of advanced materials for proton exchange membrane fuel cells. Energy Fuel **28**(12), 7303–7330 (2014)
118. Y. Sone, P. Ekdunge, D. Simonsson, Proton conductivity of Nafion 117 as measured by a four-electrode AC Impedance method. J. Electrochem. Soc. **143**(4), 1254–1259 (1996)
119. J. Yang, G. Goenaga, A. Call, D.J. Liu, Polymer electrolyte fuel cell with vertically aligned carbon nanotubes as the electrocatalyst support. Electrochem. Solid-State Lett. **13**(6), B55–B57 (2010)
120. J. Yang, D.J. Liu, N.N. Kariuki, L.X. Chen, Aligned carbon nanotubes with built-in FeN_4 active sites for electrocatalytic reduction of oxygen. Chem. Commun. **3**, 329–331 (2008)
121. J. Wu, X.Z. Yuan, J.J. Martin, H. Wang, J. Zhang, J. Shen, W. Merida, A review of PEM fuel cell durability: degradation mechanisms and mitigation strategies. J. Power Sources **184**(1), 104–119 (2008)
122. S.M. Haile, Fuel cell materials and components. Acta Mater. **51**(19), 5981–6000 (2003)
123. V. Kamavaram, V. Veedu, A.M. Kannan, Synthesis and characterization of platinum nanoparticles on in situ grown carbon nanotubes based carbon paper for proton exchange membrane fuel cell cathode. J. Power Sources **188**(1), 51–56 (2009)
124. Y. Yuan, J.A. Smith, G. Goenaga, D.J. Liu, Z. Luo, J. Liu, Platinum decorated aligned carbon nanotubes: electrocatalyst for improved performance of proton exchange membrane fuel cells. J. Power Sources **196**(15), 6160–6167 (2011)
125. J.W. Fergus, Electrolytes for solid oxide fuel cells. J. Power Sources **162**(1), 30–40 (2006)
126. A.B. Stambouli, E. Traversa, Solid oxide fuel cells (SOFCs): a review of an environmentally clean and efficient source of energy. Renew. Sust. Energ. Rev. **6**(5), 433–455 (2002)
127. S.P. Jiang, A comparison of O_2 reduction reactions on porous (La, Sr) MnO_3 and (La, Sr) (Co, Fe) O_3 electrodes. Solid State Ionics **146**(1), 1–22 (2002)
128. Z. Liu, D. Elbert, C.L. Chien, P.C. Searson, FIB/TEM Characterization of the composition and structure of core/shell Cu- Ni nanowires. Nano Lett. **8**(8), 2166–2170 (2008)
129. Y. Matsuzaki, I. Yasuda, Electrochemical properties of reduced-temperature SOFCs with mixed ionic–electronic conductors in electrodes and/or interlayers. Solid State Ionics **152**, 463–468 (2002)
130. J. Liu, A.C. Co, S. Paulson, V.I. Birss, Oxygen reduction at sol–gel derived $La_{0.8}$ $Sr_{0.2}$ $Co_{0.8}$ $Fe_{0.2}$ O_3 cathodes. Solid State Ionics **177**(3), 377–387 (2006)
131. B.C. Chan, The state of the art of electric, hybrid, and fuel cell vehicles. Proc. IEEE **95**(4), 704–718 (2007)
132. S. Barrett, A. Stubley, GM, Chrysler unveil luxury concept FCVs. Fuel Cells Bulletin 2-3 (2008)
133. J.M. Andújar, F. Segura, Fuel cells: history and updating. Awalk along two centuries. Renew. Sust. Energ. Rev. 13(9), 2309–2322 (2009)
134. Y. Gao, M. Ehsani, Systematic design of fuel cell powered hybrid vehicle drive train, in *Electric Machines and Drives Conference, 2001. IEMDC 2001* (IEEE International, 2001), pp. 604–611.
135. T. Ozeki, M. Umeyama, Development of TOYOTA's transaxle for mini-van hybrid vehicles (No. 2002-01-0931). SAE Technical Paper (2002)
136. Z.S. Whiteman, P. Bubna, A.K. Prasad, B.A. Ogunnaike, Design, operation, control, and economics of a photovoltaic/fuel cell/battery hybrid renewable energy system for automotive applications. Processes **3**(2), 452–470 (2015)

137. R.K. Dixon, The U.S. Hydrogen program (2003), http://unfccc.int/files/meetings/cop_10/in_session_workshops/mitigation/application/pdf/041209dixon-us_hydrogen_program.pdf
138. L.J. Murray, M. Dinca, J.R. Long, Hydrogen storage in metal–organic frameworks. Chem. Soc. Rev. **38**(5), 1294–1314 (2009)
139. P.A. Daly, J. Morrison, Understanding the potential benefits of distributed generation on power delivery systems, in *Rural Electric Power Conference* (IEEE, 2001), p. A2-1
140. R.H. Wolk, Fuel cells for homes and hospitals. Spectrum, IEEE **36**(5), 45–52 (1999)
141. M.F. Mathias, R. Makharia, H.A. Gasteiger, J.J. Conley, T.J. Fuller, C.J. Gittleman, S.G. Van, Two fuel cell cars in every garage. Electrochem. Soc. Interface **14**(3), 24–35 (2005)
142. IPCC, Global greenhouse gas emissions data (2014), https://www3.epa.gov/climatechange/ghgemissions/global.html. Accessed Apr 2016
143. J.D. Hamilton, Historical oil shocks (No. w16790). National Bureau of Economic Research. NBER Working Paper No. 16790, 1–51 (2011)
144. S.L. Johnson, D.M. Pekelney, Economic assessment of the regional clean air incentives market: a new emissions trading program for Los Angeles. Land Econ. **72**, 277–297 (1996)
145. G. Collantes, D. Sperling, The origin of California's zero emission vehicle mandate. Transp. Res. A Policy Pract. **42**(10), 1302–1313 (2008)
146. D.J. Griggs, M. Noguer, Climate change 2001: the scientific basis. Contribution of working group I to the third assessment report of the intergovernmental panel on climate change. Weather **57**(8), 267–269 (2002)
147. F.R. Kalhammer, B.M. Kopf, D.H. Swan, V.P. Roan, M.P. Walsh, Status and prospects for zero emissions vehicle technology. Rep. ARB Independ. Expert Panel **1**(1), 12–36 (2007). https://www.google.com/url?sa=t&rct=j&q=&esrc=s&source=web&cd=1&cad=rja&uact=8&ved=0ahUKEwizyJPlJ_MAhVBw2MKHVHlCccQFggcMAA&url=http%3A%2F%2Fwww.arb.ca.gov%2Fmsprog%2Fzevprog%2Fzevreview%2Fzev_pael_report.pdf&usg=AFQjCNHSHkTIpV2oHH9CbYvQEQjkwx4y5Q&bvm=bv.119967911,d.cGc. Accessed Apr 2016
148. J. Cobb, July 2015 dashboard (HybridCars.com and Baum & Associates, 2015). Accessed Apr 2016
149. M. Ni, D.Y. Leung, M.K. Leung, K. Sumathy, An overview of hydrogen production from biomass. Fuel Process. Technol. **87**(5), 461–472 (2006)
150. E.S. Rubin, H. Mantripragada, A. Marks, P. Versteeg, J. Kitchin, The outlook for improved carbon capture technology. Prog. Energy Combust. Sci. **38**(5), 630–671 (2012)
151. C.C. Black Jr., Photosynthetic carbon fixation in relation to net CO_2 uptake. Annu. Rev. Plant Physiol. **24**(1), 253–286 (1973)
152. A.G. Condon, R.A. Richards, G.J. Rebetzke, G.D. Farquhar, Improving intrinsic water-use efficiency and crop yield. Crop Sci. **42**(1), 122–131 (2002)
153. B. Glaser, J. Lehmann, W. Zech, Ameliorating physical and chemical properties of highly weathered soils in the tropics with charcoal–a review. Biol. Fertil. Soils **35**(4), 219–230 (2002)
154. S. Steinbeiss, G. Gleixner, M. Antonietti, Effect of biochar amendment on soil carbon balance and soil microbial activity. Soil Biol. Biochem. **41**(6), 1301–1310 (2009)
155. A. Grübler, M. Jefferson, N. Nakicenovic, Global energy perspectives: a summary of the joint study by the International Institute for Applied Systems Analysis and World Energy Council. Technol. Forecast. Soc. Chang. **51**(3), 237–264 (1996)
156. C. Azar, K. Lindgren, B.A. Andersson, Global energy scenarios meeting stringent CO_2 constraints – cost-effective fuel choices in the transportation sector. Energy Policy **31**(10), 961–976 (2003)
157. I. Dincer, M.A. Rosen, A worldwide perspective on energy, environment and sustainable development. Int. J. Energy Res. **22**(15), 1305–1321 (1998)
158. G. Fischer, L. Schrattenholzer, Global bioenergy potentials through 2050. Biomass Bioenergy **20**(3), 151–159 (2001)
159. J. Staniforth, K. Kendall, Biogas powering a small tubular solid oxide fuel cell. J. Power Sources **71**(1), 275–277 (1998)

160. J. Xuan, M.K. Leung, D.Y. Leung, M. Ni, A review of biomass-derived fuel processors for fuel cell systems. Renew. Sust. Energ. Rev. **13**(6), 1301–1313 (2009)
161. U. Bossel, B. Eliasson, G. Taylor, The future of the hydrogen economy: bright or bleak? Cogen. Distrib. Gen. J. **18**(3), 29–70 (2003)
162. R.D. Cortright, R.R. Davda, J.A. Dumesic, Hydrogen from catalytic reforming of biomass-derived hydrocarbons in liquid water. Nature **418**(6901), 964–967 (2002)
163. J.R. Hess, C.T. Wright, K.L. Kenney, Cellulosic biomass feedstocks and logistics for ethanol production. Biofuels Bioprod. Biorefin. **1**(3), 181–190 (2007)
164. M. Hadj-Kali, V. Gerbaud, J.M. Borgard, P. Floquet, X. Joulia, P. Carles, Thermodynamic modeling of HIx part of the Iodine–Sulfur thermocycle. AIChE Annual Meeting, 4 - 9 Nov 2007, Salt Lake City - Utah - USA (2007). http://72.3.180.220/Conferences/Past/Annual07.aspx
165. T. Nakamura, Hydrogen production from water utilizing solar heat at high temperatures. Sol. Energy **19**(5), 467–475 (1977)
166. S. Fujiwara, S. Kasai, H. Yamauchi, K. Yamada, S. Makino, K. Matsunaga, E. Hoashi, Hydrogen production by high temperature electrolysis with nuclear reactor. Prog. Nucl. Energy **50**(2), 422–426 (2008)
167. W. Doenitz, R. Schmidberger, E. Steinheil, R. Streicher, Hydrogen production by high temperature electrolysis of water vapour. Int. J. Hydrog. Energy **5**(1), 55–63 (1980)
168. B. Yildiz, M.S. Kazimi, Efficiency of hydrogen production systems using alternative nuclear energy technologies. Int. J. Hydrog. Energy **31**(1), 77–92 (2006)
169. J. De Vries, The industrial revolution and the industrious revolution. J. Econ. Hist. **54**(02), 249–270 (1994)
170. N.L. Stokey, A quantitative model of the British industrial revolution, 1780–1850, in *Carnegie-Rochester Conference Series on Public Policy*, vol. 55(1) (North-Holland, 2001), pp. 55–109
171. R. Fox, A. Guagnini, Laboratories, workshops, and sites. Concepts and practices of research in industrial Europe, 1800–1914 (concluded). Hist. Stud. Phys. Biol. Sci. **29**(2), 191–294 (1999)
172. R.M. MacLeod, The Alkali Acts Administration, 1863–84: the emergence of the civil scientist. Vic. Stud. **9**(2), 85–112 (1965)
173. M.L. Bell, D.L. Davis, T. Fletcher, A retrospective assessment of mortality from the London smog episode of 1952: the role of influenza and pollution. Environ. Health Perspect. **112**(1), 6 (2004)
174. Kyoto Protocol, United Nations framework convention on climate change. Kyoto Protocol, Kyoto, 19 (1997)
175. N. Grunewald, I. Martinez-Zarzoso, Did the Kyoto Protocol fail? An evaluation of the effect of the Kyoto Protocol on CO_2 emissions. Environ. Dev. Econ. **21**(01), 1–22 (2016)
176. R. Lal, Beyond COP 21: potential and challenges of the "4 per Thousand" initiative. J. Soil Water Conserv. **71**(1), 20A–25A (2016)
177. C. Change, Intergovernmental Panel on Climate Change. World Meteorological Organization. (2007). http://ipcc.ch/meetings/session19/final-report.pdf
178. A. Valadkhani, I. Roshdi, R. Smyth, How successful was Kyoto? A multiplicative environmental DEA approach to measure efficiency changes in the world's major polluters. Energy Econ. (2016). doi:10.1016/j.eneco.2015.12.018
179. L.F. Truett, *Literature Review for the Baseline Knowledge Assessment of the Hydrogen, Fuel Cells, and Infrastructure Technologies Program (No. ORNL/TM-2003/258)* (ORNL, 2003)
180. A. Sun, R. Davis, M. Starbuck, A. Ben-Amotz, R. Pate, P.T. Pienkos, Comparative cost analysis of algal oil production for biofuels. Energy **36**(8), 5169–5179 (2011)
181. M. Betsill, N.K. Dubash, M. Paterson, H. van Asselt, A. Vihma, H. Winkler, Building productive links between the UNFCCC and the broader global climate governance landscape. Global Environ. Polit. **15**, 1–10 (2015)
182. K. Blok, R.H. Williams, R.E. Katofsky, C.A. Hendriks, Hydrogen production from natural gas, sequestration of recovered CO_2 in depleted gas wells and enhanced natural gas recovery. Energy **22**(2), 161–168 (1997)

183. H.F. Abbas, W.W. Daud, Hydrogen production by methane decomposition: a review. Int. J. Hydrog. Energy **35**(3), 1160–1190 (2010)
184. C. Koroneos, A. Dompros, G. Roumbas, N. Moussiopoulos, Life cycle assessment of hydrogen fuel production processes. Int. J. Hydrog. Energy **29**(14), 1443–1450 (2004)
185. S. Shafiee, E. Topal, When will fossil fuel reserves be diminished? Energy Policy **37**(1), 181–189 (2009)
186. J.D. Holladay, J. Hu, D.L. King, Y. Wang, An overview of hydrogen production technologies. Catal. Today **139**(4), 244–260 (2009)
187. R. Kemp, Technology and the transition to environmental sustainability: the problem of technological regime shifts. Futures **26**(10), 1023–1046 (1994)
188. E. Porpatham, A. Ramesh, B. Nagalingam, Investigation on the effect of concentration of methane in biogas when used as a fuel for a spark ignition engine. Fuel **87**(8), 1651–1659 (2008)
189. S. Zaitlin, Landfill: gas to energy. Maine Policy Rev. **17**(2), 105–106 (2008)
190. T.S. Collett, Energy resource potential of natural gas hydrates. AAPG Bull. **86**(11), 1971–1992 (2002)
191. D. Cao, Y. Sun, G. Wang, Direct carbon fuel cell: fundamentals and recent developments. J. Power Sources **167**(2), 250–257 (2007)
192. X. Li, Z.H. Zhu, R.D. Marco, A. Dicks, J. Bradley, S. Liu, G.Q. Lu, Factors that determine the performance of carbon fuels in the direct carbon fuel cell. Ind. Eng. Chem. Res. **47**(23), 9670–9677 (2008)
193. L. Carrette, K.A. Friedrich, U. Stimming, Fuel cells: principles, types, fuels, and applications. ChemPhysChem **1**(4), 162–193 (2000)
194. B.C. Steele, A. Heinzel, Materials for fuel-cell technologies. Nature **414**(6861), 345–352 (2001)
195. S. Freni, G. Calogero, S. Cavallaro, Hydrogen production from methane through catalytic partial oxidation reactions. J. Power Sources **87**(1), 28–38 (2000)
196. N.J. Cherepy, R. Krueger, K.J. Fiet, A.F. Jankowski, J.F. Cooper, Direct conversion of carbon fuels in a molten carbonate fuel cell. J. Electrochem. Soc. **152**(1), A80–A87 (2005)
197. X. Li, Z. Zhu, J. Chen, R. De Marco, A. Dicks, J. Bradley, G. Lu, Surface modification of carbon fuels for direct carbon fuel cells. J. Power Sources **186**(1), 1–9 (2009)
198. A. Hermann, T. Chaudhuri, P. Spagnol, Bipolar plates for PEM fuel cells: a review. Int. J. Hydrog. Energy **30**(12), 1297–1302 (2005)
199. D. Haeseldonckx, W. D'haeseleer, The use of the natural-gas pipeline infrastructure for hydrogen transport in a changing market structure. Int. J. Hydrog. Energy **32**(10), 1381–1386 (2007)
200. J. Weitkamp, M. Fritz, S. Ernst, Zeolites as media for hydrogen storage. Int. J. Hydrog. Energy **20**(12), 967–970 (1995)
201. J.J. Reilly, G.D. Sandrock, Hydrogen storage in metal hydrides. Sci. Am. (United States) **242** (2) (1980)
202. M.C. Williams, J.P. Strakey, W.A. Surdoval, The US department of energy, office of fossil energy stationary fuel cell program. J. Power Sources **143**(1), 191–196 (2005)
203. J. Sinha, Y. Yang, *Direct Hydrogen PEMFC Manufacturing Cost Estimation for Automotive Applications* (2010 DOE Annual Merit Review, Washington, DC, 2010)
204. N. Demirdöven, J. Deutch, Hybrid cars now, fuel cell cars later. Science **305**(5686), 974–976 (2004)
205. H.P. Chang, C.L. Chou, Y.S. Chen, T.I. Hou, B.J. Weng, The design and cost analysis of a portable PEMFC UPS system. Int. J. Hydrog. Energy **32**(3), 316–322 (2007)
206. J. Zhang, Z. Xie, J. Zhang, Y. Tang, C. Song, T. Navessin, Z.S. Liu, High temperature PEM fuel cells. J. Power Sources **160**(2), 872–891 (2006)
207. B.P. Vinayan, R. Nagar, N. Rajalakshmi, S. Ramaprabhu, Novel platinum–cobalt alloy nanoparticles dispersed on nitrogen-doped graphene as a cathode electrocatalyst for PEMFC applications. Adv. Funct. Mater. **22**(16), 3519–3526 (2012)

208. H. Zhong, X. Chen, H. Zhang, M. Wang, S.S. Mao, Proton exchange membrane fuel cells with chromium nitride nanocrystals as electrocatalysts. Appl. Phys. Lett. **91**(16), 163103 (2007)
209. A.F. Ghenciu, Review of fuel processing catalysts for hydrogen production in PEM fuel cell systems. Curr. Opinion Solid State Mater. Sci. **6**(5), 389–399 (2002)
210. M. Voldsund, K. Jordal, R. Anantharaman, Hydrogen production with CO_2 capture. Int. J. Hydrog. Energy **41**(9), 4969–4992 (2016)
211. S. Czernik, A.V. Bridgwater, Overview of applications of biomass fast pyrolysis oil. Energy Fuel **18**(2), 590–598 (2004)
212. H. Chen, P. Pei, M. Song, Lifetime prediction and the economic lifetime of Proton Exchange Membrane fuel cells. Appl. Energy **142**, 154–163 (2015)
213. A.A.A. Agll, T.A. Hamad, Y.M. Hamad, S.G. Bapat, J.W. Sheffield, Development of design a drop-in hydrogen fueling station to support the early market buildout of hydrogen infrastructure. Int. J. Hydrog. Energy **41**(10), 5284–5295 (2016)
214. D. Sanfilippo, One-step hydrogen through water splitting with intrinsic CO_2 capture in chemical looping. Catalysis Today x-1-11 (2016). doi:10.1016/j.cattod.2016.02.0210920-5861
215. S. Schiebahn, T. Grube, M. Robinius, V. Tietze, B. Kumar, D. Stolten, Power to gas: technological overview, systems analysis and economic assessment for a case study in Germany. Int. J. Hydrog. Energy **40**(12), 4285–4294 (2015)

Conclusion

This book discussed various energy technologies related to hydrogen production and storage. It also outlined a look at the infrastructure, usage, and monetary aspects of an economy based upon hydrogen.

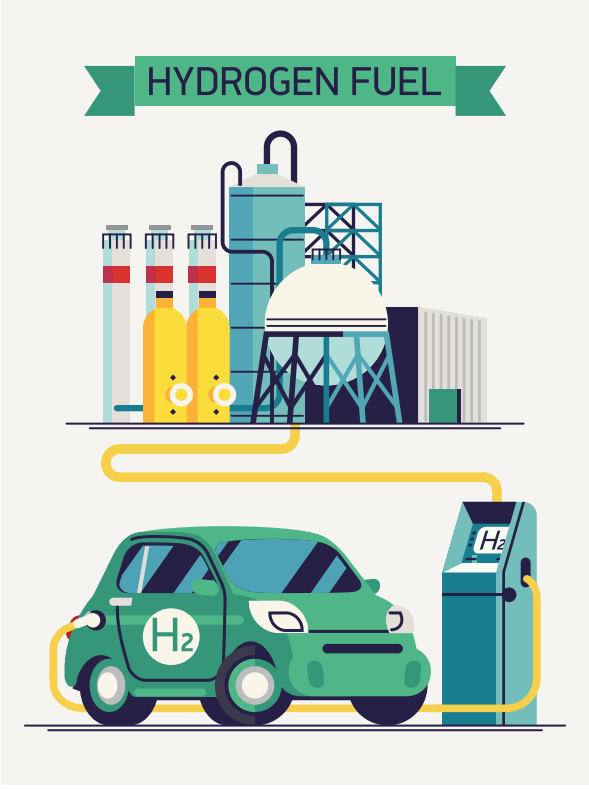

Y.-P. Chen et al. (eds.), *Nanostructured Materials for Next-Generation Energy Storage and Conversion*, DOI 10.1007/978-3-662-53514-1

Index

Y.-P. Chen et al. (eds.), *Nanostructured Materials for Next-Generation Energy Storage and Conversion*, DOI 10.1007/978-3-662-53514-1